



Whittier
College

Jordan C. Hanson

Jordan C. Hanson
Assistant Professor
Department of Physics and Astronomy
13406 East Philadelphia Street
Whittier CA 90602
Email: jhanson2@whittier.edu

July 1, 2022

Cover Letter: Application for Tenure

Greetings,

My name is Prof. Jordan C. Hanson, and I am currently an Assistant Professor in the Department of Physics and Astronomy at Whittier College. We are contacting you for your consideration as an external reviewer for our tenure and promotion process at Whittier College. This dossier contains my curriculum vitae, tenure and promotion guidelines, and my recent scholarship. Whittier College is a 130-year-old liberal arts college in Whittier, California, near East Los Angeles. We are recognized as a Title-V Hispanic Serving Institution (HSI) with a mission to provide access to higher education for historically marginalized students.

I have focused my scholarship on three broad areas: advancing the field of ultra-high energy neutrino (UHE- ν) research as part of IceCube Gen2 (<https://wipac.wisc.edu>), RF engineering research through the Office of Naval Research (ONR: <https://www.nre.navy.mil>), and contributions to diversity, equity, and inclusion (DEI). It is important to note that, at Whittier College, we typically teach six courses per year. I make my research contributions while teaching physics, math, and computer science courses. I have found creative ways to deliver a unique and intellectually enriching environment for my students, often by connecting my research and teaching. I regularly involve undergraduate students in my research, and I have published scholarship with undergraduate authors.

Within this dossier, you will find several types of examples of my scholarship. These are primarily peer-reviewed journal articles in the UHE- ν and RF engineering areas, but also include *applied* scholarship produced with undergraduates. I provide descriptions of how the applied science or engineering concept connects to our mission at Whittier College, the ONR, and IceCube Gen2. The UHE- ν and RF engineering research for the ONR is categorized into five areas: computational electromagnetism (CEM), the Askaryan effect, RF antenna design and fabrication, Antarctic ice properties, and drones. The ONR research also adds workforce development in the form of interactive engineering courses.

Finally, I have included three examples of DEI contributions. First, I highlight my participation in the Artemis program, a STEM recruitment and research program for young women from local high schools. The second describes an DEI grant I have earned to develop a mobile application that will help foster inclusion and belonging in introductory STEM courses. The third is an example of my participation in the Whittier Scholars Program (WSP: <https://scholars.domains/>). This program allows students to customize a major within our curriculum, and the interdisciplinary results tend to diversify scholarship within fields by forming new connections.

I am grateful for your consideration, and we at Whittier College want to thank you for taking the time to read and process this dossier.

Sincerely,

Jordan C. Hanson

Jordan C. Hanson, PhD

Science and Learning Center, 212 • Dept. of Physics and Astronomy, Whittier College • Whittier, CA, 90602

• Office: 562-907-5130 • Mobile: 562-351-0047 • email: jhanson2@whittier.edu*Member of the IceCube Gen2 Collaboration**Summer Faculty Research Fellow for the Office of Naval Research**Recipient of the CCAPP Post-doctoral fellowship at The Ohio State University*

Position	Assistant Professor of Physics, Department of Physics and Astronomy, Whittier College, 2017-Present
Skills	<i>Extensive experience in high-energy physics research, engineering research, physics education, mentorship, and committee service at Whittier College.</i> <ul style="list-style-type: none">• Physics instruction at high-school, college, and graduate levels: introductory and advanced level• Computer science teaching: digital signal processing, digital circuit design at college level• Mathematics teaching: elementary statistics at college level, developed the first summer online statistics program in Whittier College history• Computational Electromagnetism (CEM) research in RF antenna and phased array design for IceCube Gen2 and the Office of Naval Research (Whittier College)• Workforce development and reliability analysis for the Office of Naval Research (Whittier College)• Terabyte-scale data analysis and high-performance computing (Ohio State Univ. and UC Irvine)• Building simulations and mathematical physics models (Ohio State Univ. and Whittier College)• Organizing and leading expeditions to Antarctica to deploy physics hardware (UC Irvine)• Performing radio-frequency field measurements and anechoic chamber measurements in support of physics objectives (UC Irvine, Univ. of Kansas)• RF circuit design and testing/validation (UC Irvine, Univ. of Kansas)• Created the RF design lab at Whittier College; extensive experience in RF test bench equipment, e.g. oscilloscopes, vector network analyzers/spectrum analyzers, power meters, and signal generators (UC Irvine, Univ. of Kansas, OSU, Whittier College)• Software skill: C++, Python, MATLAB, Octave, Jupyter, MEEP, WaveDROM, LaTeX• Organizing workshops and conferences, public speaking, outreach coordination• Organizing and operating STEM recruitment and research programs for young women from local high school students interested in studying STEM at Whittier College• Recipient of DEI grant for application development to foster inclusion in introductory STEM courses• Studying DEI in introductory STEM through Cottrell Scholars Network
Education	<ul style="list-style-type: none">• Doctor of Philosophy (PhD), Physics, University of California, Irvine (March 2013)• Master of Science (M.S), Physics, University of California, Irvine (August 2008)• Bachelor of Science (B.S), Intensive Track, in Physics, Yale University (June 2007)
Research Experience	<u>Whittier College</u> Fall 2017 – Present <ul style="list-style-type: none">• Initiated a radio-frequency (RF) testing and design laboratory• Awarded three Summer Faculty Research Fellowships through the Office of Naval Research• Mentoring students in firmware and software design, electrical engineering• Mentoring students in mathematical physics research, publication on Askaryan radiation• Helped a student create a firmware/software solution in order to upgrade ARIANNA detector boards• Helped a student build a from-scratch drone, with designs for solar recharge and polar deployment• Published research regarding RF propagation in polar ice and firn, interactions with ice/ocean floor• Published mathematical physics model of Askaryan radiation with undergraduate researcher• Developed a python-based FDTD model of broadband RF phased arrays for Navy radar testing with two undergraduate researchers• Participated in workshop series entitled “Inclusivity in Introductory STEM Courses” through the Cottrell Scholars Network, research focusing on methodology for boosting inclusion and belonging in Introductory STEM courses for marginalized students• Received Whittier College DEI grant for application development to boost inclusion in introductory STEM courses

- Created a fully analytic model of the Askaryan effect adopted by the physics community
- Leading the data analysis to discover the world-record highest energy neutrinos
- Organized a workshop at Ohio State pertaining to improved analysis efficiency and machine learning
- Investigating ways to use smartphones as cosmic ray detection arrays

University of Kansas

Spring 2013 – Fall 2015

- Simulated radar-echoes of cosmic ray extensive air showers for the TARA collaboration
- Deployed radar detectors as part of the TARA remote station program
- Performed anechoic chamber measurements to calibrate the ARIANNA and TARA detectors
- Gained teaching and mentoring experience through the QuarkNet program
- Created and taught a summer physics course

University of California, Irvine

Summer 2007 - Spring 2013

- Designed, constructed, tested, and deployed the first ARIANNA neutrino detector in Antarctica
- Led the analysis of the first data collected by ARIANNA stations, constraining the ultra-high energy cosmogenic neutrino flux
- Independently organized and led expeditions to Antarctica to perform glaciological measurements in support of physics objectives
- Ran high-performance computing (HPC) codes, using machine learning, to train software to distinguish low-SNR impulses from RF thermal noise

Yale University

Summer 2006

- Performed Monte Carlo calculations of the interaction length of relativistic electrons in super-fluid helium in support of the XENON dark-matter detector innovation
- Designed a laser-scanning system to reveal helium molecules in superfluid helium

Los Alamos National Laboratory

Summer 2005

- Measured the muon Cherenkov tank event-rates over an altitude range of 0-14,000 ft. from the base to the summit of Mt. Evans, in Colorado, as part of the Milagro collaboration (now High Altitude Water Cherenkov detector)
- Compared results to cosmic-ray theory and presented at Milagro collaboration meeting

References

- Amy Connolly, PhD ... Prof. of Physics, The Ohio State University
- Steven Barwick, PhD ... Prof. of Physics, University of California, Irvine
- Dave Besson, PhD ... Prof. of Physics, University of Kansas
- Albrecht Karle, PhD ... Prof. of Physics, University of Wisconsin
- Gary Yeakley ... Retired Engineer at the Naval Surface Warfare Center, Corona, CA
- Jeffery Benson... Engineer at the Naval Surface Warfare Center, Corona, CA
- Allan Halgren, PhD ... Professor of Physics at Uppsala University, Uppsala, Sweden
- Stephanie Wissel, PhD ... Professor of Physics at Pennsylvania State University, State College, PA

Published Papers

*Primary or Corresponding author

- *J.C. Hanson and R. Hartig “Complex Analysis of Askaryan Radiation: A Fully Analytic Model in the Time-Domain” *Physical Review D*, **105** 123019 (2022).
- The RNO-G Collaboration “In situ, broadband measurement of the radio frequency attenuation length at Summit Station, Greenland” arXiv:2201.07846 (2022). *Accepted for publication in the Journal of Glaciology.*
- *J.C. Hanson “Broadband RF Phased Array Design with MEEP: Comparisons to Array Theory in Two and Three Dimensions” *Electronics Journal (MDPI)* **10** 4 (2021). *Acknowledged by editor as one of the top 10 papers in Electronics Journal for Dec. 2020 to May. 2021.*
- *J.C. Hanson “Broadband RF Phased Array Design for UHE neutrino detection.” Proceedings of 37th International Cosmic Ray Conference, Berlin, Germany (2021).
- The RNO-G Collaboration “Design and sensitivity of the Radio Neutrino Observatory in Greenland (RNO-G)” *Journal of Instrumentation* **16** P03025 (2021).
- The ARIANNA Collaboration. “Probing the Angular and Polarization Reconstruction of the ARI-

- ANNA Detector at the South Pole.” Journal of Instrumentation (JINST) **15** (2020) p. 09039
- C. Glaser *et al* “NuRadioMC: simulating the radio emission of neutrinos from interaction to detector.” European Physical Journal C (**80**) n. 77 (2020).
- The ARIANNA Collaboration. “White Paper: ARIANNA-200 high energy neutrino telescope.” arXiv:2004.09841
- The ARIANNA Collaboration. “Neutrino Vertex Reconstruction with In-Ice Radio Detectors using Surface Reflections and Implications for the Neutrino Energy Resolution.” Journal of Cosmology and Astroparticle Physics (JCAP) **11** (2019) p. 030
- The ARIANNA Collaboration. “A Search for Cosmogenic Neutrinos with the ARIANNA Test-Bed using 4.5 Years of Data.” Journal of Cosmology and Astroparticle Physics (JCAP) **03** (2020) p. 053
- *J.C. Hanson et al. “Observation of classically ‘forbidden’ electromagnetic wave propagation and implications for neutrino detection.” Journal of Cosmology and Astroparticle Physics. (**2018**) (2018)
- P. Allison et al. “Measurement of the real dielectric permittivity ϵ_r of glacial ice.” Astroparticle Physics Journal **108** (2019) pp. 63-73
- *J.C. Hanson and A. Connolly. “Complex Analysis of Askaryan Radiation: A Fully Analytic Treatment including the LPM effect and Cascade Form Factor.” Astroparticle Physics. (**91**) pp. 75-89 (2017).
- The ARIANNA Collaboration. “Radio detection of air showers with the ARIANNA experiment on the Ross Ice Shelf”, Astroparticle Physics (**90**) pp. 50-68 (2017).
- The TARA Collaboration. “First Upper Limits on the Radar Cross Section of Cosmic-Ray Induced Extensive Air Showers”, Astroparticle Physics (**87**) pp. 1-17 (2017).
- The ARIANNA Collaboration. “Live-time and sensitivity of the ARIANNA Hexagonal Radio Array.” Proceedings of the International Cosmic-Ray Conference 2015, The Hague, The Netherlands (2015).
- The ARIANNA Collaboration. “Performance of the ARIANNA Hexagonal Radio Array.” Proceedings of the International Cosmic-Ray Conference 2015, The Hague, The Netherlands (2015).
- The ARIANNA Collaboration. “A First Search for Cosmogenic Neutrinos with the ARIANNA Hexagonal Radio Array.” Astroparticle Physics Journal (70) pp. 12-36 (2015)
- *J.C. Hanson et al. “Time-Domain Response of the ARIANNA Detector.” Astroparticle Physics Journal (62) pp. 139-151 (2015).
- *J.C. Hanson et al. “Radar absorption, basal reflection, thickness and polarization measurements from the Ross Ice Shelf, Antarctica.” Journal of Glaciology (**61**) 227, pp. 438-446(9) (2015)
- The ARIANNA Collaboration. “Design and Performance of the ARIANNA HRA-3 Neutrino Detector Systems.” IEEE Transactions on Nuclear Science (**62**) 5 pp. 2202-2215 (2015).
- The TARA Collaboration. “Telescope Array Radar (TARA) observatory for Ultra-High Energy Cosmic Rays.” Nuclear Instrumentation and Methods in Physics Research, A (**767**) 322-338 (2014).
- S. Kleinfelder et al. “Design and Performance of the Autonomous Data Acquisition System for the ARIANNA High Energy Neutrino Detector.” IEEE Transactions on Nuclear Science (**60**) 2, 612-618 (2013).
- *J.C. Hanson, for the ARIANNA Collaboration. “Ross Ice Shelf Thickness, Radio-Frequency Attenuation and Reflectivity: Implications for the ARIANNA UHE Neutrino Detector”. Proceedings of the 32nd International Cosmic Ray Conference, Beijing, China (2011).
- L. Gerhardt, S.R. Klein, T. Stezelberger, S.W. Barwick, K. Dookayka, J.C. Hanson, R. Nichol. “A prototype station for ARIANNA: A detector for cosmic neutrinos.” Nuclear Instrumentation and Methods in Physics Research, A (**634**) 85-91, (2010).
- W.G. Rellergert, S.B. Cahn, A. Garvan, J.C. Hanson, W.H. Lippincott, J.A. Nikkel, and D.N. McKinsey. “Detection and Imaging of He₂ Molecules in Superfluid Helium.” Physical Review Letters (**100**) 025301 (2008).

Invited Lectures

- Invited to teach source entitled “Introduction to GPS Signals for Onboarding of Navy Personnel” (2022). *In service of the Office of Naval Research.*
- Invited to teach source entitled “RF Field Engineering: A practical introduction” (2021). *In service of the Office of Naval Research.*
- “IceCube-Gen2 Radio Array Surface Calibration: Opportunities from Unique Transmitter and Receiver Systems” (2021). *IceCube Generation 2 Calibration Workshop.*
- “Finite Difference Time-Domain Methods for Askaryan Propagation Modeling in IceCube-Gen2” (2021). *IceCube Generation 2 Calibration Workshop.*
- “Classically Forbidden Askaryan Radiation: A decade of exploration in Antarctica in the search for

- cosmic neutrinos” (2018) *Departmental Colloquium for Whittier College*
- “Ultra-high Energy Neutrinos, Antarctica, Greenland, and the Askaryan Effect: A Summary.” (2016) *Invited speaker for the particle physics seminars at Weizmann Institute, Rehovot, Israel, and at Technion University, Haifa, Israel.*
- “Ultra-high Energy Neutrinos, Antarctica, Greenland, and the Askaryan Effect: A Summary.” (2016) *Invited speaker to the TeV Particle Astrophysics (TeVPA) conference at CERN, Geneva, Switzerland.*
- “A Review of UHE neutrino detection using the Askaryan effect.” (2016) *Invited speaker to the Very High Energy particle Astrophysics (VHEPA) conference at the University of Hawaii, Honolulu, Hawaii.*
- “A Review of UHE neutrino detection using the Askaryan effect.” (2016) *Invited speaker to the KICP Workshop, UHEAP 2016, University of Chicago, Chicago, IL.*
- “A Review of UHE neutrino detection using the Askaryan effect.” (2015) *Invited speaker to the KICP Workshop on the Giant Radio Array for Neutrino Detection, University of Chicago, Chicago, IL.*
- “Future Prospects of UHE neutrino detection with Electromagnetic Fields.” (2014) *Invited speaker to the Very High Energy particle Astrophysics (VHEPA) conference at the University of Tokyo (Kashiwa), Kashiwa, Japan.*
- “Searching for Cosmic Rays with the Telescope Array Radar Experiment.” (2014) *Department colloquium at the University of Kansas.*
- “Ultra-high Energy Neutrino Detection in Antarctica with ARIANNA and ARA.” (2013) *Invited seminar in High Energy Physics at the University of Wichita.*
- “Under-water and Under-Ice Neutrino Astronomy.” (2013) *Invited speaker to the 14th ICATPP Conference on Astroparticle, Particle, Space Physics and Detectors for Physics Applications, Villa Olmo, Como, Italy.*
- “Developing the Next Generation of UHE Neutrino Detectors in Antarctica.” (2012) *Seminar in High Energy Physics at the University of Kansas.*

Service

- **Whittier College Committees:**
 - Enrollment and Student Affairs Committee (ESAC), 2018-2020
 - Educational Resources and Digital Liberal Arts Committee (ERC/DLAC), 2020-2021.
 - Educational Policy Committee (EPC), 2021-present
 - Appointed to Whittier Scholars Program Advisory Board, present
 - Artemis Program: STEM recruitment and training for young women in local area high schools
- **Service to the Navy:**
 - Creating online course for engineers in the Navy tasked with maintaining radar and RF infrastructure (2021-present)
- **Whittier College Awards:**
 - Student Life Award for Outstanding Organization Adviser, CRU (Campus Crusade Christian Fellowship), 2018
- Public Panels and Lectures:
 - The Artemis Program: Introducing high-school aged women to physics research at Whittier College 2019-2020 and 2020-2021.
 - “Hunting for Wild Antarctic Astroparticles.” Los Nietos Middle School, Los Nietos, CA (2018)
 - “Our Home.” (2016) *Upper Arlington Library Summer Astronomy Series.*
 - “Experimental Particle Astrophysics in Antarctica.” (2016) *New Vistas in Astronomy Public Lecture Series, Columbus Astronomical Society. Columbus, OH.*
 - “The Martian.” *Participated in a public question/answer panel following screening of The Martian at The Gateway Independent Theater.*
- Current Volunteer Work
 - Volunteer as a Knight of Columbus, Our Lady of the Miraculous Medal Parish, Montebello, CA (2017-present)
 - Repairing parish buildings and fundraising for parish
 - Volunteer at the Knights of Columbus, St. Matthew the Apostle Parish, Gahanna, OH (2016-2017):
 - Serving food for the homeless at YWCA Women and Family Center
 - Volunteer at Columbus Catholic Diocese Soccer Tournament
 - Volunteer Cook/Dishwasher, St. Matthew’s Parish Annual Fish Fry
 - Volunteer, Ohio State Department of Astronomy Observatory (2015-present) (public observing)

- *Providing and operating a 114-mm Newtonian reflector for public observing*
- Instructor for Young Scholars Program (YSP), Ohio State Department of Physics
- Volunteer at the Knights of Columbus, St. John the Evangelist Parish, Lawrence, Kansas (2013-2015)
 - *Volunteer Cook/Dishwasher, St. John's Parish Annual Fish Fry*
 - *Volunteer Groundskeeper, St. John's Parish*

Tenure and Promotion Guidelines
Physics and Astronomy Department
Whittier College

Teaching

Physics and Astronomy Department expects, in general, all its faculty members to teach the full load of courses, unless some other arrangement is agreed upon, with the approvals of the Dean of Faculty and the department. Faculty members are expected to contribute not only to the physics major program but also to our college's Liberal Education program by developing, designing, and teaching Lib-Ed courses such as Connections 1, Connections 2, and Communications 1.

Physics and Astronomy faculty must strive to establish excellent teaching practices regardless of their year or rank, as evaluated and judged by their students and colleagues.

Advising

Physics and Astronomy faculty are encouraged to mentor students at least once during their probation period. In general, all Physics and Astronomy faculty are expected to share the advising load of the department as equitably as the circumstances would allow.

Service

All our faculty must participate in our campus-wide faculty-governance system by serving on faculty committees. Tenure-track faculty are encouraged, but not required, to participate in the major committees. Post-tenure promotion seeking faculty are expected to serve on at least one of the major faculty committees, such as the Faculty Executive Council (FEC) or the Faculty Personnel Committee (FPC).

Research/Scholarship

For Tenure and/or Promotion to Associate Professor

The tenure-track candidate must strive to be a productive researcher/scholar in accord with the relevant Boyer category of scholarship as outlined and explained in the College Faculty Handbook. The Faculty Personnel Committee (FPC) leaves the extent and nature of the research/scholarship demonstration that is expected of every faculty member who is up for tenure to individual departments.

To this end, the following is the expectations, in tangible terms, of the Department of Physics and Astronomy from its tenure-seeking candidate regarding research/scholarship category.

We expect our tenure-track faculty to establish a sustainable research program on campus — although it can be part of a collaboration with external institutions such as research universities and national research labs — that will enable meaningful and high-quality research to take place in our department. To ensure that that is the case, the following requirements exclude any work completed elsewhere by the faculty member prior to his/her appointment by our department. Having said that, the faculty member can engage in research that is a continuation of his/her prior work, and that, if published, will perfectly count toward satisfying the following criteria.

By the end of his/her probationary period, the tenure candidate shall have created at least 3 externally peer-reviewed products. These can be:

- i- Three scientific journal articles in the main research area of the candidate, or
- ii- Two such articles and one external grant for which the candidate is a major and indispensable contributor.

With the approval and discretion of the department, any one of the following would also be an acceptable demonstration of research/scholarship:

- i- One peer-reviewed scientific journal article and one major external grant in the particular research area of the candidate, and two peer-reviewed articles on pedagogy and physics-education topics.
- ii- Two peer-reviewed scientific journal articles, and two peer-reviewed articles on pedagogy and physics-education topics.

The last two scenarios would thus mix the scholarship of discovery with the scholarship of teaching and integration.

In the same context, we also expect the faculty member to engage students in some form of research or projects outside of regular course work.

For Promotion to Full Professor

Regarding the research/scholarship criterion for tenured members seeking promotion to full professor echelon, the Physics and Astronomy Department hitherto did not have any tangible requirement, with the understanding that FPC would itself assess and judge the work of the faculty member in light of Boyer's four categories of scholarship, giving the faculty member the latitude

of choosing any single one, or a combination of several, of the four categories of Boyer scholarship. Involving students in research/scholarship activities is also highly encouraged.

Dossier Research Documents, by Title and Category

Jordan C. Hanson, PhD
Assistant Professor of Physics and Computer Science
Department of Physics and Astronomy, Whittier College

In the tables below, I have provided a list of scholarly works for your consideration. I have indicated **in bold** which ones are included in this dossier. All works **included in bold** in this dossier represent work in which I was the corresponding or primary author, or for which I was a major contributor. If a work is given in *italics*, this indicates that I served as an internal collaboration reviewer for the work.

Internal collaboration reviewers perform a task similar to anonymous reviewers for journal publications, except that we are members of the collaboration publishing the article. Internal collaboration reviewers are tasked with improving the logic and polishing the text of articles. In large physics collaborations, article manuscripts are sent from the collaboration to the journal editor for anonymous peer-review after passing internal review.

These tables go beyond the works listed in the C.V., because applied and DEI research are also included. Since these items represent projects I started on my own, they are all included **in bold**, and evidence of their progress is included in the dossier. If a work is not listed **in bold** or *in italics*, it is not included in the dossier. Such listings represent articles or works where my ideas were used, or for which I made a contribution, but was not the main contributor.

Document Title (Research Papers)	Journal	Category
Complex Analysis of Askaryan Radiation: A Fully Analytic Model in the Time-Domain	Physical Review D	The Askaryan Effect, neutrino physics and IceCube Gen2
<i>In situ, broadband measurement of the radio frequency attenuation length at Summit Station, Greenland</i>	<i>Accepted for publication in the Journal of Glaciology</i>	Antarctic and Greenlandic ice properties
Broadband RF Phased Array Design with MEEP: Comparisons to Array Theory in Two and Three Dimensions (This article won Top 10 Most Notable Articles in Electronics Journal from Dec 2020 – May 2021).	Electronics Journal	Computational Electromagnetism, RF antenna design and fabrication
Broadband RF Phased Array Design for UHE neutrino detection	Proceedings of 37th ICRC	Computational Electromagnetism, RF antenna design and fabrication
Design and sensitivity of the Radio Neutrino Observatory in Greenland (RNO-G)	Journal of Instrumentation	Neutrino physics, drones
Probing the Angular and Polarization Reconstruction of the ARIANNA Detector at the South Pole	Journal of Instrumentation	Neutrino physics, Antarctic ice properties
NuRadioMC: simulating the radio emission of neutrinos from interaction to detector	European Physical Journal C	The Askaryan effect, Antarctic ice properties
White Paper: ARIANNA-200 high energy neutrino telescope.	The arXiv: arXiv:2004.09841	The Askaryan effect, Antarctic ice properties
Neutrino Vertex Reconstruction with In-Ice Radio Detectors using Surface Reflections and Implications for the Neutrino Energy Resolution	Journal of Cosmology and Astroparticle Physics	Antarctic ice properties, the Askaryan effect
<i>A Search for Cosmogenic Neutrinos with the ARIANNA Test-Bed using 4.5 Years of Data</i>	<i>Journal of Cosmology and Astroparticle Physics</i>	Neutrino physics, the Askaryan effect, Antarctic ice properties

Observation of classically ‘forbidden’ electromagnetic wave propagation and implications for neutrino detection	Journal of Cosmology and Astroparticle Physics	Antarctic ice properties
Measurement of the real dielectric permittivity of glacial ice	Astroparticle Physics Journal	Antarctic ice properties
Complex Analysis of Askaryan Radiation: A Fully Analytic Treatment including the LPM effect and Cascade Form Factor	Astroparticle Physics Journal	The Askaryan effect
<i>Radio detection of air showers with the ARIANNA experiment on the Ross Ice Shelf</i>	<i>Astroparticle Physics Journal</i>	<i>Cosmic ray physics, the Askaryan effect</i>
First Upper Limits on the Radar Cross Section of Cosmic-Ray Induced Extensive Air Showers	Astroparticle Physics Journal	Cosmic ray physics
Live-time and sensitivity of the ARIANNA Hexagonal Radio Array	Proceedings of the 36 th ICRC	Neutrino physics, Antarctic ice properties, the Askaryan effect
Performance of the ARIANNA Hexagonal Radio Array	Proceedings of the 36 th ICRC	Neutrino Physics, Antarctic ice properties, the Askaryan effect
<i>A First Search for Cosmogenic Neutrinos with the ARIANNA Hexagonal Radio Array</i>	<i>Astroparticle Physics Journal</i>	<i>Neutrino Physics, Antarctic ice properties, the Askaryan effect</i>
Time-Domain Response of the ARIANNA Detector	Astroparticle Physics Journal	Computational Electromagnetism, RF antenna design and fabrication
Radar absorption, basal reflection, thickness and polarization measurements from the Ross Ice Shelf, Antarctica	Journal of Glaciology	Antarctic ice properties
Design and Performance of the ARIANNA HRA-3 Neutrino Detector Systems.	IEEE Transactions on Nuclear Science	RF antenna design and fabrication
Telescope Array Radar (TARA) observatory for Ultra-High Energy Cosmic Rays.	Nuclear Instrumentation and Methods in Physics Research A	Computational Electromagnetism, RF antenna design and fabrication
Design and Performance of the Autonomous Data Acquisition System for the ARIANNA High Energy Neutrino Detector	IEEE Transactions on Nuclear Science	Computational Electromagnetism, RF antenna design and fabrication
Ross Ice Shelf Thickness, Radio-Frequency Attenuation and Reflectivity: Implications for the ARIANNA UHE Neutrino Detector	Proceedings of the 32nd ICRC	Antarctic ice properties
A prototype station for ARIANNA: A detector for cosmic neutrinos	Nuclear Instrumentation and Methods in Physics Research A	Computational Electromagnetism, RF antenna design and fabrication
Detection and Imaging of He2 Molecules in Superfluid Helium	Physical Review Letters	Nuclear physics, particle physics

Applied Research Projects Documentation	Project origin	Category
Research Application: Exploration of Antarctic Ice Sheets with Drones	Whittier College internal project	Antarctic exploration with drones
Research Application: Workforce Development for Naval Surface Warfare Systems (NSWC), Corona Division	Office of Naval Research project	Workforce development
RF Field Engineer Course: A Practical Introduction	Office of Naval Research project	Workforce development
Introduction to GPS M-Code Signals for Onboarding of Navy Personnel	Office of Naval Research project	Workforce development

Diversity, Equity, and Inclusion Documentation	Project origin	Category
Schedule of activities for the Artemis Program, a STEM recruitment and research opportunity for young women from local high schools	Whittier College internal project	STEM recruitment and development
Diversity, Equity & Inclusion Innovative Initiatives Grant Proposal	Whittier College internal project	DEI in intro. STEM
Changing Glaciers: So Much More than Sea Level Rise	Whittier Scholars Program Undergraduate Thesis	Interdisciplinary research

Complex analysis of Askaryan radiation: A fully analytic model in the time domain

Jordan C. Hanson^{*} and Raymond Hartig

Department of Physics and Astronomy, Whittier College, 13406 East Philadelphia Street, Whittier, California 90602, USA



(Received 10 June 2021; accepted 1 June 2022; published 21 June 2022)

The detection of ultra-high-energy (UHE, ≥ 10 PeV) neutrinos via detectors designed to utilize the Askaryan effect has been a long-time goal of the astroparticle physics community. The Askaryan effect describes radio-frequency radiation from high-energy cascades. When a UHE neutrino initiates a cascade, cascade properties are imprinted on the radiation. Thus, observed radiation properties must be used to reconstruct the UHE neutrino event. Analytic Askaryan models have three advantages when used for UHE neutrino reconstruction. First, cascade properties may be derived from the match between analytic function and observed data. Second, analytic models minimize computational intensity in simulation packages. Third, analytic models can be embedded in firmware to enhance the real-time sensitivity of detectors. We present a fully analytic Askaryan model in the time domain for UHE neutrino-induced cascades in dense media that builds upon prior models in the genre. We then show that our model matches semianalytic parametrizations used in Monte Carlo simulations for the design of IceCube-Gen2. We find correlation coefficients greater than 0.95 and fractional power differences $<5\%$ between the fully analytic and semianalytic approaches.

DOI: 10.1103/PhysRevD.105.123019

I. INTRODUCTION

The extrasolar flux of neutrinos with energies between [0.01–1] PeV has been measured by the IceCube collaboration [1]. Previous analyses have shown that the discovery of ultra-high-energy neutrinos ($\text{UHE-}\nu$) will require an expansion in detector volume because the flux is expected to decrease with energy [2–6]. The $\text{UHE-}\nu$ flux could potentially explain the origin of UHE cosmic rays (UHECR), and provides the opportunity to study electro-weak interactions at record-breaking energies [7,8]. Utilizing the Askaryan effect expands the effective volume of $\text{UHE-}\nu$ detector designs, because this effect offers a way to detect $\text{UHE-}\nu$ with radio pulses that travel more than 1 km in sufficiently RF-transparent media such as Antarctic and Greenlandic ice [9–11].

The Askaryan effect occurs within a dense medium with an index of refraction n . A relativistic particle with $v > c/n$ initiates a high-energy cascade with negative total charge. The charge radiates energy in the RF bandwidth, and the radiation may be detected if the medium does not significantly attenuate the signal [12,13]. The IceCube EHE analysis has constrained the $\text{UHE-}\nu$ flux to be $E_\nu^2 \phi_\nu \leq 2 \times 10^{-8} \text{ GeV cm}^{-2} \text{ s}^{-1} \text{ sr}^{-1}$ between $[5 \times 10^{15} - 2 \times 10^{19}] \text{ eV}$ [4]. Arrays of $\mathcal{O}(100)$ *in situ* detectors encompassing effective areas of $\approx 10^4 \text{ m}^2 \text{ sr}$ per station, spaced by $\mathcal{O}(1)$

RF attenuation length could discover a $\text{UHE-}\nu$ flux beyond the EHE limits. The most suitable ice formations exist in Antarctica and Greenland, and a group of prototype Askaryan-class detectors has been deployed. These detectors seek to probe unexplored $\text{UHE-}\nu$ flux parameter space from astrophysical and cosmogenic sources [5,6,14,15].

Askaryan radiation was first measured in the laboratory in silica sand, and later ice [16–18]. Cascade properties affect the amplitude and phase of the radiation. At RF wavelengths, cascade particles radiate coherently, and the radiation amplitude scales with the total track length of the excess negative charge. The RF pulse shape is influenced by the *longitudinal length* of the cascade, and the pulse is strongest when the viewing angle is close to the Cherenkov angle, θ_C . The *excess charge profile* describes the excess negative charge versus longitudinal position on the cascade axis. Radiation wavelengths shorter than the *lateral width* of the cascade, perpendicular to the cascade axis, are attenuated. At energies far above 10 PeV in ice, however, excess charge profiles generated by *electromagnetic* cascades experience the Landau-Pomeranchuk-Migdal (LPM) effect and can have multiple peaks [19,20]. This theoretical foundation has been constructed from a variety of experimental and simulation results.

The field of Askaryan-class detectors requires this foundation for at least two reasons. First, the theoretical form of the Askaryan RF pulse is used to optimize RF detector designs. Askaryan models are incorporated into

*jhanson2@whittier.edu

simulations [21–23] in order to calculate expected signals and aid in detector design. For example, reconstruction tools for the radio component of IceCube-Gen2 combine machine learning and insights from Askaryan radiation physics [24–26]. Second, Askaryan models are used as templates to search large data sets for signal candidates [5,27]. The signal-to-noise ratios (SNRs) at RF channels are expected to be small ($\text{SNR} \approx 3$), because the amplitude of the radiated field decreases with the vertex distance ($1/r$), and the signal is attenuated by the ice [9,28,29]. Low SNR signals require correspondingly low RF trigger thresholds, but signals must be sampled for a bandwidth of [0.1–1] GHz. Thus, RF channels are triggered at high rates by thermal noise. UHE- ν signals will be hidden within millions of thermal triggers. Template-waveform matching between models and data is a powerful technique for isolating RF signals from high-energy particles [27,30].

Askaryan models fall into three categories: full Monte Carlo (MC), semianalytic, and fully analytic. The original work by Zas *et al.* (ZHS) [13] was a full MC model. The properties of cascades with total energy ≤ 1 PeV were examined. A parametrization for the Askaryan field below 1 GHz was offered, attenuating modes above 1 GHz via a frequency-dependent form factor tied to the lateral cascade width. The semianalytic approach was introduced by Alvarez-Muñiz *et al.* (ARVZ) [31]. This approach accounts for fluctuations in the charge excess profile, and provides an analytic vector potential observed at the Cherenkov angle. The vector potential at the Cherenkov angle is labeled the form factor, and observed fields are derived from the derivative of the vector potential once convolved with a charge excess profile from MC. Recent work also accounts for differences in fit parameters from electromagnetic and hadronic cascades, and other interaction channels, while matching full MC simulations [32].

Finally, fully analytic models of Askaryan radiation from first principles have been introduced. Ralston and Bunyi (RB) gave a fully analytic model valid for observations of cascades in the near and far field, with the transition encapsulated by a parameter η [33]. The result was a complex frequency-domain model. Recently, a model and software implementation was given by Hanson and Connolly (JCH + AC) that built upon RB by providing an analytic form factor derived from GEANT4 simulations, and accounted for LPM elongation [34]. This work connected the locations of poles in the complex frequency plane to η and the form factor. The poles combine to form a low-pass filter for the Askaryan radiation. The JCH + AC results match the ZHS results while demonstrating the physical origins of model parameters. The RB and JCH + AC results are given in the Fourier domain, but most UHE- ν searches (like template matching) have taken place in the time domain. The goals of this work are to produce a fully analytic time-domain model accounting for complex poles, valid for all viewing

angles θ and $\eta < 1$, and to demonstrate that it matches semianalytic models.

In Sec. II, the cascade geometry, units, and vocabulary are defined. In Sec. III, we describe how the JCH + AC form factor fits into the current model [34]. In Sec. IV, the analytic Askaryan field, observed at $\theta = \theta_C$ (*on-cone*), is presented. In Sec. V, the analytic Askaryan field observed for $\theta \neq \theta_C$ (*off-cone*) is presented. In Sec. VI, fully analytic fields are matched to semianalytic fields generated with NuRadioMC [23] at 10 PeV (electromagnetic cascades) and 100 PeV (hadronic cascades). Though the LPM effect is activated in NuRadioMC, it has a negligible influence on the waveform comparison at these energies. In Sec. VII, the results are summarized and potential applications of the model are described.

II. UNITS, DEFINITIONS, AND CONVENTIONS

The coordinate system of the Askaryan radiation from a vector current density \vec{J} is shown in Figs. 1(a)–1(b). Primed cylindrical coordinates refer to \vec{J} , and the unprimed spherical coordinates refer to the observer. The zenith or *viewing angle* is measured with respect to the *longitudinal axis* (z'). The observer displacement is $r = |\vec{x} - \vec{x}'|$, in the \hat{r} direction. The origin is located where the cascade has the highest instantaneous charge density (ICD). The ICD is treated with cylindrical symmetry, so it has no ϕ' dependence. This assumption is based on the large number of cascade particles and momentum conservation. The lateral extent of the ICD is along the *lateral axis* (ρ'). The viewing angle is θ in spherical coordinates, and the Cherenkov angle occurs when θ satisfies $\cos(\theta_C) = 1/n_{\text{ice}}$ with $n_{\text{ice}} = 1.78 \pm 0.003$ [35].

In Fig. 1(c), an example excess charge profile $n(z')$ is shown with characteristic longitudinal length a . The individual ICDs represent the excess charge density for small windows of time, and $n(z')$ refers to the total excess charge as a function of z' . Approximating the central

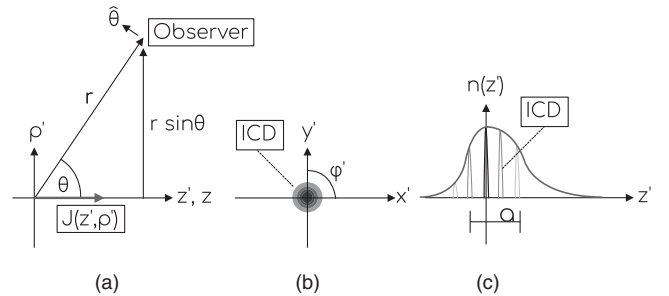


FIG. 1. (a) Side view of the coordinate systems used in the analysis. Spherical unprimed coordinates refer to the observer. Primed cylindrical coordinates refer to $\vec{J}(\rho', z')$. (b) Front view of the coordinate system. The ICD is assumed to have no ϕ' dependence. (c) The function $n(z')$ describes the total cascade excess charge, and it has a characteristic width a . The ICD has an instantaneous width much smaller than a [34].

portion of $n(z')$ as a Gaussian distribution $N(\mu, \sigma)$ corresponds to setting $a = 2\sigma$. Askaryan radiation occurs because $n(z')$ represents excess negative charge [13,34,36]. Cascades may be characterized as *electromagnetic*, initiated by charged outgoing leptons from UHE- ν interactions, or *hadronic*, initiated by the interaction between the UHE- ν and the nucleus. Electromagnetic cascades follow the Greisen distribution and hadronic cascades follow the Gaisser-Hillas distribution. An example of such an implementation via the ARVZ semianalytic parametrization is AraSim [11].

The units of the electromagnetic field in the Fourier domain are V/m/Hz, often converted in the literature to V/m/MHz. To make the distance dependence explicit, both sides of field equations are multiplied by r , as in $r\vec{E} = \dots$, making the units V/Hz. Throughout this work, an overall field normalization constant E_0 is used. E_0 may be linearly scaled with energy, as in other Askaryan models. We show that the on-cone field amplitude is proportional to E_0 times a characteristic frequency squared, so the units of E_0 are V/Hz². For off-cone results, we show that the field amplitude is proportional to E_0 times a characteristic frequency divided by a characteristic pulse width, and the units of E_0 remain V/Hz².

In Sec. III B, we review briefly the energy dependence of the longitudinal length a in both the electromagnetic and hadronic cases. For the Greisen distribution with critical energy E_{crit} , it can be shown that if $n_{\max} = n(z_{\max})$, where $z_{\max} = \ln(E_C/E_{\text{crit}})$, then $n_{\max}a \sim E_C/E_{\text{crit}}$. Thus, the area under the curve $n(z')$ scales with the total cascade energy E_C . RB demonstrated that the Askaryan radiation amplitude is proportional to $n_{\max}a$ and therefore E_C . The cascade develops over a length $\approx a$, but the radiation is coherent over a length $\Delta z'_{\text{coh}}$ for which the displacement is constant to first order relative to a wavelength. The η parameter is the square of the ratio of a to $\Delta z'_{\text{coh}}$:

$$\eta = \left(\frac{a}{\Delta z'_{\text{coh}}} \right)^2 = \frac{k}{r} (a \sin \theta)^2. \quad (1)$$

In the far field, $\eta < 1$. In the first JCH + AC model, a limiting frequency ω_C was shown to filter the Askaryan radiation [34]:

$$\eta = \frac{\omega}{\omega_C}. \quad (2)$$

The effect of ω_C is described in Sec. IV. The Askaryan radiation is primarily polarized in the $\hat{\theta}$ direction, with a small amount along \hat{r} [31,34]. The wave vector is $k = (2\pi)/(n\lambda)$, where n is the index of refraction. A 3D wave vector was defined by RB, equivalent to $\vec{q} = nk(1, \vec{\rho}/R)$. The vector current density is treated by RB as a charge density times the velocity of the ICD: $\vec{J}(t, \vec{x}') = \rho(z' - vt, \rho') \vec{v}$. Further, the charge density is factored into $n(z')$ times the ICD:

$\rho(z' - vt, \rho') = n(z')f(z' - vt, \rho')$. The form factor \tilde{F} is the three-dimensional spatial Fourier transform of the ICD [33].

The result for \tilde{F} was derived analytically by JCH + AC [34], and that derivation is briefly described in Sec. III A. JCH + AC define a parameter σ , and \tilde{F} is a function of σ : $\tilde{F}(\sigma)$. The variable σ is related to the ratio of the lateral ICD width to the radiated wavelength. In the derivation of \tilde{F} , it is convenient to set σ equal to the ratio of the angular frequency to the low-pass cutoff frequency ω_{CF} of \tilde{F} :

$$\sigma = \frac{\omega}{\omega_{\text{CF}}}. \quad (3)$$

Armed with \tilde{F} , the longitudinal length a and the corresponding energy dependence on E_0 , the RB field equations $\vec{\mathcal{E}}$, and the displacement r , the Askaryan electromagnetic field may be assembled according to the following form [33]:

$$r\vec{E}(\omega, \theta) = E_0 \left(\frac{\omega}{2\pi} \right) \psi \vec{\mathcal{E}}(\omega, \theta) \tilde{F}(\omega, \theta). \quad (4)$$

The factor E_0 is proportional to the cascade energy. The factor ω is the angular frequency. The variable ψ is $\psi = -i \exp(ikr) \sin \theta$. The function $\vec{\mathcal{E}}(\omega, \theta)$ contains the vector and complex pole structure of the field (see Refs. [33,34]). The model represented by Eq. (4) is an *all-θ, all-ω* model. That is, Eq. (4) is valid at all frequencies and all viewing angles, provided one accepts the approximation of the central portion of $n(z')$ as Gaussian. The first goal of this work is to build an *all-θ, all-t* model in the time domain, derived from Eq. (4), and the second goal is to compare it to semianalytic parametrizations.

III. THE FORM FACTOR AND LONGITUDINAL LENGTH PARAMETER

To arrive at the main electromagnetic field in the time domain, the individual pieces of Eq. (4) must first be assembled. The first piece will be the form factor \tilde{F} that accounts for the 3D ICD, followed by some remarks about the energy dependence of the longitudinal length parameter a .

A. The form factor

The form factor is the 3D Fourier transform of the ICD $f(z', \rho')$, with $\vec{q} = nk(1, \vec{\rho}/R)$ [33]:

$$F(\vec{q}) = \int d^3x' f(z', \rho') e^{-i\vec{q}\cdot\vec{x}'}. \quad (5)$$

The goal is to evaluate \tilde{F} in the Fourier domain for an ICD definition informed by cascade simulations. Simulations of the cascade induced by UHE- ν indicate a

thin wave of charge in z' spread uniformly in ϕ' , that decreases exponentially in ρ' . Using these observations JCH + AC completed the derivation in Ref. [34]. The final result was a simple analytic formula:

$$\tilde{F} = \frac{1}{(1 + (\omega/\omega_{\text{CF}})^2)^{3/2}} \quad (6)$$

The form factor acts as a low-pass filter with the cutoff frequency ω_{CF} :

$$\tilde{F} \approx \frac{\omega_0^2}{(\omega + i\omega_0)(\omega - i\omega_0)}. \quad (7)$$

The definition $\omega_0 = \sqrt{2/3}\omega_{\text{CF}}$ has been used. The effect of the approximation is illustrated in Fig. 2. Equation (7) matches the original ZHS parametrization (see Eq. 20 of Ref. [13]).

1. A note about the Molière radius

In Sec. VI B, the decay constant l of the lateral component of the ICD is inferred from best-fit values of ω_0 . The connection between the l parameter and ω_0 was described by JCH + AC [34]. Put simply, the ICD decays by a factor of $1/e$ a lateral distance l from the cascade axis. Note, however, that the l parameter is not the Molière radius. The Molière radius is the lateral radius which forms a cylinder containing 90% of the energy deposition of the cascade. For ice with a density of 0.917 g cm^{-3} , one can estimate $R_M \approx 9.2 \text{ cm}$ using standard formulas. Although it is tempting to compare l to R_M , these parameters have different definitions. Knowing that l is related to ω_0 , l may be estimated as $\lambda/2$ in ice at the cutoff frequency. At 3 GHz in ice, $\lambda/2 \approx 2.8 \text{ cm}$, and at 1 GHz in ice, $\lambda/2 \approx 8.4 \text{ cm}$. Although the results are at the same order of magnitude as R_M , there are three effects limiting the high-frequency spectrum of the radiation: ω_0 , ω_C , and the viewing angle. Thus, $l < R_M$ is possible for a radiation spectrum limited to $\lesssim 1 \text{ GHz}$.

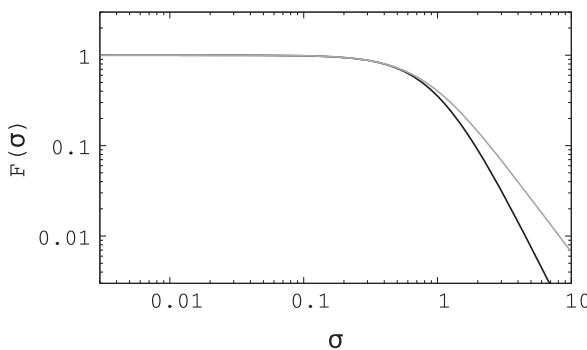


FIG. 2. Black: Eq. (6), graphed versus $\sigma = \omega/\omega_{\text{CF}}$. Gray: the two-pole approximation.

B. The longitudinal length parameter

The next piece required in the assembly of the main electromagnetic field is the energy dependence of the overall amplitude, and the energy dependence of the longitudinal length parameter, a , which is a part of $\vec{\mathcal{E}}$ in Eq. (4) [33]. What follows are two separate discussions, one for electromagnetic cascades, and one for hadronic cascades. Though we share these calculations for convenience, note that a variety of theoretical and experimental results on this topic are available [16,37,38].

1. Electromagnetic case

The number of charged particles versus distance in radiation lengths $n(z')$ in an electromagnetic cascade taking place in a dense medium with initial cascade energy E_C , critical energy E_{crit} , normalization parameter n_0 , and age s is [34]

$$n(z') = \frac{n_0}{\sqrt{\ln(E_C/E_{\text{crit}})}} \exp \left\{ z' \left(1 - \frac{3}{2} \ln(s) \right) \right\}. \quad (8)$$

To find the energy-dependent width of the Greisen distribution, four steps are necessary: (1) normalization of $n(z')$ as a fraction of the maximum excess charge, (2) conversion of $n(z')$ to $n(s)$, (3) determination of the width of $n(s)$ by approximating the central portion as a Gaussian distribution, and (4) conversion of the width from s units to radiation lengths z' , and then converting those results to a distance. Define the ratio $R = n(z_{\text{max}} \pm a/2)/n_{\text{max}}$, so the FWHM occurs when $R = 0.5$. The final result in radiation lengths is

$$a = \sqrt{\ln(E_C/E_{\text{crit}})} \sqrt{-6 \ln(R)} \quad (9)$$

Since $R < 1$, $\ln(R) < 0$ and a is real valued, and a in Eq. (9) is in radiation lengths. In solid ice the density is $\rho_{\text{ice}} = 0.917 \text{ g cm}^{-3}$, and the electromagnetic radiation length is $z_0 = 36.08 \text{ g cm}^{-2}$ [34]. Converting to distance gives

$$a = \frac{z_0}{\rho_{\text{ice}}} \sqrt{\ln(E_C/E_{\text{crit}})} \sqrt{-6 \ln(R)} \quad (10)$$

Note that $a \propto \sqrt{\ln(E_C)}$, as shown by RB and others. The product $n_{\text{max}}a$ is proportional to the energy E_C/E_{crit} . For this reason RB took $n_{\text{max}}a$ as the field normalization rather than E_C [33]. As an example, letting $R = 0.4$, and $E_{\text{crit}} \approx 10^8 \text{ eV}$, gives $a \approx 4 \text{ meters}$ for $E_C = 10^{16} \text{ eV}$. We show in Sec. VI that our fitted a values are close to 4 meters when matched to semianalytic parametrizations.

2. Hadronic case

The Gaisser-Hillas distribution describes hadronic cosmic-ray air showers, but has also been applied to hadronic cascades in dense media in codes like AraSim [11,22]. The original function reads

$$n(z') = n_{\max} \left(\frac{z' - z_0}{z_{\max} - z_0} \right)^{(z_{\max} - z_0)/\lambda} e^{\frac{z_{\max} - z'}{\lambda}}. \quad (11)$$

The variables are defined as follows: n_{\max} is the instantaneous maximum number of particles in the cascade, z' is the longitudinal distance in radiation lengths, z_0 is the initial starting point, λ is the interaction length, and z'_{\max} is the location of n_{\max} . Using the same steps as the electromagnetic case, we find

$$a = \sqrt{z'_{\max}} \sqrt{-8 \ln(R)} \quad (12)$$

The a parameter again goes as $\sqrt{z_{\max}} \propto \sqrt{\ln(E_C)}$ which produces similar lengths as the electromagnetic case when scaled by the appropriate interaction length and ice density.

IV. ON-CONE FIELD EQUATIONS

The $\hat{\theta}$ component of the electromagnetic field at $\theta = \theta_C$ will now be built in the time domain from Eq. (4). Setting $\theta = \theta_C$ in the general RB field equations (Appendix A), with Eq. (6) for \tilde{F} , $\sigma = \omega/\omega_{\text{CF}}$ and $\eta = \omega/\omega_{\text{CF}}$, and letting E_0 be proportional to the cascade energy E_C produces Eq. 45 from JCH + AC [34]:

$$r\tilde{E}(\omega, \theta_C) = \frac{(-i\omega)E_0 \sin(\theta_C)e^{i\omega r/c}}{(1 - i\omega/\omega_C)^{1/2}(1 + (\omega/\omega_{\text{CF}})^2)^{3/2}}. \quad (13)$$

More detail is provided in Appendix A. Let the retarded time be $t_r = t - r/c$ (with the appropriate value for c given the index versus depth), and let $\omega_0 = \sqrt{\frac{2}{3}}\omega_{\text{CF}}$ and $\hat{E}_0 = E_0 \sin \theta_C$. Finally, let $\epsilon = \omega_0/\omega_C$. The inverse Fourier transform of Eq. (13) is

$$\begin{aligned} rE(t, \theta_C) \\ = \frac{\hat{E}_0 i\omega_C \omega_0^2}{\pi} \frac{d}{dt_r} \int_{-\infty}^{\infty} \frac{e^{-i\omega t_r}}{(2i\omega_C + \omega)(\omega + i\omega_0)(\omega - i\omega_0)} d\omega. \end{aligned} \quad (14)$$

In Eq. (14), the derivative with respect to the retarded time d/dt_r is introduced to remove a factor of $(-i\omega)$ from the numerator. Accounting for the complex poles and the sign of t_r , complex integration and expansion to first order in ϵ yields

$$rE(t, \theta_C) = \frac{1}{3} \hat{E}_0 \omega_{\text{CF}}^2 \begin{cases} (1 - \frac{1}{2}\epsilon)e^{\omega_0 t_r} & t_r < 0 \\ (2e^{-2\omega_C t_r} - (1 + \frac{1}{2}\epsilon)e^{-\omega_0 t_r}) & t_r > 0 \end{cases} \quad (15)$$

Equation (15) represents the time-domain solution for the on-cone $\hat{\theta}$ component of the Askaryan electric field. The expansion to first order in ϵ is only performed so the final result resembles semianalytic results for $\vec{E} = -\partial \vec{A}/\partial t_r$ [31,32]. Table I summarizes the definitions of the parameters in Eq. (15). Fit results for the parameters of Table I are shown in Sec. VI.

Notice that the amplitude is asymmetric, and the parameter ϵ influences the asymmetry. The ϵ parameter was studied by JCH + AC in detail. For example, Fig. 10 of Ref. [34] shows that $\epsilon \approx [0.1 - 1]$ for an inverse lateral width $l^{-1} = \sqrt{2\pi\rho_0} \approx 20 \text{ m}^{-1}$ and $a \approx 4 \text{ m}$. The best-fit results for ϵ and a are shown in Sec. VI. JCH + AC showed that the expression for ϵ is the product of the ratio of the lateral to longitudinal length, and the ratio of the longitudinal length to the observer displacement, making it a physical parameter connecting the event geometry to the cascade shape [34]. Figure 3 displays normalized examples of Eq. (15) for different values of ω_0 , ω_C , and ϵ .

A. Verification of the uncertainty principle

As a check on the procedures used to perform the inverse Fourier transform that produces Eq. (15), we verify below that the uncertainty principle holds, for $\Delta\theta \rightarrow 0$. JCH + AC provided the Gaussian width of the radiation in the Fourier domain: σ_ν , where ν represents the frequency in Hz. Generally speaking, Fourier transform pairs must obey $\sigma_\nu \sigma_t \geq 1/(2\pi)$. The following procedure is used to compute the width σ_t of the on-cone field. First, the $t_r < 0$ and $t_r > 0$ cases are each treated as probability distributions and normalized. Next, the average positive and negative retarded times, $\bar{t}_{r,+}$ and $\bar{t}_{r,-}$, are computed. Finally, subtracting the two averages yields σ_t :

TABLE I. Parameters used to build Eq. (15). Fitted values in comparison to semianalytic parametrizations are shown in Sec. VI.

Parameter	Definition
\hat{E}_0	$E_0 \sin(\theta_C)$
E_0	$\approx n_{\max} a$
ω_0	$\sqrt{\frac{2}{3}}\omega_{\text{CF}}$
ω_{CF}	$(c\sqrt{2\pi\rho_0})/(n \sin \theta)$ (see Eqs. 22, 23, and 46 of Ref. [34])
ω_C	$(rc)/(na^2 \sin^2 \theta)$ (see Eq. 39 of Ref. [34])
ϵ	ω_0/ω_C
t_r	$t - r/c$

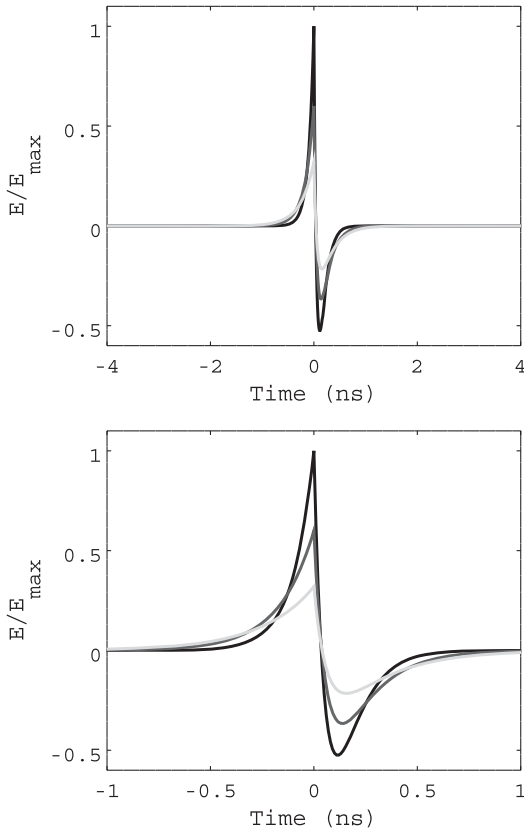


FIG. 3. Top: Eq. (15) from $[-4, 4]$ ns, with (black) $\omega_C = 2\pi(1.25)$ GHz, $\omega_0 = 2\pi(1.56)$ GHz, $\epsilon = 1.25$, (gray) $\omega_C = 2\pi(1.25)$ GHz, $\omega_0 = 2\pi(0.94)$ GHz, $\epsilon = 0.75$, (light gray) $\omega_C = 2\pi(1.25)$ GHz, $\omega_0 = 2\pi(0.625)$ GHz, and $\epsilon = 0.5$. The amplitudes of all curves are normalized to the peak of the $\epsilon = 1.25$ (black) data. Bottom: same as top panel, plotted between $[-1, 1]$ ns.

$$\sigma_t = \bar{t}_{r,+} - \bar{t}_{r,-} = \frac{\epsilon + 2}{\omega_0} = \frac{1}{\omega_C} + \frac{2}{\omega_0}. \quad (16)$$

The result has the correct units and the limiting cases are sensible. If $\epsilon \rightarrow 0$ ($\omega_C \gg \omega_0$), then $\sigma_t \rightarrow 2/\omega_0$, which is expected from observing Eq. (15) if the ω_C exponential disappears. If $\epsilon = 1$ ($\omega_C = \omega_0$), then $\sigma_t = 3/\omega_0$. That is, the pulse is wider if there is more than one relevant cutoff frequency.

The expression for σ_ν is given by Eq. 36 of JCH + AC [34]:

$$\sigma_\nu = \frac{c}{2\pi a \Delta \cos(\theta)} (1 + \eta^2)^{1/2}. \quad (17)$$

Expanding to first order in $\Delta \cos(\theta) = \cos(\theta) - \cos(\theta_C)$,

$$\sigma_\nu \approx \frac{c}{2\pi a \sin(\theta_C) \Delta \theta} (1 + \eta^2)^{1/2}. \quad (18)$$

From Table I: $\omega_C^{-1} = na^2 \sin^2(\theta_C)/(rc)$, and $\omega_0^{-1} = nl \sin(\theta_C)/c$, with $l = \sqrt{3/2}/(\sqrt{2}\pi\rho_0)$. (Recall that ρ_0

is a parameter discussed in Ref. [34]). Multiplying σ_t and σ_ν with the far-field limit ($\eta < 1$) gives the inequality

$$\sigma_\nu \sigma_t \geq \frac{n}{2\pi} \left(\left(\frac{a}{r} \right) \frac{\sin(\theta_C)}{\Delta \theta} + 2 \left(\frac{l}{a} \right) \frac{1}{\Delta \theta} \right). \quad (19)$$

Therefore, in order to satisfy $\sigma_\nu \sigma_t > 1/(2\pi)$,

$$n \left(\frac{a}{r} \right) \sin(\theta_C) + 2n \left(\frac{l}{a} \right) > \Delta \theta. \quad (20)$$

Although $a/r \ll 1$ and $l/a \ll 1$, as long as these expressions do not approach zero as fast as $\Delta \theta \rightarrow 0$ in Eq. (20), the uncertainty principle holds. Yet these are exactly the conditions of the problem: a displacement r in the far field (but not infinitely far away) and a longitudinal length a much larger (but not infinitely larger) than the lateral ICD width l . Thus, $\sigma_\nu \sigma_t > 1/(2\pi)$ holds.

V. OFF-CONE FIELD EQUATIONS

Turning to the case for which $\theta \neq \theta_C$, the $\hat{\theta}$ component of the electromagnetic field will now be built in the time domain. The RB field equations for the $\hat{\theta}$ and \hat{r} components were summarized by both RB and JCH + AC [33,34], and are included here in Appendix A. Recall the general form of the electromagnetic field, given in Eq. (4):

$$r \vec{E}(\omega, \theta) = E_0 \left(\frac{\omega}{2\pi} \right) \psi \vec{\mathcal{E}}(\omega, \theta) \tilde{F}(\omega, \theta). \quad (21)$$

The first task is to simplify $\vec{\mathcal{E}}(\omega, \theta)$ before taking the inverse Fourier transform. The simplification involves expanding $\vec{\mathcal{E}}(\omega, \theta)$ in a Taylor series such that $u = 1 - i\eta \approx 1$, restricting $\eta < 1$ (far-field). Once $\vec{\mathcal{E}}(\omega, \theta)$ is simplified, the inverse Fourier transform of Eq. (21) may be evaluated to produce the result. Table II contains useful variable definitions, Table III contains useful function definitions, and Table IV contains special cases of the functions in Table III.

The original form of $\vec{\mathcal{E}}(\eta, \theta)$ is shown in Appendix A. Changing variables to u and x (Table II) and using the

TABLE II. Useful variables for the derivation of the off-cone Askaryan electromagnetic field.

Variable	Definition
u	$1 - i\eta$
x	$\cos(\theta)$
x_C	$\cos(\theta_C)$
q	$(xx_C - x_C^2)/(1 - x^2)$
y	$(\frac{1}{2})(ka)^2(\cos \theta - \cos \theta_C)^2$
p	$\frac{1}{2}(\frac{q}{c})^2(\cos \theta - \cos \theta_C)^2$

TABLE III. Useful functions for the derivation of the off-cone Askaryan electromagnetic field. The last row contains the vector structure of the $\hat{\theta}$ component of the field.

Function	Definition
$f(u, x)$	$(u + 3 \frac{(1-u)^2 x^2 - x x_C}{u - 1 - x^2})^{-1/2}$
$g(u, x)$	$\exp(-\frac{1}{2}(ka)^2(x - x_C)^2 u^{-1})$
$h(u, x)$	$(\frac{1-u}{u})q$
$\vec{\mathcal{E}}(u, x) \cdot \hat{\theta}$	$f(u, x)g(u, x)(1 - h(u, x))$

TABLE IV. Special cases of the functions defined in Table III, when $u = 1$.

Function ($u = 1$)	Result
$f(x, 1)$	1
$\dot{f} _{u=1}$	$-\frac{1}{2}$
$g(x, 1)$	$\exp(-y)$
$\dot{g} _{u=1}$	$y \exp(-y)$
$h(x, 1)$	0
$\dot{h} _{u=1}$	$-q$

function definitions and values in Tables III–IV, $\vec{\mathcal{E}}(u, x) \cdot \hat{\theta} = \mathcal{E}(u, x)$ becomes

$$\mathcal{E}(u, x) = f(u, x)g(u, x)(1 - h(u, x)). \quad (22)$$

Expanding $\mathcal{E}(u, x)$ near $u = 1$ gives

$$\mathcal{E}(u, x) = \mathcal{E}(x, 1) + (u - 1)\dot{\mathcal{E}}(x, 1) + \mathcal{O}(u - 1)^2. \quad (23)$$

The details of the expansion are shown in Appendix B. The result is.

$$\mathcal{E}(x, u) = e^{-y} \left(1 - \frac{1}{2} j\eta(2y + 2q - 1) \right). \quad (24)$$

The inverse Fourier transform of the $\hat{\theta}$ component gives the time-domain results, after including the expanded $\mathcal{E}(u, x)$:

$$rE(t, \theta) = \mathcal{F}^{-1} \left\{ E_0 \left(\frac{\omega}{2\pi} \right) \tilde{F}\psi\mathcal{E} \right\}. \quad (25)$$

Intriguingly, the result is proportional to the *line-broadening function*, H (DLMF 7.19, [39]) common to spectroscopy applications. There are three terms in Eq. (24). Two terms ultimately vanish, being integrals over odd integrands (see Appendix B). The integral that remains contains H , with $\omega_1 = t_r/(2p)$:

$$I_0 = 2\pi i \left(\frac{\omega_C}{\omega_0} \right) e^{-\frac{t_r^2}{4p}} H(\sqrt{p}\omega_0, i\omega_1\sqrt{p}). \quad (26)$$

The line-broadening function is similar to a convolution between a Gaussian function and a Lorentzian function, and cannot be expressed analytically, though there are examples of polynomial expansions [40]. Note that, for situations relevant to the current problem, $\omega > \omega_1$. Requiring that $\omega > \omega_1$ amounts to a restriction between $\Delta\theta$ and $|t_r|$:

$$|t_r| < |2p\omega|. \quad (27)$$

It is shown in the next section that \sqrt{p} is the pulse width σ_t , so $|2p\omega|$ has units of time. Using the results of Sec. V A below, the restriction on the retarded time may be written as $|t_r|/\sigma_t < \omega\sigma_t = 2\pi(\sigma_t/T)$. That is, the accuracy of the waveform should be trusted within a number of pulse widths that is less than 2π times the ratio of the pulse width to the period of the lowest frequency. This is not a strong requirement, since the field quickly approaches zero after several pulse widths. Hereafter, this step will be called the *symmetric approximation*, because the result for $r\vec{E}(t_r, \theta)$ in Eq. (28) has equal positive and negative amplitudes. Evaluating the line-broadening function numerically would account for amplitude asymmetry. The restriction on $\Delta\theta$ is formalized in Sec. V B. Solving I_0 using the symmetric approximation clears the way for the final result (see Appendix B):

$$rE(t, \theta) = -\frac{E_0 \omega_0 \sin(\theta)}{8\pi p} t_r e^{-\frac{t_r^2}{4p} + p\omega_0^2} \text{erfc}(\sqrt{p}\omega_0) \quad (28)$$

Equation (28) represents the time-domain solution for the off-cone $\hat{\theta}$ component of the Askaryan electric field. Equation (28) is graphed in Figs. 4 and 5. In Fig. 4 (top), $E(t, \theta)$ is shown normalized to the maximum value for the angular range displayed, $[\theta_C + 1.5^\circ, \theta_C + 5.5^\circ]$, from $t = [-5, 5]$ ns. Pulses with viewing angles closer to θ_C have larger relative amplitudes and shorter pulse widths. Figure 4 (bottom) contains the same results, but for $t = [-1.5, 1.5]$ ns. The pulses are symmetric and all zero crossings are at $t_r = 0$ ns as a result of the symmetric approximation. Figure 5 contains contours of the same results as in Fig. 4.

As in the on-cone result, the overall field amplitude scales with energy ($E_0 \sim n_{\max} a$). However, the amplitude also scales with ω_0/p . The argument of the complementary error function, $\sqrt{p}\omega_0$, is unitless. This factor is strictly positive, so the range of the complementary error function is (0,1). The factor $\sqrt{p}\omega_0$ cannot be zero without setting $\theta = \theta_C$, or setting $\omega_{CF} = 0$. Both cases are not allowed. Equation (28) represents the *off-cone* ($\theta \neq \theta_C$) solution, so $p \neq 0$. Setting $\omega_{CF} = 0$ is not physical, for

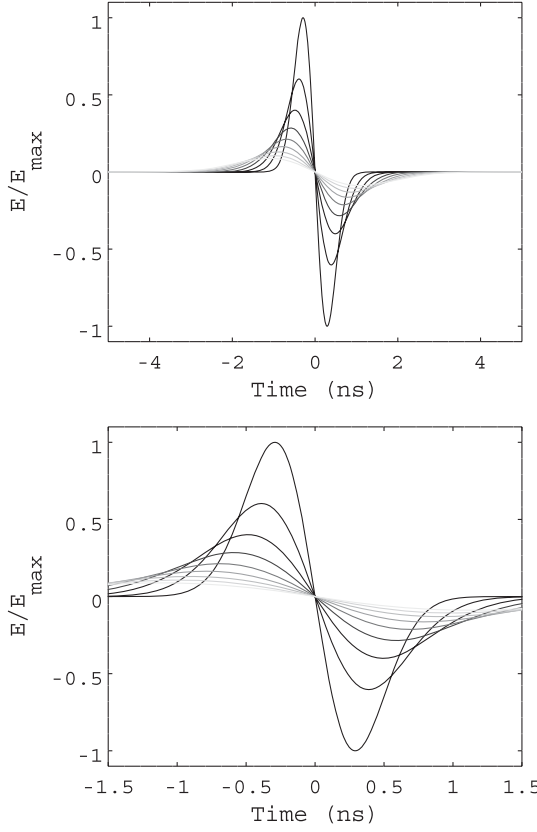


FIG. 4. $E(t, \theta)$ versus t_r [Eq. (28)], normalized. The viewing angle θ is varied from $\theta_C + 1.5^\circ$ to $\theta_C + 5.5^\circ$ in steps of 0.5° . Top: $\omega_0/(2\pi) = 1.0$ GHz. Bottom: same as top, but zoomed in on the central region.

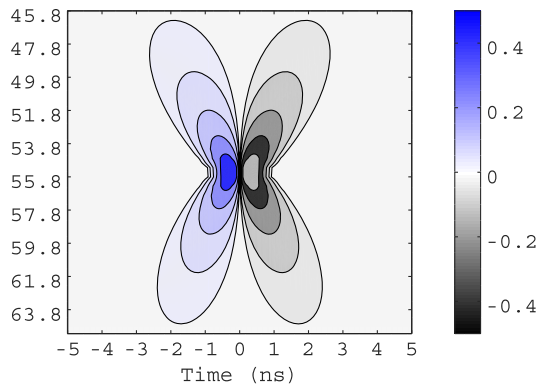


FIG. 5. Contours of $E(t, \theta)$ versus θ versus t_r [Eq. (28)], normalized. The normalization is the same as in Fig. 4. Although the contour lines extend into the region near θ_C , Eq. (5) is only being evaluated at $\Delta\theta > 1.5^\circ$ (see text for details).

this implies infinite lateral width (l) and cascade particles have finite transverse momentum. Another possibility is that $p = 0$ if $a = 0$, but this implies $E_0 = 0$. Therefore, $0 < \text{erfc}(\sqrt{p}\omega_0) < 1$.

A. Verification of the uncertainty principle

As in Sec. IV A, the uncertainty principle should be checked. Equation (28) is an antisymmetric Gaussian function with pulse width $\sigma_t = \sqrt{2p}$. Let $\Delta \cos \theta = (\cos \theta - \cos \theta_C)$. Using Table II, the expression $\sqrt{2p}$ evaluates to

$$\sigma_t = \sqrt{2p} = \left(\frac{a}{c}\right)(\Delta \cos \theta). \quad (29)$$

Recall that σ_ν is given by

$$\sigma_\nu = \frac{c}{2\pi a \Delta \cos \theta} (1 + \eta^2)^{1/2}. \quad (30)$$

The uncertainty product is

$$\sigma_t \sigma_\nu = \frac{1}{2\pi} (1 + \eta^2)^{1/2}. \quad (31)$$

In the far field, $\eta < 1$, so $\sigma_t \sigma_\nu \geq 1/(2\pi)$ holds.

B. Usage of the on-cone versus off-cone fields

The form of Eq. (28), and the restriction between $\Delta\theta$ and $|t_r|$ from the symmetric approximation suggests the limit $\Delta\theta \rightarrow 0$ must be examined carefully. Since $p \propto (\cos \theta - \cos \theta_C)^2$, probing the model near $\theta = \theta_C$ is equivalent to taking the limit that $p \rightarrow 0$. Intriguingly, the p^{-1} dependence in the field does not lead to a divergence. As the field grows in amplitude from p^{-1} as $p \rightarrow 0$, the field width, $\sqrt{2p}$, approaches zero.

Equations (16) and (29) contain the pulse widths of the on-cone and off-cone fields, respectively. Power in the off-cone case is limited by the pulse width $\sqrt{2p}$, and the observed power increases as $\Delta\theta$ and $\sqrt{2p}$ both decrease. Thus, a reasonable constraint on when $\Delta\theta_{\min}$ is large enough to use Eq. (28) is given by setting the off-cone pulse width to the on-cone pulse width:

$$\frac{1}{\omega_C} + \frac{2}{\omega_0} = \sqrt{2p}. \quad (32)$$

Expanding the expression for p near $\theta = \theta_C$, and evaluating the square root leads to

$$\frac{1}{\omega_C} + \frac{2}{\omega_0} = \frac{a}{c} \sin \theta_C \Delta\theta_{\min}. \quad (33)$$

Using $\epsilon = \omega_0/\omega_C$, and letting $k_0 = \omega_0/c$, the formula may be rearranged:

$$\epsilon + 2 = ak_0 \sin \theta_C \Delta\theta_{\min}. \quad (34)$$

Squaring both sides, and then dividing both sides by r yields

$$\frac{(\epsilon + 2)^2}{r} = k_0 \left(\frac{k_0(a \sin \theta_C)^2}{r} \right) \Delta\theta_{\min}^2. \quad (35)$$

The quantity in parentheses on the right-hand side is η , with $\omega = \omega_0$. Setting $\omega = \omega_0$ means $\eta = \epsilon$. Solving for $\Delta\theta_{\min}$ gives

$$\Delta\theta_{\min} = \frac{\epsilon + 2}{\sqrt{\epsilon k_0 r}}. \quad (36)$$

Assuming $\epsilon \approx 1$, $f_0 \approx 1$ GHz, $n = 1.78$ for solid ice, and $c = 0.3$ m ns⁻¹ (see Sec. VI A), $k_0 \approx 35$ m⁻¹. Taking $r = 1000$ m, $\Delta\theta_{\min} \approx 1^\circ$. Simple rules of thumb for the application of Eq. (28) field are

$$\Delta\theta_{\min} \geq 1^\circ, \quad (37)$$

$$\Delta\theta_{\min} \propto \frac{1}{\sqrt{kr}}. \quad (38)$$

VI. COMPARISON TO SEMIANALYTIC PARAMETRIZATIONS

The fully analytic model will now be compared to the ARVZ semianalytic parametrization used in NuRadioMC to predict signals in IceCube-Gen2 Radio [23]. Specifically, the comparison is between Eqs. (15) and (28) and the NuRadioMC implementation of the semianalytic parametrization given in Ref. [32]. To provide concrete comparisons, a small set of waveforms was generated with NuRadioMC, for both electromagnetic and hadronic cascades, on- and off-cone. The electromagnetic cascades have $E_C = 10^{16}$ eV, while the hadronic cascades have $E_C = 10^{17}$ eV. These choices minimize the impact of the LPM effect, though the LPM effect was activated in the NuRadioMC code.

The comparison involves three stages. First, waveforms and a values are generated for each cascade type, energy, and angle: $\theta = \theta_C + 3.0^\circ$, and $\theta = \theta_C$. Second, Eqs. (15) and (28) are tuned to match the waveforms. In each fit, the Pearson correlation coefficient (ρ) is maximized, and the sum squared of amplitude differences [$(\Delta E)^2$] is minimized. Finally, best-fit parameters are tabulated.

Two remarks are important regarding the fit criteria. First, the Pearson correlation coefficient is not sensitive to changes in amplitude because it is normalized:

$$\rho = \frac{\text{cov}(f_{\text{data}}, f_{\text{model}})}{\sigma_{\text{data}} \sigma_{\text{model}}}. \quad (39)$$

If E_i represent the samples of the models, then

$$(\Delta E)^2 = \sum_{i=1}^N (E_{i,\text{data}} - E_{i,\text{model}})^2. \quad (40)$$

A. Waveform comparison: $\theta = \theta_C$

1. Electromagnetic case

Six different electromagnetic cascades and the corresponding Askaryan fields were generated using the ARZ2019 model from NuRadioMC [23,32] for comparison to Eq. (15). The cascades have $E_C = 10$ PeV, and $r = 1000$ meters. The LPM effect is activated in NuRadioMC for all comparisons in this work. The units of $\vec{E}(t_r, \theta_C)$ are mV/m versus nanoseconds, so the units of $r\vec{E}$ are volts. The sampling rate of the digitized semianalytic parametrizations was 100 GHz, with $N = 2048$ samples. Let $f_C = \omega_C/(2\pi)$ and $f_0 = \omega_0/(2\pi)$. The frequencies f_C and f_0 were varied from [0.6–6.0] GHz. The parameter E_0 was varied from [0.05 – 5.0] V GHz⁻². In a simple two-level for loop, the Pearson correlation coefficient ρ was maximized by varying f_0 and f_C . Next, the sum of the squared amplitude differences $(\Delta E)^2$ was minimized by varying E_0 , while holding f_0 and f_C fixed. Several other schemes were studied, including a three-level for loop, but the two-stage process produced the best results. The results are shown in Fig. 6.

Maximizing ρ corresponds to minimizing $(\Delta E)^2$. In Fig. 7, $(\Delta E)^2$ is graphed versus ρ for one event. Best-fit ρ values are ≈ 0.97 for this set, corresponding to best-fit $(\Delta E)^2$ values of $\approx 7\%$. Contours of $\rho > 0.95$ for f_0 versus f_C are shown in Fig. 6 (left column). The crosses represent the best-fit locations. The dashed gray line at $y = x$ corresponds to $f_0/f_C = \epsilon = 1$. Though Eq. (15) contains an expansion to first order in ϵ , making it resemble the derivative of the vector potential from the ARVZ semianalytic parametrization [32], the expansion is optional. There is a restriction that $\epsilon \neq 2$ [see Eq. (A14) of Appendix A]. Thus, the best-fit ϵ values avoid the solid black lines ($\epsilon = 2$) in Fig. 6, but are large enough to account for pulse asymmetry. The best-fit waveforms are shown in Fig. 6 (right column). The gray curves correspond to the semianalytic parametrization, and the black curves represent Eq. (15).

Table V contains the best-fit results for the Eq. (15) parameters, along with best-fit ρ values and $(\Delta E)^2$ values. The horizontal and vertical distances from the crosses to the $\rho > 0.95$ contour are used as error estimates for f_0 and f_C in Table V. The a errors typically encompass the a values from NuRadioMC. The full region in $[f_0, f_C]$ space for which UHE- ν signals are expected the radio component of the IceCube Gen2 detector will be the topic of future studies, along with the apparent difference in ϵ values depending on the electromagnetic or hadronic classification of the cascade (see Fig. 8).

2. Hadronic case

Using the same procedure as in the electromagnetic case, NuRadioMC was used to generate six hadronic cascades at 100 PeV for comparison to Eq. (15). The energy was

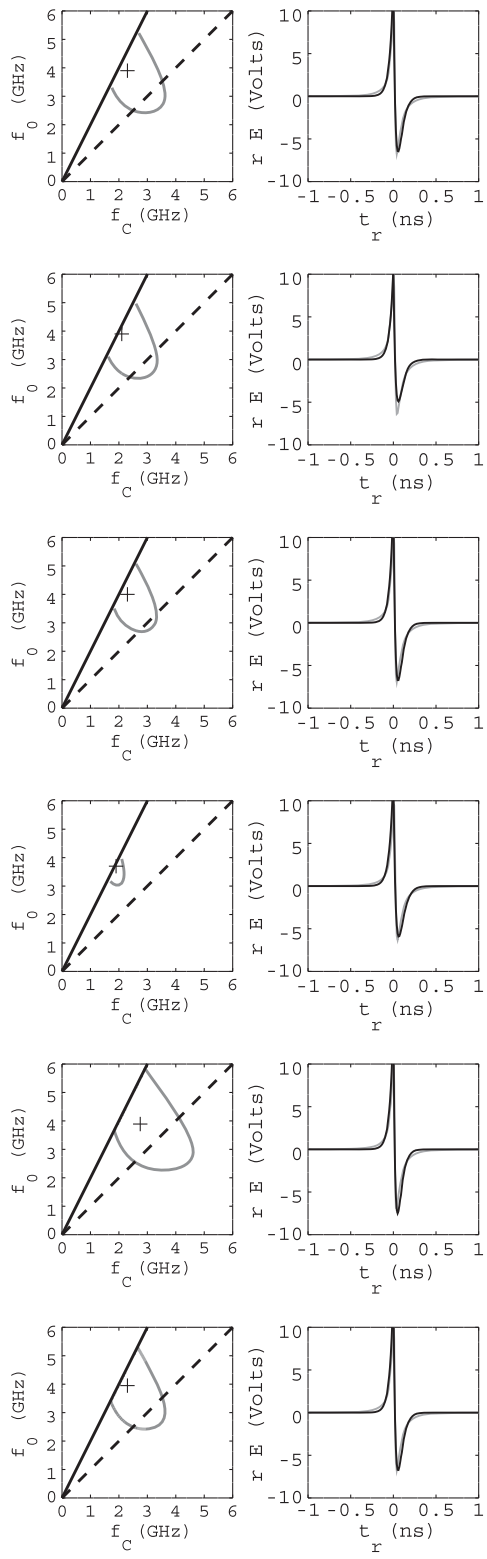


FIG. 6. Fit results: electromagnetic case, $\theta = \theta_C$, $E_C = 10$ PeV. The rows correspond to NuRadioMC waveforms 1–6, with 10 PeV electromagnetic cascades. Left column: best fits for f_0 and f_C . Dashed line: $\epsilon = 1$. Solid line: $\epsilon = 2$. Gray contour: $\rho > 0.95$. Black cross: best fit. Right column: best-fit waveforms. Gray: semianalytic parametrizations from Ref. [23]. Black: Eq. (15).

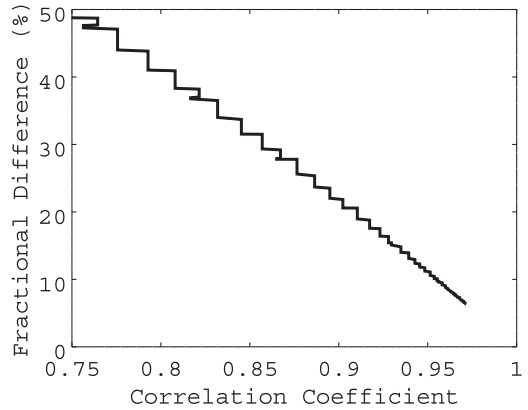


FIG. 7. Fractional difference in the sum of amplitude differences squared $[(\Delta E)^2]$ versus correlation coefficient (ρ) for waveform 1 at $E_C = 10$ PeV, for the electromagnetic case.

increased to show that the model describes a range of energies, so the waveform amplitudes are larger by a factor of 10 relative to the 10 PeV case. The LPM effect is activated in NuRadioMC for all comparisons in this work. The main results are shown in Fig. 8, and the correlation contours represent $\rho = 0.985$.

The results shown in Fig. 8 demonstrate that modeling hadronic cascades at $\theta = \theta_C$ is similar to the electromagnetic case, with one interesting difference. The contours enclose best-fit ϵ values below the dashed line, whereas the fits to the electromagnetic cases were above the dashed line. This could indicate a potential discriminator for cascade classification. Another difference between the electromagnetic and hadronic cases is that the gray contours in Fig. 8 correspond to $\rho = 0.985$, as opposed to $\rho = 0.95$ in the electromagnetic case.

TABLE V. Fit results: electromagnetic case, $\theta = \theta_C$, $E_C = 10$ PeV. The six rows (from top to bottom) correspond to NuRadioMC waveforms 1–6, WITH 10 PeV electromagnetic cascades. From left to right: the form-factor cutoff frequency, coherence cutoff frequency, energy-scaling normalization, longitudinal length parameter, the best-fit correlation coefficient, and the relative power difference between the NuRadioMC semianalytic parametrization and the fully analytic model. The parameter means and errors in the mean are quoted in the bottom two rows.

No.	f_0 (GHz)	f_C (GHz)	E_0 (V GHz $^{-2}$)	a_{wave} (m), a_{MC} (m)	ρ	$(\Delta E)^2$ (%)
1	$3.9^{+0.2}_{-1.9}$	$2.3^{+1.3}_{-0.3}$	0.3	$4.1^{+1.2}_{-0.3}$, 4.85	0.97	6.5
2	$3.9^{+0.3}_{-1.5}$	$2.1^{+0.9}_{-0.1}$	0.5	$4.3^{+1.8}_{-0.2}$, 6.35	0.97	10.9
3	$4.0^{+1.2}_{-1.0}$	$2.3^{+0.8}_{-0.4}$	0.35	$4.1^{+0.7}_{-0.4}$, 4.48	0.96	7.5
4	$3.7^{+0.1}_{-0.5}$	$1.9^{+0.5}_{-0.1}$	1.85	$4.5^{+1.1}_{-0.3}$, 5.6	0.955	8.9
5	$3.9^{+1.4}_{-0.9}$	$2.7^{+1.4}_{-0.8}$	0.18	$4.0^{+2.0}_{-1.2}$, 4.48	0.97	5.7
6	$3.9^{+1.3}_{-1.9}$	$2.3^{+1.3}_{-0.3}$	0.31	$4.1^{+2.0}_{-0.5}$, 4.85	0.97	6.4
Average	3.88	2.3	0.6	4.18	0.966	7.7
Error	3.08	0.1	0.3	0.07	0.003	0.8

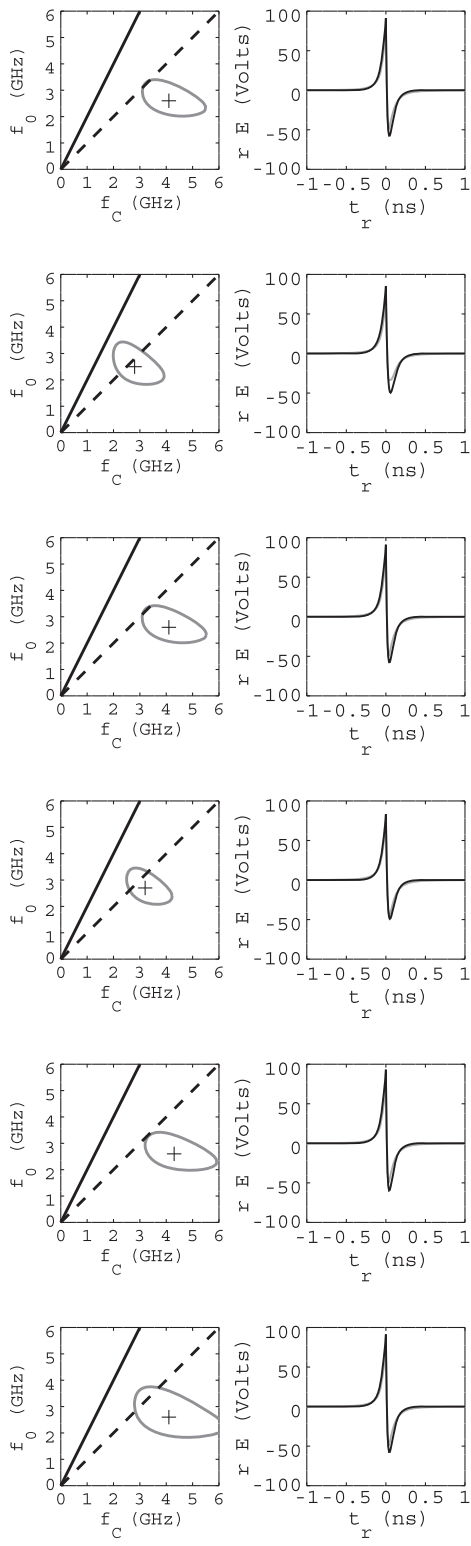


FIG. 8. Fit results: hadronic case, $\theta = \theta_C$, $E_C = 100$ PeV. The six rows (from top to bottom) correspond to NuRadioMC waveforms 1–6, with 100 PeV hadronic cascades. Left column: best fits for f_0 and f_C . Dashed line: $\epsilon = 1$. Solid line: $\epsilon = 2$. Gray contour: $\rho > 0.985$. Black cross: best fit. Right column: best-fit waveforms. Gray: semianalytic parametrizations from Ref. [23]. Black: Eq. (15).

Table VI contains the best-fit parameters corresponding to Fig. 8. The typical power difference $(\Delta E)^2$ has decreased with respect to the electromagnetic case. The ρ values all exceed 0.985, and the $(\Delta E)^2$ results are typically below 2 percent. Intriguingly, $\epsilon < 1$ means higher f_C values, which in turn yields systematically low a values relative to those generated in NuRadioMC, despite the increased energy. Reconstructed a values are still within a factor of 2 of the MC-true values. Despite the systematic offset, the best-fit a and the NuRadioMC a values are tightly correlated (see Fig. 11 below).

B. Waveform comparison: $\theta \neq \theta_C$

1. Electromagnetic case

The general comparison procedure of Sec. VIA was repeated with the same semianalytic parametrization from NuRadioMC, but with 12 new events each viewed at $\theta = \theta_C + 3.0^\circ$ (six electromagnetic cascades, six hadronic). One difference is that ω_0 only changes the waveform amplitude, along with E_0 . The pulse width $\sigma_t = \sqrt{2}p$ connects the longitudinal length a and the viewing angle with respect to the Cherenkov angle.

The fit procedure was performed in two stages. First, θ values and a values were scanned from $[\theta_C + 1.5^\circ, \theta_C + 10.0^\circ]$ and $[0.1, 10]$ meters, respectively, to maximize ρ . Once the best-fit values for a and θ were determined, $(\Delta E)^2$ was minimized by varying $f_0 = \omega_0/(2\pi)$ and E_0 from $[0.3, 3.0]$ GHz and $[0.1, 2.0]$ V GHz $^{-2}$, respectively. The (θ, a) scan and the (f_0, E_0) scan were each separate two-level for loops. The results are shown in Fig. 9.

TABLE VI. Fit results: hadronic case, $\theta = \theta_C$, $E_C = 100$ PeV. The six rows (from top to bottom) correspond to NuRadioMC waveforms 1–6, with 100 PeV hadronic cascades. From left to right: the form-factor cutoff frequency, coherence cutoff frequency, energy-scaling normalization, longitudinal length parameter, the best-fit correlation coefficient, and the relative power difference between the NuRadioMC semianalytic parametrization and the fully analytic model. The parameter means and errors in the mean are quoted in the bottom two rows.

No.	f_0 (GHz)	f_C (GHz)	E_0 (V GHz $^{-2}$)	a_{wave} (m), a_{MC} (m)	ρ (%)	$(\Delta E)^2$
1	$2.6^{+0.6}_{-0.6}$	$4.1^{+1.1}_{-1.0}$	1.0	$3.1^{+0.8}_{-0.8}$, 5.23	0.99	1.86
2	$2.5^{+0.7}_{-0.6}$	$2.8^{+0.9}_{-0.8}$	1.25	$3.75^{+1.2}_{-1.1}$, 6.35	0.99	1.83
3	$2.6^{+0.7}_{-0.6}$	$4.1^{+1.2}_{-0.9}$	1.0	$3.1^{+0.7}_{-0.7}$, 5.23	0.99	1.83
4	$2.7^{+0.6}_{-0.5}$	$3.2^{+0.8}_{-0.6}$	1.0	$3.5^{+0.9}_{-0.7}$, 6.35	0.99	2.5
5	$2.6^{+0.7}_{-0.6}$	$4.3^{+1.4}_{-1.1}$	1.0	$3.0^{+1.0}_{-0.75}$, 4.85	0.99	1.755
6	$2.6^{+1.4}_{-0.7}$	$4.1^{+1.9}_{-1.2}$	1.0	$3.1^{+1.4}_{-0.9}$, 5.23	0.99	1.86
Average	2.60	3.75	1.04	3.3	0.99	1.9
Error	0.03	0.25	0.04	0.1	0.0	0.1

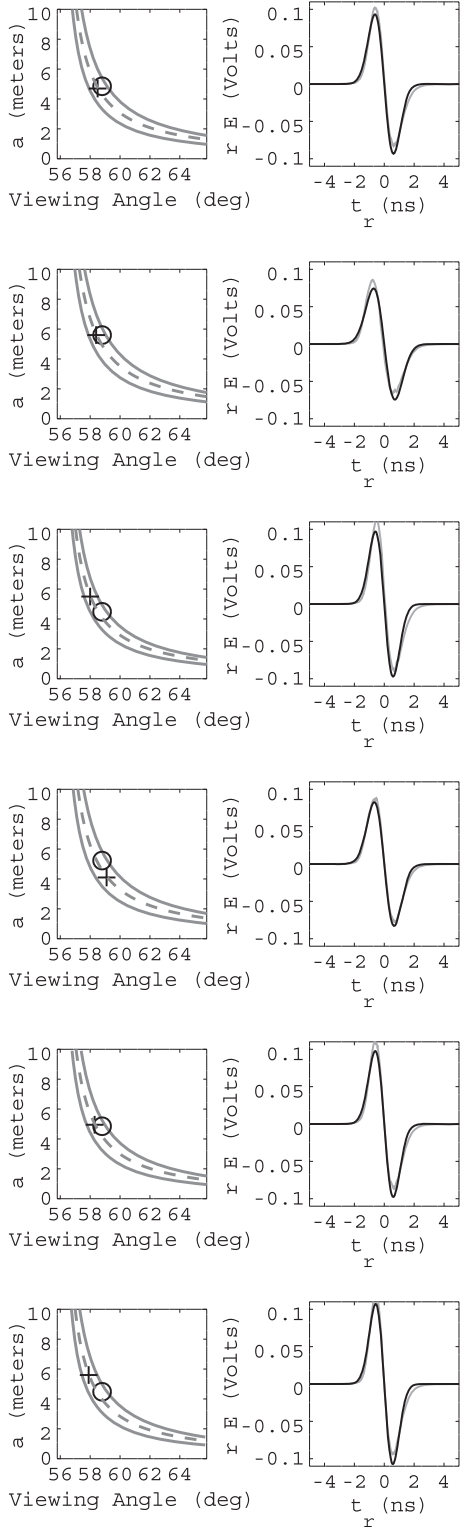


FIG. 9. Fit results: electromagnetic case, $\theta \neq \theta_C$, $E_C = 10$ PeV. The six rows (from top to bottom) correspond to NuRadioMC waveforms 1–6, with 10 PeV electromagnetic cascades. Left column: best-fit θ and a values. Crosses: best fits. Circles: MC true values. Gray contour: $\rho > 0.95$. Dashed line: a versus θ from Eq. (29). Right column: best-fit waveforms. Gray: semianalytic parametrizations from Ref. [23]. Black: Eq. (28).

In Fig. 9 (left column), the best-fit a values and θ values are marked with a cross. The circles represent the MC-true values. Circles and crosses lie on the dashed lines, because an uncertainty principle connects a values to θ values (see Sec. V A). Specifically, Eq. (29) may be used to show, to first order in $\Delta\theta = \theta - \theta_C$,

$$a\Delta\theta = \frac{c\sqrt{2p}}{\sin\theta_C} = \text{const.} \quad (41)$$

The pulse width $\sigma_t = \sqrt{2p}$ is a constant derived from the waveform, implying that the product of a and $\Delta\theta$ is constant. The parameters a and $\Delta\theta$ are therefore inversely proportional: $a \propto \Delta\theta^{-1}$. The shape of the $\rho > 0.95$ contour follows this inverse proportionality. The dashed lines represent Eq. (41). These results suggest that a measurement of the Askaryan pulse width would constrain the cascade shape and geometry. The best-fit waveforms are shown in Fig. 9 (right column). Typical correlation coefficients exceed $\rho = 0.98$. Table VII contains the fit results. The fit results include estimates of the lateral width parameter, l , derived from f_0 (see Sec. III A). Despite making the symmetric approximation to arrive at Eq. (28), the fits include fractional power differences of $\approx 3\%$.

TABLE VII. Fit results: electromagnetic case, $\theta \neq \theta_C$, $E_C = 10$ PeV. The six rows (from top to bottom) correspond to NuRadioMC waveforms 1–6, with 10 PeV electromagnetic cascades. From left to right: the viewing angle, longitudinal length parameter, form-factor cutoff frequency, the energy-scaling normalization, the lateral width of the cascade, the best-fit correlation coefficient, and the relative power difference between the NuRadioMC semianalytic parametrization and the fully analytic model. The parameter means and errors in the mean are quoted in the bottom two rows.

No.	θ_{wave} (deg), θ_{MC} (deg)	a_{wave} (m), a_{MC} (m)	f_0 (GHz)	E_0 (V GHz $^{-2}$)	l (cm)	ρ	$(\Delta E)^2$
1	$58.5^{+0.7}_{-0.6}$, 58.8	$4.7^{+1.3}_{-1.0}$, 4.85	0.75	1.2	$3.4^{+0.9}_{-0.7}$	0.99	1.93
2	$58.4^{+0.6}_{-0.5}$, 58.8	$5.6^{+1.4}_{-1.1}$, 5.60	1.0	1.2	$2.6^{+0.4}_{-0.3}$	0.99	2.61
3	$58.0^{+0.5}_{-0.4}$, 58.8	$5.5^{+1.3}_{-1.0}$, 4.48	1.0	1.1	$2.6^{+0.3}_{-0.2}$	0.98	4.47
4	$59.1^{+0.9}_{-0.7}$, 58.8	$4.1^{+1.2}_{-0.9}$, 5.23	0.75	1.2	$3.4^{+0.5}_{-0.5}$	0.995	0.80
5	$58.3^{+0.7}_{-0.5}$, 58.8	$4.95^{+1.4}_{-1.1}$, 4.85	0.75	1.2	$3.4^{+0.4}_{-0.3}$	0.99	1.8
6	$57.9^{+0.6}_{-0.4}$, 58.8	$5.6^{+1.5}_{-1.2}$, 4.48	0.75	1.2	$3.5^{+0.5}_{-0.4}$	0.99	1.83
Average	58.4	5.1	0.83	1.18	3.2	0.989	2.2
Error	0.2	0.2	0.05	0.02	0.2	0.002	0.5

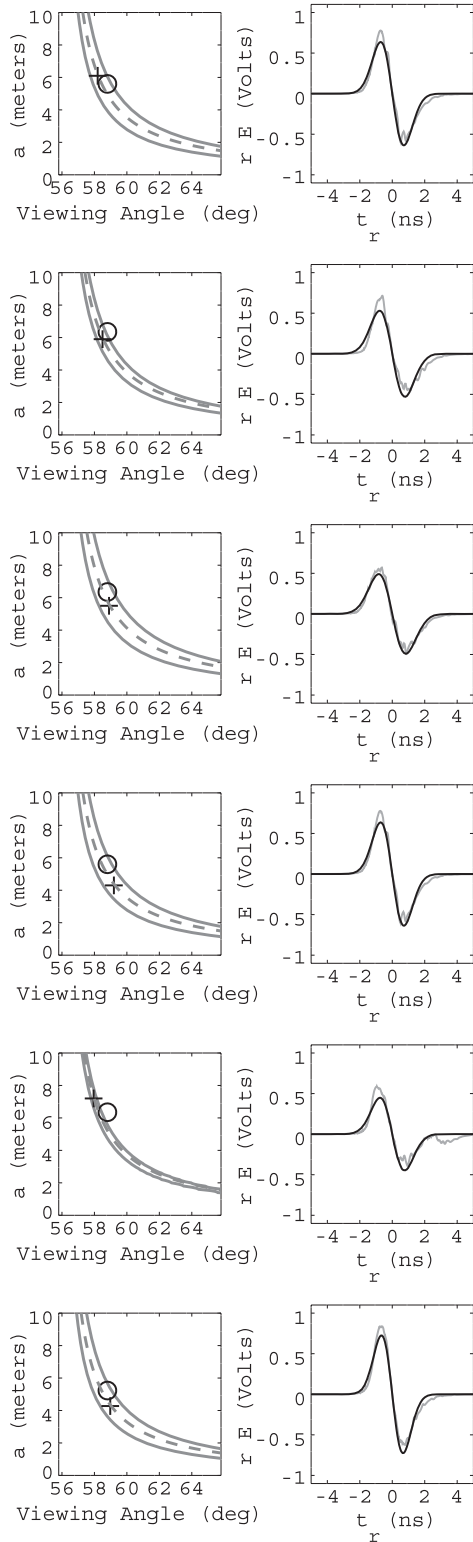


FIG. 10. Fit results: hadronic case, $\theta \neq \theta_C$, $E_C = 100$ PeV. The six rows (from top to bottom) correspond to NuRadioMC waveforms 1–6, with 100 PeV hadronic cascades. Left column: best-fit θ and a values. Crosses: best fits. Circles: MC true values. Gray contour: $\rho > 0.95$. Dashed line: a versus θ from Eq. (29) (uncertainty principle). Right column: best-fit waveforms. Gray: semianalytic parametrizations from Ref. [23]. Black: Eq. (28).

2. Hadronic case

The fit procedure for the hadronic cascades was the same as the electromagnetic case, except that the range for E_0 was expanded to $[1.0, 20.0]$ V GHz $^{-2}$. As in the on-cone procedure, the hadronic cascade energy was $E_C = 100$ PeV. The results are shown in Fig. 10.

As with the electromagnetic case, ρ is maximized and $(\Delta E)^2$ is minimized. Table VIII contains the best-fit parameters, along with ρ and $(\Delta E)^2$. Solutions with $\rho \approx 0.98$ and $(\Delta E)^2 \approx 5\%$ were found. Similar to the results shown in Table VII, the results in Table VIII are in agreement with the MC values from NuRadioMC. The E_0 values match expectations for 100 PeV cascades, because they are a factor of 10 higher than those of the 10 PeV electromagnetic case. The results for a , l , and f_0 , however, are not statistically different between Tables VII and VIII. Future studies will require computing the probability distributions of these parameters from large numbers of UHE- ν cascades.

As a first exercise for statistical energy reconstruction from waveform parameters, assume that $\theta = \theta_C + 3.0^\circ$ is already measured. For example, θ could be determined by measuring the cutoff frequency in the Fourier domain below 1 GHz (see Fig. 5 of Ref. [34], for example). Scanning Eq. (28) over all NuRadioMC waveforms at fixed $\theta = \theta_C + 3.0^\circ$ yields Fig. 11, in which the fitted a value from each waveform

TABLE VIII. Fit results: hadronic case, $\theta \neq \theta_C$, $E_C = 100$ PeV. The six rows (from top to bottom) correspond to NuRadioMC waveforms 1–6, with 100 PeV hadronic cascades. From left to right: the viewing angle, longitudinal length parameter, form-factor cutoff frequency, the energy-scaling normalization, the lateral width of the cascade, the best-fit correlation coefficient, and the relative power difference between the NuRadioMC semianalytic parametrization and the fully analytic model. The parameter means and errors in the mean are quoted in the bottom two rows.

No.	θ_{wave} (deg), θ_{MC} (deg)	a_{wave} (m), a_{MC} (m)	f_0 (GHz) 5.5 6.35	E_0 (V GHz $^{-2}$) 10.6 5.6	l (cm) 3.2 5.6	ρ (%) 0.98 7.1	$(\Delta E)^2$ 3.55 7.1
1	$58.2^{+0.6}_{-0.4}$, 58.8	$6.1^{+1.5}_{-1.2}$, 5.6	0.8	10.6	$3.2^{+0.5}_{-0.5}$	0.98	3.55
2	$58.5^{+0.4}_{-0.3}$, 58.8	$5.9^{+0.9}_{-0.8}$, 6.35	0.85	10.3	$3.0^{+0.3}_{-0.2}$	0.96	7.1
3	$58.9^{+0.8}_{-0.6}$, 58.8	$5.5^{+1.4}_{-1.1}$, 6.35	0.9	10.8	$2.8^{+0.5}_{-0.5}$	0.98	2.64
4	$59.2^{+0.8}_{-0.7}$, 58.8	$4.3^{+1.1}_{-0.8}$, 5.6	0.85	10.5	$3.0^{+0.5}_{-0.5}$	0.98	3.10
5	$58.0^{+0.2}_{-0.2}$, 58.8	$7.2^{+0.6}_{-0.6}$, 6.35	0.9	8.2	$2.9^{+0.3}_{-0.3}$	0.955	8.76
6	$59.0^{+0.8}_{-0.6}$, 58.8	$4.3^{+1.1}_{-0.9}$, 5.23	0.85	10.4	$3.0^{+0.5}_{-0.5}$	0.985	3.00
Average	58.6	5.5	0.86	10.1	3.2	0.973	5
Error	0.2	0.5	0.015	0.4	0.2	0.005	1

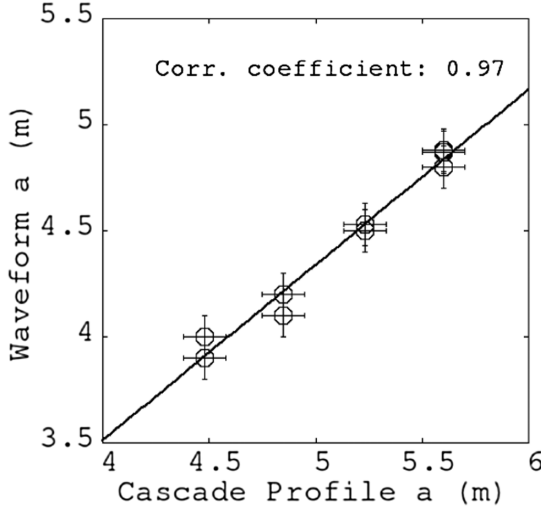


FIG. 11. The longitudinal length parameter a derived from the Eq. (28) best fit versus the a value derived from the cascade profile in NuRadioMC. A linear fit and correlation coefficient are shown (slope: 0.83 ± 0.05 ; intercept: 0.2 ± 0.2 (m); correlation coefficient = 0.97).

is graphed versus the MC-true a value. The a errors in all cases are taken to be ± 10 cm (\pm two Δa step sizes). A least-squares linear fit was applied to the data. The linear function fits the data, and the correlation coefficient is 0.97. The results in Fig. 11 imply an energy reconstruction technique using the formulas found in Sec. III B. Consider the relationship between a and $\ln(E_C/E_{\text{crit}})$: $a = c_1 \sqrt{\ln(E_C/E_{\text{crit}})}$. The fractional error in $\ln(E_C/E_{\text{crit}})$ is proportional to the fractional error in a :

$$\frac{\sigma_{\ln(E_C/E_{\text{crit}})}}{\ln(E_C/E_{\text{crit}})} = 2c_1 \left(\frac{\sigma_a}{a} \right). \quad (42)$$

If a reliable fit for the a parameter is obtained from observed Askaryan waveforms, Eq. (42) shows that the logarithm of the energy can be constrained.

VII. CONCLUSION

We have presented a fully analytic Askaryan model in the time domain, and we have shown that it matches results generated with semianalytic parametrizations used in NuRadioMC. Pearson correlation coefficients between the fully analytic and semianalytic parametrizations were found to be greater than 0.95, and typical fractional differences in total power were found to be $\approx 5\%$. New results and potential applications are summarized in the following sections.

A. Summary of new results

The main results are summarized in Table IX. This work represents the first time the two distinct pole frequencies f_0 and f_C have been used to characterize the time-domain

TABLE IX. Summary of results in this work.

Result	Location
$r\vec{E}(t_r, \theta_C)$, on-cone field ($\hat{\theta}$)	Eq. (15), Sec. IV
$\sigma_t \sigma_\nu \geq 1/(2\pi)$, on-cone	Eq. (20), Sec. IVA
$r\vec{E}(t_r, \theta)$, off-cone field ($\hat{\theta}$)	Eq. (28), Sec. V
$\sigma_t \sigma_\nu \geq 1/(2\pi)$, off-cone	Eq. (31), Sec. VA
On-cone EM comparison to [32]	Fig. 6, Table V
On-cone HAD comparison to [32]	Fig. 8, Table VI
Off-cone EM comparison to [32]	Fig. 9, Table VII
Off-cone HAD comparison to [32]	Fig. 10, Table VIII

field equations of the Askaryan effect for both $\theta = \theta_C$ and $\theta \neq \theta_C$. The uncertainty principle was verified on-cone ($\theta = \theta_C$), serving as a check on the model. By fitting on-cone cascade parameters, we have shown that an analytic model matches semianalytic predictions. The ϵ parameter reveals a potential cascade classification scheme. Next, the off-cone ($\theta \neq \theta_C$) field equations were derived, and again the uncertainty principle was verified. Off-cone cascade parameters were fit, and the results are in excellent agreement with semianalytic results. Fitting a values has revealed a potential energy reconstruction.

To obtain the fields on- and off-cone, $\eta < 1$ was assumed. The restriction $\eta < 1$ means that Eqs. (15) and (28) must be applied to the far field. Given that a and θ_C are fixed by cascade physics and ice density, and that the relevant Askaryan bandwidth for ice is [0.1–1] GHz, the parameter most easily varied within η is the observer distance r . Taking $\nu = 0.5$ GHz, $n = 1.78$, $c = 0.3$ m GHz, $\theta = \theta_C$, and $a = 5$ m, requiring that $\eta = 1$ gives $r \geq 0.4$ km. Scaling to $\nu = 0.25$ GHz gives $r \geq 0.2$ km. According to NuRadioMC [23] (Fig. 13), the r corresponding to UHE- ν at 10^{18} eV ranges from 0.7–3.2 km, and 0.2 km is rare.

The “acceleration argument” invoked by RB in Ref. [33] states that if $r(t)$ points to the ICD, $r(t)$ must be constant enough to ensure that $\Delta r < \lambda$. Using the law of cosines, with two sides being r and $r + \Delta r$, and a third being a , the criteria that $(a/r)^2 \ll 1$ leads to $|\Delta r| \approx a/n$ which is $\mathcal{O}(2)$ m. When in doubt about usage and event geometry, determining if $(a/r)^2 \ll 1$ is a good check. If the UHE- ν event is a charged-current interaction with an electromagnetic cascade far above the LPM energy for ice, a grows faster than $\sqrt{\ln(E_C/E_{\text{crit}})}$ [20].

B. Utility of the analytic model

There are at least four advantages of fully analytic Askaryan models. First, when analytic models are matched to observed data, cascade properties may be derived directly from the waveforms. Second, in large-scale simulations, evaluating a fully analytic model technically provides a speed advantage over other approaches. Third, fully analytic models, combined with RF channel

response, can be embedded in firmware to form a *matched filter* that enhances UHE- ν detection probability. Fourth, parameters in analytic models may be *scaled* to produce results that apply to media of different density than ice. This application is useful for understanding potential signals in the Antarctic firn, or the upper layer of snow and ice that is of lower density than the solid ice beneath it.

The ability to fit cascade properties from waveforms will be a useful tool for the radio component of IceCube-Gen2. Examples of current reconstruction techniques include the forward-folding method [25] and information field theory [26]. In particular, the longitudinal length parameter a leads to a reconstruction of $\ln(E_C)$, given knowledge of $\Delta\theta$ [Fig. 11 and Eq. (42)]. Further, all designs for detector stations in IceCube-Gen2 radio include many distinct RF channels and one phased array of channels. Matching our analytic model to each channel waveform will provide a separate measurement of parameters like a and θ (see gray contours of Figs. 4 and 5). The ensuing global fit should constrain the event energy and geometry.

The most intriguing usage for a fully analytic Askaryan model would be to embed the model as a *matched filter* in detector firmware. Because cascade properties are unknown *a priori*, an array of matched filters could be implemented to form a *matched filter bank*. One example of this approach was the TARA experiment [41], which was designed to detect low-SNR cosmic ray radar echoes. This is similar to the challenge faced by the radio component of the IceCube Gen2 detector: pushing the limit of low-SNR RF pulse detection in a remote setting. For example, a matched filter bank could be formed with an array of off-cone field formulas with fixed a value and varying θ values, which would then be convolved with the RF channel impulse response (see Sec. 6 of Ref. [27]).

Finally, a fully analytic model enhances the ability of IceCube-Gen2 radio to identify signals that originate in the firn. At the South Pole, the RF index of refraction begins around 1.35 and does not reach the solid ice value of 1.78 until 150–200 meters [28]. There are at least two signals that could originate in the firn: UHE- ν events that create Askaryan radiation, and UHE cosmic-ray cascades partially inside or fully inside the firn. The altitude of the South Pole makes the latter possible. The Askaryan radiation of the firn UHE- ν events could be modeled via appropriate density scaling of the cascade parameters.

ACKNOWLEDGMENTS

We would like to thank our colleagues for helpful discussions regarding analysis techniques. In particular, we want to thank Profs. Steve Barwick, Dave Besson, and Christian Glaser for useful discussions. Finally, we would like to thank the Whittier College Fellowships Committee, and specifically the Fletcher-Jones Fellowship Program for providing financial support for this work. This work was

partially funded by the Fletcher-Jones Summer Fellowship of 2020, Whittier College Fellowships program.

APPENDIX A: DETAILS OF THE ON-CONE FIELD EQUATION DERIVATION

The original equations for the $\hat{\theta}$ component of $\vec{\mathcal{E}}$ are

$$\mathcal{W}(\eta, \theta) = \frac{\exp(-\frac{1}{2}(ka)^2 \frac{(\cos \theta - \cos \theta_C)^2}{1-i\eta})}{(1 - i\eta(1 - 3i\eta \frac{\cos \theta \cos \theta - \cos \theta_C}{\sin^2 \theta}))^{1/2}}, \quad (\text{A1})$$

$$\vec{\mathcal{E}}(\eta, \theta) \cdot \hat{\theta} = \mathcal{W}(\eta, \theta) \left(1 - i\eta \frac{\cos \theta_C \cos \theta - \cos \theta_C}{\sin^2 \theta} \right). \quad (\text{A2})$$

Letting $\theta = \theta_C$ yields

$$\vec{\mathcal{E}}(\eta, \theta) \cdot \hat{\theta} = \frac{1}{\sqrt{1 - i\eta}}. \quad (\text{A3})$$

The complete field from the original RB model [33], including the form factor \tilde{F} , $\psi = -i \exp(ikr) \sin \theta$, and $\vec{\mathcal{E}}$ is

$$r\vec{E}(\omega, \theta) = E_0 \left(\frac{\omega}{2\pi} \right) \psi \vec{\mathcal{E}}(\eta, \theta) \tilde{F}. \quad (\text{A4})$$

Take Eq. 6 for the form factor \tilde{F} . Let E_0 be proportional to cascade energy E_c and let $\theta = \theta_C$:

$$r\tilde{E}(\omega, \theta_C) = \frac{(-i\omega)E_0 \sin(\theta_C) e^{i\omega r/c}}{(1 - i\omega/\omega_C)^{1/2} (1 + (\omega/\omega_{CF})^2)^{3/2}}. \quad (\text{A5})$$

Suppose $\omega < \omega_C$, and $\omega < \omega_{CF}$, such that the following approximations of the factors in the denominator are valid:

$$(1 - i\omega/\omega_C)^{1/2} \approx 1 - \frac{i}{2} \frac{\omega}{\omega_C}, \quad (\text{A6})$$

$$(1 + (\omega/\omega_{CF})^2)^{3/2} \approx 1 + \frac{3}{2} \left(\frac{\omega}{\omega_{CF}} \right)^2. \quad (\text{A7})$$

Using the approximations introduces simple poles into the complex formula for the frequency-dependent electric field. Inserting the approximations in the denominator of Eq. (A5), we have

$$r\tilde{E}(\omega, \theta_C) = \frac{(-i\omega)E_0 \sin(\theta_C) e^{i\omega r/c}}{(1 - \frac{i}{2}\omega/\omega_C)(1 + \frac{3}{2}(\omega/\omega_{CF})^2)}. \quad (\text{A8})$$

The denominator can be rearranged by factoring the ω coefficients, and defining $\omega_0 = \sqrt{\frac{2}{3}}\omega_{CF}$:

$$r\tilde{E}(\omega, \theta_C) = \frac{2i\omega_C\omega_0^2(-i\omega)E_0 \sin(\theta_C)e^{i\omega r/c}}{(2i\omega_C + \omega)(\omega + i\omega_0)(\omega - i\omega_0)}. \quad (\text{A9})$$

Let $\hat{E}_0 = E_0 \sin(\theta_C)$, and let the retarded time be $t_r = t - r/c$. Taking the *inverse* Fourier transform, using the same sign convention as RB [33] [$f(t) = (2\pi)^{-1} \int_{-\infty}^{\infty} \tilde{F}(\omega) e^{-i\omega t} d\omega$], converts the field to the time domain:

$$\begin{aligned} rE(t, \theta_C) &= \frac{\hat{E}_0 i\omega_C \omega_0^2}{\pi} \frac{d}{dt_r} \int_{-\infty}^{\infty} \frac{e^{-i\omega t_r}}{(2i\omega_C + \omega)(\omega + i\omega_0)(\omega - i\omega_0)} d\omega. \\ &\quad (\text{A10}) \end{aligned}$$

- (1) If $t_r > 0$: Consider the contour comprised of the real axis and the clockwise-oriented negative infinite semicircle. On the contour, the exponential phase factor in Eq. (A10) goes as

$$\exp(-i\omega t_r) = \exp(-i(R \cos \phi + iR \sin \phi)t_r). \quad (\text{A11})$$

For the semicircle, $\phi \in [\pi, 2\pi]$, so $\sin \phi < 0$ and $t_r > 0$. Exponential decay occurs and the integrand vanishes on the semicircle for $|\omega| = R \rightarrow \infty$.

- (2) If $t_r < 0$: Consider the contour comprised of the real axis and the counterclockwise-oriented positive infinite semicircle. On the contour, the exponential phase factor in Eq. (A10) goes again as

$$\exp(-i\omega t_r) = \exp(-i(R \cos \phi + iR \sin \phi)t_r). \quad (\text{A12})$$

For the semicircle, $\phi \in [0, \pi]$, so $\sin \phi > 0$ and $t_r < 0$. Exponential decay occurs and the integrand vanishes on the semicircle for $|\omega| = R \rightarrow \infty$.

Using cases 1 and 2, Eq. (A10) can be solved using the Cauchy integral formula. Beginning with $t_r > 0$, two poles are enclosed in the semicircle: one that originated from the coherence cutoff frequency, and the other that originated from the form factor. The Cauchy integral formula yields

$$\begin{aligned} rE(t, \theta_C) &= 2\hat{E}_0 \omega_C \omega_0^2 \frac{d}{dt_r} \left(\frac{e^{-2\omega_C t_r}}{i^2(-2\omega_C + \omega_0)(-2\omega_C - \omega_0)} \right. \\ &\quad \left. + \frac{e^{-\omega_0 t_r}}{i^2(-\omega_0 + 2\omega_C)(-2\omega_0)} \right). \quad (\text{A13}) \end{aligned}$$

Define the ratio of the cutoff frequencies: $\epsilon = \omega_0/\omega_C$. After evaluating the time derivatives, Eq. (A13) becomes

$$rE(t, \theta_C) = \hat{E}_0 \omega_0^2 \left(\frac{e^{-2\omega_C t_r}}{(1 - \frac{\epsilon}{2})(1 + \frac{\epsilon}{2})} - \frac{e^{-\omega_0 t_r}}{(2)(1 - \frac{\epsilon}{2})} \right). \quad (\text{A14})$$

Expanding to linear order in ϵ , assuming $\epsilon < 1$, and recalling that $\omega_0^2 = \frac{2}{3}\omega_{\text{CF}}^2$,

$$rE(t, \theta_C) \approx \frac{1}{3} \hat{E}_0 \omega_{\text{CF}}^2 \left(2e^{-2\omega_C t_r} - \left(1 + \frac{\epsilon}{2} \right) e^{-\omega_0 t_r} \right). \quad (\text{A15})$$

Turning to the case of $t_r < 0$, consider integrating Eq. (A10) along the contour comprised of the real axis and the counterclockwise-oriented positive infinite semicircle. The contour encloses one pole, and the exponent ensures convergence:

$$rE(t, \theta_C) = (2\pi i) \hat{E}_0 (\pi)^{-1} i\omega_C \omega_0^2 \frac{d}{dt_r} \left(\frac{e^{\omega_0 t_r}}{(2i\omega_C + i\omega_0)(2i\omega_0)} \right). \quad (\text{A16})$$

After evaluating the derivative, the expression simplifies with $\epsilon = \omega_0/\omega_C$:

$$rE(t, \theta_C) = \frac{1}{2} \hat{E}_0 \omega_0^2 \left(\frac{e^{\omega_0 t_r}}{1 + \frac{1}{2}\epsilon} \right). \quad (\text{A17})$$

Finally, using the same first-order approximation in ϵ as the $t_r > 0$ case,

$$rE(t, \theta_C) \approx \frac{1}{3} \hat{E}_0 \omega_{\text{CF}}^2 \left(1 - \frac{1}{2}\epsilon \right) e^{\omega_0 t_r}. \quad (\text{A18})$$

Collecting the $t_r > 0$ and $t_r < 0$ results together,

$$rE(t, \theta_C) = \frac{1}{3} \hat{E}_0 \omega_{\text{CF}}^2 \begin{cases} (1 - \frac{1}{2}\epsilon) e^{\omega_0 t_r}, & t_r < 0, \\ (2e^{-2\omega_C t_r} - (1 + \frac{1}{2}\epsilon) e^{-\omega_0 t_r}), & t_r > 0. \end{cases} \quad (\text{A19})$$

APPENDIX B: DETAILS OF THE OFF-CONE FIELD EQUATION DERIVATION

Using Tables II–IV, Eq. (A2) reduces to

$$\mathcal{E}(u, x) = f(u, x)g(u, x)(1 - h(u, x)). \quad (\text{B1})$$

Expanding to first order with respect to u near ($u = 1$) gives

$$\mathcal{E}(u, x) = \mathcal{E}(x, 1) + (u - 1)\dot{\mathcal{E}}(x, 1) + \mathcal{O}(u - 1)^2. \quad (\text{B2})$$

The first term is $fg(1 - h)$ evaluated at $u = 1$: $\exp(-y)$ (Table IV). The second term requires the first derivative of $\mathcal{E}(u, x)$ with respect to u , evaluated at $u = 1$:

$$\dot{\mathcal{E}}(u, x) = f\dot{g} + \dot{f}g - (fgh + f\dot{g}h + \dot{f}gh) \quad (\text{B3})$$

$$\dot{\mathcal{E}}(1, x) = (f\dot{g} + \dot{f}g - (fgh + f\dot{g}h + \dot{f}gh))|_{u=1} \quad (\text{B4})$$

The first derivatives of f , g , and h , evaluated at $u = 1$, are given in Table IV. Because $h(x, 1) = 0$, terms proportional to h will vanish. The result is

$$\dot{\mathcal{E}}(1, x) = \frac{1}{2} e^{-y} (2y + 2q - 1). \quad (\text{B5})$$

Inserting Eq. (B5) into Eq. (B2),

$$\mathcal{E}(u, x) = e^{-y} \left(1 + \frac{1}{2} (u - 1)(2y + 2q - 1) \right). \quad (\text{B6})$$

Using the definition of u (Table II), the result may be written as

$$\mathcal{E}(u, x) = e^{-y} \left(1 - \frac{1}{2} j\eta (2y + 2q - 1) \right). \quad (\text{B7})$$

Proceeding with the inverse Fourier transform of the $\hat{\theta}$ component,

$$rE(t, \theta) = \mathcal{F}^{-1} \left\{ E_0 \left(\frac{\omega}{2\pi} \right) \tilde{F} \psi \mathcal{E} \right\}. \quad (\text{B8})$$

Let $\eta = \omega/\omega_C$, $y = p\omega^2$ (Table II). Inserting the Taylor series for \mathcal{E} , the form factor \tilde{F} , and $\psi = -i \exp(ikr) \sin \theta$ (Sec. II), and following the same steps as the on-cone case produces

$$\begin{aligned} 2\pi rE(t, \theta) &= \frac{E_0 \omega_0^2 \sin(\theta)}{4\pi i \omega_C} \\ &\times \frac{d}{dt_r} \int_{-\infty}^{\infty} \frac{e^{-i\omega t_r - p\omega^2} (2i\omega_C + 2p\omega^3 + (2q - 1)\omega)}{\omega^2 + \omega_0^2} d\omega. \end{aligned} \quad (\text{B9})$$

Unlike the on-cone case, Eq. (B9) cannot be integrated with infinite semicircle contours, because the exponential term diverges along the imaginary axis far from the origin.

Let I_0 represent the constant term with respect to ω in the numerator:

$$I_0 = \int_{-\infty}^{\infty} \frac{e^{-i\omega t_r - p\omega^2} (2i\omega_C)}{\omega^2 + \omega_0^2} d\omega. \quad (\text{B10})$$

Further, let I_1 and I_3 represent the linear and cubic terms, respectively. Completing the square in the exponent of I_0 , with $\omega_1 = t_r/(2p)$, yields

$$I_0 = 2i\omega_C e^{-\frac{t_r^2}{4p}} \int_{-\infty}^{\infty} \frac{e^{-p(\omega + i\omega_1)^2}}{\omega^2 + \omega_0^2} d\omega. \quad (\text{B11})$$

Equation (B11) may be recast as the *line-broadening function*, H (DLMF 7.19, [39]) common to spectroscopy applications:

$$I_0 = 2\pi i \left(\frac{\omega_C}{\omega_0} \right) e^{-\frac{t_r^2}{4p}} H(\sqrt{p}\omega_0, i\sqrt{p}\omega_1). \quad (\text{B12})$$

Assume that $\omega > \omega_1$. This approximating step will be called the *symmetric approximation*:

$$I_0 \approx 2i\omega_C e^{-\frac{t_r^2}{2p}} \int_{-\infty}^{\infty} \frac{e^{-p\omega^2}}{\omega^2 + \omega_0^2} d\omega. \quad (\text{B13})$$

The result for I_0 involves the complementary error function (DLMF 7.7.1, [39]):

$$I_0 = 2i\omega_C e^{-\frac{t_r^2}{2p}} \pi \omega_0^{-1} e^{p\omega_0^2} \operatorname{erfc}(\sqrt{p}\omega_0). \quad (\text{B14})$$

The integrals I_1 and I_3 are zero by symmetry, with odd integrands over $(-\infty, \infty)$. Inserting the result for I_0 into Eq. (B9) and evaluating the derivative finishes the problem (see Sec. V).

-
- [1] The IceCube Collaboration, Evidence for high-energy extraterrestrial neutrinos at the IceCube detector, *Science* **342**, 1242856 (2013).
 - [2] M. Ahlers, L. Anchordoqui, M. Gonzalez-Garcia, F. Halzen, and S. Sarkar, GZK neutrinos after the Fermi-LAT diffuse photon flux measurement, *Astropart. Phys.* **34**, 106 (2010).
 - [3] K. Kotera, D. Allard, and A. Olinto, Cosmogenic neutrinos: Parameter space and detectability from PeV to ZeV, *J. Cosmol. Astropart. Phys.* **10** (2010) 013.
 - [4] The IceCube Collaboration, Differential limit on the extremely-high-energy cosmic neutrino flux in the presence of astrophysical background from nine years of IceCube data, *Phys. Rev. D* **98**, 062003 (2018).
 - [5] The ARIANNA Collaboration, A search for cosmogenic neutrinos with the ARIANNA test bed using 4.5 years of data, *J. Cosmol. Astropart. Phys.* **03** (2020) 053.
 - [6] The ARA Collaboration, Constraints on the diffuse flux of ultrahigh energy neutrinos from four years of Askaryan Radio Array data in two stations, *Phys. Rev. D* **102**, 043021 (2020).
 - [7] M. Ackermann *et al.*, Astrophysics uniquely enabled by observations of high-energy cosmic neutrinos, *Bull. Am. Astron. Soc.* **51**, 185 (2019).
 - [8] M. Ackermann *et al.*, Fundamental physics with high-energy cosmic neutrinos, *Bull. Am. Astron. Soc.* **51**, 215 (2019).

- [9] J. C. Hanson *et al.*, Radar absorption, basal reflection, thickness and polarization measurements from the Ross Ice Shelf, Antarctica, *J. Glaciol.* **61**, 438 (2015).
- [10] J. Avva, J. Kovac, C. Miki, D. Saltzberg, and A. Vieregg, An in situ measurement of the radio-frequency attenuation in ice at Summit Station, Greenland, *J. Glaciol.* **61**, 1005 (2015).
- [11] The ARA Collaboration, Design and initial performance of the Askaryan Radio Array prototype EeV neutrino detector at the south pole, *Astropart. Phys.* **35**, 457 (2012).
- [12] G. Askaryan, On the coherent emission of radio frequency radiation from high energy particle showers, Sov. Phys. JETP **15** (1962).
- [13] E. Zas, F. Halzen, and T. Stanev, Electromagnetic pulses from high-energy showers: Implications for neutrino detection, *Phys. Rev. D* **45**, 362 (1992).
- [14] I. Kravchenko, S. Hussain, D. Seckel, D. Besson, E. Fensholt, J. Ralston, J. Taylor, K. Ratzlaff, and R. Young, Updated results from the RICE experiment and future prospects for ultra-high energy neutrino detection at the south pole, *Phys. Rev. D* **85**, 062004 (2012).
- [15] The ANITA Collaboration, Constraints on the ultrahigh-energy cosmic neutrino flux from the fourth flight of ANITA, *Phys. Rev. D* **99**, 122001 (2019).
- [16] D. Saltzberg, P. Gorham, D. Walz, C. Field, R. Iverson, A. Odian, G. Resch, P. Schoessow, and D. Williams, Observation of the Askaryan Effect: Coherent Microwave Cherenkov Emission from Charge Asymmetry in High-Energy Particle Cascades, *Phys. Rev. Lett.* **86**, 2802 (2001).
- [17] P. Miocinovic, R. Field, P. Gorham, E. Guillian, R. Milincic, D. Saltzberg, D. Walz, and D. Williams, Time-domain measurement of broadband coherent Cherenkov radiation, *Phys. Rev. D* **74**, 043002 (2006).
- [18] P. W. Gorham, S. W. Barwick, J. J. Beatty, D. Z. Besson, W. R. Binns, C. Chen, P. Chen, J. M. Clem, A. Connolly, P. F. Dowkontt *et al.* (ANITA Collaboration), Observations of the Askaryan Effect in Ice, *Phys. Rev. Lett.* **99**, 171101 (2007).
- [19] J. Alvarez-Muñiz, C. James, R. Protheroe, and E. Zas, Thinned simulations of extremely energetic showers in dense media for radio applications, *Astropart. Phys.* **32**, 100 (2009).
- [20] L. Gerhardt and S. R. Klein, Electron and photon interactions in the regime of strong Landau-Pomeranchuk-Migdal suppression, *Phys. Rev. D* **82** (2010).
- [21] K. Dookayka, Characterizing the search for ultra-high energy neutrinos with the ARIANNA detector, Ph.D. thesis, University of California, Irvine, 2011.
- [22] The ARA Collaboration, First constraints on the ultra-high energy neutrino flux from a prototype station of the Askaryan Radio Array, *Astropart. Phys.* **70**, 62 (2015).
- [23] C. Glaser *et al.*, NuRadioMC: Simulating the radio emission of neutrinos from interaction to detector, *Eur. Phys. J. C* **80**, 77 (2020).
- [24] C. Glaser, A. Nelles, I. Plaisier, C. Welling, S. W. Barwick, D. García-Fernández, G. Gaswint, R. Lahmann, and C. Persichilli, NuRadioReco: A reconstruction framework for radio neutrino detectors, *Eur. Phys. J. C* **79**, 464 (2019).
- [25] The ARIANNA Collaboration, Probing the angular and polarization reconstruction of the ARIANNA detector at the south pole, *J. Instrum.* **15**, P09039 (2020).
- [26] C. Welling, P. Frank, T. A. Enßlin, and A. Nelles, Reconstructing non-repeating radio pulses with information field theory, *J. Cosmol. Astropart. Phys.* **04** (2021) 071.
- [27] J. C. Hanson *et al.*, Time-domain response of the ARIANNA detector, *Astropart. Phys.* **62**, 139 (2015).
- [28] The ARIANNA Collaboration, Observation of classically ‘forbidden’ electromagnetic wave propagation and implications for neutrino detection, *J. Cosmol. Astropart. Phys.* **07** (2018) 055.
- [29] The ARA Collaboration, Measurement of the real dielectric permittivity ϵ_r of glacial ice, *Astropart. Phys.* **108**, 63 (2019).
- [30] S. Barwick, E. Berg, D. Besson, G. Binder, W. Binns, D. Boersma, R. Bose, D. Braun, J. Buckley, V. Bugaev *et al.*, A first search for cosmogenic neutrinos with the ARIANNA Hexagonal Radio Array, *Astropart. Phys.* **70**, 12 (2015).
- [31] J. Alvarez-Muniz, A. Romero-Wolf, and E. Zas, Practical and accurate calculations of Askaryan radiation, *Phys. Rev. D* **84**, 103003 (2011).
- [32] J. Alvarez-Muniz, P. M. Hansen, A. Romero-Wolf, and E. Zas, Askaryan radiation from neutrino-induced showers in ice, *Phys. Rev. D* **101**, 083005 (2020).
- [33] R. V. Buniy and J. P. Ralston, Radio detection of high energy particles: Coherence versus multiple scales, *Phys. Rev. D* **65** (2001).
- [34] J. C. Hanson and A. L. Connolly, Complex analysis of Askaryan radiation: A fully analytic treatment including the LPM effect and cascade form factor, *Astropart. Phys.* **91**, 75 (2017).
- [35] V. Bogorodsky, C. Bentley, and P. Gudmandsen, *Radio-glaciology* (Springer, Netherlands, 1985).
- [36] S. Razzaque, S. Seunarine, D. Z. Besson, D. W. McKay, J. P. Ralston, and D. Seckel, Coherent radio pulses from GEANT generated electromagnetic showers in ice, *Phys. Rev. D* **65**, 103002 (2002).
- [37] S. Andringa, R. Conceição, and M. Pimenta, Mass composition and cross-section from the shape of cosmic ray shower longitudinal profiles, *Astropart. Phys.* **34**, 360 (2011).
- [38] K. F. Fadhel, A. Al-Rubaiee, H. A. Jassim, and I. T. Al-Alawy, Estimating the lateral distribution of high energy cosmic ray particles by depending on Nishimura-Kamata-Greisen function, *J. Phys.* **1879**, 032089 (2021).
- [39] DLMF, *NIST Digital Library of Mathematical Functions*, <http://dlmf.nist.gov/>, Release 1.1.1 of 2021-03-15, edited by f. W. J. Olver, A. B. Olde Daalhuis, D. W. Lozier, B. I. Schneider, R. F. Boisvert, C. W. Clark, B. R. Miller, B. V. Saunders, H. S. Cohl, and M. A. McClain, <http://dlmf.nist.gov/>.
- [40] T. T. García, Voigt profile fitting to quasar absorption lines: An analytic approximation to the Voigt–Hjerting function, *Mon. Not. R. Astron. Soc.* **369**, 2025 (2006).
- [41] The Telescope Array Collaboration, First upper limits on the radar cross section of cosmic-ray induced extensive air showers, *Astropart. Phys.* **87**, 1 (2017).

In situ, broadband measurement of the radio frequency attenuation length at Summit Station, Greenland

J. A. Aguilar¹, P. Allison², J. J. Beatty², D. Besson^{3,4}, A. Bishop⁵, O. Botner⁶, S. Bouma⁷, S. Buitink⁸, M. Cataldo⁷, B. A. Clark⁹, Z. Curtis-Ginsberg¹⁰, A. Connolly², P. Dasgupta¹, S. de Kockere¹¹, K. D. de Vries¹¹, C. Deaconu¹⁰, M. A. DuVernois⁵, C. Glaser⁶, A. Hallgren⁶, S. Hallmann¹², J. C. Hanson¹³, B. Hendricks¹⁴, C. Hornhuber³, K. Hughes¹⁰, A. Karle⁵, J. L. Kelley⁵, I. Kravchenko¹⁵, R. Krebs¹⁴, R. Lahmann⁷, U. Latif¹¹, J. Mammo¹⁵, Z. S. Meyers^{12,7}, K. Michaels¹⁰, K. Mulrey¹⁶, A. Nelles^{12,7}, A. Novikov³, A. Nozdrina³, E. Oberla¹⁰, B. Oeyen¹⁷, Y. Pan¹⁸, H. Pandya⁸, I. Plaisier^{7,12}, N. Punzuebsay¹⁸, L. Pyras^{12,7}, D. Ryckbosch¹⁷, O. Scholten^{11,19}, D. Seckel¹⁸, M. F. H. Seikh³, D. Smith^{*10}, D. Southall¹⁰, J. Torres², S. Toscano¹, D. Tosi⁵, D. J. Van Den Broeck^{11,8}, N. van Eijndhoven¹¹, A. G. Vieregg¹⁰, C. Welling^{7,12}, D. R. Williams²⁰, S. Wissel^{14,21}, R. Young³, A. Zink⁷

¹Université Libre de Bruxelles, Science Faculty CP230, B-1050 Brussels, Belgium

²Dept. of Physics, Center for Cosmology and AstroParticle Physics, Ohio State University, Columbus, OH 43210, USA

³University of Kansas, Dept. of Physics and Astronomy, Lawrence, KS 66045, USA

⁴National Nuclear Research University MEPhI, Kashirskoe Shosse 31, 115409, Moscow, Russia

⁵Wisconsin IceCube Particle Astrophysics Center (WIPAC) and Dept. of Physics,
University of Wisconsin-Madison, Madison, WI 53703, USA

⁶Uppsala University, Dept. of Physics and Astronomy, Uppsala, SE-752 37, Sweden

⁷Erlangen Center for Astroparticle Physics (ECAP),

Friedrich-Alexander-University Erlangen-Nuremberg, 91058 Erlangen, Germany

⁸Vrije Universiteit Brussel, Astrophysical Institute, Pleinlaan 2, 1050 Brussels, Belgium

⁹Dept. of Physics and Astronomy, Michigan State University, East Lansing MI 48824, USA

¹⁰Dept. of Physics, Enrico Fermi Inst., Kavli Inst. for Cosmological Physics, University of Chicago, Chicago, IL 60637, USA

¹¹Vrije Universiteit Brussel, Dienst ELEM, B-1050 Brussels, Belgium

¹²DESY, Platanenallee 6, 15738 Zeuthen, Germany

¹³Whittier College, Whittier, CA 90602, USA

¹⁴Dept. of Physics, Dept. of Astronomy & Astrophysics, Penn State University, University Park, PA 16801, USA

¹⁵Dept. of Physics and Astronomy, Univ. of Nebraska-Lincoln, NE, 68588, USA

¹⁶Department of Astrophysics/IMAPP, Radboud University, PO Box 9010, 6500 GL, The Netherlands

¹⁷Ghent University, Dept. of Physics and Astronomy, B-9000 Gent, Belgium

¹⁸Dept. of Physics and Astronomy, University of Delaware, Newark, DE 19716, USA

¹⁹Kapteijn Institute, University of Groningen, Groningen, The Netherlands

²⁰Dept. of Physics and Astronomy, University of Alabama, Tuscaloosa, AL 35487, USA

²¹Physics Dept. California Polytechnic State University, San Luis Obispo CA 93407, USA

ABSTRACT. Over the last 25 years, radiowave detection of neutrino-generated signals, using cold polar ice as the neutrino target, has emerged as perhaps the most promising technique for detection of extragalactic ultra-high energy neutrinos (corresponding to neutrino energies in excess of 0.01 Joules, or 10^{17} electron volts). During the summer of 2021 and in tandem with the initial deployment of the Radio Neutrino Observatory in Greenland (RNO-G), we conducted radioglaciological measurements at Summit Station, Greenland to refine our understanding of the ice target. We report the result of one such measurement, the radio-frequency electric field attenuation length L_α . We find an approximately linear dependence of L_α on frequency with the best fit of the average field attenuation for the upper 1500 m of ice: $\langle L_\alpha \rangle = ((1024 \pm 50) - (0.65 \pm 0.06)(\nu/\text{MHz})) \text{ m}$ for frequencies $\nu \in [145 - 350] \text{ MHz}$.

Article

Broadband RF Phased Array Design with MEEP: Comparisons to Array Theory in Two and Three Dimensions

Jordan C. Hanson

Science & Learning Center, Whittier College, Whittier, CA 90602, USA; jhanson2@whittier.edu

Abstract: Phased array radar systems have a wide variety of applications in engineering and physics research. Phased array design usually requires numerical modeling with expensive commercial computational packages. Using the open-source MIT Electromagnetic Equation Propagation (MEEP) package, a set of phased array designs is presented. Specifically, one and two-dimensional arrays of Yagi-Uda and horn antennas were modeled in the bandwidth [0.1–5] GHz, and compared to theoretical expectations in the far-field. Precise matches between MEEP simulation and radiation pattern predictions at different frequencies and beam angles are demonstrated. Given that the computations match the theory, the effect of embedding a phased array within a medium of varying index of refraction is then computed. Understanding the effect of varying index on phased arrays is critical for proposed ultra-high energy neutrino observatories which rely on phased array detectors embedded in natural ice. Future work will develop the phased array concepts with parallel MEEP, in order to increase the detail, complexity, and speed of the computations.

Keywords: FDTD methods; MEEP; phased array antennas; antenna theory; Askaryan effect; UHE neutrinos



Citation: Hanson, J.C. Broadband RF Phased Array Design with MEEP: Comparisons to Array Theory in Two and Three Dimensions. *Electronics* **2021**, *10*, 415. <https://doi.org/10.3390/electronics10040415>

Academic Editor: Hirokazu Kobayashi

Received: 28 December 2020

Accepted: 27 January 2021

Published: 8 February 2021

Publisher's Note: MDPI stays neutral with regard to jurisdictional claims in published maps and institutional affiliations.



Copyright: © 2021 by the authors. Licensee MDPI, Basel, Switzerland. This article is an open access article distributed under the terms and conditions of the Creative Commons Attribution (CC BY) license (<https://creativecommons.org/licenses/by/4.0/>).

1. Introduction

Radio-frequency phased array antenna systems with design frequencies of order 0.1–10 GHz have applications in 5G mobile telecommunications, ground penetrating radar (GPR) systems, and scientific instrumentation [1–4]. In the one-dimensional case, a series of three-dimensional antenna elements are arranged in a line with fixed spacing [5]. Common antenna designs like loops and dipoles can be used to limit the *elements* to two dimensions. In this special case, phased array radiation may be modeled in two spatial dimensions plus time. In the two-dimensional case, a series of three-dimensional antenna elements are arranged in a two-dimensional pattern, often a grid with fixed element spacing in both dimensions. The elements may be strictly two-dimensional, but there is still an increase in computational complexity and the radiation is calculated in three dimensions plus time.

Proprietary RF modeling packages like XFDTD and HFSS are often used to model the response of elements within phased arrays and the behavior of arrays [6–9]. The XFDTD package, for example, relies on the finite difference time domain (FDTD) method. The FDTD approach is a computational electromagnetics (CEM) technique in which spacetime and Maxwell's equations are broken into discrete form. One variant of the FDTD method is the conformal FDTD method (CFDTD), recently used to study phased array concepts on a large scale [9]. The NEC2 and NEC4 family of codes relies on the method-of-moments (MoM) approach [10]. Aside from the cost, a drawback of proprietary modeling software can be a lack of fine control over each individual object in the simulation. Because Maxwell's equations are scale-invariant, in principle open-source FDTD codes designed for optical regimes could be re-purposed for RF design workflows. One such open-source package is the MIT Electromagnetic Equation Propagation (MEEP) package [11].

A recent review [12] covered how open radio design software like openEMS [13], gprMax [14], and the NEC2 family of codes [10] facilitate design workflows. In this work, the radiation patterns of one-dimensional and two-dimensional phased array designs

are simulated with the MEEP package. MEEP takes advantage of the scale-invariance of Maxwell's equations. Common MEEP applications are found in optical wavelength μm -scale designs, but scale-invariance allows the user to treat designs as cm-scale RF elements (see Appendix A for details). Although MEEP has been used to optimize antenna designs [15], this work appears to be the first to model entire phased arrays in MEEP with a variable index of refraction. Two classes of phased array element are considered: Yagi-Uda and horn antennas. The former is applied to single-frequency designs, while the latter is applied to broadband design. Each element class is treated in both the one-dimensional and two-dimensional cases. The phase-steering properties and radiation patterns of all designs are shown to match theoretical predictions. The appropriate array theory is shown in Section 2, based on Chapter 1 of Reference [16]. Section 3 contains comparisons between theory and simulation for one-dimensional cases, and Section 4 contains the corresponding two-dimensional comparisons. In Section 5, the varying index of refraction is introduced. Results and future work are summarized in Section 6.

A workflow using MEEP for phased array design is outlined in Figure 1 based on Figure 1 from Reference [12]. Examples of decisions within the *specifications* category are: single-frequency or broadband, desired directivity and beamwidth, side-lobe tolerance, and number of antenna elements. These decisions lead to the choice of element type which must be implemented in MEEP. Simple shapes like dipoles can be modeled with built-in MEEP objects. Complex shapes like horns and dishes can be assembled from groups of objects. Radiation sources and current functions must be defined. For these studies, pure sinusoidal currents are passed to radiators which in turn radiate sinusoidal fields. The dielectric constant and boundary conditions of the simulation volume and objects within the volume are defined in the next step. The information is loaded into a simulation object and run for a number of time-steps. Once complete, near-to-far field routines are called to produce the power at a set of angles. The power versus angle is converted to normalized E and H-plane array radiation patterns and compared to theoretical models. Given a match, the frequency is updated and the process is repeated. If there is not a match, element separation and other array parameters are adjusted.

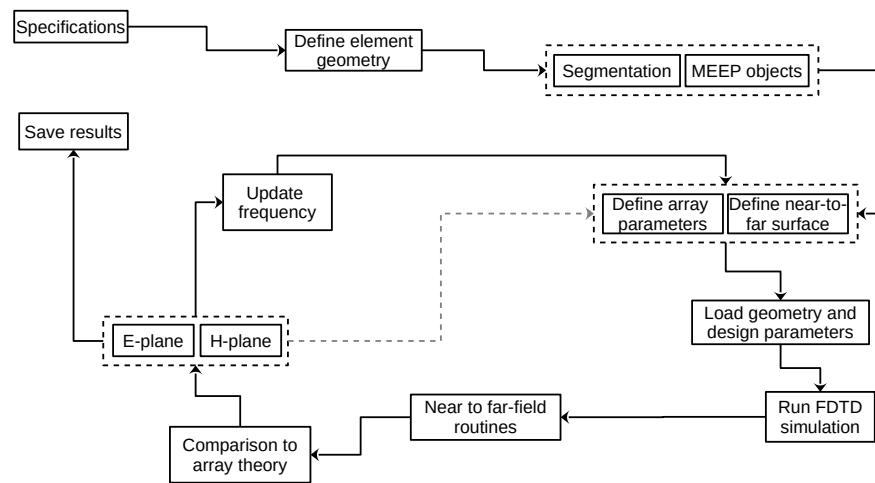


Figure 1. A detailed workflow for phased array design with MEEP. See text for details.

The workflow in Figure 1 represents a non-parallelized approach. Much development has gone into enhancing the speed, accuracy, and utility of the FDTD method. First, MEEP itself may be run in parallel mode, providing a speed enhancement. In a high-performance computing (HPC) environment, where each node has allocated memory (implying local RAM is not the limiting factor) running MEEP in parallel would speed up results. There has also been CEM research devoted to enhancing the FDTD approach itself. Decreasing

memory usage and avoiding repetitive computations in favor of a more subtle approach is presented in [7]. A three-dimensional implementation of FDTD algorithms on GPUs via CUDA has also been explored [17]. The results of this work were obtained using the simplest version of MEEP: non-parallel with the python3 interface run in Jupyter notebooks on a laptop. Therefore the results shown in Sections 3 and 4 could benefit from speed and memory enhancements in future studies.

2. Phased Array Antenna Theory

The basic structure of a one-dimensional phased array of RF radiating elements is shown in Figure 2. Two important numerical constants that determine the beam angle $\Delta\phi$ of the array are the inter-element spacing d_y and the phase shift per antenna $\Delta\Phi$. Letting the subscript i label each of the N elements, the one-dimensional inter-element spacing in Figure 2 is $d_y \hat{f} = \vec{r}_{i+1} - \vec{r}_i$, where \vec{r}_i records the position of element i . The phase shift per antenna is $\Delta\Phi = \Phi_{i+1} - \Phi_i$. The relationship between d_y , $\Delta\Phi$, and $\Delta\phi$ is derived in Section 2.1. The radiation pattern for a given $\Delta\phi$ is derived in Section 2.2. For all coordinate systems, the azimuthal angle in the xy-plane is ϕ , and the polar angle from the z-axis is θ .

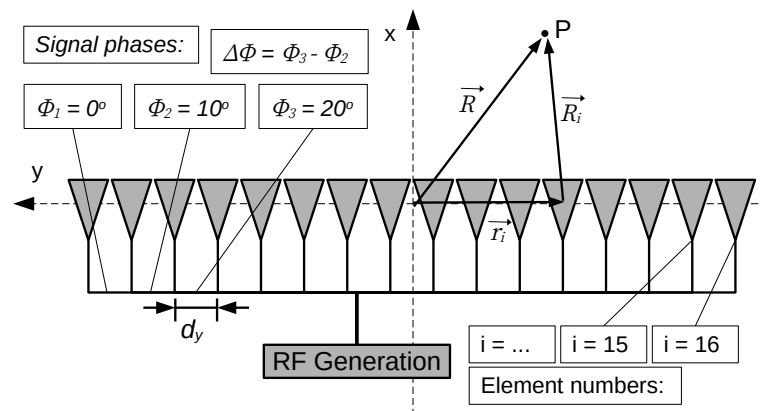


Figure 2. Definitions for the coordinate system, element label i , position vectors, and phase shift per antenna for a one-dimensional phased array of RF radiating elements. An example phase shift per antenna of $\Delta\Phi = \Phi_2 - \Phi_1 = \Phi_3 - \Phi_2 = \Phi_{i+1} - \Phi_i = 10^\circ$ value is shown. Example position vectors for the 12th element are shown: $\vec{R} = \vec{r}_{12} + \vec{R}_{12}$.

2.1. Phase Steering and Beam Angle

The beam angle $\Delta\phi$ of the array given $\Delta\Phi$ and d_y will now be derived for the coordinate system in Figure 2. First, the relevant far-field approximation will be described. Second, it will be assumed that the elements all radiate at the same frequency ω and have the same vector radiation pattern $\vec{f}(\theta, \phi)$ that accounts for co-polarized and cross-polarized radiated power. Third, the \vec{E} -field at point P will be treated as a sum of the \vec{E}_i radiated from each element. Fourth, the calculations will be restricted to the xy-plane and the relationship between the beam angle $\Delta\phi$ and array parameters will be obtained for a one-dimensional array.

According to Figure 2, the position of P can be written

$$\vec{R} = \vec{r}_i + \vec{R}_i \quad (1)$$

Rearranging, the displacement between the i -th element and P is

$$\vec{R}_i = \vec{R} - \vec{r}_i \quad (2)$$

The magnitude of the displacement is

$$R_i = \sqrt{(\vec{R} - \vec{r}_i) \cdot (\vec{R} - \vec{r}_i)} = (R^2 - 2\vec{R} \cdot \vec{r}_i + r_i^2)^{1/2} \quad (3)$$

Factoring an R^2 , and neglecting the third term because it is small compared to the others,

$$R_i \approx R \left(1 - \frac{2\vec{R} \cdot \vec{r}_i}{R^2} \right)^{1/2} \quad (4)$$

Expanding in a Taylor series to first order in $2\vec{R} \cdot \vec{r}_i/R^2$, with $\hat{r} = \vec{R}/R$, yields

$$R_i \approx R \left(1 - \frac{\hat{r} \cdot \vec{r}_i}{R} \right) \quad (5)$$

Distributing the R gives the approximation:

$$R_i \approx R - \hat{r} \cdot \vec{r}_i \quad (6)$$

The electric field at P due to the i -th element with individual radiation pattern $\vec{f}_i(\theta, \phi)$ is

$$\vec{E}_i(R, \theta, \phi) = \frac{\vec{f}_i(\theta, \phi) \exp(-jkR_i)}{R_i} \quad (7)$$

Substituting Equations (6) into (7):

$$\vec{E}_i(R, \theta, \phi) = \vec{f}_i(\theta, \phi) \frac{\exp(-jkR)}{R} \exp(jk\vec{r}_i \cdot \hat{r}) \quad (8)$$

The element positions are written in Cartesian coordinates, while P is written in spherical coordinates using $u = \sin \theta \cos \phi$ and $v = \sin \theta \sin \phi$:

$$\vec{r}_i = \hat{x}x_i + \hat{y}y_i + \hat{z}z_i \quad (9)$$

$$\hat{r} = \hat{x}u + \hat{y}v + \hat{z}\cos \theta \quad (10)$$

The total field \vec{E} at P requires summing over elements. The current delivered to the i -th element could have a potentially complex amplitude a_i . The details of how the currents a_i are converted to radiated \vec{E} -field are taken to be part of $\vec{f}(\theta, \phi)$. The summation for \vec{E} over elements is

$$\vec{E}(R, \theta, \phi) = \frac{\exp(-jkR)}{R} \sum_i a_i \vec{f}_i(\theta, \phi) \exp(jk\vec{r}_i \cdot \hat{r}) \quad (11)$$

For identical radiating elements: $\vec{f}_i = \vec{f}$:

$$\vec{E}(R, \theta, \phi) = \vec{f}(\theta, \phi) \frac{\exp(-jkR)}{R} \sum_i a_i \exp(jk\vec{r}_i \cdot \hat{r}) \quad (12)$$

Define the *array-factor* $F(\theta, \phi) = \sum_i a_i \exp(jk\vec{r}_i \cdot \hat{r})$:

$$\vec{E}(R, \theta, \phi) = \vec{f}(\theta, \phi) \frac{\exp(-jkR)}{R} F(\theta, \phi) \quad (13)$$

Thus, if $F = 1$, then the \vec{E} -field is a plane wave, modified only by the elemental radiation pattern. Complex amplitudes a_i that cause a plane wave with wavevector pointed to (θ_0, ϕ_0) are

$$a_i = |a_i| \exp(-jk\vec{r}_i \cdot \hat{r}_0) \quad (14)$$

The notation for beam angle $\Delta\phi = \phi - \phi_0$ will be introduced shortly. For \hat{r}_0 , u_0 and v_0 take the corresponding θ_0 and ϕ_0 for the angles: $\hat{r}_0 = \hat{x}u_0 + \hat{y}v_0 + \hat{z}\cos \theta_0$. The angles (θ_0, ϕ_0) correspond to the plane wave because the phases in the array factor in Equation (13)

are cancelled by those in Equation (14), and the summation is over just the magnitudes $|a_i|$. For a *linear array* in one-dimension, oriented along the y-axis as shown in Figure 2, $\theta_0 = \pi/2$ and $\vec{r}_i = id_y\hat{y}$:

$$\vec{E}(R, \theta, \phi) = \vec{f}(\theta, \phi) \frac{\exp(-jkR)}{R} \sum_i a_i \exp(jk(id_y v)) \quad (15)$$

The summation is $F(\pi/2, \phi_0)$, $v = \sin(\phi)$ and $v_0 = \sin(\phi_0)$. The weights a_i may be arranged to produce a plane wave at ϕ_0 :

$$a_i = |a_i| \exp(-jki d_y v_0) \quad (16)$$

The i -th phase of \vec{E} in the array factor is

$$\Phi_i = k i d_y (\sin \phi - \sin \phi_0) \quad (17)$$

The difference $\Delta\Phi = \Phi_{i+1} - \Phi_i$ for angles not far from the x-axis, $|\phi| < 1$ and $|\phi_0| < 1$, is

$$\Delta\Phi \approx d_y k (\phi - \phi_0) = 2\pi(d_y/\lambda)(\phi - \phi_0) = 2\pi(d_y/\lambda)\Delta\phi \quad (18)$$

The *beam angle* is $\Delta\phi = \phi - \phi_0$, the angular distance between a reference angle and the angle at which all contributions to \vec{E} are in phase. Equation (18) reveals that the relationship between $\Delta\phi$ and $\Delta\Phi$ is linear, with slope $\lambda/(2\pi d_y)$. In Section 3, the relationship between $\Delta\Phi$ and $\Delta\phi$ obtained from FDTD calculations via MEEP are shown to match precisely the theoretical prediction. For two-dimensional grid arrays, the relationship “factors,” in that phase shift per element row and phase shift per element column govern $\Delta\phi$ and $\Delta\theta$ independently. This theoretical prediction is matched precisely by the FDTD calculations shown in Section 4 as well.

2.2. Radiation Patterns and Beam Width

The radiation pattern, or relative power P emitted versus beam angle, is obtained from the array factor $F(\pi/2, \phi)$ summation. Summation over the phased array with identical elements causes the vector element pattern $\vec{f}(\theta, \phi)$ and the common phase and amplitude factors $\exp(jkR)/R$ to cancel upon normalization. The parameters that characterize the radiation patterns of arrays are N , the number of elements, and d_y/λ . The magnitude of the complex current to each element is assumed to be the same, $|a_i| = a$. Recall the array factor from Equation (13), with $\theta = \pi/2$ and $a_i = a$:

$$F(\phi, \phi_0) = a \sum_i \exp(jk i d_y (v - v_0)) \quad (19)$$

Let $\chi = k d_y (v - v_0)$ so that $z = \exp(j\chi)$. The sum is a geometric series from $i = 1$ to $i = N$, the number of elements:

$$F(z) = a \sum_{i=1}^N z^i = a \left(\frac{1 - z^N}{1 - z} \right) \quad (20)$$

Using the Euler formula for $\sin(\chi)$, the array factor simplifies to

$$F(\chi) = -a \exp(j(N-1)\chi/2) \left(\frac{\sin(N\chi/2)}{\sin(\chi/2)} \right) \quad (21)$$

The radiation pattern is proportional to power, so it is prudent to take the magnitude of $F(\phi)$:

$$|F(\chi)| = a \left(\frac{\sin(N\chi/2)}{\sin(\chi/2)} \right) \quad (22)$$

The normalized radiation pattern will be $(F/F_{max})^2$, so it is necessary to find F_{max} :

$$\lim_{\chi \rightarrow 0} |F(\chi)| = a \lim_{\chi \rightarrow 0} \left(\frac{\sin(N\chi/2)}{\sin(\chi/2)} \right) = aN \quad (23)$$

So $|F(\chi)|/F_{max}$ is

$$\frac{F(\chi)}{F_{max}} = \frac{\sin(N\chi/2)}{N \sin(\chi/2)} \quad (24)$$

Finally, with $\chi = kd_y(v - v_0)$, $v = \sin(\phi)$, and $v_0 = \sin(\phi_0)$, the radiation pattern P is $|F(\chi)/F_{max}|^2$:

$$P(\phi) = \left(\frac{\sin(\pi N(d_y/\lambda)(\sin(\phi) - \sin(\phi_0)))}{N \sin(\pi(d_y/\lambda)(\sin(\phi) - \sin(\phi_0)))} \right)^2 \quad (25)$$

The -3 dB beamwidth is $0.886\lambda/L$, where $L = (N - 1)d_y$. In fact, Equation (19) is a function of $v - v_0$, so altering the $\Delta\Phi$ in the a_i only rotates $P(\phi)$ in ϕ -space, corresponding to a translation in v -space. The radiation pattern in Equation (25) is shown to match precisely the main beam of FDTD calculations via MEEP for one-dimensional arrays in Section 3. For two-dimensional grid arrays, the E and H plane radiation patterns “factor,” in that $P(\theta, \phi) = P(\theta)P(\phi)$. In Section 4, precision matches for two-dimensional grid arrays are shown.

2.3. Regarding Array Radiation Patterns

Because one-dimensional and two-dimensional arrays are considered, some notes about radiation patterns are necessary. First, all one-dimensional array radiation patterns correspond to the E-plane (the xy-plane). The arrays are specified using elements situated in the xy-plane, and the array extends along the y-axis. Radiators are linearly polarized such that the E-plane at some radius r is $(r \cos(\phi), r \sin(\phi), 0)$. The H-plane at r would be $(r \sin(\theta), 0, r \cos(\theta))$, but this data is not relevant for a one-dimensional array. Second, the MEEP python routine `get_farfield` is evaluated at a radius $r \gg L$, the length of the array, to obtain the far-fields \vec{E} and \vec{H} . Notice that not all open-source FDTD codes offer near-field to far-field transition modeling [12].

All two-dimensional phased array elements presented in Section 4 are arrayed in the yz-plane, and the E and H-planes have the same definitions as the one-dimensional case. However, the H-plane results have been shifted so that the main beam occurs at $\theta = 0$ degrees, rather than the expected 90 degrees. This is purely for visual comparison to Equation (25) cast as $P(\theta)$ with $\theta_0 = 0$, and does not mean the phased array is radiating orthogonally to broadside. Equation (25) is matched to E and H-plane two-dimensional patterns, and both are normalized to 0 dB at peak power.

3. Phased Array Designs in One Dimension: Two-Dimensional Fields

Two antenna designs were considered in modeling one-dimensional phased arrays: Yagi-Uda and horn, corresponding to narrowband and wideband applications, respectively. The two designs are depicted in Figure 3 with associated parameters described in Section 3.1 below. The Yagi-Uda antennas have 6 elements with the same radius, oriented in the xy-plane: one reflector, one radiator, three directors and a connecting boom. The current a_i is connected only to the radiator. The horn antennas have three structures: the box containing the linearly polarized radiator, the radiator which is connected to a_i , and the curves of the horn. An exponential function $y = f(x) = k_1 \exp(k_2(x - a))$ describes the curves (see Figure 3), and the origin is taken to be at the center of the back edge of the box. The constants are $k_1 = a/2$ and $k_2 = (1/c) \ln(2d/a)$. The curves are built from n slices where $n = c/dx$. All objects comprising the antenna elements have the same metallic conductivity, and the surrounding volume has an index of refraction $n = 1$. At the edge of

the space is a layer $1 \Delta x$ unit thick called the perfectly matched layer (PML) which cancels reflections.

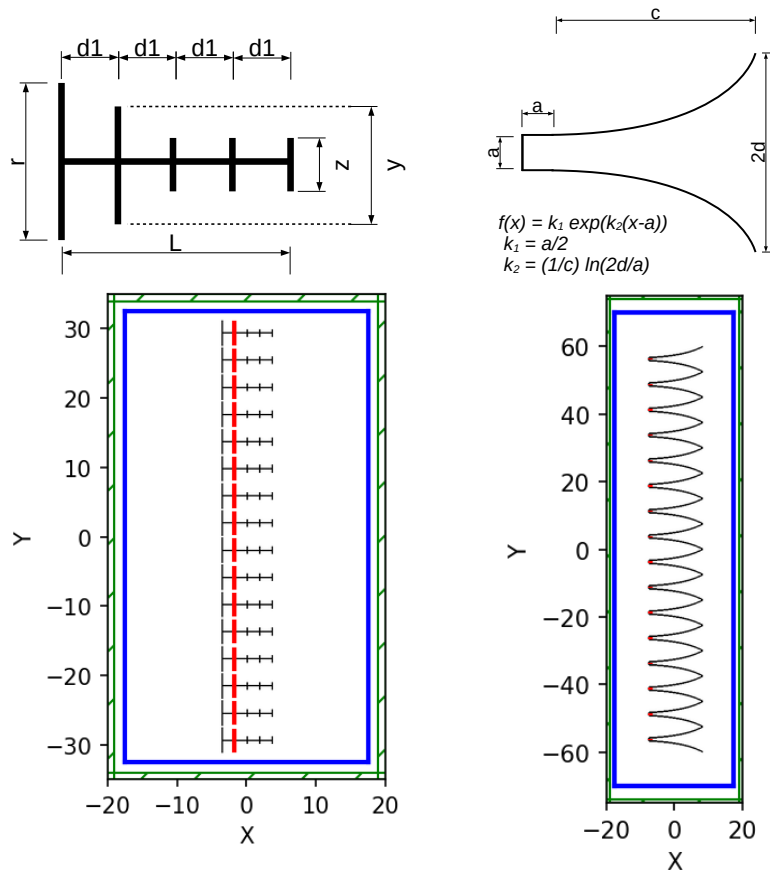


Figure 3. The two-dimensional antenna designs used in the one-dimensional phased array simulations. (See Section 3.1 for details). (Left) The Yagi-Uda antenna, and the $N = 16$ array. (Right) The horn antenna, and the $N = 16$ array. The white regions have $\epsilon = \epsilon_0$, the green borders are perfectly matched layers (PML), and the blue surfaces are MEEP *Near2FarRegion* objects where flux is recorded for near-to-far projection. The black lines represent metal structures, and the red lines represent the radiating elements. All dimensions are in centimeters.

3.1. Phase Steering, Beam Angle, and Beamwidth

As described in Section 2, the beam angle is controlled by the phase shift per antenna. Simulation results were run with the parameters in Table 1 for the one-dimensional arrays. The main results are shown in Figure 4. A discussion about scan loss below references data from Table 1.

The phase-steering results are shown in Figure 4. The y-axes of Figure 4 (top left) and (top right) are the beam angles of the Yagi-Uda arrays, divided by the beam widths. The x-axes for these graphs are the phase shifts per element. The top left plot and top right plots correspond to $N = 8$ and $N = 16$, respectively. For the $N = 16$ horn case (bottom left and right), the value of $d_y/\lambda = fd_y/c$ varies because the elements can radiate from $\approx 0.3\text{--}5.0$ GHz. The black solid lines in the top left and top right graphs of Figure 4 are linear fits to the Yagi-Uda data. The gray lines represent the function $f(x) = bx$, with $b = \lambda/(2\pi d_y)$. For these models, $d_y = 3.92$ cm and $\lambda = 6$ cm (Table 1). The slopes match almost exactly, with slight errors arising from radiation pattern distortion at high beam angle $\Delta\phi$. At such large $\Delta\Phi$ values, side lobes can shift the location of the main beam by $\mathcal{O}(1)$ degree by merging with the main beam. In the $N = 8$ case the fitted slope is slightly higher, and in the $N = 16$ case the fitted slope is slightly lower. In each model, the observed beamwidths are within 1% of the value predicted by Equation (18).

Table 1. Yagi-Uda: The first and second columns contain the geometric parameters describing the antenna elements for the Yagi-Uda array. Horn: The third and fourth columns contain those for the horn array. Scan-loss: The fifth through eighth columns contain scan loss (SL_{dB}) data, reported for different frequencies and different d_y/λ values for the $N = 16$ horn array.

Yagi-Uda		Horn		SL_{dB}			
Parameter	Value	Parameter	Value	f (GHz)	$\Delta\Phi$ (degrees)	d_y/λ	SL_{dB}
N	8.16	N	8.16	0.5	80	0.125	-11.6
L	7.20	a	0.95	1.0	80	0.25	-1.2
d_1	1.80	c	15.0	2.0	80	0.5	-1.0
r	3.75	d	3.8	4.0	80	1.0	-0.9
y	2.81	dx	0.1				
z	1.24	$n = c/dx$	150				
d_y	3.92	d_y	2d				
resolution	6	resolution	6				

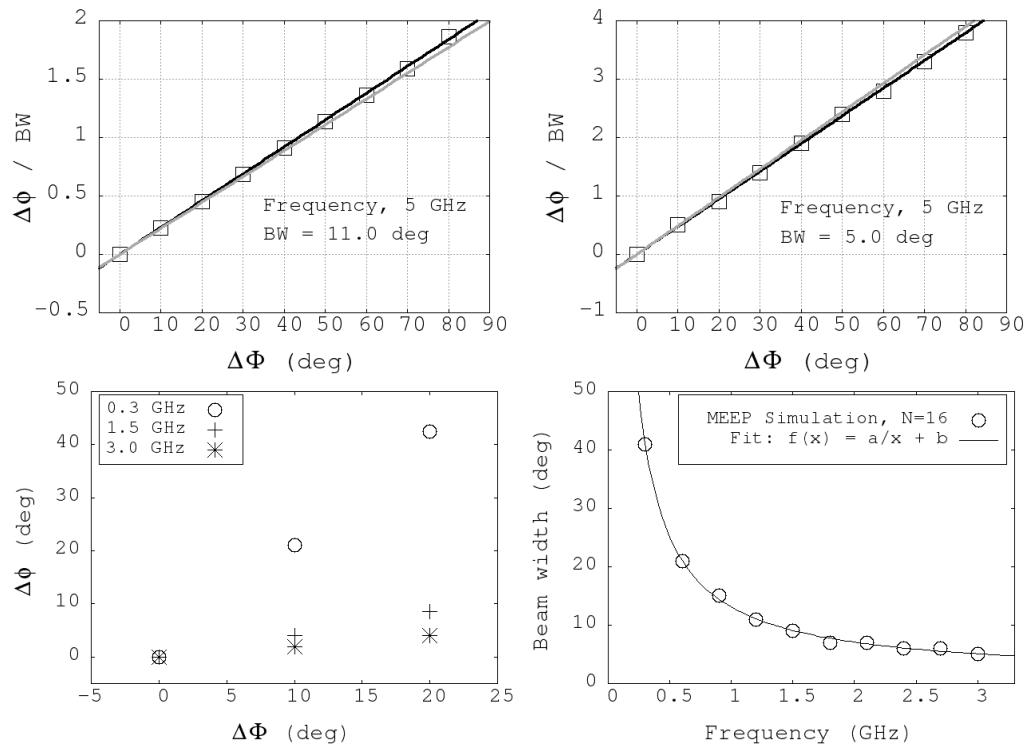


Figure 4. (Top left) The beam angle $\Delta\phi$ divided by the beam width BW for the $N = 8$ one-dimensional Yagi array versus $\Delta\Phi$, the phase shift per element. (Top right) The same results for the $N = 16$ array. (Bottom left) $\Delta\phi$ versus $\Delta\Phi$ for the $N = 16$ version of the one-dimensional horn array, for several frequencies. (Bottom right) The dependence of the beam width on frequency for the one-dimensional $N = 16$ horn array.

For the broadband horn case in the bottom left of Figure 4, three frequency cases are shown: 0.3, 1.5, and 3.0 GHz. The intercepts are all consistent with zero and the slopes scale correctly: dividing the frequency by a factor of 2 increases the slope by a factor of 2, and dividing by a factor of 10 increases it by a factor of 10. Graphs like the top left and top right of Figure 4 would be misleading for horn antennas since the beamwidth depends on frequency (bottom right). The fit parameters for beam width were $a = 12.0 \pm 0.1$ degree GHz, and $b = 1.1 \pm 0.2$ degrees. For these two-dimensional antennas, the $1/f$ -dependence

is a good description of the beamwidth across the [0.3–5 GHz] bandwidth. The constant term b is only necessary since the array has finite length L . The beamwidth (BW) scales inversely with array length L : $BW \approx 0.886\lambda/L$, from Equation (25).

A discussion of scan loss is merited when analyzing normalized radiation patterns, which are shown below in Section 3.2. Scan loss may be quantified as the peak power at the given beam angle divided by the peak power at a beam angle of zero degrees. In the form of an equation in decibels, scan loss becomes a subtraction:

$$SL_{dB} = P_\phi - P_{\phi=0} \quad (26)$$

The scan loss SL_{dB} is shown for the $N = 16$ one-dimensional horn array in Table 1 (right), as it varies with frequency and d_y/λ . The conservative value $\Delta\Phi = 80$ degrees was chosen because it is associated with the largest beam angles that do not generate side lobes larger than -15 dB. Given the beam width of the $N = 16$ design (5.04 degrees), this corresponds to a scan range of ± 20.16 degrees. The largest beam angles tend to have the largest scan losses, so the numbers in Table 1 should be the most conservative. Scan losses of less than 1 dB are observed at high frequencies, but at d_y/λ values that begin to admit large side lobes (Section 3.2).

3.2. Radiation Patterns

Radiation patterns in the E-plane from $N = 16$ one-dimensional Yagi and horn arrays are shown in Figures 5 and 6, respectively. As described above, the x-direction ($\Delta\phi = 0$) corresponds to no phase shift per element ($\Delta\Phi = 0$). The radiation patterns are normalized to the power at the beam angle, and are shown in blue. The red curves represent Equation (25) with the correct N -value and d_y/λ -value. Equation (25) is symmetric, with identical forward and backward lobes. The front-to-back or FB ratio would be 1.0 or 0 dB for a row of ideal point sources. Although there is no backplane in either simulated one-dimensional array, the FB ratios of ≤ -15 dB are observed.

The Yagi-Uda results are shown for 2.5 and 5.0 GHz frequencies in Figure 5, with $\Delta\Phi = 0, 20, 40$, and 60 degrees. Though the radiating elements are 6 cm long, good agreement between simulation and Equation (25) is observed at both 2.5 GHz and 5.0 GHz, including side-lobes. The beamwidth is proportionally larger at 2.5 GHz relative to 5.0 GHz, and at 5.0 GHz, the theoretical -3 dB beam width of 5.0 degrees is achieved. The amplitudes of all side-lobes are limited to ≈ -15 dB, except at the highest beam angles where scan losses are experienced. Finally, the effect of frequency on beam steering is evident. The same $\Delta\Phi$ does not generate as large a $\Delta\phi$ at higher frequencies because the slope implied by Equation (18) is proportional to λ .

The horn results are shown in Figure 6 for 0.5 GHz and 5.0 GHz frequencies, corresponding to the lower and upper end of the bandwidth. The phase shifts per element are $\Delta\Phi = 0, 10, 20$, and 30 degrees. The angular range of $\Delta\Phi$ is restricted relative to the Yagi-Uda case. Wideband systems experience a natural trade-off in angular range versus bandwidth. A d_y/λ value that is acceptably smaller than one at low frequencies can grow larger with increasing frequency, leading to interference patterns. At 5.0 GHz, the horns radiate at ± 45 degrees from $\Delta\phi = 0$. The prediction from Equation (25) is that these side-lobes, or *grating lobes*, are equal in relative power to the main beam. The actual array limits them to -15 dB, but only if $|\Delta\Phi| < 35$ degrees. For larger phase shifts per element, the opposite side-lobe grows above -15 dB. If the beam is steered too far in the $-\hat{\phi}$ -direction, the side-lobe on the $\hat{\phi}$ side grows, and vice versa.

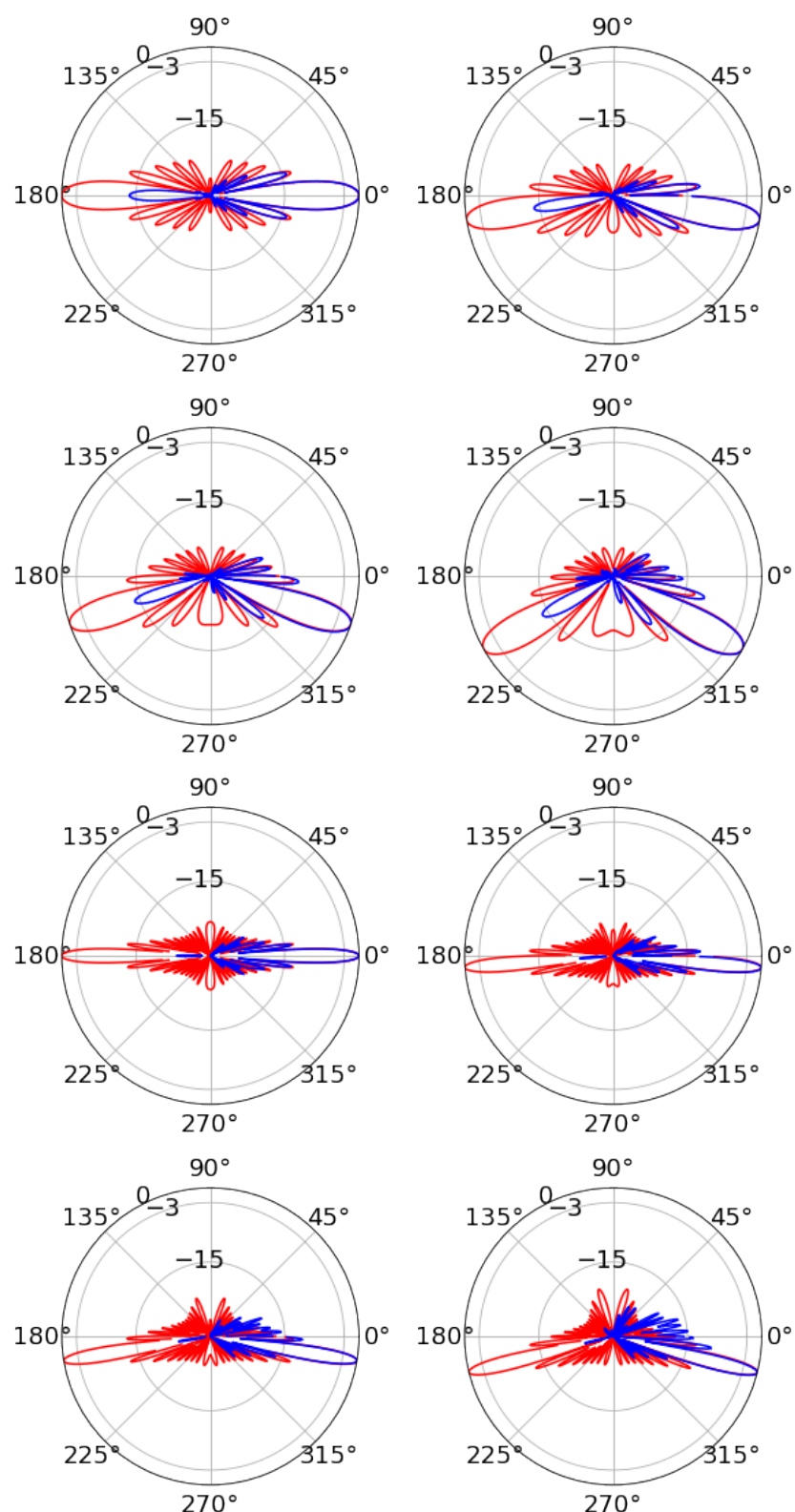


Figure 5. Yagi-Uda results, two-dimensional elements, one-dimensional array. **(Top row)** $f = 2.5 \text{ GHz}$, and $\Delta\Phi = 0, 20$ degrees from left to right. **(Second row)** $f = 2.5 \text{ GHz}$, and $\Delta\Phi = 40, 60$ degrees from left to right. **(Third row)** $f = 5.0 \text{ GHz}$, and $\Delta\Phi = 0, 20$ degrees from left to right. **(Bottom row)** $f = 5.0 \text{ GHz}$, and $\Delta\Phi = 40, 60$ degrees from left to right. The radial units are dB, and the angular units are degrees.

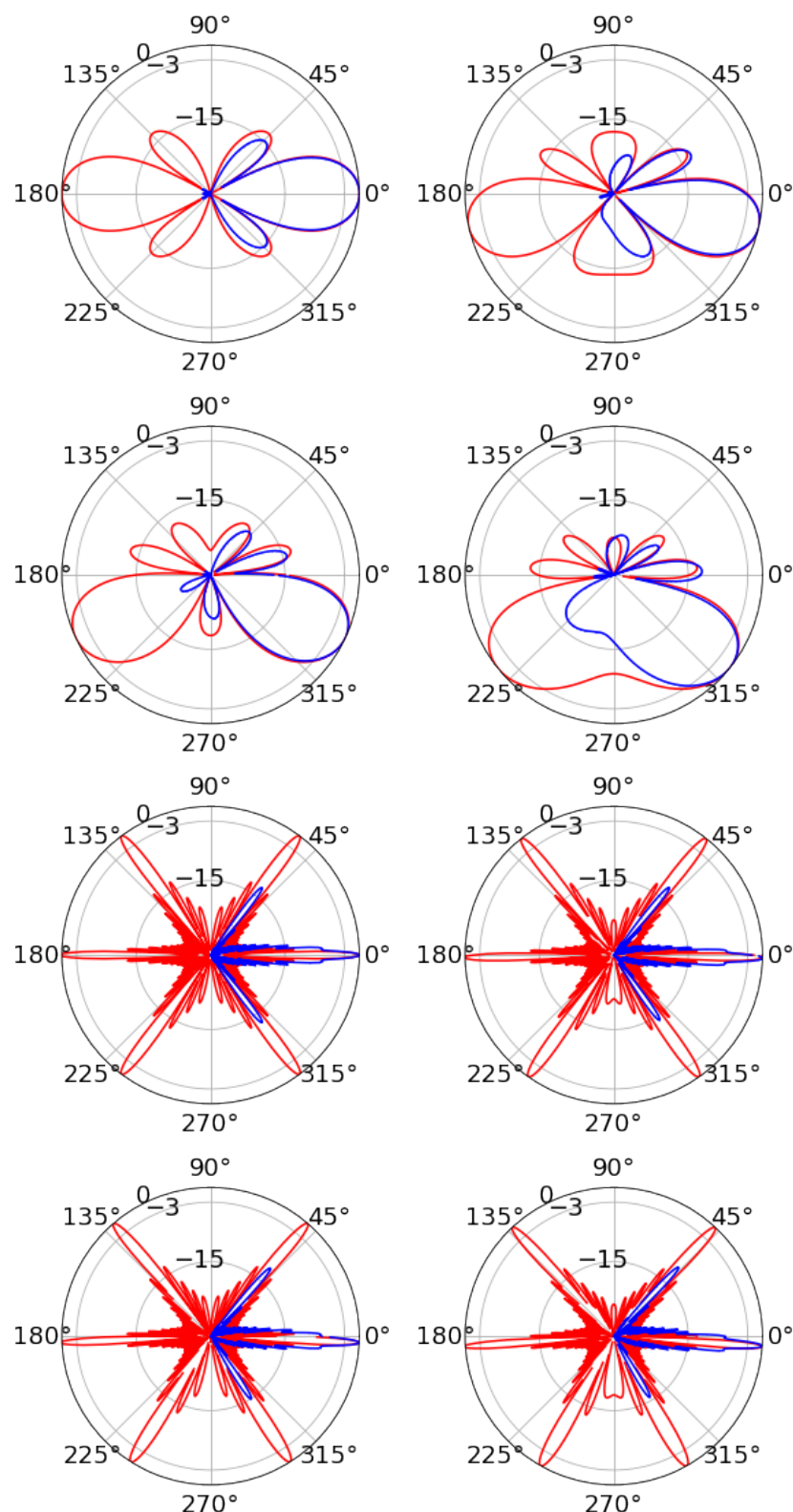


Figure 6. Horn results, two-dimensional elements, one-dimensional array. (**Top row**) $f = 0.5$ GHz, and $\Delta\Phi = 0, 10$ degrees from left to right. (**Second row**) $f = 0.5$ GHz, and $\Delta\Phi = 20, 30$ degrees from left to right. (**Third row**) $f = 5.0$ GHz, and $\Delta\Phi = 0, 10$ degrees from left to right. (**Bottom row**) $f = 5.0$ GHz, and $\Delta\Phi = 20, 30$ degrees from left to right.

The general features of the radiation pattern compare well to the theoretical prediction. The $1/f$ -dependence of the main beamwidth is evident in Figure 6. Like the Yagi-Uda

array, the minimum theoretical beamwidth is reached at the highest frequencies (Figure 4 bottom right). The mini-lobes that are partially merged with the main beam widen the beam, however, the beamwidth is calculated at angles corresponding to -3 dB relative power. Since the mini-lobes are below -3 dB, the beamwidth calculation is unaffected. The simulation also matches the location and width of side-lobes to the theoretical prediction across the bandwidth. The six grating lobes at 5 GHz are a result of the pattern multiplication theorem, which states that the normalized radiation pattern is a product of the horn pattern and the pattern of an array of point sources. At 5 GHz, this multiplication suppresses the horn element pattern in the multiplication.

The field magnitude $|\vec{E}(x, y, t)|$ for the $N = 16$ horn array is shown in Figure 7 for $t = 0.5, 1.0, 1.5, 2.0$ ns at a frequency of 2.5 GHz, along with the radiation pattern (far right). The original amplitude of the radiation source within the horns is ± 1 units, and the color scale for radiated $|\vec{E}(x, y, t)|$ is ± 0.002 . The $\Delta\phi$ is 9 degrees, with $\Delta\Phi = -35$ degrees, and the beamwidth is 5.5 ± 0.5 degrees. The area is 480×900 pixels describing $80 \times 150 \text{ cm}^2$ with a resolution of 6 pixels per Δx . The dimensions of the box (Table 1: $a = 0.95 \text{ cm}$) are smaller than $\lambda = 12 \text{ cm}$. As the radiation escapes to free space, the wavefront forms several λ in front of the horns. Higher-frequency modes with $f \gg 2.5 \text{ GHz}$ are observed at the wavefront that correspond to start-up effects at $t = 0$ ns. With 72 pixels per wavelength, minute features of $|\vec{E}(x, y, t)|$ can be interpreted as physical rather than numerical. These features can be eliminated with amplitude smoothing near $t = 0$ ns, a feature available in the MEEP CustomSource class. Amplitude smoothing, however, makes the location of the wavefront less precise.

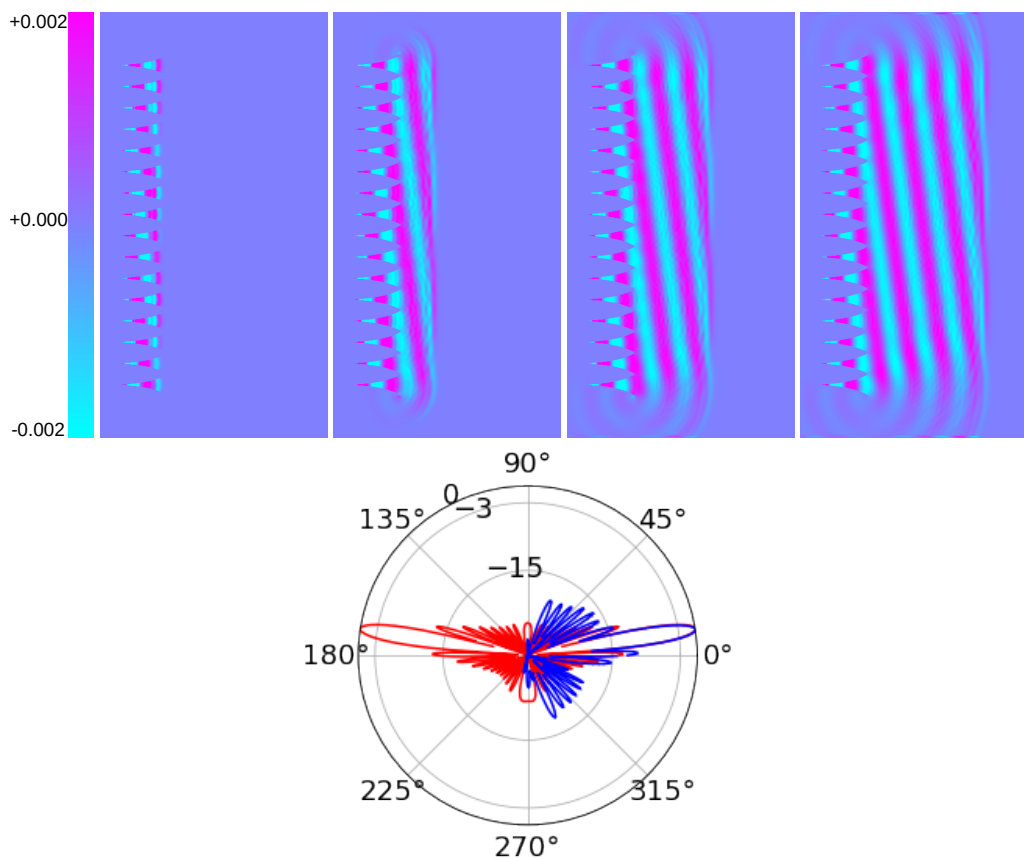


Figure 7. (From top left to top right) The $N = 16$ horn one-dimensional linearly polarized electric field $|\vec{E}(x, y, t)|$ at $t = 0.5$ ns, $t = 1.0$ ns, $t = 1.5$ ns, and $t = 2.0$ ns. The 2D area is $80 \times 150 \text{ cm}^2$, with resolution of 6 pixels per distance unit (480×900 pixels). The frequency is 2.5 GHz, and the beam angle is 9 degrees from broadside. (Bottom) The corresponding radiation pattern.

The radiation pattern in Figure 7 matches the theoretical prediction for the main lobe and first few side lobes. The origin of the side lobes is apparent from the $|\vec{E}(x, y, t)|$ images, where diffraction patterns at the edges of the array are visible. At 0.5 ns, radiation in an element is confined to the horn. By 1.0 ns, that radiation joins the waves from horns on either side. However, horns at the end of the array have no partner on one side, and some radiation leaks outside the main lobe. The side lobes can change if the total run time is not sufficient. The `get_farfield` routine in MEEP requires `Near2FarRegion` surfaces that form the near-field box that collects flux information at the radiation frequency. The parameters of the near-field box are set by the `add_near2far` routine. The `get_farfield` routine performs a near-to-far field projection to the given radius ($r = 1000$ cm) where the field is computed for the radiation pattern. The propagation code must be run for sufficient units of Δt so that enough radiation can cross the near-field box. The code is run for 6.67 ns to generate the radiation pattern in Figure 7. Thus, the side lobes are averaged over many radiation periods.

4. Phased Array Designs in Two Dimensions: Three-Dimensional Fields

For two-dimensional grids of radiating elements, the array-factor $F(u, v)$ factors:

$$F(\theta, \phi) = F(u - u_0)F(v - v_0) \quad (27)$$

The radiation pattern in Equation (25) applies to the E and H plane separately. The two-dimensional arrays modeled below are square $N \times N$ arrays, so beamwidths implied by Equation (25) are equal for the E and H planes. The complex phasing of Equation (27) also indicates that $\Delta\phi_E \propto \Delta\Phi_E$, and $\Delta\phi_H \propto \Delta\Phi_H$, as shown in Equation (18) for the one-dimensional case. For the designs presented, the H-plane corresponds to the xz-plane, and to varying the phase in the z-direction (by array row). The E-plane corresponds to the xy-plane, and to varying the phase in the y-direction (by array column). In Figure 8, the basic shape of the two-dimensional array is shown in the yz-plane with $\Delta\Phi_E = 15$ degrees, and $\Delta\Phi_H = 15$ degrees. Section 4.1 contains results along the lines of Section 3.1 but for two-dimensional Yagi and horn arrays, and Section 4.2 contains results along the lines of Section 3.2 but for two-dimensional Yagi and horn arrays. As before, Table 1 contains the typical run parameters, with a few important exceptions.

The first exception is that for the two-dimensional case N becomes $N \times N$. However, squaring the number of antennas raises the memory requirements. In order to stay within a 16 GB memory limit, the two-dimensional *horn array* results had to be restricted to $N \times N = 8 \times 8$. The 2D horn array still has over $\mathcal{O}(10^4)$ metal objects, compared to the $\mathcal{O}(10^3)$ objects for the $N \times N = 16 \times 16$ 2D Yagi-Uda. The typical memory consumption is listed in Table 2, along with modified run parameters. Further, the resolution parameter was restricted to 4.0 for the horns. Restricting to 4 pixels per Δx unit limits memory consumption, but then the box containing the radiator has too few pixels. Enlarging the box allows the proper sized radiator to be fully contained. A final object was added to reduce the FB ratio: a back-plane with parameters listed in Table 2. One interesting modification is the doubling of the ratio of the box size (a) and the final horn width (d). This had the effect of limiting the maximum frequency to ≈ 1 GHz. At 1 GHz, $d/\lambda \approx 0.5$. A full optimization study on the horn parameters is warranted, though outside the present scope.

The horn elements radiate linearly polarized radiation in the y-direction, so the width in the z-direction does not follow the exponential functions but remains fixed at a . Initial runs were performed with horn elements that simultaneously widened according to the exponential function defined in Section 3. That design allowed reflections internal to the horns to distort the initial wavefront. Holding the horn-width constant in the z-direction produces radiation patterns that match Equation (25) because it follows the one-dimensional example of Section 3. To obtain z-polarized wavefronts, all that is necessary is to rotate the array. Practically, there are already examples of dually polarized RF band horns used in particle astrophysics [18,19], meaning that if this design were created with such elements, no rotation would be necessary.

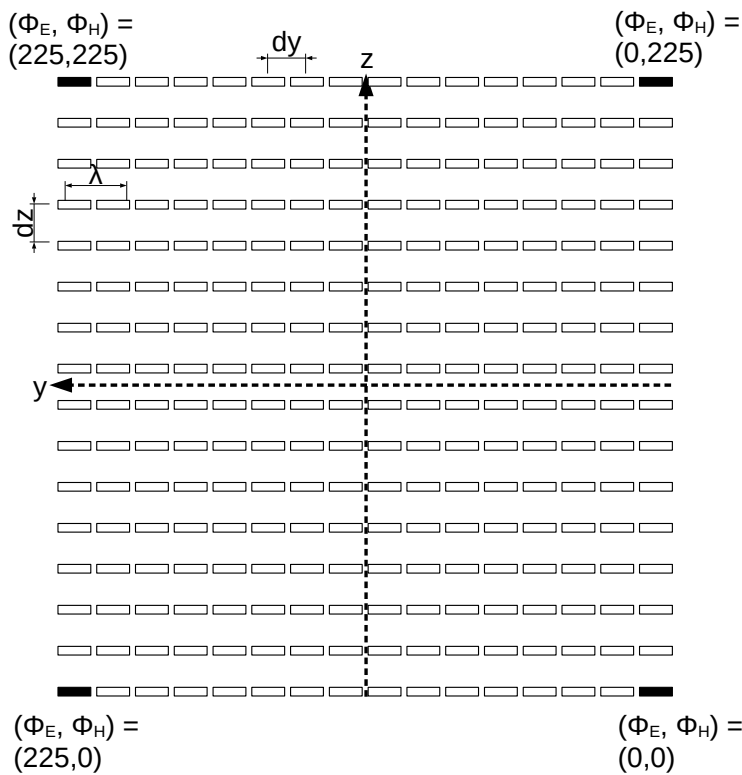


Figure 8. The two-dimensional $N \times N = 16 \times 16$ Yagi-Uda/horn y-polarized array layout. The alignment with 3D Cartesian coordinates is depicted, along with the array spacing variables d_y and d_z , the wavelength λ (to scale), and the phases for each row and column if $\Delta\Phi_E = \Delta\Phi_H = 15$ degrees.

Table 2. The parameters for the $N \times N = 8 \times 8$ horn array, modified from Table 1. The Yagi-Uda $N \times N = 16 \times 16$ array did not require modification. The number of CPU cores was 4 in hardware, but was effectively 8 with hyperthreading. The most memory-intensive simulation was the 8×8 horn array, which consumed 11.7 GB of memory out of 15.5 GB free. The code was written with the Python3 interface to MEEP, installed with the conda package manager, and run in Jupyter notebooks.

Horn		System Information	
Parameter	Value		
$N \times N$	8×8	Memory Consumption	
a	2.0	11.7 GB out of 15.5 GB	
c	15.0	CPU cores	
d	8.0	Intel i7 1.80 GHz (8)	
dx	0.5	MEEP installation	
$n = c/dx$	30	Python3 interface (conda)	
d_y	16		
resolution	4		
backplane location	$-2a$		
backplane thickness	0.5		
backplane dim.	142×142		

4.1. Phase Steering, Beam Angle, and Beamwidth

The $\Delta\phi$ vs. $\Delta\Phi$ results for the two-dimensional $N \times N = 16 \times 16$ Yagi-Uda array are shown in Figure 9. Figure 9 (top left) contains $\Delta\phi_E$ versus $\Delta\Phi_E$ data at 5 GHz. The data match the theoretical linear slope $\lambda/(2\pi d_y)$ and $\lambda/(2\pi d_z)$, with $d_y = d_z$. The phase shift per antenna is varied over $[0, 75]$ degrees in 15 degree increments independently by row and column. The circles and squares correspond to $\Delta\Phi_H = 0$ and 45 degrees, respectively. Both the circles and squares follow the same line, implying the correct phase independence: when $\Delta\Phi_H$ is held at either constant, $\Delta\phi_E$ still varies with $\Delta\Phi_E$ correctly. Figure 9 (bottom

left) contains $\Delta\phi_H$ versus $\Delta\Phi_H$ data at 5 GHz. The circles and squares correspond to $\Delta\Phi_E = 0$ and 45 degrees, respectively. Beyond $\Delta\Phi_E = 75$ degrees or $\Delta\Phi_H = 75$ degrees, side lobes appear (>-15 dB). Figure 9 (right) contains the beam angle results after steering the beam to 36 of the possible 11×11 positions in the E and H plane using increments of $\Delta\Phi_{E/H} = 15$ degrees. The xy-errorbars correspond to the beamwidths.

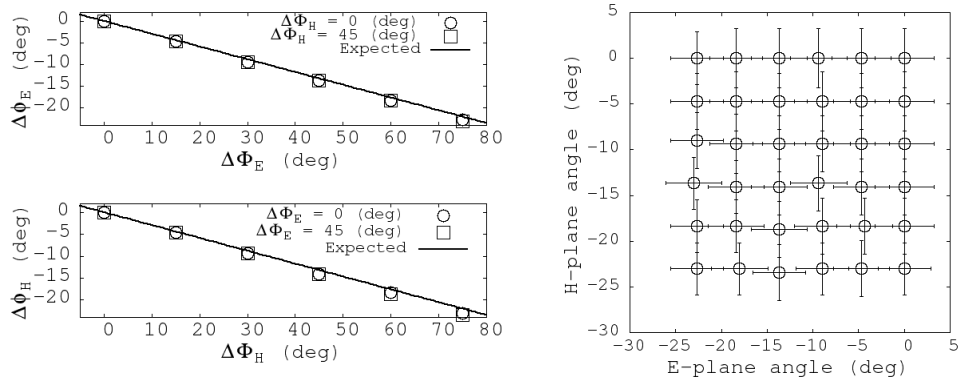


Figure 9. (Left) The beam angles $\Delta\phi_E$ and $\Delta\phi_H$ versus the phase shifts for the $N \times N = 16 \times 16$ Yagi-Uda array at 5 GHz. The black lines represent the theoretical prediction of a linear dependence with slope $\lambda/(2\pi d_y)$ or $\lambda/(2\pi d_y)$, ($d_y = d_z$). In each graph, the circles and squares correspond to two different $\Delta\Phi$ constant values for the other array plane. In these examples, location of zero phase on the array is chosen to cause a negative beam angle. (Right) The data points correspond to beam angles in the E and H-planes, with the associated beamwidths as errorbars. These data represent one-quarter of the possible scan positions with $\Delta\Phi_{E/H} = 15$ degrees.

The $\Delta\phi$ vs. $\Delta\Phi$ results for the two-dimensional $N \times N = 8 \times 8$ horn array are shown in Figure 10 (left). Figure 10 (top left) contains $\Delta\phi_E$ versus $\Delta\Phi_E$ data at 1 GHz. The larger horn size relative to those in Section 3 means the upper frequency is ≈ 1.2 GHz. The data match the theoretical slopes just as in Figure 9. The phase shift per antenna is varied in the same pattern as in Figure 9. The circles and squares correspond to $\Delta\Phi_H = 0$ and 45 degrees, respectively, and both data sets follow the theory. Figure 10 (bottom left) contains $\Delta\phi_H$ versus $\Delta\Phi_H$ data at 1 GHz. The circles and squares correspond to $\Delta\Phi_E = 0$ and 45 degrees, respectively, and both data sets follow the theory. The beamwidth as a function of frequency across the bandwidth for the design is shown in Figure 10 (right). The fit parameter mean values and standard errors are: $a = 10.6 \pm 0.2$ degree GHz, $b = 2.8 \pm 0.3$ degrees, $c = 8.7 \pm 0.4$ degree GHz, and $d = 5.0 \pm 0.9$ degrees. The width of the mouth of the horns is 16 cm in the E-plane direction and 2 cm in the H-plane direction, so some small difference in beamwidth is not surprising.

4.2. Radiation Patterns

The radiation patterns in the E and H plane for the two-dimensional Yagi-Uda array are shown in Figure 11. The phase combinations $(\Delta\Phi_E, \Delta\Phi_H) = (0, 0), (30, 60), (60, 30)$ degrees are shown for E and H planes at 3 and 4 GHz. As in Section 3.2, Equation (25) is shown in red, and the simulation results are shown in blue. The main beam and first several side lobes are modeled correctly in each case, and the FB ratio is ≤ -15 dB. The side lobes are also at the ≈ -15 dB level. Following Figure 10 (right), the main beam is narrower at 4 GHz than at 3 GHz. Though not generally designed to be broadband elements, the Yagi-Uda elements do display some flexibility in frequency. The log-periodic dipole array (LPDA) is a broadband example constructed from dipoles as the Yagi is [20].

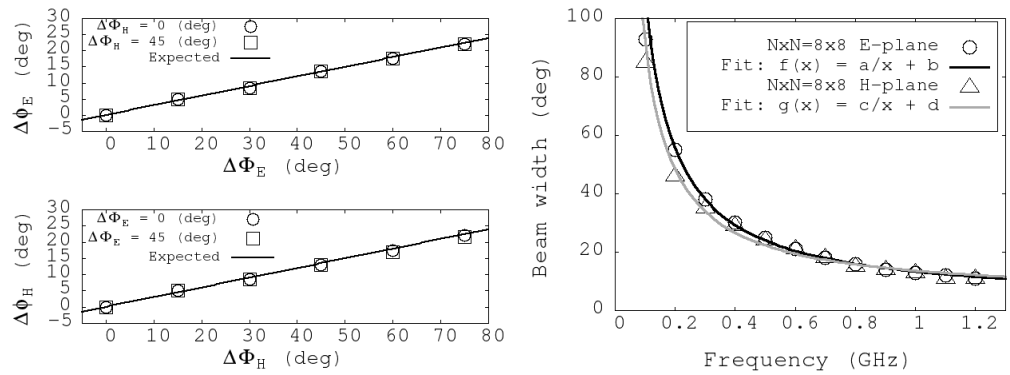


Figure 10. (Left) The beam angles $\Delta\phi_E$ and $\Delta\phi_H$ versus the phase shifts per column (for the E-plane) and per row (for the H-plane) for the $N \times N = 8 \times 8$ horn array at 1 GHz. The black lines represent the theoretical prediction. In each graph, the circles and squares correspond to two different $\Delta\Phi$ constant values for the other array plane. (Right) The beamwidth in the E and H-planes versus frequency.

Producing the radiation patterns in Figure 11 requires only $\mathcal{O}(10)$ seconds to run near-field calculations, and only another ≈ 5 min each to run the `get_farfield` routine over the E and H-planes. Modeling arrays constructed from dipole elements is orders of magnitude faster than for the array of horns, due to the two-dimensional nature of the dipole elements. Producing the radiation patterns of Figure 12 for the two-dimensional horn array requires ≈ 60 min combined for the E and H-plane patterns, *per frequency*. Unlike the Yagi case, the vast majority of time is not dedicated to the `get_farfield` routine, but to the near-field calculations. The near-field calculations require “sub-pixel smoothing” for the many edges of the blocks that comprise the horn structure.

The radiation patterns in the E and H plane for the two-dimensional horn array are shown in Figure 12. The phase combinations $(\Delta\Phi_E, \Phi_H) = (0, 0), (30, 60), (60, 30)$ degrees are shown for E and H planes at 0.5 and 1.0 GHz. As in Section 3.2, Equation (25) is shown in red, and the simulation results are shown in blue. The main beam and first several side lobes are modeled correctly in each case, and the FB ratio is ≤ -15 dB. The side lobes are also at the ≈ -15 dB level. Due to the higher bandwidth, a wider range of beamwidths is available (see Figure 10). The main beam is narrower at 1 GHz than at 0.5 GHz. The horns produce the correct pattern for $(\Delta\Phi_E, \Delta\Phi_H) = (0, 0)$ degrees from 0.1 to 1.2 GHz. However, grating lobes above -15 dB are a known problem that occur when attempting to steer phased arrays built from broadband horns to wide angles (see Chapter 9 of Reference [16]). The addition of the backplane limits diffraction of the radiation around the edges of the array and therefore limits the FB ratio, but grating lobes appear at ± 45 degrees from the main beam. There is occasionally a back lobe, which can be attributed to the diffraction of fields around the edge of the backplane. This effect is more pronounced when the main beam is steered to a wide angle and occurs in the hemisphere opposite to the main beam.

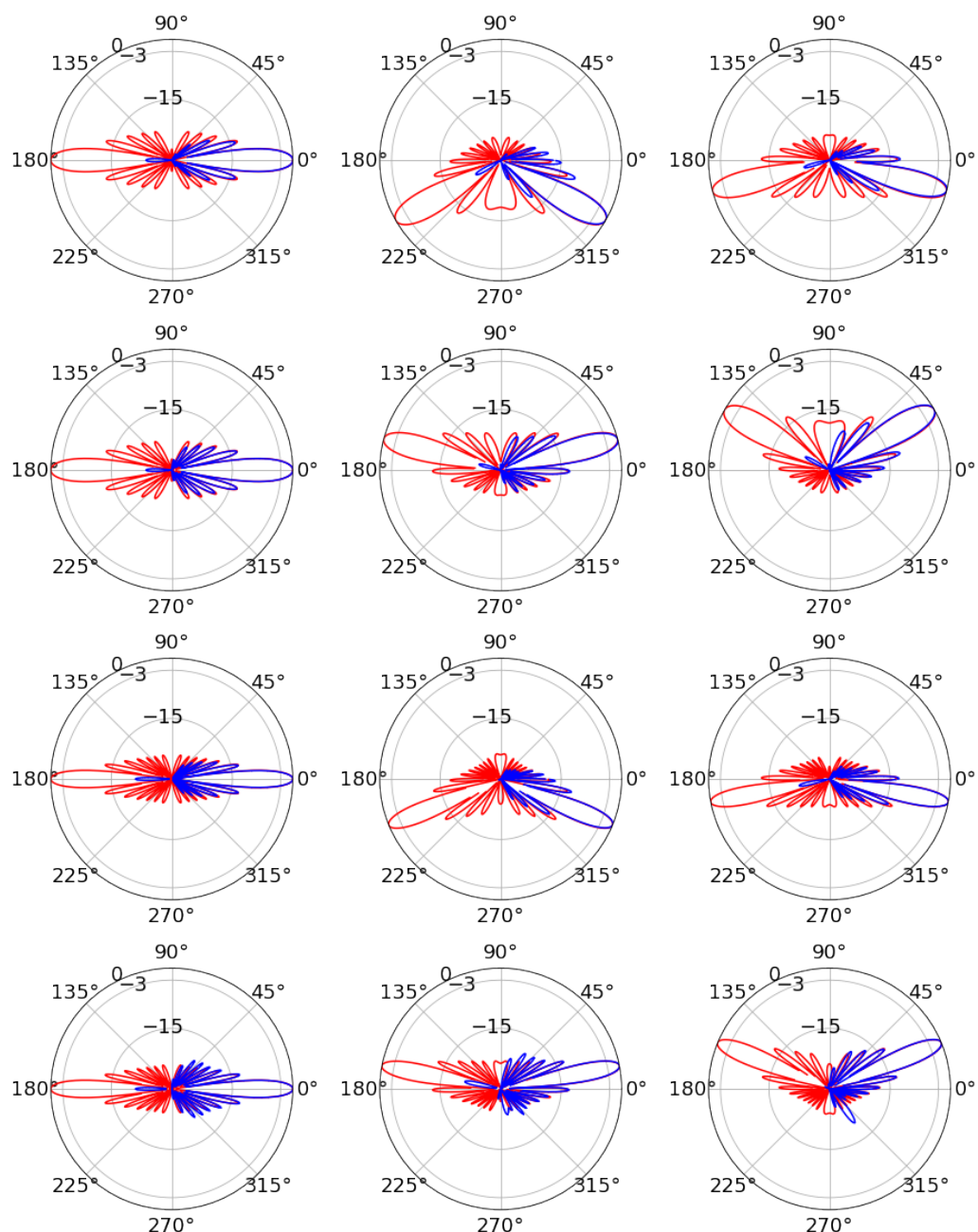


Figure 11. Yagi-Uda results, two-dimensional array (**First row**) $f = 3$ GHz, with (from left to right) E-plane $(\Delta\Phi_E, \Delta\Phi_H) = (0, 0)$ degrees, E-plane $(\Delta\Phi_E, \Delta\Phi_H) = (60, 30)$ degrees, E-plane $(\Delta\Phi_E, \Delta\Phi_H) = (30, 60)$ degrees. (**Second row**) $f = 3$ GHz, with (from left to right) H-plane $(\Delta\Phi_E, \Delta\Phi_H) = (0, 0)$ degrees, H-plane $(\Delta\Phi_E, \Delta\Phi_H) = (60, 30)$ degrees, H-plane $(\Delta\Phi_E, \Delta\Phi_H) = (30, 60)$ degrees. (**Third row**) $f = 4$ GHz, with (from left to right) E-plane $(\Delta\Phi_E, \Delta\Phi_H) = (0, 0)$ degrees, E-plane $(\Delta\Phi_E, \Delta\Phi_H) = (60, 30)$ degrees, E-plane $(\Delta\Phi_E, \Delta\Phi_H) = (30, 60)$ degrees. (**Fourth row**) $f = 4$ GHz, with (from left to right) H-plane $(\Delta\Phi_E, \Delta\Phi_H) = (0, 0)$ degrees, H-plane $(\Delta\Phi_E, \Delta\Phi_H) = (60, 30)$ degrees, H-plane $(\Delta\Phi_E, \Delta\Phi_H) = (30, 60)$ degrees.

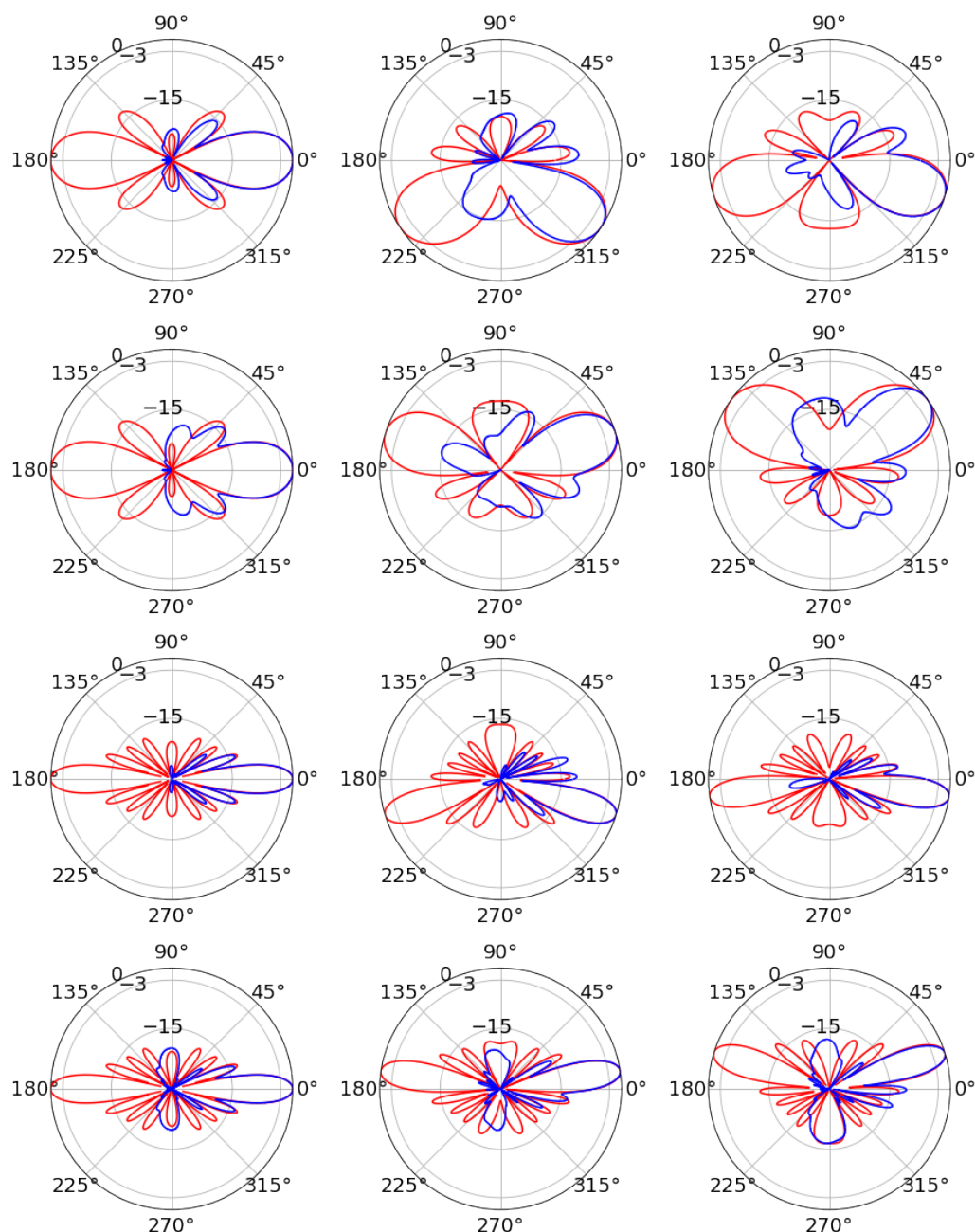


Figure 12. Horn results, two-dimensional array (**First row**) $f = 0.5$ GHz, with (from left to right) E-plane $(\Delta\Phi_E, \Delta\Phi_H) = (0, 0)$ degrees, E-plane $(\Delta\Phi_E, \Delta\Phi_H) = (60, 30)$ degrees, E-plane $(\Delta\Phi_E, \Delta\Phi_H) = (30, 60)$ degrees. (**Second row**) $f = 0.5$ GHz, with (from left to right) H-plane $(\Delta\Phi_E, \Delta\Phi_H) = (0, 0)$ degrees, H-plane $(\Delta\Phi_E, \Delta\Phi_H) = (60, 30)$ degrees, H-plane $(\Delta\Phi_E, \Delta\Phi_H) = (30, 60)$ degrees. (**Third row**) $f = 1.0$ GHz, with (from left to right) E-plane $(\Delta\Phi_E, \Delta\Phi_H) = (0, 0)$ degrees, E-plane $(\Delta\Phi_E, \Delta\Phi_H) = (60, 30)$ degrees, E-plane $(\Delta\Phi_E, \Delta\Phi_H) = (30, 60)$ degrees. (**Fourth row**) $f = 1.0$ GHz, with (from left to right) H-plane $(\Delta\Phi_E, \Delta\Phi_H) = (0, 0)$ degrees, H-plane $(\Delta\Phi_E, \Delta\Phi_H) = (60, 30)$ degrees, H-plane $(\Delta\Phi_E, \Delta\Phi_H) = (30, 60)$ degrees.

5. Variation of the Index of Refraction

The behavior of a one-dimensional phased array embedded within a dielectric medium with spatially-dependent index of refraction $n(z)$ is interesting to the ultra-high energy (UHE) neutrino community [3,5]. Phased arrays represent an opportunity to lower the RF detection threshold for RF pulses generated by UHE neutrinos via the Askaryan effect. Antarctic ice is the most convenient and natural medium for Askaryan pulse detection, due to the RF transparency and large pristine volumes located in Antarctic and Greenlandic

ice sheets and shelves [21–23]. The index of refraction varies within the ice because of the transition between surface snow ($\rho \approx 0.4 \text{ g/cm}^3$) and the solid ice below ($\rho = 0.917 \text{ g/cm}^3$). Most recent and intricate studies of phased array beam behavior still assume a uniform medium [24–26]. Embedded phased arrays with varying $n(z)$ emit signals that curve in the direction of increasing $n(z)$.

The *shadow zone* is the volume of ice from which RF signals do not reach a receiver due to the excess curvature of the ray trace [27]. While there is evidence that RF signals can propagate horizontally through Antarctic ice [28], data from Greenland suggests the relative strength of the effect is small compared to the curved radiation [29]. Using the tools developed in this work, it is possible to map out the shadow zone for an embedded phased array radiating sinusoidal signals at fixed frequency. Intriguingly, when the phased array *radiates*, the grating lobe power reflect downward from the snow-air interface, and radiates into the shadow zone. Grating lobe power also refracts into the air above the interface. Grating lobe power leaves the array at a different angle than the main beam, so their presence in the shadow zone does not represent forbidden RF propagation.

A two-parameter fit to the $n(z)$ data versus depth z below the surface is given by [28]

$$n(z) = \begin{cases} 1 & z > 0 \\ n_{\text{ice}} - \Delta n \exp(z/z_0) & z \leq 0 \end{cases} \quad (28)$$

The fit parameters in Equation (28) come from Reference [28]: $\Delta n = 0.423 \pm 0.004$ and $z_0 = 77 \pm 2 \text{ m}$, with $n_{\text{ice}} = 1.78$ for RF frequencies. These values are derived from the SPICE core data taken in 2015 near the South Pole, and are in statistical agreement with fits from data obtained by the RICE experiment (see also Reference [28]). Equation (28) was implemented in the one-dimensional horn array case, but the horn structure surrounding each radiating element was removed. The array is therefore a one-dimensional dipole array. Further, the length scale was reinterpreted to be meters rather than centimeters, which is an ability conferred by the scale invariant FDTD algorithms. In this medium, there is no fixed *in-situ* value of λ so the $\lambda/4$ dipoles were spaced by $\lambda/2$ according to their free space λ value. At the selected frequency of 200 MHz, the dipole length is 0.375 m, and the spacing is 0.75 m.

Figures 13 and 14 contain the results of a $N = 8$ one-dimensional dipole array embedded in a medium with the index profile in Equation (28). Figure 13 shows the schematic of the calculation, and Figure 14 shows the magnitude of the z-component of the z-polarized array. Figure 14 represents the same physical dimensions as Figure 13. Equation (28) was sampled 100 times vertically, and with a resolution parameter of 10, the effective Δz is 0.1 m. The units in Figure 13 are meters, and the unit-less frequency in MEEP was scaled accordingly, to correspond to 200 MHz. The distances between the air-snow interface and the first phased array element is 15 m (top) and 35 m (bottom).

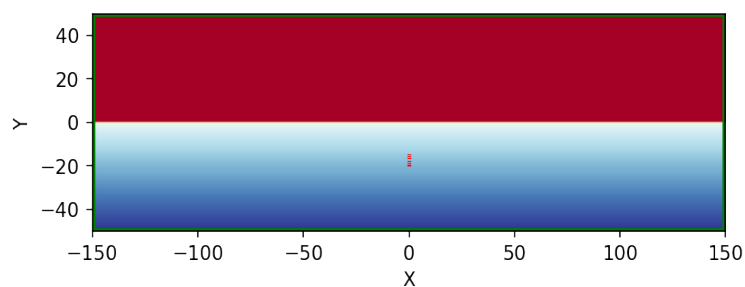


Figure 13. The simplified $N = 8$ one-dimensional vertical phased array with dimensions in meters. For this array, $d_z = \lambda/2.0$, and the length of the dipole radiators is $\lambda/4.0$. The colorscale represents $n(z)$ in Equation (28).

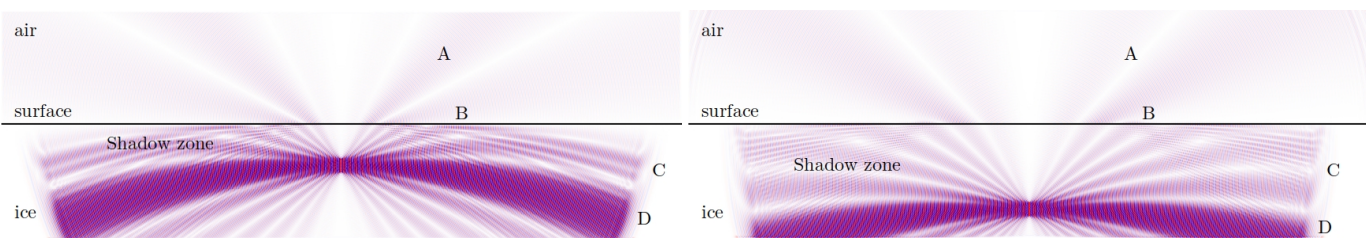


Figure 14. The magnitude of the z -component of the z -polarized dipoles as they radiate as a phased array with $\Delta\Phi = 0$ degrees. The air, surface, and ice regions are the same as Figure 13, with the same dimensions. (Top) The array depth is -15 m. (Bottom) The array depth is -35 m. (A) Radiation refracting through the surface into the air. (B) Grating lobes reflect from the surface into the shadow zone. (C) Grating lobes propagating through the shadow zone. (D) The main beam bent downward due to the gradient in $n(z)$.

The color scale in Figure 14 is ± 0.05 with the signal amplitude of the elements ± 1.0 at 200 MHz. The amplitude scale is less important than observing *where* the radiation has penetrated the ice after 200 time steps. In Figure 14 (top), the main beam has curved downwards in the direction of increasing $n(z)$, while grating lobes have both diffracted to the air and reflected into the shadow zone. The rate of curvature of the main beam is controlled by the fit parameter z_0 in Equation (28). In Figure 14 (bottom), the physics is the same as Figure 14 (top), but the effect of $n(z)$ curvature is weakened. The beam travels farther horizontally because the gradient of $n(z)$ is smaller at the larger depth. The geometry of the larger depth is such that the reflected grating lobe power is interfering with grating lobe power that was curved downwards without reflection. This can be seen just above the C marker in Figure 14 (bottom).

6. Summary and Future Analysis

Four phased array designs have been modeled with the MIT Electromagnetics Equation Propagation (MEEP) package in non-parallel mode. Two types of individual radiating element were explored: the narrow-band Yagi-Uda and broadband horn antennas. Two phased array geometries were explored: *one-dimensional* and *two-dimensional*. The one and two-dimensional Yagi-Uda phased arrays were designed for ≤ 5 GHz, however, scale-invariance makes this design scalable to a variety of frequencies. The one-dimensional horn array performs in the range [0.3–5] GHz, using two-dimensional versions of the horn elements. The two-dimensional horn array had to be modified due to memory constraints. The result was an array that performed in the range [0.1–1.2] GHz. In all cases, comparisons to array theory were shown.

The one-dimensional array of Yagi-Uda antennas was analyzed in Section 3. The array demonstrated the correct linear relationship between $\Delta\phi$ and $\Delta\Phi$ (Figure 4) (top left and right). Although any row of point sources would obey the relationship in Equation (18), a row of point sources has two main beam solutions by symmetry. Thus Figure 4 could not be interpreted correctly were it not for the proper functioning of the Yagi elements. The radiation patterns produced with the one-dimensional Yagi array were compared to Equation (25) in Figure 5. The radiation pattern in the E-plane is shown to agree with Equation (25) in both the main beam and the first several grating lobes. The calculation takes place in two-dimensions, so an H-plane comparison is not relevant.

The one-dimensional array of horn antennas was analyzed in Section 3. The array demonstrated the correct linear relationship between $\Delta\phi$ and $\Delta\Phi$ (Figure 4). In that case, the slope of $\Delta\phi$ vs. $\Delta\Phi$ was *increased* by a factor of 2 and then 10 by *decreasing* the frequency by a factor of 2 and then 10. The bandwidth of the two-dimensional versions of the horns allows the variation of scan range. The scan range is smaller at high frequencies, as indicated in Figure 4 (bottom left). However, the beamwidth is also smaller at high frequencies, as indicated in Figure 4 (bottom right). The design trade-off is between small beamwidth and large scan range. In Figure 6 the one-dimensional horn array radiation pattern is shown to match Equation (25) at both 0.5 and 5.0 GHz. There are 2–4 side lobes

at 0.5 GHz to match per pattern, and the simulation results match them as well as the wide main beam. At 5.0 GHz, the main beam is accompanied by two prominent grating lobes at ± 45 degrees that should be as powerful as the main beam. The simulation finds them at the -15 dB level. The grating lobes are being suppressed by the the pattern null from the horn element pattern [16]. At lower frequencies, however, scan loss takes a toll on radiated power (Table 1).

The two-dimensional, $N \times N = 16 \times 16$ Yagi-Uda array was analyzed in Section 4. The array demonstrated the correct linear relationships between $\Delta\phi_E$ and $\Delta\Phi_E$, and $\Delta\phi_H$ and $\Delta\Phi_H$ (Figure 9) (left). Given the narrow beamwidth, the array design can be scanned ± 5 beamwidths in the E-plane and ± 5 beamwidths in the H-plane before side lobes become too large. One fourth of these scan positions are shown in Figure 9 (right). The radiation pattern of the full two-dimensional array was displayed in Figure 11 at 3 and 4 GHz, for several scan angles. In each case, the pattern matched Equation (25) in the E and H-planes in the main beam and dominant side lobes. The addition of a metal back plane helps to suppress back lobes. Peculiarly, the two-dimensional array did not match the theoretical prediction at 5 GHz as well as the one-dimensional case when scanned.

The two-dimensional, $N \times N = 8 \times 8$ horn array was analyzed in Section 4. The array demonstrated the correct linear relationships between $\Delta\phi_E$ and $\Delta\Phi_E$, and $\Delta\phi_H$ and $\Delta\Phi_H$ (Figure 10) (left). The beamwidth is again inversely proportional to frequency (Figure 10) (right). It is not surprising that the fits differ slightly in the E and H-planes, since the horn width changes in the E-plane but does not in the H-plane. The quality of the fits to $1/f + const$ are excellent. The additive constants in these fits are only necessary because the array cannot be infinitely long. Technically, Equation (25) implies that the beamwidth would go to zero as $N \rightarrow \infty$. The radiation patterns of the two-dimensional horn array are displayed in Figure 12 at 0.5 and 1.0 GHz, for the same sampling of scan angles as in Figure 11. The high-frequency beam is narrower and accompanied by grating lobes at ± 45 degrees. The patterns agree with theoretical expectations, with the exception of the H-plane lobes at ± 90 degrees. At low frequency, the beam is wider and is accompanied by grating lobes at ± 45 degrees from the main beam. The results match in the main lobe, but the simulation does not match the theoretical grating lobes. This is pronounced when the beam is moved far from broadside in the H-plane.

Finally, a simplified version of the $N = 8$ one-dimensional case of dipoles was embedded in a medium with varying index of refraction, $n(z)$. The model for $n(z)$ was a simple fit to the profile of the ice at the South Pole, which is a location of interest for planned phased array detectors designed to record Askaryan signals from UHE neutrinos passing through ice. Though the studies in this work are restricted to phased-arrays as transmitters, and not receivers, the shadow zone of the array was mapped at 200 MHz under realistic conditions. An interesting side effect of the phased array being the radiating system was that the grating lobes managed to propagate into the shadow zone.

Future work would include several enhancements to the simulations. Calculations of S-parameters for individual elements should be added, and optimization studies on horn and Yagi geometric parameters are warranted. However, other RF element types should also be studied. Due to the relevance of one-dimensional phased array receivers for UHE neutrino physics, one interesting choice is the wide-radius dipole used by the Radio Neutrino Observatory Greenland (RNO-G) collaboration [30]. Such elements already have low VSWR measurements in the relevant bandwidth. Finally, upgrading the simulation code to utilize parallel MEEP capabilities will increase the potential speed and complexity. Additional complexity will come in the form of more accurate antenna structure modeling, thereby improving the precision across a wide bandwidth.

Funding: This research was funded by the Office of Naval Research (ONR) under the Summer Faculty Research Program (SFRP).

Institutional Review Board Statement: Not applicable.

Informed Consent Statement: Not applicable.

Data Availability Statement: The data presented in this study are available on request from the corresponding author. Due to large file sizes and restricted bandwidth, please contact corresponding author to set up collaborative sharing.

Acknowledgments: We would like to thank the Office of Naval Research (ONR) for helping to support this research. In particular, we would like to thank the Naval Surface Warfare Center Corona Division and their continued support of the ONR Summer Faculty Research Program (SFRP). Conversations with Christopher Clark and Gary Yeakley were especially helpful. We are also grateful to Van Nguyen, Jeffery Benson, and Golda McWhorter. Karon Myles deserves our special thanks for helping to coordinate the SFRP program.

Conflicts of Interest: The authors declare no conflict of interest.

Appendix A

MEEP FDTD is more often applied to 1 μm scale lengths than the 1 cm-scale RF elements, so scale-invariance must be highlighted. Scale invariant units with $c = 1$ are used in MEEP when solving Maxwell's equations with the FDTD technique. The typical length scale in MEEP analysis is usually called the "a-value." Systems with dimensions of order 1 μm are said to have an "a-value of 1 μm ." A value of $a = 1 \text{ cm}$ is chosen for models presented in Sections 3 and 4. For example, if the frequency $f = 7.5 \text{ GHz}$, the wavelength is $4.0 \text{ cm} = 4.0a$, or simply 4.0 with $f = 1/\lambda = 0.25$. Since $c = 1$, $\lambda = f^{-1} = T$. The period is 4.0, so a simulation run of $50T = 200$ time units corresponds to 6.67 ns. Assuming 1 pixel/a-value, simulated radiation would therefore propagate 200 units of Δx in a straight line before time was up. A *resolution* parameter sets the number of pixels per distance unit and is usually larger than 1.0. Selecting the right resolution is often a subtle balance between capturing the most relevant effects while limiting the memory usage of the simulation results.

References

1. Syrytsin, I.; Zhang, S.; Pedersen, G.F. Circularly Polarized Planar Helix Phased Antenna Array for 5G Mobile Terminals. In Proceedings of the 2017 International Conference on Electromagnetics in Advanced Applications (ICEAA), Verona, Italy, 11–15 September 2017; pp. 1105–1108. [[CrossRef](#)]
2. Kikuchi, K.; Mikada, H.; Takekawa, J. Improved Imaging Capability of Phased Array Antenna in Ground Penetrating Radar Survey. In Proceedings of the Conference Proceedings, 79th EAGE Conference and Exhibition, Paris, France, 12–15 June 2017. [[CrossRef](#)]
3. Vieregg, A.; Bechtol, K.; Romero-Wolf, A. A technique for detection of PeV neutrinos using a phased radio array. *J. Cosmol. Astropart. Phys.* **2016**, *2016*, 005. [[CrossRef](#)]
4. Munekata, T.; Yamamoto, M.; Nojima, T. A Wideband 16-Element Antenna Array Using Leaf-Shaped Bowtie Antenna and Series-Parallel Feed Networks. In Proceedings of the 2014 IEEE International Workshop on Electromagnetics (iWEM), Sapporo Hokkaido, Japan, 4–6 August 2014; pp. 80–81. [[CrossRef](#)]
5. Avva, J.; Bechtol, K.; Chesebro, T.; Cremonisi, L.; Deaconu, C.; Gupta, A.; Ludwig, A.; Messino, W.; Miki, C.; Nichol, R.; et al. Development Toward a Ground-Based Interferometric Phased Array for Radio Detection of High Energy Neutrinos. In *Nuclear Instruments and Methods in Physics Research Section A: Accelerators, Spectrometers, Detectors and Associated Equipment*; Elsevier: Amsterdam, The Netherlands, 2016.
6. Ansys, Inc. *3D Electromagnetic Field Simulator for RF and Wireless Design*; Ansys, Inc.: Canonsburg, PA, USA, 2020.
7. Feng, N.; Zhang, Y.; Tian, X.; Zhu, J.; Joines, W.T.; Wang, G.P. System-Combined ADI-FDTD Method and Its Electromagnetic Applications in Microwave Circuits and Antennas. *IEEE Trans. Microw. Theory Tech.* **2019**, *67*, 3260–3270. [[CrossRef](#)]
8. Zhu, L.; Hwang, H.S.; Ren, E.; Yang, G. High Performance MIMO Antenna for 5G Wearable Devices. In Proceedings of the 2017 IEEE International Symposium on Antennas and Propagation & USNC/URSI National Radio Science Meeting, San Diego, CA, USA, 9–15 July 2017; pp. 1869–1870. [[CrossRef](#)]
9. Ho, T.Q.; Hunt, L.N.; Hewett, C.A.; Ready, T.G.; Mittra, R.; Yu, W.; Zolnick, D.A.; Kragalott, M. Analysis of Electrically Large Patch Phased Arrays via CFDTD. In Proceedings of the 2006 IEEE Antennas and Propagation Society International Symposium, Albuquerque, New Mexico, 9–14 July 2006; pp. 1571–1574. [[CrossRef](#)]
10. Burke, G.J.; Miller, E.K.; Poggio, A.J. The Numerical Electromagnetics Code (NEC)—A Brief History. *IEEE Antennas Propag. Soc. Symp.* **2004**, *3*, 2871–2874. [[CrossRef](#)]
11. Oskooi, A.F.; Roundy, D.; Ibanescu, M.; Bermel, P.; Joannopoulos, J.; Johnson, S.G. Meep: A flexible free-software package for electromagnetic simulations by the FDTD method. *Comput. Phys. Commun.* **2010**, *181*, 687–702. [[CrossRef](#)]
12. Fedeli, A.; Montecucco, C.; Gragnani, G.L. Open-Source Software for Electromagnetic Scattering Simulation: The Case of Antenna Design. *Electronics* **2019**, *8*, 1506. [[CrossRef](#)]

13. Liebig, T.; Rennings, A.; Held, S.; Erni, D. openEMS—A free and open source equivalent-circuit (EC) FDTD simulation platform supporting cylindrical coordinates suitable for the analysis of traveling wave MRI applications. *Int. J. Numer. Model. Electron. Networks Dev. Fields* **2013**, *26*, 680–696. [[CrossRef](#)]
14. Warren, C.; Giannopoulos, A.; Giannakis, I. gprMax: Open source software to simulate electromagnetic wave propagation for Ground Penetrating Radar. *Comput. Phys. Commun.* **2016**, *209*, 163–170. [[CrossRef](#)]
15. Richie, J.E.; Ababei, C. Optimization of patch antennas via multithreaded simulated annealing based design exploration. *J. Comput. Des. Eng.* **2017**, *4*, 249–255. [[CrossRef](#)]
16. Mailloux, R. *The Phased Array Antenna Handbook*; Artech House: Norwood, MA, USA, 2018.
17. Wahl, P.; Gagnon, D.S.L.; Debaes, C.; Erps, J.V.; Vermeulen, N.; Miller, D.A.B.; Thienpont, H. B-CALM: An Open-Source Multi-GPU-based 3D-FDTD with Multi-pole dispersion for Plasmonics. *Prog. Electromagn. Res.* **2013**, *138*, 467–478. [[CrossRef](#)]
18. Gorham, P.; Allison, P.; Barwick, S.; Beatty, J.; Besson, D.; Binns, W.; Chen, C.; Chen, P.; Clem, J.; Connolly, A.; et al. The Antarctic Impulsive Transient Antenna ultra-high energy neutrino detector: Design, performance, and sensitivity for the 2006–2007 balloon flight. *Astropart. Phys.* **2009**, *32*, 10–41. [[CrossRef](#)]
19. Gorham, P.; Barwick, S.; Beatty, J.; Besson, D.; Binns, W.; Chen, C.; Chen, P.; Clem, J.; Connolly, A.; Dowkontt, P. Observations of the Askaryan effect in ice. *Phys. Rev. Lett.* **2007**, *99*, 171101. [[CrossRef](#)] [[PubMed](#)]
20. Barwick, S.; Berg, E.; Besson, D.; Duffin, T.; Hanson, J.; Klein, S.; Kleinfelder, S.; Piasecki, M.; Ratzlaff, K.; Reed, C.; et al. Time-domain response of the ARIANNA detector. *Astropart. Phys.* **2015**, *62*, 139–151. [[CrossRef](#)]
21. Hanson, J.C. Ross Ice Shelf Thickness, Radio-frequency Attenuation and Reflectivity: Implications for the Arianna Uhe Neutrino Detector. In Proceedings of the 32nd International Cosmic Ray Conference, Beijing, China, 11–18 August 2011. [[CrossRef](#)]
22. Hanson, J.C.; Barwick, S.W.; Berg, E.C.; Besson, D.Z.; Duffin, T.J.; Klein, S.R.; Kleinfelder, S.A.; Reed, C.; Roumi, M.; Stezelberger, T.; et al. Radar absorption, basal reflection, thickness and polarization measurements from the Ross Ice Shelf, Antarctica. *J. Glaciol.* **2015**, *61*, 438–446. [[CrossRef](#)]
23. Avva, J.; Kovac, J.; Miki, C.; Saltzberg, D.; Vieregg, A. An in situ measurement of the radio-frequency attenuation in ice at Summit Station, Greenland. *J. Glaciol.* **2014**. [[CrossRef](#)]
24. Adamidis, G.A.; Vardiambasis, I.O.; Ioannidou, M.P.; Kapetanakis, T.N. Design and implementation of an adaptive beamformer for phased array antenna applications. *Microw. Opt. Technol. Lett.* **2020**, *62*, 1780–1784. [[CrossRef](#)]
25. Ahn, B.; Hwang, I.J.; Kim, K.S.; Chae, S.C.; Yu, J.W.; Lee, H.L. Wide-Angle Scanning Phased Array Antenna using High Gain Pattern Reconfigurable Antenna Elements. *Sci. Rep.* **2019**, *9*, 18391. [[CrossRef](#)] [[PubMed](#)]
26. Gampala, G.; Reddy, C.J. Advanced Computational Tools for Phased Array Antenna Applications. In Proceedings of the 2016 IEEE International Symposium on Phased Array Systems and Technology (PAST), Waltham, MA, USA, 18–21 October 2016; pp. 1–5. [[CrossRef](#)]
27. Dookayka, K. Characterizing the Search for Ultra-High Energy Neutrinos with the ARIANNA Detector. Ph.D. Thesis, University of California at Irvine, Irvine, CA, USA, 2011.
28. Barwick, S.W.; Berg, E.C.; Besson, D.Z.; Gaswint, G.; Glaser, C.; Hallgren, A.; Hanson, J.C.; Klein, S.R.; Kleinfelder, S.; Köpke, L.; et al. Observation of classically ‘forbidden’ electromagnetic wave propagation and implications for neutrino detection. *J. Cosmol. Astropart. Phys.* **2018**, *2018*, 055. [[CrossRef](#)]
29. Deaconu, C.; Vieregg, A.G.; Wissel, S.A.; Bowen, J.; Chipman, S.; Gupta, A.; Miki, C.; Nichol, R.J.; Saltzberg, D. Measurements and Modeling of Near-Surface Radio Propagation in Glacial Ice and Implications for Neutrino Experiments. *Physic. Rev. D* **2018**, *98*, 043010. [[CrossRef](#)]
30. Aguilar, J.A.; Allison, P.; Beatty, J.J.; Bernhoff, H.; Besson, D.; Bingefors, N.; Botner, O.; Buitink, S.; Carter, K.; Clark, B.A.; et al. Design and Sensitivity of the Radio Neutrino Observatory in Greenland (RNO-G). *arXiv* **2020**, arXiv:2010.12279.

Subject: [Electronics] Most Notable Articles (December 2020–February 2021)



electronics

IMPACT
FACTOR
2.412

Most Notable Articles (December 2020–February 2021)

New CMOS Devices and Their Applications
One-Transistor Dynamic Random-Access Memory Based on Gate-All-Around Junction-Less Field-Effect Transistor with a Si/SiGe Heterostructure
Young Jun Yoon et al.

Reliability Assessment and Modeling of Optical and Semiconductor Devices
LTPS TFTs with an Amorphous Silicon Buffer Layer and Source/Drain Extension
Hye In Kim et al.

Applications of Thin Films in Microelectronics
Electrical Performance and Stability Improvements of High-Mobility Indium-Gallium-Tin Oxide Thin-Film Transistors Using an Oxidized Aluminum Capping Layer of Optimal Thickness
Hyun-Seok Cha et al.

Microwave and Wireless Communications
Broadband RF Phased Array Design with MEEP: Comparisons to Array Theory in Two and Three Dimensions
Jordan C. Hanson

10th Anniversary of Electronics: Recent Advances in Computer Science & Engineering
Muon–Electron Pulse Shape Discrimination for Water Cherenkov Detectors Based on FPGA/SoC
Luis Guillermo Garcia et al.

AI-Based Transportation Planning and Operation
Estimating Micro-Level On-Road Vehicle Emissions Using the K-Means Clustering Method with GPS Big Data
Hyejung Hu et al.

Microelectronics and Optoelectronics
A Compact and Robust Technique for the Modeling and Parameter Extraction of Carbon Nanotube Field Effect Transistors
Laura Falaschetti et al.

Evolutionary Machine Learning for Nature-Inspired Problem Solving
Data Analytics and Mathematical Modeling for Simulating the Dynamics of COVID-19 Epidemic—A Case Study of India
Himanshu Gupta et al.

Ubiquitous Sensor Networks
Low-Cost Distributed Acoustic Sensor Network for Real-Time Urban Sound Monitoring
Ester Vidaña-Vila et al.

10th Anniversary of Electronics: Advances in Circuit and Signal Processing
Circuit Model and Analysis of Molded Case Circuit Breaker Interruption Phenomenon
Kun-A Lee et al.

Data according to Altmetric, a service collecting metrics and qualitative data that are complementary to traditional, citation-based metrics.

Call for Papers



Emerging Internet of Things Solutions and Technologies

edited by Franco Cicirelli, Antonio Guerrieri, Carlo Mastroianni and Andrea Vinci
submission deadline **31 March 2021**



Smart Processing for Systems under Uncertainty or Perturbation

edited by Sanghyuk Lee, Mihail Popescu and Eneko Osaba
submission deadline **9 April 2021**

Electronics 2021 Best Paper Awards for Women
Winner announcement date: 31 March 2022

Journal Awards

Why Submit to *Electronics*?

- **Open Access** Unlimited and free access for readers.
- **No Copyright Constraints** Retain copyright of your work and free use of your article.
- **Impact Factor 2.412** (2019 Journal Citation Reports®).
- **Thorough Peer-Review**
- **Coverage by Leading Indexing Services** Chemical Abstracts (American Chemical Society), Current Contents - Engineering, Computing & Technology/Web of Science (Clarivate), DOAJ, Inspec (IET), SCIE/Web of Science (Clarivate), Scopus (Elsevier).
- **Rapid Publication** Manuscripts are peer-reviewed and a first decision provided to authors approximately 15.1 days after submission; acceptance to publication is undertaken in 3.4 days (median values for papers published in this journal in the second half of 2020).
- **No Space Constraints, No Extra Space or Color Charges** No restriction on the length of the papers, number of figures or colors.
- **Discounts on Article Processing Charges (APC)** If you belong to an institute that participates with the MDPI Institutional Open Access Program (IOAP).

Open Access Journals for Academic Conferences

<p>PROCEEDINGS CHEMISTRY PROCEEDINGS ENGINEERING PROCEEDINGS</p> <p> proceedings</p> <p> chemistry proceedings</p> <p> engineering proceedings</p>	<p>MATERIALS PROCEEDINGS ENVIRONMENTAL SCIENCES PROCEEDINGS</p> <p> materials proceedings</p> <p> environmental sciences proceedings</p> <p> engineering proceedings</p>	<p>MDPI</p>
---	---	--------------------

Journal Information

Electronics (ISSN 2079-9292) is an international, peer-reviewed, open access journal on the science of electronics and its applications.

To submit to the journal click [here](#).

[Unsubscribe](#)

[Manage your subscriptions](#)



Academic Open Access Publishing
since 1996

MDPI

www.mdpi.com

St. Alban-Anlage 66, 4052 Basel, Switzerland

Tel. +41 61 683 77 34

Fax +41 61 302 89 18

Disclaimer: MDPI recognizes the importance of data privacy and protection. We treat personal data in line with the General Data Protection Regulation (GDPR) and with what the community expects of us. The information contained in this message is confidential and intended solely for the use of the individual or entity to whom they are addressed. If you have received this message in error, please notify me and delete this message from your system. You may not copy this message in its entirety or in part, or disclose its contents to anyone.



Subject: [Electronics] Most Notable Articles (February–May 2021)



IMPACT
FACTOR
2.412

Most Notable Articles (February–May 2021)

Bioelectronics

Evaluation of Large-Area Silicon Photomultiplier Arrays for Positron Emission Tomography Systems
Minjee Seo et al.

Circuit and Signal Processing

Area-Time Efficient Two-Dimensional Reconfigurable Integer DCT Architecture for HEVC
Pramod Kumar Meher et al.

Bioelectronics

Evaluation Method of Immediate Effect of Local Vibratory Stimulation on Proprioceptive Control Strategy: A Pilot Study
Yohei Ito et al.

Artificial Intelligence

Evaluating the Quality of Machine Learning Explanations: A Survey on Methods and Metrics
Jianlong Zhou et al.

Microwave and Wireless Communications Broadband RF Phased Array Design with MEEP: Comparisons to Array Theory in Two and Three Dimensions
Jordan C. Hanson

Networks

Identity and Access Management Resilience against Intentional Risk for Blockchain-Based IOT Platforms
Alberto Partida et al.

Circuit and Signal Processing

Investigating the Effects of Training Set Synthesis for Audio Segmentation of Radio Broadcast
Satvik Venkatesh et al.

Computer Science & Engineering

An Assessment of Deep Learning Models and Word Embeddings for Toxicity Detection within Online Textual Comments
Danilo Dessì et al.

Networks

UAV Forensic Analysis and Software Tools Assessment: DJI Phantom 4 and Matrice 210 as Case Studies
Fahad E. Salamh et al.

Computer Science & Engineering

When Data Fly: An Open Data Trading System in Vehicular Ad Hoc Networks
Markus Lücking et al.

Data according to Altmetric, a service collecting metrics and qualitative data that are complementary to traditional, citation-based metrics.

10th Anniversary of Electronics: Advances in Networks

Guest Editors: Prof. Dr. Dongkyun Kim, Prof. Dr. Qinghe Du, Dr. Mehdi Sookhak, Prof. Dr. Lei Shu, Assoc. Prof. Dr. Nurul I. Sarkar, Prof. Dr. Jemal H. Abawajy, Prof. Dr. Francisco Falcone
Deadline : 31 October 2021

mdpi.com/si/66341

Special Issue
Invitation to submit

Call for Papers



Application of Neural Networks in Biosignal Process

edited by Andrzej Czyżewski and Piotr Szczykło
submission deadline **30 June 2021**



Recent Advances in Antenna Design for 5G Heterogeneous Networks

edited by Issa Tamer Elfergani, Raed A. Abd-Alhameed and Abubakar Sadiq Hussaini
submission deadline **30 June 2021**

Why Submit to *Electronics*?

- **Open Access** Unlimited and free access for readers.
- **No Copyright Constraints** Retain copyright of your work and free use of your article.
- **Impact Factor 2.412** (2019 Journal Citation Reports®).
- **Thorough Peer-Review**
- **Coverage by Leading Indexing Services** Chemical Abstracts (American Chemical Society), Current Contents - Engineering, Computing & Technology/Web of Science (Clarivate), DOAJ, Inspec (IET), SCIE/Web of Science (Clarivate), Scopus (Elsevier).
- **Rapid Publication** Manuscripts are peer-reviewed and a first decision provided to authors approximately 15.1 days after submission; acceptance to publication is undertaken in 3.4 days (median values for papers published in this journal in the second half of 2020).
- **No Space Constraints, No Extra Space or Color Charges** No restriction on the length of the papers, number of figures or colors.
- **Discounts on Article Processing Charges (APC)** If you belong to an institute that participates with the MDPI Institutional Open Access Program (IOAP).

Journal Information

Electronics (ISSN 2079-9292) is an international, peer-reviewed, open access journal on the science of electronics and its applications.

To submit to the journal click [here](#).

[Unsubscribe](#)

[Manage your subscriptions](#)



Academic Open Access Publishing
since 1996

MDPI
www.mdpi.com
St. Alban-Anlage 66, 4052 Basel, Switzerland
Tel. +41 61 683 77 34
Fax +41 61 302 89 18

Disclaimer: MDPI recognizes the importance of data privacy and protection. We treat personal data in line with the General Data Protection Regulation (GDPR) and with what the community expects of us. The information contained in this message is confidential and intended solely for the use of the individual or entity to whom they are addressed. If you have received this message in error, please notify me and delete this message from your system. You may not copy this message in its entirety or in part, or disclose its contents to anyone.



Broadband RF Phased Array Design for UHE neutrino detection

Jordan C. Hanson^{a,*}

^aWhittier College,
13406 East Philadelphia Street, Los Angeles, California, 90602
E-mail: jhanson2@whittier.edu

Radio-frequency (RF) phased array systems have a wide variety of applications in engineering and physics research. Among these applications is ultra-high energy neutrino (UHE- ν) detection above 100 PeV via the Askaryan effect. Phased array design usually requires numerical modeling with expensive commercial computational packages. Using the open-source MIT Electromagnetic Equation Propagation (MEEP) package, a set of phased array designs relevant for UHE- ν detection is presented. Specifically, one-dimensional arrays of Yagi-Uda and horn antennas were modeled in the bandwidth of the Askaryan effect [0.1 - 5] GHz, and compared to theoretical expectations. Precise matches between MEEP simulation and radiation pattern predictions at different frequencies and beam angles are demonstrated. Finally, the effect of embedding a phased array within Antarctic ice is studied. Askaryan-class UHE- ν detectors are being constructed in Antarctic ice because it is an ideal detection medium for UHE- ν . Future work will develop the phased array concepts with parallel MEEP, in order to increase the detail, complexity, and speed of the computations.

37th International Cosmic Ray Conference (ICRC 2021)
July 12th – 23rd, 2021
Online – Berlin, Germany

*Presenter

1. Introduction

Phased arrays have applications in 5G, ground penetrating radar (GPR), and scientific instrumentation [13, 14, 16]. A series of three-dimensional antenna elements are arranged in a line with fixed spacing [2]. Proprietary RF modeling packages like XFDTD and HFSS are often used to model phased arrays [1, 8, 12]. The XFDTD package, for example, relies on the finite difference time domain (FDTD) method. The FDTD approach is a computational electromagnetics (CEM) technique in which Maxwell's equations are solved in discrete spacetime. Two advantages of the open-source approach to RF design are zero-cost and fine control over simulation objects. Maxwell's equations are scale-invariant, so FDTD codes designed for μm -wavelengths can be re-purposed for RF designs. One such package is the MIT Electromagnetic Equation Propagation (MEEP) package [15].

A recent review [7] covered open-source software facilitates RF antenna design. In this work, the radiation patterns of one-dimensional phased array designs are simulated with the MEEP package. Common MEEP applications have μm -scale wavelengths, but scale-invariance allows the user to treat designs as cm-scale RF elements. Two classes of phased array element are considered: Yagi-Uda and horn antennas. The former is applied to single-frequency designs, while the latter is applied to broadband design. The phase-steering properties and radiation patterns of all designs are shown to match theoretical predictions. The appropriate array theory is shown in Section 2. Section 3 contains comparisons between theory and simulation. In Section 4, the effect of a varying index of refraction is introduced.

2. Phased Array Antenna Theory

The structure of a one-dimensional phased array is shown in Figure 1. Two constants that determine the beam angle $\Delta\phi$ of the array are the spacing d_y and the phase shift per antenna $\Delta\Phi$. Letting the subscript i label each of the N elements, the one-dimensional spacing in Figure 1 is $d_y \hat{j} = \vec{r}_{i+1} - \vec{r}_i$. The phase shift per antenna is $\Delta\Phi = \Phi_{i+1} - \Phi_i$. The relationship between d_y , $\Delta\Phi$, and $\Delta\phi$ is quoted in Section 2.1. The radiation pattern for a given $\Delta\phi$ is quoted in Section 2.2. For all coordinate systems, the azimuthal angle in the xy-plane is ϕ , and the polar angle from the z-axis is θ .

2.1 Phase Steering and Beam Angle

According to [10], the beam angle $\Delta\phi$ of the array given $\Delta\Phi$ and d_y is

$$\Delta\Phi \approx 2\pi(d_y/\lambda)\Delta\phi \quad (1)$$

Equation 1 relates $\Delta\phi$, the beam angle, and $\Delta\Phi$, the phase shift per element, via a linear relationship with slope $\lambda/(2\pi d_y)$.

2.2 Radiation Patterns and Beam Width

Let N be the number of radiating elements in the phased array. Further, let the beam angle be $\Delta\phi = \phi - \phi_0$, where ϕ_0 is some reference angle (usually in the direction orthogonal to the phased array). According to [10], the radiation pattern is

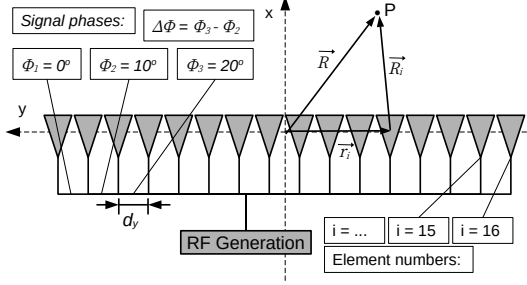


Figure 1: Definitions for the coordinate system, element label i , position vectors, and phase shift per antenna for a one-dimensional phased array of RF radiating elements. An example phase shift per antenna of $\Delta\Phi = \Phi_2 - \Phi_1 = \Phi_3 - \Phi_2 = \Phi_{i+1} - \Phi_i = 10^\circ$ value is shown. Example position vectors for the 12th element are shown: $\vec{R} = \vec{r}_{12} + \vec{R}_{12}$.

$$P(\phi) = \left(\frac{\sin(\pi N(d_y/\lambda)(\sin(\phi) - \sin(\phi_0)))}{N \sin(\pi(d_y/\lambda)(\sin(\phi) - \sin(\phi_0)))} \right)^2 \quad (2)$$

The radiation pattern in Equation 2 is shown to match precisely the main beam of FDTD calculations via MEEP for one-dimensional arrays in Section 3. All one-dimensional array radiation patterns correspond to the E-plane (the xy-plane). The MEEP python routine `get_farfield` is evaluated at a radius $r \gg L$, the length of the array, to obtain the far-fields \vec{E} and \vec{H} . Notice that not all open-source FDTD codes offer near-field to far-field projection [7].

3. Results: Phase Steering, Beam Angle, Beamwidth, and Radiation Pattern

The two element designs are depicted in Figure 2. The Yagi-Uda antennas have 6 elements with the same radius, oriented in the xy-plane: one reflector, one radiator, three directors and a connecting boom. The horn antennas have three structures: the box containing the linearly polarized radiator, the radiator, and the curves of the horn. An exponential function describes the curves. All antenna elements have metallic conductivity, and the edge of space consists of a perfectly matched layer (PML) to cancel reflections.

3.1 Phase Steering, Beam Angle, and Beamwidth

Phase steering, beam angle, and beamwidth results are shown in Figure 3. The y-axes of Figure 3 (top left) and (top right) are the beam angles of the Yagi-Uda arrays, divided by the beam widths. The x-axes are the phase shifts per element. The top left and top right plots correspond to $N = 8$ and $N = 16$, respectively. For the $N = 16$ horn case (bottom left and right), the value of $d_y/\lambda = f d_y/c$ varies because the elements can radiate from $\approx 0.3 - 5.0$ GHz. The black solid lines in the top left and top right graphs of Figure 3 are linear fits to the Yagi-Uda data. The gray lines represent the function $f(x) = bx$, with $b = \lambda/(2\pi d_y)$. The slopes match, with 1% errors arising from pattern distortion for large $\Delta\phi$. At large $\Delta\Phi$, side lobes can merge with the main beam to shift the location of the main beam by $O(1)$ degree.

For the broadband horn case in the bottom left of Figure 3, data from three frequencies are shown: 0.3, 1.5, and 3.0 GHz. The intercepts are all zero and the slopes scale correctly. The fit

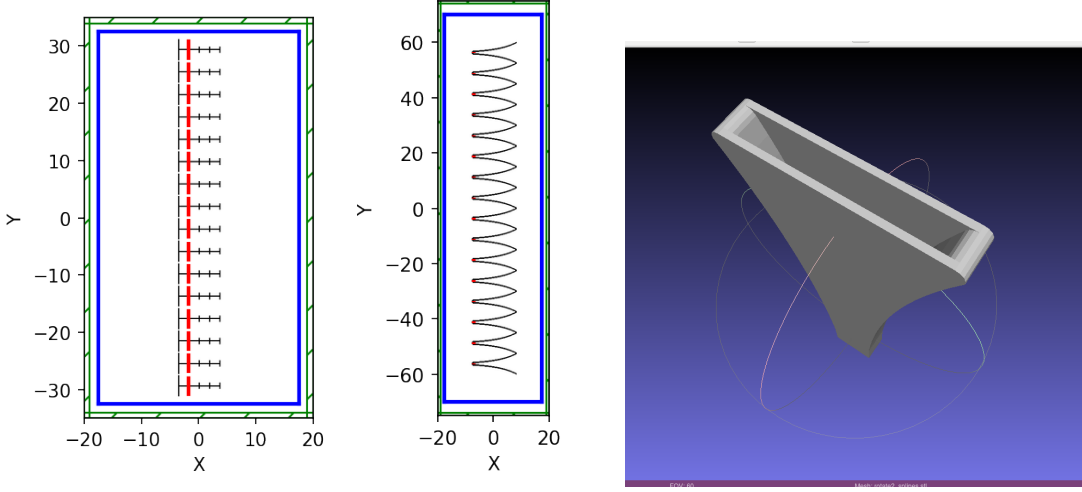


Figure 2: The 2D antenna designs used in the 1D phased array simulations. (Left) The $N = 16$ Yagi-Uda array. (Middle) The $N = 16$ horn array. The blue surfaces are MEEP *Near2FarRegion* objects for near-to-far projection. All dimensions are in centimeters. (Right) Example STL file for 3D version of horn.

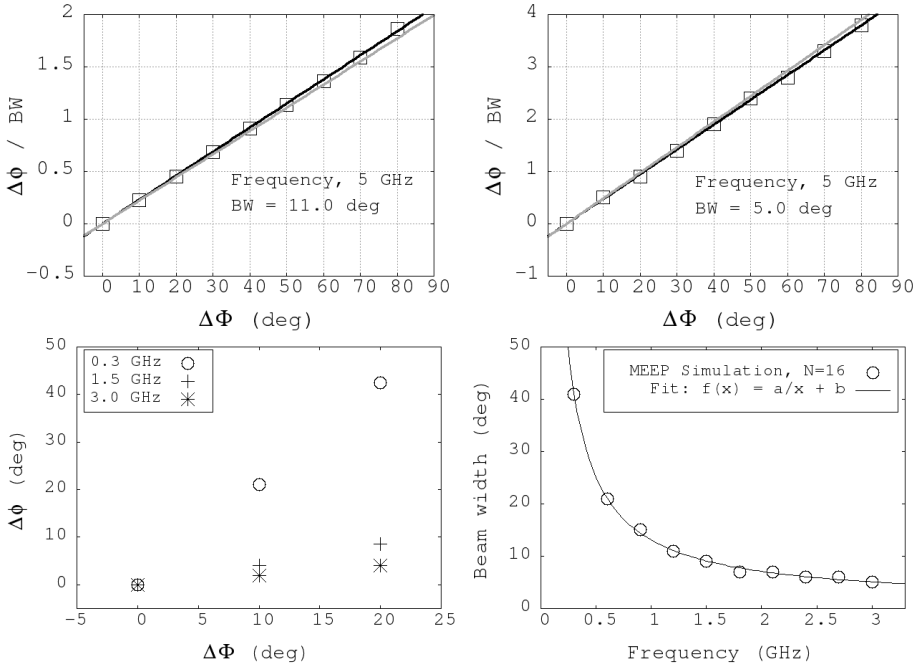


Figure 3: (Top left) The beam angle $\Delta\phi$ divided by the beam width BW for the $N = 8$ one-dimensional Yagi array versus $\Delta\Phi$, the phase shift per element. (Top right) The same results for the $N = 16$ array. (Bottom left) $\Delta\phi$ versus $\Delta\Phi$ for the $N = 16$ version of the one-dimensional horn array, for several frequencies. (Bottom right) The dependence of the beam width on frequency for the one-dimensional $N = 16$ horn array.

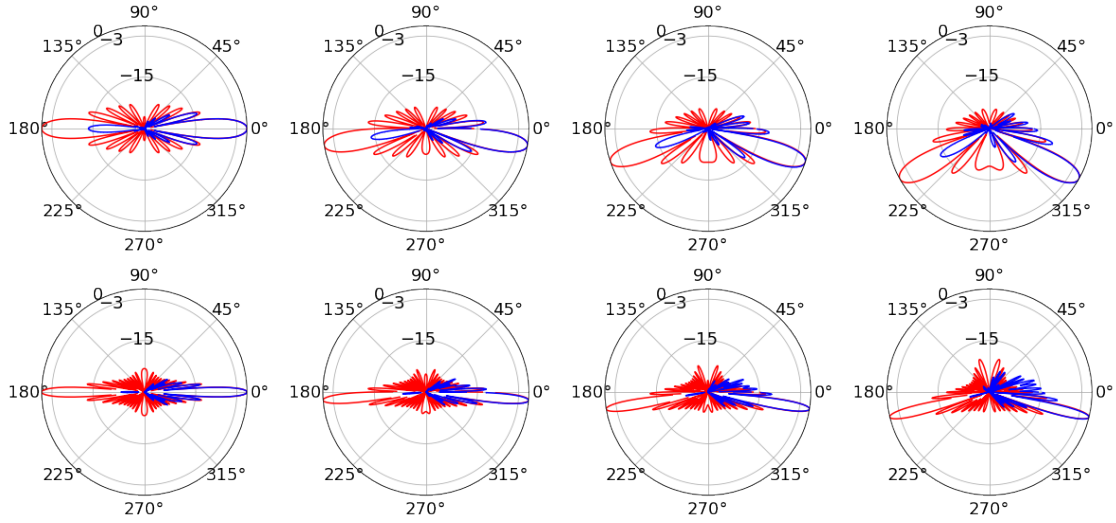


Figure 4: Yagi-Uda results. (Top row) $f = 2.5$ GHz, and $\Delta\Phi = 0, 20, 40, 60$ degrees from left to right. (Second row) $f = 5.0$ GHz, and $\Delta\Phi = 0, 20, 40, 60$ degrees from left to right. The radial units are dB, and the angular units are degrees.

parameters for beam width $f(x) = a/x + b$ were $a = 12.0 \pm 0.1$ degree GHz, and $b = 1.1 \pm 0.2$ degrees. The $1/f$ -dependence is a good description of the beamwidth across the [0.3 - 5 GHz] bandwidth. The constant term b is only necessary since the array has finite length L .

3.2 Radiation Patterns

Radiation patterns for $N = 16$ one-dimensional arrays are shown in Figures 4 and 5, respectively. As described above, the x-direction ($\Delta\phi = 0$) corresponds to no phase shift per element ($\Delta\Phi = 0$). The radiation patterns are shown in blue, and the red curves represent Equation 2. Equation 2 is symmetric, with identical forward and backward lobes.

The Yagi-Uda results are shown for 2.5 and 5.0 GHz frequencies in Figure 4, with $\Delta\Phi = 0, 20, 40$, and 60 degrees. The amplitudes of all side-lobes are limited to ≈ -15 dB, except at the highest beam angles where scan losses are experienced. The effect of frequency on beam steering is evident. The same $\Delta\Phi$ does not generate as large a $\Delta\phi$ at higher frequencies because the slope implied by Equation 1 is proportional to λ .

The horn results are shown in Figure 5 for 0.5 GHz and 5.0 GHz frequencies. The phase shifts per element are $\Delta\Phi = 0, 10, 20$, and 30 degrees. Wideband systems experience a natural trade-off in angular range versus bandwidth. A d_y/λ value that is acceptably smaller than one at low frequencies can grow larger with increasing frequency, leading to interference patterns. At 5.0 GHz, the horns radiate at ± 45 degrees from $\Delta\phi = 0$. The prediction from Equation 2 is that these *grating lobes* are equal in relative power to the main beam. The horns limit them to -15 dB if $|\Delta\Phi| < 35$ degrees.

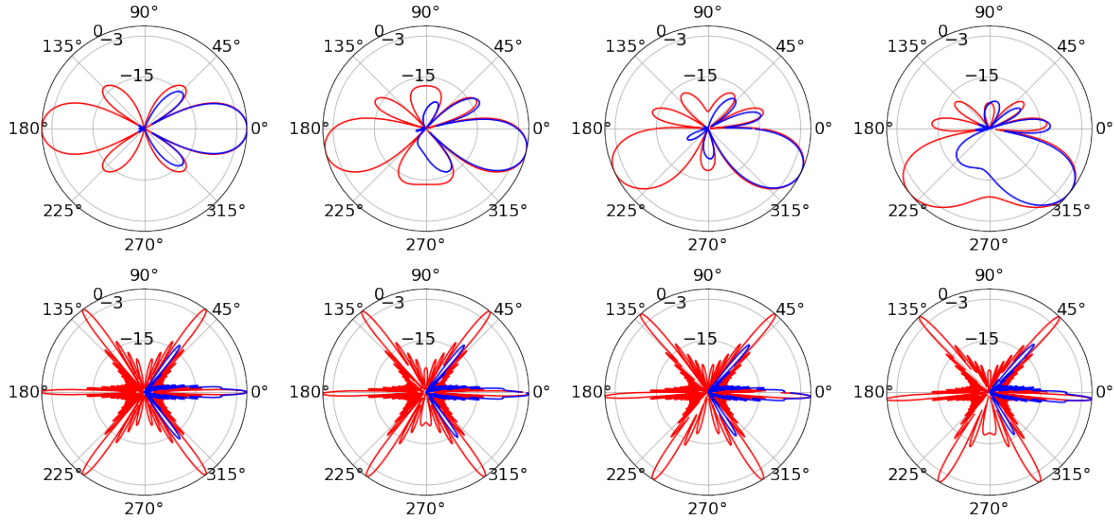


Figure 5: Horn results. (Top row) $f = 0.5$ GHz, and $\Delta\Phi = 0, 10, 20, 30$ degrees from left to right. (Second row) $f = 5.0$ GHz, and $\Delta\Phi = 0, 10, 20, 30$ degrees from left to right. The radial units are dB, and the angular units are degrees.

4. Variation of the Index of Refraction

The behavior of a phased array embedded within a spatially-dependent index of refraction $n(z)$ is interesting to the UHE- ν community [2, 16]. Phased arrays represent an opportunity to lower the RF detection threshold for RF pulses generated by UHE- ν via the Askaryan effect. Ice is the most convenient medium for Askaryan pulse detection due to the RF transparency and large pristine volumes located in Antarctic and Greenlandic ice sheets and shelves [3, 9, 11]. The index of refraction varies within the ice because of the transition between surface snow ($\rho \approx 0.4$ g/cm 3) and the solid ice below ($\rho = 0.917$ g/cm 3). Embedded phased arrays with varying $n(z)$ emit signals that curve in the direction of increasing $n(z)$.

The *shadow zone* is the volume of ice from which RF signals do not reach a receiver due to the excess curvature of the ray trace [6]. While there is evidence that RF signals can propagate horizontally through Antarctic ice [4], data from Greenland suggests the relative strength of the effect is small compared to the curved radiation [5]. It is possible to map out the shadow zone for an embedded phased array radiating at fixed frequency. Grating lobe power reflects downward from the snow-air interface, and radiates into the shadow zone. Grating lobe power also refracts into the air above the interface.

A two-parameter fit to the $n(z)$ data versus depth z below the surface is given by [4]

$$n(z) = \begin{cases} 1 & z > 0 \\ n_{\text{ice}} - \Delta n \exp(z/z_0) & z \leq 0 \end{cases} \quad (3)$$

The fit parameters in Equation 3 come from Reference [4]: $\Delta n = 0.423 \pm 0.004$ and $z_0 = 77 \pm 2$ meters, with $n_{\text{ice}} = 1.78$. These values are derived from the SPICE core near the South Pole. Equation 3 was implemented in a volume surrounding a horn array with all but the radiators removed. Further, the length scale was reinterpreted to be meters rather than centimeters. The $\lambda/4$

dipoles were spaced by $\lambda/2$ according to their free space λ value. At 200 MHz, the dipole length is 0.375 meters, and the spacing is 0.75 meters.

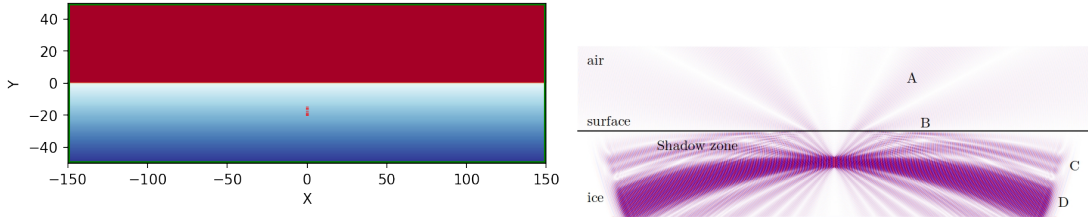


Figure 6: (Left) The simplified $N = 8$ phased array with dimensions in meters. The colorscale represents $n(z)$ in Equation 3. (Right) The magnitude of the z-component of the E-field from the vertical dipoles. The air, surface, and ice regions are the same as (left). The array depth is -15 meters. (A) Radiation refracting through the surface into the air. (B) Grating lobes reflect from the surface into the shadow zone. (C) Grating lobes propagating through the shadow zone. (D) The main beam bent downward due to the gradient in $n(z)$.

Figure 6 contains the results of a $N = 8$ dipole array embedded in a medium with the index profile in Equation 3. Figure 6 (left) shows the schematic of the calculation, and Figure 6 (right) shows the magnitude of the z-component of the radiated E-field. The units in Figure 6 are meters, and the radiation frequency is 200 MHz. The distance between the air-snow interface and the first phased array element is 15 meters. The color scale in Figure 6 (right) is ± 0.05 with the signal amplitude of the elements ± 1.0 at 200 MHz. The amplitude scale is less important than observing *where* the radiation has penetrated the ice after 200 radiation periods. In Figure 6 (right), the main beam has curved downwards in the direction of increasing $n(z)$, while grating lobes have both diffracted to the air and reflected into the shadow zone. The rate of curvature of the main beam is controlled by the fit parameter z_0 in Equation 3.

References

- [1] Ansys, Inc., Canonsburg, Pennsylvania. *3D Electromagnetic Field Simulator for RF and Wireless Design*, 2020.
- [2] J. Avva, K. Bechtol, T. Chesebro, L. Cremonesi, C. Deaconu, A. Gupta, A. Ludwig, W. Messino, C. Miki, R. Nichol, E. Oberla, M. Ransom, A. Romero-Wolf, D. Saltzberg, C. Schlupf, N. Shipp, G. Varner, A. Vieregg, and S. Wissel. Development toward a ground-based interferometric phased array for radio detection of high energy neutrinos. *Nuclear Instruments and Methods in Physics Research Section A: Accelerators, Spectrometers, Detectors and Associated Equipment*, 869:46 – 55, 2017.
- [3] J. Avva, J. Kovac, C. Miki, D. Saltzberg, and A. Vieregg. An in situ measurement of the radio-frequency attenuation in ice at Summit Station, Greenland. *Journal of Glaciology*, 2014.
- [4] S. W. Barwick, E. C. Berg, D. Z. Besson, G. Gaswint, C. Glaser, A. Hallgren, J. C. Hanson, S. R. Klein, S. Kleinfelder, L. Köpke, I. Kravchenko, R. Lahmann, U. Latif, J. Nam, A. Nelles, C. Persichilli, P. Sandstrom, J. Tatar, and E. Unger. Observation of classically ‘forbidden’ electromagnetic wave propagation and implications for neutrino detection. *Journal of Cosmology and Astroparticle Physics*, 2018(07):055–055, 2018.

- [5] C. Deaconu, A. G. Vieregg, S. A. Wissel, J. Bowen, S. Chipman, A. Gupta, C. Miki, R. J. Nichol, and D. Saltzberg. Measurements and modeling of near-surface radio propagation in glacial ice and implications for neutrino experiments. *Phys. Rev. D*, 98:043010, Aug 2018.
- [6] K. Dookayka. *Characterizing the Search for Ultra-High Energy Neutrinos with the ARIANNA Detector*. PhD thesis, Univeristy of California at Irvine, 2011.
- [7] A. Fedeli, C. Montecucco, and G. L. Gragnani. Open-Source Software for Electromagnetic Scattering Simulation: The Case of Antenna Design. *Electronics*, 8(12):1506, 2019.
- [8] N. Feng, Y. Zhang, X. Tian, J. Zhu, W. T. Joines, and G. P. Wang. System-Combined ADI-FDTD Method and Its Electromagnetic Applications in Microwave Circuits and Antennas. *IEEE Transactions on Microwave Theory and Techniques*, 67(8):3260–3270, 2019.
- [9] J. C. Hanson. Ross Ice Shelf Thickness, Radio-frequency Attenuation and Reflectivity: Implications for the ARIANNA UHE Neutrino Detector. In *Proceedings of the 32nd International Cosmic Ray Conference, Beijing, China, August 2011*, 2011.
- [10] J. C. Hanson. Broadband rf phased array design with meep: Comparisons to array theory in two and three dimensions. *Electronics*, 10(4), 2021.
- [11] J. C. Hanson, S. W. Barwick, E. C. Berg, D. Z. Besson, T. J. Duffin, S. R. Klein, S. A. Kleinfelder, C. Reed, M. Roumi, T. Stezelberger, J. Tatar, J. A. Walker, and L. Zou. Radar absorption, basal reflection, thickness and polarization measurements from the Ross Ice Shelf, Antarctica. *Journal of Glaciology*, 61(227):438–446, 2015.
- [12] T. Q. Ho, L. N. Hunt, C. A. Hewett, T. G. Ready, R. Mittra, W. Yu, D. A. Zolnick, and M. Kragalott. Analysis of Electrically Large Patch Phased Arrays via CFDTD. *2006 IEEE Antennas and Propagation Society International Symposium, Albuquerque, New Mexico, July 2006*.
- [13] K. Kikuchi, H. Mikada, and J. Takekawa. Improved Imaging Capability of Phased Array Antenna in Ground Penetrating Radar Survey. *Conference Proceedings, 79th EAGE Conference and Exhibition 2017, Paris, France, June 2017*, 2017.
- [14] T. Munekata, M. Yamamoto, and T. Nojima. A Wideband 16-Element Antenna Array Using Leaf-Shaped Bowtie Antenna and Series-Parallel Feed Networks. *2014 IEEE International Workshop on Electromagnetics (iWEM), Sapporo Hokkaido, Japan, August 2014*, pages 80–81, 2014.
- [15] A. F. Oskooi, D. Roundy, M. Ibanescu, P. Bermel, J. Joannopoulos, and S. G. Johnson. Meep: A flexible free-software package for electromagnetic simulations by the FDTD method. *Computer Physics Communications*, 181(3):687–702, 2010.
- [16] A. Vieregg, K. Bechtol, and A. Romero-Wolf. A technique for detection of PeV neutrinos using a phased radio array. *Journal of Cosmology and Astroparticle Physics*, 2016(02):005, feb 2016.



NuRadioMC: simulating the radio emission of neutrinos from interaction to detector

C. Glaser^{1,a}, D. García-Fernández^{2,3,b}, A. Nelles^{2,3,c}, J. Alvarez-Muñiz⁴, S. W. Barwick¹, D. Z. Besson⁵, B. A. Clark⁶, A. Connolly⁶, C. Deaconu⁷, K. D. de Vries⁸, J. C. Hanson⁹, B. Hokanson-Fasig¹⁰, R. Lahmann^{1,3}, U. Latif⁵, S. A. Kleinfelder¹¹, C. Persichilli¹, Y. Pan¹², C. Pfendner¹³, I. Plaisier^{2,3}, D. Seckel¹², J. Torres⁶, S. Toscano¹⁴, N. van Eijndhoven⁸, A. Vieregg⁷, C. Welling^{2,3}, T. Winchen^{8,15}, S. A. Wissel¹⁶

¹ Department of Physics and Astronomy, University of California, Irvine, CA 92697, USA

² DESY, Platanenallee 6, 15738 Zeuthen, Germany

³ Erlangen Centre for Astroparticle Physics, Friedrich-Alexander-Universität Erlangen-Nürnberg, 91058 Erlangen, Germany

⁴ IGFAE, Depto. de Física de Partículas, Universidade de Santiago de Compostela, Santiago de Compostela, Spain

⁵ Department of Physics and Astronomy, University of Kansas, Lawrence, USA

⁶ Department of Physics and Center for Cosmology and Astroparticle Physics, The Ohio State University, Columbus, USA

⁷ Kavli Institute for Cosmological Physics, University of Chicago, Chicago, USA

⁸ Vrije Universiteit Brussels, Brussels, Belgium

⁹ Department of Physics, Whittier College, Whittier, CA, USA

¹⁰ Department of Physics and Wisconsin IceCube Particle Astrophysics Center, University of Wisconsin, Madison, USA

¹¹ Department of Electrical Engineering and Computer Science, University of California, Irvine, CA 92697, USA

¹² Department of Physics and Astronomy, Bartol Research Institute, University of Delaware, Newark, USA

¹³ Otterbein University, Westerville, OH, USA

¹⁴ Université Libre, Brussels, Belgium

¹⁵ Max-Planck Institute for Radio Astronomy, Bonn, Germany

¹⁶ Physics Department, California Polytechnic State University, San Luis Obispo, CA 93407, USA

Received: 3 June 2019 / Accepted: 5 January 2020 / Published online: 31 January 2020

© The Author(s) 2020

Abstract NuRadioMC is a Monte Carlo framework designed to simulate ultra-high energy neutrino detectors that rely on the radio detection method. This method exploits the radio emission generated in the electromagnetic component of a particle shower following a neutrino interaction. NuRadioMC simulates everything from the neutrino interaction in a medium, the subsequent Askaryan radio emission, the propagation of the radio signal to the detector and finally the detector response. NuRadioMC is designed as a modern, modular Python-based framework, combining flexibility in detector design with user-friendliness. It includes a state-of-the-art event generator, an improved modelling of the radio emission, a revisited approach to signal propagation and increased flexibility and precision in the detector simulation. This paper focuses on the implemented physics processes and their implications for detector design. A variety of models and parameterizations for the radio emission of neutrino-induced showers are compared and reviewed. Comprehensive examples are used to discuss the capabilities of

the code and different aspects of instrumental design decisions.

1 Introduction

High-energy neutrino astronomy is a most promising approach to address the still unanswered question of the origin of high-energy cosmic rays [1]. Neutrinos are the perfect messenger. Because they have negligible mass, are electrically neutral and have an extremely low interaction probability, they traverse the universe essentially unimpeded and point directly back to their sources. However, measuring neutrinos requires the instrumentation of large volumes to observe sufficient target material in which a rare interaction of these particles may occur. Currently the largest detector having observed neutrinos is IceCube, which uses the Antarctic ice as a target medium and instruments it with optical sensors [2].

Neutrino astronomy recently took a significant leap forward when the IceCube detector at the South Pole was used to measure a yet unexplained excess of events that provides

^a e-mail: christian.glaser@uci.edu

^b e-mail: daniel.garcia@desy.de

^c e-mail: anna.nelles@desy.de

the first strong evidence for astrophysical neutrino sources [3]. The sources have not yet been identified, though compelling evidence for a first source was delivered with the observation of a spatial and temporal coincidence between a flaring blazar, observed with gamma-ray telescopes, and a high-energy neutrino [4]. However, detection of astrophysical neutrinos above a few tens of PeV has not been achieved yet, possibly due to the neutrino flux expected to steeply fall with energy, which calls for instrumented volumes larger than those currently existing. A two orders of magnitude increase in the volume instrumented by IceCube is considered cost-prohibitive due to the attenuation and scattering of optical light in ice [5]. Such a detector may measure the continuation of the neutrino flux, as well as the expected fluxes in the ultra-high energy regime [1].

1.1 Experimental and physical context of radio detection

High-energy neutrinos ($E_\nu > 10^{16}$ eV) can be most efficiently observed with the radio technique. Radio signals are produced via the Askaryan effect [6] from particle cascades generated in the ice following interactions of the neutrinos. The Askaryan effect arises from the development of a charge excess in the shower front as it accumulates electrons from the surrounding medium. The resulting changing current leads to measurable radio emission in the MHz–GHz frequency range. The Antarctic ice is transparent to these radio signals which allows for a cost-effective instrumentation of large volumes with sparse arrays. The attenuation length is about 1 km, depending on the frequency and ice temperature [7]. This results in an effective volume in the order of 1km^3 per single detector station, similar to the size of the entire IceCube detector.

The radio technique has already been successfully piloted with detectors at the South Pole and at Moore’s Bay on the Ross ice-shelf. The ARIANNA project [8,9] uses an array of autonomous detector stations with antennas located close to the ice surface, whereas the ARA project [10] uses antennas at a depth of up to 200 m below the firn layer. The experimental techniques matured substantially over the last years [11,12] and the community is well prepared for the construction of a large scale Askaryan detector with enough exposure to measure the continuation of the astrophysical neutrino flux to higher energies [1], to potentially discover cosmogenic neutrinos [13–15], and measure particle physics properties at yet unachieved energies [16].

With the developments on the experimental side, improved Monte Carlo simulations became imperative, leading to the development of NuRadioMC, which is presented in this article. A versatile and validated simulation of the radio signal in an Askaryan detector is crucial in many areas: for the determination of the sensitivity of a specific detector, for the optimization of the detector layout, to establish the require-

ments of the hardware to record the relevant parts of the signal, for the computation of a realistic signal expectation that is used to search for neutrino induced signals out of a large background of thermal and anthropogenic triggers, and finally, for the development of reconstruction techniques to determine the neutrino properties from the short radio flashes. In particular, the usage of modern deep-learning techniques requires a large and precise training data set.

The diversity of possible station layouts (e.g. compare the ARA and ARIANNA approach) requires a flexible software which is one of the main limitations of existing codes that were each targeted at a very specific experimental layout [17–19]. NuRadioMC is not tailored to a specific experimental design, and a detector station can have any number of antennas at arbitrary positions. In addition, the Askaryan radio technique is not limited to in-ice detectors. For example the lunar regolith has similar radio properties as ice and provides a immense neutrino target that can be observed from Earth with radio telescopes [20,21], providing the opportunity for synergies in simulations. Hence, from the beginning NuRadioMC was designed for maximum flexibility while maintaining user-friendliness.

1.2 Structure of NuRadioMC

The Monte-Carlo simulation of Askaryan signals from neutrino induced in-ice¹ particle showers is logically split up into four independent steps, the four pillars of NuRadioMC:

- 1. Event generation** The simulation of a neutrino flux. This includes the simulation of different neutrino properties (energy, direction, flavor, etc.), lepton propagation, the position of the interaction vertices, and the properties of the induced particle shower, i.e., how much neutrino energy is transferred into the shower, whether it is an electromagnetic or hadronic shower, etc.
- 2. Signal generation** The calculation of the Askaryan radio pulse generated from the particle shower.
- 3. Signal propagation** The propagation of the radio signal through the medium, from its origin to each antenna. Naturally occurring media typically have a density gradient resulting in bent rather than straight trajectories of the radio signal. Also, multiple distinct paths from the interaction vertex to the antenna may exist for typical geometries and ice typically shows a frequency-dependent attenuation length.
- 4. Detector simulation** The simulation of all components of the detector hardware. This step includes the conver-

¹ We will continue to refer to the standard case of a neutrino interaction in ice, when describing NuRadioMC. However, the code is designed in such a way that it can also support media other than ice, and exotic particles such as for instance dark photons [22].

sion from the electric-field pulses at the antenna positions to the measured voltages of each antenna channel, as well as the simulation of the trigger. It accounts for frequency dependent gain and group-delay, sampling-speed, record-length, etc.

The separation of the four steps follows the temporal structure of the physical processes. In a MC simulation this sequence will be different and not linear, e.g., we determine the signal path before generating it, so that we only need to calculate the Askaryan signal at the particular emission angle leading to that path. Moreover, after having calculated the signal, we need to use the propagation module again to determine the signal attenuation along the path.

We note that the separation of signal generation and propagation is a valid approximation when the difference in travel time from different points of the emission region to an observer in a homogeneous medium and one in a medium with a density gradient (bent trajectories) is small with respect to the observation frequency. We find that this assumption holds for all but rare and extreme geometries of an in-ice detector at frequencies up to 1 GHz.

The four pillars are complemented by a set of utility classes that are accessible at all times throughout the simulation such as a model of the medium, or a model of the signal attenuation. To ensure maximum flexibility and ease of use of different codes and programming languages the four pillars are separated as much as possible. The modules can be written in any language but Python wrappers of the relevant functions are required (this can be achieved e.g. with Cython [23]), so that the simulation can be steered from Python. This design was chosen to maximize user-friendliness and allow for the interfacing with other existing frameworks.

1.3 Improvements on the simulated physics in NuRadioMC

NuRadioMC does not only improve in flexibility and ease of use over existing codes, but also includes more physics processes in the simulation than previous codes and improves on precision. In the event generation, the subsequent decay of taus following a tau-neutrino interaction is modelled and the interface to simulate any *multi-bang* model is provided. Hence, models predicting several spatially-separated interactions can be implemented and simulated.

In the signal generation pillar, various Askaryan signal generation models are implemented. Previous MC codes relied on parameterizations of the frequency spectrum of radio emission [24] or on time-domain calculations mostly restricted to electromagnetic shower profiles [25]. NuRadioMC improves this approach by providing a time-domain calculation from an extensive library of electromagnetic, hadronic and tau-initiated showers. In particular, this

allows for a realistic treatment of the Landau–Pomeranchuk–Migdal effect (LPM effect) [26,27].

In the signal propagation pillar, new ray-tracing techniques based on an analytic solution of possible signal paths are implemented. This implementation results in unprecedented combination of speed and accuracy. Furthermore, we provide the interface to a more detailed numerical calculation that can simulate the signal paths in arbitrary 3D density profiles.

In the detector simulation pillar, we use the *NuRadioReco* code [28] that allows for the simulation of any detector geometry. In particular, it includes a detailed antenna response for a variety of antenna types and arbitrary orientations, treating the full set of complex gains as well as complex triggers such as phased-arrays.

In this article, we first describe each of the four pillars in detail and discuss different approaches. Then, we present three examples of how to use NuRadioMC and discuss the implications for the design of a high-energy neutrino radio detector.

2 Event generation

The event generation is logically separated from the simulation and provides general event parameters as input to the simulation. The results of the event generation are stored in an HDF5 file [29], which ensures that the event generator is easy to change in order to cover a variety of physics cases, as well as practical cases such as the simulation of calibration pulser data. This section describes the standard case implemented in NuRadioMC and provides an outlook for future implementation and special cases.

Having the event generation separated from the other simulation steps is beneficial because it allows the user to test the influence of different parameters on the same events. For example, the influence of different signal generation models, ice properties that influence the signal propagation or attenuation, and trigger schemes and thresholds, while using the same set of events.

2.1 Considerations concerning the coordinate system

All coordinates are specified in a local Cartesian coordinate system with its origin centered at the surface of the ice (see Fig. 1). The implementation of a global coordinate system that takes into account the curvature of the Earth is not required at this stage of precision: Due to attenuation of radio signals in the ice, the maximum propagation distance of radio signals is $\mathcal{O}(1 - 5)$ km where the impact of Earth attenuation is less than 2 m. Thus, effects of Earth curvature can be ignored from the signal propagation step onwards. The maximum propagation distance also defines the neces-

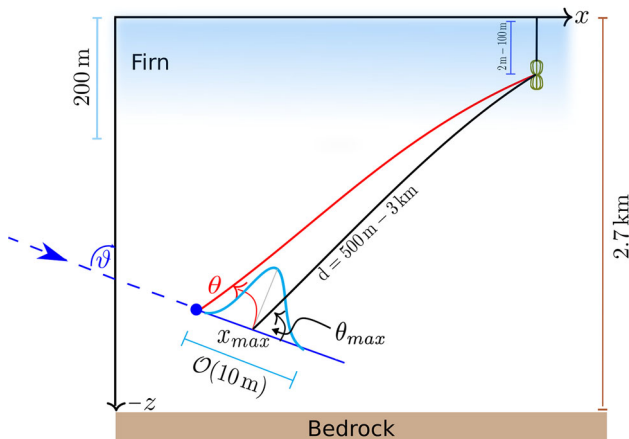


Fig. 1 Sketch of the coordinate system used by NuRadioMC and typical dimensions in the radio detection of neutrino interactions. The coordinate origin is at the ice surface. A quantity of particular interest is the viewing angle θ , i.e., the angle at which the in-ice shower is observed. Due to the longitudinal extent of the shower, the viewing angle is not uniquely defined. By default, we measure the angle with respect to the neutrino interaction vertex, but sometimes it is appropriate to measure the angle with respect to the maximum of the charge-excess profile, which we denote with $\theta_{X\max}$. It should be noted that this is just one typical set-up, other choices of geometry are supported

sary volume where neutrino interactions are simulated in. Thus, also for the standard event generation, a flat Cartesian coordinate system is sufficient.

Earth curvature starts to matter in the tracking of tau leptons and simulation of their subsequent decay as the tau decay length can reach values above 10 km. At 10 km distance, the difference between a flat and curved surface is 8 m which is still small compared to the thickness of the ice sheet at the South Pole of 2.7 km. Hence, the difference in target volume is also small. Another effect is that the probability of a neutrino reaching the simulation volume (referred to as *neutrino event weight*, see Sect. 6.2) is calculated based on the angle between the incident neutrino direction and the (flat) surface. Consequently, the neutrinos originating close to the horizon will have a systematic uncertainty in their assigned weights. However, at 10 km distance, this effect is again small with a displacement of only 0.1°. In the future, effects of Earth curvature can be considered by correcting this angle in the neutrino event weight calculation. The additional complexity of implementing a global coordinate system does not seem required at this point.

2.2 Default event generator and file format details

The default event generator creates a list of neutrino interaction vertices, specifies all relevant neutrino properties, and stores everything in an HDF5 file (see structure in Appendix A).

The event generator specifies the following parameters:

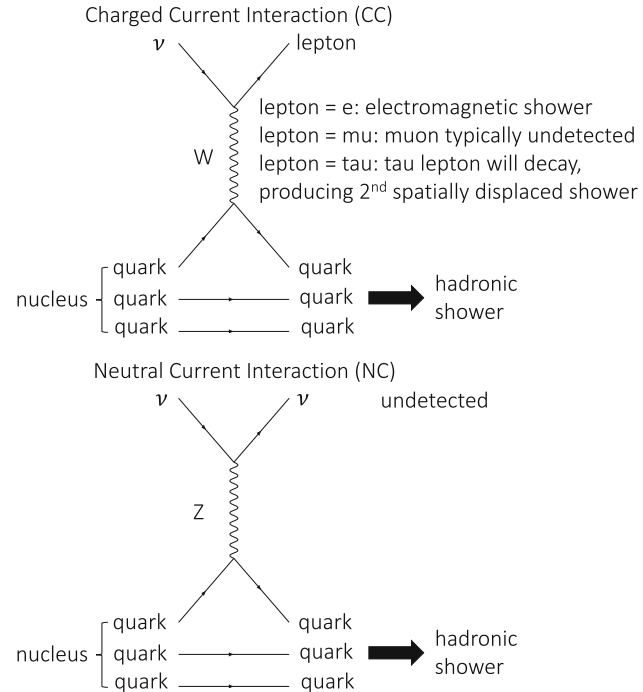


Fig. 2 Feynman diagrams of a charged current and neutral current neutrino interaction

- the position of the neutrino interaction, randomly placed in a cylindrical volume surrounding the detector. The user can control the minimum and maximum radius and the vertical extent.
- the neutrino energy, drawn from a user definable energy spectrum between a minimal and maximal energy. We also allow to specify the *deposited* energy instead, i.e., the amount of neutrino energy that ends up in a particle shower producing an Askaryan signal.
- the neutrino flavor. By default all flavors and particle/anti-particle nature have equal probability. Internally, this is specified using the Particle Data Group ID (PDGID) [30], which allows for cross-referencing with other Monte-Carlo codes.
- the neutrino direction. By default the full sky is uniformly covered but the user can restrict neutrino directions to specific ranges in zenith and azimuth angles.
- whether the neutrino undergoes a neutral current (NC) or charged current (CC) interaction (see Fig. 2 for an illustration of the two interaction types). We use a constant ratio CC:NC 0.7064:0.2936 according to the CTEQ4-DIS cross sections for the neutrino energy between 10^{16} eV and 10^{21} eV [31].
- the inelasticity, i.e., the fraction of the neutrino energy going into the hadronic part of the interaction. The inelasticity distributions from [32–34] have been implemented.

We note that we place neutrino vertices with equal probability per volume. The probability of a neutrino reaching the detection volume is taken into account later by assigning a *weight* to each event (see Sect. 6.2 for how the neutrino absorption is calculated). Similarly, it is currently ignored, if the density of the simulation volume is not uniform which changes the neutrino interaction cross section and thereby the interaction probability. As the density of the typical use-case of ice, only changes in the upper ~ 100 m this effect is ignored at this stage of precision. It can be taken into account in the future by an additional weighting factor or by an event-by-event calculation of the neutrino cross section.

All these parameters are saved in a HDF5 table. This has several advantages. The data is saved efficiently, the format is platform and programming-language independent, stand-alone viewers exist to quickly inspect the files, and apart from storing the actual data tables, it allows saving meta attributes such as the parameters the event set was generated for.

Typical data sets consist of millions of events which would take too long to simulate in a single process. Therefore, the event generator allows to automatically split up the data set into smaller chunks, i.e., into separate HDF5 files with typically 10,000 to 100,000 events per file. Then, the NuRadio-MC simulation can be performed for each file separately, and we provide the tools to merge the individual output files back together.

2.3 Multiple showers

Previous radio simulations only considered particle showers created by the initial neutrino interaction. However, in case of charged current interactions of muon and tau neutrinos, the produced muons and taus might interact or decay producing a second spatially displaced particle shower that generates Askaryan radiation.

The typical decay length of a tau lepton range from 50 m at tau energies of 1 PeV to 50 km at tau energies of 1 EeV. This increases the sensitivity of an Askaryan detector because tau neutrinos can interact far away from the detector but still produce a visible signal if the tau happens to decay close enough to the detector.

Muons in turn are unlikely to decay but they can undergo a catastrophic dE/dX energy loss, depositing a substantial fraction of their energy into the ice and initializing a hadronic shower [35, 36]. In general, more exotic models can also be considered that predict multiple spatially displaced showers per neutrino. Hence, NuRadioMC offers the flexibility to specify an arbitrary number of interaction vertices per event. This is incorporated into the file format by inserting additional events into the event list with the same event ID.

We consider several levels of detail. While a simple treatment of tau decays exists in NuRadioMC itself, we also foresee the inclusion of more complete particle decay codes,

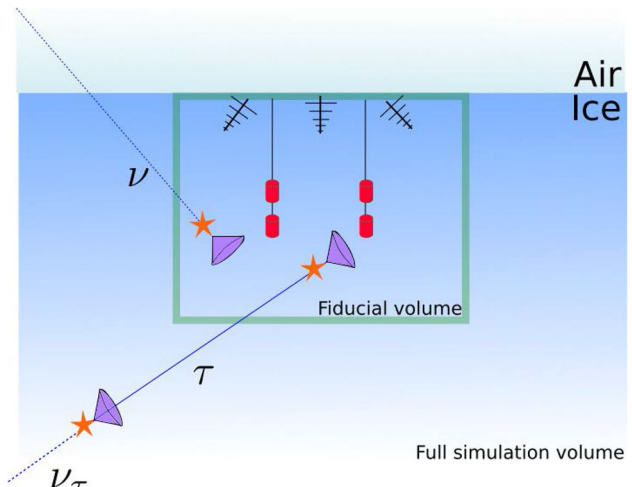


Fig. 3 Sketch of the geometry and the concept of a fiducial volume of the event generator. Neutrino tracks are generated in a full simulation volume, but only the radio emission of primary or secondary interactions are considered, when they take place in a fiducial volume encompassing the detector

such as PROPOSAL [35, 36] that tracks secondary losses of all types of lepton.

2.4 Tau neutrinos

In NuRadioMC, for the first time in an in-ice simulation, we provide the inclusion of secondary sub-showers from tau-decays that add additional detection channels, flavor sensitivity and contribute to the effective volume.

Due to the large decay length of tau leptons, a large volume needs to be simulated to catch the few cases in which there is a secondary interaction close enough to the detector. This increases the computation time enormously as it scales proportionally to the simulated volume, and makes this brute-force approach unfeasible. Therefore, we developed the following technique: we generate neutrino interactions in an arbitrarily large volume including all secondary interaction vertices (e.g. from tau decays) but save only those primary and secondary interactions that take place in a much smaller fiducial volume surrounding the detector while keeping track of the total number of simulated events (see Fig. 3 for an illustration). The user needs to make sure that the fiducial volume is chosen large enough such that the probability to trigger the detector is negligible for interaction vertices outside of this volume. This allows for a computationally efficient simulation of complex physics models.

Once a tau is created after the interaction of a tau neutrino in the volume, we calculate its decay time t_{decay} and energy at decay. We first randomly sample a decay time τ_{decay} in the tau particle rest frame from an exponential distribution using a mean tau decay lifetime 2.903×10^{-13} s [37]. If the tau energy is less than $E_\tau = 1$ PeV, we do not account for tau

energy losses along the path, and the decay time is simply given by the product of the Lorentz factor γ and the sampled decay time τ_{decay} in the tau rest frame

$$t_{\text{decay}} = \gamma(E_\tau)\tau_{\text{decay}}. \quad (1)$$

The decay length l_τ is calculated multiplying t_{decay} by the particle speed, while the energy of the τ at decay is equal to the initial tau energy.

In the case the tau has an energy greater than 1 PeV, we include photonuclear tau energy losses in our calculation. These are not very well constrained and we use a simple model inspired by the results in [38]. We take the mean energy loss per amount of traversed matter in ice to be,

$$\left\langle \frac{dE_\tau}{dX} \right\rangle \approx f(E_\tau) = b_1 E_\tau + b_2 E_\tau \log_{10}(E_\tau/E_0), \quad (2)$$

with $b_1 = 1 \times 10^{-7} \text{ cm}^2/\text{g}$, $b_2 = 1.8 \times 10^{-7} \text{ cm}^2/\text{g}$, and $E_0 = 1 \text{ PeV}$. Above $E_\tau = E_0$, it is a good approximation to assume that the tau speed is equal to the speed of light in vacuum c . This allows us to write the time t that it takes a tau with initial energy $E_{\tau,i}$ to reach a lower energy E_τ as,

$$t(E_\tau) = \frac{1}{c\rho_{\text{ice}}} \int_{E_{\tau,i}}^{E_\tau} \frac{dE'}{f(E')}. \quad (3)$$

Once $t(E_\tau)$ is known, we numerically obtain the inverse function $E_\tau(t)$ for equally-spaced times by interpolation. The decay time is obtained by solving the following integral equation for t_{decay} :

$$\int_0^{t_{\text{decay}}} \frac{m_\tau}{E_\tau(t)} dt = \tau_{\text{decay}}, \quad (4)$$

from which the tau decay length above 1 PeV is obtained as:

$$l_\tau \approx ct_{\text{decay}}. \quad (5)$$

In Fig. 4, left, we show the decay length l_τ as a function of tau energy. The straight dashed line represents the mean decay length without tau energy losses, which increases linearly with energy. The solid line indicates the decay length assuming that the decay time in the rest frame is equal to the mean decay time τ_{decay} and accounting for deterministic tau-energy losses during propagation given in Eq. (2). The shaded band represents an 80% confidence interval for the decay length, where the decay time has been drawn from an exponential distribution. Stochastic energy losses have not been accounted for. In Fig. 4, right, we show the tau energy at decay obtained with the same assumptions used for obtaining the tau decay length shown in the left panel. Tau energy losses become important around 100 PeV.

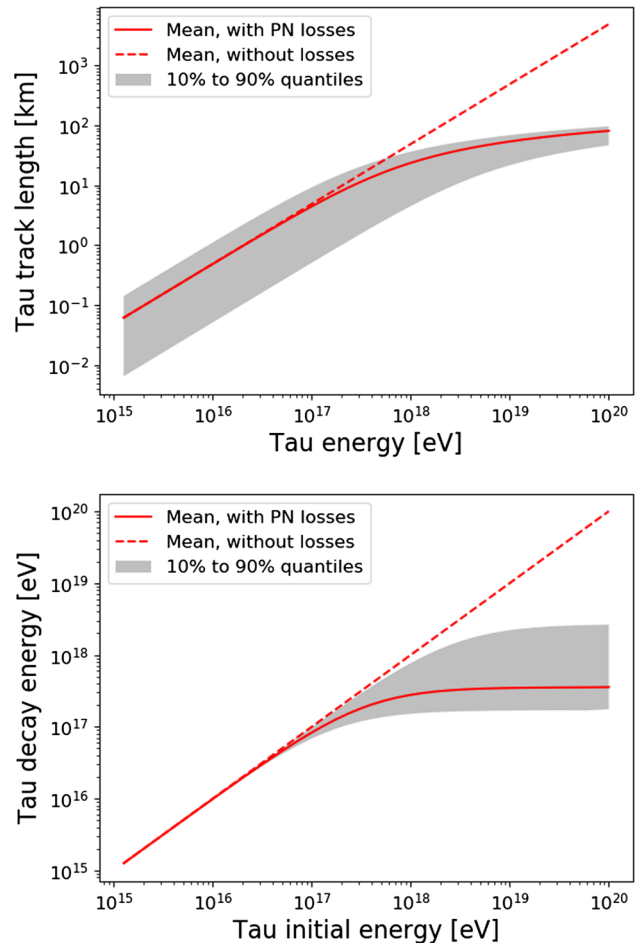


Fig. 4 Top: Tau decay length as a function of the tau energy. Bottom: Tau decay energy as a function of the initial tau energy. Due to the one-tailed nature of the exponential decay function, we show the decay length for the mean proper decay time with photonuclear losses (solid line) and without any losses (dashed line). The shaded band represents the area spanning from the 10% proper decay time quantile to the 90% quantile (80% of total probability). This implementation matches what has been shown previously in [39]

2.5 Options for additional physics processes or calibration purposes

The event generation described above is the default event generator in NuRadioMC. However, emission from a standard-model neutrino-induced shower is only one possible scenario that can be covered. The users have the freedom to implement their own event generators according to other physics assumptions, e.g., new physics or for simulating calibration signal generators. We provide an example to simulate a calibration measurement online [40]. As long as the events are saved according to the well-defined file structure, NuRadioMC can process any input files. A skeleton event generator is provided as an example [41].

3 Signal generation

NuRadioMC provides several modules for the generation of the radio signal from showers. The user may choose from a selection ranging from well-known frequency-domain parameterizations of the Askaryan signal to a state-of-the art semi-analytic calculation.

A uniform interface in the form of a simple function is provided for all models (see [42] and List. 3 in Appendix D.3). In this way the NuRadioMC code also serves as a reference implementation for all models. Furthermore, the well-defined interface allows for an easy extension of NuRadioMC with additional models. Even calibration emitters can be (and are) implemented to simulate a calibration measurement with NuRadioMC.

In the following, we first present the different signal generation models available in NuRadioMC before discussing their differences and giving recommendations for use in different cases. We discuss a variety of models, some for more pedagogical reasons, others because they are fast, and others because they are accurate. We hope that this section also serves as reference discussion of several widely used emission models, however, it is not an attempt at completeness.

3.1 Frequency-domain parametrizations

NuRadioMC currently provides two frequency-domain parameterizations of the Askaryan signal. One, referred to as *Alvarez2000*, is also used in the simulation code for the ANITA detector (IceMC) [19] and for the ARIANNA array (ShelfMC) [17,43], and is an implementation of the parameterization of [24], which was validated against a full simulation of Askaryan radiation performed with the ZHS Monte Carlo [44]. This is a microscopic simulation of the shower and its radio emission, that does not contain signal propagation and detector simulation.

The other parameterization (*Alvarez2009*) is an updated version of the first one. It is based on the so-called “box model” of shower development [45] and separate parameterizations for electromagnetic [46] and hadronic [47] showers are provided. Both parameterizations are the product of three functions. The first is a scaling function A that grows linearly with the primary energy E_0 , frequency f , and the sine of the observing angle θ . The second and third functions are two continuous cutoff frequency factors d_L and d_R that account for deviations from linearity due to incoherence effects associated to the longitudinal and lateral extensions of the shower. For electromagnetic showers, the LPM effect is modelled including random fluctuations of the size of the effect.

Although we encourage the use of the *Alvarez2009* parameterization, we have also included the older parameterization *Alvarez2000* for comparison with previous work and other

codes. The latter can be understood as a simplified version of the former, with constant factors, a simple continuous cut-off factor instead of two, and a Gaussian function for the dependence of emission on viewing angle. Because of its simplicity, it provides qualitative and easily understandable, however, not necessarily precise insights into the main dependencies of the Askaryan signal. For pedagogical reasons, we explicitly provide the parameterization of this model here and give an example of the resulting Askaryan signals.

If the shower is observed on the Cherenkov angle, the electric field (scaled to a distance of 1 m) according to *Alvarez2000* is given by

$$\frac{\varepsilon_c^{lm}}{V/m/MHz}(E_{sh}, f) = 2.53 \times 10^{-7} \cdot \frac{E_{sh}}{\text{TeV}} \cdot \frac{f}{f_0} \cdot \frac{1}{1 + (\frac{f}{f_0})^{1.44}}, \quad (6)$$

with the shower energy E_{sh} , frequency f and $f_0 = 1.15$ GHz. Signal amplitudes off the Cherenkov cone, ε^{lm} , are modeled as a Gaussian profile according to

$$\varepsilon^{lm}(E_{sh}, f, \theta_v) = \varepsilon_c^{lm}(E_{sh}, f) \cdot \frac{\sin \theta_v}{\sin \theta_c} \cdot \exp \left[-\ln 2 \cdot \left(\frac{\theta_v - \theta_c}{\sigma_\theta} \right)^2 \right] \quad (7)$$

with ε_c^{lm} given in Eq. (6), and where θ_v is the viewing angle relative to the shower axis. The angular width of the cone around the Cherenkov angle σ_θ is a function of both frequency and energy. For hadronic showers σ_θ is given in Eq. (6) of [48], for which a factor to account for the so-called missing energy, energy going mainly into muons and neutrinos that does not contribute to the Askaryan signal, is included in Eq. (6).

For electromagnetic showers above 2 PeV, the shower profile becomes elongated due to the Landau–Pomeranchuk–Migdal (LPM) effect. In the simple model of *Alvarez2000* such an elongation corresponds to a reduced σ_θ which is modeled according to the prescription in [49]. This in turn manifests itself as a rapid decrease in the high frequency content of the Askaryan signal off the Cherenkov cone for EM showers, as seen in Fig. 5.

For NuRadioMC, the time-domain signal based on *Alvarez2000* and *Alvarez2009* is generated by taking the simple approximation of a phase that is constant with frequency and equal to 90°, yielding a bipolar pulse in the time domain.

3.2 Fully analytic treatment including the LPM effect and Cascade Form Factor

NuRadioMC provides an implementation of the analytic model of Askaryan radiation (*HCRB2017*) [50] that builds on previous work by [51]. This fully analytic model accounts

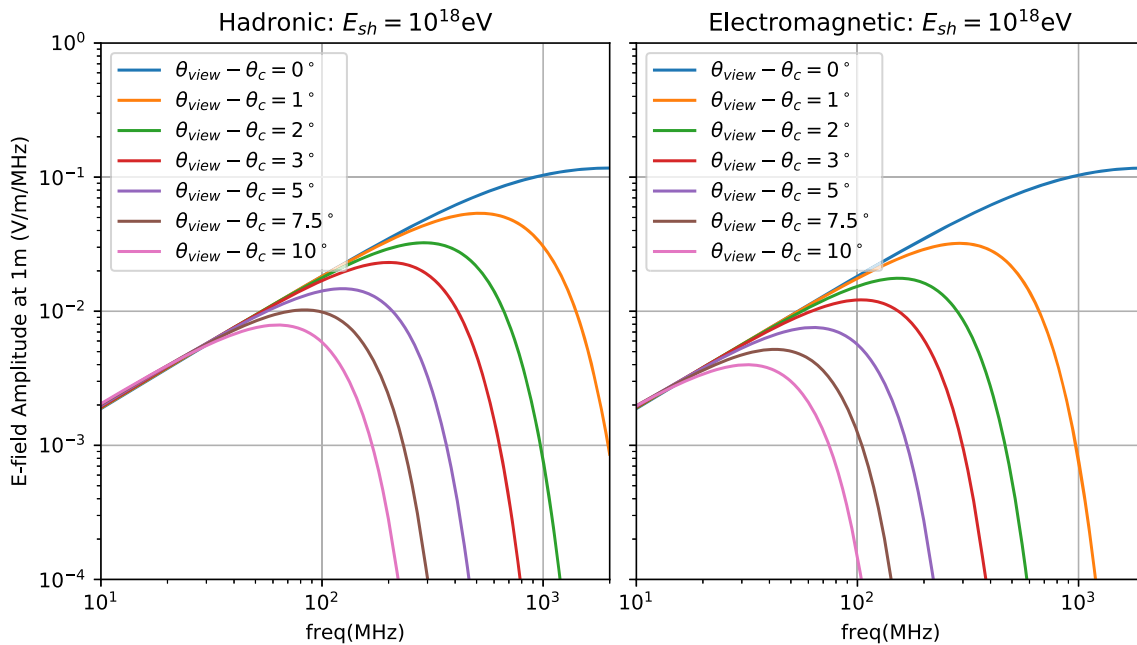


Fig. 5 Electric field amplitude ε^{1m} , 1 m from the neutrino interaction vertex (Eq. (7)) for hadronic (left) and electromagnetic (right) showers with $E_{sh} = 10^{18}$ eV using the parameterization Alvarez2000. Note that

as the viewing angle shifts away from the Cherenkov cone angle, high frequency components fall off. For the EM showers, the cone width σ_θ is reduced due to the LPM effect

simultaneously for the three-dimensional *form factor* of the cascade, and the cascade elongation. The form factor is the spatial Fourier transform of the instantaneous charge distribution of the cascade. The form factor affects the Askaryan signal properties in the same way a multi-pole filter affects any time-domain signal. Although some authors have provided partial solutions for the three-dimensional form-factor in the past [52], in [50] a complete solution is presented that includes dependence on the viewing angle θ . This allows for the analytic exploration of the relevant parameter space affecting σ_θ and σ_v , the width of the Cherenkov cone and the Fourier spectrum, respectively.

This module builds upon the work of [51] where the authors provide analytic functions for Askaryan radiation correct in both the near and far-field regimes. When a cascade is elongated due to the LPM effect, both regimes become important given the three-dimensional nature of the form-factor. *HCRB2017* treats the LPM effect as a smooth stretching of the shower profile using the results of [53].

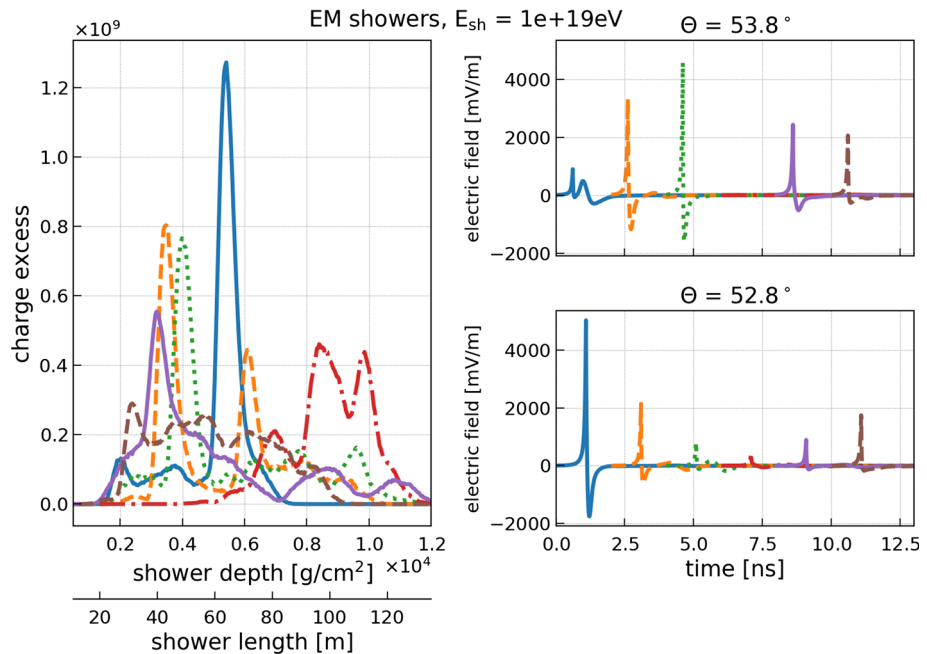
The fully analytic nature of this model has the advantage that it gives direct insights into the physical dependencies of the Askaryan signal. However, as shown in the radio emission of air showers [54] a purely analytic model comes at the cost of a poorer accuracy.

3.3 Semi-analytic model in the time domain

A third option for the signal generation is to calculate the Askaryan radiation individually from detailed charge-excess profiles in the time domain, following the approach in [55]. The implementation in NuRadioMC referred to as *ARZ*, is based on a realistic shower library. This allows to precisely model the effects of LPM elongation [26,27] and the resulting large shower-to-shower fluctuations on the Askaryan signal on a single event basis, rather than describing an average behaviour. The model also captures subtle features of the cascades like sub-showers and accounts for stochastic fluctuations in the shower development which can alter the Askaryan signal amplitudes significantly (see e.g. discussion in [47] or Fig. 6). This model is the most accurate treatment of Askaryan radiation implemented in NuRadioMC, but it comes at the expense of larger computation times as it involves computationally expensive convolutions of the Askaryan vector-potential with Monte-Carlo generated cascade profiles.

The main idea behind the *ARZ* method is that the electromagnetic vector potential \mathbf{A} in Coulomb gauge can be expressed as an integral in shower depth containing the shower profile, a factor that accounts for polarization, another factor that accounts for distance to the emitting point of the shower, and a form factor F_p :

Fig. 6 Charge-excess profiles and resulting Askaryan signal (unfiltered). (left) Charge-excess, i.e., number of electrons minus number of positrons, as a function of shower depth and length of six electromagnetic shower with an initial energy of 10^{19} eV. The variation in the charge-excess profile is due to the stochastic nature of the shower development effected by the LPM elongation. (right) The resulting Askaryan signal for the charge-excess profiles according to the ARZ model for two different viewing angles at 1 km distance. The pulse start time is shifted for a better visibility of all pulses



$$\mathbf{A}(r, z, t) = \frac{\mu}{4\pi} \int_{-\infty}^{\infty} dz' \frac{Q(z')}{\sqrt{r^2 + (z - z')^2}} \mathbf{p}(z') F_p \left(t - \frac{z'}{v} - \frac{n\sqrt{r^2 + (z - z')^2}}{c} \right), \quad (8)$$

where r is the radial distance of the observer to the shower, z is the vertical coordinate of the observer, z' is the shower depth, $Q(z')$ the excess charge profile, \mathbf{p} is the polarization vector and F_p is the form factor (see [55] for more details). This form factor F_p has approximately the same shape for every particle shower in ice, which allows us to treat it as a constant function. It only depends on the type of the shower, i.e., hadronic or electromagnetic, and a parameterization of the form factor for both shower types is provided.

The charge profile $Q(z')$ depends on the nature of the shower (hadronic or electromagnetic), the shower energy, and is also subject to random fluctuations. The LPM effect, for instance, modifies the charge profile, which in turns modifies \mathbf{A} through Eq. (8). All the physical processes that are relevant for the electric-field calculation contribute to $Q(z')$, so as long as a correct description of the charge profile is available in the shower library, an accurate electromagnetic potential \mathbf{A} can be calculated with Eq. (8).

Once \mathbf{A} is known, the radiation electric field can be calculated with a derivative, since in Coulomb gauge $\mathbf{E}_{\text{rad}} = -\frac{\partial \mathbf{A}}{\partial t}$. The agreement between the electric field predicted by the ZHS Monte Carlo and the one obtained with the ARZ model is quite satisfactory, yielding a few percent of error up to 2 GHz (see Fig. 3 in [25]). The ARZ model considers that the shower has a volume and therefore is adequate for computing the fields of observers near the shower as long as the con-

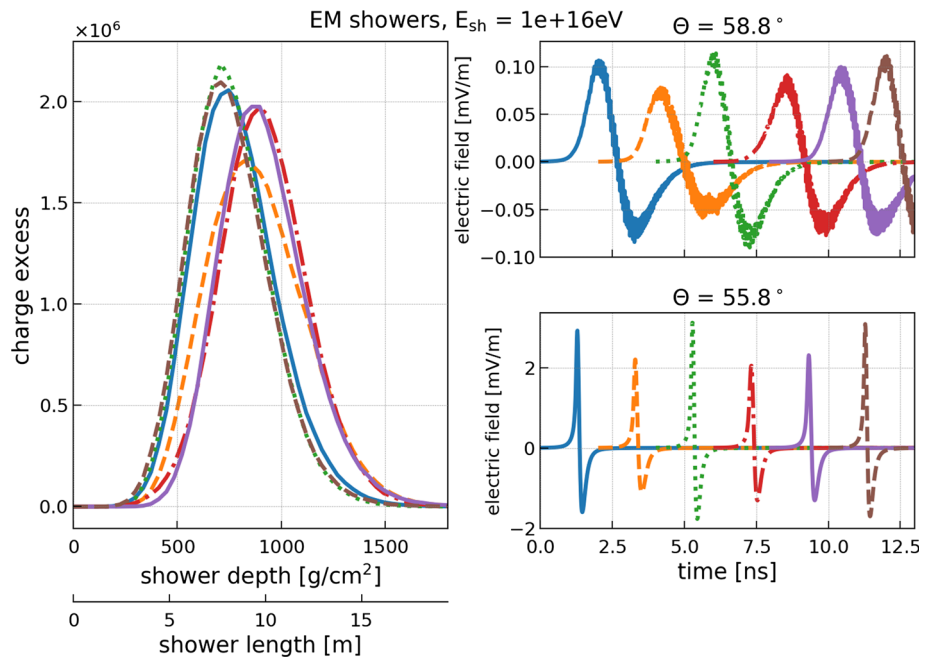
sidered wavelengths are small with respect to the distance to the shower.

NuRadioMC provides a modern Python-based implementation of the code used in [55] and optimized routines for numerical integration. The code includes a shower library of charge-excess profiles for different shower types:

1. electromagnetic: purely electromagnetic showers from ν_e charge current interactions.
2. hadronic (neutrino): showers started by the fragmentation of the nucleon struck by the neutrino, i.e., the result of neutrino neutral current interactions and the hadronic part of an electron neutrino charged current interaction.
3. hadronic (tau): showers initiated by a hadronic decay of a tau lepton. A tau decay into muons will not produce any significant shower, and tau decays into electrons correspond to purely electromagnetic showers.

The last category is not simulated explicitly. Instead, the branching ratios of a tau decay and the fraction of energy ending up in the particle cascades is parameterized using the results of [35, 36]. Then, the shower library of electromagnetic (category 1) or hadronic (category 2) showers is used with the appropriate shower energy. We note that the initial hadronic particles that start the hadronic shower are different between a fragmenting nucleon and a hadronic tau decay. This might lead to small differences in the hadronic shower developments. However, for now we ignore this subtle difference and use category 2 also for hadronic tau decays. In the future, we will provide a separate shower library for category 3. Currently, NuRadioMC comes with version 1.2

Fig. 7 Charge-excess profiles and resulting Askaryan signal (unfiltered). Same as Fig. 6 but for electromagnetic showers with an initial energy of 10^{16} eV. At this energy the LPM effect only has a small influence on the shower development and stochastic shower-to-shower fluctuations are small



of the shower library that will be described in the following.

The showers were simulated using HERWIG [56] for the simulation of the first neutrino nucleon interaction, and ZHAireS [57] for the subsequent simulation of the particle shower in ice. The charge-excess profiles are binned in bins of 37 g/cm^2 for electromagnetic showers and 18 g/cm^2 for hadronic showers. To optimize the computation speed, we integrate Eq. (8) numerically using the trapezoid rule given the binning of the charge-excess profile. The form factor is a strongly peaked function which requires a more precise integration around the peak. This is achieved by dynamically interpolating the charge-excess profile at the positions corresponding to the peak of the form factor.

The shower library (version 1.2) contains 10 showers for every shower energy ranging from 10^{15} eV to $10^{20.5}$ eV in steps of $\Delta \log_{10}(E) = 0.1$ for both electromagnetic and hadronic showers. To obtain charge-excess profiles for shower energies that were not explicitly simulated we do the following: At first order, the charge-excess amplitude scales with shower energy. Hence, in a simulation, we pick one shower realization randomly from the nearest energy bin and re-scale the charge-excess amplitude by $E_{\text{event}}/E_{\text{library}}$.

To discuss and illustrate the improvement in accuracy when using the ARZ approach as opposed to a parameterization, we consider the influence of the LPM effect on the radio signal. The main consequence of the LPM effect is that the interaction probability of high-energy electrons, positrons and photons is suppressed leading to an elongation of the shower profile. The strength of the effect is proportional to the energy of the particle. Therefore, it mostly affects highly-

energetic electromagnetic showers above a few PeV in ice, in which a large amount of energy is carried by individual particles. Previously in the literature (e.g. [50, 57]), the effect was often modelled via stretching of a smooth shower profile. However, this does not take into account the stochastic nature of the process and the fact that the first few particles of an electromagnetic shower are impacted differently by the LPM effect as the energy is not equally distributed. As a consequence, one gets multiple spatially displaced EM showers as shown in Fig. 6. In this figure, also the resulting Askaryan signals are shown for two different viewing angles θ which are significantly different for different realizations of the shower (see Fig. 1 for a sketch of the coordinate system). Low energy EM showers are less influenced by the LPM effect and the resulting Askaryan signals are similar for all shower realizations (cf. Fig. 7). Hadronic showers exhibit little shower-to-shower fluctuations except for the rare cases where a high-energy electromagnetic shower is initiated in one of the first interactions that then gets LPM elongated (see Fig. 8).

3.4 Comparison of models

Each signal generation module in NuRadioMC has its own strengths and shortcomings. We first compare the signal models with respect to their resulting signal properties and then discuss practical considerations. We provide a quick overview of the discussion in Table 1. In Fig. 9, a comparison of the predicted peak-to-peak amplitudes in a typical detector bandwidth of 100 MHz–500 MHz is presented that will be discussed below.

Fig. 8 Charge-excess profiles and resulting Askaryan signal (unfiltered). Same as Fig. 6 but for hadronic showers with an initial energy of 10^{17} eV. Most hadronic showers are not influenced by the LPM effect and show only very little shower-to-shower fluctuations. Different energies mostly scale the charge-excess and electric-field amplitudes approximately linear with energy but have a small effect on the shower length. However, sometimes a high-energy π^0 that is created in one of the first interactions decays instead of interacting leading to an electromagnetic sub-shower that experiences significant LPM elongation (green dotted curve in this figure)

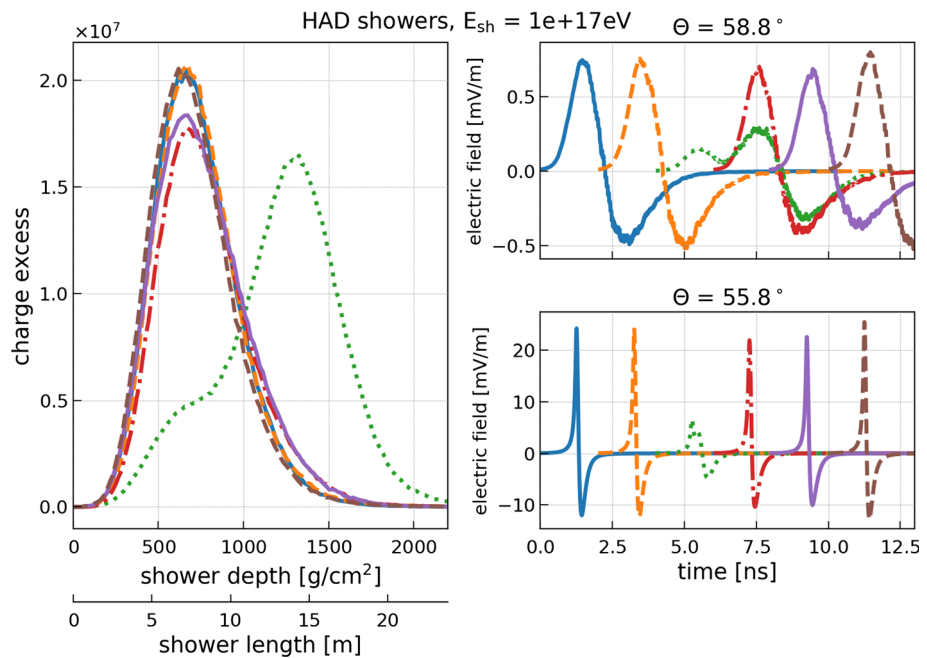


Table 1 Overview of alternative methods implemented in NuRadioMC to calculate the signal following a neutrino interaction

Model	Advantages	Shortcomings
Parameterization (<i>Alvarez2009</i>)	Fast, accurate representation of the signal amplitudes, includes statistical fluctuations from LPM	No phase information, only valid in far-field
Fully analytic (<i>HCRB2017</i>)	Fast, phase information provided, valid in near and far-field, LPM is treated as elongated shower	No statistical fluctuations from LPM, generalization, absolute amplitudes less accurate
Semi analytic (<i>ARZ</i>)	Phase information provided, near and far-field, realistic LPM treatment based on simulated shower library	Computationally expensive
Full MC	Precise modelling of all details of shower development	Slow, no implementation in NuRadioMC yet

The frequency-domain parameterizations are based on a detailed full Monte Carlo simulation of the particle shower and a calculation of the resulting radio signal using the ZHAireS code [46]. Thus, their predictions of the signal amplitudes are accurate, the narrowing of the Cherenkov cone due to the LPM effect is modelled and even statistical fluctuations in the shower development are parameterized (only *Alvarez2009*). The models are fast to evaluate and the computing time is negligible compared to the other parts of the simulation. We also provide an older version, *Alvarez2000*, that was most commonly used in previous simulation frameworks and is therefore important for comparison. However, we strongly recommend the usage of the newer model *Alvarez2009* as the older model typically overestimates the Askaryan amplitudes by roughly 20–30%. The

Alvarez2009 model is in good agreement with the more precise *ARZ* time-domain calculation (cf. Fig. 9).

The main shortcomings of such parametrizations are that no phase information is provided which leads to inaccuracies in the time domain. Typically, the phases are approximated as constant 90° as function of frequency, which results in a perfectly symmetric bipolar pulse. While this may be a reasonable approximation for many cases, it does not capture the details of the shape of the pulses and does not account for physical time delays. Thus, these models are suitable for general sensitivity calculations given the correct prediction of amplitudes. However, more detailed models are recommended to study trigger efficiencies and event reconstruction that are based on pulse shape and timing.

Another option is the fully analytic model *HCRB2017* that also calculates the phases and is thus suitable for the time-

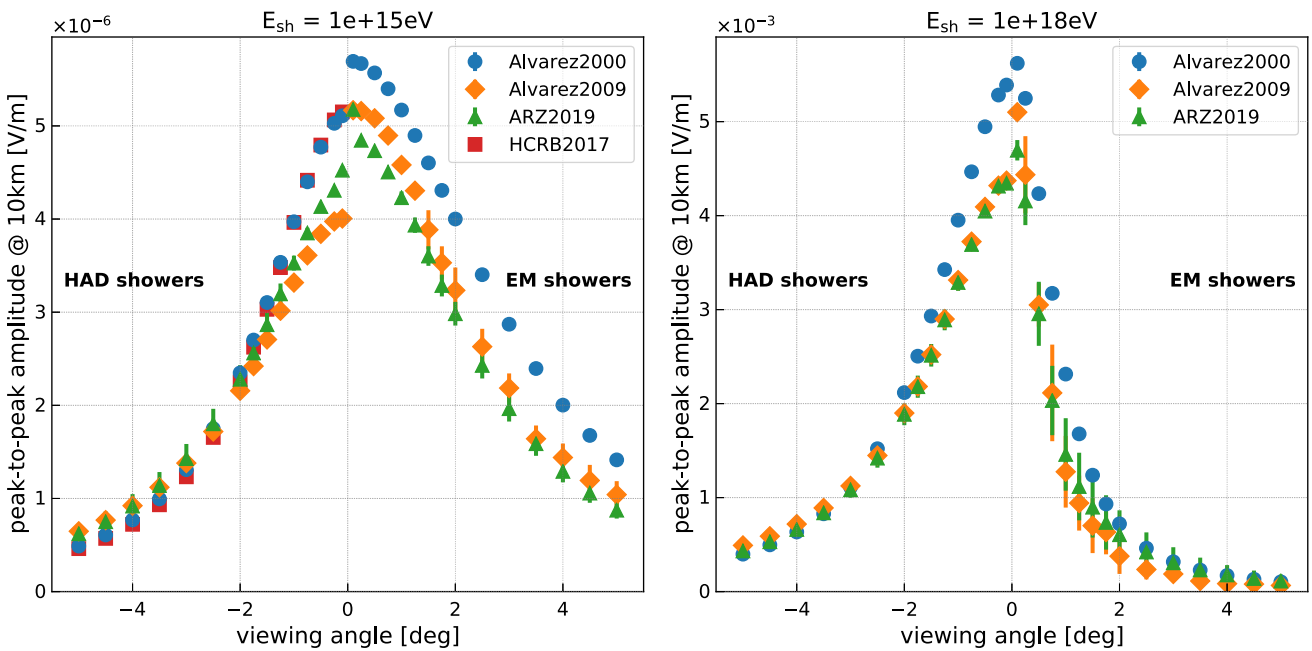


Fig. 9 Comparison of Askaryan models. Shown the peak-to-peak amplitude (the difference between the maximum and the minimum of the Askaryan pulse) as a function of viewing angle. The pulses are filtered in a typical experimental bandwidth of 100 MHz to 500 MHz. The

left part of the plot (negative angles) shows the prediction for hadronic showers and the right part of the plot (positive angles) the prediction for electromagnetic showers of the same shower energy. (left) 10^{15} eV shower energy. (right) 10^{18} eV shower energy

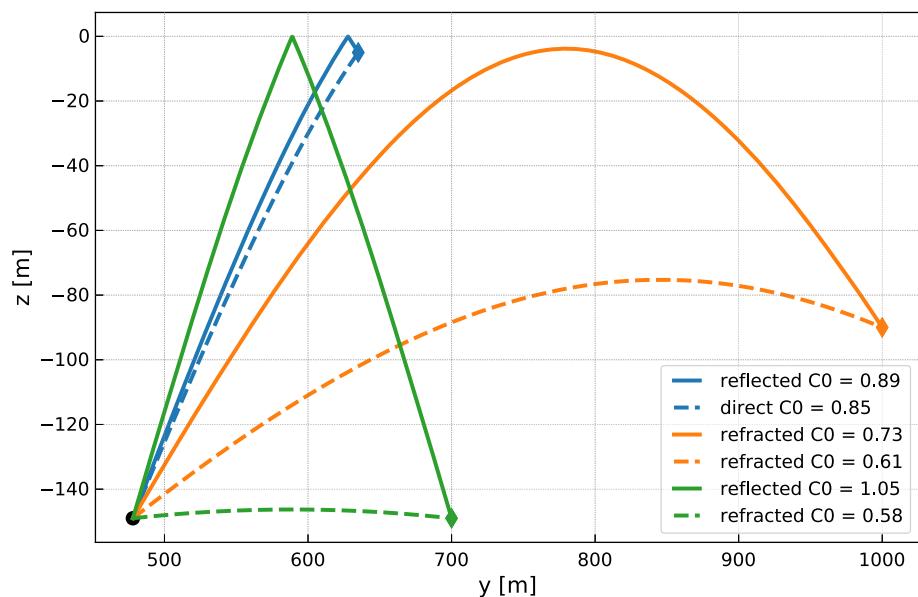
domain. It provides helpful insights into the dependencies of the Askaryan signals on shower elongation and shower width. As being analytically it does not model the statistical fluctuations occurring in showers that can be substantial as shown in Fig. 6. The signal strength prediction depends strongly on the longitudinal cascade width a , which has to be approximated with a Gaussian function for different cases (electromagnetic, hadronic and LPM showers). The approximations lead to a mis-match between the predictions of this model and the ones of the other models that are based on a microscopic Monte Carlo simulation where the calculation of the radio signal is based on first principles resulting in a few percent accuracy as shown in the radio emission of air showers [58]. In particular, the HCRB2017 model overpredicts the amplitudes at higher shower energies and the reduction of the cone width due to the LPM effect. Therefore, we only show the HCRB2017 model for low-energy hadronic showers in Fig. 9. Furthermore, the treatment of pulse arrival times is complex in an analytic model, complicating the integration with the different signal propagation modules (see Sect. 4). Naturally, the model is computationally very fast given its analytic approach.

The semi-analytic model ARZ builds on a shower library of charge-excess profiles and thus models all details like sub-showers including statistical fluctuations in the shower development. The calculation is performed in the time domain. It therefore includes all phase information and gives an accurate

prediction of the pulse shape and timing. The model provides valid results even when the distance from observer to shower is comparable to or smaller than the shower dimensions, as long as the distance is large compared the considered wavelengths. Above 100 MHz, and at distances greater than 10 m, the use of the ZHS formula, on which the ARZ model is based, is justified [59]. It is the most precise model available and recommended for the development of neutrino identification and reconstruction algorithms. Its disadvantage is that it is computationally more expensive. In a full end-to-end simulation it takes up roughly 90% of the computing time. When using this model, the computing time increases roughly by a factor of 10.

The next level of precision can be achieved with full Monte Carlo simulations where each shower particle is tracked and the radio emission is calculated from the acceleration and creation of each charged particle. This is done for air showers in codes like CoREAS [60] and ZHAireS [57], which are required to achieve the necessary accuracy for modern air shower experiments that are pushing the reconstruction uncertainties (e.g. [58, 61–63]). Currently, there is no urgency to require this level of accuracy for neutrino predictions, given the experimental uncertainties and the computational costs of a full Monte Carlo. However, future developments like a next generation of CORSIKA [64] are followed closely to allow for synergies and compatibility with NuRadioMC.

Fig. 10 Example of typical ray-tracing solutions for receiver locations differing in depth and horizontal distance to a given emitter. The emitter is indicated by the black circle at the bottom left. Lines of the same color belong to the same receiver location. Shown are the combinations of direct and reflected ray (blue), refracted and reflected ray (green), and two refracted rays (orange). The numbers in the legend show the C_0 parameter of Eq. (10) that defines the shape of the curve



One could also consider another future improvement in the combination of signal generation and propagation. As discussed earlier, the decoupling of signal generation and propagation leads to noticeable inaccuracies in an inhomogeneous medium (where the signal trajectories are bent, cf. next section) if the extent of the emission region becomes large with respect to the distance to the receiver and if the trajectory is substantially refracted in the firn. Then, the time delay of the propagation time from different emission points to the receiver vary between a homogeneous and inhomogeneous medium, so that signal generation and propagation cannot be separated without loss of accuracy. This effect can be taken into account naturally in a microscopic Monte Carlo simulation by calculating the (curved) path from each emission point to the observer. In an intermediate step, one could use the ARZ2019 model, where the Askaryan signal is calculated from the charge-excess profile to address the issue: Instead of calculating the emission from the full charge-excess profile at once, a shower can be subdivided into small chunks. The Askaryan radiation can then be calculated per chunk and propagated individually to the receiver.

4 Signal propagation

The signal propagation pillar of NuRadioMC handles the propagation of the Askaryan signal through the medium to the observer positions. Like the other pillars, this part of the code is clearly separated so that different signal propagation modules can be implemented and exchanged by the user. This is achieved by defining an interface in form of a Python class (see general example in [65]).

The signal propagation problem is typically approximated via ray tracing but more general techniques such as a finite difference time-domain (FDTD) method that evolves Maxwell's equation can be foreseen in the future [66, 67]. In the ray-tracing approximation, the different ray paths connecting an emitter and receiver can be classified as *direct*, if the depth is monotonously decreasing or increasing along the path between emitter and receiver, as *refracted*, if the path shows a turning point, and as *reflected*, if the ray is reflected off the ice-air interface at the surface which acts as a perfect mirror for most geometries. A few typical ray-tracing solutions are presented in Fig. 10.

4.1 Analytic ray tracing

The default signal propagation module in NuRadioMC is an analytic ray-tracing technique that provides an unprecedented combination of speed and precision relative to traditional ray-tracing techniques. Traditional ray-tracing techniques locate the path connecting an emitter and receiver by time intensive trial-and-error methods, where numerous rays are “thrown” until a ray which connects the emitter and receiver is found. This is necessary because the index-of-refraction (n) of glacial ice is known to vary with depth, and so a light ray is bent and follows a curved path as it travels from an emitter to a receiver. Because the index-of-refraction does not need to be a well-behaved function it is impossible to predict the path traversed by the ray with full generality.

However, ice density measurements and the resulting index-of-refraction profiles from the South Pole and Moore’s Bay site exhibit a simple, depth-dependent index-of-refraction $n(z)$. The data can be described to within a few percent

[68] by an exponential function of the following form:

$$n(z) = n_{\text{ice}} - \Delta_n e^{z/z_0}, \quad (9)$$

where z is the depth and n_{ice} , Δ_n , z_0 are the parameters of the model. For this specific exponential $n(z)$ profile, an *analytic* solution of the ray path as a function of depth ($y(z)$) exists and is given by

$$y(z) = \pm z_0 \sqrt{n_{\text{ice}}^2 C_0^2 - 1} \cdot \ln \left(\gamma / \left[2\sqrt{c(\gamma^2 - b\gamma + c)} - b\gamma + 2c \right] \right) + C_1, \quad (10)$$

with $\gamma = \Delta_n e^{z/z_0}$, $b = 2n_{\text{ice}}$, and $c = n_{\text{ice}}^2 - C_0^{-2}$. We provide a derivation of this equation in Appendix C.1. The parameters C_0 and C_1 uniquely describe the ray path and need to be determined from two initial conditions which are given by the two points the ray goes through, e.g., the neutrino interaction vertex (the point of emission) and the observer position.

The parameter C_1 corresponds to a vertical translation in the coordinate system and can be calculated analytically from the initial conditions. The parameter C_0 must be determined numerically, and is found through a least-squares minimization. For each receiver-emitter coordinate pair, we can either have no, one or two solutions, corresponding to no connecting ray, one connecting ray, or two connecting rays. To quickly and stably find all possible solutions, we leverage numerical algorithms as documented in Appendix C.2.

4.1.1 Derived quantities

Once a ray path is found, several derived quantities are needed in the simulation. The *launch vector* of the ray is needed to calculate the *viewing angle* (the angle between shower axis and launch vector) which is required to calculate the Askaryan emission. The *receive vector* is needed to evaluate the antenna response for the arrival direction of the incident radiation. As discussed in Appendix C.2, the ray-tracing problem can be reduced to the y-z plane with a simple coordinate rotation. Hence, only the launch and receive angles are required, which can be calculated analytically from the derivative $dy(z)/dz$ which we specify in appendix Appendix C.4.

The path length can be calculated numerically via the following line integral

$$d = \int_{z_1}^{z'_2} \left| \frac{d\mathbf{x}}{dz} \right| dz = \int_{z_1}^{z'_2} \sqrt{1 + \left(\frac{dy(z)}{dz} \right)^2} dz, \quad (11)$$

where $\mathbf{x} = (y(z), z)^T$, and $z_1/2$ refer to the z position of the emitter/receiver. In case of a direct ray we have $z'_2 = z_2$. In case of a refracted or reflected ray, we first need to integrate from z_1 to the turning point and then the same path backwards to z_2 .

Similarly, the travel time t and the signal attenuation $\exp(-A)$ can be calculated as

$$t = \int_{z_1}^{z'_2} n(z)/c \left| \frac{d\mathbf{x}}{dz} \right| dz = \int_{z_1}^{z'_2} n(z)/c \sqrt{1 + \left(\frac{dy(z)}{dz} \right)^2} dz, \quad (12)$$

and

$$A = \int_{z_1}^{z'_2} \left| \frac{d\mathbf{x}}{dz} \right| / L(z, f) dz \quad (13)$$

$$= \int_{z_1}^{z'_2} \sqrt{1 + \left(\frac{dy(z)}{dz} \right)^2} / L(z, f) dz \quad (14)$$

where $L(z, f)$ is the attenuation length as a function of depth and frequency which is discussed in Sect. 6.5.

If the index of refraction profile is described with an exponential function as in Eq. 9, an analytic expression for the path length and travel time can be derived. This analytic function is used by default due to its improved computing time. The derivation can be found in Appendix C.5. For the attenuation factor no analytic solution has been found and a numerical integration is required.

4.1.2 Computational speed

We provide a Python implementation of the analytic ray-tracing technique described above which leverages the NumPy [69] and SciPy [70] computational packages. In addition, we implemented the time critical operations of finding the ray-tracing solution and determining the signal attenuation in a standalone C++ module. This C++ module leads to a substantial speed improvement of a factor of 20, so that the calculation of the ray-tracing solutions and the calculation of travel time and distance as well as the signal attenuation takes less than 4 ms in ice. The C++ module utilizes the highly optimized and broadly supported GNU Scientific Library (GSL) [71] for numerical integration and root-finding.

We provide a Cython wrapper to the C++ implementation so that it can be called as a sub-routine. Selection of routine (C++ or Python) is done in a transparent fashion. If the user compiled the C++ extension, NuRadioMC will automatically pick the faster C++ implementation, and otherwise utilize the Python implementation. In this way, the

NuRadioMC code works out-of-the-box without additional dependencies. The Python implementation is still sufficiently fast to be used for many problems.

4.2 Focusing effect due to ray bending

Applying the ray approximation to signals from neutrinos in case of ray bending, requires an additional correction factor on the signal amplitude. In general, when considering many rays which are bent there can either be a convergence or divergence of rays. If there is a convergence the ray density and thereby the amplitude of the signal will increase, and conversely so for a divergence. For the ice geometry, refraction contains the signal within the ice, and an amplification is expected if the receiver is above the point of emission and the ray is not reflected from the surface.

We calculate a correction factor from an energy conservation argument: The intensity along the ray is given by

$$I = \sqrt{\frac{\epsilon \varepsilon^2}{\mu c}} = \frac{n \varepsilon^2}{c}, \quad (15)$$

for $\mu = \mu_0$ where ε is the electric-field amplitude, c the speed of light and n the index of refraction. The total power contained in a ray bundle is $P = I A$ with A being an area perpendicular to the propagation direction, so the electric field strength propagates as

$$\varepsilon' = \varepsilon \sqrt{\frac{n A}{n' A'}}. \quad (16)$$

The power radiated into a given solid angle is fixed by the source. For a spherical geometry we have

$$dA = R^2 d\Omega = R d\theta \times R \sin \theta d\phi. \quad (17)$$

For refracted rays the relation $\frac{dA}{d\Omega}$ changes during propagation. Assuming a planar index of refraction model, i.e., it only depends on the depth z , only the $R d\theta$ part changes and is given by

$$dA' = \frac{dz}{d\theta} \sin \theta' d\theta \times R \sin \theta' d\phi. \quad (18)$$

See Appendix C.6 for a derivation of this relation. Then, the ratio of electric field amplitudes is given by

$$\frac{\varepsilon'^2}{\varepsilon^2} = \frac{n}{n'} \frac{dA}{dA'} = \frac{n}{n'} \frac{R}{\sin \theta' \frac{dz}{d\theta}} \quad (19)$$

in the limit of $\theta \approx \theta'$, which is applied as a correction factor to the calculated electric field amplitude from the signal generation module. The factor $\frac{dz}{d\theta}$ is calculated numerically using the ray tracing code by calculating a new ray to the

receiver position which is vertically displaced by a small amount $\Delta z \approx 1$ cm.

Emitter positions very close to the shadow zone boundary require special attention as the correction diverges because $\frac{dz}{d\theta}$ approaches zero. This is not physical but an artifact from treating both emitter and receiver as a point. However, in reality the emission region is extended over several meters due to the extent of the particle shower (cf. Fig. 7) and also the antenna is an extended object. Thus, we studied the stability of the correction factor under small changes of the emitter position by ± 5 m corresponding to typical dimensions of the emission region. We find that correction factors below about a factor of $2\times$ in amplitude vary by less than 10% when the emitter position is varied. Larger amplification factors in-turn are not stable. Hence, limiting the amplification to a maximum of $2\times$ removes unphysical correction factors. Furthermore, we studied the effect of the limit value. Limiting the focusing correction to a factor of $1.5\times$, $2\times$ and $3\times$ results in essentially the same effective volume (i.e. sensitivity of the detector) over a broad range of neutrino energies. Thus, the exact choice limit value is not that important as long as very large amplification factors are removed. As default we limit the focusing correction to a factor of $2\times$ but allow the user to configure this value via the config file.

The effect of focusing is strongest when the rays pass near the surface and experience significant refraction. For a receiver close to the surface we find an increase in the effective volume of the order of 10% due to this correction.

4.3 Numerical ray tracing for arbitrary density fields

In the future, it may become necessary to describe the ice in more detail than an exponential profile that only depends on the depth. This will require a more detailed ray tracing that takes into account an arbitrary 3D index of refraction profile $n(x, y, z)$. We have already foreseen this case and ensured that necessary hooks are available in the code.

Interestingly, the computational problem of the propagation of ultra-high energy cosmic rays through the universe is similar to propagating a ray through the ice. Instead of magnetic fields bending the trajectories of charged cosmic-ray particles, the ray is bend according to the spatial distribution of the index of refraction. Where the cosmic ray can spallate into secondaries, a ray can be partly transmitted and reflected. Consequently, we considered the cosmic-ray propagation code CRPropa [72] as one option and have started to modify it for our needs.

The resulting code RadioPropa [73] solves the Eikonal equation in a local paraxial approximation thus enabling casting of rays through materials with arbitrary varying refractive index as may be required here. In addition, RadioPropa handles effects from boundary traversals such as reflection or partial reflection and allows for the implementation of prop-

agating components of the electric field differently, such as needed for birefringence. It automatically tracks several parts of the original ray, making it also suitable for other less well understood phenomena in the ice. In the same way as NuRadioMC, RadioPropa is modular and flexible, leaving room for future developments. It is currently under heavy development and therefore not yet fully included in NuRadioMC.

4.4 Signal propagation beyond ray tracing

Ray tracing describes the path taken by light in the limit where the wavelength is much smaller than any relevant feature sizes. While this is appropriate in most practical cases, i.e., when the ice is uniform or has a slowly-varying index of refraction, ray tracing does not offer a full description of light propagation near dielectric interfaces, where additional solutions to Maxwell's equations exist, (see e.g. [74] for a pedagogical tutorial on some of the solutions, or [75] for a complete solution for the field of a particle track). In addition to the ice-air interface at the surface, variations in ice density are present below the surface, producing a set of dielectric interfaces. These may result in signals being observed at locations, where simple models assuming a smooth gradient predict no radio signals [68]. While adaptations to the analytic ray-tracing requiring a smooth gradient of the index of refraction, deliver solutions for special cases, the finite-difference time-domain (FDTD) method may be used to model propagation in ice even in the presence of inhomogeneities in all its aspects [66, 67].

Interesting phenomena that arise include the existence of potentially detectable (though generally small) signals coming from regions where there is no ray-tracing solution, diffraction and interference of the radio waves, and the presence of caustics, where the small electric field may be significantly amplified in some geometries [67].

While these effects will slightly modify the effective volume of a detector and provide additional opportunities for event reconstruction, direct integration of an FDTD solver into NuRadioMC is challenging for the purpose of providing a simulation framework. FDTD methods are very computationally and memory intensive, requiring discretization on the scale of a tenth of the smallest relevant wavelength in all spatial dimensions as well as time. Directly simulating the entire volume seen by a typical in-ice station is extremely computationally challenging in three dimensions with our present capabilities – we estimate a single simulation of a cubic kilometer volume valid up to 500 MHz would take $\mathcal{O}(10^7)$ CPU-hours. One can envision the usage for a single event (in case of re-simulation of a detected shower for example), the integration for all events is, however, impractical.

By considering only azimuthally-symmetric antennas and density variations dependent only on depth, it is possible to simulate a transmitting in-ice antenna in just two dimensions,

greatly reducing the computational burden. We are investigating techniques exploiting reciprocity in order to tabulate the propagation properties of the equivalent time-reversed geometry, corresponding to a receiving antenna. Such tabulated properties could then be incorporated into NuRadioMC in an efficient manner.

5 Detector simulation

The fourth pillar of NuRadioMC is the detector simulation, i.e., the calculation of the detector response to an electric field at the antenna and subsequent trigger simulation. We use the software *NuRadioReco* for this task [28]. NuRadioReco is a software for the detector simulation and event reconstruction of radio neutrino and cosmic-ray detectors. It is written in Python and also follows a modern modular design so that it nicely integrates into NuRadioMC.

5.1 Antenna simulation

The most important part in the simulation of the detector response is the impact of the antenna. NuRadioReco provides antenna response pattern of typically used antennas such as LPDAs, dipoles or bicone antennas that were simulated with dedicated codes such as WIPL-D [76] and XFDTD [77]. NuRadioReco also provides an interface to the output of these codes such that new antenna models can be added if necessary.

In earlier software, the response of the antennas was typically treated in a simplified way, only assuming real gain factors and a simple polarization response, i.e. ignoring contributions polarized orthogonal to the main antenna sensitivity. According to methods already standard in the treatment of radio signal from cosmic rays (e.g. [63, 78]), the antenna response is modelled fully frequency-dependent in NuRadioReco, also taking into account the group delay induced by the antenna and its sensitivity to two orthogonal polarization components.

5.2 Trigger simulation

Especially when looking for small signals, as expected from neutrinos, the simulation of the trigger mechanism is essential. The trigger simulation is set up as such that any instrumental trigger can be rebuilt in software. NuRadioReco offers modules to simulate different trigger conditions, e.g., a simple threshold trigger, a high and low trigger as implemented on the SST electronic [79] used by ARIANNA [8] that also allows to specify temporal coincidences between different channels, or more complex triggers such as the phased array concept used by ARA [12] have been included to model the instrument response as implemented in the fields.

5.3 Usage in complex detectors

NuRadioReco was built to reconstruct data from an existing detector. In order to facilitate complex detectors without creating too much overhead, the detector description is stored in a database allowing for a description of every single detector component. While this functionality will be helpful to simulate specific events for an existing detector, it is much too complex for design studies. Therefore, NuRadioReco also allows the user to define the detector description in a human readable JSON format, with reduced complexity. This means both that the detector description only needs to be as complex as minimally required and it significantly speeds up simulations. The information ranges from basic parameters such as the positions of the antennas, their type and orientation to more detailed properties such as the sampling rate of the digitizing electronics, the cable lengths or details about the amplifier and ADC. The detector simulation modules have access to these properties and will simulate the detector response accordingly. An example of a typical detector simulation is provided in Appendix E.

6 Utilities

The four pillars of NuRadioMC are complemented by a set of utility classes that are available to all modules, such as units and medium properties.

6.1 Cross-sections and inelasticities

The cross-section of neutrinos at energies relevant for radio detection are still subject to study, given that these energies have never been probed. Different current extrapolations [31, 33, 34] have been implemented in NuRadioMC in the central utilities, so that the cross-sections can easily be exchanged throughout the code, if so desired.

6.2 Earth models for neutrino absorption

To simulate the sensitivity of a neutrino detector, we need to calculate the probability of a neutrino reaching the detection volume. The Earth atmosphere has negligible absorption for high energy neutrinos but the Earth becomes opaque at high neutrino energies. Hence, NuRadioMC comes with multiple models to calculate the Earth absorption so that we can assign each simulated neutrino a weight, i.e., a probability of reaching the detection volume.

Right now, NuRadioMC provides two Earth models: a simple Earth model with a constant density and a core-mantle-crust Earth model with three layers of different densities. Due to the modularity, it is straight forward to add more detailed models if deemed necessary.

Currently, we do not model *tau regeneration*: A tau lepton that is created following a tau neutrino interaction can propagate significantly through the Earth and potentially decay with a relatively large energy and producing another tau neutrino that can interact close to the detector. We plan to include this effect in a future version of NuRadioMC using e.g. the code of [80, 81].

6.2.1 Simple Earth model

This model uses a constant density of 2900 kg/m^3 and by default uses the cross section (σ) based on [31]. It then calculates the distance the neutrino goes through the Earth as

$$d = 2R_e \cos(\pi - \vartheta), \quad (20)$$

where R_e is the radius of the Earth and ϑ is the zenith angle of the neutrino direction. The weight of an event is then

$$\text{weight} = e^{-d\sigma\rho/\text{AMU}}, \quad (21)$$

where ρ is the constant density of the Earth and AMU is the atomic mass unit in kg.

6.2.2 Core-mantle-crust Earth model

NuRadioMC provides a more realistic Earth model with three layers of different densities which is the default model. In this model, the cross section is per default calculated based on [33] and the propagation distance is calculated through three different layers. The weight is calculated as

$$\text{weight} = e^{-(d_1\rho_1 + d_2\rho_2 + d_3\rho_3)\sigma/\text{AMU}}, \quad (22)$$

where d_1, d_2, d_3 are the distances through three layers and ρ_1, ρ_2, ρ_3 are the three densities.

6.3 Handling of Fourier transforms

NuRadioMC provides a consistent internal handling of Fourier transforms. A common source of errors when using time- and frequency-domain calculations simultaneously is the normalization of the Fourier transforms. There are several reasons for different normalizations depending on the purpose and context. All NuRadioMC Fourier transforms adhere to Parseval's theorem and previously existing Askaryan signal parameterizations have been adjusted to match the FFT definition used in NuRadioMC. Details are discussed in Appendix D.

6.4 Handling of units

In simulations, typical errors occur during the handling of units. To prevent that, NuRadioMC (just like NuRadioReco)

employs a default system of units, a concept borrowed from the Pierre Auger Observatory offline analysis framework [82]: every time a physical variable is defined, it is multiplied by its unit, and every time a variable is plotted or printed out in a certain unit, it is divided by the unit of choice. All other calculations within the code can then be done without considering units.

```
from NuRadioMC.utilities import units
time = 132. * units.ms # define 132 milliseconds
distance = 5. * units.mm # define 5 mm
speed = distance/time
print("the speed is {:.2f} km/h"
      .format(speed/units.km*units.hour))
# the speed is 0.14 km/h
```

The units utilities are available to modules written in both Python and C. In order to facilitate this, no standard Python package was used.

6.5 Attenuation length and other medium characteristics

As discussed in Sect. 4 the signal propagation is a significant part of the neutrino simulation and an area where lots of development is still to be expected. Consequently characteristics of the interaction medium are stored centrally in the utilities to avoid contradicting definitions in modules. We describe the index-of-refraction profile and signal attenuation properties separately to allow for simulation with different combinations of the two. Which model is being used in a NuRadioMC simulation is controlled via the central config file (see Sect. 7.2).

Currently, a signal attenuation model for South Pole ice is provided that is based on a custom model used by the ARA experiment [83]. For the index-of-refraction profile we provide exponential parameterizations to data from for the South Pole and Moore's Bay [68], as well as from Greenland [84, 85].

6.6 Flux calculations and sensitivity limits

In order to compare the performance of different experimental designs, typically quantities like the effective area, volume or expected limits are compared. Since also here, many definitions are common (e.g. 90% confidence upper limits vs. 5σ discovery fluxes), utility functions are provided centrally.

7 Example 1: calculation of the sensitivity of an Askaryan neutrino detector

In this section we present a full example of the capabilities of NuRadioMC to simulate the sensitivity of an Askaryan

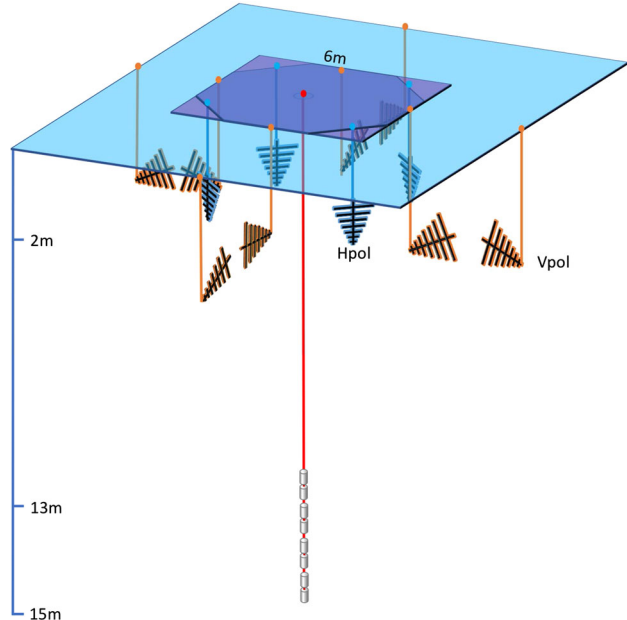


Fig. 11 Sketch of the station layout simulated in Example 1

detector. We choose a station layout that combines log-periodic dipole antennas (LPDA) near the surface with slim dipoles deployed in a borehole deeper in the ice. The specific layout is depicted in Fig. 11. This station layout does not necessarily reflect the authors' opinion on the optimal detector layout but was chosen because it highlights NuRadioMC's capabilities: Antennas of different type, orientation and depth are simulated, the location close to the surface makes a detailed propagation of the signal through the firn necessary, and multiple trigger conditions need to be calculated for different sets of antennas. In the following, only the relevant code snippets are shown. A comprehensive tutorial can be found online [86].

7.1 Event generation

The first step in the simulation is the event generation. The event generation is done stand-alone and produces a list of neutrino interactions in the ice with all necessary properties saved in a simple HDF5 format (see Sect. 2 for details and advantages of separating this step). We choose to generate several input lists, each for a fixed neutrino energy to study the energy dependence. We only consider the initial neutrino interaction. A discussion of the impact of additional Askaryan signals from decaying taus or interacting muons goes beyond the scope of this publication.

A list of one million neutrino interactions with an energy of $E_\nu = 10^{18}$ eV in a cylindrical volume saved in chunks of 10,000 events can be generated with

```
generate_eventlist_cylinder('1e18_n1e6.hdf5',
    n_events=1e6, n_events_per_file=1e4,
    Emin=1e18 * units.eV, Emax=1e18 * units.eV,
    fiducial_rmin=0, fiducial_rmax=5 * units.km,
    fiducial_zmin=-2.7 * units.km, fiducial_zmax=0)
```

The radius needs to be set large enough to include all events that can trigger the detector and is set to 4 km here. For larger neutrino energies, the radius needs to be extended and for lower energies the simulation volume can be decreased to save computing time. The vertical extent of the volume ranges from the surface to the bottom of the ice layer at a depth of 2.7 km at the South Pole.

7.2 Configuration of simulation parameters

The settings of the simulation are controlled with a config file in the human-readable yaml format. The user only needs to specify a parameter if it should be different from its default value. An example configuration with typical settings is shown in listing 1. Typical parameters are the choice of signal generation model (*Alvarez2009* in this example), the ice model, or if noise should be generated and added to the signal in the simulation.

```
noise: False # specify if simulation should be
    run with or without noise
sampling_rate: 5. # sampling rate in GHz used
    #internally in the simulation.
speedup:
    minimum_weight_cut: 1.e-5
    delta_C_cut: 0.698 # 40 degree
propagation:
    ice_model: southpole_2015
signal:
    model: Alvarez2009
trigger:
    noise_temperature: 300 # in Kelvin
weights:
    weight_mode: core_mantle_crust # core_mantle_crust:
        #use the three layer earth model,
        #which considers the different densities of the
        #core, mantle and crust.
        #Simple: use the simple earth model,
        #which applies a constant earth density
```

Listing 1: Example of NuRadioMC’s config file. All parameters are specified in a default system of units. See text for details.

7.3 Detector description

The detector description consists of two parts. First, we need to define the layout of the detector (position, type, and orientation of the antennas), and the sampling rate. Additional parameters such as cable delays and amplifiers can be specified if needed (cf. Sect. 5.3 and NuRadioReco [28]). However, in this example we will perform a simplified detec-

tor simulation sufficient to estimate the sensitivity of an Askaryan detector. The detector description is specified in a JSON file presented in List. 2.

```
{
    "channels": {
        "1": {
            "station_id": 101,
            "channel_id": 0,
            "ant_type": "createLPDA_100MHz",
            "ant_position_x": 3,
            "ant_position_y": 0,
            "ant_position_z": -2.0,
            "ant_rotation_phi": 180,
            "ant_rotation_theta": 90,
            "ant_orientation_phi": 0,
            "ant_orientation_theta": 180,
        },
        ...
    },
    "stations": {
        "1": {
            "pos_altitude": 0,
            "pos_easting": 0,
            "pos_northing": 0,
            "pos_site": "southpole",
            "station_id": 101
        }
    }
}
```

Listing 2: Example of detector description. Only the first channel is shown which defines a downward facing LPDA at a depth of 2 m with its tines oriented along the Northing direction.

Second, we need to specify basic details of the signal chain, i.e., what filter is being used and which triggers are calculated. These tasks are done by dedicated NuRadioReco modules [28] (see Sect. 5.3) that interface directly with NuRadioMC. Instead of simulating just a single trigger condition as shown in the example, a separate trigger can be simulated for each parallel pair of LPDA antennas and for the dipole antennas. This is achieved by calling the same trigger module several times with different arguments. The full example can be found in the online tutorial [86].

7.4 Running the simulation, results, and visualization tools

The NuRadioMC simulation is run by executing the steering script from the command line. The flexibility to split up the input data set into smaller chunks is part of the event generator, so multi-processing computing resources can be used right away. A detailed example on how to run NuRadioMC on a cluster is available in the online tutorial [87].

The sensitivity of the detector is quantified in terms of effective volume to an isotropic neutrino flux. It is given by the weighted sum of all triggered events divided by the total

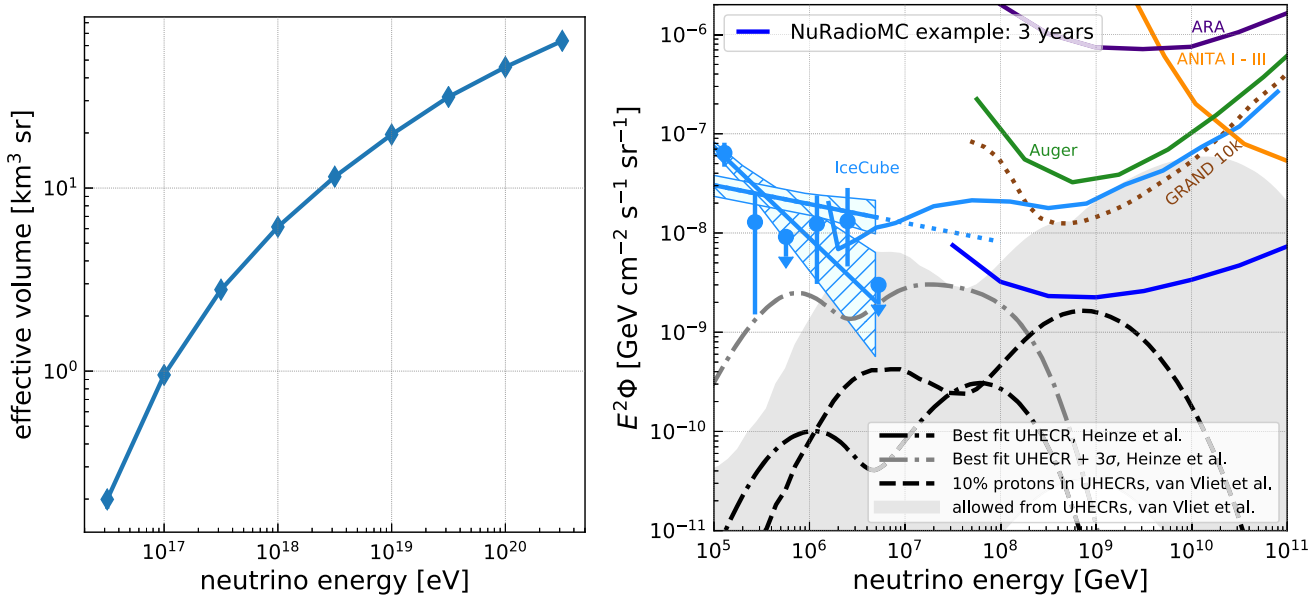


Fig. 12 (left) Effective volume of one example detector station (right) corresponding expected limit for a diffuse neutrino flux for a detector comprising 100 stations and an uptime of 3 years. Shown are for comparison neutrino flux measurements from IceCube [88–90], the Pierre

Auger Observatory [91], ANITA [92], and ARA [10], as well as neutrino flux prediction models from [93,94] calculated using the restrictions from ultra-high energy cosmic rays. We also compare to other proposed arrays [95]

number of events multiplied by the simulation volume and the simulated solid angle (typically 4π). The weighting factor is the probability of a neutrino reaching the simulation volume (and not being absorbed by the Earth). The effective volume of our example detector station is presented in Fig. 12 (left). This effective volume can be converted into an expected limit on the diffuse neutrino flux which is shown in the right panel of Fig. 12. The required tools to make these standard post-processing plots are also part of NuRadioMC.

Furthermore, a standard set of debug plots can be automatically generated from the output files. The distribution of the neutrino interaction vertices of events that triggered the detector is shown in Fig. 13 (left). The upper right (triangular) part of the volume correspond to positions in the *shadow zone* where signals cannot reach the detector according to the ray tracing. The lower left region has little events because the Askaryan signal is only emitted towards the antennas if the neutrino is up-going, i.e., it travelled through the Earth and its probability of reaching the detector is small. The right panel shows the ratio of neutrino flavors and interaction types that triggered the detector. In this case, most triggered events were electron neutrino charged-current (CC) interactions where the full neutrino energy is deposited in particle showers producing an Askaryan signal.

8 Example 2: calculation of the efficiency to detect a signal from both the direct and reflected path

In this example, we calculate the efficiency of an in-ice antenna to observe both the direct Askaryan signal and the signal reflected at the ice surface. For most shower geometries there is total internal reflection of the Askaryan signal at the ice surface, i.e., the ice-air interface acts as a mirror. Consequently, an antenna installed within the ice has the chance to see two pulses: one pulse that propagated straight to the antenna and a second pulse that was reflected off the surface. Detecting this *D'n'R* (direct and reflected) signature is advantageous and an Askaryan neutrino detector will benefit strongly from detecting both pulses: First, it provides a unique method to identify a neutrino interaction in the ice as origin of the detected radio signal, and second, the time difference between the two pulses allows for an improvement in the reconstruction of the distance to the neutrino interaction vertex which is a crucial ingredient for the reconstruction of the neutrino energy. See [9] and [96] for first experimental results concerning this effect using pulsars deployed in the Antarctic ice at South Pole.

There are several effects that influence the efficiency of detecting both pulses that are all taken into account in the NuRadioMC simulation:

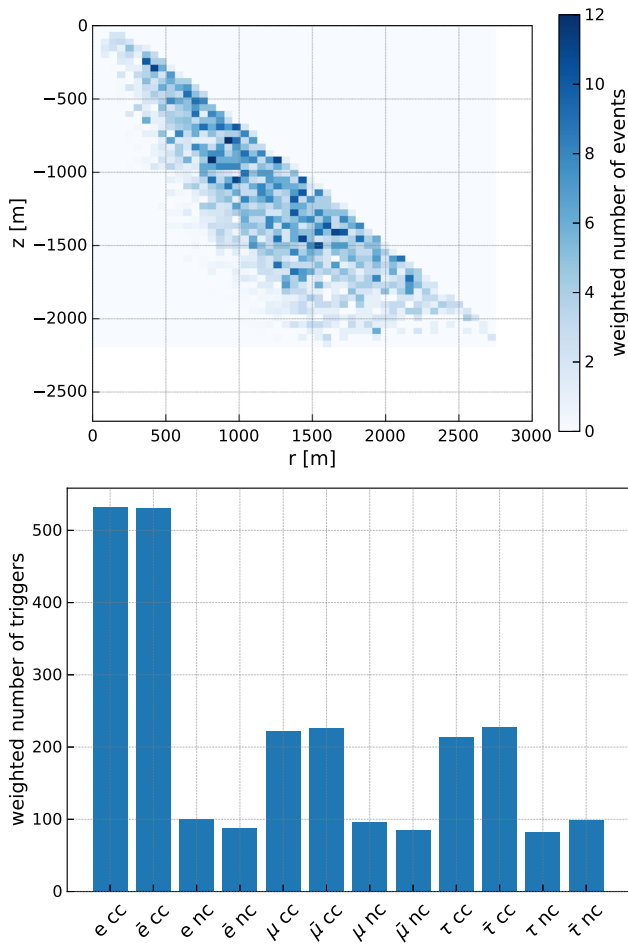


Fig. 13 Visualization for the energy bin of 10^{18} eV neutrino energy. (top) Distribution of neutrino interaction vertices of all triggered events. (bottom) Flavor and interaction type (charged or neutral current) distribution of triggered events

- The reflection coefficient depends on the incident angle of the radio pulse at the ice surface and can range from 1 (total internal reflection) to 0 (no reflection) at the Brewster angle.
- The reflection results in a phase shift of the Askaryan pulse which can alter the amplitude of the pulse. This is modelled using the complex Fresnel coefficients.
- Due to the changing index of refraction in the upper ice layers the signal propagates on curved paths. We find all possible paths to each antenna via ray-tracing. We note that not only a ‘direct’ and ‘reflected’ path will provide a useful signature but any two distinct paths through the ice to the antenna. In case only one solution exists, the efficiency to detect two pulses is of course zero.
- The different ray paths correspond to different launch angles of the signal. This results in a potentially large difference of the amplitude of the Askaryan signal as the launch angles correspond to different viewing angles.

- Antennas have a different sensitivity to different incoming signal directions.
- The two ray paths have different propagation distances and potentially propagate through ice with different attenuation lengths.

In the following we describe an example of how to simulate the D’n’R detection efficiency with NuRadioMC and explain the relevant parts of the code. The full code of this example can be found online at [97].

The D’n’R efficiency depends on the depth of an antenna, hence, we want to define a detector with several antennas of the same kind at different depths. As antenna type we choose a bicone antenna as used by the ARA experiment as such an antenna is sensitive to the dominant vertical polarization, fits into narrow boreholes, and has very little signal dispersion which helps to measure the time difference between the two pulses. Hence, we set up a detector with vertically oriented bicone antennas every 10 m down to a depth of 100 m.

It does make sense to study the D’n’R efficiency as a function of neutrino energy. Therefore, we can use the same script to generate the input event list as in the previous example.

8.1 Set-up of detector simulation

In the previous example we have discussed how to simulate the detector response and the trigger. In the detector simulation so far, all signals that reach the antenna from the different ray path solutions, are combined into a single voltage trace on which the trigger condition is determined. However, for the D’n’R study, we not only need to determine if the detector could observe/trigger a certain event, but also if both pulses are visible. Hence, a dedicated *NuRadioReco* module called *calculateAmplitudePerRaySolution* was written, which simulates the antenna response to each pulse separately and calculates and saves the resulting maximum amplitude. Following this we can calculate if a triggered event has two visible pulses.

As trigger condition we choose a simple threshold trigger of $2 V_{rms}$ that runs on all channels (i.e. antennas) independently. The NuRadioMC simulation is then executed as described in Example 1.

8.2 Results

We now assume a more stringent cut in which all events that produce at least a 3σ ($3 V_{rms}$) signal can be recorded. For the second pulse the requirement for identification is assumed smaller at 2σ . Furthermore, we require that the time difference between the two pulses is smaller than 430 ns

which is assumed as typical record length. We then calculate if an event has triggered via

$$B_i = A_1^i \geq 3 V_{\text{rms}} \quad \text{or} \quad A_2^i \geq 3 V_{\text{rms}} \quad (23)$$

and if both pulses are visible via

$$C_i = ((A_1^i \geq 3 V_{\text{rms}}) \text{ or } (A_2^i \geq 3 V_{\text{rms}})) \quad (24)$$

$$\text{and } ((A_1^i \geq 2 V_{\text{rms}}) \text{ and } (A_2^i \geq 2 V_{\text{rms}})) \quad (25)$$

$$\text{and } (\Delta T < 430 \text{ ns}), \quad (26)$$

where A_1^i and A_2^i are the amplitudes of the two pulses of event i .

Then the D'n'R efficiency is then given by

$$\epsilon = \sum_i C_i / \sum_i B_i \quad (27)$$

where the summation runs over all simulated events i . This calculation is performed for each simulated antenna depths, and for each set of simulated neutrino energy separately.

We simulated 10 million events per neutrino energy and obtain the result presented in Fig. 14. The D'n'R efficiency depends strongly on depth and energy and is best at shallow depth and high energies.

It should be noted that D'n'R efficiency is not the only parameter that one should optimize an array for. For example, a shallower station generally has a smaller effective volume than a deep station, and the fraction of sky coverage also depends of depth. Together with a diverse choice of antennas influencing reconstruction capabilities, data volume restrictions, and instrument costing, optimizing a detector layout is a complex problem, for which NuRadioMC provides guidance.

9 Example 3: Optimization of station spacing for an Askaryan neutrino detector

In this example we calculate the probability to detect a signal from the same neutrino in multiple stations of an array. For a discovery detector, one objective is a large sensitivity which means that it is beneficial to separate stations far enough to minimize station coincidences. However, one may want to optimize differently in the future to have a large fraction of coincidences to improve reconstruction quality. Here, we show how the coincidence fraction can be studied as a function of station separation distance, neutrino energy, and antenna depth. The full code of this example can be found online at [98].

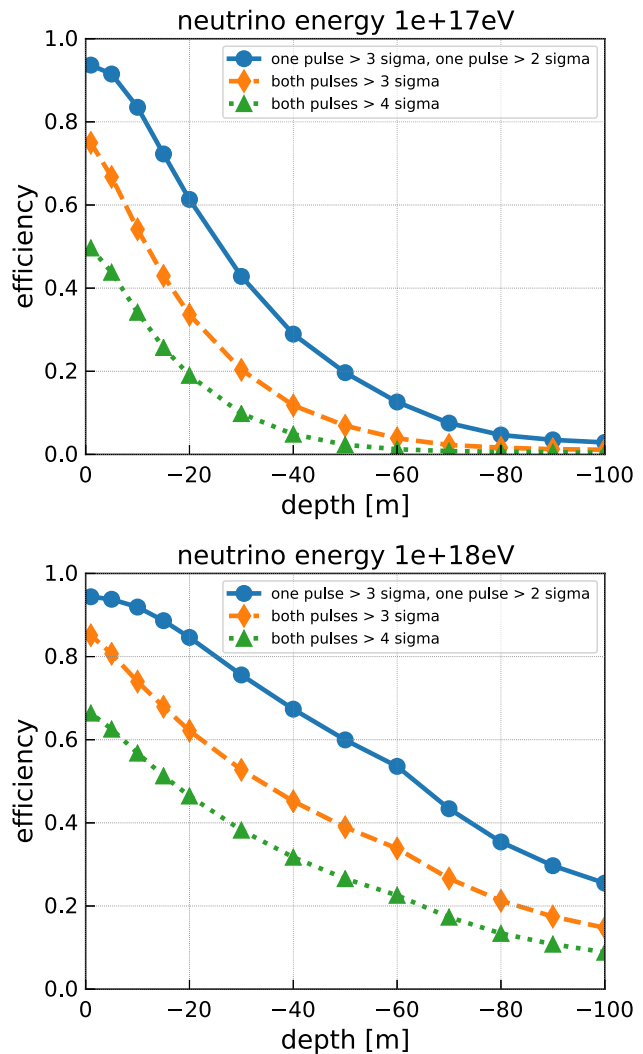


Fig. 14 Efficiency to detect both the direct and reflected Askaryan pulse as a function of depth of the receiver. (top) For a neutrino energy of 10^{17} eV. (bottom) For a neutrino energy of 10^{18} eV. Different markers and colors correspond to different trigger thresholds. All events with a signal of at least a 3σ in any of the pulses were considered which explains the smaller efficiency at the surface for the 'both pulses $> 4\sigma$ ' criterion

9.1 Simulation strategy

We consider a simplified detector with two components. The first one is a surface oriented component consisting of LPDAs and dipoles. To save computing time, we only simulate two orthogonally-oriented horizontal LPDAs at 2 m depth and one dipole at 5 m depth to be sensitive to all signal polarizations. The second component is a deep one, approximated with a single dipole antenna at 50 m depth. We combine the four antennas into a single station so that only one simulation needs to be run, but we can still evaluate the coincidence fraction independently.

In principle, one would need to simulate a full 2D grid for every station separation distance that one wanted to test, because there might be cases where not the nearest station triggered but the next-to nearest neighboring station or stations even further out. However, as this will drastically increase computing time (which scales linearly with the number of stations) this small second order effect is ignored in this example. Our analysis will show that the coincidence rate is dominated by the nearest neighbors, i.e., the coincidence rate quickly drops if the separation between stations is doubled, justifying this approximation.

For every station separation distance we consider the eight nearest stations around the central station as illustrated in Fig. 15 on the left. We consider distances ranging from 100 m to 3 km.

We run the NuRadioMC simulation for event lists of different neutrino energies. The Askaryan signal is filtered from 80 MHz - 500 MHz and all events are saved that exceed a signal threshold of $1V_{\text{RMS}}$ for a noise temperature of 300 K.

9.2 Accessing the results and coincidence fraction

Part of the HDF5 output file is the maximum amplitude of each channel of each event stored in a two dimensional array. This allows for a quick calculation of the coincidence requirements. We first check if the central station fulfilled the trigger condition which we assume to be a signal above $3V_{\text{RMS}}$ in any channel. Then, for each simulated distance, we select the channels corresponding to this distance and check if any channel fulfills the trigger condition. The coincidence rate is then given by the ratio of events where both the central station and any of its nearest neighbors triggered, divided by the number of triggers of the central station alone. The result is presented in Fig. 15 (right). It shows that the coincidence fraction increases with energy. At a station distance of 1 km more than 20% of the events at 10^{18} eV for a surface station (and more than 40% for a 50 m deep station) are detected in at least two stations. This suggests that for a design optimizing on effective volume, stations should be separated further than 1 km from each other, or even further when optimizing for the highest energies. An array of surface stations shows in general a smaller coincidence fraction.

10 Summary and outlook

We have presented NuRadioMC as a versatile framework to simulate different aspects of radio neutrino detectors. NuRadioMC provides a state-of-the-art implementation of the four pillars of a radio neutrino simulation: *event generation*, *signal generation*, *signal propagation*, and *detector simulation*. All properties of the simulation chain can be adapted and compared to each other. Following the design goals of flex-

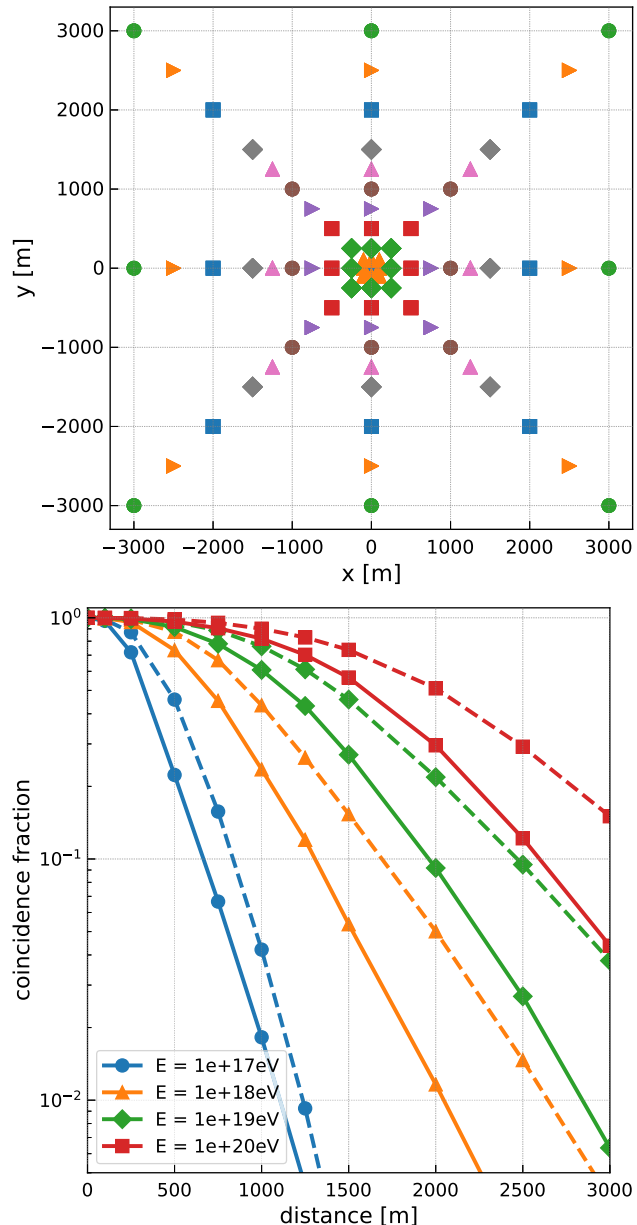


Fig. 15 (top) Station layout of example 3 to determine the station coincidence rate. Each color and symbol combination corresponds to the nearest neighbors of one station separation distance. (bottom) The probability to detect the same neutrino in multiple stations as a function of separation between the stations. The different colors/symbols correspond to different neutrino energies. The solid line is the result for a surface detector, the dashed line is the result for a 50 m deep detector

ibility and usability, NuRadioMC combines the knowledge and experience from all previous radio detectors for neutrino and cosmic-rays. We have presented a detailed discussion of many radio emission models and documented an improved time-domain approach using a shower library which provides a realistic treatment of the LPM effect and its random fluctuations. In three comprehensive examples, we have shown how to calculate effective volumes and sensitivities,

the efficiency to detect multiple pulses from the same shower (multi-path events), and the coincidence fraction between stations in a large array, depending on the distance between stations. This provides valuable tools for design decisions, depending on the goals one wants to optimize for. Proposed radio neutrino experiments such as RNO, ARIANNA, GRAND, ANITA/PUEO or BEACON [9, 95, 99, 100] may soon or already have profited from the capabilities of NuRadioMC.

NuRadioMC provides a solid foundation for reliable simulations, but also leaves room for future developments from the radio neutrino community. NuRadioMC is publicly available on github [101] and is open to low-threshold further code development from interested parties. As experiments progress and as soon as neutrinos are detected through their radio emission, the areas of prioritized need for development will be indicated by the data.

Acknowledgements This article and NuRadioMC itself would not exist without the constructive spirit of the InIceMC working group of the ARA and ARIANNA collaborations. We acknowledge funding from the German research foundation (DFG) under grant GL 914/1-1 (CG) and grant NE 2031/2-1 (DGF, AN, IP, and CW). JAM is supported by Ministerio de Economía, Industria y Competitividad (FPA 2017-85114-P), Xunta de Galicia (ED431C 2017/07), Feder Funds, RENATA Red Nacional Temática de Astropartículas (FPA2015-68783-REDT) and María de Maeztu Unit of Excellence (MDM-2016-0692). We are grateful to the U.S. National Science Foundation-Office of Polar Programs, the U.S. National Science Foundation-Physics Division (grant NSF-1607719) and the U.S. Department of Energy (SWB and CP). BAC thanks the National Science Foundation for support through the Graduate Research Fellowship Program Award DGE-1343012. AC acknowledges funding from the NSF CAREER award 28820 and NSF award 49285. We acknowledge Belgian Funds for Scientific Research (FRS-FNRS and FWO) (ST and NvE), the FWO programme for International Research Infrastructure, and funds from the ERC-StG (No. 805486) of the European Research Council (KDdV).

Data Availability Statement This manuscript has associated data in a data repository. [Authors' comment: The source code and example data files are available open source on github: <https://github.com/nuradio/NuRadioMC>.]

Open Access This article is licensed under a Creative Commons Attribution 4.0 International License, which permits use, sharing, adaptation, distribution and reproduction in any medium or format, as long as you give appropriate credit to the original author(s) and the source, provide a link to the Creative Commons licence, and indicate if changes were made. The images or other third party material in this article are included in the article's Creative Commons licence, unless indicated otherwise in a credit line to the material. If material is not included in the article's Creative Commons licence and your intended use is not permitted by statutory regulation or exceeds the permitted use, you will need to obtain permission directly from the copyright holder. To view a copy of this licence, visit <http://creativecommons.org/licenses/by/4.0/>.

Funded by SCOAP³.

Appendix A: HDF5 event files structure

The HDF5 files created by the event generator consist of a collection of arrays containing the properties of the neutrinos and other secondary particles (taus, for instance). The array keys and contents are the following:

- *azimuths*, the arrival azimuth angles in radians.
- *zeniths*, the arrival zenith angles in radians.
- *xx*, *yy*, and *zz*, the *x*, *y* and *z* coordinates in meters for the point where the particles interact or decay.
- *event_ids*, the event identification numbers
- *n_interaction*, the interaction number. 1 indicates a neutrino interaction, 2 and greater indicates decay or interaction of a lepton created after the neutrino interaction.
- *flavors*, neutrino flavors. 12 for electron neutrino, 14 for muon neutrino, and 16 for tau neutrino. Antineutrinos are represented by –12, –14, and –16. A value of 15 indicates a tau lepton. The numbers are following the standard of [30].
- *energies*, the particle energies in electronvolts
- *interaction_type*, the interaction type. 'cc' for charged current, and 'nc' for neutral current. 'tau_had', 'tau_em', 'tau_mu' indicate the tau decays into the hadronic, electromagnetic and muonic channels respectively.
- *inelasticities*, the inelasticities for the neutrino interactions and the tau decays, that is, the energy fractions taken by the product cascades.

In these HDF5 files we also save as attributes the number of events and the characteristics of the fiducial and total simulated volumes, along with maximum and minimum energies and angles for the neutrinos.

Appendix B: NuRadioMC HDF5 output files structure

NuRadioMC creates as output an HDF5 file with information on the events and on the simulation outcome. The user can choose between saving all the information for all events or only for those that have triggered. The NuRadioMC HDF5 output files contain all the values that can be found in the event files (Appendix A), along with the following additional arrays:

- *triggered*, with ones indicating a triggering event and zeroes a non-triggering event.
- *weights*, the weights given to each event as a consequence of propagation through the Earth.
- *multiple_triggers*, indicates if the triggering condition has been met individually for each simulated trigger. The first axis of this array gives the event number, and the second the type of trigger.

The rest of the output arrays are stored in several HDF5 groups, each group corresponding to a simulated station. The following arrays (except for the SNRs array) contained within the station group are multidimensional. Their first axis is the event number, and the second one the antenna. Each group for a given station contains:

- *SNRs*, the signal to noise ratios for each event defined as the maximum signal amplitude divided by the RMS noise.
- *triggered*, with ones indicating a triggering station and zeroes a non-triggering station.
- *multiple_triggers*, indicates if the triggering condition has been met individually for each simulated trigger. The first axis of this array gives the event number, and the second the type of trigger.
- *maximum_amplitudes*, the maximum amplitudes for the voltages of each antenna.
- *maximum_amplitudes_envelope*, the maximum amplitudes of the voltage envelope of each antenna.
- *travel_distances*, the distances traveled by the rays. There can be up to two, one for each ray-tracing solution. The third axis of the array indicates the ray-tracing solution. The same principle applies to all arrays containing ray-tracing information.
- *travel_times*, the times taken by the rays from emitter to observer.
- *ray_tracing_C0*, C_0 parameters for the ray tracing solutions.
- *ray_tracing_C1*, C_1 parameters for the ray tracing solutions.
- *ray_tracing_solution_type*, strings containing the type of ray tracing solutions: direct, reflected, or refracted.

The following arrays of the HDF5 group contain three-dimensional vectors, and therefore they have a fourth axis that allows us to find the x , y , and z components of said vectors.

- *launch_vectors*, the launch vectors for the ray tracing solutions.
- *receive_vectors*, the receive vectors for the ray tracing solutions.
- *polarization*, the polarization of the electric field.

In the attributes of the output files the names of the simulated triggers (using the string *trigger_names*) can be found.

Appendix C: Analytic ray tracing

The analytic ray tracing in NuRadioMC provides a novel and fast solution of the ray-tracing problem. For completeness we

provide the full derivation of the analytic solution, the path, the path length and the travel time.

Appendix C.1: Derivation of analytic solution

In this section, we will derive the analytic solution to the ray tracing problem. Fermat's principle states that the optical path of a ray of light travelling between two points is stationary. Suppose the index of refraction depends on one coordinate in a three-dimensional Cartesian coordinate system:

$$n(x, y, z) = n(z) \quad (C.1)$$

Further, let $dx/dz = \dot{x}$ and $dy/dz = \dot{y}$, so that the metric may be expressed as:

$$ds = \sqrt{dx^2 + dy^2 + dz^2} = dz\sqrt{\dot{x}^2 + \dot{y}^2 + 1} \quad (C.2)$$

The symmetry of $n(z)$ implies that the coordinate system may be rotated such that $\dot{x} = 0$. Thus the metric becomes

$$ds = dz\sqrt{\dot{y}^2 + 1} \quad (C.3)$$

Inserting this metric into Fermat's Principle gives

$$S = \int_A^B n ds \quad (C.4)$$

$$\delta S = 0 \quad (C.5)$$

$$\delta \int_A^B n(z)\sqrt{1 + \dot{y}^2} dz = 0 \quad (C.6)$$

Defining $u = \dot{y}$ and applying the Euler-Lagrange equations yields

$$\dot{u} = -\frac{\dot{n}}{n}(u^3 + u) \quad (C.7)$$

Letting $v = -\ln n$, Eq. C.7 simplifies to

$$\dot{u} = \dot{v}(u^3 + u) \quad (C.8)$$

Noting that $\dot{v} = dv/dz$, and applying the chain rule gives

$$\frac{du}{dz} \frac{dz}{dv} = \frac{du}{dv} = u^3 + u \quad (C.9)$$

Rearranging and then integrating gives

$$\int \frac{du}{u^3 + u} = \int dv \quad (C.10)$$

$$\ln u - \frac{1}{2} \ln(u^2 + 1) = v + C_0 \quad (C.11)$$

Equation C.11 may be solved for dz/dy after re-scaling C_0 :

$$\frac{dz}{dy} = \pm \sqrt{C_0^2 n^2 - 1} \quad (\text{C.12})$$

In the case of South Pole and Moore's Bay glacial ice, it is found that $n(z)$ is described to within a few percent by an exponential function [68] which allows us to proceed further in solving for the ray-path.

$$n(z) = n_{ice} - \Delta_n \exp(z/z_0) \quad (\text{C.13})$$

Let $\gamma = \Delta_n \exp(z/z_0)$, which implies

$$n(z) = n_{ice} - \gamma \quad (\text{C.14})$$

$$dz = \gamma^{-1} z_0 d\gamma \quad (\text{C.15})$$

Inserting Eq. C.13 into Eq. C.12 and integrating, with $b = 2n_{ice}$ and $c = n_{ice}^2 - C_0^{-2}$:

$$\int \frac{d\gamma}{\gamma(\gamma^2 - b\gamma + c)^{1/2}} = \pm C_0 \left(\frac{\gamma}{z_0} + C_1 \right) \quad (\text{C.16})$$

The second integration constant is C_1 . Intriguingly, for depths much greater than the scale height ($|z_i| \gg z_0, z_i < 0$), the integral in Eq. C.16 has a singularity in the denominator when the ray is initially horizontal. This is discussed further below. The solution to Eq. C.16 is available in standard tables. The solution with y as a function of z via γ is:

$$y(z) = \pm C_0^{-1} c^{-1/2} z_0 \ln \left(\frac{\gamma}{2c^{1/2}(\gamma^2 - b\gamma + c)^{1/2} - b\gamma + 2c} \right) \mp z_0 C_1 \quad (\text{C.17})$$

Let the function within the logarithm in Eq. C.17 be $F(\gamma)$:

$$F(\gamma) = \frac{\gamma}{2c^{1/2}(\gamma^2 - b\gamma + c)^{1/2} - b\gamma + 2c} \quad (\text{C.18})$$

Inserting Eq. C.18 into Eq. C.17, we recover a function which returns the ray path as a function of depth:

$$y(z) = \pm C_0^{-1} c^{-1/2} z_0 \ln(F(\gamma)) \mp z_0 C_1 \quad (\text{C.19})$$

Because the ice model is horizontally symmetric, the constant C_1 is set by the choice of origin. All that remains is to understand the physical meaning of C_0 . Let the initial angle

with respect to the horizontal be θ_i , which should obey

$$\frac{dy}{dz} = \cot(\theta_i) \quad (\text{C.20})$$

$$\frac{dy}{d\gamma} = z_0 \gamma^{-1} \cot(\theta_i) \quad (\text{C.21})$$

Given Eq. C.19, Eq. C.21 may be solved in terms of $F(\gamma)$. The result is

$$\tan \theta_i = \pm C_0 c^{1/2} \frac{F(\gamma)}{\gamma F'(\gamma)} \quad (\text{C.22})$$

Inserting the definition of c and solving for C_0 :

$$C_0(\gamma, \theta_i) = \pm n_{ice}^{-1} \left(\frac{\gamma^2 F'^2(\gamma)}{F^2(\gamma)} \tan^2 \theta_i + 1 \right)^{1/2} \quad (\text{C.23})$$

The right-hand side of Eq. C.23 resembles a secant function. Restricting to initial depths much greater than the scale depth ($|z_i| \gg z_0, z_i < 0$) causes

$$\frac{\gamma^2 F'^2(\gamma)}{F^2(\gamma)} \rightarrow 1 \quad (\text{C.24})$$

If this limit is taken, then Eq. C.23 simplifies:

$$C_0(\gamma, \theta_i) = \pm n_{ice}^{-1} \left(\tan^2 \theta_i + 1 \right)^{1/2} = \pm n_{ice}^{-1} \sec \theta_i \quad (\text{C.25})$$

C_0 is a constant that depends on the boundary conditions, so Eq. C.25 may be inverted:

$$n_{ice} \cos \theta_i = \pm C_0^{-1} \quad (\text{C.26})$$

Equation C.26 is Snell's Law, because C_0 is constant and θ_i is defined with respect to the horizontal. Thus, in the limit ($|z_i| \gg z_0, z_i < 0$) the singularity in Eq. C.16 is for $\cos \theta_i = \pm 1$, i.e. horizontal propagation. Further, in the limit ($|z_i| \gg z_0, z_i < 0$) the factor in front of Eq. C.19, $C_0^{-1} c^{-1/2}$, simplifies:

$$c = n_{ice}^2 - C_0^{-2} \quad (\text{C.27})$$

$$c^{-1/2} = \left(n_{ice}^2 - C_0^{-2} \right)^{-1/2} \quad (\text{C.28})$$

$$C_0^{-1} c^{-1/2} = \left(C_0^2 n_{ice}^2 - 1 \right)^{-1/2} \quad (\text{C.29})$$

$$C_0^{-1} c^{-1/2} = \cot(\theta_i) \quad (\text{C.30})$$

In the last step, Eq. C.12 has been used. Thus, the closed form of $y(z)$ is

$$y(z) = \pm z_0 \cot \theta_i \ln(F(\gamma)) \quad (\text{C.31})$$

If the depth z does not satisfy the limit ($|z_i| \gg z_0, z_i < 0$), C_0 must first be obtained from Eq. C.23, and then inserted into Eq. C.19 to obtain the ray-tracing path.

Appendix C.2: Putting the analytic solution into practical usability

In this section, we demonstrate how to efficiently solve the analytic equations for the ray path derived in Appendix C.1. Without loss of generality, we can use only the positive solution which corresponds to rays propagating into the positive y direction. Equally, we can only consider rays in the $y - z$ plane. This is because such a start configuration can always be achieved with a simple coordinate transformation.

In addition, it is sufficient to only compute solution from a deeper to a shallower position without loss of generality by flipping the initial condition. Hence we can always reduce the problem to finding all possible path's between two points

$$\mathbf{x}_1 = (y_1, z_1)^T \quad \text{and} \quad \mathbf{x}_2 = (y_2, z_2)^T \\ \text{with } y_1 < y_2 \quad \text{and} \quad z_1 < z_2. \quad (\text{C.32})$$

The analytic solution only describes the “first part” of the solution until the *turning point*. This is the position where the ray either hits the surface and is reflected down, or it reaches the point where the propagation direction of the ray becomes horizontal (i.e. into the y direction) due to continuous refraction. This is of course a consequence of the solution being $y(z)$ and not $z(y)$ which is needed to describe the ray path in a single analytic function (because $z(y)$ is not bijective).

The turning point is the position where the second root of Eq. (10) becomes undefined, i.e., for

$$\gamma^2 - b\gamma + c = 0 \Rightarrow \gamma_{\text{turn}} = \frac{1}{2}b - \sqrt{\frac{b^2}{4} - c}. \quad (\text{C.33})$$

The z_{turn} position can be calculated from γ_{turn} . If z_{turn} is positive, the turning points is above the surface. Hence, the ray is reflected off the surface and z_{turn} is set to zero. Then, y_{turn} can be calculated by inserting z_{turn} into Eq. (10).

Hence, from an implementation perspective, we have two distinct cases: either we have a direct ray ($y_2 < y_{\text{turn}}$) or we have a reflected or refracted ray ($y_2 > y_{\text{turn}}$).

Appendix C.3: Determination of free parameters

Now, we present how to determine the two free parameters C_0 and C_1 in a fast and robust way from the initial condition that the ray path goes through the points \mathbf{x}_1 and \mathbf{x}_2 . The parameter C_1 is given by

$$C_1 = y_1 - y(z_1, C_0 = C'_0, C_1 = 0) \quad (\text{C.34})$$

with $y()$ being Eq. (10) evaluated for $C_0 = C'_0$ and $C_1 = 0$.

The parameter C_0 needs to be determined numerically by minimizing the following objective function:

$$\chi^2 = (y_2 - y'(z_2, C_0, C_1))^2. \quad (\text{C.35})$$

As Eq. (10) describes only half of the solution, we first check if \mathbf{x}_2 is before or after the turning point. It is after the turning point if $y_{\text{turn}} < y_2$. Then the following coordinate transformation is performed.

$$y'(z_2, C_0, C_1) = 2y_{\text{turn}} - y(z_2, C_0, C_1). \quad (\text{C.36})$$

To increase the numerical stability of the minimizer it is useful to perform the following coordinate transformation

$$D = \ln(C_0 - 1/n_{\text{ice}}). \quad (\text{C.37})$$

Then Eq. (10) is defined for all values of D .

For typical geometries not just one but two solutions are present. Once one solution is found, the second solution can be determined fast and efficiently using the Brent root finding algorithm [102], and using the displacement in y at position \mathbf{x}_2 as objective function (cf. Fig. 16 right). Utilization of Brent’s algorithm is possible because for a second solution to exists, Δy needs to change sign in one of the open intervals $(-\infty, C_0^1)$ and (C_0^1, ∞) , where C_0^1 is the first solution.

Appendix C.4: Derivative of analytic ray tracing path

The derivative of the analytic ray tracing solution is given by

$$\begin{aligned} & \frac{dy(z)}{dz} \\ &= \left(-\sqrt{c} e^{\frac{z}{z_0}} b \Delta_n + 2 \sqrt{-b \Delta_n e^{\frac{z}{z_0}} + \Delta_n^2 e^{2 \frac{z}{z_0}} + c} c + 2 c^{3/2} \right) \\ & \times \left(2 \sqrt{c} \sqrt{-b \Delta_n e^{\frac{z}{z_0}} + \Delta_n^2 e^{2 \frac{z}{z_0}} + c} - b \Delta_n e^{\frac{z}{z_0}} + 2 c \right)^{-1} \\ & \times \frac{1}{\sqrt{-b \Delta_n e^{\frac{z}{z_0}} + \Delta_n^2 e^{2 \frac{z}{z_0}} + c}} \frac{1}{\sqrt{C_0^2 n_{\text{ice}}^2 - 1}}. \end{aligned} \quad (\text{C.38})$$

Appendix C.5: Analytic solution of path length and travel time

In this section, the analytic solution of the path length and travel time for an exponential index-of-refraction profile is derived.

To find the path(s) between two given points in the ice, (r_0, z_0) and (r_1, z_1) , we need to find the launch angle(s) θ_0 of the ray(s). The radial coordinate r is equivalent to the y coordinate used in the previous sections, since we are restricted to the vertical plane where the wave propagates. Given the

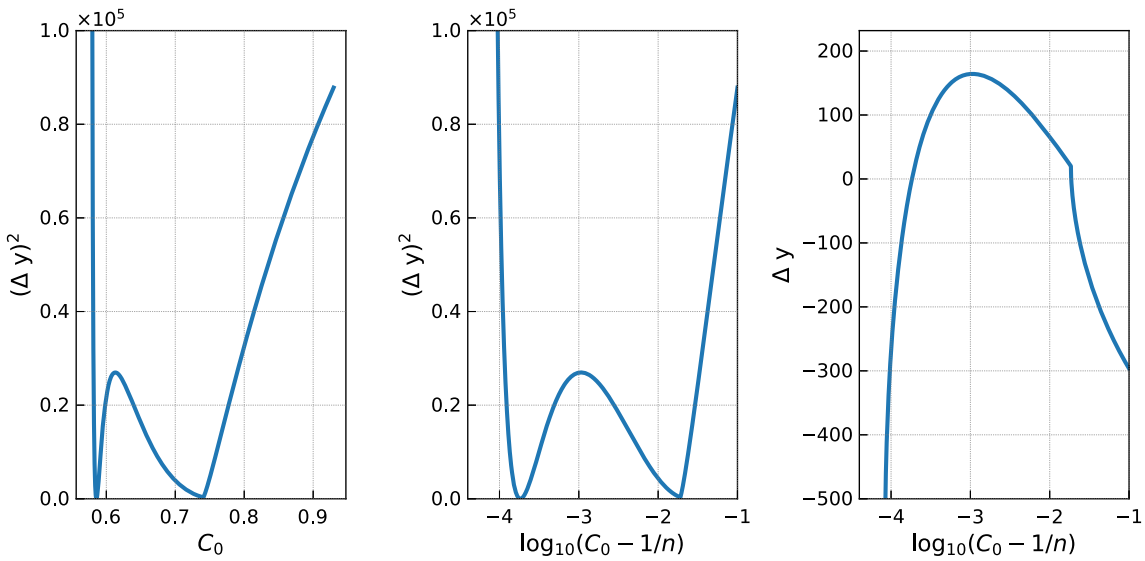


Fig. 16 Example of a typical objective function as a function of C_0 (left) and $\log_{10}(C_0 - 1/n)$ (center). Displacement in y as used for the determination of the second solution via the root finding algorithm (right)

launch angle θ_0 then we can find θ as a function of z using Snell's Law:

$$n(z) \sin(\theta(z)) = n(z_0) \sin(\theta_0) \quad (\text{C.39})$$

$$\theta(z) = \arcsin\left(\frac{n(z_0) \sin(\theta_0)}{n(z)}\right) \quad (\text{C.40})$$

Since we know the radial distance between our starting and ending points, we can calculate the launch angle by first working out the radial distance integral as a function of launch angle, and then inverting it.

$$\begin{aligned} \frac{dr}{dz} &= \frac{dr}{ds} \frac{ds}{dz} = \tan(\theta) \\ \int_{r_0}^{r_1} dr &= \int_{z_0}^{z_1} \tan(\theta) dz \end{aligned}$$

And then using Eq. C.40, this becomes

$$r_1 - r_0 = \int_{z_0}^{z_1} \tan\left(\arcsin\left(\frac{n(z_0) \sin(\theta_0)}{n(z)}\right)\right) dz \quad (\text{C.41})$$

To calculate the launch angle(s) for ray(s) between our two points, solve this equation for θ_0 . While we will continue solving this problem in generality for any $n(z)$ now, in a following section we will simplify the answer for a specific ice model.

Once we know the launch angle of our path we have all we need to calculate its properties. The total path length can be calculated by integrating $\frac{dz}{ds}$:

$$s = \int_{z_0}^{z_1} \frac{1}{\cos(\theta)} dz \quad (\text{C.42})$$

$$= \int_{z_0}^{z_1} \sec\left(\arcsin\left(\frac{n(z_0) \sin(\theta_0)}{n(z)}\right)\right) dz \quad (\text{C.43})$$

The time of flight t along the path can be calculated by combining $\frac{dz}{ds}$ with the following differential equation for the time of flight (where c is the speed of light):

$$\frac{dt}{ds} = \frac{n(z)}{c} \quad (\text{C.44})$$

Which then gives

$$\begin{aligned} \frac{dt}{dz} &= \frac{dt}{ds} \frac{ds}{dz} = \frac{n(z)}{c} \frac{1}{\cos(\theta)} \\ t &= \int_{z_0}^{z_1} \frac{n(z)}{c} \frac{1}{\cos(\theta)} dz \end{aligned} \quad (\text{C.45})$$

$$= \frac{1}{c} \int_{z_0}^{z_1} n(z) \sec\left(\arcsin\left(\frac{n(z_0) \sin(\theta_0)}{n(z)}\right)\right) dz \quad (\text{C.46})$$

For an exponential index-of-refraction profile of the form

$$n(z) = n_{\text{ice}} - \Delta_n e^{z/z_0} \quad (\text{C.47})$$

we can finish the calculations. We will use a few substitutions to make our equations clearer. The substitutions are as follows, where $n(z)$ is as above, z_0 is the starting depth, and θ_0 is the launch angle:

$$\begin{aligned}\beta &= n(z_0) \sin(\theta_0) \\ \alpha &= n_{\text{ice}}^2 - \beta^2 \\ \gamma &= n(z)^2 - \beta^2 \\ \ell_1 &= n_{\text{ice}} n(z) - \beta^2 - \sqrt{\alpha \gamma} \\ \ell_2 &= n(z) + \sqrt{\gamma}\end{aligned}\quad (\text{C.48})$$

Plugging in our ice model, the radial distance integral in equation C.41 becomes

$$r_1 - r_0 = \frac{\beta}{\sqrt{\alpha}} (-z + z_0 \log(\ell_1)) \Big|_{z_0}^{z_1} \quad (\text{C.49})$$

after equation C.48's substitutions. Solving this equation for the launch angle is an alternative approach to find the ray tracing path. Unfortunately, since the launch angle appears in so many places (α , β , and ℓ_1), this equation is not invertible and so cannot be directly solved for θ_0 . As a result, root-finding algorithms will need to be used to calculate the launch angle(s) for the ray(s) between (r_0, z_0) and (r_1, z_1) . In the NuRadioMC code, we calculate the ray paths using the approach of Sect. Appendix C.2 and just calculate the launch angle from the parameter C_0 of the analytic ray-tracing path.

Plugging in our ice model and substituting according to equation C.48, the path length (equation C.42) becomes

$$s = \frac{n_{\text{ice}}}{\sqrt{\alpha}} (-z + z_0 \log(\ell_1)) + z_0 \log(\ell_2) \Big|_{z_0}^{z_1} \quad (\text{C.50})$$

By the same process, the time of flight (equation C.45) becomes

$$t = \frac{1}{c} \left(z_0 \left(\sqrt{\gamma} + n_{\text{ice}} \log(\ell_2) + \log(\ell_1) \frac{n_{\text{ice}}^2}{\sqrt{\alpha}} \right) - z \frac{n_{\text{ice}}^2}{\sqrt{\alpha}} \right) \Big|_{z_0}^{z_1} \quad (\text{C.51})$$

Note that these integrals are specifically for a direct path. For an indirect path, the bounds must be changed to reflect the fact that the path goes up to z_{turn} before coming back down to z_1 .

Appendix C.6: Derivation of focusing correction

Here, we derive how ray density per unit area changes. The geometry in case of straight line propagation is depicted in Fig. 17. We read off that $a = R \sin \Delta\theta$. In the limit of $\Delta\theta \ll 1$ we get $a = R \Delta\theta$. The relation between the length a and vertical displacement Δz is given by $a = \sin \theta \Delta z$. Thus, we get

$$R = \frac{\Delta z}{\Delta\theta} \sin \theta \quad (\text{C.52})$$

and in the limit $\Delta z \Rightarrow 0$

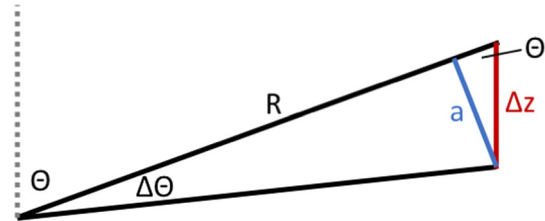


Fig. 17 Sketch of geometry for focusing correction

$$R = \frac{dz}{d\theta} \sin \theta . \quad (\text{C.53})$$

The area dA perpendicular to a ray is given by

$$dA = R d\theta \times R \sin \theta d\phi , \quad (\text{C.54})$$

and will change due to ray bending to

$$dA = \frac{dz}{d\theta} \sin \theta d\theta \times R \sin \theta d\phi . \quad (\text{C.55})$$

Appendix D: FFT normalization in NuRadioMC

In NuRadioMC we use a real fast Fourier transform (rFFT) as it only deals with real valued signals in the time-domain. Furthermore, we assume that the number of samples in the time domain is even. Then, n_t bins (with real values) in the time domain correspond to $n_f = n_t/2 + 1$ bins (with complex values) in the frequency domain where the first bin is the zero frequency component. This is because we exploit the symmetry between negative and positive frequencies for real valued input and only compute the positive frequency components.

The rFFT is normalized such that Parseval's theorem holds without any additional normalization factor, i.e.,

$$\sum_{m=0}^{n_t-1} x_m^2 = \sum_{k=0}^{n_t/2} \tilde{X}_k^2 . \quad (\text{D.56})$$

where x_m are the time domain samples of the signal, and \tilde{X}_k are the frequency domain samples. In the case of electric fields, the dimensions of both x_m and \tilde{X}_k are voltage/length.

This means that the energy fluence, i.e., the time integral over the pulse amplitudes, calculated in the frequency domain and in the time domain give the same results which is a useful physical property. Then, the rFFT and inverse rFFT is defined as

$$\tilde{X}_k = \frac{\sqrt{2}}{\sqrt{N}} \times \sum_{m=0}^{n_t-1} x_m \exp \left(-2\pi i \frac{mk}{n_t} \right) , k = 0, \dots, n_t/2 \quad (\text{D.57})$$

and

$$x_m = \frac{1}{\sqrt{2}\sqrt{N}} \times 2 \sum_{k=0}^{n_t/2} \tilde{X}_k \exp\left(2\pi i \frac{mk}{n_t}\right), m = 0, \dots, n_t - 1 \quad (\text{D.58})$$

We added an additional factor of $\sqrt{2}$ with respect to the standard orthogonal normalization to compensate for the negative frequencies that we did not compute so that the Eq. (D.56) holds.

Appendix D.1: Relation to a continuous Fourier transform

In literature, one also finds the continuous Fourier transform with different conventions for the normalization. One typical choice is to define the Fourier transform as

$$\tilde{E}(v) = \int_{-\infty}^{\infty} dt \exp(i2\pi vt) E(t) \quad (\text{D.59})$$

and

$$E(t) = \int_{-\infty}^{\infty} dv \exp(-i2\pi vt) \tilde{E}(v). \quad (\text{D.60})$$

If the signal in the time domain has units V/m the units in the frequency domain become V/m/Hz. A common task is to transform a frequency-domain parameterization of the Askaryan signal into the time domain via a discrete Fourier transform. For the definition of Eq. (D.59), the corresponding discrete inverse transform is

$$x_m = \frac{1}{n_t} \times 2 \sum_{k=0}^{n_t/2} \tilde{X}_k / \Delta t \exp\left(2\pi i \frac{mk}{n_t}\right) \quad (\text{D.61})$$

$$= 2 \sum_{k=0}^{n_t/2} \tilde{X}_k \Delta f \exp\left(2\pi i \frac{mk}{n_t}\right) \quad (\text{D.62})$$

where we exploit the relation $\Delta t = 1/(n_t \Delta f)$ of a discrete Fourier transform. The additional factor of 2 was added because we only sum over the positive frequencies here. This factor of 2 is already part of real FFT packages such as `numpy.fft` and does not need to be taken into account by the user (see Sect. Appendix D.3 for details).

Appendix D.2: Adjustments to different normalizations

All publications of a frequency-domain parameterization of the Askaryan signal that is based on the *ZHS* model use an unusual normalization of the continuous Fourier transform

where an additional factor of 2 is added to the forward transform (Eq. D.59), and correspondingly a factor of 1/2 in the backward transform (Eq. D.60) (see e.g. [47]). Therefore, Eq. (D.62) needs an additional factor of 1/2 if a ZHS parameterization is used.

Appendix D.3: Implementation details

Most parts of the code use the `numpy` real fft routines. The default normalization has the direct transforms unscaled and the inverse transforms are scaled by $1/n_t$. Hence, a analytic parametrization of the amplitudes in the frequency domain $A(v)$ with units V/m/Hz can be transformed into the time domain via

```
import numpy as np
n = 2**12 # number of bins in time domain
dt = 0.5 * units.ns # bin width in time domain
ff = np.fft.rfftfreq(n, dt)
# get array of frequencies
trace = np.fft.irfft(A(ff) / dt)
```

If $A(v)$ is a parametrization from a ZHS paper, we get the correct time domain representation via

```
trace = 0.5 * np.fft.irfft(A(ff) / dt)
# additional factor of 2 due to
# ZHS Fourier transform normalization
```

All other Fourier transforms are normalized such that Eq. (D.56) is satisfied which is achieved with `numpy` via:

```
def time2freq(trace):
    """
    performs forward FFT with correct
    normalization that conserves the power
    """
    return np.fft.rfft(trace,
axis=-1, norm="ortho") * 2 ** 0.5
# an additional sqrt(2) is added because
# negative frequencies are omitted.
```

```
def freq2time(spectrum):
    """
    performs backward FFT with correct
    normalization that conserves the power
    """
    return np.fft.irfft(spectrum, axis=-1,
norm="ortho") / 2 ** 0.5
```

Appendix E: Detector simulation

The code snippet in List. 4 shows a typical detector simulation. With just a few lines of code, we can calculate the antenna response, downsample the time trace to the detec-

tor sampling rate, bandpass filter the signal and simulate a high/low trigger with a 2 out of 4 antennas coincidence logic.

```
def get_time_trace(energy, theta, N, dt, shower_type, n_index, R, model,
                   interp_factor=None, interp_factor2=None,
                   same_shower=False, **kwargs):
    """
    returns the Askaryan pulse in the time domain of the eTheta component

    We implement only the time-domain solution and obtain the frequency spectrum
    via FFT (with the standard normalization of NuRadioMC). This approach assures
    that the units are interpreted correctly. In the time domain, the amplitudes
    are well defined and not details about fourier transform normalizations needs
    to be known by the user.

    Parameters
    -----
    energy : float
        energy of the shower
    theta: float
        viewangle: angle between shower axis (neutrino direction) and the line
        of sight between interaction and detector
    N : int
        number of samples in the time domain
    dt: float
        time bin width, i.e. the inverse of the sampling rate
    shower_type: string (default "HAD")
        type of shower, either "HAD" (hadronic), "EM" (electromagnetic) or
        "TAU" (tau lepton induced), note that TAU showers
        are currently only implemented in the ARZ2019 model
    n_index: float
        index of refraction
    R: float
        distance from vertex to observer
    model: string
        specifies the signal model
        * ZHS1992: the original ZHS parametrization from E. Zas, ...
        * Alvarez2000: parameterization based on ZHS mainly based on J. Alvarez-...
        * Alvarez2009: parameterization based on ZHS from J. Alvarez-...
        * HCRB2017: analytic model from J. Hanson, A. Connolly ...
        * ARZ2019 semi MC time domain model
    interp_factor: float or None
        controls the interpolation of the charge-excess profiles in the ARZ model
    interp_Factor2: float or None
        controls the second interpolation of the charge-excess profiles in the ARZ model
    same_shower: bool (default False)
        controls the random behaviour of picking a shower from the library in the ARZ model,
        see description there for more details

    Returns
    -----
    time trace: array
        the amplitudes for each time bin
    """


```

Listing 3: Signature of the signal generation interface. NuRadioMC provides a uniform interface in form of simple function to all implemented Askaryan modules. This allows to use the Askaryan modules outside of a NuRadioMC simulation and is a well tested resource/reference implementation for the radio community.

```

class mySimulation(simulation.simulation):
    def _detector_simulation(self):
        # 1st convolve efield with antenna pattern
        efieldToVoltageConverterPerChannel.run(self._evt, self._station, self._det)
        # downsample trace back to detector sampling rate
        channelResampler.run(self._evt, self._station, self._det, sampling_rate=1. / self._dt)
        # bandpass filter the signal
        channelBandPassFilter.run(self._evt, self._station, self._det,
                                  passband=[80 * units.MHz, 500 * units.GHz],
                                  filter_type='butter', order=2)
        # run a high/low trigger on the 4 downward pointing LPDAs
        triggerSimulatorHighLow.run(self._evt, self._station, self._det,
                                     threshold_high=4 * self._Vrms,
                                     threshold_low=-4 * self._Vrms,
                                     coinc_window=40 * units.ns,
                                     triggered_channels=[0, 1, 2, 3], # select the LPDA channels
                                     number_cedicences=2, # 2/4 majority logic
                                     trigger_name='LPDA_2of4_4sigma')

```

Listing 4: Example of performing a detector simulation using NuRadioReco.

References

1. M. Ackermann et al., Astrophysics uniquely enabled by observations of high-energy cosmic neutrinos, astro 2020 decadal whitepaper (2019). [arXiv:1903.04334](https://arxiv.org/abs/1903.04334)
2. IceCube collaboration, The IceCube Neutrino Observatory: instrumentation and online systems. *J. Instrum.* **12**, P03012 (2017). [arXiv:1612.05093](https://arxiv.org/abs/1612.05093). <https://doi.org/10.1088/1748-0221/12/03/P03012>
3. IceCube collaboration, A combined maximum-likelihood analysis of the high-energy astrophysical neutrino flux measured with IceCube. *Astrophys. J.* **809**, 98 (2015). [arXiv:1507.03991](https://arxiv.org/abs/1507.03991). <https://doi.org/10.1088/0004-637X/809/1/98>
4. IceCube collaboration, Neutrino emission from the direction of blazar TXS 0506+056 prior to the IceCube-170922A alert. *Science* **361**, 147 (2018)
5. IceCube collaboration, Measurement of South Pole ice transparency with the IceCube LED calibration system. *Nucl. Instrum. Methods* **A711**, 73 (2013). [arXiv:1301.5361](https://arxiv.org/abs/1301.5361). <https://doi.org/10.1016/j.nima.2013.01.054>
6. G.A. Askar'yan, Coherent radio emission from cosmic showers in air and in dense media. *Sov. J. Exp. Theor. Phys.* **21**, 658 (1965)
7. S. Barwick, D. Besson, P. Gorham, D. Saltzberg, South polar in situ radio-frequency ice attenuation. *J. Glaciol.* **51**, 231–238 (2005). <https://doi.org/10.3189/172756505781829467>
8. ARIANNA collaboration, Design and performance of the ARIANNA HRA-3 neutrino detector systems. *IEEE Trans. Nucl. Sci.* **62**, 2202 (2015). [arXiv:1410.7369](https://arxiv.org/abs/1410.7369). <https://doi.org/10.1109/TNS.2015.2468182>
9. ARIANNA collaboration, Targeting ultra-high energy neutrinos with the ARIANNA experiment. *Adv. Space Res.* **64**(12), 2595–2609 (2019). [arXiv:1903.01609](https://arxiv.org/abs/1903.01609) <https://doi.org/10.1016/j.asr.2019.06.016>
10. ARA collaboration, Performance of two Askaryan Radio Array stations and first results in the search for ultrahigh energy neutrinos. *Phys. Rev. D* **93**, 082003 (2016). [arXiv:1507.08991](https://arxiv.org/abs/1507.08991). <https://doi.org/10.1103/PhysRevD.93.082003>
11. ARIANNA collaboration, A first search for cosmogenic neutrinos with the ARIANNA Hexagonal Radio Array. *Astropart. Phys.* **70**, 12 (2015). [arXiv:1410.7352](https://arxiv.org/abs/1410.7352). <https://doi.org/10.1016/j.astropartphys.2015.04.002>
12. P. Allison et al., Design and performance of an interferometric trigger array for radio detection of high-energy neutrinos. *Nucl. Instrum. Methods Phys. Res. A* **930**, 112 (2019). <https://doi.org/10.1016/j.nima.2019.01.067>. [arXiv:1809.04573](https://arxiv.org/abs/1809.04573)
13. K. Greisen, End to the cosmic-ray spectrum? *Phys. Rev. Lett.* **16**, 748 (1966). <https://doi.org/10.1103/PhysRevLett.16.748>
14. G.T. Zatsepin, V.A. Kuz'min, Upper limit of the spectrum of cosmic rays. *Sov. J. Exp. Theor. Phys. Lett.* **4**, 78 (1966)
15. V.S. Beresinsky, G.T. Zatsepin, Cosmic rays at ultra high energies (neutrino?). *Phys. Lett. B* **28**, 423 (1969). [https://doi.org/10.1016/0370-2693\(69\)90341-4](https://doi.org/10.1016/0370-2693(69)90341-4)
16. M. Ackermann et al., Fundamental physics with high-energy cosmic neutrinos, Astro 2020 Decadal Whitepaper (2019). [arXiv:1903.04333](https://arxiv.org/abs/1903.04333)
17. K. Dookayka, *Characterizing the Search for Ultra-High Energy Neutrinos with the ARIANNA Detector*; Ph.D. thesis (University of California, Irvine, 2011)
18. ARA collaboration, First constraints on the ultra-high energy neutrino flux from a prototype station of the Askaryan Radio Array. *Astropart. Phys.* **70**, 62 (2015). [arXiv:1404.5285](https://arxiv.org/abs/1404.5285). <https://doi.org/10.1016/j.astropartphys.2015.04.006>
19. ANITA collaboration, ICEMC: a Monte Carlo Simulation for Cosmogenic Neutrinos interacting in the Antarctic ice as viewed by the Antarctic Impulsive Transient Antenna (ANITA). [arXiv:1903.11043](https://arxiv.org/abs/1903.11043)
20. T. Winchen et al., Realtime processing of LOFAR data for the detection of nano-second pulses from the Moon, in *Journal of Physics Conference Series*, vol. 898, p. 032004 (2017). [arXiv:1612.06592](https://arxiv.org/abs/1612.06592). <https://doi.org/10.1088/1742-6596/898/3/032004>
21. C.W. James et al., Overview of lunar detection of ultra-high energy particles and new plans for the SKA, in *European Physical Journal Web of Conferences*, vol. 135, p. 04001 (2017). [arXiv:1704.05336](https://arxiv.org/abs/1704.05336). <https://doi.org/10.1051/epjconf/201713504001>
22. R. Essig et al., Dark sectors and new, light, weakly-coupled particles, FERMILAB-CONF-13-653 (2013). [arXiv:1311.0029](https://arxiv.org/abs/1311.0029)
23. “Cython.” <http://cython.org>
24. J. Alvarez-Muñiz, R.A. Vázquez, E. Zas, Calculation methods for radio pulses from high energy showers. *Phys. Rev. D* **62** (2000). <https://doi.org/10.1103/physrevd.62.063001>

25. J. Alvarez-Muñiz, A. Romero-Wolf, E. Zas, Practical and accurate calculations of Askaryan radiation. *Phys. Rev. D* **84**, 103003 (2011). [arXiv:1106.6283](https://arxiv.org/abs/1106.6283). <https://doi.org/10.1103/PhysRevD.84.103003>
26. L.D. Landau, I. Pomeranchuk, Limits of applicability of the theory of bremsstrahlung electrons and pair production at high-energies. *Dokl. Akad. Nauk Ser. Fiz.* **92**, 535 (1953)
27. A.B. Migdal, Bremsstrahlung and pair production in condensed media at high-energies. *Phys. Rev.* **103**, 1811 (1956). <https://doi.org/10.1103/PhysRev.103.1811>
28. C. Glaser, A. Nelles, I. Plaisier, C. Welling, S.W. Barwick, D. Garca-Fernndez, et al., NuRadioReco: A reconstruction framework for radio neutrino detectors. *Eur. Phys. J. C* **79** (2019). [arXiv:1903.07023](https://arxiv.org/abs/1903.07023). <https://doi.org/10.1140/epjc/s10052-019-6971-5>
29. The HDF Group, Hierarchical Data Format, version 5, 1997-NNNN
30. C. Amsler et al., (Particle Data Group), Monte Carlo particle numbering scheme. *Phys. Lett. B* **667** (2018)
31. R. Gandhi, C. Quigg, M.H. Reno, I. Sarcevic, Neutrino interactions at ultrahigh energies. *Phys. Rev. D* **58**, 58 (1998). <https://doi.org/10.1103/PhysRevD.58.093009>
32. R. Gandhi, C. Quigg, M.H. Reno, I. Sarcevic, Ultrahigh-energy neutrino interactions. *Astropart. Phys.* **5**, 81–110 (1996). [https://doi.org/10.1016/0927-6505\(96\)00008-4](https://doi.org/10.1016/0927-6505(96)00008-4)
33. A. Connolly, R.S. Thorne, D. Waters, Calculation of high energy neutrino-nucleon cross sections and uncertainties using the MSTW parton distribution functions and implications for future experiments. *Phys. Rev. D* **83**, 113009 (2011). [arXiv:1102.0691](https://arxiv.org/abs/1102.0691). <https://doi.org/10.1103/PhysRevD.83.113009>
34. A. Cooper-Sarkar, P. Mertsch, S. Sarkar, The high energy neutrino cross-section in the Standard Model and its uncertainty. *JHEP* **08**, 042 (2011). [arXiv:1106.3723](https://arxiv.org/abs/1106.3723). [https://doi.org/10.1007/JHEP08\(2011\)042](https://doi.org/10.1007/JHEP08(2011)042)
35. J.H. Koehne, K. Frantzen, M. Schmitz, T. Fuchs, W. Rhode, D. Chirkov et al., PROPOSAL: a tool for propagation of charged leptons. *Comput. Phys. Commun.* **184**, 2070 (2013). <https://doi.org/10.1016/j.cpc.2013.04.001>
36. M. Dunsch, J. Soedingrekso, A. Sandrock, M. Meier, T. Menne, W. Rhode, Recent improvements for the lepton propagator PROPOSAL. [arXiv:1809.07740](https://arxiv.org/abs/1809.07740)
37. Particle Data Group collaboration, Review of particle physics. *Phys. Rev. D* **98**, 030001 (2018). <https://doi.org/10.1103/PhysRevD.98.030001>
38. T. De Young, S. Razzaque, D.F. Cowen, Astrophysical tau neutrino detection in kilometer-scale Cherenkov detectors via muonic tau decay. *Astropart. Phys.* **27**, 238 (2007). [arXiv:astro-ph/0608486](https://arxiv.org/abs/astro-ph/0608486). <https://doi.org/10.1016/j.astropartphys.2006.11.003>
39. S. Iyer Dutta, M.H. Reno, I. Sarcevic, D. Seckel, Propagation of muons and taus at high energies. *Phys. Rev. D* **63**, 094020 (2001). <https://doi.org/10.1103/PhysRevD.63.094020>
40. NuRadioMC, “Example: Pulser calibration measurement.” <https://github.com/nu-radio/NuRadioMC/wiki/Example:-Pulser-calibration-measurement>
41. NuRadioMC, “Event generation skeleton.” https://github.com/nu-radio/NuRadioMC/blob/master/NuRadioMC/EvtGen/generator_skeleton.py
42. NuRadioMC, “Online documentation.” <https://github.com/nu-radio/NuRadioMC/wiki/Interface-to-Askaryan-modules>
43. C.R. Persichilli, *Performance and Simulation of the ARIANNA Pilot Array, with Implications for Future Ultra-high Energy Neutrino Astronomy*, Ph.D. thesis (University of California, Irvine, 2018)
44. E. Zas, F. Halzen, T. Stanev, Electromagnetic pulses from high-energy showers: implications for neutrino detection. *Phys. Rev. D* **45**, 362 (1992). <https://doi.org/10.1103/PhysRevD.45.362>
45. J. Alvarez-Muñiz, E. Marqués, R.A. Vázquez, E. Zas, Coherent radio pulses from showers in different media: a unified parameterization. *Phys. Rev. D* **74**, 023007 (2006). [arXiv:astro-ph/0512337](https://arxiv.org/abs/astro-ph/0512337). <https://doi.org/10.1103/PhysRevD.74.023007>
46. J. Alvarez-Muñiz, W.R. Carvalho, M. Tueros, E. Zas, Coherent Cherenkov radio pulses from hadronic showers up to EeV energies. *Astropart. Phys.* **35**, 287 (2012). [arXiv:1005.0552](https://arxiv.org/abs/1005.0552). <https://doi.org/10.1016/j.astropartphys.2011.10.002>
47. J. Alvarez-Muñiz, C. James, R. Protheroe, E. Zas, Thinned simulations of extremely energetic showers in dense media for radio applications. *Astropart. Phys.* **32**, 100 (2009). <https://doi.org/10.1016/j.astropartphys.2009.06.005>
48. J. Alvarez-Muñiz, E. Zas, The LPM effect for EeV hadronic showers in ice: implications for radio detection of neutrinos. *Phys. Lett. B* **434**, 396 (1998). [https://doi.org/10.1016/s0370-2693\(98\)00905-8](https://doi.org/10.1016/s0370-2693(98)00905-8)
49. J. Alvarez-Muñiz, E. Zas, Cherenkov radio pulses from EeV neutrino interactions: the LPM effect. *Phys. Lett. B* **411**, 218 (1997). [https://doi.org/10.1016/s0370-2693\(97\)01009-5](https://doi.org/10.1016/s0370-2693(97)01009-5)
50. J.C. Hanson, A.L. Connolly, Complex analysis of askaryan radiation: a fully analytic treatment including the LPM effect and cascade form factor. *Astropart. Phys.* **91**, 75 (2017). [arXiv:1605.04975](https://arxiv.org/abs/1605.04975). <https://doi.org/10.1016/j.astropartphys.2017.03.008>
51. R.V. Buniy, J.P. Ralston, Radio detection of high energy particles: coherence versus multiple scales. *Phys. Rev. D* **65**, 016003 (2001). <https://doi.org/10.1103/PhysRevD.65.016003>
52. C.-Y. Hu, C.-C. Chen, P. Chen, Near-field effects of Cherenkov radiation induced by ultra high energy cosmic neutrinos. *Astropart. Phys.* **35**, 421 (2012). [arXiv:1012.5155](https://arxiv.org/abs/1012.5155). <https://doi.org/10.1016/j.astropartphys.2011.11.008>
53. L. Gerhardt, S.R. Klein, Electron and photon interactions in the regime of strong LPM suppression. *Phys. Rev. D* **82**, 074017 (2010). [arXiv:1007.0039](https://arxiv.org/abs/1007.0039). <https://doi.org/10.1103/PhysRevD.82.074017>
54. K. Werner, K.D. de Vries, O. Scholten, A realistic treatment of geomagnetic Cherenkov radiation from cosmic ray air showers. *Astropart. Phys.* **37**, 5 (2012). [arXiv:1201.4471](https://arxiv.org/abs/1201.4471). <https://doi.org/10.1016/j.astropartphys.2012.07.007>
55. J. Alvarez-Muñiz, A. Romero-Wolf, E. Zas, Čerenkov radio pulses from electromagnetic showers in the time domain. *Phys. Rev. D* **81**, 123009 (2010). [arXiv:1002.3873](https://arxiv.org/abs/1002.3873). <https://doi.org/10.1103/PhysRevD.81.123009>
56. J. Bellm et al., Herwig 7.1 Release Note. [arXiv:1705.06919](https://arxiv.org/abs/1705.06919)
57. J. Alvarez-Muñiz, W.R. Carvalho, Jr., E. Zas, Monte Carlo simulations of radio pulses in atmospheric showers using ZHAireS. *Astropart. Phys.* **35**, 325 (2012). [arXiv:1107.1189](https://arxiv.org/abs/1107.1189). <https://doi.org/10.1016/j.astropartphys.2011.10.005>
58. M. Gottowik, C. Glaser, T. Huege, J. Rautenberg, Determination of the absolute energy scale of extensive air showers via radio emission: systematic uncertainty of underlying first-principle calculations. *Astropart. Phys.* **103**, 87 (2018). [arXiv:1712.07442](https://arxiv.org/abs/1712.07442). <https://doi.org/10.1016/j.astropartphys.2018.07.004>
59. D. García-Fernández, J. Alvarez-Muñiz, W.R. Carvalho, A. Romero-Wolf, E. Zas, Calculations of electric fields for radio detection of ultrahigh energy particles. *Phys. Rev. D* **87**, 023003 (2013). <https://doi.org/10.1103/PhysRevD.87.023003>
60. T. Huege, M. Ludwig, C.W. James, Simulating radio emission from air showers with CoREAS, in American Institute of Physics Conference Series, R. Lahmann, T. Eberl, K. Graf, C. James, T. Huege, T. Karg et al. (eds.) American Institute of Physics Conference Series, vol. 1535, pp. 128–132 (2013). [arXiv:1301.2132](https://arxiv.org/abs/1301.2132). <https://doi.org/10.1063/1.4807534>
61. Pierre Auger collaboration, Measurement of the radiation energy in the radio signal of extensive air showers as a universal estimator of cosmic-ray energy. *Phys. Rev. Lett.* **116**, 241101

- (2016). arXiv:1605.02564. <https://doi.org/10.1103/PhysRevLett.116.241101>
62. C. Glaser, M. Erdmann, J.R. Hörandel, T. Huege, J. Schulz, Simulation of radiation energy release in air showers. *JCAP* **1609**, 024 (2016). arXiv:1606.01641. <https://doi.org/10.1088/1475-7516/2016/09/024>
63. LOFAR collaboration, Detecting cosmic rays with the LOFAR radio telescope. *Astron. Astrophys.* **560**, A98 (2013). arXiv:1311.1399. <https://doi.org/10.1051/0004-6361/201322683>
64. R. Engel, D. Heck, T. Huege, T. Pierog, M. Reininghaus, F. Riehn et al., Towards a next generation of CORSIKA: a framework for the simulation of particle cascades in astroparticle physics. *Comput. Softw. Big Sci.* **3**, 2 (2019). arXiv:1808.08226. <https://doi.org/10.1007/s41781-018-0013-0>
65. NuRadioMC, “Signal propagation base class.” https://github.com/nu-radio/NuRadioMC/blob/master/NuRadioMC/SignalProp/propagation_base_class.py
66. S. Buitink, Using FDTD simulations to study radio propagation effects, Proceedings of the ARENA 2018, Catania Sicily (2018)
67. C. Deaconu, A.G. Vieregg, S.A. Wissel, J. Bowen, S. Chipman, A. Gupta et al., Measurements and modeling of near-surface radio propagation in glacial ice and implications for neutrino experiments. *Phys. Rev. D* **98**, 043010 (2018). arXiv:1805.12576. <https://doi.org/10.1103/PhysRevD.98.043010>
68. S. Barwick et al., Observation of classically ‘forbidden’ electromagnetic wave propagation and implications for neutrino detection. *J. Cosmol. Astropart. Phys.* **07**, 055 (2018). arXiv:1804.10430. <https://doi.org/10.1088/1475-7516/2018/07/055>
69. S. van der Walt, S.C. Colbert, G. Varoquaux, The numpy array: a structure for efficient numerical computation. *Comput. Sci. Eng.* **13**, 22 (2011). <https://doi.org/10.1109/MCSE.2011.37>
70. E. Jones, T. Oliphant, P. Peterson et al., “SciPy: Open source scientific tools for Python.” <http://www.scipy.org/> (2001)
71. M. Galassi et al., “GNU Scientific Library Reference Manual.” <http://www.gnu.org/software/gsl/%22>
72. R.A. Batista, A. Dundovic, M. Erdmann, K.-H. Kampert, D. Kuempel, G. Müller et al., CRPropa 3—a public astrophysical simulation framework for propagating extraterrestrial ultrahigh energy particles. *JCAP* **1605**, 038 (2016). arXiv:1603.07142. <https://doi.org/10.1088/1475-7516/2016/05/038>
73. T. Winchen, RadioPropa—a modular raytracer for in-matter radio propagation, in *Proceedings of the ARENA 2018*, Catania Sicily (2018). arXiv:1810.01780
74. F. Frezza, N. Tedeschi, Electromagnetic inhomogeneous waves at planar boundaries: tutorial. *J. Opt. Soc. Am. A* **32**, 1485 (2015). <https://doi.org/10.1364/JOSAA.32.001485>
75. D. García-Fernández, B. Revenu, A. Escudie, L. Martin, Influence of a planar boundary on the electric field emitted by a particle shower. *Phys. Rev. D* **99**, 063009 (2019). arXiv:1811.11003. <https://doi.org/10.1103/PhysRevD.99.063009>
76. B. Kolundzija, WIPL-D: from university software to company product, in *Proceedings of the 5th European Conference on Antennas and Propagation (EUCAP)*, pp. 2844–2846 (2011)
77. K.S. Kunz, R.J. Luebers, *The Finite Difference Time Domain Method for Electromagnetics* (CRC Press, Boca Raton, 1993)
78. Pierre Auger collaboration, Advanced functionality for radio analysis in the Offline software framework of the Pierre Auger Observatory. *Nucl. Instrum. Methods Phys. Res. A* **635**, 92 (2011). arXiv:1101.4473. <https://doi.org/10.1016/j.nima.2011.01.049>
79. S.A. Kleinfelder, E. Chiem, T. Prakash, The SST Multi-G-Sample/s Switched Capacitor Array Waveform Recorder with Flexible Trigger and Picosecond-Level Timing Accuracy. arXiv:1508.02460
80. J. Alvarez-Muñiz, W. R. Carvalho, K. Payet, A. Romero-Wolf, H. Schoorlemmer, E. Zas, Comprehensive approach to tau-lepton production by high-energy tau neutrinos propagating through the earth. *Phys. Rev. D* **97** (2018). <https://doi.org/10.1103/physrevd.97.023021>
81. J. Alvarez-Muñiz, W.R. Carvalho, A.L. Cummings, K. Payet, A. Romero-Wolf, H. Schoorlemmer et al., Erratum: Comprehensive approach to tau-lepton production by high-energy tau neutrinos propagating through the earth [Phys. Rev. D 97, 023021 (2018)]. *Phys. Rev. D* **99** (2019). <https://doi.org/10.1103/physrevd.99.069902>
82. S. Argirò et al., The offline software framework of the Pierre Auger Observatory. *Nucl. Instrum. Methods Phys. Res. A* **580**, 1485 (2007). <https://doi.org/10.1016/j.nima.2007.07.010>. arXiv:0707.1652
83. ARA Project, “Attenuation model.” <https://icecube.wisc.edu/araproject/radio/#icetabsorption>
84. R.L. Hawley, E.M. Morris, J.R. McConnell, Rapid techniques for determining annual accumulation applied at Summit. Greenland. *J. Glaciol.* **54**, 839 (2008). <https://doi.org/10.3189/00221430878779951>
85. R. Alley, B. Koci, Ice-Core analysis at site A, Greenland: preliminary results. *Ann. Glaciol.* **10**, 1–4 (1988). <https://doi.org/10.3189/S026030550004067>
86. NuRadioMC, “Tutorial.” <https://github.com/nu-radio/NuRadioMC/wiki/Tutorial>
87. NuRadioMC, “Cluster documentation.” <https://github.com/nu-radio/NuRadioMC/wiki/Running-on-a-cluster>
88. IceCube collaboration, A measurement of the diffuse astrophysical muon neutrino flux using eight years of IceCube data. *PoS ICRC2017*, 1005 (2018). arXiv:1710.01191. <https://doi.org/10.22323/1.301.1005>
89. IceCube collaboration, Observation of astrophysical neutrinos in six years of IceCube data, *PoS ICRC2017*, 981 (2018). arXiv:1710.01191. <https://doi.org/10.22323/1.301.0981>
90. IceCube collaboration, Differential limit on the extremely-high-energy cosmic neutrino flux in the presence of astrophysical background from nine years of IceCube data. *Phys. Rev. D* **98**, 062003 (2018). arXiv:1807.01820. <https://doi.org/10.1103/PhysRevD.98.062003>
91. Pierre Auger collaboration, Improved limit to the diffuse flux of ultrahigh energy neutrinos from the Pierre Auger Observatory. *Phys. Rev. D* **91**, 092008 (2015). arXiv:1504.05397. <https://doi.org/10.1103/PhysRevD.91.092008>
92. ANITA collaboration, Constraints on the diffuse high-energy neutrino flux from the third flight of ANITA. *Phys. Rev. D* **98**, 022001 (2018). arXiv:1803.02719. <https://doi.org/10.1103/PhysRevD.98.022001>
93. J. Heinze, A. Fedynitch, D. Boncioli, W. Winter, A new view on Auger data and cosmogenic neutrinos in light of different nuclear disintegration and air-shower models. arXiv:1901.03338
94. A. van Vliet, R. Alves Batista, J.R. Hörandel, Determining the fraction of cosmic-ray protons at ultra-high energies with cosmogenic neutrinos. arXiv:1901.01899
95. GRAND collaboration, The Giant Radio Array for Neutrino Detection (GRAND): science and design. arXiv:1810.09994
96. ARA collaboration, Measurement of the real dielectric permittivity ϵ_r of glacial ice. *Astropart. Phys.* **108**, 63 (2019). <https://doi.org/10.1016/j.astropartphys.2019.01.004>
97. NuRadioMC, “Example: D’n’r analysis.” <https://github.com/nu-radio/NuRadioMC/wiki/Example:-D'n'R-analysis>
98. NuRadioMC, “Example: Multi station coincidences.” <https://github.com/nu-radio/NuRadioMC/wiki/Example:-Multi-station-coincidences>

99. A. Karle, A. Nelles, The Radio Neutrino Observatory, in *Proceedings of the XVIII International Workshop on Neutrino Telescopes*, Venice (2019)
100. S. Wissel, *A new concept for high-elevation radio detection of tau neutrinos*, in *Proceedings of the ARENA 2018* (Catania, Sicily, 2018)
101. “NuRadioMC.” <https://github.com/nu-radio/NuRadioMC>
102. R.P. Brent, *An algorithm with guaranteed convergence for finding a zero of a function*, in *Algorithms for Minimization without Derivatives* (Prentice-Hall, Englewood Cliffs, 1973)

A search for cosmogenic neutrinos with the ARIANNA test bed using 4.5 years of data

A. Anker^a S. W. Barwick^a H. Bernhoff^b D. Z. Besson^{c,d} N. Bingefors^e D. García-Fernández^{f,g} G. Gaswint^a C. Glaser^a A. Hallgren^e J. C. Hanson^h S. R. Kleinⁱ S. A. Kleinfelder^j R. Lahmann^{a,g} U. Latif^c J. Nam^k A. Novikov^{c,d} A. Nelles^{f,g} M. P. Paul^a C. Persichilli^{a,1} I. Plaisier^{f,g} T. Prakashⁱ S. R. Shively^a J. Tatar^{a,l} E. Unger^e S.-H. Wang^k C. Welling^{f,g}

^aDepartment of Physics and Astronomy, University of California, Irvine, CA 92697, USA

^bUppsala University Department of Engineering Sciences, Division of Electricity, Uppsala, SE-752 37 Sweden

^cDepartment of Physics and Astronomy, University of Kansas, Lawrence, KS 66045, USA

^dNational Research Nuclear University MEPhI (Moscow Engineering Physics Institute), Moscow 115409, Russia

^eUppsala University Department of Physics and Astronomy, Uppsala, SE-752 37, Sweden

^fDESY, 15738 Zeuthen, Germany

^gECAP, Friedrich-Alexander-Universität Erlangen-Nürnberg, 91058 Erlangen, Germany

^hWhittier College Department of Physics, Whittier, CA 90602, USA

ⁱLawrence Berkeley National Laboratory, Berkeley, CA 94720, USA

^jDepartment of Electrical Engineering and Computer Science, University of California, Irvine, CA 92697, USA

^kDepartment of Physics and Leung Center for Cosmology and Particle Astrophysics, National Taiwan University, Taipei 10617, Taiwan

^lResearch Cyberinfrastructure Center, University of California, Irvine, CA 92697 USA

¹Corresponding author

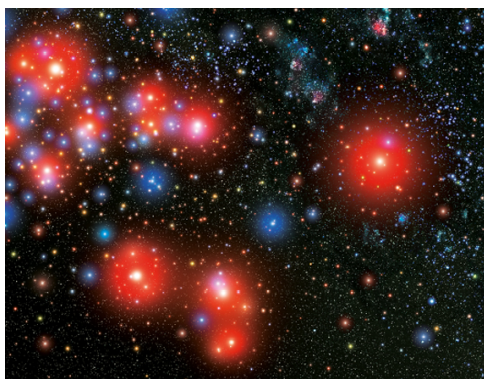
Observation of classically 'forbidden' electromagnetic wave propagation and implications for neutrino detection.

To cite this article: S.W. Barwick *et al* JCAP07(2018)055

Related content

- [The IceCube Neutrino Observatory: instrumentation and online systems](#)
M.G. Aartsen, M. Ackermann, J. Adams et al.
- [Feasibility of determining diffuse ultra-high energy cosmic neutrino flavor ratio through ARA neutrino observatory](#)
Shi-Hao Wang, Pisin Chen, Jiwoo Nam et al.
- [Status of RadioWave Neutrino Detection](#)
Dave Besson

View the [article online](#) for updates and enhancements.



IOP Astronomy ebooks

Part of your publishing universe and your first choice for astronomy, astrophysics, solar physics and planetary science ebooks.

iopscience.org/books/aas

Observation of classically ‘forbidden’ electromagnetic wave propagation and implications for neutrino detection.

S.W. Barwick,^a E.C. Berg,^a D.Z. Besson,^{b,c} G. Gaswint,^a C. Glaser,^a A. Hallgren,^d J.C. Hanson,^e S.R. Klein,^f S. Kleinfelder,^g L. Köpke,^h I. Kravchenko,ⁱ R. Lahmann,^j U. Latif,^b J. Nam,^k A. Nelles,^{l,m} C. Persichilli,^a P. Sandstrom,ⁿ J. Tatar^{a,o} and E. Unger^d

^aDept. of Physics & Astronomy, University of California,
4129 Frederick Reines Hall, Irvine, CA 92697, U.S.A.

^bDept. of Physics and Astronomy, Univ. of Kansas,
1082 Malott Hall, Lawrence, KS 66045, U.S.A.

^cNational Research Nuclear University, Moscow Engineering Physics Institute,
31 Kashirskoye Highway, Moscow 115409, Russia

^dUppsala University Department of Physics and Astronomy,
Regementsvägen 1, SE-752 37 Uppsala, Sweden

^eWhittier College Department of Physics,
13406 E. Philadelphia St., Whittier, CA 90602, U.S.A.

^fLawrence Berkeley National Laboratory,
1 Cyclotron Rd., Berkeley, CA 94720, U.S.A.

^gDept. of Electrical Engineering and Computer Science, University of California,
5200 Engineering Hall, Irvine, CA 92697, U.S.A.

^hInstitute of Physics, University of Mainz,
Staudinger Weg 7, D-55099 Mainz, Germany

ⁱDept. of Physics and Astronomy, Univ. of Nebraska-Lincoln,
Theodore Jorgensen Hall 208, Lincoln, NE 68588, U.S.A.

^jECAP, Friedrich-Alexander Universität Erlangen-Nürnberg,
Erwin-Rommel-Str. 1, 91058 Erlangen, Germany

^kLeung Center for Cosmology and Particle Astrophysics, National Taiwan University,
No. 1, Sec. 4, Roosevelt Road Taipei, 10617, Taiwan, R.O.C

^lInstitut für Physik, Humboldt-Universität zu Berlin,
Newtonstraße 15, 12489 Berlin, Germany

^mDESY,
Platanenallee 6, 15738 Zeuthen, Germany

ⁿDept. of Physics and Wisconsin IceCube Particle Astrophysics Center,
University of Wisconsin,
Thomas C Chamberlin Hall, Madison, WI 53706, U.S.A.

^oResearch Cyberinfrastructure Center, University of California,
100 Campus Dr., Irvine, CA 92697, U.S.A.

E-mail: sbarwick@uci.edu, gravity@ecberg.com, zedlam@ku.edu,
ggaswint@uci.edu, christian.glaser@uci.edu, allan.hallgren@physics.uu.se,
jhanson2@whittier.edu, srklein@lbl.gov, stuartk@uci.edu,
lutz.koepke@uni-mainz.de, ikrav@unl.edu,
robert.lahmann@physik.uni-erlangen.de, uzair.latif@ku.edu, namjiwoo@gmail.com,
anna.nelles@desy.de, cperish@uci.edu, sandstrom@icecube.wisc.edu,
jetatar@gmail.com, lisa.unger@physics.uu.se

Received April 30, 2018

Revised July 6, 2018

Accepted July 13, 2018

Published July 24, 2018

Abstract. Ongoing experimental efforts in Antarctica seek to detect ultra-high energy neutrinos by measurement of radio-frequency (RF) Askaryan radiation generated by the collision of a neutrino with an ice molecule. An array of RF antennas, deployed either in-ice or in-air, is used to infer the properties of the neutrino. To evaluate their experimental sensitivity, such experiments require a refractive index model for ray tracing radio-wave trajectories from a putative in-ice neutrino interaction point to the receiving antennas; this gives the degree of signal absorption or ray bending from source to receiver.

The gradient in the density profile over the upper 200 meters of Antarctic ice, coupled with Fermat’s least-time principle, implies ray “bending” and the existence of “forbidden” zones for predominantly horizontal signal propagation at shallow depths. After re-deriving the formulas describing such shadowing, we report on experimental results that, somewhat unexpectedly, demonstrate the existence of electromagnetic wave transport modes from nominally shadowed regions. The fact that this shadow-signal propagation is observed both at South Pole and the Ross Ice Shelf in Antarctica suggests that the effect may be a generic property of polar ice, with potentially important implications for experiments seeking to detect neutrinos.

Keywords: cosmic ray experiments, ultra high energy photons and neutrinos

ArXiv ePrint: [1804.10430](https://arxiv.org/abs/1804.10430)

Contents

1	Introduction	1
2	Formalism	3
2.1	Fermat’s principle and ray tracing	3
2.2	Horizontal and near-surface propagation	5
2.3	Density and propagation-time measurements in Antarctica	6
3	Observation of signal propagation from shadow zones	7
3.1	Measurements made by the RICE experiment at South Pole	7
3.1.1	Comparison with expectation	9
3.1.2	Estimate of attenuation length from shadowed transmissions	12
3.1.3	Cross-checks and possible systematic errors	13
3.2	Observation of horizontal propagation with the ARIANNA experiment at Moore’s Bay, Ross Ice-Shelf, Antarctica	13
3.2.1	Experimental technique	14
3.2.2	Measurements between boreholes	14
3.2.3	Measurements in ARIANNA stations	16
3.2.4	Measurement from single borehole to buried LPDA	18
4	Conclusions	19

1 Introduction

Owing to its remote location and isolation from anthropogenic sources, excellent transparency at wavelengths ranging from optical through radio, and also the presence of extensive scientific support at several locations, Antarctica now supports multiple astronomy and astrophysics-oriented projects. Within the last five years, the IceCube experiment, sensitive to optical and near-optical Cherenkov radiation resulting from neutrino interactions in-ice, has reported on the first observation of a diffuse flux of extraterrestrial neutrinos at energies greater than 10 TeV [1], with a ‘hard’ spectrum extending to 10^{15} eV. At higher energies, in-ice detection of longer-wavelength (radio) radiation is likely a more sensitive measurement strategy, owing to the Askaryan effect [2–4], combined with the measured kilometer-scale radio-wave attenuation length for cold polar ice [5, 6]. This has prompted several experimental initiatives based on experimental radio receiver arrays either elevated 35–40 km (ANITA [7]), near the Antarctic ice-air interface at Moore’s Bay, Antarctica (ARIANNA [8]), or at depths of up to 200 m at South Pole (pioneering RICE [9] and successor ARA [10]). In addition, exploratory work has been conducted within the last few years at Summit, Greenland to assess the radio-glaciological suitability of that site for a future neutrino-detection experiment [11]. Each of the possible neutrino-observation schemes (synoptic, surface detection of antennas, or antennas embedded in the ice sheet) has its own inherent advantages and trade-offs.

The variable specific gravity through the firn [12], over which the ice density varies between approximately 40–100% of the asymptotic value (917 kg/m^3), results in an electromagnetic wave-speed decreasing with depth. By Fermat’s principle, this results in not only curved ray trajectories, but also the expectation that, for the case where transmitter

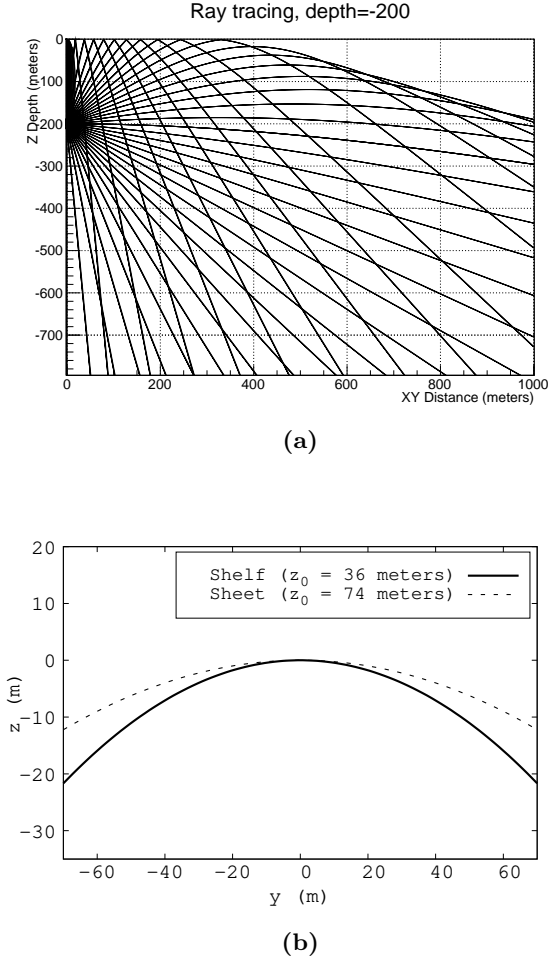


Figure 1. (a) Simulation of rays emitted from a transmitter at the South Pole at $z=-200$ m, showing curved paths. The shadow zone in the upper right is expected in the case of a smoothly-varying $n(z)$ profile in the absence of impurities. For the RICE measurements described later, the XY-distance was approximately 3000 meters, at typical depths of 100 meters (b) Examples of quadratic ray-paths in media with index of refraction profiles with the form of eq. (1.1). The dashed line corresponds to a particular solution of eq. (2.7) with $z_0 = 74$ m. The solid line corresponds to eq. (2.7) with $z_0 = 36$ m.

(Tx) and/or receiver (Rx) is deployed either on the surface or at near-surface depths, signals emanating from sufficiently large horizontal angles may be refracted downwards before they can be observed (“shadowing”). In the Huygens picture, these shadowed regions correspond to volumes for which the superposition of all contributing wavelets, properly weighted by distance, sum to zero net amplitude for all observation times t , as illustrated in figure 1.

We note that the standard Huygens picture is typically applicable in the case where phase information is preserved by each scatterer, assumed to be small compared to one wavelength (i.e., the Rayleigh limit), and results (assuming zero signal absorption in the medium) in the usual $1/r$ length scaling of the electric field \vec{E} . If the scatterer is not point-like (e.g., scattering size $\sim \lambda$) or, if, for any other reason, the phase shift across the scatterer is random, this leads to $|\vec{E}| \propto 1/r^2$.

For dielectric materials like snow and ice, the signal wave-speed is determined by the local index of refraction, which can be approximated as a linear equation of density:

$n(z) \approx 1 + b\rho(z)$, with $z=0$ at the surface and increasingly negative with depth. The specific dependence for ice is given by the Schytt equation: $n(x, y, z) = 1 + 0.78\rho(x, y, z)/\rho_0$, where $\rho(x, y, z)$ is the local ice density and ρ_0 is the density for solid ice (917 kg/m^3). Designating n_s as the index of refraction of snow (see section 2.3), n_{ice} that of solid ice, and $\Delta n = n_{\text{ice}} - n_s$, then it can be shown from classical gravity and density considerations that the index versus scale depth z/z_0 ($z_0 > 0$) dependence follows:

$$n(z) = n_{\text{ice}} - \Delta n e^{z/z_0}. \quad (1.1)$$

From the same classical treatment that produces eq. (1.1), it may be shown that $z_0^{-1} = (g\chi_0\rho_s)$, where g is the gravitational acceleration, and ρ_s and χ_0 are the density and volumetric compressibility of snow, respectively. The snow density and compressibility are inversely proportional, while measurements of natural snow compressibility vary in the literature and depend on the measurement technique [13]. Taking compressibility values from fit F of figure 3 of [14] at $\rho_s = 300 \text{ kg m}^{-3}$ yields a z_0 value of 25 m. Rather than measure χ and ρ independently, we fit z_0 as a free-parameter obtained from $\rho(z)$ data from various locations around Antarctica (see figure 2 and table 1). We find agreement with prior measurements [5, 15], and also find that z_0 varies by a factor of ≈ 2 between Moore's Bay and the South Pole. Snow formation conditions near the surface vary considerably across polar regions, so there is no reason to expect the compressibility of surface snow to be uniform across different glaciological regions.

Allowing χ to vary with z in the density versus depth model yields the following boundary-value relation for χ_s , the compressibility of surface snow, χ_{ice} the compressibility of deep ice, and χ_f , the compressibility of the firn:

$$(\Delta\rho)\chi_f = \rho_s\chi_s - \rho_{\text{ice}}\chi_{\text{ice}}. \quad (1.2)$$

In eq. (1.2), χ_f is a density-weighted difference between snow and ice compressibility, which serves as a useful average for the firn, as a whole. Although the depth-dependence of the compressibility of the firn $\chi(z)$ is outside the scope of this work, we note that if χ depends monotonically on depth, eq. (1.1) disallows horizontal ray tracing solutions. To explain horizontal ray tracing, a perturbation in the index profile can be added to eq. (2.2) (see section 2).

2 Formalism

In this section, ray tracing theory is reviewed. We begin with Fermat's principle and conclude with a discussion of conditions that lead to horizontal ray propagation, anticipating the experimental results described below.

2.1 Fermat's principle and ray tracing

Fermat's Principle states that optical lengths of light ray trajectories are minimized. Ray paths that satisfy Fermat's Principle depend on the index of refraction n . If n depends only on z , Fermat's Principle can be expressed in variational form as:

$$\delta \int_A^B n(z)(1 + \dot{y}^2)^{1/2} dz = \delta \int_A^B L(z, \dot{y}) dz = 0. \quad (2.1)$$

Derivatives indicated with a dot are with respect to z . Because $n(z)$ does not depend on x or y , the problem exhibits cylindrical symmetry. Without loss of generality we can choose

$x = \dot{x} = 0$. Note that $\dot{y} = dy/dz$ is unit-less, and \ddot{y} has units of inverse length. Minimizing the variation in the path, and substituting $u = \dot{y}$ gives

$$\dot{u} = -\left(\frac{\dot{n}}{n}\right)(u^3 + u). \quad (2.2)$$

Inserting eq. (1.1) for $n(z)$, the equation of motion is

$$\dot{u} = z_0^{-1} \left(\frac{\Delta n e^{z/z_0}}{n_{\text{ice}} - \Delta n e^{z/z_0}} \right) (u^3 + u). \quad (2.3)$$

As a check, note the deep ice limit: $|z| \gg z_0$, $z < 0$:

$$\dot{u} = 0. \quad (2.4)$$

The solution to this equation of motion is

$$z(y) = a + by. \quad (2.5)$$

Eq. (2.5) shows that rays propagate in straight lines far below the firn where n is constant, as expected.¹ Another straight-line solution to eq. (2.3) is the vertical ray ($u = 0$), which remains straight while progressing through all regions of $n(z)$.

For the case of a shallow ray ($z \rightarrow 0$) with $n \approx n_{\text{ice}} - \Delta n(1 + z/z_0)$ and $\dot{n} \approx -\Delta n/z_0$ initially propagating with a horizontal velocity component satisfying $u^3 \gg u$, the main equation of motion (eq. (2.3)) reduces to

$$\frac{du}{dz} = \frac{1}{z_0} \left(\frac{\Delta n}{n_{\text{ice}} - \Delta n(1 + z/z_0)} \right) u^3, \quad (2.6)$$

Keeping only first order terms in (z/z_0) , a particular solution is

$$z(y) = -\frac{1}{2z_0} \left(\frac{n_{\text{ice}} - n_s}{n_s} \right) (y - y_1)^2. \quad (2.7)$$

Equation (2.7) shows that the shortest travel time between two near-surface points is given by a quadratic path, if the initial velocity vector is mostly horizontal.

For example, take $z_0 = 36$ m and $n_s = 1.30$ to describe refraction at Moore's Bay, Antarctica (site of the ARIANNA experiment), and $z_0 = 74$ m, $n_s = 1.35$ to describe South Polar refraction (see table 1 for measured values). These two ray paths are compared in figure 1. The curvature of the quadratic in eq. (2.7) is controlled by z_0^{-1} .

The ray tracing framework yields near-surface ray paths that are downward bending quadratic curves, with *smaller* z_0 values corresponding to steeper bending. The data presented in section 3 include observations of rays that not only do not propagate with quadratic downward bending, but propagate horizontally in Moore's Bay where the value of z_0 is approximately a factor two smaller than that of the South Pole. If rays are not shadowed in Moore's Bay, it should be even less likely that they are shadowed in the firn of the South Pole, and data presented in section 3 also support this hypothesis.

¹Note that a horizontal solution to eq. (2.3) would imply $\dot{u} \rightarrow \infty$, requiring $\dot{n} \rightarrow 0$ in eq. (2.2). However, $\dot{n} = 0$ cannot occur without an under-density or over-density in the firn, since index and density are proportional.

2.2 Horizontal and near-surface propagation

Perturbations from the smooth profile can be introduced by variable yearly melting and sintering mechanisms, and bulk re-alignment of the crystal orientation fabric. Chapter 2 of [16] summarizes these mechanisms, and such observations of layers are common [17, 18]. We observe layering in Moore’s Bay and South Pole data as $\approx 5\%$ deviations from a smooth fit to the density profile (see figures 2 and 10). Over-densities (such as those observed near the South Polar surface) and under-densities can lead to local minima and maxima in the index of refraction profile.

Let one such local feature be described by a quadratic perturbation from an otherwise constant n_0 value, with a strength a at a depth z_d :

$$n(z) = n_0 + a(z - z_d)^2 \quad (2.8)$$

$$\dot{n} = 2a(z - z_d) \quad (2.9)$$

$$q = z - z_d, \quad (2.10)$$

Let $\omega^2 = 2 \left(\frac{a}{n_0} \right)$. Introducing $n(z)$ from eq. (2.8) into eq. (2.2), and neglecting terms higher than order q^2 , the variables-separable differential equation may be solved near $q = 0$:

$$q(y) = C_0 \sin(\pm C_1 \omega y - C_2) \quad (2.11)$$

The constants C_i are determined by the boundary conditions and the shape of the perturbation, and two of them are independent. The approximation is accurate as long as $\omega^4 q^4 \ll 1$. Solving the problem in the same limit with $a \rightarrow -a$ in eq. (2.8) amounts to replacing the sine function with a sinh function in eq. (2.11), making the path $q(y)$ unbounded.

A quadratic perturbation in q can only be added in a piecewise-continuous fashion to eq. (1.1), if the boundary conditions $n \rightarrow n_{\text{ice}}$ as $z \rightarrow -\infty$ and $n(0) = n_s$ are to be preserved. Admitting a Gaussian perturbation yields the physical behavior of the locally quadratic perturbation, while keeping $n(z)$ fully continuous and differentiable:

$$n(z) = n_0 + a \exp \left(-\frac{1}{2} \left(\frac{q}{\sigma} \right)^2 \right) \quad (2.12)$$

The prior definition of ω with the a -value from eq. (2.8) has units of inverse length. The a -value in eq. (2.12) is unit-less, but the perturbation width σ has units of length. Repeating the procedure leading to eq. (2.11), in the limit that $(\omega q / \sigma)^4 \ll 1$, the solution is

$$q(y) = C_0 \sin \left(\pm C_1 \frac{\omega y}{\sigma} - C_2 \right) \quad (2.13)$$

If horizontal ray-propagation were observed, there would be several potential conclusions. First, the $n(z)$ profile could be described by eq. (1.1) with local density perturbations. According to eq. (2.13), the rays would oscillate about the perturbation with a spatial frequency and amplitude determined by the shape of the perturbation. A second possibility is that the perturbations could have such large a -values and such small σ -values that rays are simply reflected by them. Groups of such internal layers could form reflective channels, trapping rays in horizontal states through total internal reflection. Although we do not discern from the data which mechanism is present in the ice sheets and ice shelves, we note that ice layers are common in the upper firn, and that over- and under-densities do appear in residual fits of eq. (1.1) to the $n(z)$ data (see figure 2).

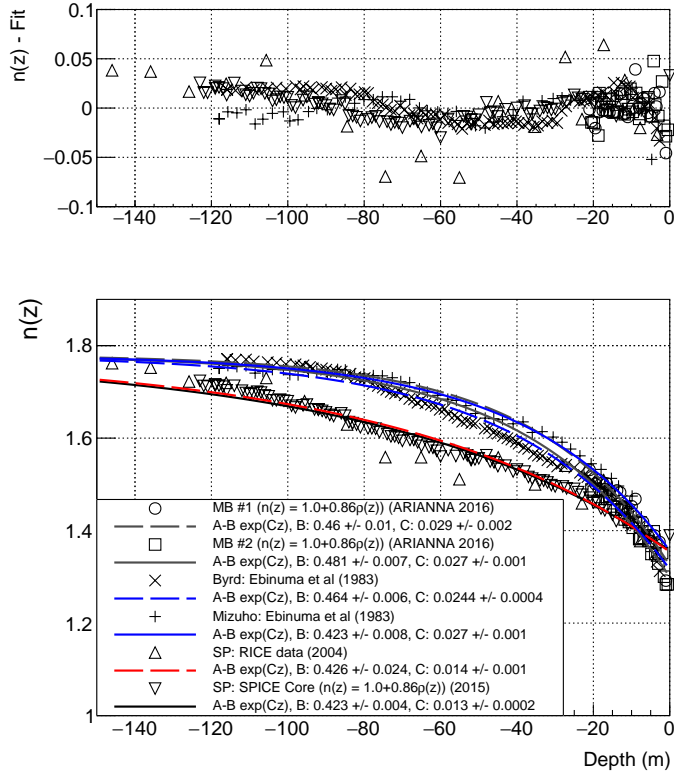


Figure 2. Compilation of density and index of refraction measurements. “MB” results (circles and squares) refer to density measurements made by the authors during the 2016-17 austral season at Moore’s Bay, Antarctica, and expressed here as index of refraction via the Schytt equation. The Byrd and Mizuho density data (x’s and crosses) are taken from [19] and translated to index of refraction in the same fashion. The RICE data (triangles) are direct measurements of index using RF signals from [20]. The SPICE-core data (upside-down triangles) come from the 2015 SPICE core density measurements from the South Pole, and are translated via the Schytt equation. The residual difference between the fit lines and the data are plotted in the upper panel.

2.3 Density and propagation-time measurements in Antarctica

Measurements of density and index of refraction have been compiled in figure 2 for a variety of Antarctic locations. Table 1 contains the coefficients $A = n_{\text{ice}}$, $B = \delta n$, and $C = z_0^{-1}$ determined from a fit of the form $n(z) = A - B \exp(Cz)$. Relative to a smooth functional dependence, variations in measured density are observed at the level of a few percent, larger than the intrinsic systematic errors (estimated at less than 1% relative), and decreasing with depth.

In Moore’s Bay, the parameter n_s (index of refraction of the snow near the surface), has been measured in two ways. First, surface snow density measurements were recorded and converted to index via the usual Schytt equation to determine $n_s = 1.3$ [21]. Second, the absolute timing of an RF pulse transmitted at 2–4 wavelengths below the surface through the snow along a 543 meter baseline corresponded to a measurement of $n_s = 1.29 \pm 0.02$ [15]. These results are in agreement with the fits to the density data versus depth shown in figure 2 and table 1, and in agreement with n_s values obtained from density measurements at the South Pole and two other locations.

ref./Location	$B = \Delta n$	$n_s = n_{\text{ice}} - B$	$C^{-1} = z_0$ (m)
MB#1/Moore’s Bay	0.46 ± 0.01	1.32 ± 0.01	34.5 ± 2
MB#2/Moore’s Bay	0.481 ± 0.007	1.299 ± 0.007	37 ± 1
Ebinuma (1983)/Byrd	0.464 ± 0.006	1.316 ± 0.006	41 ± 1
Ebinuma (1983)/Mizuho	0.423 ± 0.008	1.357 ± 0.008	37 ± 1
RICE (2004)/South Pole	0.43 ± 0.02	1.35 ± 0.02	71 ± 5
SPICE (2015)/South Pole	0.423 ± 0.004	1.357 ± 0.004	77 ± 2

Table 1. Fit parameters for the curves shown in figure 2. The function fit to the data is $n(z) = A - B \exp(Cz)$. The second-order differential equation derived in the first section requires $A = n_{\text{ice}} = 1.78$ and $B = \Delta n$ as the two boundary conditions.

The RICE data presented in figure 2 was collected with a 0.5-km distance between RF transmitter and receiver, and relied on relative timing between stationary RF receiver channels as a single transmitter is lowered into an ice borehole. A direct RF-based measurement of the South Pole $n(z)$ was conducted in December 2003 using two RF antennas co-lowered into boreholes separated by 30 m horizontally; those data are presented in figure 3. The absolute timing between RF transmitter and receiver provides a direct measurement of $n(z)$. By contrast, the “MB” data in figure 2 is density data that has been converted to $n(z)$ via the Schytt equation. The near-surface comparison of the 2003 RICE measurements with the density data is particularly interesting — here, the local-minimum in SPICE density measurements at $z=-12$ m suggestively correlates with a local minimum in RF propagation time at that same depth. This is consistent with the presence of ‘inversion’ layers which, as demonstrated in section 2 of this document, owing to the least-time principle, can result in signals arriving horizontally from nominally ‘shadowed’ regions.

3 Observation of signal propagation from shadow zones

Experimental measurements of the radio-frequency dielectric permittivity have been made over the last 15 years in Antarctica [6] and also more recently in Greenland [11]. In those previous measurements, radio wave signals propagate vertically from a surface or near-surface transmitter, and are observed in a surface or a near-surface receiver via their reflection either from an in-ice horizontal conducting layer, e.g., or the underlying bedrock. This approach has the advantage that the transmitter and receiver can be easily moved on the surface, and flexible triggers configured. However, since the solid angle for neutrino acceptance varies with polar angle θ as $\sin \theta$, the neutrino effective target volume becomes diminishingly small viewing vertically, and such measurements therefore have limited applicability to neutrino sensitivity estimates.

3.1 Measurements made by the RICE experiment at South Pole

Given its importance vis-a-vis neutrino sensitivity, verification of shadowing was given high priority in the early stages of the RICE experiment [9, 20]. During the period Dec. 2003–Jan. 2004, microsecond-duration “tone” signals were transmitted horizontally over a baseline of 3.3–3.5 km, at depths of 70, 120 and 125 meters from a borehole drilled originally for the National Oceanic and Atmospheric Administration (NOAA). The 20-channel RICE antenna

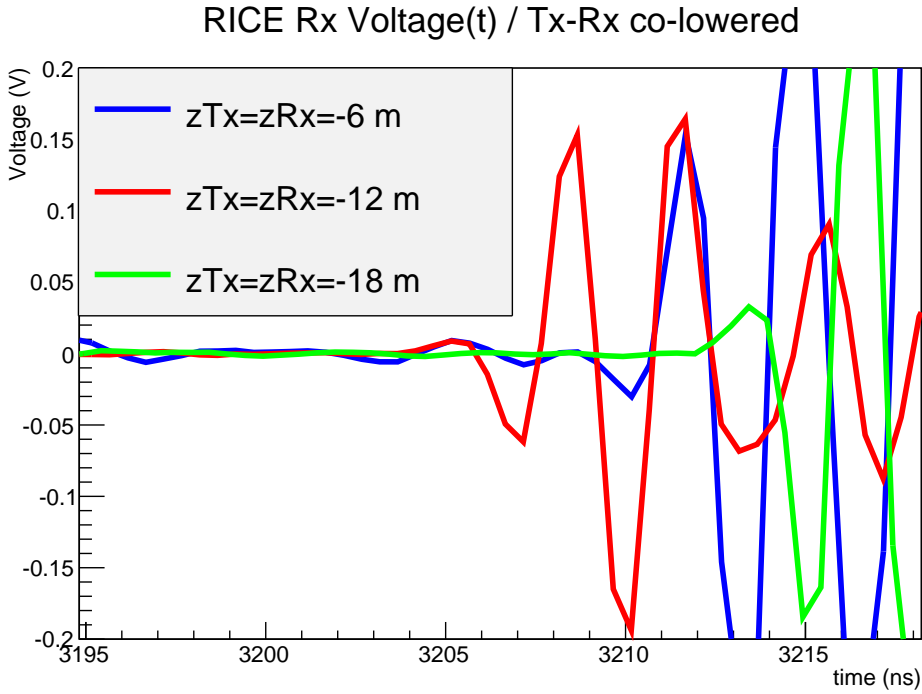


Figure 3. Received signals for cases where transmitter/receiver depths are 6 m (red), 12 m (blue) and 18 m (green), from dedicated, 2003 data taken with RICE experimental hardware, illustrating earlier arrival time for 12-meter depth compared to 6-meter depth, consistent with observed local fluctuation in SPICE density profile. Horizontal separation between transmitter and receiver is approximately 30 m for these data. Systematic error on relative signal arrival time is of order 0.1 ns.

array, based at South Pole and including 17 receiver antennas deployed at depths between 105 and 350 meters, was located in the nominal ‘shadow’ zone, as evident from figure 1 above.

For reference, and to simplify a calculation of attenuation length based on relative received signal strengths, data were also collected, using exactly the same transmitter set-up, from a closer location embedded within the RICE array itself, and unshadowed. With two such transmitter locations, L_{atten} can be numerically extracted using the ratio of signal amplitudes measured at the far transmitter location (A_{far}) relative to the ‘near’ transmitter location (A_{near}), and assuming that electric field strengths vary inversely with distance

$$A_{\text{far}}/A_{\text{near}} = (\cos \theta_{Tx \rightarrow Rx}^{\text{near}} / \cos \theta_{Tx \rightarrow Rx}^{\text{far}}) |r_{\text{near}}/r_{\text{far}}| \times e^{-(r_{\text{far}}-r_{\text{near}})/L_{\text{atten}}}, \quad (3.1)$$

with the values of r defined individually for each Tx/Rx pair; the $\cos \theta$ term accounts for the antenna dipole beam pattern of the dipoles.

Broadcast signals were produced as follows:

1. A signal generator (SG), producing continuous waves in the interval 211–500 MHz, is gated open once per second by a GPS pulse per second (pps) trigger, for a period of between one and 20 microseconds.
2. This signal generator output is then split into two copies: one copy is routed to an above-surface TV log-periodic-dipole-antenna (LPDA) (TV) pointed at a similar above-surface receiver LPDA antenna co-located with the RICE receiver array and fed (arbi-

trarily) into RICE channel 11. Receipt of that above-ice signal in channel 11 provides the event trigger for the RICE array, initiating readout of the remaining channels.

3. The second copy is passed through a 100W amplifier, and then routed into a 300-meter length of 7/8" Andrews coaxial cable, at the end of which is the buried RICE Dipole (*DI*) antenna transmitter, efficient over the interval 200-500 MHz, and used to broadcast under-ice signal to the RICE Dipole (*DI*) receiver array. An additional delay unit staggers the $SG \rightarrow TV$ vs. $SG \rightarrow DI$ signals to ensure that they are emitted roughly simultaneously.

In principle, multiple signal paths are possible from the two transmitters to the RICE receivers, which we designate as $TV \rightarrow TV$ (signals measured in the above-air receiver from the above-air TV transmitter, and providing the RICE event trigger), $TV \rightarrow DI$ (signals measured in the in-ice RICE Dipole receiver channels from the above-air TV transmitter), and $DI \rightarrow DI$ (signals measured in the in-ice RICE Dipole receiver channels from the in-ice Dipole transmitter). These multiple signal paths are indeed seen as signals in the RICE channels.

Although signals cannot be averaged during data-taking, to improve the signal-to-noise of the $DI \rightarrow DI$ signal, the in-ice receiver traces were phase-aligned, event-by-event, using the event-by-event relative phase shifts derived from the bright $TV \rightarrow TV$ signals, which are observed as nearly pure sinusoids. Figure 4 shows the signals observed in three RICE channels (channel 0: top row, receiver $z = -166$ m; channel 6: middle row, receiver $z = -170$ m; channel 15: bottom row, receiver $z = -367$ m), for data taken at the three transmitter depths (left column: $z = -70$ m, middle column: $z = -120$ m, and right column: $z = -125$ m), after phase alignment. Figure 5 shows the same traces after filtering around the carrier.

Clearly observed in these dipole receiver plots are two signals, offset in time by approximately 10 microseconds, which we interpret as the $TV \rightarrow DI$ and $DI \rightarrow DI$ signals, respectively.

3.1.1 Comparison with expectation

Since the entire RICE array is in the nominal shadow zone for this geometry, observation of the latter of these signals is immediately in conflict with naive expectations. For non-shadowed signal propagation, received signals should: i) be of time duration identical to the broadcast signal, and ii) for each RICE channel, exhibit a signal strength which is independent of the depth of the transmitter, since the difference in path-length between 70 meter transmitter depth (the experimental minimum) and 125 meter transmitter depth (the experimental maximum) is negligible, given the approximately 3 km horizontal propagation baseline. By contrast, the experimentally received signals show unexpectedly large variation in amplitude, compared to the simple $1/r$ expectation, for relatively small vertical displacements (120 m vs. 125 m, e.g.); a model that adequately describes these variations is currently under development. We note that the large variations observed in received signal strength, for 5-meter variations in transmitter depth, cannot be explained by channel-to-channel gain uncertainties, as those uncertainties are inherent, and identical for the transmitter at any depth.

To determine the possible ray trajectories consistent with the observed timing of these signals, we compare these data with simplified models of ray propagation. Owing to uncertainties in the surface elevation map, and thus the point-of-entry into the ice for the $TV \rightarrow DI$ path, our model for the $TV \rightarrow DI$ ray is ‘extreme’ (and unphysical) — namely, we calculate the expected timing for a ray traveling horizontally through air, then bending ninety degrees into the ice to the in-ice receiver. Nevertheless, this model differs from the expected signal

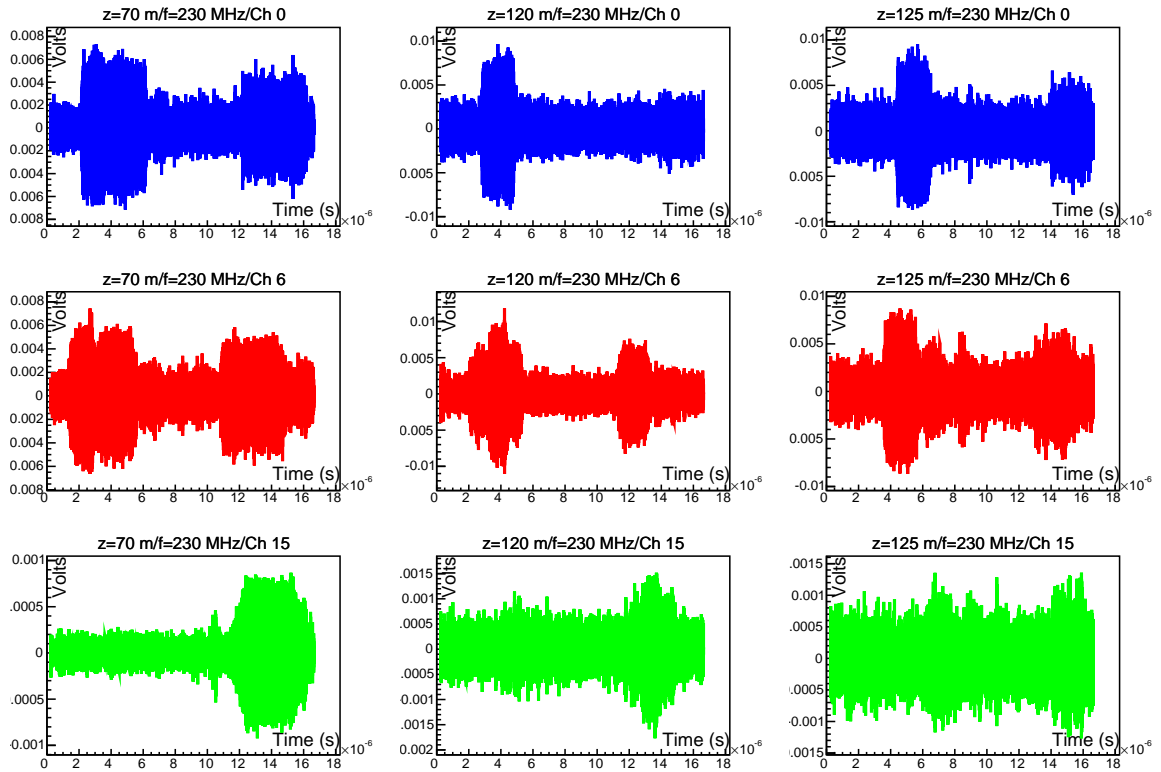


Figure 4. Phase-aligned sum of signals observed for three RICE channels, with transmitter at indicated depths -70 m , -120 m , or -125 m . Receiver depths are -166 m (Ch 0), -170 m (Ch 6) and -367 m (Ch 15), respectively.

trajectory by only $\mathcal{O}(100\text{ ns})$ in transit time, which is commensurate with the magnitude of our overall total timing uncertainties. For the $DI \rightarrow DI$ path, we use the ARA Collaboration experimental model [22] for the index-of-refraction profile, which we integrate, assuming straight-line ray propagation from source in-ice dipole transmitter to in-ice receiver, to determine the total transit time. These predictions are overlaid with data in figure 6. In general, our very crude model matches data to within $\sim 0.5\text{ }\mu\text{s}$, commensurate with the sum of uncertainties due to ray trajectory, cable delays, trigger time delays, etc. Expressed fractionally, that uncertainty is $\sim 5\%$ on the total travel time, or $\sim 0.02\text{--}0.03$ in the refractive index.

Figure 6 (right) overlays the signal arrival for the case where the transmitter is at a depth of -70 m vs. -120 m . We observe $\sim 0.8\text{ }\mu\text{s}$ time delay stagger in the latter relative to the former, compared with $\sim 0.75\text{ }\mu\text{s}$ assuming least-time propagation to the RICE channel 12 receiver ($z = -110\text{ m}$). This observed time delay difference is incompatible with through-air or surface signal propagation from the transmitter at the two depths ($z = -70\text{ m}$ and $z = -120\text{ m}$) to the receiver, which would imply a much shorter time stagger in their received signals of no more than $0.2\text{ }\mu\text{s}$. We also note an extended period of signal onset, indicating a wide range of contributing ray trajectories, consistent with the observation that many of the received $DI \rightarrow DI$ signals are apparently temporally broadened compared to the nominal tone signal duration.

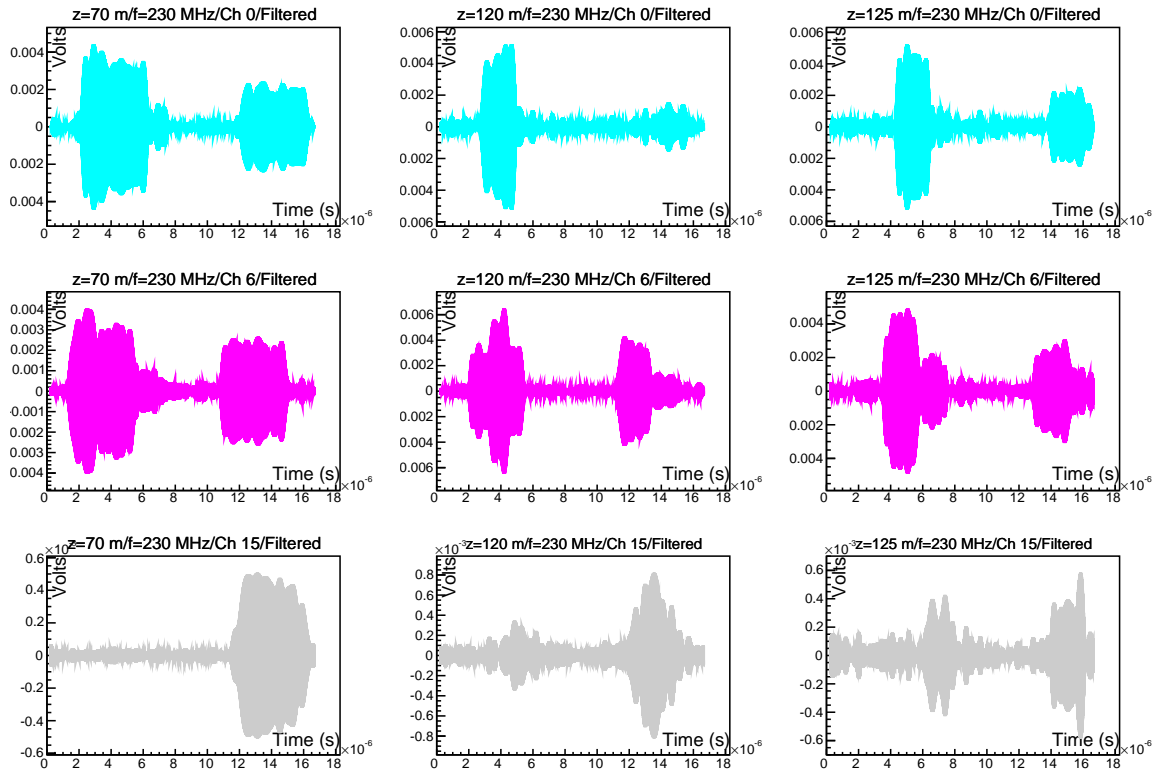


Figure 5. Same signals as in previous plot, after filtering ± 2 MHz around known broadcast frequency. Vertical axis: Volts; Horizontal axis: time (s).

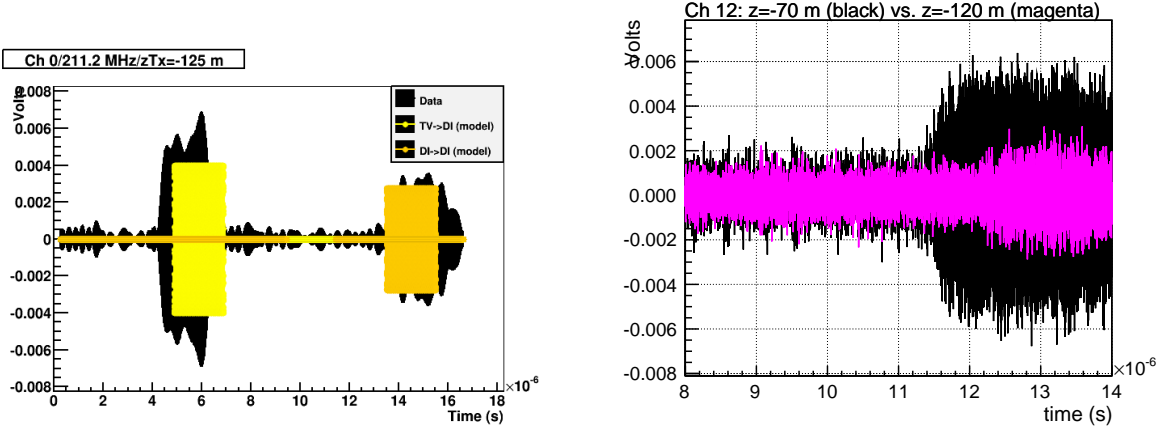


Figure 6. Left: overlay of raw data obtained in 2003 horizontal propagation experiments with model predictions for $TV \rightarrow DI$ (light yellow) and also $DI \rightarrow DI$ (dark yellow). Right: comparison of $DI \rightarrow DI$ signal arrival times in RICE channel 12 ($z = -110$ m) for transmitter in NOAA borehole, at depths $z = -70$ m (black) vs. $z = -120$ m (magenta; scaled), illustrating time delay of latter relative to former.

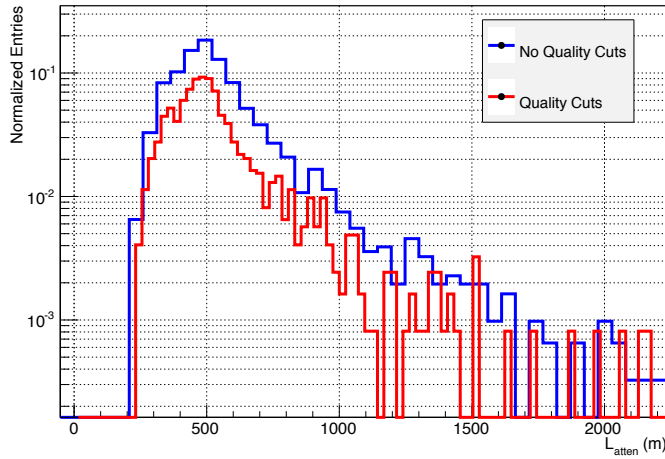


Figure 7. Distribution of field attenuation lengths calculated using RICE signal amplitudes measured from ‘far’ transmitter relative to ‘near’ transmitter. “Quality Cuts” refers to restricting data sample for which receiver Signal-to-Noise Ratio (SNR) exceeds 6:1 in amplitude.

3.1.2 Estimate of attenuation length from shadowed transmissions

Given multi-channel RICE receiver data, and using multiple data runs taken at both the near and far locations to sample a variety of depths and frequencies as well as a range of possible systematics, the attenuation length for horizontal propagation can be calculated by normalizing the signal strengths measured, channel-by-channel and run-by-run, for broadcasts over 3.3–3.5 km baselines, to signal strengths measured, channel-by-channel and run-by-run, to broadcasts when the transmitter is located within the RICE array itself (“near” transmission). Assuming the simplest $1/r$ electric field dependence, we apply corrections for the distance difference between the near and far locations, and also for the $\cos \theta$ dependence of the dipole beam pattern, as outlined previously. The ensemble of electric field attenuation lengths extracted in this manner is presented in figure 7. As a systematic check, we have sub-divided our samples by depth of the transmitter at the far location and also frequency of signal broadcast (table 2). Our observed scatter in calculated attenuation lengths is consistent with our estimated systematic errors. In principle, possible dispersive effects for shadow propagation can be probed by measuring the signal onset time, relative to the $TV \rightarrow TV$ trigger, over the frequency range probed in this experiment. In practice, uncertainties in such a measurement were comparable to the determination of the signal onset time, and must therefore await more precise future measurements.

The ice is expected to have complete horizontal translational symmetry, with vertical symmetry broken by the presence of conducting layers within the ice (primarily due to deposits following volcanic eruptions) and/or fluctuations in the vertical density profile. As noted earlier, such vertical asymmetries suggest models in which signal emitted isotropically might be ‘trapped’ in a horizontal channel, thus circumventing the otherwise-expected shadowing. We have therefore searched for a possible inverse dependence of the calculated attenuation length on the vertical separation between transmitter and receiver. Our data suggest a possible slight decrease in attenuation length with the magnitude of $z_{Tx} - z_{Rx}$, although insufficient to be conclusive.

Numerically, our extracted attenuation length for all possible near/far combinations (550 ± 10 m, where the error shown is the error on the mean) is consistent with the result

z_{Tx}	$\langle SNR \rangle$	L_{atten} (m)
70	13.9 ± 1.9	521 ± 12.2
120	11.4 ± 0.8	476 ± 8.5
125	13.4 ± 1.3	491.2 ± 9.8

frequency (MHz)	L_{atten} (m)
211.2	484.4 ± 4.5
230	495.7 ± 2.8
490	563.2 ± 27.3

Table 2. Observed signal-to-noise ratio and calculated average field attenuation length dependence on transmitter depth (top, and summing over all frequency data), and on frequency (bottom, and summing over all transmitter depth values); statistical errors only are shown. Estimated systematic errors are comparable in magnitude to the spread observed in the data points.

obtained when we restrict our calculation to those ‘high-quality’ combinations having high signal-to-noise only (542 ± 16 m).

We also note that similar broadcasts from the 8-km distant SPRESO hole (South Pole Remote Earth Science and Seismological Observatory), with transmitter at $z=-300$ m, yielded no observable signal in the RICE channels. This is consistent with the large number of implied e-foldings (~ 16) to the RICE receiver array by a 550 m attenuation length. Unshadowed propagation from that source point should have yielded SNR values approximately $2-3 \times$ larger than those observed from the NOAA source location.

3.1.3 Cross-checks and possible systematic errors

For the RICE measurements described herein, the uncertainty in the signal arrival times is estimated as approximately one time sampling bin (i.e., one nanosecond), which is insignificant compared to the ~ 10 microsecond total travel times. Uncertainties in the attenuation length measurement are reflected in the width of the distribution shown in figure 7, or approximately 25 meters. Additional cross-checks were made to ensure that signal was not otherwise being lost in the signal path from generator to in-ice dipole, including checks for: a) faulty cables, connectors, antennas, or amplifiers (checked by swapping in/out other cables, connectors, antennas, or amplifiers), b) non-linearity of the power amplifier to the in-field transmitter, which was checked by direct measurement, c) sensitivity to possible coupling of the in-ice dipole antennas to the sides of the borehole, which was checked by taking multiple measurements after successively entirely raising and lowering the transmitter dipole, and d) saturation of the near-hole receiver amplifiers, which was also checked by verifying the linearity of the received near-hole signals with transmitter gain.

3.2 Observation of horizontal propagation with the ARIANNA experiment at Moore’s Bay, Ross Ice-Shelf, Antarctica

After earlier prototypes, deployment of the pilot-stage ARIANNA Hexagonal Array (HRA) began in 2014 and has since demonstrated successful operation under harsh Antarctic conditions [23]. ARIANNA employs high-gain log-periodic dipole antennas (*LPDAs*) with excellent broad-band response between 100 MHz and 900 MHz, primarily sensitive to signals polar-

ized parallel to the antenna tines. ARIANNA comprises multiple *stations*, each acting as an independent autonomous neutrino and cosmic ray detector and including four (or more) LP-DAs deployed just below the snow surface, admitting easy access and repair when necessary. The sensitivity to radio signals from neutrino interactions is enhanced by the high dielectric contrast at the ice-water interface at the bottom of the Ross Ice-Shelf, resulting in efficient reflection of down-going emission back towards the antennas [15, 24].

The first installed HRA stations have been used to derive limits on the neutrino flux [8] and to measure the radio emission of air showers, which are an important background for arrays with antennas close to the surface, while simultaneously providing equally important proof-of-concept and calibration [25]. ARIANNA measurement of air showers has demonstrated that the hardware response of the experiment, including antennas and amplifiers, is well-understood, as the predicted signal shape is well-matched by the detected signal shapes [25]. ARIANNA is, thus far, the only ground-based experiment to successfully self-trigger on radio emissions from air showers, with a high purity and efficiency independent of particle detectors.

The deployment of the HRA was accompanied by several ice properties measurements in subsequent years [15]. For many tests, such as studies of signals reflected off the ice-water interface on the bottom of the ice-shelf, early signals were measured in stations for which in-ice propagation was believed to be forbidden by the shadowing effect. These were initially not emphasized because they were considered as either potential in-air propagation or artifacts of the measurement set-up [26]. Additional analysis ruled out those possibilities, indicating that such signals were likely due to horizontal propagation, putative shadowing notwithstanding, prompting recent direct measurements of this phenomenon.

3.2.1 Experimental technique

During the 2016-17 polar season, two dedicated boreholes, separated by about 100 meters, were drilled to a depth of 20 meters in the ice, to permit the detailed study of horizontally propagating signals. (In practice, snow infall in the hole resulted in data taken at $z = -19$ m, rather than $z = -20$ m.) While transmitting and receiving between the two boreholes, multiple ARIANNA stations, schematically outlined in figure 8, were also regularly recording data, allowing for redundant cross-checks of propagation over multiple baselines. Signals were broadcast from the same RICE fat-dipoles used in the 2003 RICE study described previously.

3.2.2 Measurements between boreholes

High-amplitude (few kV), short-duration signals (< 20 ns) were generated using a Pockels Cell Driver (*PCD*), which was routed directly to the transmitting antenna located in one borehole. Absolute timing was achieved by using a BNC Model 555 pulser to simultaneously trigger the PCD and send a triggering pulse to an oscilloscope for monitoring the signals received in the other borehole.

For reference, the entire set-up was lifted into the air, both on the ice-shelf and also pre-deployment in a park in California (i.e. dry ground, very little conductivity, flat area, little high vegetation); recorded signals were observed to be of similar strength at both locales.

For all tested in-ice configurations of different depths, strong pulses are observed. This is despite the fact that simple ray tracing would only allow for signals in certain combinations as shown on the left in figure 9. The figure also shows sample pulses recorded in different configurations of Tx/Rx. The signal shapes are observed to be very similar, despite the fact that, absent shadowed propagation, only the in-air configurations and the Tx/Rx depth of

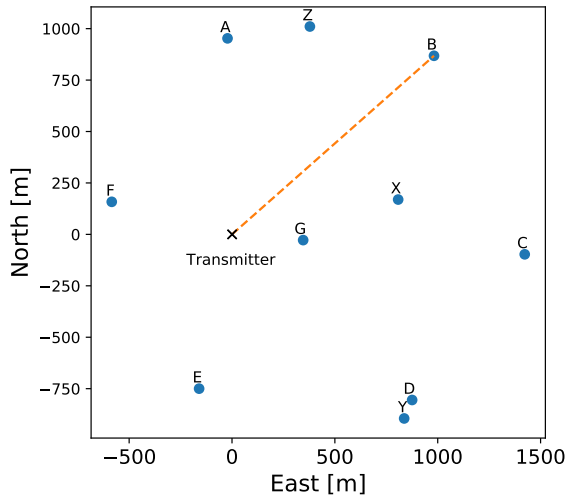


Figure 8. ARIANNA HRA array in the Antarctic season 2016/17. The transmitter for these studies was positioned at the origin in these coordinates. An example path of propagation to the station at position B is indicated by the dashed line.

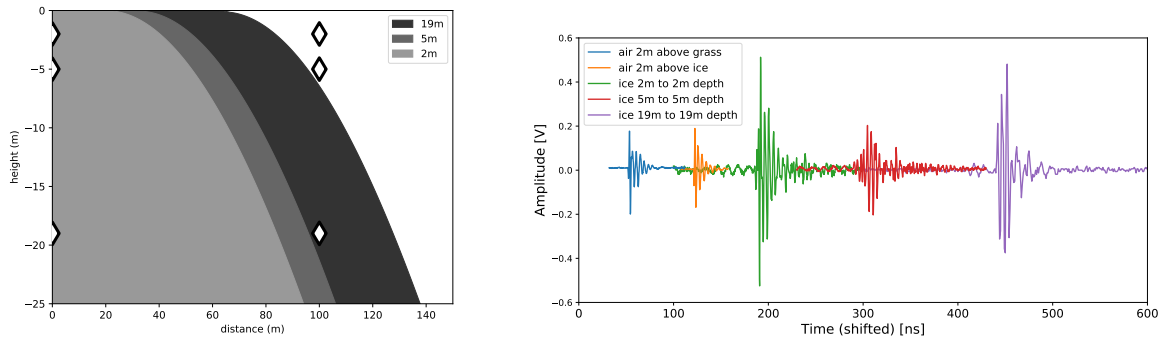


Figure 9. Left: illustration of shadowing at the ARIANNA site. Shaded regions indicate the horizon visible to a receiver (right) at the indicated depths of each transmitter (left). Diamonds show the location of the different transmitters and receiver positions in the first and second bore-hole, respectively. Right: pulses as recorded when transmitting from a RICE dipole to a receiving RICE dipole at varying transmitter/receiver depths at Moore's Bay. For reference measurements in air (in Moore's Bay and in California) are also depicted. Pulses have been arbitrarily shifted horizontally to better illustrate signal shapes.

19 meters should be visible. Interestingly, the amplitudes vary quite significantly, despite no changes in the set-up. This can at this point only tentatively be attributed to multi-path effects which lead to constructive and destructive interference.

We note that a) signal timing is consistent with horizontal propagation (as we quantify below), and b) no special transition was experimentally observed when the transmitter was moved across the shadow/non-shadow zone boundary.

In order to confirm that the observed pulses propagate through ice vs. air, the average index of refraction was measured for every combination of dipole depths from the signal arrival times, and then compared to the index-of-refraction calculated from ice density measurements obtained during hole-drilling. As figure 10 shows, the timing is fully compatible

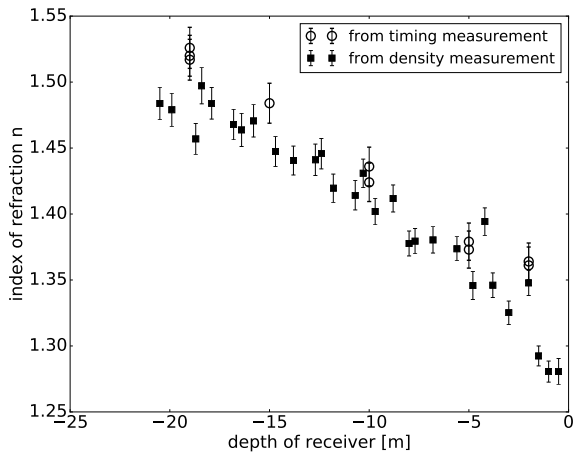


Figure 10. Measured index of refraction as function of depth. Filled squares indicate the index of refraction as calculated from ice density measurements of the bore holes. The open circles show the index of refraction calculated from absolute timing of the propagation of the pulses, using the leading edge of each pulse to obtain signal arrival times.

with propagation through the ice, and incompatible with through-air propagation ($n \approx 1.0$), for a variety of depths. It is also incompatible with the ice-water boundary bounce hypothesis, as the measured timing cannot be reconciled with two-way propagation through the ice-shelf (~ 1000 m) and an index of refraction $n > 1.0$.

It should be noted that there seems to be a systematic offset between the index of refraction derived from the timing measurements and the ice density measurements (perhaps resulting from multi-path effects). As the index of refraction obtained from the air \rightarrow air measurement ($n=1.016$) is approximately 1.6% higher than expectation, this offset may also be a systematic effect. To exclude the possibility that signals were the result of accidental emission of the PCD itself, it was also verified that no signals were observed when the transmitting antenna in the ice was disconnected from the PCD.

The pulses received in the shadow zone (Tx 19 to Rx 2) have an average signal-to-noise ratio (SNR) of 25. Albeit being longer than the pulses received in the allowed zone (SNR = 193) the signals are still well-above the noise floor and contain significant power.

3.2.3 Measurements in ARIANNA stations

While pulsing in the boreholes, signals were captured in all normally operational ARIANNA stations with their nominal trigger settings. Figure 11 shows signals as recorded in a station at a distance of 953 meters from the transmitter, for which shadowing would otherwise prohibit signal observation. Since there is no absolute timing information between the transmitter and the ARIANNA station, to demonstrate that observed radio signals are propagating horizontally and are not the result of reflections from the underlying Ross Sea-Ross Ice Shelf boundary, one can consider arrival times within a station. Every HRA station is equipped with two co-polarized pairs of 6-meter separated LPDAs, with different pairs oriented perpendicularly, allowing direct polar angle-of-incidence inference based on a single antenna pair.

Figure 12 shows the contrast between expected and measured arrival directions when using the *bounce* hypothesis vs. the horizontal propagation hypothesis. For both hypotheses the time difference between pulses in antenna pairs are calculated (y-axis) and compared to

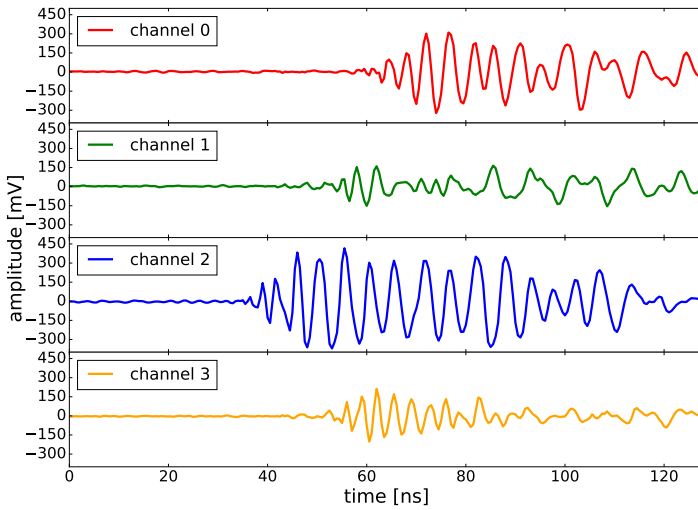


Figure 11. Horizontally propagating signals recorded in ARIANNA station *A*, at a horizontal distance of 953 meters from the transmitter. All pulses show a sharp leading edge with signal persisting for tens of nanoseconds, possibly extending beyond the length of the ARIANNA waveform record. The antennas of channels 0 and 2 are aligned roughly perpendicular to the arrival direction from the transmitter, while channels 1 and 3 are almost parallel. Channel 2 is closest to the transmitter and channel 0 furthest away, with a difference in distance of about 6 meters.

the measured time difference (x-axis). A good agreement is reached, when the points follow the dashed line through the origin and prediction matches measurement.

While there is significant scatter (partly due to the rather simple method chosen to identify the timing of the signal, as well as the short waveform length), the observed signals clearly favor horizontal propagation. We also observe no strong polarization dependence in those received signals.

The time structure of the pulses suggests some dispersion, as the received signal is elongated in time as compared to the emitted signal (figure 11). Some dispersion is expected from the antenna and amplifier response of the ARIANNA stations [27]. Amplifiers with a small group-delay are difficult to accommodate in low-power, broadband systems and the LPDAs are also slightly dispersive due to their broadband nature. However, even assuming the least sensitive direction for the LPDAs (a fully vertically polarized signal arriving in the null of the antenna i.e. parallel to the tines) cannot account for the dispersion of the signal observed.

Dispersive effects have the negative consequence of stretching the signal in the time domain and thereby reducing the instantaneous amplitude, but also offer the possibility that the relative arrival time of different frequency components can provide information on the distance-to-vertex for future in-ice neutrino searches, which is essential for a neutrino energy estimate.

The electric field attenuation lengths extracted from the data collected with all ARIANNA stations and the neighboring borehole are compiled in figure 13. Two calculations have been made to cross-check whether there is a significant difference when accounting for possible dispersive effects. Neglecting differences in the systematic uncertainties between the data obtained with an oscilloscope and ARIANNA station data, the best fit results in an attenuation length of 447 ± 146 meters for the time-integrated absolute amplitude and

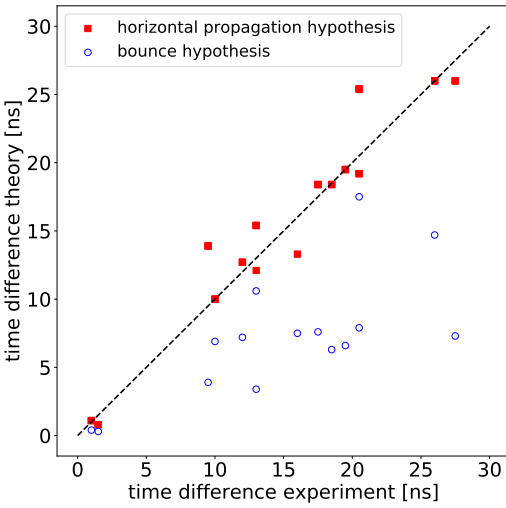


Figure 12. Measured (x-axis) vs. expected (y-axis) signal arrival times in ARIANNA stations for two different propagation hypotheses. The filled squares correspond to the *bounce*-hypothesis, while the open circles represent the hypothesis of horizontal propagation. The proximity to the dashed line through the origin with slope one illustrates that the arrival times match horizontal propagation through the ice better than a reflection from the underlying Ross Sea.

651 ± 270 meters based on the peak observed pulse amplitude only. These values are commensurate with those obtained at South Pole for horizontal propagation. These results imply that $1/r$ geometric signal reduction dominates over attenuation for horizontal propagation, which is an intriguing perspective for the effective volume for an ARIANNA-like detector with a station spacing of about one kilometer.

3.2.4 Measurement from single borehole to buried LPDA

The same set-up with the PCD was also used to recorded pulses between the transmitter in a borehole and an LPDA buried at a depth of one meter in December of 2017. The LPDA was placed at a distance of 500 meters, which corresponds to the longest signal cable available. The tines of the LPDA were rotated perpendicular to the line connecting its position and the borehole for maximum gain. Using a cabled set-up and the long record of an oscilloscope allows for absolute timing.

Three pulses were observed as shown in figure 14. Solely from timing, the three pulses can be attributed to different paths between transmitter and receiver. The first small pulse has to travel (mainly) through the air, as its arrival time corresponds to a propagation with the speed of light in air ($n = 1.0$). The signal is no longer present when the Tx antenna is disconnected from the PCD, so the signal is emitted by the antenna and has to propagate up and out of the firn first and then along the surface. The second pulse is compatible with the horizontal propagation through the firn, as its start-time corresponds to a propagation through a medium having $n = 1.36$. At a distance of 500 meters this horizontal propagation is not an allowed solution of classical ray tracing. The third pulse is found at the time required to travel twice through the ice-shelf and is therefore the reflection of the original signal off the bottom of the ice-shelf.

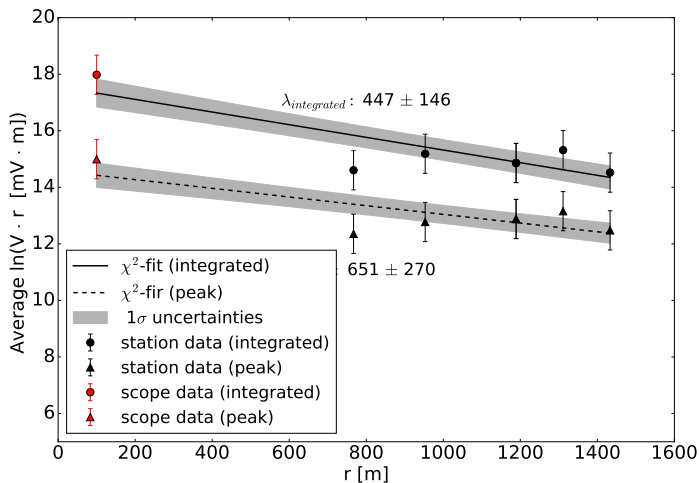


Figure 13. Field attenuation derived from all measured signals. Two calculations are made, one using the peak amplitudes of the signals and one using integrated absolute amplitudes (150–250 MHz), to account for possible dispersion. The reconstructed attenuation lengths from the pulse amplitude is 651 ± 270 meters; for the integrated amplitude, the corresponding value is 447 ± 146 meters. Note that exclusion of the left-most data point, which has been measured with an oscilloscope and not a station and therefore might be subject to different uncertainties, results in an even longer estimated attenuation length.

The figure depicts the raw data waveforms recorded in the field, with no applied gain correction. As an LPDA is rather insensitive to signals arriving perpendicular to the plane formed by the dipole elements (at least 3 dB compared to its front-lobe), the signals arriving horizontally are suppressed in this measurement, and may well contain more power than the reflected signal. An exact quantification requires knowledge of the precise arrival direction and the polarization of the incoming signal, which is impossible with the single LPDA which has been used to conduct these measurements. The reported signal strength is therefore a lower limit on the true power in the horizontally propagating signal.

Additional data, taken during the 2017-18 Antarctic field season, is currently being analyzed and should improve the understanding of signal propagation at Moore’s Bay. Additional studies, focusing of signal polarization, are foreseen for the 2018-19 season.

4 Conclusions

We have presented evidence for electromagnetic signals propagating from nominally shadowed source locations. Although forbidden in the ray optics picture for the case of a smooth and monotonic variation of wave-speed with depth, reflective layers or local deviations from the smooth $n(z)$ profile can result in local signal channeling.

The measured attenuation length of ~ 500 m, from both the South Polar and the Ross Ice Shelf locales, is slightly larger than the average unshadowed attenuation length measured at Moore’s Bay [15], and approximately one-third that observed for unshadowed radio signal propagation at South Pole [28] in the upper 1.5 km of ice. This value is also compatible with what might be expected in a model where microscopic scattering occurs entirely incoherently, and phase information is lost in the scattering process.

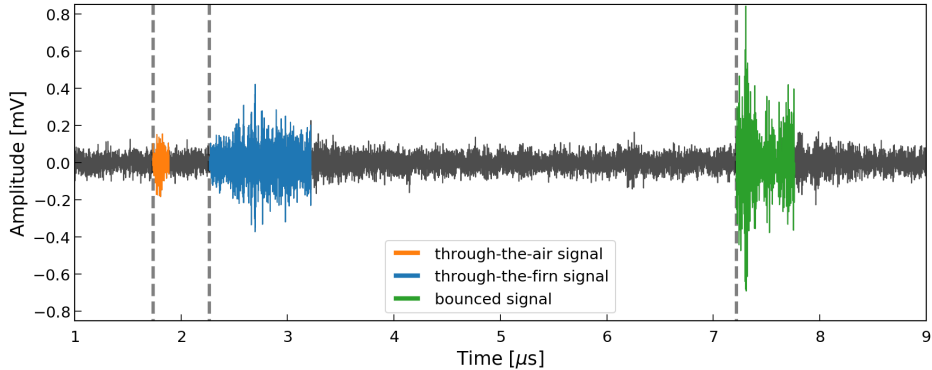


Figure 14. Pulses recorded with an LPDA buried at one meter depth, transmitted from a dipole at 19 meters depth at 500 meters distance. The dashed lines correspond to the calculated travel times in air ($n = 1.0$, + propagation up through firn), firn ($n=1.36$) and the ray tracing solution for a pulse reflecting from the bottom of the ice-shelf, assuming a thickness of 578 meters.

The attenuation length for horizontal propagation presented herein is comparable to the maximum detectable range for ~ 10 PeV neutrinos using the radio technique. Contrary to previous expectation, experimental observation of such neutrinos is therefore not limited by shadowing. This neutrino energy regime is particularly interesting experimentally, as it represents the maximum upper energy reach of the IceCube experiment and the detected astrophysical neutrino flux. A radio detector with such an energy threshold may measure the continuation of the IceCube flux, which is likely orders of magnitude larger than the flux caused by the interaction of cosmic rays with the cosmic microwave background at 100 PeV. As the horizontally propagating signals are well above the noise floor, this result therefore suggests that a future neutrino detector constructed at relatively shallow depths (< 30 meters) might optimize the balance between science return and the logistical overhead associated with hole drilling.

During the 2017-18 austral season, a transmitter based on the HiCal [29] piezo-electric model was lowered into the SPICE core hole [30] and broadcast to both the ARA array (deep) as well as a single ARIANNA station at the surface, allowing a more systematic map of signal transmission over a range of depths. Data analysis is currently in progress. A second generation of those studies will be conducted in 2018-19.

Acknowledgments

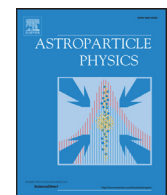
We are grateful to the U.S. National Science Foundation-Office of Polar Programs, the U.S. National Science Foundation-Physics Division and the U.S. Department of Energy. We thank generous support from the German Research Foundation (DFG), grant NE 2031/1-1, NE 2031/2-1 and GL 914/1-1, the Taiwan Ministry of Science and Technology, the “Wallenbergs-tiftelsen” (Wallenberg Foundation) and the “Liljewalch stipendier” (Liljewalch scholarships).

References

- [1] ICECUBE collaboration, M.G. Aartsen et al., *Observation and characterization of a cosmic muon neutrino flux from the northern hemisphere using six years of IceCube data*, *Astrophys. J.* **833** (2016) 3 [[arXiv:1607.08006](https://arxiv.org/abs/1607.08006)] [[INSPIRE](#)].
- [2] G.A. Askaryan, *Excess negative charge of an electron-photon shower and its coherent radio emission*, *Sov. Phys. JETP* **14** (1962) 441 [*Zh. Eksp. Teor. Fiz.* **41** (1961) 616] [[INSPIRE](#)].

- [3] G.A. Askaryan, *Excess negative charge of electron-photon shower and the coherent radiation originating from it. Radiorecording of showers under the ground and on the moon*, *J. Phys. Soc. Jpn.* **17** (1962) 257.
- [4] G.A. Askaryan, *Coherent radio emission from cosmic showers in air and in dense media*, *Sov. Phys. JETP* **21** (1965) 658.
- [5] T. Barrella, S.W. Barwick and D. Saltzberg, *Ross Ice Shelf (Antarctica) in situ radio-frequency attenuation*, *J. Glaciol.* **57** (2011) 61.
- [6] S.W. Barwick, D. Besson, P. Gorham and D. Saltzberg, *South polar in situ radio-frequency ice attenuation*, *J. Glaciol.* **51** (2005) 231.
- [7] ANITA collaboration, P.W. Gorham et al., *The Antarctic Impulsive Transient Antenna ultra-high energy neutrino detector design, performance and sensitivity for 2006–2007 balloon flight*, *Astropart. Phys.* **32** (2009) 10 [[arXiv:0812.1920](#)] [[INSPIRE](#)].
- [8] ARIANNA collaboration, S.W. Barwick et al., *A first search for cosmogenic neutrinos with the ARIANNA hexagonal radio array*, *Astropart. Phys.* **70** (2015) 12 [[arXiv:1410.7352](#)] [[INSPIRE](#)].
- [9] RICE collaboration, I. Kravchenko et al., *Performance and simulation of the RICE detector*, *Astropart. Phys.* **19** (2003) 15 [[astro-ph/0112372](#)] [[INSPIRE](#)].
- [10] ARA collaboration, P. Allison et al., *Performance of two Askaryan Radio Array stations and first results in the search for ultrahigh energy neutrinos*, *Phys. Rev. D* **93** (2016) 082003 [[arXiv:1507.08991](#)] [[INSPIRE](#)].
- [11] J. Avva, J.M. Kovac, C. Miki, D. Saltzberg and A.G. Vieregg, *An in situ measurement of the radio-frequency attenuation in ice at Summit Station, Greenland*, *J. Glaciol.* **61** (2015) 1005.
- [12] D. Pearce and J. Walker, *An empirical determination of the relative dielectric constant of the Greenland Ice Cap*, *J. Geophys. Res.* **72** (1967) 5743.
- [13] Cold Regions Research and Engineering Laboratory (U.S.), M. Mellor, *A review of basic snow mechanics*, U.S. Army Cold Regions Research and Engineering Laboratory, U.S.A., (1974).
- [14] B. Gerling, H. Löwe and A. van Herwijnen, *Measuring the elastic modulus of snow*, *Geophys. Res. Lett.* **44** (2017) 11,088.
- [15] J.C. Hanson et al., *Radar absorption, basal reflection, thickness and polarization measurements from the Ross Ice Shelf*, *J. Glaciol.* **61** (2015) 438.
- [16] V.V. Bogorodsky, C.R. Bentley and P.E. Gudmansen, *Radioglaciology*, Reidel, Dordrecht, Netherlands, (1985).
- [17] S. Gerland, H. Oerter, J. Kipfstuhl, F. Wilhelms, H. Miller and W.D. Miners, *Density log of a 181 m long ice core from Berkner Island, Antarctica*, *Ann. Glaciol.* **29** (1999) 215.
- [18] J.A. Dowdeswell and S. Evans, *Investigations of the form and flow of ice sheets and glaciers using radio-echo sounding*, *Rept. Prog. Phys.* **67** (2004) 1821.
- [19] N. Maeno and T. Ebinuma, *Pressure sintering of ice and its implication to the densification of snow at polar glaciers and ice sheets*, *J. Phys. Chem.* **87** (1983) 4103.
- [20] I. Kravchenko, D. Besson and J. Meyers, *In situ index-of-refraction measurements of the south polar firn with the RICE detector*, *J. Glaciol.* **50** (2004) 522.
- [21] L. Gerhardt et al., *A prototype station for ARIANNA: a detector for cosmic neutrinos*, *Nucl. Instrum. Meth. A* **624** (2010) 85 [[arXiv:1005.5193](#)] [[INSPIRE](#)].
- [22] U. Abdul et al., *Measurement of the real dielectric permittivity ϵ_r of glacial ice*, [arXiv:1712.03301](#) [[INSPIRE](#)].
- [23] S.W. Barwick et al., *Design and performance of the ARIANNA HRA-3 neutrino detector systems*, *IEEE Trans. Nucl. Sci.* **62** (2015) 2202 [[arXiv:1410.7369](#)] [[INSPIRE](#)].

- [24] C.S. Neal, *The dynamics of the Ross Ice Shelf revealed by radio echo-sounding*, *J. Glaciol.* **24** (1979) 295.
- [25] S.W. Barwick et al., *Radio detection of air showers with the ARIANNA experiment on the Ross Ice Shelf*, *Astropart. Phys.* **90** (2017) 50 [[arXiv:1612.04473](#)] [[INSPIRE](#)].
- [26] J. Hanson, *The performance and initial results of the ARIANNA prototype*, Ph.D. thesis, University of California, Irvine, CA, U.S.A., July 2013.
- [27] S.W. Barwick et al., *Time domain response of the ARIANNA detector*, *Astropart. Phys.* **62** (2015) 139 [[arXiv:1406.0820](#)] [[INSPIRE](#)].
- [28] P. Allison et al., *Design and initial performance of the Askaryan Radio Array prototype EeV neutrino detector at the South Pole*, *Astropart. Phys.* **35** (2012) 457 [[arXiv:1105.2854](#)] [[INSPIRE](#)].
- [29] P.W. Gorham et al., *The HiCal 2 instrument: calibration and Antarctic surface reflectivity measurement for the ANITA experiment*, [arXiv:1710.11175](#) [[INSPIRE](#)].
- [30] K.A. Casey et al., *The 1500 m South Pole ice core: recovering a 40 ka environmental record*, *Ann. Glaciol.* **55** (2014) 137.



Complex analysis of Askaryan radiation: A fully analytic treatment including the LPM effect and Cascade Form Factor[☆]



Jordan C. Hanson*, Amy L. Connolly

Center for Cosmological and AstroParticle Physics, Department of Physics, The Ohio State University, Columbus, OH 43210, United States

ARTICLE INFO

Article history:

Received 16 May 2016

Revised 8 March 2017

Accepted 28 March 2017

Available online 30 March 2017

Keywords:

Cosmogenic neutrinos

GZK effect

Askaryan effect

ABSTRACT

The Askaryan effect describes coherent electromagnetic radiation from high-energy cascades in dense media with a collective charge. We present an analytic model of Askaryan radiation that accounts simultaneously for the three-dimensional form factor of the cascade, and quantum mechanical cascade elongation via the Landau-Pomeranchuk-Migdal effect. These calculations, and the associated open-source code, allow the user to avoid computationally intensive Monte Carlo cascade simulations. Searches for cosmogenic neutrinos in Askaryan-based detectors benefit from computational speed, because scans of Askaryan parameter-space are required to match neutrino signals. The Askaryan field is derived from cascade equations verified with Geant4 simulations, and compared with prior numerical and semi-analytic calculations. Finally, instructive cases of the model are transformed from the Fourier domain to the time-domain. Next-generation *in situ* detectors like ARA and ARIANNA can use analytic time-domain signal models to search for correlations with event candidates.

© 2017 Published by Elsevier B.V.

1. Introduction

The landmark observation of PeV neutrino interactions in Antarctic ice by the IceCube collaboration [1] has highlighted the urgency for progress in ultra-high energy cosmogenic neutrino (UHE- ν) searches, at energies $10^{16} - 10^{20}$ eV [2–4]. Cosmogenic neutrinos represent a long awaited prize in both astrophysics and particle physics, because of the potential to explain the origin of UHE cosmic rays (UHECR), as well as the chance to study electroweak interactions at record-breaking energies.

The GZK process is a $p\gamma$ interaction yielding UHE- ν from the UHECR flux through the cosmic microwave background (CMB) [5,6]. UHECR models lead to the conclusion that 100 km³-volume detectors are required to measure cosmogenic UHE- ν flux [7–10]. UHE- ν also present the possibility revealing physics beyond the Standard Model, via measurements of UHE- ν deep-inelastic scattering cross-sections [11,12]. Models matching simultaneously the PeV- ν flux from IceCube, the diffuse GeV gamma-ray flux, and the UHECR flux, are now placing constraints on cosmogenic UHE- ν flux [9,13,14].

The next generation of UHE- ν detectors is based on the Askaryan effect, in which a UHE- ν interaction produces a cascade

that radiates radio-frequency (RF) pulses from within a dielectric medium [15–17]. These detectors use the special RF properties of Antarctic ice, in order to search for UHE- ν cascades efficiently [18–20]. The Radio Ice Cernekov Experiment (RICE) conducted the pioneering search [21]. The Antarctic Impulsive Transient Antenna (ANITA) is a balloon-borne detector [22,23]. The Askaryan Radio Array (ARA), and the Antarctic Ross Ice Shelf Neutrino Array (ARIANNA) are two *in situ* detectors similar to RICE, but designed on a much larger scale [24–28]. The ExaVolt Antenna (EVA) is a proposed design to improve on the ANITA detection scheme [29].

The expected Askaryan RF pulse in the detectors must be understood in detail. Zas, Halzen, and Stanev (ZHS) created a Monte Carlo (MC) simulation which yielded the Askaryan field by tracking the radiation from every cascade particle above ≈ 1 MeV, using the Fraunhofer approximation [30]. This technique is computationally intensive and is difficult to scale to UHE- ν energies. Semi-analytic models [31–33] by Alvarez-Muniz, Romero-Wolf, Vazquez, and Zas (AVZ, ARVZ) solve Maxwell's equations, treating the cascade charge excess as a source current. These models require only the MC profile (charge versus depth) of the cascade. Semi-classical methods become fully analytic when the Greisen and Gaisser–Hillas treatments provide the profile [34].

Ralston and Buniy (RB) [35] presented a complex analysis of Askaryan radiation. This approach yields theoretical insight into observable properties of the field, while matching the ZHS MC. The model includes an explanation of signal causality, and merges

* Open-source code associated with this work: <https://github.com/918particle/AskaryanModule>

* Corresponding author.

E-mail addresses: hanson.369@osu.edu, 918particle@gmail.com (J.C. Hanson).

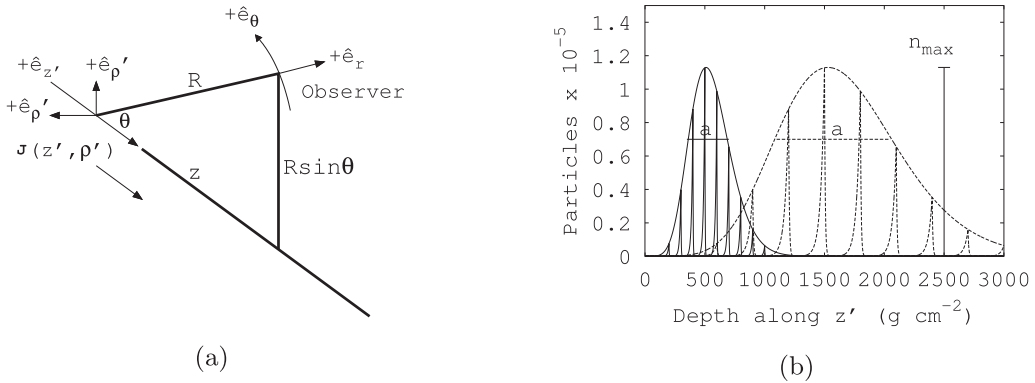


Fig. 1. (a) Coordinate systems. Un-primed coordinates refer to the observer, and primed coordinates refer to the reference frame of the vector current. (b) The curves represent the total charge content, with the instantaneous charge density (ICD) shown by the internal curves, versus depth after the first interaction in the medium. The solid curves were made for shower energy 10^{14} eV and the dashed curves for a shower profile having been stretched by either the LPM effect, or simply by going to a higher energy. The Greisen model was used for the form of the cascade profile. The n_{\max} parameter will refer to the negative charge excess.

coherence zones (Near-Field, Fresnel, Fraunhofer) continuously. A proper handling of non-Fraunhofer zones is vital for lowering energy thresholds in the *in situ* Askaryan detectors, because the lowest-energy events are only detectable above thermal backgrounds when the neutrino vertex is in coherence zones other than the Fraunhofer zone. Lowering energy thresholds is critical for maximizing detected UHE- ν , because the flux is expected to increase with decreasing energy.

We generalize the RB model by including two effects. We derive and implement the three-dimensional Cascade Form Factor from lateral MC charge diffusion, $\tilde{F}(\omega, \theta)$, and we introduce smooth cascade-elongation from the Landau-Pomeranchuk-Migdal (LPM) effect. Among the consequences of these extensions to RB are the constraint of the high-frequency (≈ 1 GHz) Fourier modes and the solid angle of the radiation. Parameters in $\tilde{F}(\omega, \theta)$ are derived from Geant4 MC (> 1 PeV) using a sub-cascade technique, and the electromagnetic MC cascades match the Greisen treatment, laterally and longitudinally [36]. Finally, the functional form of the Askaryan field is derived for special cases useful for Askaryan signal template-creation for UHE- ν searches with ARA/ARIANNA.

1.1. Advantages of a fully analytic treatment with the form factor and LPM elongation

The challenge of detecting UHE- ν with ARA/ARIANNA is one of distinguishing natural RF pulses from backgrounds. Every RF antenna observes thermal radiation associated with the temperature of the observed medium. ARA/ARIANNA background rates are a mixture of thermal radiation from ice, the sky, and the Milky Way [24,28,37]. Thermal noise is uncorrelated with digital signal templates generated by convolving theoretical Askaryan pulses with detector response. Signal templates have been used recently to detect UHECR with the ARIANNA Hexagonal Radio Array (HRA) [38]. More significantly, vibrational signal templates were used to detect gravitational wave signals in the Advanced LIGO detector [39]. In each case, a *template library* was created, in which individual templates share a physical origin, but use different functional parameters that span parameter-space.

Creating template libraries with semi-analytic and fully analytic models is far more efficient than creating them with particle MC codes. The Askaryan field is derived in semi-analytic models from cascade profiles computed via MC codes, accounting for stochastic effects in cascade profiles [31]. Fully analytic models are derived mathematically, where every model parameter has a physical origin and explanation. Template libraries may then be generated by tuning continuously parameters, accounting for regions of

parameter-space where the form factor $\tilde{F}(\omega, \theta)$ and LPM elongation dominate. Although the resulting template library would not account for stochastic processes, it would contain the effects of the form factor and LPM elongation, which control the sensitivity and design of Antarctic detectors. Examples of parameter-space variables are: the range to the interaction R , the frequencies ν , the length of the cascade a , the viewing angle θ , the fraction of the cascade that is electromagnetic or hadronic, the total cascade energy E_C , and the lateral width of the cascade $\sqrt{2\pi}\rho_0$.

2. Units, definitions, and conventions

All calculations in this work have been encapsulated into an open-source C++ class, available online.¹ The primary function of this code is to predict the electric fields that Askaryan-based detectors would detect. In all sections, this class will be called the *associated code*, or simply *the code*.

The coordinate systems are shown in Fig. 1a. Observer coordinates are un-primed, and charge excess coordinates are primed. The cascade current $\mathbf{J}(t')$ is described in Section 3.2, and will be called the instantaneous charge distribution (ICD) in subsequent sections. The vectors ρ and ρ' refer to the lateral distance from the cascade axis, and z and z' refer to the cascade axis. The origin for both systems is the location of the cascade maximum, with $z' = z = 0$ and $\rho = \rho' = 0$. The viewing angle is θ . Bold variables, and variables with a circumflex, \hat{e}_i , refer to vectors. The observer distance is $R = |\mathbf{x} - \mathbf{x}'|$, ω refers to the angular frequency, and $k = (2\pi)/n\lambda$ and $\mathbf{q} = n(\omega R, \omega \rho)/(cR)$ refer to one- and three-dimensional wavevectors in the dielectric, with a refractive index n . Although the code takes $n = 1.78$ as a default value, it may be altered to apply to other uniform media. The Cherenkov angle is defined by the index of refraction: $\cos\theta_C = 1/n$. The index of refraction at RF frequencies for bulk ice in Antarctica is 1.783 ± 0.003 [40].

The archetypal cascade profile is shown in Fig. 1b, in which the total number of cascade particles is shown, versus depth along the z' axis. The depth is Pz' , where P is the bulk density of ice (0.917 g/cm^3). The parameter n_{\max} will refer to the net number of negatively charged particles (typically $\approx 20\%$ of the total – see Section 3.4.1 and the Appendix Section A.2 for details). The parameter a is the Gaussian width of the cascade profile near cascade maximum. The cascade is initiated by an electroweak neutrino interaction, where the neutrino energy is E_ν , and the total energy of the cascade is E_C .

¹ <https://github.com/918particle/AskaryanModule>.

The units of the electromagnetic field in the Fourier domain are V/m/Hz, often converted in the literature to V/m/MHz. To make the distance-dependence explicit, both sides of field equations are multiplied by R , making the units V/Hz. In Section 4, the field normalization constant is E_0 , and it contains the energy-dependence. E_0 may be linearly scaled with energy, provided the parameters a and n_{\max} are derived consistently from the Greisen model. Equations in Section 4 are proportional to ωE_0 , so the units of E_0 are V/Hz².

In the original RB work, the following convention for the Fourier transform $\tilde{G}(\omega)$ of a function $g(t)$ was used:

$$\tilde{G}(\omega) = \int_{-\infty}^{\infty} e^{i\omega t} g(t) dt \quad (1)$$

$$g(t) = \frac{1}{2\pi} \int_{-\infty}^{\infty} e^{-i\omega t} \tilde{G}(\omega) dt \quad (2)$$

The sign convention shown in the exponent is used in RB, though the opposite sign convention is more common in mathematical physics. The definitions in Eqs. (1), (2) have been kept for consistency with Section V of [35]. The sign convention may be toggled in the code, but the output does not depend on this choice, because the appropriate transformation in time is applied. All frequencies are shown in MHz in spectral plots, for comparison to the literature. The symbol \sim above a function denotes a Fourier-domain quantity. In Sections 3.2 and 3.4, the three-dimensional Fourier transform is used to describe the form factor in three-dimensional frequency-space, with the normal sign convention:

$$\tilde{F}(\mathbf{q}) = \int d^3x' f(\mathbf{x}') e^{-i\mathbf{q}\cdot\mathbf{x}'} \quad (3)$$

3. Combination of the RB model, the LPM effect, and the Cascade Form Factor

In Section 3.1, the RB model [30] is presented for clarity, beginning with all assumptions made. Next, the model is enhanced by treating two new effects: the LPM effect (Section 3.3) and the Cascade Form Factor, \tilde{F} (Section 3.4).

3.1. General assumptions, and the basic RB model

The conventions are taken from Section 2 to build the RB model in the code [35]. RB derive the Askaryan fields from Maxwell's equations in the Lorentz gauge for a dielectric medium, by expanding with a special scalar parameter η . The source current, $\mathbf{J}(t', \mathbf{x}')$, is described by an ICD $f(z' - vt, \rho')$, excess charge profile $n(z')$, and cascade speed \mathbf{v} :

$$\mathbf{J}(t', \mathbf{x}') = \mathbf{v}n(z')f(z' - vt, \rho') \quad (4)$$

$$\eta = \left(\frac{a}{\Delta z_{\text{coh}}} \right)^2 = \frac{k}{R}(a \sin \theta)^2 \quad (5)$$

The function $f(z' - vt, \rho')$ is the 3D ICD. Eq. (5) is the squared ratio of a , and Δz_{coh} , the longitudinal range where the Askaryan radiation must be coherent. To understand Δz_{coh} , consider Feynman's formula [30]. Radiation from an accelerating point charge is proportional to the angular acceleration $\ddot{\theta}$ relative to the observer. The coherence regime is defined by $|z'| \lesssim \Delta z_{\text{coh}}$, where $\ddot{\theta}$ and $R(z')$ are constant in time to first order, and $\ddot{\theta}$ is maximized. RB show that if $\Delta R(z') < \lambda$ in this limit, $\Delta z_{\text{coh}} < (R/(ks \sin^2 \theta))^{1/2}$.

The dominant Askaryan radiation occurs when $|z'| \lesssim \Delta z_{\text{coh}}$. In the Fresnel and Fraunhofer (far-field) regimes, $\eta < 1$. The calculations, however, are valid for any η , rather than only the in the far-field ($\eta \rightarrow 0$, and $kR \gg 1$, $R \gg a$). If $a \ll \Delta z_{\text{coh}}$, then the fields have spherical symmetry, and the limit $kR \gg 1$ corresponds to the

far-field. Conversely, if $a \gg \Delta z_{\text{coh}}$, then $\eta \rightarrow \infty$, the fields have cylindrical symmetry.

The longitudinal cascade width a , and therefore η , is derived in the code from either the Greisen (electromagnetic) or Gaisser-Hillas (hadronic) cascade profile functions (Sections 3.4–3.4.1), and can be elongated by the LPM effect. The associated code requires the type of cascade profile (hadronic or electromagnetic) as an input, and whether the LPM effect must be applied. If the user specifies a purely hadronic cascade, no further action is taken if the LPM effect is activated [31].

3.2. The RB field equations

RB insert the vector current $\mathbf{J}(t', \mathbf{x}')$ into Maxwell's equations, and solve for the vector potential:

$$c\mathbf{A}(\mathbf{x}') = \int d^3x' \frac{e^{ik|\mathbf{x}-\mathbf{x}'|}}{|\mathbf{x}-\mathbf{x}'|} \int dt' e^{i\omega t'} \mathbf{J}(t', \mathbf{x}') \quad (6)$$

RB then define $R(z') = \sqrt{(z-z')^2 + \rho'^2}$, and expand around $\rho' = 0$:

$$|\mathbf{x}-\mathbf{x}'| \approx R(z') - \frac{\rho \cdot \rho'}{R(z')} + \frac{\rho'^2}{2R(z')} \quad (7)$$

In Eq. (7), the third term on the right-hand side is dropped, because $\rho' \ll R(z')$. The vector potential in Eq. (6) is then factored into the form factor $\tilde{F}(\omega)$ and a vector potential. $\tilde{F}(\omega)$ is the three-dimensional Fourier transform of the ICD, and the vector potential is governed by $n(z')$. Thus, $\tilde{F}(\omega)$ describes the charge distribution, and the vector potential describes the charge evolution. Eqs. (8) and (9) summarize the result. In Eqs. (8) and (9), $\tilde{\mathbf{A}}^{\text{FF}}$ is the vector potential, named the Fresnel-Fraunhofer (FF) potential in RB.

$$\tilde{\mathbf{A}}(\omega, \theta) = \tilde{\mathbf{A}}^{\text{FF}}(\omega, \theta) \int d^3x' e^{-i\mathbf{q}\cdot\mathbf{x}'} f(\mathbf{x}') \quad (8)$$

$$\tilde{\mathbf{A}}(\omega, \theta) = \tilde{F}(\omega, \theta) \tilde{\mathbf{A}}^{\text{FF}}(\omega, \theta) \quad (9)$$

Eqs. (10)–(13) express the general RB result for the electric field $\mathbf{E} = -\partial\mathbf{A}/\partial t$, in terms of the frequency ν , viewing angle θ , and η :

$$\frac{R\tilde{\mathbf{E}}(\nu, \theta, \eta)}{\left[\frac{\nu}{\text{MHz}} \right]} = 2.52 \times 10^{-7} \frac{a}{[\text{m}]} \frac{n_{\max}}{[1000]} \frac{\nu}{[\text{GHz}]} \tilde{F}(\mathbf{q}) \psi \mathcal{E} \quad (10)$$

$$\psi = -ie^{ikR} \sin \theta \quad (11)$$

$$\begin{aligned} \mathcal{E} &= \mathcal{W}(\eta, \theta) \left(\frac{\cos \theta_C - \cos \theta}{\sin \theta} \right) \hat{e}_r \\ &\quad + \mathcal{W}(\eta, \theta) \left(1 - i\eta \frac{\cos \theta_C}{\sin^2 \theta} \frac{\cos \theta - \cos \theta_C}{1 - i\eta} \right) \hat{e}_\theta \end{aligned} \quad (12)$$

$$\begin{aligned} \mathcal{W}(\eta, \theta) &= \left(1 - i\eta \left(1 - 3i\eta \frac{\cos \theta}{\sin^2 \theta} \frac{\cos \theta - \cos \theta_C}{1 - i\eta} \right) \right)^{-1/2} \\ &\quad \times \exp \left(-\frac{1}{2} (ka)^2 \frac{(\cos \theta - \cos \theta_C)^2}{1 - i\eta} \right) \end{aligned} \quad (13)$$

Eq. (10) is the total field, with an overall phase factor defined in Eq. (11). Eq. (12) contains the vector structure, and Eq. (13) governs the phase and angular structure.

3.3. The Landau-Pomeranchuk-Migdal (LPM) effect

The Landau-Pomeranchuk-Migdal (LPM) effect is a suppression of the pair-creation and bremsstrahlung cross-sections at cascade energies above a material-dependent constant known as the LPM energy or E_{LPM} [41]:

$$E_{\text{LPM}} = \frac{(mc^2)^2 \alpha X_0}{4\pi c \hbar} = 7.7 \text{ TeV/cm} \cdot X_0 \quad (14)$$

In Eq. (14), m is the electron mass, α is the fine-structure constant, and X_0 is the radiation distance ($E_{\text{LPM}} = 0.303$ PeV for ice). If $E_C > E_{\text{LPM}}$, the quantum mechanical *formation length* of these interactions is longer than atomic separations, leading to quantum interference and suppressing cross-sections. The result is a *longitudinal shower elongation*, from the non-interacting, higher-energy particles. The LPM effect is reviewed by S.R. Klein in Ref. [41].

The LPM changes how the RB model must be applied. Under normal circumstances, the quantity $n_{\text{max}}a$ approximates the area under the cascade profile for particles with energy greater than some critical energy: $n_{\text{max}}a \propto E_C$. It is shown in Ref. [42] that in the LPM-regime, $a \propto \sqrt{E_C/E_{\text{crit}}}$. While it may appear that changing the energy scaling of a violates energy conservation through the field normalization $n_{\text{max}}a$, this is not necessarily the case.

First, the amount of *radiated* energy does not have to track the *total* energy, if the cascade shape is modified. The Frank-Tamm radiation distribution for a charge moving through a track of length L states: $d^2P/d\Omega d\omega \propto L^2$ [35]. The LPM effect would increase L , increasing the radiated energy. The increase is contingent on L remaining comparable to Δz_{coh} , avoiding spectral cut-off. It is shown in Section 3.6 (graphically) and Section 4 (mathematically) that enhancements due to cascade elongation are attenuated by a combination of decoherence, \tilde{F} , and narrowed Cherenkov cone-width.

Second, it should not be assumed naively that n_{max} must be decreased in direct proportion to the increase in a , under LPM elongation. Absent the LPM effect, the inverse relationship between a and n_{max} merely reflects that E_C is a constant, with $\approx 10^{-7}$ of the energy in TeV passing to Askaryan radiation in V/m/MHz. Figs. 12–13 of Ref. [43] demonstrate LPM elongation, but n_{max} is not reduced in direct proportion to a . Fig. 12 of Ref. [43] shows that X_{max} grows and fluctuates at energies above E_{LPM} . However, Fig. 13 of Ref. [43] shows that the energy-dependence of n_{max} stays approximately the same, and n_{max} fluctuates mildly. Further, Fig. 3 of [31] suggests that charged-current induced cascades, with mixed hadronic and electromagnetic components, have no reduction in n_{max} relative to neutral-current induced cascades, for which the LPM effect is not relevant [44].

Physically, all particle energies must decrease below E_{LPM} eventually. This takes place before the cascade maximum, so to first order n_{max} is still governed by non-LPM physics, even if $E_C > E_{\text{LPM}}$. Conversely, ZHS and others have shown that the radiated field strength below 500 MHz is proportional to the weighted, projected track length of charged particles [30]. The LPM effect cannot enhance dramatically the weighted projected track length, because the number of LPM-elongated tracks is a small fraction of the total number. The associated code contains a flag (*strictLowFreqLimit*) which directs the model to retain this limit by inversely scaling n_{max} in direct proportion to the increase in a . Requiring this limit is equivalent to stating that sub-showers with $E < E_{\text{LPM}}$ occur both *before* and *after* cascade maximum, *smearing* $n(z')$. From the arguments and references above, this is the most conservative approach.

Finally, S.R. Klein notes in Ref. [41] that the LPM effect may influence $\tilde{F}(\omega, \theta)$. The lateral ICD is influenced by multiple scattering (MSC) effects that lead to a mean scattering angle $\langle \theta_{\text{MSC}} \rangle$ for cascade particles incident on atoms [36,41]. In Ref. [41], $\langle \theta_{\text{MSC}} \rangle$ takes the following form for a particle of energy E :

$$\langle \theta_{\text{MSC}} \rangle = \frac{E_s}{E} \sqrt{\frac{d}{X_0}} \quad (15)$$

X_0 is the radiation distance, d is the distance over which the scattering occurs, and E_s is the Molière scattering energy ($E_s = mc^2/\sqrt{4\pi/\alpha} \approx 21.2$ MeV). The LPM effect increases d relative to X_0 , increasing $\langle \theta_{\text{MSC}} \rangle$. Although $\langle \theta_{\text{MSC}} \rangle$ is enhanced by the LPM effect, it is also inversely proportional to energy. This implies that the

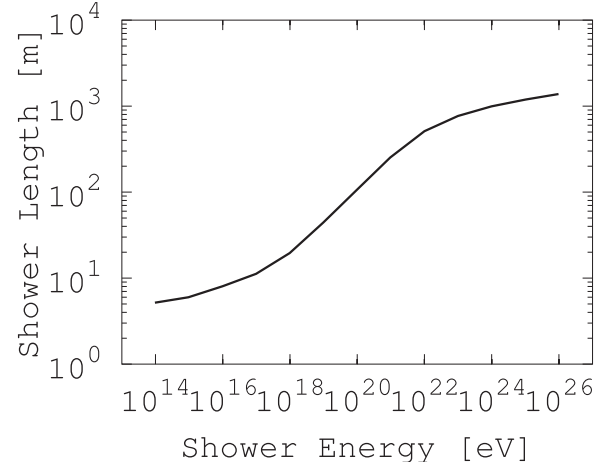


Fig. 2. The length of the neutrino-induced cascade, including the LPM effect, from ref. [42].

pile-up of particle energies at $E_{\text{crit}} \approx E_s$ actually governs the ICD width.

Finally, a remark about “shower fluctuations” is prudent. While the LPM effect may cause the cascade maximum location to fluctuate, the *location* of cascade maximum is irrelevant, because Askaryan radiation is independent of the origin of the coordinate system. The origin in the associated code is the location of cascade maximum, *wherever it occurs*. Stochastic features of the LPM effect, such as the multi-peaked cascade profile, are not treated in this work. However, it is shown in Ref. [45] that the sub-peaks only alter the waveform in certain circumstances, such as being off-cone by $\approx 10^\circ$ in the Fraunhofer regime. The waveforms in Ref. [45] all contain the basic bi-polar structure produced by the associated code, despite the multi-peaked cascade profile.

In summary, the main effect LPM physics has on Askaryan radiation is the angular and frequency filtering via the cascade elongation. The effect is quantified in the code by drawing an elongated shower width a from calculations by Klein and Gerhardt shown in Fig. 2 [42]. In scenarios where LPM is unimportant, such as initial hadronic-dominated processes [44] and cascades with $E_C < E_{\text{LPM}}$, the associated code draws the width and height of the negative charge excess profile from the usual Greisen and Gaisser–Hillas formulations [36,46].

3.4. The Cascade Form Factor, \tilde{F}

The factorization of the longitudinal charge excess evolution, $\tilde{A}^{FF}(\omega, \theta)$, and the instantaneous properties of the lateral charge distribution, $\tilde{F}(\omega)$, leads to the interpretation of $\tilde{F}(\omega)$ as a filter. Filters are fully described by pole-zero diagrams, which display the Laplace transform of the filter transfer function. Impulsive E-fields with no DC-component automatically approach 0 as $|\omega| \rightarrow 0$, meaning \tilde{F} should not require any zeros. Thus, $\tilde{F}(\omega)$ should be completely defined by poles in the complex ω -plane.

D. Garcia-Fernandez *et. al.* (Ref. [47]) show that the integrals over individual tracks in the ZHS algorithm can be generalized to all coherence regimes, when integrated numerically. The authors of Ref. [47] then insert the form factor chosen in Ref. [48] into the RB framework to demonstrate agreement (Fig. 7 of Ref. [47]). This agreement occurs at frequencies below 120 MHz, below the bandwidths of ARA/ARIANNA. The lateral ρ' -dependence of the chosen form factor is Gaussian ($f \propto \exp(-\rho'^2)$), yielding gaussian behavior in the Fourier domain ($|\tilde{F}| \propto \exp(-\omega^2)$). Geant4 simulations and the Greisen model show that $f(x')$ is not Gaussian (Section 3.4.1 and Appendix Section A.2). Additionally, the ultra-violet divergence

in Ref. [47] is attributed to the assumption that the dielectric constant $\epsilon(\omega)$ is not absorptive, however, the effect of $\tilde{F}(\omega)$ is apparent in that model near 1 GHz. This is because the filtering effect of $\tilde{F}(\omega, \theta)$ occurs when the Askaryan radiation of all finite tracks in a cascade are summed.

The ZHS form factor, $\tilde{F}_{\text{ZHS}}(\omega)$, is constructed of poles which imply that the lateral ICD $f \propto \exp(-\rho')$. The key result for $\tilde{F}(\omega)$ is given in Eq. (16), in terms of the viewing angle θ , the angular frequency ω , and $(\sqrt{2\pi}\rho_0)^{-1}$, the distance from the cascade axis ($\rho' = 0$) at which the negative charge excess has decreased by $1/e$.

$$\tilde{F}(\omega, \theta) = \frac{1}{(1 + (\frac{(\omega/c)\sin\theta}{\sqrt{2\pi}\rho_0})^2)^{3/2}} \quad (16)$$

Intuitively, the squared ratio in the denominator of Eq. (16) compares the lateral projection of the wavevector with the physical extent of the charge excess. If the charge excess is laterally large, compared to the wavelength, then Eq. (16) begins to act as a low-pass filter. By substituting Eq. (16) into Eq. (10), the RB model is completed, properly accounting for LPM elongation and the ICD. The form factor $\tilde{F}(\omega, \theta)$ is derived from fits to Geant4 cascades, for $E_C = 1\text{--}100$ PeV. Once the quality of these fits is established, one may proceed with the theoretical cascade models, with no need of further numerical simulation.

3.4.1. The Greisen model

K. Greisen provided a comprehensive review of the longitudinal charge evolution, and lateral distribution, within electromagnetic cascades [36], by combining earlier work by Molière, Nishimura and Kamata, Landau, and others. The integrated charge at depth z_0 in the medium is

$$n_{\text{tot}}(z_0) = \frac{0.31}{\sqrt{\ln(E_C/E_{\text{crit}})}} \exp\left\{z_0\left(1 - \frac{3}{2}\ln(s)\right)\right\} \quad (17)$$

In Eq. (18), z_0 is in units of radiation length (36.08 g cm^{-2}), and the cascade energy E_C in units of GeV ($E_{\text{crit}} = 73 \text{ MeV}$) [30,34]. The shower age is $s = 3z_0/(z_0 + 2\ln(E_C/E_{\text{crit}}))$. Eq. (17) contains the cascade maximum $z_{\text{max}} = \ln(E_C/E_{\text{crit}})$. Additionally, $\langle \ln n_{\text{tot}} \rangle \approx 0.7(s - 1 - 3\ln s)$. When $s = 1$ at z_{max} , $\langle \ln n_{\text{tot}} \rangle = 0$, implying negligible n_{max} fluctuation. Approximating $n_{\text{tot}}(z_0)$ by a Gaussian, $a \propto \sqrt{z_{\text{max}}}$. For $n_{\text{max}} = n_{\text{tot}}(z_{\text{max}})$, $n_{\text{max}}a \propto E_C/E_{\text{crit}}$. The factor $n_{\text{max}}a$ approximates the area under the peak of Eq. (17).

The lateral ICD arises from multi-scattering effects (MSC processes in Geant4), with average scattering angle $\langle \theta_{\text{MSC}} \rangle$ (Eq. (15)), and a Molière radius defined by $\rho_1 = E_{\text{MSC}}/E_c$, in radiation lengths. Large errors arise for angles $\theta \gg \langle \theta_{\text{MSC}} \rangle$, or ($\rho' > \rho_1$), but few particles have $\rho' > \rho_1$. The $\langle \theta_{\text{MSC}} \rangle$ is expressed in Eq. (18), for particles of energy ϵ in electromagnetic cascades [41]:

$$\langle \theta_{\text{MSC}} \rangle = \frac{E_{\text{MSC}}}{\epsilon} \sqrt{z_0} = \frac{m_e c^2 \sqrt{4\pi z_0/\alpha}}{\epsilon} \approx \frac{21.2[\text{MeV}]}{\epsilon} \sqrt{z_0} \quad (18)$$

Eq. (18) implies the lateral ICD should be widest near n_{max} , where ϵ is minimized. The widening lateral ICD causes most particles to lag behind the cascade front by $\mathcal{O}(1\text{--}10)$ cm at n_{max} (see Eq. (13) of [41]). Nishimura and Kamata refine the approximation, providing the lateral charged particle density, D . The result is known as the NKG-function, shown in Eq. (19).

$$D = \frac{n_{\text{tot}}}{2\pi\rho_1^2} \frac{\Gamma(4.5-s)}{\Gamma(s)\Gamma(4.5-2s)} \left(\frac{\rho'}{\rho_1}\right)^{s-2} \left(1 + \frac{\rho'}{\rho_1}\right)^{s-4.5} \quad (19)$$

Agreement between this work and Eqs. (17)–(19) is shown Section A.2 in the Appendix. The ICD is assigned a three-dimensional function $f(\mathbf{x}')$, and in Section 3.4.2, $\tilde{F}(\omega)$ is derived analytically from $f(\mathbf{x}')$. Other efforts to model the ICD and the resulting Askaryan radiation can be found in Refs. [49–51].

3.4.2. Analytic formula for $\tilde{F}(\omega, \theta)$

The definition of $\tilde{F}(\omega, \theta)$ is

$$\tilde{F}(\mathbf{q}) = \int d^3x' e^{-i\mathbf{q}\cdot\mathbf{x}'} f(\mathbf{x}') \quad (20)$$

The ICD $f(\mathbf{x}')$ is given by a general parameterization of the Greisen model:

$$f(\mathbf{x}') = \rho_0^2 \delta(z') \exp(-\sqrt{2\pi}\rho_0\rho') \quad (21)$$

The choice of Eq. (21) is motivated by Section 3.4.1 (see Appendix Section A.2 for more detail). Recall that the ICD is meant to describe the number density of the negative charge excess, not the total charged particle number density. Geant4 MC calculations and the Greisen model predict the exponential form, and the ZHS parameterization suggests it in the Fourier domain. Hu *et al* chose a double-Gaussian form [48], which is not accurate near $\rho' = 0$, but highlights the relationship between theoretical parameters and numerical fields. Note that the units of the $1/e$ width $\sqrt{2\pi}\rho_0$ and $\delta(z')$ are inverse length, giving $f(\mathbf{x}')$ units of number density.

Fitted results for the parameter $\sqrt{2\pi}\rho_0$ for times between 20–30 ns ($s \approx 1$) indicate that $\sqrt{2\pi}\rho_0 \sim$ is constant with respect to cascade depth. The solution to Eq. (20) is as follows: the trivial z' integration is performed, setting $z' = 0$ without loss of generality. Next, two convenient variables are defined, and shown in Eqs. (22) and (23).

$$\gamma = \frac{\omega}{c} \sin\theta \quad (22)$$

$$\sigma = \frac{\gamma}{\sqrt{2\pi}\rho_0} \quad (23)$$

The variable γ is the lateral projection of the wavevector, and σ is the product of γ and the lateral charge extent. The variable σ compares the laterally-projected wavelength to the lateral extent of cascade excess charge. In Section 4, $\sigma = \omega/\omega_{\text{CF}}$, so that ω_{CF} is the limiting frequency. Substituting Eqs. (21)–(23) into Eq. (20), $\tilde{F}(\omega, \theta)$ becomes

$$\tilde{F}(\omega, \theta) = \rho_0^2 \int_0^\infty d\rho' \rho' \exp\left\{-\frac{\gamma}{\sigma}\rho'\right\} \int_{-\pi}^\pi d\phi' \exp\{-i\rho'\gamma \cos(\phi')\} \quad (24)$$

From the cylindrical symmetry of $f(\mathbf{x}')$, the ϕ' coordinate may be rotated. With $\phi' \rightarrow \phi' - \pi/2$, the ϕ' -integral becomes a 0th-order Bessel function. A similar result in Ref. [49] contains the Bessel function in Eq. (24). In Ref. [49], however, the lateral ICD is not evaluated analytically, but through numeric integrals. After making the substitution $u' = \gamma\rho'$, the remaining ρ' -integral may be found in standard tables.

$$\tilde{F}(\omega, \theta) = \sigma^{-2} \int_0^\infty du' u' \exp\left\{-\frac{u'}{\sigma}\right\} J_0(u') \quad (25)$$

$$\tilde{F}(\omega, \theta) = \frac{1}{(1 + \sigma^2)^{3/2}} \quad (26)$$

The result for $\tilde{F}(\omega, \theta)$ is shown in Eq. (26). The Askaryan spectrum is attenuated like ω^{-3} for $\sigma \gg 1$, for wavelengths much smaller than the lateral ICD. For $\sigma \lesssim 1$, $\tilde{F}(\omega, \theta) \approx (1 + (3/2)\sigma^2)^{-1}$. Given the location of complex poles for $\sigma \ll 1$, one might suspect problems with causality. It is important to note, upon transforming the model to the time domain, including the LPM effect and the effect of $\tilde{F}(\omega, \theta)$, that the fields do not violate the causality criterion stated by RB [35].

Eq. (16) in Ref. [32] contains the Askaryan vector potential versus retarded time (t_r), matched to MC at $\theta = \theta_C$, with six numerical parameters, not counting the overall normalization. This

equation is restated as Eq. (27), and the x_i have unique values for $t_r > 0$ and $t_r < 0$.

$$\frac{R\mathbf{A}(t_r, \theta_C)}{[V \cdot s]} = -E'_0 \sin(\theta_C) \hat{e}_\theta (\exp(-2|t_r|/x_0) + (1+x_1|t_r|)^{-x_2}) \quad (27)$$

Eq. (26) fully describes the cascade shape, is analytic, and when combined with $\tilde{\mathbf{A}}^{FF}$, produces fields that obey causality (see Section 3.5). Additionally, \tilde{F} only needs one MC constant: $\sqrt{2\pi}\rho_0$. Although the second term in Eq. (27) accounts for the asymmetric MC vector potential in an ad-hoc fashion, this asymmetry flows directly from Eq. (26) (Section 4), and special cases of the x_i are derived. Rather than requiring six raw MC numbers, the associated code relies on Eq. (26), and one MC parameter ($\sqrt{2\pi}\rho_0$).

3.4.3. Generalization of Eq. (26)

In the Appendix Section A.2, the lateral distribution of excess charge near cascade maximum is shown to follow Eq. (21) for $\rho' < \rho_1$, where ρ_1 is the Molière radius. To include the effect of charges beyond a single Molière radius, the following form for $f(\mathbf{x}')$ may be taken:

$$f(\mathbf{x}') = \delta(z') \sum_i^N a_i \exp(-\sqrt{2\pi}\rho_i\rho') \quad (28)$$

The normalization requirement for the ICD provides the following constraint on the $2N$ free parameters:

$$\sum_i^N \left(\frac{a_i}{\rho_i^2} \right) = 2\pi \quad (29)$$

Note that the units of the a_i parameters are the same as the normalization ρ_0^2 in the single-exponential case. Let α_i and σ_i take the following definitions:

$$a_i = \alpha_i \rho_i^2 \quad (30)$$

$$\sigma_i = \frac{\gamma}{\sqrt{2\pi}\rho_i} \quad (31)$$

With this definition, Eq. (26) may be generalized to arbitrary Molière radii, taking the following form:

$$\tilde{F}(\omega, \theta) = \sum_i^N \frac{\alpha_i}{(1+\sigma_i^2)^{3/2}} \quad (32)$$

It is shown in Section 4.2 that in the far-field limit, at $\theta = \theta_C$, the effect of extending the form factor \tilde{F} to arbitrary Molière radii is equivalent to adding a set of additional poles to the Askaryan field in the complex ω -plane. In the time domain, the Askaryan field picks up a series of exponential terms corresponding to the added poles.

3.5. Results of the Model: RB+LPM+ $\tilde{F}(\omega, \theta)$

The associated code output $\hat{e}_\theta \cdot \mathbf{E}(t)$, including all effects is shown in Fig. 3, with $E_C = 1000$ PeV. Fig. 3 contains contour graphs, in units of mV/m, versus the retarded time in nanoseconds, and θ in degrees. The quadratic grey dashed line on the contours is a causal requirement from RB, showing how the arrival time (e.g. group delay) of the signal depends on θ . Phase delays t_ϕ about the quadratic are allowed: $t_\phi = -\phi(\omega)/\omega$. Phase delays are most prominent when $\tilde{F} \neq 1$, $\theta \neq \theta_C$, and when the LPM effect is strong. See Appendix Section 3.6 for further detail.

The fields are shown for $R = 200$ m (panels c and d) and 1000 m (panels a and b), $(\sqrt{2\pi}\rho_0)^{-1} = 5$ cm (panels a and c) and 10 cm (panels b and d) in Fig. 3. The causality requirement from RB leads to off-cone regions have a higher effective velocity. A larger R

value leads to wider separation in arrival times, as these off-cone modes have longer to outpace the other modes (earlier times correspond to more negative retarded times).

An enticing implication of the effective velocity variation is that the degeneracy between a low-energy event interacting close to the observer, and a high-energy event interacting correspondingly farther from the observer would be broken. Recall that $\tilde{\mathbf{E}} \propto R^{-1}$ in the far-field. An event with $R = 100$ m and $E_C = 10$ PeV would have the same amplitude as an event with $R = 1000$ m and $E_C = 100$ PeV, neglecting secondary effects like ice absorption. The temporal signature shown by the quadratics in Fig. 3 would be different in the two cases.

From Eq. (12), the field $\tilde{\mathbf{E}}$ has both \hat{e}_r and \hat{e}_θ components. For the extreme Fraunhofer limit, as $\eta \rightarrow 0$, the ratio of the amplitudes of these components is independent of frequency:

$$\frac{\hat{e}_r \cdot \tilde{\mathbf{E}}}{\hat{e}_\theta \cdot \tilde{\mathbf{E}}} = -\left(\frac{\cos \theta - \cos \theta_C}{\sin \theta} \right) \quad (33)$$

Eq. (33) shows that the \hat{e}_r -component of $\mathbf{E}(t)$ is positive above the Cherenkov angle, and negative below it. Since the $\hat{e}_r \cdot \mathbf{E}(t) = 0$ at θ_C , the maximum in the \hat{e}_r -component is always at some angle $\theta \neq \theta_C$. The contour graphs of Fig. 4 represent the \hat{e}_r -component of the same fields as Fig. 3. Because $\hat{e}_r \cdot \tilde{\mathbf{E}} < \hat{e}_\theta \cdot \tilde{\mathbf{E}}$, the Askaryan field is usually given with a pure \hat{e}_θ -polarization. Though the \hat{e}_r -component is small compared to the \hat{e}_θ -component, the code does not neglect it. The polarization ratio (Eq. (33)) is both complex, and frequency-dependent if $\eta \neq 0$.

3.6. Spectral, phase, and angular comparisons to previous work

It is shown in Figs. 5 and 6 where the associated code agrees with the ZHS parameterization for $E_C < E_{LPM}$. Eqs. (10)–(13), via the associated code, are compared in Figs. 5–6 to Eqs. 20–21 from [30], with $\Delta\theta = 2.4^\circ(v_0/\nu)$, and $v_0 = 0.5$ GHz, shown for convenience in Eqs. (34) and (35). In Fig. 5, the spectra are scaled by $R[m]/E_C[\text{TeV}]$, where E_C is the cascade energy in TeV.

$$\frac{R|\tilde{\mathbf{E}}(\omega, \theta = \theta_C)|}{\left[\frac{V}{\text{MHz}} \right]} = 1.1 \times 10^{-7} \frac{E_0}{[\text{TeV}]} \left(\frac{\nu}{v_0} \right) \frac{1}{1 + (\nu/v_0)^2} \hat{e}_\theta \quad (34)$$

$$\tilde{\mathbf{E}}(\omega, \theta) = \tilde{\mathbf{E}}(\omega, \theta = \theta_C) \exp \left[-\frac{1}{2} \left(\frac{\theta - \theta_C}{\Delta\theta} \right)^2 \right] \hat{e}_\theta \quad (35)$$

The $|\tilde{\mathbf{E}}(\omega, \theta_C)|$ derived from Eq. (16) from ARVZ [32] is also shown in Fig. 5(a) for comparison, as well as an off-cone example given in Fig. 3 of ARVZ [32]. The on-cone ARVZ case is given as a vector potential, so $\mathbf{E}(t) = -\tilde{\mathbf{A}}(t, \theta_C)$ is applied before extracting $|\tilde{\mathbf{E}}(\omega, \theta_C)|$. When $\theta = \theta_C$, the various $\tilde{F}(\omega)$ are the cause of the attenuation above 1 GHz. The choice of $\tilde{F}(\omega)$ for the associated code corresponds to a lateral cascade width of ≈ 5 cm, and $\tilde{F}(\omega)$ attenuates the spectrum above 1 GHz more realistically than ZHS. When $\theta \neq \theta_C$, the width of the Cherenkov cone is the cause of the high-frequency attenuation. The associated code is compared to ZHS at several angles, and the off-cone ARVZ lies in between the other results above 1 GHz, due to the smaller off-cone angle (0.3°). In Fig. 5(b), the angular dependence of the associated code and ZHS is compared at 0.25, 0.5 and 1.0 GHz. The cone-width is also inversely proportional to a in the RB model - an important feature that accounts for cone-width narrowing when LPM elongation is important (see Figs. 7 and 8 below). In Fig. 5 (b), the results with $\tilde{F} \neq 1$ are systematically lower than those with $\tilde{F} = 1$, as expected.

The phase $\phi(\omega)$ of $\hat{e}_\theta \cdot \tilde{\mathbf{E}}$ versus frequency is shown in Fig. 6, for several values of $\theta - \theta_C$. The phase $\phi(\omega)$ is unwrapped after taking the arctangent of the ratio of the imaginary to the real parts of the Fourier transform of the model waveforms. Shown for comparison are the phases of Eq. (16) of ARVZ [32], and ZHS (Fig. 16 of

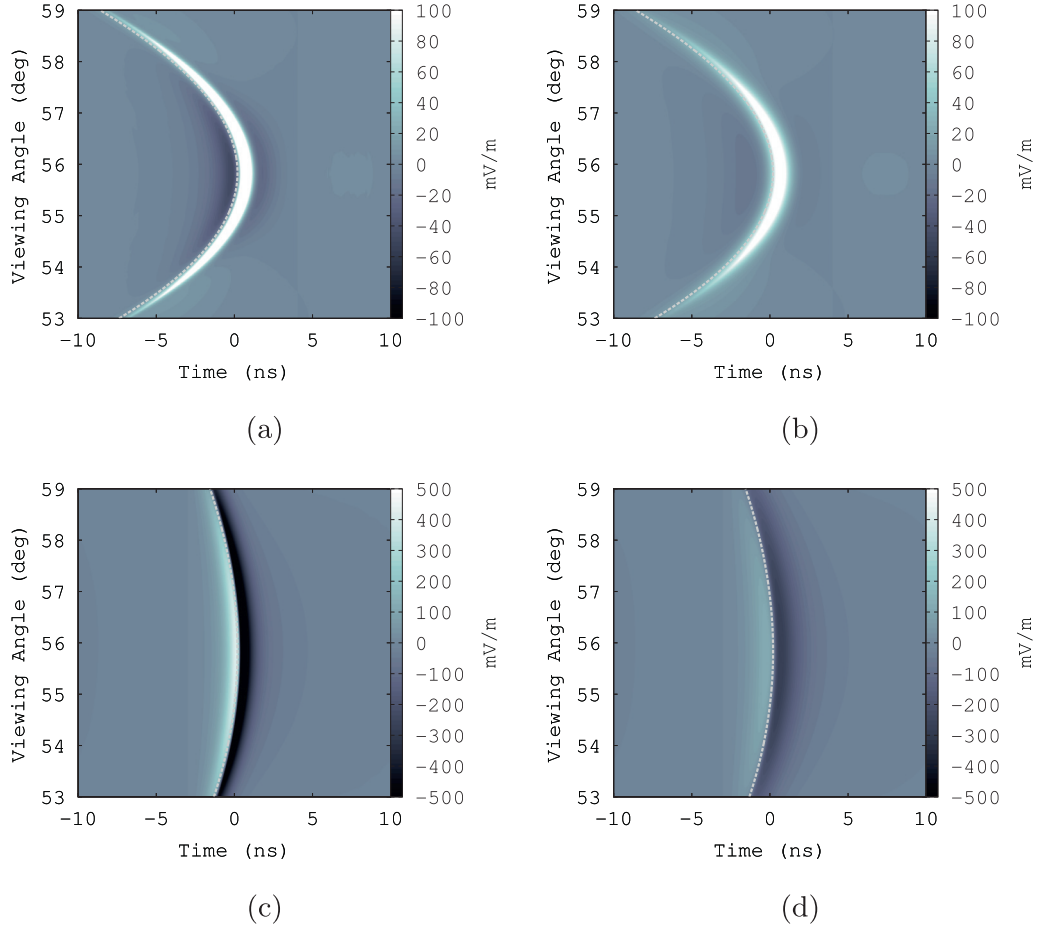


Fig. 3. Contours of $\hat{e}_\theta \cdot \mathbf{E}(t)$, for a cascade energy of 1000 PeV. (a) $R=1000$ m, lateral ICD width of 5 cm. (b) $R=1000$ m, lateral ICD width of 10 cm. (c) $R=200$ m, lateral ICD width of 5 cm. (d) $R=200$ m, lateral ICD width of 10 cm. The LPM effect has been taken into account. See text for details.

[30]), both at $\theta = \theta_C$. For the ARVZ case, which is a vector potential $\mathbf{A}(t, \theta_C)$, $\mathbf{E}(t) = -\dot{\mathbf{A}}(t, \theta_C)$ is applied before extracting the phase. All the models have $\phi(\omega) \sim 90^\circ$ for $\nu < 100$ MHz.² The $\phi(\omega)$ functions diverge above 100 MHz, where the radiated power is reduced off-cone. The group delay ($-d\phi/d\omega$) in this regime is roughly constant. Therefore, the ARVZ model and the associated code differ in phase above 100 MHz, but not group delay. Exploring all effects on $\phi(\omega)$, including LPM elongation and coherence, is outside the scope of this work.

The influence of LPM elongation on $|\hat{e}_\theta \cdot \tilde{\mathbf{E}}(\omega)|$ is shown in Fig. 7, revealing two effects relative to other models. First, there is a mild enhancement below 100 MHz in panels (b) and (d). Fig. 7, panels (a) and (c) show spectra with the *strictLowFreqLimit* flag activated in the associated code (see Section 3.3). Fig. 7, panels (b) and (d) show spectra without the *strictLowFreqLimit* flag, by default. As long as $\eta = ka^2 \sin^2 \theta / R \lesssim 1$, so that the stretched a is still $\lesssim \Delta z_{coh}$, the mild low-frequency enhancement in panels (b) and (d) may be attributed to radiation from an elongated cascade.

Second, spectra in panels (a) and (b) have different values of η than the spectra in panels (c) and (d), leading to a counter-intuitive high-frequency dependence. Eq. (13) at fixed θ implies a Gaussian frequency distribution: $|\mathcal{W}(\eta, \theta)| \propto \exp(-\frac{1}{2}(\Delta \cos \theta)^2(ka)^2)/(1 + \eta^2)$, with $\Delta \cos \theta = \cos \theta - \cos \theta_C$. The Gaussian width in ν is

$$\sigma_\nu(a, \eta, \theta) = \frac{c}{2\pi a \Delta \cos \theta} (1 + \eta^2)^{1/2} \quad (36)$$

² $\mathcal{F}_\omega(-\dot{\mathbf{A}}(t, \omega_C)) = \tilde{\mathbf{E}}(\omega, \theta_C) = -i\omega \tilde{\mathbf{A}}(\omega, \theta_C) = -e^{i\pi/2}\omega \tilde{\mathbf{A}}(\omega, \theta_C)$, so a low-frequency phase of $\pi/2$ (see Section A.1)

For $a \lesssim R$, as in panels (a) and (b), the η -term on the right side of Eq. (36) dominates for large ν because $\eta > 1$, which leads to $\sigma_\nu \sim \nu(a/R)$. The spectra in panels (a) and (b) are wider than the low-energy spectra in panels (c) and (d) due to the frequency-dependent σ_ν , which changes the high-frequency attenuation from Gaussian to linear attenuation at high-frequencies. Conversely, the low-energy spectra in panels (c) and (d) have $a \ll R$, and $\eta \ll 1$, implying from Eq. (36) that $\sigma_\nu \sim 1/a$, while the high-energy spectra encounter the former limit, because the a values are enlarged by LPM elongation. Thus, the low-energy spectra do not have the enhancement at high-frequencies, but the high-energy spectra have the enhancement. These various limits are important because the simulated range of neutrino interaction ranges detectable to ARA/ARIANNA are typically 100–1000 m [28,52].

Finally, $|\hat{e}_\theta \cdot \tilde{\mathbf{E}}|$ versus θ is compared with ZHS and AVZ [31] in Fig. 8. As with Fig. 7, a counter-intuitive situation arises when $\eta > 1$. Similar to the derivation of Eq. (36) from Eq. (13), the angular distribution at fixed frequency is Gaussian in $\Delta \cos \theta = \cos \theta - \cos \theta_C$: $|\mathcal{W}(\eta, \theta)| \propto \exp(-\frac{1}{2}(\Delta \cos \theta/\sigma_{\Delta \theta})^2)$, with Cherenkov cone-width

$$\sigma_{\Delta \theta}(a, \nu, \eta) = \frac{c}{2\pi a \nu} (1 + \eta^2)^{1/2} \quad (37)$$

LPM elongation has been applied in Fig. 8, implying that the width of the Cherenkov cone-width should be narrower than ZHS curves. In panel (a), the electromagnetic case agrees with AVZ at 100 MHz ($E_C = 10$ EeV). The AVZ field for large $|\theta - \theta_C|$ corresponds to radiation from sub-dominant peaks in the cascade profile not modelled by RB. The LPM effect is not applied

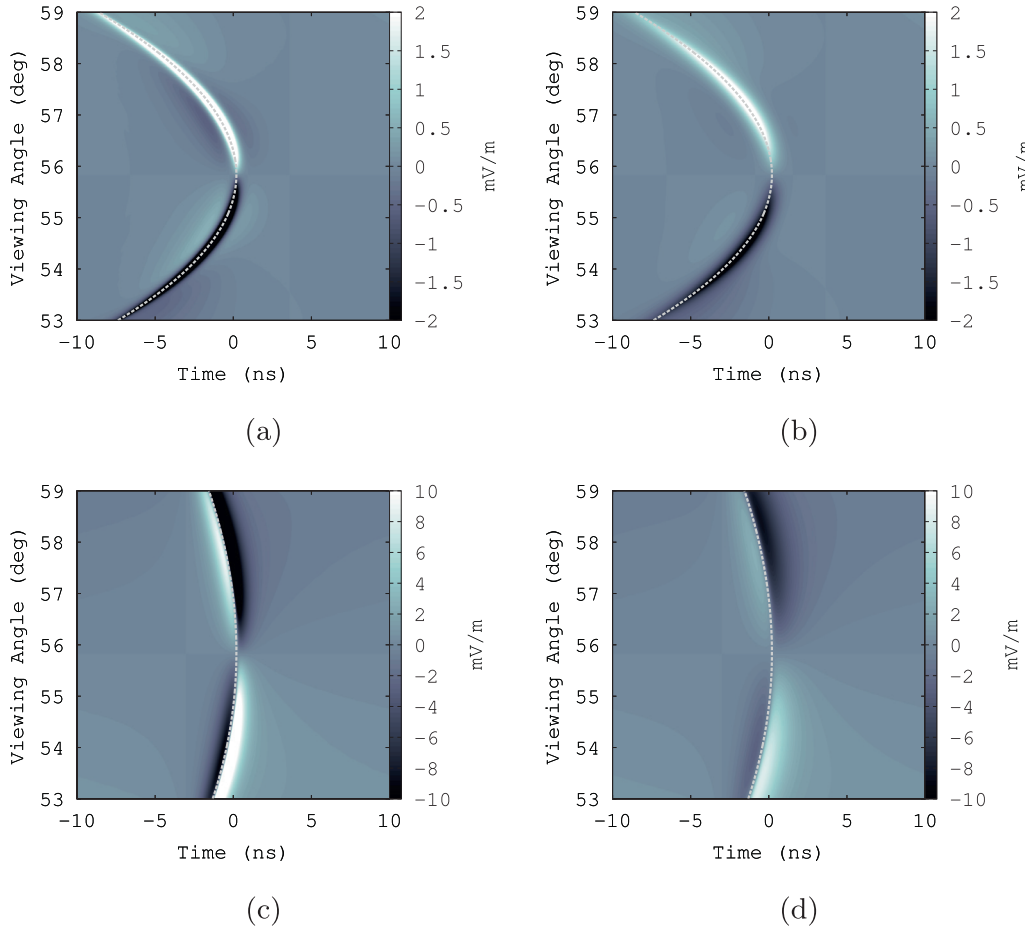


Fig. 4. Contours of $\hat{e}_r \cdot \mathbf{E}(t)$, for a cascade energy of 1000 PeV. (a) $R=1000$ m, lateral ICD width of 5 cm. (b) $R=1000$ m, lateral ICD width of 10 cm. (c) $R=200$ m, lateral ICD width of 5 cm. (c) $R=200$ m, lateral ICD width of 10 cm. In all cases, the gray dashed line represents the causality requirement. See text for details.

to the hadronic case in the associated code [44]. The hadronic case is therefore wider in panel (a), because $\eta < 1$ and from Eq. (37), $\sigma_{\Delta\theta} \sim 1/a\nu$. This result follows past far-field approximations in the literature: the Cherenkov-cone is narrower for higher frequencies, and narrower for larger a . However, pure hadronic cone-widths from the code should be narrower than AVZ pure hadronic cases, because AVZ do not have the $1/a$ dependence of Eq. (37). In panel (b) ($E_C = 1$ EeV), the code is compared to a mixed hadronic/electromagnetic cascade from [31]. AVZ note that pure electromagnetic cascades do not result from electroweak neutrino interactions, because the charged-current case always has a hadronic component. Thus, a linear combination of the solid black and solid gray curves that sum to the black dashed curve will be observed for charged-current interactions. The lower energy in panel (b) relative to panel (a) leads to a wider cone-width because LPM elongation is proportional to E_C .

In panel (c) of Fig. 8, the same scenario as in panel (a) is depicted, but the frequency is an order of magnitude larger. In panel (d), the same scenario as in panel (b) is depicted, but the frequency is an order of magnitude larger as well. For both scenarios, $\eta \gg 1$, so the Cherenkov cone *loses dependence on frequency*: $\sigma_{\Delta\theta} \sim \frac{a}{R} \sin^2 \theta$. This result is that the electromagnetic contribution to the Cherenkov cone is actually *wider* than the hadronic contribution, because the LPM elongation increases the a of the electromagnetic component, but not the hadronic component. Note that the solid black and solid gray curves do not have to agree with the dashed curves, because they represent different frequencies. The AVZ and ZHS results are identical in all panels, and kept for reference in panels (c) and (d).

4. Time-domain properties at the Cherenkov angle

The analytic RB+LPM+ $\tilde{F}(\omega, \theta)$ model is derived in the time-domain for limiting cases, and parameters from the semi-analytic treatment in Ref. [32] are derived analytically. The purpose of this section is to connect each parameter in the analytic Askaryan pulse to a physical origin in the cascade. Similar efforts have been attempted. The authors of [49] provide a formula along the lines of Eqs. (26) and (32) involving Bessel function evaluation, but rely on MC techniques to complete the model. The authors of [48] chose a mathematically tractable ICD and connected ICD parameters to simulated Askaryan radiation properties. However, the choice of ICD in [48] was for convenience, and does not necessarily agree with MC results. Here, we have attempted to both choose a 3D ICD that matches Geant4 results, and evaluate the Askaryan field analytically. See Appendix (Section A.2) for further detail.

Two cases are considered: $\tilde{F} = 1$, followed by $\tilde{F}(\omega, \theta) \neq 1$. The limiting frequency of the former, ω_C , is governed by coherence. The latter has two limiting frequencies, ω_C and ω_{CF} , which leads to an asymmetry in the vector potential, and therefore, asymmetry in $\tilde{\mathbf{E}}$. The SI units of terms like $R\tilde{\mathbf{E}}$ in the Fourier domain are [V/Hz], while they are just [V] for $R\mathbf{E}$ in the time-domain. The overall scale of the field is not relevant in this section, so the unit of frequency is left as [Hz], rather than [MHz]. In each derivation, the viewing angle is $\theta = \theta_C$.

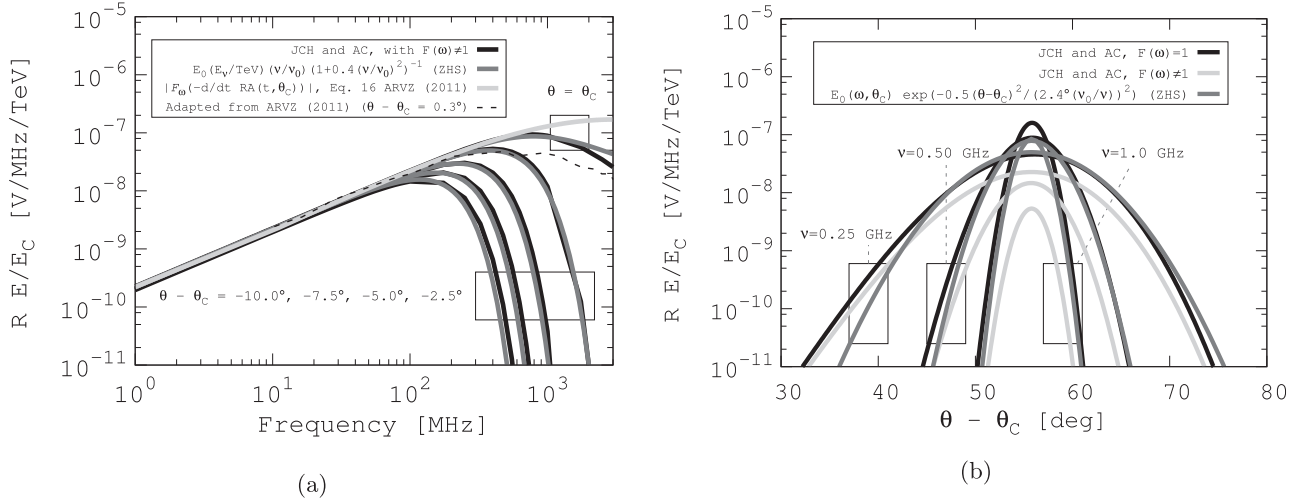


Fig. 5. (a) A comparison of the magnitude of the Askaryan field in different models versus v for $E_C = 100$ TeV scaled by R/E_C . Models shown are: the associated code $|\hat{e}_\theta \cdot \tilde{\mathbf{E}}(\omega)|$ (black), ZHS parameterization (dark gray), the $|\hat{e}_\theta \cdot \tilde{\mathbf{E}}(\omega)|$ from Eq. (16) from ARVZ [32] (light gray), and the spectrum adapted from Fig. 3 of [32] (dashed line). For the associated code (black), $a = 1.5$ m, $R = 1000$ m, $\tilde{F} \neq 1$. The upper right box encompasses cases for which $\theta = \theta_C$, and the lower left box encompasses cases for which $\theta \neq \theta_C$. The cases are (from right to left) $\theta_C - 2.5^\circ$, $\theta_C - 5.0^\circ$, $\theta_C - 7.5^\circ$, and $\theta_C - 10.0^\circ$. (b) The angular dependence of the associated code $|\hat{e}_\theta \cdot \tilde{\mathbf{E}}(\omega)|$, $\tilde{F}(\omega) = 1$ (black), ZHS parameterization (dark gray), and the associated code $|\hat{e}_\theta \cdot \tilde{\mathbf{E}}(\omega)|$, $\tilde{F}(\omega) \neq 1$ (light gray).

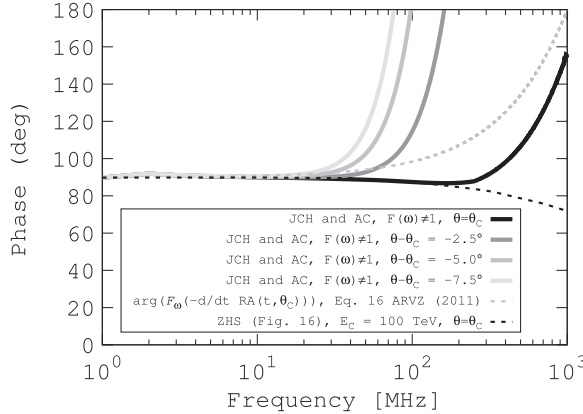


Fig. 6. A comparison of the phase of the Askaryan field in different models versus v for $E_C = 100$ TeV, $R = 1000$ m. The associated code produces the solid lines at viewing angles of θ_C and $\theta - \theta_C = \{-2.5^\circ, -5.0^\circ, -7.5^\circ\}$. The gray dashed line is the phase of Eq. (16) of [32] ($\theta = \theta_C$), and the black dashed line is the ZHS result.

4.1. The limit $\eta < 1$, $\tilde{F}(\omega, \theta_C) = 1$

Recall from Eq. (10) of Section 3.2 that the vector-form of the on-cone field from the RB formalism takes the form:

$$\frac{R\tilde{\mathbf{E}}(\omega, \theta_C)}{[V/\text{Hz}]} = -\frac{i\omega E_0 \sin \theta_C e^{i\omega R/c}}{(1 - i\eta)^{1/2}} \hat{e}_\theta \quad (38)$$

Let $\hat{E}_0 = E_0 \sin \theta_C \hat{e}_\theta$, and define ω_C from η : $\eta = \omega/\omega_C$. Eq. (38) may be approximated to first order in the limit $\eta < 1$, or $\omega < \omega_C$, equivalent to requiring $\lambda R \gtrsim 5a^2$. Using the definition of η , $\nu_C = \omega_C/(2\pi)$ is

$$\nu_C = \frac{cR}{2\pi a^2 \sin^2 \theta_C} \quad (39)$$

Applying the given limit to Eq. (38), and taking the inverse Fourier transform, yields

$$RE(t_r, \theta_C) \approx \frac{i\omega_C \hat{E}_0}{\pi} \frac{d}{dt_r} \int_{-\infty}^{\infty} d\omega \frac{e^{-it_r\omega}}{\omega + 2i\omega_C} \quad (40)$$

The sign convention in the exponential in Eq. (40) is chosen to remain consistent with the RB formalism. The integral may be performed using the Cauchy integral formula, provided that

the numerator is analytic ($\exp(-i\omega t_r)$) obeys the Cauchy–Riemann equations.

Contour integration of Eq. (40) requires a contour C that satisfies Jordan's lemma and includes all $\omega \in [-\infty, \infty]$. For the $t_r > 0$ case, the integral converges along the contour defined by the infinite lower semi-circle because the magnitude of the numerator decreases like $\exp(\text{Im}\{\omega\})$. Note that this is a negatively-oriented contour. For the case $t_r < 0$, use the fact that $\mathcal{F}_\omega(x(-t)) = \tilde{X}(-\omega)$, so $x(-t) = \mathcal{F}_\omega^{-1}(\tilde{X}(-\omega))$, where $\mathcal{F}_\omega(x) = \tilde{X}(\omega)$ is the Fourier transform of a function $x(t)$. The final solution is piecewise:

$$\frac{RE(t_r, \theta_C)}{[V]} \approx 4\hat{E}_0 \omega_C^2 \begin{cases} \exp(2\omega_C t_r) & t_r \leq 0 \\ -\exp(-2\omega_C t_r) & t_r > 0 \end{cases} \quad (41)$$

MC calculations show the transition at $t_r = 0$ to be smooth [34]. Eq. (41) has a characteristic width of $1/\omega_C = 1/(2\pi\nu_C)$, implying that the pulse-width is controlled by coherence, in the absence of a form factor. Fig. 9 shows ν_C versus the observer distance R and the shower width a .

Under the Lorentz gauge condition for Maxwell's equations, in the absence of static potentials, the negative derivative of the vector potential yields the electric field: $-\partial\mathbf{A}/\partial t = \mathbf{E}$. Using Eq. (41), the vector potential is

$$\frac{R\mathbf{A}(t_r, \theta_C)}{[V \cdot s]} \approx -2\hat{E}_0 \omega_C \begin{cases} \exp(2\omega_C t_r) & t_r \leq 0 \\ \exp(-2\omega_C t_r) & t_r > 0 \end{cases} \quad (42)$$

Eq. (16) of [32] is the vector potential at $\theta = \theta_C$:

$$\frac{R\mathbf{A}(t_r, \theta_C)}{[V \cdot s]} = -E'_0 \sin(\theta_C) \hat{e}_\theta (\exp(-2|t_r|/x_0) + (1 + x_1|t_r|)^{-x_2}) \quad (43)$$

Eq. (43) is a formula that is used in MC by ARA/ARIANNA [28,34,53], corresponding to a fit to MC similar to ZHS. By comparing Eqs. (42) and (43), a natural, theoretical explanation of the fit parameters in [32] arises, albeit from a special case: $\tilde{F} = 1$, and $x_0 = 1/(\omega_C)$, with $x_2 \gg 1$, or $x_1 \sim 0$. Thus, the result from [32] has been derived from first principles, rather than fitting to MC.

The fits in Ref. [32] have $x_2 \approx x_1 \approx 3$. The fact that x_1 and x_2 are not relevant to Eq. (42) is precisely because stipulating that $\tilde{F}(\omega, \theta_C) = 1$ leaves the spectral limiting to ν_C rather than $\tilde{F}(\omega, \theta)$. Such a scenario can be important when dealing with observations of cascades with $R = \mathcal{O}(100)$ m, under the influence of the LPM

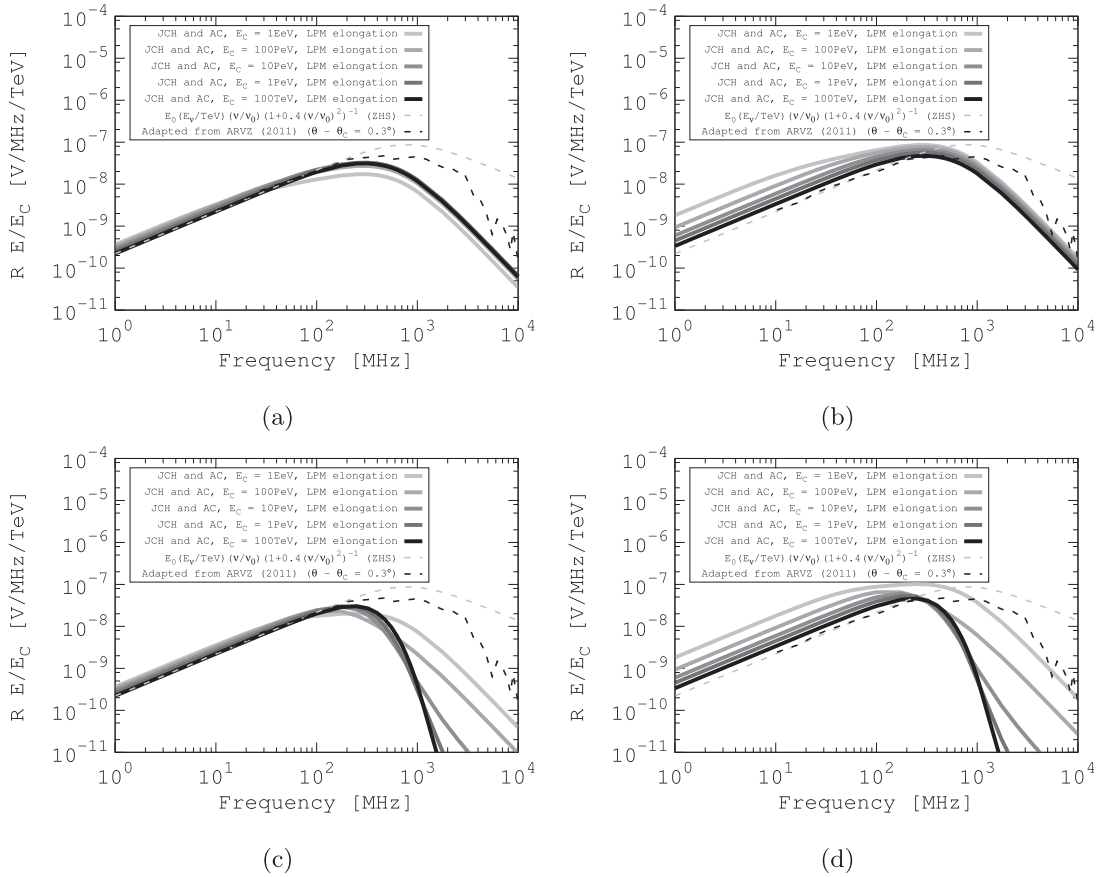


Fig. 7. The influence of LPM elongation on $|\hat{e}_\theta \cdot \tilde{\mathbf{E}}(\omega)|$, for different values of η . (a) $|\hat{e}_\theta \cdot \tilde{\mathbf{E}}(\omega)|$, for $R = 200$ m, and $\theta = 57^\circ$, low-frequency restricted. (b) $|\hat{e}_\theta \cdot \tilde{\mathbf{E}}(\omega)|$, for $R = 200$ m, and $\theta = 57^\circ$. (c) $|\hat{e}_\theta \cdot \tilde{\mathbf{E}}(\omega)|$, for $R = 1000$ m, and $\theta = 57^\circ$, low-frequency restricted. (d) $|\hat{e}_\theta \cdot \tilde{\mathbf{E}}(\omega)|$, for $R = 1000$ m, and $\theta = 57^\circ$. In all graphs, the black dashed line is the ZHS result with no LPM elongation, and the gray dashed line is the ARVZ result adapted from Fig. 3 of [32]. See text for detail.

effect. In this case, only a small fraction of the shower excess profile is within Δz_{coh} , and ν_C cuts off the spectrum. Another example in which spectral limiting is due to ν_C , rather than $\tilde{F}(\omega, \theta)$, is when the dielectric medium is denser than ice. The Askaryan spectra extends to $\approx \mathcal{O}(10)$ GHz at $\theta = \theta_C$ in salt, for example [54]. Higher density leads to a more compact ICD, suppressing the effect of $\tilde{F}(\omega, \theta)$. Fig. 9 shows a parameter space for ν_C relevant to ARA/ARIANNA.

The result $x_0 = 1/(\omega_C)$ also has a useful physical analogy for the shower width, a . Let the signal propagation time be T , such that (to first order) $R = cT/n$. Eq. (44) then relates the pulse width x_0 from Eq. (43) to the shower width a :

$$x_0 = \left(\frac{a \sin \theta_C}{c} \right) \left(\frac{a \sin \theta_C}{R} \right) = T \left(\frac{a \sin \theta_C}{\sqrt{n} R} \right)^2 \quad (44)$$

Eq. (44) demonstrates that the pulse width is a fraction of the propagation time T , and proportional to $(a/R)^2$.

4.2. The limit $\eta < 1$, $\sigma < 1$, $\tilde{F}(\omega, \theta_C) \neq 1$

Askaryan radiation from cascades experiences further low-pass filtering from $\tilde{F}(\omega, \theta) \neq 1$ (Section 3.4). The parameter σ can be used to define a limiting frequency: $\sigma = \omega/\omega_{\text{CF}}$, similar to $\eta = \omega/\omega_C$. The electric field of Eq. (38), combined with the form factor $\tilde{F}(\omega, \theta_C)$ of Eq. (26), is

$$\begin{aligned} \frac{\tilde{\mathbf{E}}(\omega, \theta_C)}{[\text{V}/\text{Hz}]} &= -\tilde{F}(\omega, \theta) \frac{i\omega E_0 \sin \theta_C e^{i\omega R/c}}{(1 - i\omega/\omega_C)^{1/2}} \hat{e}_\theta \\ &= -\frac{i\omega E_0 \sin \theta_C e^{i\omega R/c}}{(1 - i\omega/\omega_C)^{1/2} (1 + (\omega/\omega_{\text{CF}})^2)^{3/2}} \hat{e}_\theta \end{aligned} \quad (45)$$

In the limit $\sigma < 1$, and $\eta < 1$, Eq. (45) may be approximated as shown in Eq. (46), using $t_r = t - R/c$, and $\omega_0 = \sqrt{2/3} \omega_{\text{CF}}$.

$$\frac{R\mathbf{E}(t_r, \theta_C)}{[\text{V}]} \approx \frac{i\omega_0^2 \omega_C}{\pi} \hat{E}_0 \frac{d}{dt_r} \oint d\omega \frac{e^{-it_r \omega}}{(\omega + 2i\omega_C)(\omega + i\omega_0)(\omega - i\omega_0)} \quad (46)$$

There are two poles in the lower-half complex plane, and one in the upper-half plane. If $t_r > 0$, the contour integral around the lower infinite semi-circle converges because the numerator approaches zero exponentially as $\text{Im}\{\omega\} \rightarrow -\infty$. Conversely for $t_r < 0$, the contour integral converges along the upper infinite semi-circle. The final field is given by Eq. (47), to first-order in ϵ , with $\epsilon = \omega_0/\omega_C$.

$$\frac{R\mathbf{E}(t_r, \theta_C)}{[\text{V}]} \approx \frac{\hat{E}_0 \omega_{\text{CF}}^2}{3} \begin{cases} (1 - \frac{1}{2}\epsilon) \exp(\omega_0 t_r) & t_r \leq 0 \\ -\exp(-\omega_0 t_r) + 2 \exp(-2\omega_C t_r) & t_r > 0 \end{cases} \quad (47)$$

Consulting Fig. 9 reveals regions of parameter space where $\omega_C \leq 1$ GHz. Consulting Eq. (23) and (39) shows that $\epsilon < 1$ is typical for cascades with $a \leq \mathcal{O}(1 - 10)$ m. The relative strengths of ω_C and $\omega_{\text{CF}} = \sqrt{3/2} \omega_0$ are shown in Fig. 10, versus the longitudinal and lateral cascade widths. The vector potential corresponding to Eq. (47) is

$$\frac{R\mathbf{A}(t_r, \theta_C)}{[\text{V} \cdot \text{s}]} \approx -\frac{\hat{E}_0 \omega_{\text{CF}}}{\sqrt{6}} \begin{cases} (1 - \frac{1}{2}\epsilon) \exp(\omega_0 t_r) & t_r \leq 0 \\ \exp(-\omega_0 t_r) - \epsilon \exp(-2\omega_C t_r) & t_r > 0 \end{cases} \quad (48)$$

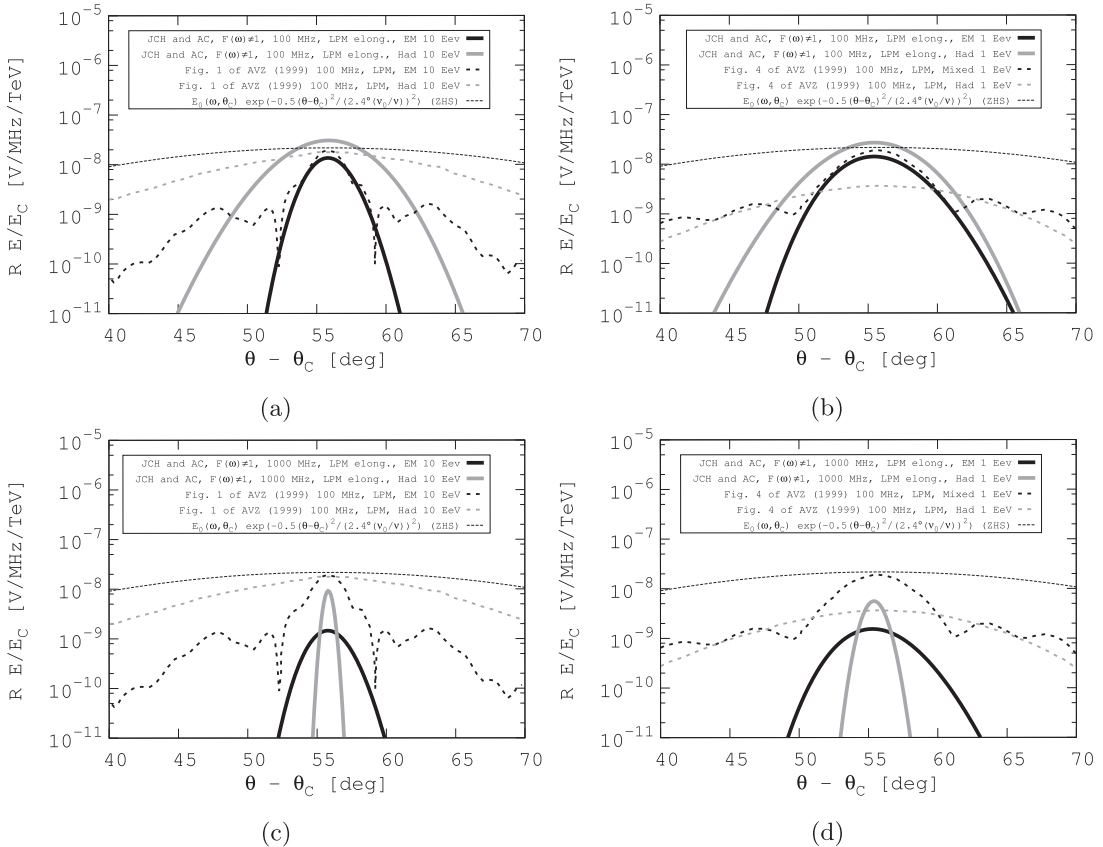


Fig. 8. (a) $|\hat{e}_0 \cdot \tilde{\mathbf{E}}(\omega)|$ versus θ , for $v = 100$ MHz, $E_c = 10$ EeV, and $R = 2000$ m, accounting for LPM elongation, in the pure electromagnetic (solid black) and pure hadronic (solid gray) cases. Shown for comparison are the pure electromagnetic (dashed black) and pure hadronic (dashed gray) from Fig. 1 of [31]. (b) $|\hat{e}_0 \cdot \tilde{\mathbf{E}}(\omega)|$ versus θ , for $v = 100$ MHz, $E_c = 1$ EeV, and $R = 500$ m, accounting for LPM elongation, in the pure electromagnetic (solid black) and pure hadronic (solid gray) cases. Shown for comparison are the mixed (dashed black) and pure hadronic (dashed gray) from Fig. 4 of [31]. (c) Same as (a), but with $v = 1000$ MHz. (d) Same as (b), but with $v = 1000$ MHz. Notice that for $v = 1000$ MHz, the electromagnetic cone-width is larger than the hadronic cone-width. See text for details.

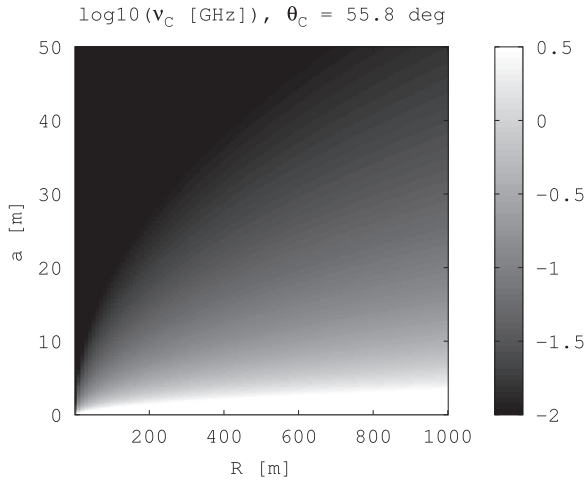


Fig. 9. A contour graph of $\log_{10} v_C$, for a parameter space relevant for ground-based radio-Askaryan detectors. Notice that $v_C < 1$ GHz if $a \gtrsim 1$ m.

Eqs. (47) and (48) show that the field remains bipolar but asymmetric, and asymmetric in time, from the interplay between coherence and the form factor. The pulse width is enhanced due to the presence of two different limiting frequencies, $\omega_0 = \sqrt{2/3}\omega_{\text{CF}}$, and ω_C . Eq. (49) defines a parameter showing the relative importance of the two limiting frequencies:

$$\epsilon' = \omega_{\text{CF}}/\omega_{\text{C}} = (\sqrt{2\pi} \rho_0 \rho) \left(\frac{a}{R}\right)^2 \quad (49)$$

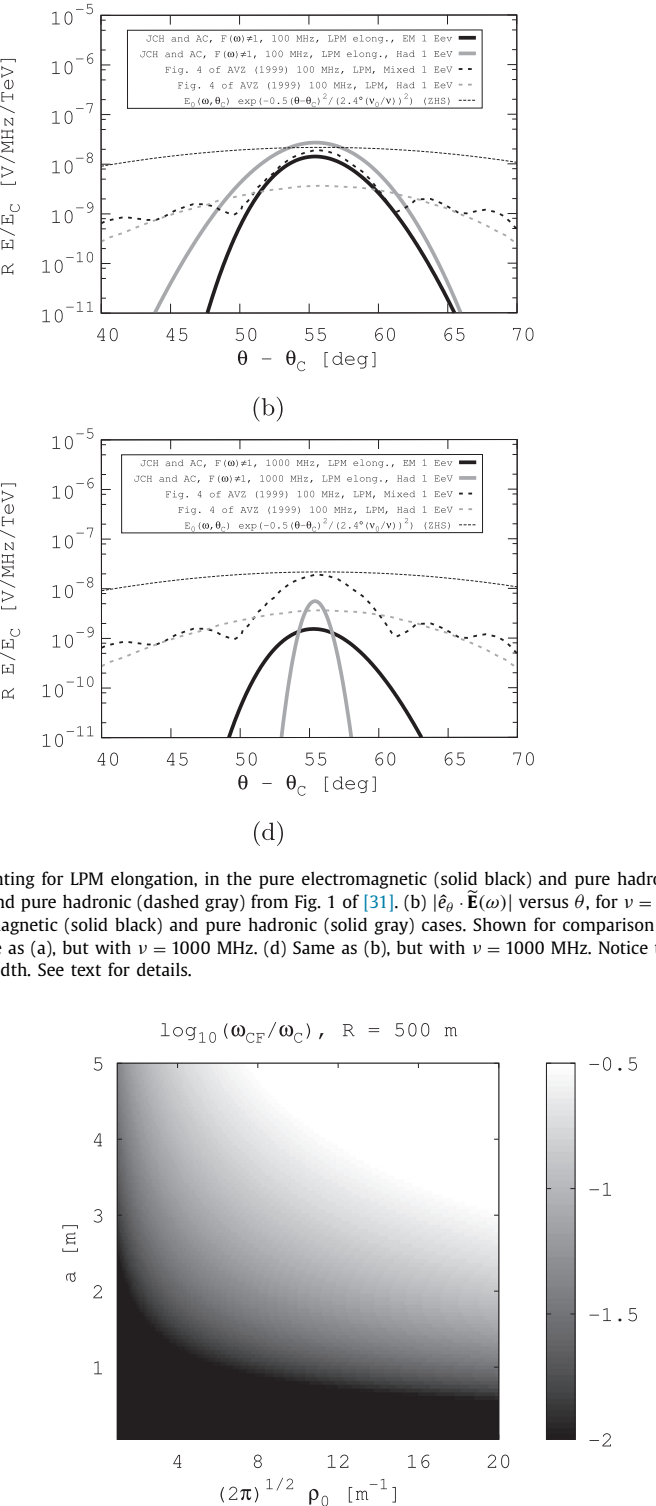


Fig. 10. A contour plot of $\omega_{\text{CF}}/\omega_{\text{C}} = v_{\text{CF}}/v_{\text{C}}$, for a parameter space relevant for ground-based radio-Askaryan detectors.

Fig. 10 is a contour graph of ϵ' in a parameter space relevant for ARA/ARIANNA. The first term in parentheses in Eq. (49) represents the relative importance of $\tilde{F}(\omega, \theta)$. The second term in parentheses is the ratio of the longitudinal cascade width to the observer distance, and it represents the quality of the Fraunhofer limit.

4.3. Generalization of Eq. (45)

The purpose of Eq. (32) is to account for excess charge at lateral distances greater than one Molière radius. Consequently, Eq. (45) may be generalized to

$$\frac{R\tilde{\mathbf{E}}(\omega, \theta_C)}{[V/\text{Hz}]} = - \sum_{j=0}^N \frac{\alpha_j i\omega \hat{E}_0 e^{i\omega R/c}}{(1 - i\omega/\omega_C)^{1/2} (1 + (\omega/\omega_{CF,j})^2)^{3/2}} \quad (50)$$

Making the same approximations leading up to Eq. (46), and exchanging the order of summation and integration, yields

$$\begin{aligned} \frac{R\mathbf{E}(t_r, \theta_C)}{[V]} &\approx \sum_{j=0}^N \alpha_j \frac{i\omega_C \omega_{0,j}^2}{\pi} \hat{E}_0 \frac{d}{dt_r} \oint d\omega \\ &\quad e^{-it_r\omega} \\ &\quad \frac{(\omega + 2i\omega_C)(\omega + i\omega_{0,j})(\omega - i\omega_{0,j})}{(51)} \end{aligned}$$

Thus, accounting for wider lateral scales in the ICD (here in the far-field case) amounts to adding more poles in the complex- ω plane. The problem mirrors the addition of complex poles to digital filters to achieve a desired filter impulse response. The summation terms of Eq. (51) are equal to Eq. (47), with the substitution $\omega_0 \rightarrow \omega_{0,j}$:

$$\begin{aligned} \frac{R\mathbf{E}(t_r, \theta_C)}{[V]} \\ \approx \sum_{j=0}^N \alpha_j \frac{\hat{E}_0 \omega_{0,j}^2}{2} \begin{cases} (1 - \frac{1}{2} \frac{\omega_{0,j}}{\omega_C}) \exp(\omega_{0,j} t_r) & t_r \leq 0 \\ -\exp(-\omega_{0,j} t_r) + 2 \exp(-2\omega_C t_r) & t_r > 0 \end{cases} \quad (52) \end{aligned}$$

The pair of poles in Eq. (45) from the form factor \tilde{F} follow from fitting the ρ' -component of the ICD with a single exponential function. The next-most complex case is to fit the ICD ρ' -component with two exponentials ($N = 1$ in Eq. (52), with $\Delta_{0,j} = 2\omega_C - \omega_{0,j}$):

$$\begin{aligned} \frac{R\mathbf{E}(t_r, \theta_C)}{[V]} \\ \approx \begin{cases} \hat{E}_0 (\alpha_0 \omega_{0,0} \epsilon_0 \Delta_{0,0} e^{\omega_{0,0} t_r} + \alpha_1 \omega_{0,1} \epsilon_1 \Delta_{0,0} e^{\omega_{0,1} t_r}) & t_r \leq 0 \\ \hat{E}_0 e^{-2\omega_C t_r} (\alpha_0 \omega_{0,0}^2 (1 - \frac{1}{2} e^{-\Delta_{0,0} t_r}) + \alpha_1 \omega_{0,1}^2 (1 - \frac{1}{2} e^{-\Delta_{0,1} t_r})) & t_r > 0 \end{cases} \quad (53) \end{aligned}$$

5. Summary

The Askaryan fields for a UHE- ν induced cascade have been presented, accounting for LPM elongation, and the 3D ICD of the cascade. The calculations are analytic, and the associated code encapsulates them into a model that is computationally efficient and in agreement with prior studies. The entire field in both \hat{e}_r and \hat{e}_θ components is computed in the code, for any set of initial conditions chosen by users. The cascade model was verified with Geant4, and the 3D MC cascade structure formed the shape of the 3D ICD model. Evaluating the spatial Fourier transform of the 3D ICD yielded the form factor, $\tilde{F}(\omega, \theta)$. The effects of $\tilde{F}(\omega, \theta)$ and LPM elongation were explored mathematically and graphically. Table 1 contains brief summary of the results and tools presented in this work.

The effect of LPM elongation was modelled as an energy-dependent increase in the longitudinal cascade width, a . LPM elongation is found to modify low-frequency emission, to suppress high-frequency emission, and to narrow the Cherenkov cone under far-field conditions. $\tilde{F}(\omega)$ is similar to a two-pole, low-pass filter, with the limiting frequency determined by cascade Molière radius and viewing angle θ . The θ -dependence in the form of $\tilde{F}(\omega, \theta)$ implies that the filtered radiation depends on the laterally-projected

Table 1
A summary of new results.

Effect	Eq./Fig.	Sec.
Cascade Form Factor, $\tilde{F}(\omega, \theta)$, single-pole	Eq. (26)	Section 3.4.2
Cascade Form Factor, $\tilde{F}(\omega, \theta)$, multi-pole	Eq. (32)	Section 3.4.3
Contours of complete model (RB+LPM+ $\tilde{F}(\omega, \theta)$) $\hat{e}_\theta \cdot \tilde{\mathbf{E}}(t, \theta)$	Fig. 3	Section 3.5
Contours of complete model (RB+LPM+ $\tilde{F}(\omega, \theta)$) $\hat{e}_r \cdot \tilde{\mathbf{E}}(t, \theta)$	Fig. 4	Section 3.5
Complete model (RB+LPM+ $\tilde{F}(\omega, \theta)$) $\hat{e}_\theta \cdot \tilde{\mathbf{E}}(\omega)$ comparison	Fig. 7	Section 3.6
Complete model (RB+LPM+ $\tilde{F}(\omega, \theta)$) $\hat{e}_\theta \cdot \tilde{\mathbf{E}}(\theta)$ comparison	Fig. 8	Section 3.6
$E(t, \theta_C), \tilde{F}(\omega, \theta) = 1, \eta < 1$	Eq. (41)	Section 4.1
$E(t, \theta_C), \tilde{F}(\omega, \theta) \neq 1, \eta < 1$, single-pole	Eq. (47)	Section 4.2
ω_{CF}/ω_C Figure of Merit	Eq. (49)	Section 4.2
$E(t, \theta_C), \tilde{F}(\omega, \theta) \neq 1, \eta < 1$, two-pole	Eq. (53)	Section 4.3

wavevector. Although these conclusions are in line with expectations, alternate scenarios were explored, yielding novel results (see Figs. 7 and 8). The field shows interesting causal structure that could serve as a discrimination technique between the distance R and the cascade energy, for *in situ* detectors such as ARA/ARIANNA (see Figs. 3 and 4).

Finally, time-domain field equations were derived by computing the inverse Fourier transform of the RB model. Future work will focus exclusively on the time domain, for viewing angles $\theta \neq \theta_C$, and expanded ranges of η and ω . Producing theoretical, time-dependent field equations under specific limits facilitates UHE- ν signal template generation by bypassing altogether the need for Askaryan RF code, provided the limits are satisfied. Rejecting thermal noise in the *in situ* Antarctic detectors, in favour of UHE- ν signals, is an exercise in the mathematical analysis of thermal fluctuations [55]. The associated code presented in this work has been made freely available to all researchers involved in discriminating cosmogenic UHE- ν pulses from thermal backgrounds.

Acknowledgements

We thank the NSF for the support received under the NSF CAREER award 1255557, and for support from the NSF award for the Askaryan Radio Array (Grant 1404266). We are grateful to the Ohio Supercomputing Center [56] for their staff support, training, and resources. Contributions were also received from The Ohio State University, the Center for Cosmology and Astroparticle Physics (CCAPP), and the United States-Israel Binational Science Foundation Grant 2012077. We thank John Ralston and Roman Buny for their helpful remarks regarding the mathematical physics. Also, special thanks are in order for John Beacom and Steve Barwick for practical advice.

Appendix A

A1. Causal features and poles of Askaryan Radiation

The complex pole-structure of the various models each demonstrate how the models treat the issue of causality. The E-field of ZHS, on-cone in Eq. (34) takes the form

$$\frac{R\mathbf{E}}{[V/\text{Hz}]} = -E_0 \omega_0^2 \frac{i\omega}{(\omega + i\omega_0)(\omega - i\omega_0)} \hat{e}_\theta \quad (54)$$

Figure 16 of ZHS shows that the E-field phase is $\sim 90^\circ$ below 1 GHz, or a phase factor of $\exp(i\pi/2) = i$. The overall minus sign in Eq. (54) is just a convention. Taking the inverse Fourier transform, the time-domain form of the field at the Cherenkov angle may be

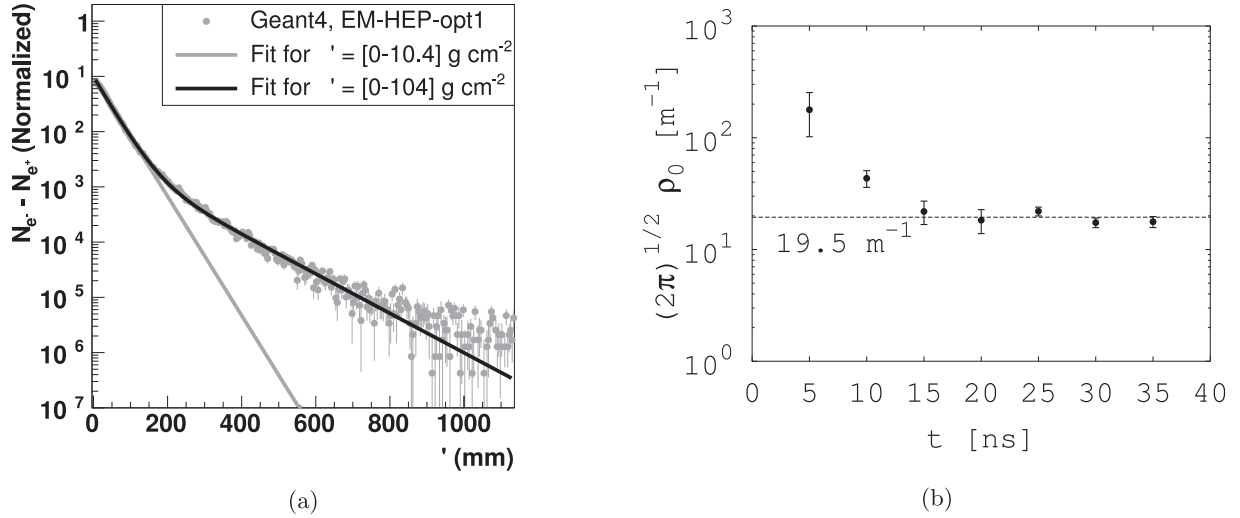


Fig. 11. (a) $N_{e^-} - N_{e^+}$, versus ρ' at 25 ns into a 100 PeV shower (gray points). A single-exponential model (gray line, Eq. (21) with slope $\sqrt{2\pi}\rho_0$ is fit for $\rho' < 10.4 \text{ g cm}^{-2}$. A double-exponential model (black line, Eq. (28)) is fit for $\rho' < 104 \text{ g cm}^{-2}$. (b) Fit results for the parameter $\sqrt{2\pi}\rho_0$ vs. time within the shower, using Eq. (21). The dashed line is the average of the points between 15–35 ns.

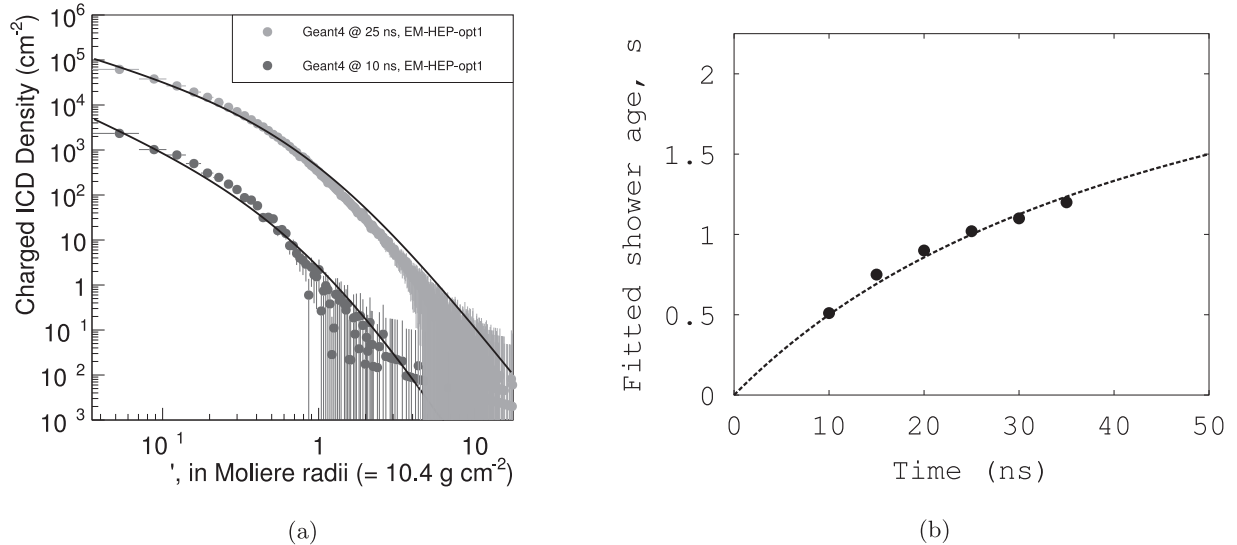


Fig. 12. (a) The charged ICD density, at 10 ns and 25 ns after the first interaction. The solid lines are fits of Eq. (19) to the points with the shower age, s , as free parameter. (b) The fitted shower age, s , versus time since first interaction. The dashed line is the theoretical expectation.

written

$$\frac{RE(t)}{|V|} = \omega_0^2 E_0 \frac{d}{dt} \int_{-\infty}^{\infty} \frac{e^{-i\omega t}}{(\omega + i\omega_0)(\omega - i\omega_0)} d\omega \quad (55)$$

The integral converges via Jordan's lemma if the contour is the infinite upper semi-circle for $t < 0$, and, for $t > 0$, the infinite lower semi-circle. There is an overall minus sign from the clockwise contour. The result is

$$\frac{RE(t)}{|V|} = \omega_0^2 E_0 \hat{e}_\theta \begin{cases} \exp(\omega_0 t) & t \leq 0 \\ -\exp(-\omega_0 t) & t > 0 \end{cases} \quad (56)$$

The existence poles above and below the real line is deemed a causality violation by RB. Physically, the field changes overall sign when the angular acceleration of the charge relative to the observer changes sign. Feynman's formula [30] states that the field from an accelerating charge goes like $\mathbf{E} \propto \text{sgn}(1 - \hat{n} \cdot \vec{\beta}) \hat{u} \times \vec{\theta}$, where $\vec{\beta}$ is the velocity of the charge, and \hat{u} is a unit vector at the charge location in the direction of the observer. \mathbf{E} changes sign as the charge crosses the plane in which R is minimized. The quan-

tit $\vec{\theta}$ increases rapidly, until the plane crossing, after which it decreases rapidly.

From Eq. (55) $\tilde{F}_{ZHS}(\omega) \propto (\omega + i\omega_0)^{-1} (\omega - i\omega_0)^{-1}$. Treating $t > 0$ and $t < 0$ separately, the inverse Fourier transform of $\tilde{F}_{ZHS}(\omega)$ with respect to the coordinate ρ' yields $f(\mathbf{x}') \propto \exp(-\rho')$. Therefore, a logical inference is that the full, 3D ICD responsible for $\tilde{F}(\omega, \theta)$ is distributed exponentially. Geant4 simulations show this to be correct in Section A.2.

A2. Numerical study of the excess charge distribution

Geant4 [57,58] is used to derive numbers for $\sqrt{2\pi}\rho_0$, and those results are checked with Eqs. (17)–(19). Refs. [49–51] are other works that used GEANT/Pythia to calculate Askaryan radiation properties. The GEANT4 high-energy electromagnetic option-1 physics list was used, with a MC threshold of 1 MeV, e^\pm primaries, and ice of density 0.917 g/cm^3 and at a temperature of 240 K. Although the LPM effect is important primarily for electro-

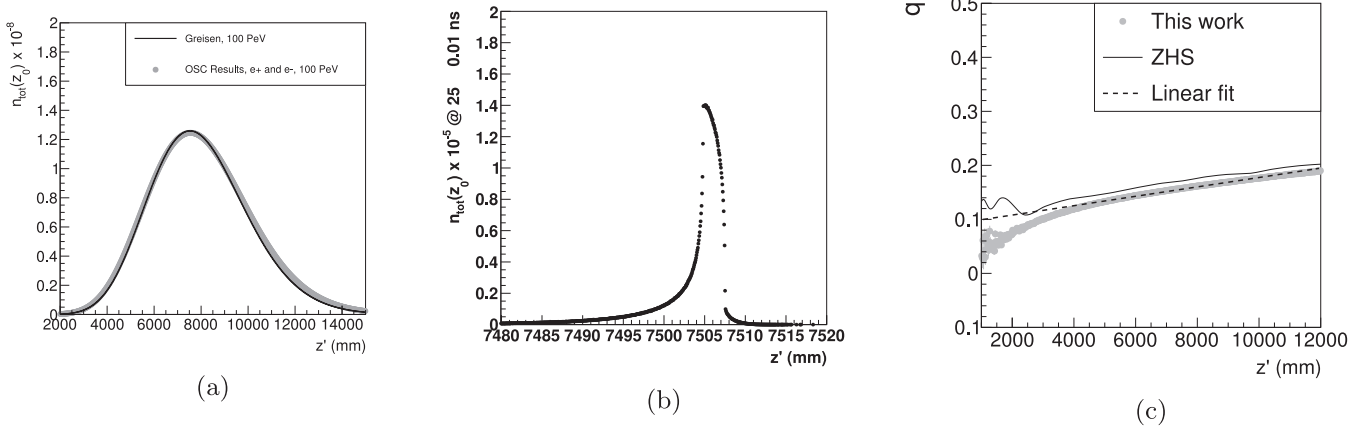


Fig. 13. (a) $n_{\text{tot}}(z')$ versus z' , for a 100 PeV cascade. (b) The ICD at 25 ± 0.01 ns after the first interaction. (c) The fractional negative charge excess of a 100 PeV shower, with a 5 MeV MC threshold from Geant4. The solid line is the ZHS result with a 5 MeV MC threshold, and the dashed line is a linear fit to the OSC results.

magnetic cascades, $\tilde{F}(\omega, \theta)$ does not depend on a , so it is also valid for hadronic cascades.

CPU memory constraints forbid accounting for all tracks, so a pre-shower/sub-shower approach is taken to access more memory. A pre-shower drops all particles with energy below 0.1 PeV. The trajectory, position and type of the pre-shower particles generated by the primary are recorded and sent to separate CPUs. Each particle in the pre-shower then becomes an independent cascade, with a second MC threshold of 1 MeV.

The lateral ICD is shown in Fig. 11 (a). The results follow $\propto \exp(-\sqrt{2\pi}\rho_0\rho')$ in the range $\rho' = [0, \rho_1/d_{\text{ice}}]$ (0–113 mm in ice, with $\rho_1 = 10.4 \text{ g cm}^{-3}$ and $d_{\text{ice}} = 0.917 \text{ g cm}^{-3}$). The gray data corresponds to Geant4 tracks inside a 100 PeV cascade, 25 ± 0.01 ns from the beginning of the first Geant4 interaction. The single exponential (single-pole) fit diverges when $\rho' > \rho_1$, however a double exponential (two-pole) model, comprised of a sum of exponential functions, fits the data for $\rho' > \rho_1$.

The results for $\sqrt{2\pi}\rho_0$ are shown in Fig. 11 (b), averaged over 10 cascades with $E_C = 100$ PeV. Each point contains tracks existing within 10 ps of the time on the x-axis. Early in the cascade, the particles have not yet diffused laterally, implying a higher value of $\sqrt{2\pi}\rho_0$. The dashed horizontal line represents the average between 15–35 ns, when lateral diffusion saturates.

The ICD per unit area, vs. Molière radius, is shown in Fig. 12 (a), plotted along with Eq. (19). Fig. 12 (b) shows the fitted shower age s as a function of time after the first interaction. Eq. (19) was fit to the MC data sets at each time bin, with s as a free parameter. The results match the definition of s , from which the gray dashed line in Fig. 12 is derived.

Fig. 13(a) matches Eq. (17) to MC data, neglecting photons, with a 1 MeV MC threshold. The Gaussian form is evident [59], justifying the RB saddle-point expansion. The ICD as a function of z' is shown in Fig. 13b. The width of $f(x')$ versus z' is proportional to the width of the time-window (10 ps), justifying its approximation as a δ -function in $f(x')$.

The parameter n_{max} in RB is the number of excess negative charges. The fractional excess charge is $\Delta q = (N_{e^-} - N_{e^+})/(N_{e^-} + N_{e^+})$, so $n_{\text{max}} = N\Delta q$. The MC shows that Δq is linear with depth. The y-intercept is sensitive to the MC threshold, but the slope is not. The associated code includes the linear dependence of Δq on depth by sampling the linear fit at z_{max} . Fig. 13(c) shows Δq and that of ZHS.

References

- [1] M.G. Aartsen, et al., First observation of PeV-energy neutrinos with icecube, Phys. Rev. Lett. 111 (2013) 021103, doi:[10.1103/PhysRevLett.111.021103](https://doi.org/10.1103/PhysRevLett.111.021103).
- [2] O.E. Kalashev, V.A. Kuzmin, D.V. Semikoz, G. Sigl, Ultrahigh-energy neutrino fluxes and their constraints, Phys. Rev. D 66 (2002) 063004, doi:[10.1103/PhysRevD.66.063004](https://doi.org/10.1103/PhysRevD.66.063004).
- [3] K. Kotera, D. Allard, A. Olinto, Cosmogenic neutrinos: parameter space and detectability from PeV to ZeV, J. Cosmol. Astropart. Phys. 2010 (10) (2010) 013.
- [4] J.G. Learned, K. Manheim, High-energy neutrino astrophysics, Nucl. Part. Sci. 50 (2000) 679–749, doi:[10.1146/annurev.nucl.50.1.679](https://doi.org/10.1146/annurev.nucl.50.1.679).
- [5] K. Greisen, End to the cosmic-ray spectrum? Phys. Rev. Lett. 16 (1966) 748–750, doi:[10.1103/PhysRevLett.16.748](https://doi.org/10.1103/PhysRevLett.16.748).
- [6] G. Zatsepin, V. Kuzmin, Phys. Lett. B 8 (1969) 423.
- [7] E. Waxman, J. Bahcall, High energy neutrinos from astrophysical sources: an upper bound, Phys. Rev. D 59 (1998) 023002, doi:[10.1103/PhysRevD.59.023002](https://doi.org/10.1103/PhysRevD.59.023002).
- [8] R. Engel, D. Seckel, T. Stanev, Neutrinos from propagation of ultrahigh energy protons, Phys. Rev. D 64 (2001) 093010, doi:[10.1103/PhysRevD.64.093010](https://doi.org/10.1103/PhysRevD.64.093010).
- [9] K. Murase, M. Ahlers, B.C. Lacki, Testing the hadronuclear origin of PeV neutrinos observed with icecube, Phys. Rev. D 88 (2013) 121301, doi:[10.1103/PhysRevD.88.121301](https://doi.org/10.1103/PhysRevD.88.121301).
- [10] J.C. Joshi, W. Winter, N. Gupta, How many of the observed neutrino events can be described by cosmic ray interactions in the Milky Way? Mon. Not. R. Astron. Soc. 439 (4) (2014) 3414–3419, doi:[10.1093/mnras/stu189](https://doi.org/10.1093/mnras/stu189).
- [11] A. Connolly, R.S. Thorne, D. Waters, Calculation of high energy neutrino-nucleon cross sections and uncertainties using the Martin-Stirling-Thorne-Watt parton distribution functions and implications for future experiments, Phys. Rev. D 83 (2011) 113009, doi:[10.1103/PhysRevD.83.113009](https://doi.org/10.1103/PhysRevD.83.113009).
- [12] P.W. Gorham, A. Connolly, Implications of ultrahigh energy neutrino flux constraints for Lorentz-invariance violating cosmogenic neutrinos, Phys. Rev. D 86 (2012) 103006, doi:[10.1103/PhysRevD.86.103006](https://doi.org/10.1103/PhysRevD.86.103006).
- [13] M. Ahlers, L. Anchordoqui, M. Gonzalez Garcia, F. Halzen, S. Sarkar, GZK neutrinos after the Fermi-LAT diffuse photon flux measurement, Astropart. Phys. 34 (2) (2010) 106–115. <http://dx.doi.org/10.1016/j.astropartphys.2010.06.003>.
- [14] K. Murase, D. Guetta, M. Ahlers, Hidden cosmic-ray accelerators as an origin of TeV-PeV cosmic neutrinos, Phys. Rev. Lett. 116 (2016) 071101, doi:[10.1103/PhysRevLett.116.071101](https://doi.org/10.1103/PhysRevLett.116.071101).
- [15] G. Askaryan, Excess negative charge of electron-Photon shower and the coherent radiation originating from it. Radiorecording of showers under the ground and on the Moon, J. Phys. Soc. Jpn. 17 (Suppl A) (1962).
- [16] D. Saltzberg, et al., Observation of the Askaryan effect: coherent microwave Cherenkov emission from charge asymmetry in high-Energy particle cascades, Phys. Rev. Lett. 86 (2001) 2802–2805, doi:[10.1103/PhysRevLett.86.2802](https://doi.org/10.1103/PhysRevLett.86.2802).
- [17] P.W. Gorham, et al., Observations of the Askaryan effect in ice, Phys. Rev. Lett. 99 (2007) 171101, doi:[10.1103/PhysRevLett.99.171101](https://doi.org/10.1103/PhysRevLett.99.171101).
- [18] J.C. Hanson, Ross ice shelf thickness, radio-frequency attenuation and reflectivity: implications for the ARIANNA UHE neutrino detector, in: International Cosmic Ray Conference, 4, 2011, p. 169, doi:[10.7529/ICRC2011/V04/0340](https://doi.org/10.7529/ICRC2011/V04/0340).
- [19] J.C. Hanson, Radar absorption, basal reflection, thickness and polarization measurements from the Ross ice shelf, Antarctica, J. Glaciol. 61 (227) (2015) 438–446.
- [20] D. Besson, et al., In situ radioglaciological measurements near Taylor Dome, Antarctica and implications for Ultra-High Energy (UHE) neutrino astronomy, Astropart. Phys. 29 (2) (2008) 130–157. <http://dx.doi.org/10.1016/j.astropartphys.2007.12.004>.
- [21] I. Kravchenko, S. Hussain, D. Seckel, D. Besson, E. Fensterholz, J. Ralston, J. Taylor, K. Ratzlaff, R. Young, Updated results from the RICE experiment and future prospects for ultra-high energy neutrino detection at the South Pole, Phys. Rev. D 85 (2012) 062004, doi:[10.1103/PhysRevD.85.062004](https://doi.org/10.1103/PhysRevD.85.062004).
- [22] P.W. Gorham, et al., Observational constraints on the ultrahigh energy cosmic neutrino flux from the second flight of the ANITA experiment, Phys. Rev. D 82 (2010) 022004, doi:[10.1103/PhysRevD.82.022004](https://doi.org/10.1103/PhysRevD.82.022004).

- [23] P. Gorham, et al., The antarctic impulsive transient antenna ultra-high energy neutrino detector: design, performance, and sensitivity for the 20062007 balloon flight, *Astropart. Phys.* 32 (1) (2009) 10–41. <http://dx.doi.org/10.1016/j.astropartphys.2009.05.003>.
- [24] S. Barwick, et al., A first search for cosmogenic neutrinos with the ARIANNA hexagonal radio array, *Astropart. Phys.* 70 (2015a) 12–26. <http://dx.doi.org/10.1016/j.astropartphys.2015.04.002>.
- [25] S. Barwick, et al., Time-domain response of the ARIANNA detector, *Astropart. Phys.* 62 (2015b) 139–151. <http://dx.doi.org/10.1016/j.astropartphys.2014.09.002>.
- [26] S.W. Barwick, E.C. Berg, D.Z. Besson, T. Duffin, J.C. Hanson, S.R. Klein, S.A. Kleinfelder, K. Ratzlaff, C. Reed, M. Roumi, T. Stezelberger, J. Tatar, J. Walker, R. Young, L. Zou, Design and performance of the ARIANNA HRA-3 neutrino detector systems, *IEEE Trans. Nucl. Sci.* 62 (5) (2015c) 2202–2215, doi:10.1109/TNS.2015.2468182.
- [27] P. Allison, et al., First constraints on the ultra-high energy neutrino flux from a prototype station of the Askaryan radio array, *Astroparticle Physics* 70 (2015) 62–80. <http://dx.doi.org/10.1016/j.astropartphys.2015.04.006>.
- [28] P. Allison, et al., Design and initial performance of the Askaryan radio array prototype EeV neutrino detector at the South Pole, *Astropart. Phys.* 35 (7) (2012) 457–477. <http://dx.doi.org/10.1016/j.astropartphys.2011.11.010>.
- [29] P. Gorham, F. Baginski, P. Allison, K. Liewer, C. Miki, B. Hill, G. Varner, The ExaVolt antenna: a large-aperture, balloon-embedded antenna for ultra-high energy particle detection, *Astropart. Phys.* 35 (5) (2011) 242–256. <http://dx.doi.org/10.1016/j.astropartphys.2011.08.004>.
- [30] E. Zas, F. Halzen, T. Stanev, Electromagnetic pulses from high-energy showers: implications for neutrino detection, *Phys. Rev. D* 45 (1992) 362–376, doi:10.1103/PhysRevD.45.362.
- [31] J. Alvarez-Muniz, R.A. Vazquez, E. Zas, Characterization of neutrino signals with radiopulses in dense media through the Landau-Pomeranchuk-Migdal effect, *Phys. Rev. D* 61 (1999) 023001, doi:10.1103/PhysRevD.61.023001.
- [32] J. Alvarez-Muñiz, A. Romero-Wolf, E. Zas, Practical and accurate calculations of Askaryan radiation, *Phys. Rev. D* 84 (2011) 103003, doi:10.1103/PhysRevD.84.103003.
- [33] J. Alvarez-Muñiz, A. Romero-Wolf, E. Zas, Čerenkov radio pulses from electromagnetic showers in the time domain, *Phys. Rev. D* 81 (2010) 123009, doi:10.1103/PhysRevD.81.123009.
- [34] E. Hong, *Searching for Ultra-high Energy Neutrinos with Data from a Prototype Station of the Askaryan Radio Array, The Ohio State University, 2014 Ph.D. thesis*.
- [35] R.V. Buniy, J.P. Ralston, Radio detection of high energy particles: coherence versus multiple scales, *Phys. Rev. D* 65 (2001) 016003, doi:10.1103/PhysRevD.65.016003.
- [36] K. Greisen, Progress in cosmic ray physics. J. G. Wilson, ed. Amsterdam: North-Holland Pub.; New York: Interscience, 1952. 557 pp., *Science* 115 (2990) (1952) 426–427, doi:10.1126/science.115.2990.426-a.
- [37] P. Allison, Performance of two Askaryan radio array stations and first results in the search for ultrahigh energy neutrinos, *Phys. Rev. D* 93 (2016) 082003, doi:10.1103/PhysRevD.93.082003.
- [38] S.W. Barwick, Radio detection of air showers with the ARIANNA experiment on the Ross ice shelf, *Astropart. Phys.* 90 (2017) 50–68. <http://dx.doi.org/10.1016/j.astropartphys.2017.02.003>.
- [39] B.P. Abbott, et al., Observation of gravitational waves from a binary black hole merger, *Phys. Rev. Lett.* 116 (2016) 061102, doi:10.1103/PhysRevLett.116.061102.
- [40] V.V. Bogorodsky, C.R. Bentley, P.E. Gudmandsen, *Radioglaciology*, D. Reidel Publishing Co., 1985.
- [41] S. Klein, Suppression of Bremsstrahlung and pair production due to environmental factors, *Rev. Mod. Phys.* 71 (1999) 1501–1538, doi:10.1103/RevModPhys.71.1501.
- [42] L. Gerhardt, S. Klein, Electron and photon interactions in the regime of strong Landau-Pomeranchuk-Migdal suppression, *Phys. Rev. D* 82 (7) (2010), doi:10.1103/physrevd.82.074017.
- [43] A. Cillis, H. Fanchiotti, G.C. Canal, S. Sciutto, Influence of the LPM effect and dielectric suppression on particle air showers, *Phys. Rev. D* 59 (11) (1999) 113012, doi:10.1103/PhysRevD.59.113012.
- [44] J. Alvarez-Muiz, E. Zas, The LPM effect for EeV hadronic showers in ice: implications for radio detection of neutrinos, *Phys. Lett. B* 434 (34) (1998) 396–406. [http://dx.doi.org/10.1016/S0370-2693\(98\)00905-8](http://dx.doi.org/10.1016/S0370-2693(98)00905-8).
- [45] C.-Y. Hu, C.-C. Chen, P. Chen, Near-field effects of Cherenkov radiation induced by ultra-high energy cosmic neutrinos, *Astropart. Phys.* 35 (7) (2012) 421–434, doi:10.1016/j.astropartphys.2011.11.008.
- [46] T. Gaisser, A. Hillas, Reliability of the method of constant intensity cuts for reconstructing the average development of vertical showers, in: *Proceedings of the 15th International Cosmic Ray Conference*, 8, 1977.
- [47] G. Daniel, A. Jaime, W.R. Carvalho, R. Andrés, E. Zas, Calculations of electric fields for radio detection of ultra-high energy particles, *Phys. Rev. D* 87 (023003) (2012), doi:10.1103/physrevd.87.023003.
- [48] Chia Yu-Hu, Chih-Ching Chen, Pisin Chen, Near-field effects of Cherenkov radiation induced by ultra high energy cosmic neutrinos, *Astropart. Phys.* 35 (2012) 421–434, doi:10.1016/j.astropartphys.2011.11.008.
- [49] S. Razzaque, Coherent radio pulses from GEANT generated electromagnetic showers in ice, *Phys. Rev. D* 65 (103002) (2002), doi:10.1103/PhysRevD.65.103002.
- [50] J. Alvarez-Muniz, Comparative study of electromagnetic shower track lengths in water and implications for Čerenkov radio emission, *Phys. Rev. D* 68 (043001) (2003), doi:10.1103/PhysRevD.68.043001.
- [51] D. McKay, S. Hussain, Comparative study of radio pulses from simulated hadron-, electron-, and neutrino-initiated showers in ice in the GeV-PeV range, *Phys. Rev. D* 70 (103003) (2004), doi:10.1103/PhysRevD.70.103003.
- [52] K. Dookayka, *Characterizing the Search for Ultra-High Energy Neutrinos with the ARIANNA Detector*, The University of California, Irvine, 2011 Ph.D. thesis.
- [53] J.C. Hanson, *The Performance and Initial Results of the ARIANNA Prototype*, The University of California, Irvine, 2013 Ph.D. thesis.
- [54] P. Miočinović, et al., Time-domain measurement of broadband coherent Čerenkov radiation, *Phys. Rev. D* 74 (2006) 043002, doi:10.1103/PhysRevD.74.043002.
- [55] S.O. Rice, Mathematical analysis of random noise, *Bell Syst. Tech. J.* 23 (3) (1944) 282–332, doi:10.1002/j.1538-7305.1944.tb00874.x.
- [56] OSC, Ohio supercomputer center, 1987, (<http://osc.edu/ark:/19495/f5s1ph73>).
- [57] S. Agostinelli, et al., Geant4 a simulation toolkit, *Nucl. Instrum. Methods Phys. Res. Sect. A* 506 (3) (2003) 250–303. [http://dx.doi.org/10.1016/S0168-9002\(03\)01368-8](http://dx.doi.org/10.1016/S0168-9002(03)01368-8).
- [58] J. Allison, et al., *Geant4 developments and applications*, *IEEE Trans. Nucl. Sci.* 53 (1) (2006) 270–278.
- [59] B. Rossi, *High-Energy Particles*, NJ, 1952.

Radio detection of air showers with the ARIANNA experiment on the Ross Ice Shelf

S. W. Barwick^a, D. Z. Besson^{b,c}, A. Burgman^d, E. Chiem^e, A. Hallgren^d, J. C. Hanson^f, S. R. Klein^{g,h}, S. A. Kleinfelder^e, A. Nelles^{a,*}, C. Persichilli^a, S. Phillips^a, T. Prakash^e, C. Reed^a, S. R. Shively^a, J. Tatar^{a,i}, E. Unger^d, J. Walker^a, G. Yodh^a

^a*Dept. of Physics and Astronomy, University of California, Irvine, USA*

^b*Dept. of Physics and Astronomy, University of Kansas, USA*

^c*National Research Nuclear University MEPhI (Moscow Engineering Physics Institute) 115409, Moscow, Russia*

^d*Dept. of Physics and Astronomy, Uppsala University, Sweden*

^e*Dept. of Electrical Engineering and Computer Science, University of California, Irvine, USA*

^f*Center for Cosmology and Astro-Particle Physics (CCAPP), Dept. of Physics, Ohio State University, USA*

^g*Lawrence Berkeley National Laboratory, USA*

^h*Dept. of Physics, University of California, Berkeley, USA*

ⁱ*Office of Information Technology, Research Computing, University of California, Irvine, USA*

Abstract

The ARIANNA hexagonal radio array (HRA) is an experiment in its pilot phase designed to detect cosmogenic neutrinos of energies above 10^{16} eV. The most neutrino-like background stems from the radio emission of air showers. This article reports on dedicated efforts of simulating and detecting the signals of cosmic rays. A description of the fully radio self-triggered data-set, the properties of the detected air shower signals in the frequency range of 100-500 MHz and the consequences for neutrino detection are given. 38 air shower signals are identified by their distinct waveform characteristics, are in good agreement with simulations and their signals provide evidence that neutrino-induced radio signals will be distinguishable with high efficiency in ARIANNA. The cosmic ray flux at a mean energy of $6.5_{-1.0}^{+1.2} \times 10^{17}$ eV is measured to be $1.1_{-0.7}^{+1.0} \times 10^{-16}$ eV $^{-1}$ km $^{-2}$ sr $^{-1}$ yr $^{-1}$ and one five-fold coincident event is used to illustrate the capabilities of the ARIANNA detector to reconstruct arrival direction and energy of air showers.

Keywords: Cosmic rays, Neutrinos, Radio emission

98.70.Sa, 95.85.Ry, 95.55.Vj, 95.55.Jz

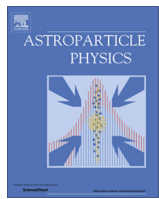
1. Introduction

The ARIANNA experiment (Antarctic Ross Ice shelf ANtenna Neutrino Array) is a surface array of radio antennas designed to detect cosmogenic neutrinos [1]. Currently in its pilot phase the hexagonal radio array (HRA) [2], the experiment has been taking data since 2014.

ARIANNA is aimed at detecting the radio emission of neutrino induced showers in ice. The radio emission is caused by the changing charge imbalance that is created in the shower front as it accumulates electrons from the medium and shower positrons are annihilated [3]. While test-beam experiments have shown that radio emission is indeed created in a shower [4], the first measurement of the radio emission due to a neutrino is still being awaited.

Considerable progress has been made in the last years in radio detection of air showers (see [5] for a review). Radio emissions of air showers are now routinely measured at various experiments, such as AERA [6], LOFAR [7] and Tunka-Rex [8] in coincidence with particle arrays or optical methods such as Fluorescence or Cherenkov detectors. Detections have also been reported from the balloon-based experiment ANITA [9].

*Corresponding author: anelles@uci.edu



A first search for cosmogenic neutrinos with the ARIANNA Hexagonal Radio Array



S.W. Barwick^a, E.C. Berg^a, D.Z. Besson^{c,g}, G. Binder^{e,f}, W.R. Binns^m, D.J. Boersma^j, R.G. Bose^m, D.L. Braun^m, J.H. Buckley^m, V. Bugaev^m, S. Buitink^k, K. Dookayka^a, P.F. Dowkontt^m, T. Duffin^a, S. Euler^j, L. Gerhardt^e, L. Gustafsson^j, A. Hallgren^j, J.C. Hanson^{c,a}, M.H. Israel^m, J. Kirylukⁱ, S.R. Klein^{e,f}, S. Kleinfelder^b, H. Niederhausenⁱ, M.A. Olevitch^m, C. Persichelli^a, K. Ratzlaff^d, B.F. Rauch^m, C. Reed^{a,*}, M. Roumi^b, A. Samanta^b, G.E. Simburger^m, T. Stezelberger^e, J. Tatar^{a,h,*}, U.I. Uggerhoj^l, J. Walker^a, G. Yodh^a, R. Young^d, ARIANNA Collaboration

^a Dept. of Physics and Astronomy, University of California, Irvine, USA

^b Dept. of Electrical Engineering and Computer Science, University of California, Irvine, USA

^c Dept. of Physics and Astronomy, University of Kansas, USA

^d Instrumentation Design Lab, University of Kansas, USA

^e Lawrence Berkeley National Laboratory, USA

^f Dept. of Physics, University of California, Berkeley, USA

^g Moscow Engineering and Physics Institute, Russia

^h Center for Experimental Nuclear Physics and Astrophysics, University of Washington, USA

ⁱ Dept. of Physics and Astronomy, Stony Brook University, USA

^j Dept. of Physics and Astronomy, University of Uppsala, Sweden

^k IMAPP, Radboud University of Nijmegen, The Netherlands

^l Dept. of Physics and Astronomy, Aarhus University, Denmark

^m Dept. of Physics and McDonnell Center for the Space Sciences, Washington University, St. Louis, USA

ARTICLE INFO

Article history:

Received 4 November 2014

Received in revised form 20 March 2015

Accepted 6 April 2015

Available online 13 April 2015

Keywords:

Radio

Antarctica

Neutrino

Cosmogenic

GZK

High energy

ABSTRACT

The ARIANNA experiment seeks to observe the diffuse flux of neutrinos in the 10^8 – 10^{10} GeV energy range using a grid of radio detectors at the surface of the Ross Ice Shelf of Antarctica. The detector measures the coherent Cherenkov radiation produced at radio frequencies, from about 100 MHz–1 GHz, by charged particle showers generated by neutrino interactions in the ice. The ARIANNA Hexagonal Radio Array (HRA) is being constructed as a prototype for the full array. During the 2013–14 austral summer, three HRA stations collected radio data which was wirelessly transmitted off site in nearly real-time. The performance of these stations is described and a simple analysis to search for neutrino signals is presented. The analysis employs a set of three cuts that reject background triggers while preserving 90% of simulated cosmogenic neutrino triggers. No neutrino candidates are found in the data and a model-independent 90% confidence level Neyman upper limit is placed on the all flavor $\nu + \bar{\nu}$ flux in a sliding decade-wide energy bin. The limit reaches a minimum of 1.9×10^{-23} GeV $^{-1}$ cm $^{-2}$ s $^{-1}$ sr $^{-1}$ in the $10^{8.5}$ – $10^{9.5}$ GeV energy bin. Simulations of the performance of the full detector are also described. The sensitivity of the full ARIANNA experiment is presented and compared with current neutrino flux models.

© 2015 Elsevier B.V. All rights reserved.

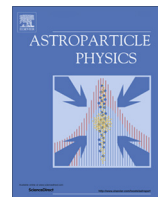
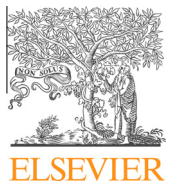
1. Introduction

While the flux of cosmic rays has been measured to energies greater than 10^{10} GeV [1], the sources of such high energy particles

remain a mystery. No known galactic source could accelerate particles to such energies, and no particular sources of the very highest energy particles, with large rigidities, have been found [2–5]. Potential sources of such ultra-high energy (UHE) cosmic rays are limited to our local supercluster (within about 50 Mpc) due to their interaction with the cosmic microwave background (CMB) [6,7]. The mesons produced by this process promptly decay to leptons, leading to a flux of UHE neutrinos [8–10].

* Corresponding authors at: Dept. of Physics and Astronomy, University of California, Irvine, USA (C. Reed, J. Tatar).

E-mail addresses: cjreed@uci.edu (C. Reed), jtatar@uci.edu (J. Tatar).



Time-domain response of the ARIANNA detector

S.W. Barwick^a, E.C. Berg^a, D.Z. Besson^{b,f}, T. Duffin^a, J.C. Hanson^{a,b,*}, S.R. Klein^d, S.A. Kleinfelder^c, M. Piasecki^e, K. Ratzlaff^e, C. Reed^a, M. Roumi^c, T. Stezelberger^d, J. Tatar^{a,g}, J. Walker^a, R. Young^e, L. Zou^c

^aDept. of Physics and Astronomy, University of California, Irvine, United States

^bDept. of Physics and Astronomy, University of Kansas, United States

^cDept. of Electrical Engineering and Computer Science, University of California, Irvine, United States

^dLawrence Berkeley National Laboratory, United States

^eInstrumentation Design Lab, University of Kansas, United States

^fMoscow Physics and Engineering Institute, United States

^gDept. of Physics, University of Washington, United States

ARTICLE INFO

Article history:

Received 5 June 2014

Received in revised form 26 August 2014

Accepted 9 September 2014

Available online xxxx

Keywords:

GZK neutrinos

Askaryan effect

Radio detector

ABSTRACT

The Antarctic Ross Ice Shelf Antenna Neutrino Array (ARIANNA) is a high-energy neutrino detector designed to record the Askaryan electric field signature of cosmogenic neutrino interactions in ice. To understand the inherent radio-frequency (RF) neutrino signature, the time-domain response of the ARIANNA RF receiver must be measured. ARIANNA uses Create CLP5130-2N log-periodic dipole arrays (LPDAs). The associated *effective height* operator converts incident electric fields to voltage waveforms at the LDPA terminals. The effective height versus time and incident angle was measured, along with the associated response of the ARIANNA RF amplifier. The results are verified by correlating to field measurements in air and ice, using oscilloscopes. Finally, theoretical models for the Askaryan electric field are combined with the detector response to predict the neutrino signature.

© 2014 Published by Elsevier B.V.

1. Introduction and theory

The origin of ultra-high energy cosmic rays (UHECRs) is an enduring mystery in astrophysics. Because cosmic-rays with energies above 4×10^{19} eV interact with the cosmic microwave background radiation, they have a limited range, so terrestrial cosmic-ray detectors can only probe UHECR sources within ≈ 75 Mpc. In these interactions, cosmic-ray protons are excited to a Δ^+ resonance; when the Δ^+ decays, it produces neutrinos with energies in the range of 10^{17} – 10^{20} eV [1–3]. These neutrinos can be used to probe UHECR sources at cosmic distances.

ARIANNA is designed to detect these neutrinos [4], by observing the coherent radio Cerenkov emission produced when UHE neutrinos interact in Antarctic ice. ARIANNA is located in Moore's Bay on the Ross Ice Shelf, about 100 miles south of McMurdo station. There, the ice is about 570 m thick [5,6], with the Ross Sea beneath it. ARIANNA is placed in Moore's Bay because aerial radar surveys show that the ice-water interface there is smooth and undisturbed, enabling clean reflections of downward-going radio waves off of the interface [7].

High energy particle cascades in ice contain an excess of negatively charged particles (mostly electrons), and radiates coherently at wavelengths that are large compared with the transverse size of the cascade [8]. For a cascade containing 10^{11} particles, the RF radiation is greatly enhanced. When observed along the Cerenkov cone, the radio signal grows linearly with frequency, up to a cutoff given by the size of the negative charge excess – about 1 GHz in ice. Away from the cone, the cutoff frequency is lower; one can use the observed spectrum to determine how far the detector is from the Cerenkov cone.

A number of experiments have used the Askaryan effect to search for cosmogenic neutrinos. One of the first was RICE, which placed antennas in holes drilled at the South Pole [9]. It pioneered the concept of using Antarctic ice to search for neutrinos via radio waves. The ANITA experiment flies an array of horn antennas in the skies above Antarctica, to search for neutrino interactions in the ice [10], having completed two missions thus far. A number of experiments have also used radio-telescopes to search for ultra-high energy ($> 10^{20}$ eV) neutrino interaction in the Moon [11]. Detectors under construction, like ARIANNA (Moore's Bay) and ARA (South Pole), seek to observe the GZK neutrino flux via surface-array detectors.

* Corresponding author at: University of Kansas, United States.

E-mail address: j529h838@ku.edu (J.C. Hanson).

ARIANNA detects the radio waves using antennas that are buried shallowly in the ice. The current prototype stations each have four log-periodic dipole antennas (LPDAs) that are buried in a square pattern, facing downward. The antennas on opposite sides of the square are separated by 6 m. The direction to the neutrino interaction can be found by cross-correlating signals in these opposite antennas. The signal polarization is measured by comparing the signals from adjacent antennas. Between this polarization measurement and the determination of the frequency spectrum, the neutrino arrival direction can be determined, given enough channels above background [12] (doubling the channel number from 4 to 8 improves the solution). The amplitude of the waveforms, corrected for distance and ice absorption, provide knowledge of the interaction energy. The shape of the initial electric field, derived from the observed waveforms, would point to variables like the angle with respect to Cerenkov angle and the hadronic/electromagnetic nature of the event.

Monte Carlo simulations have been used to predict the signals that would be produced by neutrino interactions in the ice [13,14]. Both charged current (CC) and neutral current (NC) interactions are of interest. In NC interactions, neutrinos scatter from a target nucleus, depositing an average of 20% of their energy in the ice, in the form of a hadronic cascade. Charged-current interactions are similar, except that the neutrino produces a lepton which carries the remaining energy. Charged-current ν_e interactions produce an electron, creating an additional electromagnetic cascade (this discussion does not distinguish particle from anti-particle). Tau leptons from CC interactions also produce Askaryan pulses, albeit at a significant separation (≈ 1 km) from the point of the neutrino interaction.

2. Antenna effective height

The antenna response to time-varying Askaryan electric field may be parameterized in terms of an effective height operator. This height may be determined by measuring the antenna response to a broad-band signal. To measure the LPDA effective height, two identical LPDAs were placed inside an anechoic chamber, facing each other. One LPDA transmitted an impulse, and the other received it, a distance r away. The received signal voltage is shown in Eq. (1) and derived below.

$$V_L(t) = \frac{2^2}{2\pi rc} \left(\frac{Z_L Z_0}{(Z_L + Z_{in})^2} \right) \vec{h}_{rx} \circ \vec{h}_{rx} \circ \dot{V}_{src}(t) \quad (1)$$

In Eq. (1), the circles denote the convolution operator, Z_0 is the impedance of free space ($\approx 120\pi$), Z_{in} is the antenna impedance ($\approx 50\Omega$), c is the speed of light (≈ 0.3 m/ns), V_L is the received voltage at the antenna port, V_{src} is the original voltage impulse transmitted through the first antenna, and \vec{h}_{rx} is the vector-like effective height. Measurements in this work were co-polarized, so the vector symbols will be dropped from now on. For similar measurements of LPDA effective height characterization, see [15,16]. Convolution is linear, commutative, and overall time-invariant.

Eq. (1) is now derived. A receiver with input line impedance Z_L is connected to an antenna of impedance Z_{in} . The voltage seen by the receiver is reduced by a factor

$$\frac{V_L}{V_{O.C.}} = \frac{Z_L}{Z_L + Z_{in}} \quad (2)$$

The open-circuit voltage of the antenna-receiver system is $V_{O.C.}$. The effective height is proportional to this factor [17,18]. The authors of [18] also include a factor of 2 such that the voltage delivered to the receiver is

$$V_L(t) = 2 \left(\frac{Z_L}{Z_L + Z_{in}} \right) h_{rx}(t) \circ E(t) \quad (3)$$

The factor of two out front in Eq. (5) is consistent with [18], in which the effective height operator was used to predict (correctly) the Askaryan amplitude of an electromagnetic cascade in the lab. The factor of two corrects V_L from the observed data on the 50Ω -scope to the voltage actually produced by the antenna. For the transmitter, the ratio of the voltage delivered to the antenna to the open-circuit voltage is [17]

$$\frac{V_A}{V_{O.C.}} = \left(\frac{Z_{in}}{Z_{in} + Z_L} \right) \left(\frac{Z_0}{Z_{in}} \right) \quad (4)$$

The additional factor Z_0/Z_{in} is included to account for the antenna coupling the radiated electric field to the impedance of free space. The electric field radiated by the transmitter is therefore

$$E(t) = \frac{1}{2\pi rc} \left(\frac{Z_{in}}{Z_{in} + Z_L} \right) \left(\frac{Z_0}{Z_{in}} \right) h_{tx} \circ V_{src}(t) \quad (5)$$

Before combining Eqs. (3) and (5), the relationship between h_{rx} and h_{tx} must be mentioned, and it is shown in Eq. (6). The authors of [17,16] differ on the factor of 2 in Eq. (6), but only due to slightly different definitions of antenna quantities. One motivation of the time-derivative in Eq. (6) is that antennas do not radiate DC voltages; in the Fourier domain, time-derivation becomes multiplication of the original function by the frequency, so that $h_{rx}(\omega) \rightarrow 0$ for $\omega \rightarrow 0$.

$$h_{tx} = 2\partial_t h_{rx} \quad (6)$$

Integration by parts, and the *stability condition* of the linear time-invariant system ($h_{rx}(t) \rightarrow 0$ for $t \rightarrow \pm\infty$) allows the transfer of the time-derivative to the input signal. Therefore, Eq. (5) can be rewritten:

$$E(t) = \frac{1}{\pi rc} \left(\frac{Z_{in}}{Z_{in} + Z_L} \right) \left(\frac{Z_0}{Z_{in}} \right) h_{rx} \circ \dot{V}_{src}(t) \quad (7)$$

Combining (3) and (7) produces

$$V_L(t) = \frac{2^2}{2\pi rc} \left(\frac{Z_L Z_0}{(Z_L + Z_{in})^2} \right) h_{rx} \circ h_{rx} \circ \dot{V}_{src}(t) \quad (8)$$

The LPDAs in the anechoic chamber are co-polarized and impedance matched to the 50Ω input impedance of the oscilloscope and amplifier ($Z_L \approx Z_{in}$), so (8) simplifies to

$$V_L(t) = \frac{1}{2\pi rc} \left(\frac{Z_0}{Z_L} \right) h_{rx} \circ h_{rx} \circ \dot{V}_{src}(t) \quad (9)$$

Eq. (9) provides the basis for measuring the effective height. Using the effective height, and similar *transfer functions* for the other components in the ARIANNA data acquisition, neutrino signals may be predicted for a given model of Askaryan radiation. The impedance matching criterion is discussed further in the appendix.

3. Experimental technique

Fig. 1 contains a diagram of the LPDA, a Create CLP5130-2N, and defines the terms E- and H-plane, with respect to the antenna design. The geometry of the LPDA provides the advantage of frequency-independent broadband response, similar to a radio horn. The advantage over a horn (as is revealed by the data) is the uniformity of the response over a wide range of angles. The beam width, VSWR, radiated power, and gain are all favorable over the 105–1300 MHz range. Monte Carlo simulations [12] show that such an antenna maximizes broadband neutrino signal over backgrounds.

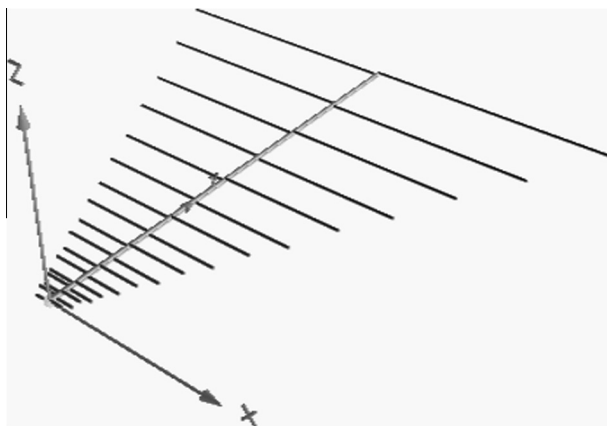


Fig. 1. A diagram of the LPDA, demonstrating the logarithmic spacing and dipole length. The x - y plane contains the dipole elements (*tines*), and is denoted the E-plane. The H-plane, in this case, is the y - z plane. The $-y$ direction is the forward direction of the LPDA. The longest ($\lambda/2$) dipole is 1.45 m, and the length ratio of adjacent dipoles is 0.83. The 1.385 m-long spine holds the dipoles in place, and the feed point is at the shortest dipole (at the origin).

Two LPDAs were arranged a distance $r = 5.72$ m apart, facing towards each other (boresight configuration), inside of an anechoic chamber. A 400 ps wide impulse from an Avtech pulser was sent through coaxial cable to the transmitter, and the received signal was recorded on a Tektronix TDS5104 oscilloscope with a nominal bandwidth of 1 GHz. The spectrum of this raw impulse signal, as measured with the oscilloscope, matches the spectrum taken with a 2.5 GHz bandwidth spectrum analyzer up to a frequency of 1.25 GHz. Above this frequency, the oscilloscope begins to attenuate the data. Results above this benchmark frequency should not be trusted. Fig. 2 shows the experimental setup. The receiving LPDA was attached to a post via a rotating flange, and the post is fixed to a rotating turntable. The flange and turntable apparatus enabled independent rotation of the receiver in both θ and ϕ .

The total system transfer function besides that of the antennas was shown to be a small correction, by comparing the raw pulse with the pulse propagated through all cables in the system (Fig. 3). The 400 ps width of the pulse sent to the transmitter was sufficiently narrow to guarantee that the highest frequencies

of the LPDA were probed. To ensure that the entire bandwidth was accessible to the instrumentation, the voltage standing wave ratio (VSWR) was measured by a network analyzer built into the chamber systems (Fig. 3). The VSWR is a standard RF probe of antenna efficiency; a VSWR of 1.0 indicates all transmitted energy is being radiated with high efficiency.

In the anechoic chamber, the antenna was properly grounded and isolated from interfering electronic equipment, and the VSWR is near 1.0 for the experimental bandwidth. The VSWR of these antennas was measured previously during the installation of the first ARIANNA prototype station [19]. Those measurements recorded a VSWR of ≈ 1.5 from 100 MHz to above 1 GHz, when the antenna was ≈ 1.5 m above the snow surface. When the antenna was buried in densely packed snow, the VSWR was 1.5 down to 80 MHz. The index of refraction of the surface snow in Moore's Bay is $n = 1.29 \pm 0.02$ [5], and this result has been measured with several techniques [19,20]. The LPDA responds to the longest wavelength that physically can exist on the longest $\lambda/2$ dipoles. In a dielectric medium, the wavelength corresponding to a given frequency decreases by one factor of the index, meaning that 80 MHz can fit onto the 1.45 m LPDA dipoles (the longest pair). This effect is confirmed in NEC4 simulations [21], where the accompanying shift in antenna impedance is not enough to reduce the efficiency. This point will be discussed further in Section 5.2.

The programmable turntable was used to rotate the receiving antenna in both the E- and H-planes. The E-plane is the plane containing the LPDA tines (associated with the spherical coordinate ϕ), and the H-plane (associated with the spherical coordinate θ) is orthogonal to the E-plane, and contains the LPDA central spine (Fig. 1). For the pulsed measurements, waveforms were measured in 10 degree increments in the E and H-planes, beginning with 0° in each. The configuration at 0° in both planes is the boresight configuration, with the LPDA receiver facing the transmitter head-on. The E-plane was fully probed by the pulsed data, and 67% of the H-plane was probed. The missing third of the H-plane arose from limitations in the rotating flange, which was not able to tilt beyond $\pm 63^\circ$ in the H-plane.

The response is not expected to vary significantly versus θ until the incident wave is outside the H-plane front lobe (Fig. 4). The network analyzer was used to map the radiation pattern, shown in Fig. 4. A simple model of log-periodic antennas [22] is shown as well. The model is tuned to have the same geometric parameters as the CLP5130-2N, and the same bandwidth and number of dipole elements. The agreement is good for the forward lobes in the E and H-planes, and the back lobe in the H-plane. The E-plane result agrees in overall scale, but fluctuates around the average model prediction. For the experimental bandwidth, a front-to-back ratio of ≈ -15 dB is observed across the bandwidth, in accordance with the manufacturer specifications. The front-to-back ratio is the ratio of received power at 180° to 0° in the E-plane, for identical transmission signals. Note that, in Fig. 4, the H-plane angle of 0° indicates the forward direction. In subsequent figures, the H-plane is associated with the polar angle, θ , in which case the forward direction is $\theta = 90^\circ$, where the antenna rests in the x - y plane.

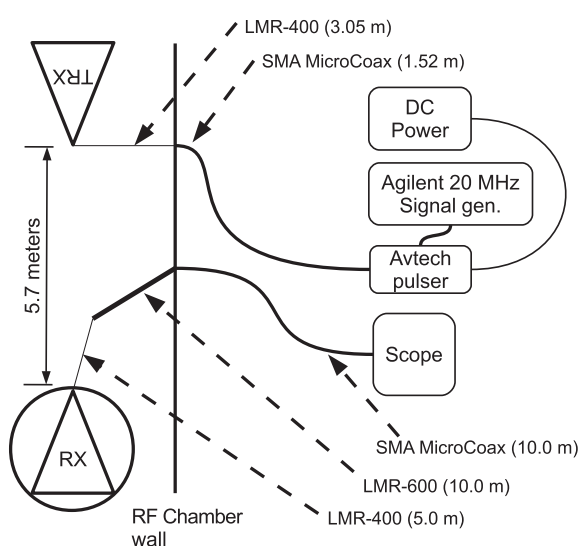


Fig. 2. The experimental setup of the bore-sight configuration. The Avtech was a model AVP-AV-1S type pulser, capable of 0.4 ns pulse widths.

4. Results and analysis

4.1. Data

The data from the boresight configuration is shown in Fig. 5. The scope recorded a downward-chirping signal approximately 40 ns wide, probing all frequencies accessible to the LPDA, according to the VSWR measurements (Fig. 3). A reflection is observed 67.5 ns after the initial pulse, and can be verified with auto-correlation

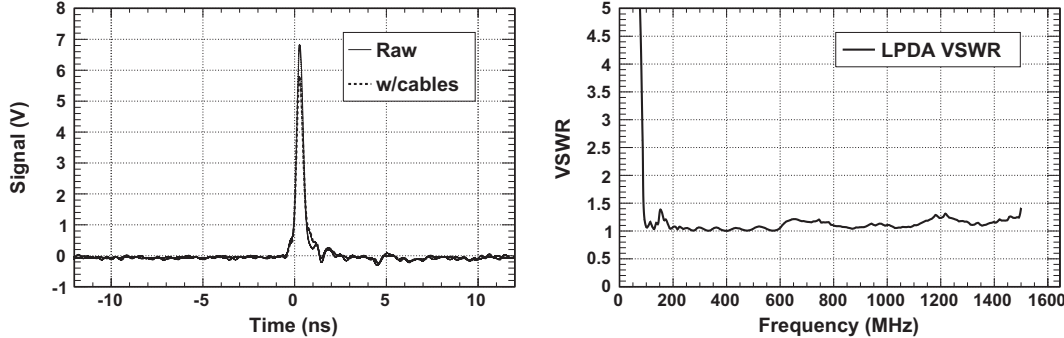


Fig. 3. (Left) The raw pulse sent to the transmitting antenna, as measured on the 1 GHz scope (Fig. 2), along with the raw pulse after having propagated through all coaxial cables in the system. (Right) The VSWR of the receiving antenna, measured by a network analyzer just outside the anechoic chamber.

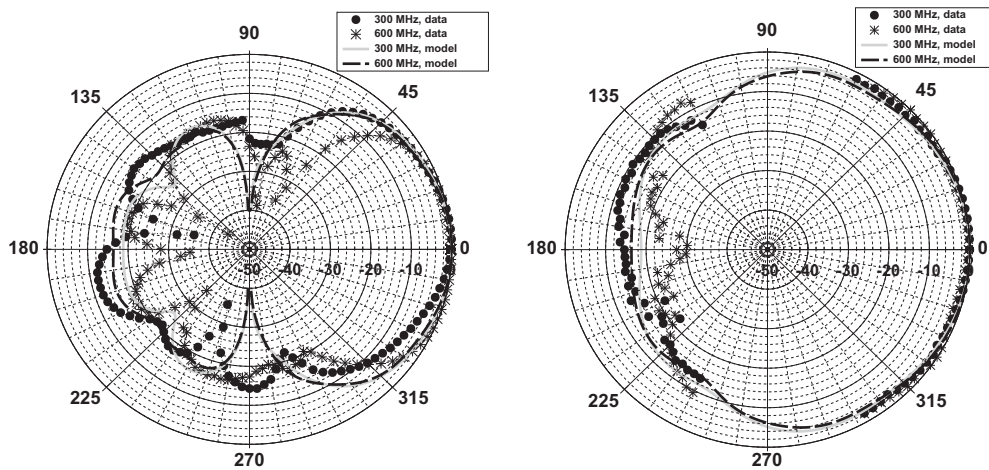


Fig. 4. The radiation pattern of the CLP-5130-2N LDPA (normalized to 0 dB maximum). The angles are relative to boresight in the counter-clockwise sense. (Left) the E-plane radiation pattern at 300 and 600 MHz, compared to a log-periodic simulation of the E-plane. (Right) the H-plane radiation pattern at 300 and 600 MHz, compared to the same simulation for H-plane. Note that 0° in the H-plane indicates the forward direction in this graph.

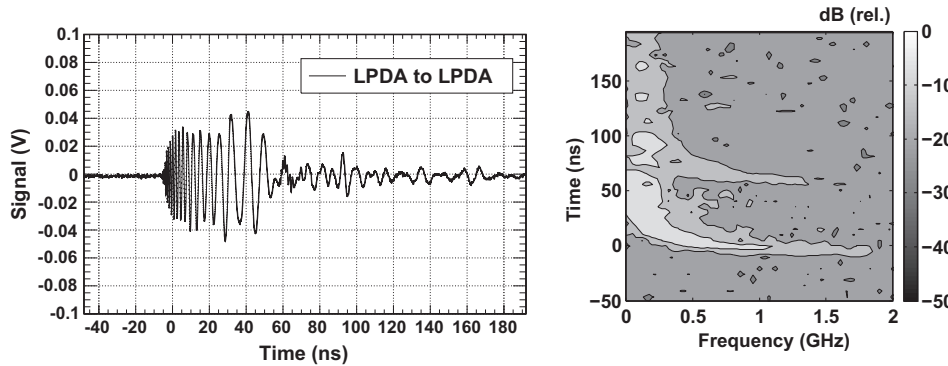


Fig. 5. (Left): The boresight time-domain results, shifted such that the trigger location is at 0 ns. (Right): a spectrogram of the boresight data, with the oscilloscope DC offset removed. The power is in units of dB, relative to maximum power.

of the data. The analysis was performed only on the first 67.5 ns of data, before the reflection. Similar pulse data was taken at all available turntable angles, and the input pulse was not changed. The chirping form of the impulse data has a simple explanation: the placement of the feed point on the LDPA causes the radiated phase, and group delay, to have predictable dependencies on frequency:

$$\phi(\omega) = \frac{\pi}{\ln \tau} \ln \left(\frac{\omega}{\omega_1} \right) \quad (10)$$

$$\tau_g(\omega) \equiv -\frac{d\phi}{d\omega} = -(2\pi \ln \tau)^{-1} \quad (11)$$

The overall minus sign in the group delay $\tau_g(\omega)$ simply indicates a physical delay, rather than an earlier signal. In Eq. (10), ω_1 is the angular frequency of the shortest radiating dipole, and τ is the ratio of the length of adjacent dipole elements. The location of the LPDA feed-point delays radiation of components with lower frequencies. Fortunately, this effect can be undone with a knowledge of the components' frequencies, and the LPDA τ -parameter

($\tau = 0.83$ for the CLP-5130-2N) [23,24]. Because of the simple form of Eq. (10), an operator which commutes with the detector response can be constructed that removes the phase dispersion.

Examples of data from off-boresight configurations are shown in Figs. 6 and 7. These data demonstrate that it is not sufficient, for a broadband antenna, to model the time-response as the bore-sight function times the relative gain versus angle of the antenna. The radiation pattern depends on frequency, and the phasing must be studied at all angles to accurately predict signals. For example, a high-frequency incident plane wave interacting with the antenna at oblique angles changes the order in which antenna elements produce a voltage. Thus, the relative phasing between elements must depend on the orientation of the system.

4.2. Analysis

Eq. (9) represents the model used to explain the time-domain data. Eq. (9) can be re-written: $xV_L(t) - h \circ h \circ \dot{V}_{src}(t) = 0$, with $x = (Z_L/Z_0)2\pi rc$. An algorithm was developed to derive the waveform representation of h that solves this equation. Fig. 8 demonstrates how, after many iterations, a solution for h was found that satisfies the equation with x defined as above. Because of the shape of the LPDA, the expectation for the solution is a rapidly oscillating chirp that decreases in frequency as time increases.

During each iteration, the algorithm adds a small amount of white noise to the effective height samples $[s_1 : s_n]$, and nothing to subsequent samples $[s_{n+1} : s_N]$, where there are N samples total. The result is kept only if the solution to $xV_L(t) - h \circ h \circ \dot{V}_{src}(t) = 0$ improves. Improvement is defined as a decrease in the mean squared-difference between model and data, denoted the score, S :

$$S = N^{-1} \sum_{i=1}^N (s_{i,data} - s_{i,model})^2 \quad (12)$$

If the score decreases, there is a 1%-percent chance that $n \rightarrow n + 1$ (a randomly drawn number between 0 and 1 must be less than 0.01). Thus, the algorithm focuses early action on the high-frequency content of the response, leaving the simpler low-frequency oscillations for the end of the calculation. The calculation terminates when the score has decreased by a factor of ≈ 100 , which is typical of convergence (subsequent iterations produce only marginal improvement).

The algorithm was applied to all the angles measured with the anechoic chamber turntable. The main lobe results converge and provide the effective height versus time. The LPDA null zones are not studied in detail, as the neutrino signals are heavily attenuated there. Several instances of the results are shown below in Fig. 9. The beam-width of the LPDA is 60° in the E-plane, meaning

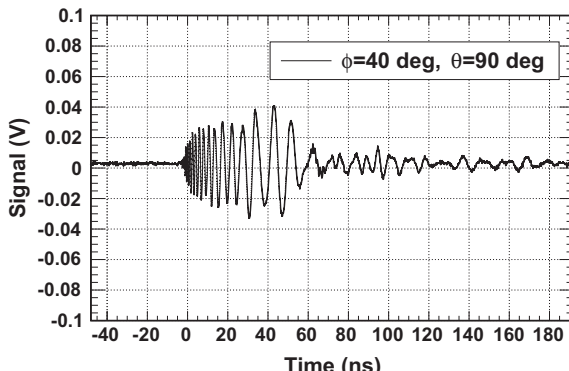


Fig. 6. The pulse data from the anechoic chamber at an angle of $\phi = 40^\circ$ (ϕ : angle in E-plane), and $\theta = 90^\circ$ (θ : angle in H-plane, with 90° corresponding to boresight).

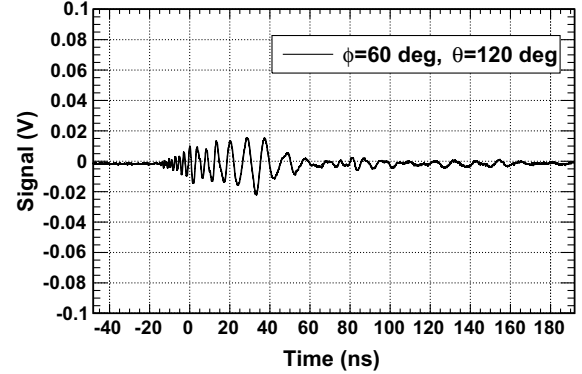


Fig. 7. Similar to Fig. 6, except at $\phi = 60^\circ$, $\theta = 120^\circ$.

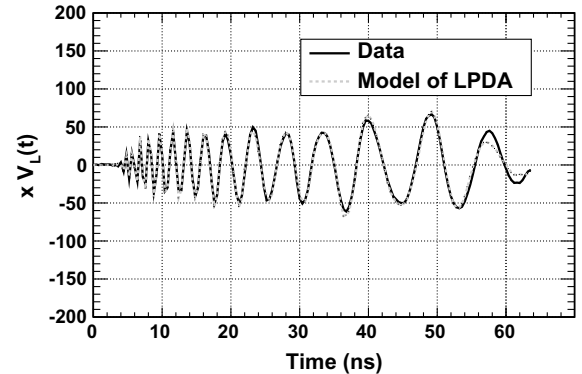


Fig. 8. The algorithm finds a solution for the effective height, $h(t)$, vs. time. The solution found by the algorithm (model of LPDA), solves the equation $xV_L(t) - h \circ h \circ \dot{V}_{src}(t) = 0$, in order to match the anechoic chamber data (data). The algorithm terminates after the mean squared-difference between model and data (the score) has improved by a factor of ≈ 100 .

radiated power is reduced by 3 dB at $\pm 30^\circ$ from boresight. As the observation in the E-plane (Fig. 9, top) begins to take place outside the beam width, the amplitude shifts more rapidly, and is concentrated at lower (100–200 MHz) frequencies. The H-plane dependence (Fig. 9, bottom) is gradual, because the beam width is wider and more consistent in frequency.

5. Confirmations of measurements

Although the solutions for the LPDA response converge such that they match laboratory data, it is necessary to show that response solutions explain multiple independent measurements. Section 5.1 demonstrates that anechoic chamber measurements with the ARIANNA low-noise amplifier can be explained with the impulse response of the amplifier, combined with the that of the LPDA. Section 5.2 involves independent measurements of the temperature-averaged RF attenuation length of the ice beneath the deployed ARIANNA stations in Moore's Bay.

In this section, pulses reflected from the ocean/ice interface are modeled using the ice properties and antenna properties. Time series data from the 2006–7 and 2013–14 Antarctic seasons are used. The 2013 oscilloscope data was observed to agree with the ARIANNA data acquisition system, a result that has been demonstrated before [25]. The measurements of the ice properties were made in the interim (2010–10 and 2011–12), and are calibrated to be independent of the antenna model. Section 5.3 uses data taken in 2010 in Aldrich Park at UC Irvine, with different antenna orientations.

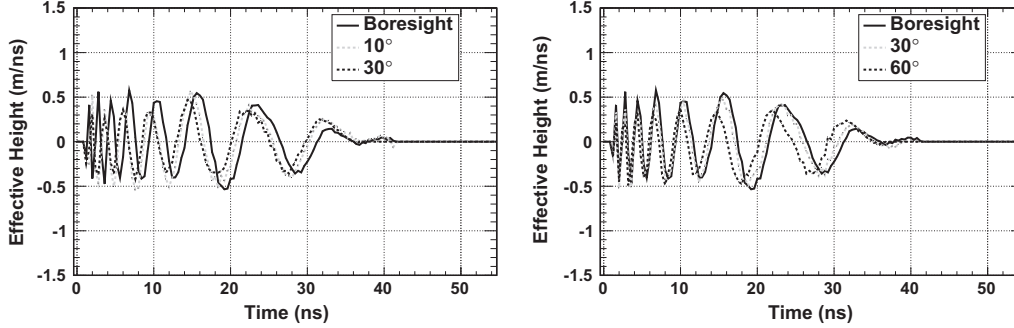


Fig. 9. The results for the effective height. (Left): selection of E-plane results, with ϕ varying, $\theta = 90^\circ$. (Right): the same for the H-plane, with θ varying, $\phi = 0^\circ$. In all cases the radiated wave polarization is parallel to the transmitter E-plane, which was kept fixed.

5.1. ARIANNA custom amplifier

The ARIANNA amplifier was designed to match the antenna signals to the ARIANNA waveform digitizers, while maintaining a high signal to noise ratio (a small noise figure). The specific design used here was developed in 2012, powered by 3.3 V DC, with a [50–1000] MHz bandwidth. The gain decreases with frequency (Fig. 10), so the impulse response function is not a δ -function. To measure the impulse response, a 0.5-ns wide pulse was attenuated and fed directly into the amplifier. The output waveform was recorded, and from that waveform the impulse response was computed such that convolution of the response and the impulse produced the output waveform. The gain versus frequency, and impulse response are plotted in Fig. 10.

The amplifier was inserted into the anechoic chamber system, between the 1 GHz oscilloscope and the LPDA receiver, with a total of 36 dB of attenuation added in the system. The resulting data in Fig. 11 has been corrected for attenuators. The data matches the model, in amplitude and shape. The (Pearson) correlation coefficient, ρ , is used to quantify agreement between signals x and y :

$$\rho = \frac{\text{Cov}(x, y)}{\sqrt{\text{Var}(x)\text{Var}(y)}} \quad (13)$$

For the result in Fig. 11, $\rho = 0.89$. The equation for the modeled waveform is identical to that of the anechoic chamber system (Eq. (9)), with the amplifier impulse response (denoted A) added. (The constant numerical factors in front of Eq. (14) commute with the convolution operators). If either the amplifier transfer function, or the LPDA response function are not included, then the correlation coefficient drops to insignificant levels. The model amplitudes for early times, corresponding to higher frequency content, are slightly smaller than the data. This has little effect on ρ , however, because ρ values are driven by the most powerful amplitudes.

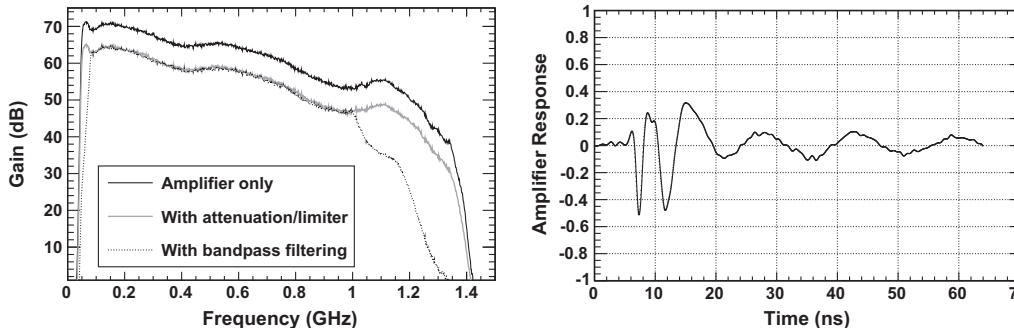


Fig. 10. (Left): The gain vs. frequency of the ARIANNA amplifier. (Right): The impulse response of the ARIANNA amplifier. The y-axis has been normalized such that the auto-correlation of this response is 1.0.

Fig. 11. Anechoic chamber amplified data, with model. The recorded data is shown as a solid line, and the dashed line is the model from Eq. (14). Agreement between the model and data is considered good because $\rho = 0.89$.

$$V_L(t) = \frac{1}{2\pi rc} \left(\frac{Z_0}{Z_L} \right) A \circ h_{rx} \circ h_{tx} \circ \dot{V}_{src}(t) \quad (14)$$

5.2. Ice shelf data

The RF attenuation length of the ice shelf in Moore's Bay has been measured several times (c.f. [5,20]), and will be updated in a forthcoming publication. In each radio echo measurement, a calibration pulse is recorded by the receiver and transmitter system. The antennas are then pointed down, and the recording oscilloscope is triggered on a delay such that it records the reflection from the ice/ocean interface beneath. By comparing the calibration pulse to the reflected pulse, the attenuation length is measured. The shelf depth is extracted from the oscilloscope time delay that captures

the reflection. The shelf-depth obtained this way is 576 ± 8 m. The attenuation length $\lambda(v)$ causes the electric field mode $E(v)$ at frequency v to be absorbed in the ice as $\propto \exp(-r/\lambda(v))$. The introduction of the reflection coefficient for electric fields accounts for the ocean/ice interface. Table 1 summarizes linear fits to the attenuation length vs. frequency data over several seasons in Moore's Bay, assuming 100% reflection at the ocean surface.

The linear fits to the data from all seasons are consistent, as demonstrated in Table 1. The attenuation lengths are conservative, because some of the returned power loss could be attributed to a non-ideal reflection coefficient. Prior measurements indicate that the interface in Moore's Bay is smooth compared to the shelf ice near the coast, [7,26]. Newer measurements of the reflection coefficient \sqrt{R} indicate that $\sqrt{R} \approx 1$ [5,6], with almost negligible surface roughness. A more detailed discussion of the ice properties of Moore's Bay can be found in [5], and in forthcoming publications. Following convention, R is the reflection coefficient for signal power, and \sqrt{R} for electric field amplitudes. To model the reflections from the ocean, Eq. (14) is applied, with an additional step to account for the frequency-dependent attenuation length, and a reflection coefficient (Eqs. (15)–(17)). The 180-degree phase-shift caused by reflection between ice and salt water requires an overall minus sign.

$$E(t) = \left(\frac{1}{2\pi c}\right) \left(\frac{Z_0}{Z_L}\right) h_{rx} \circ \dot{V}_{src}(t) \quad (15)$$

$$\tilde{E}(v) = F_v(E(t)) e^{-i\lambda(v)/r} \quad (16)$$

$$V_L(t) = -\sqrt{R} h_{rx} \circ F_v^{-1}(\tilde{E}(v)) \quad (17)$$

Eq. (15) is just Eq. (7) for the matched-impedance case, and the input pulse V_{src} was typically a 2.5 kV, 1 ns wide pulse from a Pockel Cell driver. In the 2006 measurement, the receiver and transmitter antennas were Seavey radio horns, and the measured effective height, at boresight, is shown in [10]. In the 2013 measurement, the receiving antenna was the ARIANNA LPDA. Because the attenuation length depends on frequency, the data is transformed to the Fourier domain, multiplied by the frequency-dependent attenuation factor, and transformed back to the time domain (Eqs. (16) and (17)). The operators F_v and F_v^{-1} represent the Fourier transform and inverse Fourier transform, respectively. Eq. (17) is just Eq. (3), in the matched-impedance case. No correction is made to $h_{rx}(t)$ for the effect of the surface snow, which has an index of 1.29 ± 0.02 (see below).

Fig. 12, left, presents the comparison of the 2006 data, and Fig. 12, right, the more recent data. A prototype of the ARIANNA analogue transient waveform digitizer (ATWD) was brought to Moore's Bay in 2010, and recorded similar results [25]. The linear fit $\lambda(v) = -(140 \pm 20) \text{ m/GHz} + (470 \pm 20) \text{ m}$ was used for the attenuation length, and $\sqrt{R} = 1.0$, from Table 1 (These numbers are consistent with prior measurements, and will be updated in a forthcoming publication). Notice that, in either comparison, the negative sign in front of Eq. (15) is necessary to obtain the correct phase, indicating that the reflection at the ocean/ice interface is taking place between two materials with differing indices of refraction ($n_2 > n_1$).

Table 1

Attenuation length fit parameters, assuming 100% reflection at the shelf-bottom. The year and transmitter/receiver models (TX/RX) are shown in the first and second columns, respectively. The constant and slope of the linear fits are in the third and forth columns, respectively, and the χ^2/dof is shown in the fifth column. The form of the linear fit is $\lambda(v) = L_0 + \alpha v$. The 2006 data was published with 25 MHz bins, and has a larger χ^2/dof . With 150 MHz bin-width, the χ^2/dof is reduced to 0.4. The final row indicates a fit to the average of all data collected.

Year	TX/RX	L_0 (m)	α (m/GHz)	χ^2/dof
2006	S/S	450 ± 10	-120 ± 10	2.4
2011	L/L, S/L	475 ± 30	-150 ± 60	0.42
Ave.	L/L, S/L, S/S	470 ± 20	-140 ± 20	0.3

The correlation coefficients are larger than the naive expectation for signal correlation with noise: $\rho \approx 0$. Further studies of the thermal noise environment at the temperatures of Moore's Bay with the ARIANNA system indicate that the correlation between signal and realistic noise is ≈ 0.2 for un-altered bandwidth, and ≈ 0.3 for bandwidth-limited noise in the presence of band-pass filtering [27]. A good discussion of this subject can be found in [28]. Fig. 13 demonstrates that if the pulse from Fig. 12 is sent through the air, with the same equipment, the comparison still indicates agreement. That is, the quality of the model does not depend on the frequency dependent attenuation profile of the ice.

It is important to note that the snow plays no role in the agreement between model and data in Fig. 12. Several factors that could be corrected, due to the snow, are the medium conductivity, antenna impedance and the group delay. The antenna simulation package NEC4 [21] was used to reproduce in-air properties of the LPDA (such as impedance, VSWR, and radiation pattern), by solving for the antenna current using a method-of-moments approach. The simulation package allows the antenna to be embedded in a dielectric medium, with tunable index, n , and conductivity. The conductivity of Antarctic surface snow is small ($\approx 10 \mu\text{S}/\text{m}$) [29]. Varying the conductivity by an order of magnitude technically changes the antenna impedance, but not enough to effect $h_{rx}(t)$.

The simulated NEC antenna impedance is affected mainly by n : the real and imaginary parts of Z_{in} are shifted down by a factor of n , and to lower frequencies: $v \rightarrow v/n$. However, the LPDA is designed for broadband, frequency-independent use, and the shift in lower cutoff frequency from 105 to 80 MHz has little effect on the structure of $h_{rx}(t)$ (derived from simulated parameters). The reduction by a factor n in Z_{in} could have caused a $\approx 15\%$ reduction in the amplitude of $h_{rx}(t)$ (which goes as $|\sqrt{Z_{in}}|$). However, the average $|Z_{in}|$ is 80Ω in the NEC4 model (agreeing with network analyzer measurements in air), whereas Eq. (9) assumes 50Ω . The measured $h_{rx}(t) \circ h_{rx}(t)$ must therefore be a factor of $(Z_L + Z'_{in})^2 / (Z_L + Z_{in})^2$ larger, to compensate. With $Z_L = 50\Omega$, $Z'_{in} = 80\Omega$, and $Z_{in} = 50\Omega$, this factor is 1.3^2 , which is equal to the measured n^2 . When the antennas are placed in snow (and each $h_{rx}(t)$ drops by \sqrt{n}), $Z_0 \rightarrow Z_0/n$. Thus, these effects in Eq. (9) cancel when the LPDA is placed in the snow. Ultimately, the empirical data matches the model, and it is safe to assume the role of the snow is negligible.

The NEC model was also used to check that the position of the LPDA does not strongly affect the results. The depth of the LDPA does not affect the impedance as long as n is constant near the surface. Near the air/snow interface, this is most likely a first-order approximation. However, measurements of the VSWR in [19] reveal that the LPDA bandwidth extends down to 80 MHz, verifying the NEC model prediction near the surface. Because the front-to-back (F/B) ratio of the LPDA is -15 dB, surface effects likely do not matter as long as the antenna is facing downward. Density measurements of the surface firn vs. depth [5,20] indicate that treating the index as a constant for the first few meters is reasonable. Finally, because the group delay is the derivative of the S21 phase, it is a relative quantity should not be affected as long as the index is constant. As a final check, the simulated impedance, gain, and the theoretical group delay equation were folded into the standard formula for $h_{eff}(v)$ [30] and inverse Fourier-transformed to obtain $h_{rx}(t)$. The snow and air versions of $h_{rx}(t)$ had a correlation coefficient of 0.98 in this case.

5.3. Further comparisons in air

The time-domain model derived from anechoic chamber data must be checked for a variety of situations, including locations with no ice or snow, and different band-pass filtering. In 2010, data was taken in Aldrich Park to investigate the LPDA waveform shape for a variety of angles. Filters rejecting CW noise were applied.

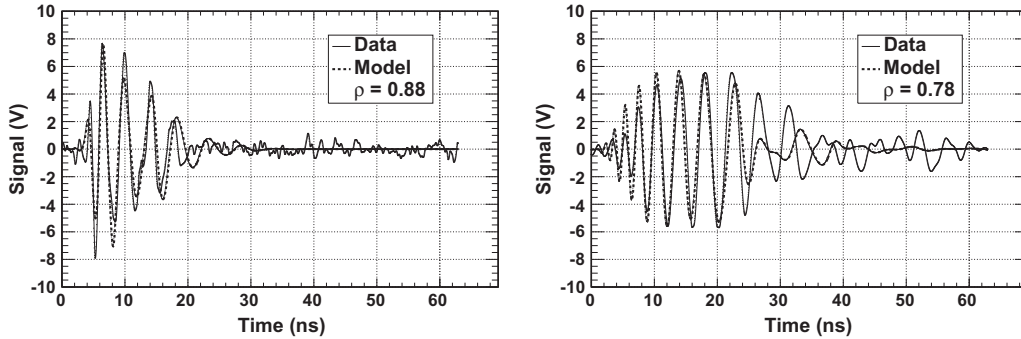


Fig. 12. (Left): 2006 Moore's Bay comparison. (Right): 2013 Moore's Bay comparison. The recorded data are shown as solid lines, and the model from Eq. (15) is shown as a dashed line. The value of ρ is 0.88 for the 2006 data and 0.78 for the 2013 data, indicating agreement. The waveforms have been corrected for attenuators used to keep amplitudes in the linear range of amplifiers and oscilloscopes.

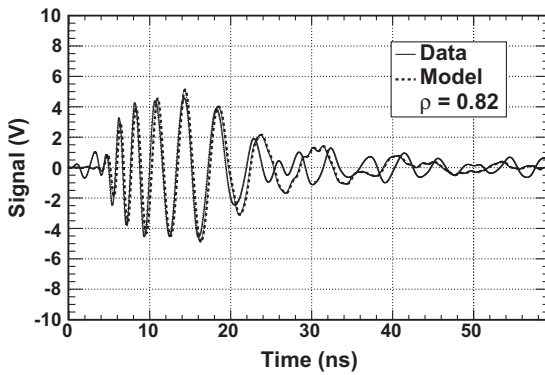


Fig. 13. In-air Seavey to LPDA calibration through 23 m of air. The recorded data is shown as a solid line, and the model from Eq. (15) is shown as a dashed line ($r = 23$ m, $\lambda = \infty$). The value of $\rho = 0.82$. The waveforms have been corrected for attenuators used to keep amplitudes in the linear range of amplifiers and oscilloscopes.

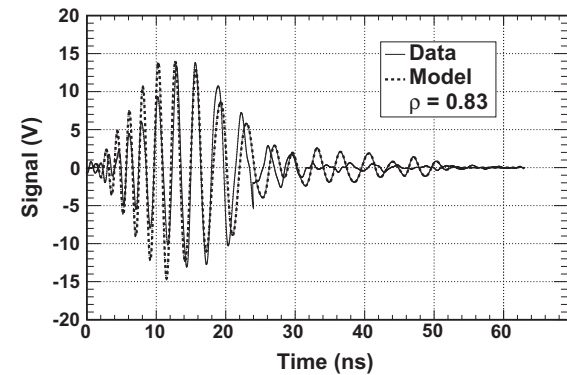


Fig. 14. A model of a pulse obtained in Aldrich Park in 2010, using two LPDA antennas, a PCD, and filters, with a separation of 5 m. The correlation coefficient is $\rho = 0.79$.

Table 2

Correlation coefficients, ρ , determined from the different measurements described in the text.

Exp. Setting	Fig.	ρ
Chamber+amplifier	11	0.89
Ice sounding (Moore's Bay 2006)	12	0.88
Ice sounding (Moore's Bay 2013)	12	0.78
In-air over ice (Moore's Bay 2012)	13	0.82
In-air (Aldrich Park 2010)	14	0.83

time from the signal, and the noise level produced the same signal to noise ratio as the data when added to the model.

6. Askaryan pulses in ARIANNA data

Given an understanding of how the Askaryan electric field would be transformed in the data acquisition, the next logical step is to predict properties of the signal based on a theoretical understanding of the neutrino interaction. Various authors have studied the problem theoretically [13,14,31], and several experimental confirmations have been achieved [32,33]. The experimental observations recreate the ultra-high energy electroweak interaction by building a cascade energy equivalent to the expectation for a cosmogenic neutrino. The total energy is equal to the sum of the separate energies of the charged particles in a beam built from photons or electrons.

The negative charge excess that develops over several meters in the dielectric material leads to RF radiation, and the shape of the pulse reflects the details of the longitudinal development of charge,

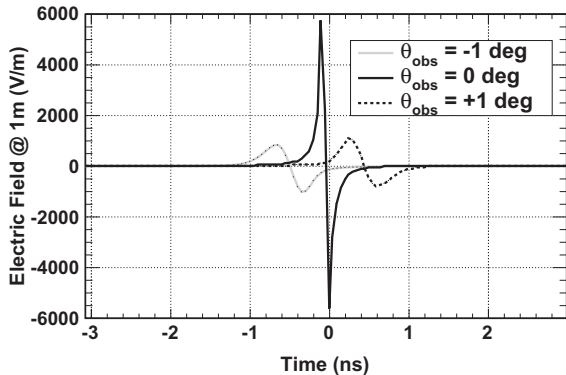


Fig. 15. The electric field pulse created by a 100 TeV event, scaled to an energy of 10 EeV, $\theta_{\text{obs}} = -1^\circ, 0^\circ$ and 1° .

and perspective from which the pulse is observed, since the highest frequencies are confined to the Cerenkov angle. In Section 6.1, signal predictions are shown with respect to the observation angle relative to the Cerenkov angle. In Section 6.2, the result of varying the angle at which the Askaryan pulse interacts with the ARIANNA antenna is presented.

6.1. Prediction vs. observation angle

A description of how Askaryan electric fields are generated from the negative charge excess profile versus cascade depth can be found in [13,14], and early Monte Carlo studies in [34]. Several key observations arise from these calculations. First, the electric field amplitude (and vector potential) scales with the total energy, due to coherence effects. Second, the shape of the electric field corresponds to a temporal derivative with respect to the retarded time of the excess negative charge profile. Because the charge excess is moving in the lab frame, the pulse shape traces the derivative of the excess charge with respect to cascade depth. The LPM effect [35] stretches the charge excess profile above 10^{16} eV, and therefore stretches the pulse, while reducing the amplitude. Secondary peaks in the charge distribution and therefore the electric field are also caused by the LPM effect. Because the pattern of energy deposition varies from event to event in the strong-LPM regime, there can be considerable event-to-event variation in the radio frequency spectrum.

Fig. 15 displays Askaryan pulses derived from the ZHS Monte Carlo [34], with subsequent modifications for non-cylindrical form factors of the charge distribution [14]. The electric fields are scaled to correspond to a total energy of 10 EeV, but were created from charge excess profiles from 100 TeV events (the scaling is linear).

Because the LPM effect becomes relevant above 10^{16} eV [12], the pulses are unaffected by it, and are smooth and unstretched. The center of graph corresponds to a retarded time of zero. The pulse asymmetry (difference in maximum and minimum values) for non-zero observation angles (color scale) is caused primarily by the non-symmetric charge distribution. For negative observation angles, the retarded time dictates that the end of the charge excess profile is observed *first*, and the electric field is anti-symmetric for reflections across the y-axis where the retarded time is zero.

The time-domain response of both the ARIANNA LPDA and the low-noise amplifier produce results that match data. Theoretical Askaryan pulses can be combined with them to produce experimental predictions for the neutrino signal, or *templates*. For electric fields not subject to the LPM effect, the accuracy of the templates is limited only by model and experimental uncertainties. Electric fields subject to the LPM effect have also been studied, to establish how the templates change. However, this study is not meant to be comprehensive. Assuming a matched coaxial cable, and including amplifier effects, Eq. (3) reduces to $V_L(t) = A(t) \circ h_{rx}(t) \circ E_v(t)$, where $A(t)$ again represents the transfer function of the amplifier. Fig. 16 shows the signal templates $V_L(t)$, while varying the observation angle. Technically, ice absorption is also taken into account over a 1000 m path length, however, it is shown below that this has a negligible effect on waveform structure.

While the signal amplitudes are predicted by the analysis, the waveforms have been scaled such that the maximum voltage is 1.0, so that shapes can be compared (Fig. 16). The only change in the templates with respect to observation angle, besides overall amplitude, is the frequency content early in the wave. Higher frequency modes are expressed early in the wave as the observation angle decreases to zero, however these modes are lost off-cone. The structure of the LPDA response causes the high frequency modes to be recorded earlier, because the smaller dipole elements are located nearer to the antenna feed point. (The next section shows templates for non-boresight angles).

The LPM versions of the templates demonstrate a stronger dependence on the observation angle than the non-LPM versions. There are three main effects. First, the on-cone (0°) versions are identical, because the electric fields are identical. That is, an extreme narrowing of the Cerenkov cone width is irrelevant, if the observation is taking place at precisely the Cerenkov angle. Second, for off-cone observations, the high frequency modes near the beginning of the waves are suppressed, because those modes are suppressed in the original electric field. Finally, the lower frequency modes (near the end of the waves) appear to be enhanced relative to the 0° case. This is an artifact of the normalization, which sets the maximum voltage (whenever it occurs) to 1.0. In the un-normalized templates, oscillations between 20 and 30 ns from the 0° case are the largest in the set. It is important to

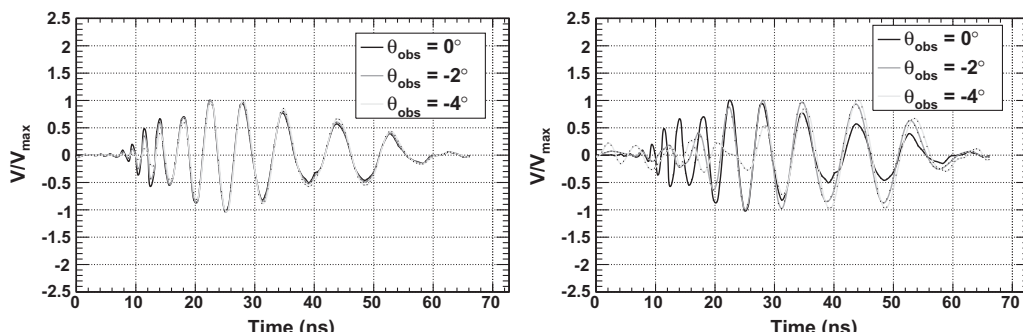


Fig. 16. Signal templates for a 10 EeV neutrino, via the Askaryan effect. The LPDA observes the cascade at boresight, and the results for observation angles of 0° , -2° and -4° are shown. (Left): Signals generated by NC neutrino interactions, appropriate for CC interactions in the absence of significant LPM suppression. (Right): the same events, with the LPM effect included, appropriate for electron-type CC interactions.

mention here that the LPM-templates shown in Fig. 16 are not meant to be comprehensive, and demonstrate the need for further analysis.

Correlating templates with each other produces an interesting result: if the E-plane angle (next section) is restricted to two beam-widths or less ($\approx 60^\circ$), the correlations between templates obey $\rho \geq 0.8$. This result includes varying the E- and H-plane angles, and the observation angle. Because 0.8 is much larger than auto-correlation coefficients produced by noise in ARIANNA analyses, typically $\rho \lesssim 0.3$, it is acceptable to use the time-dependent pulse generated from an electromagnetic cascade at energies below the influence of the LPM, and scale it to higher energies to predict the waveforms from the dominant hadronic cascades. LPM-dominated events (CC events with energies greater than 1 EeV) make up 20%–30% of the total event rate [12] in ARIANNA, and do not obey $\rho \geq 0.8$, for correlations between all templates from the LPDA forward lobe. To understand the final fraction of events which do undergo the LPM effect, future development of this work will extend template production to include LPM physics.

6.2. Prediction vs. antenna angle

Although the effect of the observation angle is interesting theoretically, the majority of detectable signals in the ARIANNA system will be electric fields with small observation angles, above the detector threshold. The effect of the LPDA on the signal must be clear, since this effect (and of the amplifier) must be deconvolved to reveal the electric field. Fig. 17 demonstrates the effect of the LPDA responses from Fig. 9, and the amplifier, on an on-cone Askaryan pulse at 10 EeV. In each case, the signal is assumed to be co-polarized. The cross-polarization fraction [5,6], which

measures how much power leaks into the cross-polarized direction due to ice propagation, is $\leq 5\%$ for the data in ice soundings taken in Moore's Bay. Fig. 17 retains the properties of Fig. 9. The LPDA response approaches uniformity within the main lobe of the E- and H-planes, especially at lower frequencies.

Although ice absorption over the total path length affects the overall amplitude in a triggered event, it has been checked that the effect on the waveform shape is small (Fig. 18). The slope of the measured attenuation length vs. frequency is not steep enough to produce a difference comparable to the shelf depth over a few hundred MHz. The differences in high and low frequency attenuation do not have enough time to warp the waveform shape. With an average (measured) shelf depth of 576 ± 8 m, the attenuation effect works out to approximately a -16 dB/km overall scale factor, which is nearly independent of frequency.

6.3. Confirmation of ARIANNA Monte Carlo amplitudes

The ARIANNA Monte Carlo simulation, ShelfMC, predicts the overall exposure and sensitivity to neutrino flux, given a variety of parameters [12]. Natural factors, such as the chemical composition of cosmic rays and the distribution of cosmic ray sources with respect to redshift [36], must be determined independently or taken as free parameters. However, once the neutrino flux interacts in the ice, it produces a cascade. The cascade electric field strength versus frequency (in ice) has been measured experimentally [32] for cascades of equivalent total energy to GZK events. The ShelfMC simulation has been adapted from that of prior experiments [9,10]. These Monte Carlo simulations multiply the electric field strength (parameterized as in [37]) with an effective height equation in the following way:

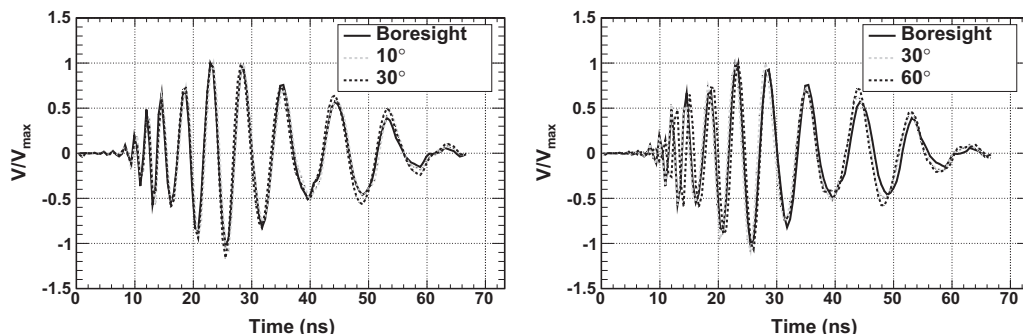


Fig. 17. Signal templates for a 10 EeV neutrino, via the Askaryan effect. The LPDA observes the cascade at varying angle with respect to boresight, and the observation angle is kept constant at 0° . (Left): Varying antenna angle in the E-plane only. (Right): Varying the antenna angle in the H-plane only.

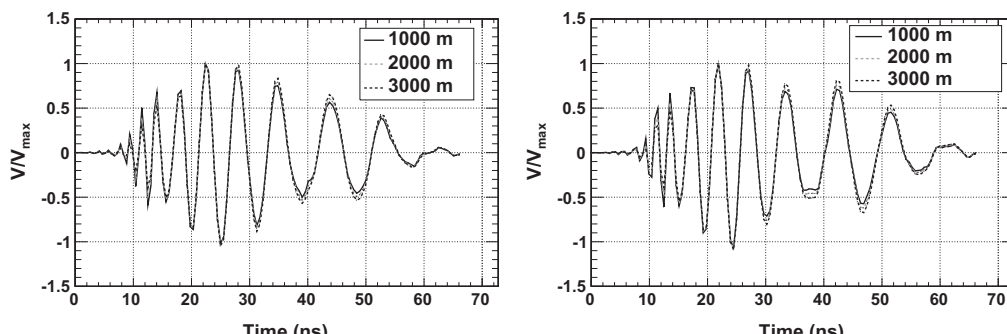


Fig. 18. These signal templates includes the usual suite of electronics effects (LPDA, filters, and amplifier), and the effect of the ice. The measured attenuation length vs. frequency is $\lambda(v) = (470 \pm 20) - (140 \pm 20)v[\text{GHz}]$ (meters). The path length is varied and shown in the legend, and the shape changes accordingly. The waveforms are normalized such that the maximum voltage is 1.0. (Left): LPDA boresight. (Right): 60° in the H-plane.

$$E_v^{1m} \left[\frac{V}{\text{m MHz}} \right] = \left(\frac{f}{f_0} \right) \frac{E[\text{TeV}] \times 2.53 \times 10^{-7}}{1 + (f/f_0)^{1.44}} \left(\frac{\sin \theta_{obs}}{\sin \theta_c} \right) \quad (18)$$

$$E_v(\theta_{obs}, r, f) = E_v^{1m}(f) \exp \left(-\ln 2 \left(\frac{\theta_{obs} - \theta_c}{\Delta \theta(f)} \right)^2 \right) \frac{e^{-r/\lambda}}{r} \quad (19)$$

$$V_{ant} = \frac{\sqrt{R} \Delta f}{2\sqrt{2}} \sum_i h_{eff}(f_i) (f_{had} + f_{em}) E_v(\theta_{obs}, r, f_i) G(\theta_E, \theta_H) \quad (20)$$

In Eq. (18), the basic electric field strength is shown, and $f_0 = 1150$ MHz. In Eq. (19), $\theta_{obs} - \theta_c$ measures how far the observation is from the Cerenkov cone, $\Delta \theta$ is the width of the Cerenkov cone, and $\theta_c = 56^\circ$ is the Cerenkov angle in ice. The cone width $\Delta \theta$ depends on frequency, and whether the event is electromagnetic or hadronic in nature. Eq. (21) below gives the electromagnetic dependence, which depends on the LPM effect. In Eq. (19), r and λ are the distance from the neutrino vertex and ice attenuation length, respectively. In Eq. (20), f_{em} and f_{had} are the fractions of energy in the electromagnetic and hadronic component of the neutrino cascade, and the function G averages (in-quadrature) Gaussian models of the forward lobe of the LPDA radiation pattern in the E- and H-planes. If the event reflects from the ocean, then R is the reflection coefficient for power. Finally, h_{eff} is the scalar expression for antenna effective height at a given wavelength [30].

$$\Delta \theta(E_v, f) = 2.7 \cdot \frac{f_0}{f} \left(\frac{E_{LPM}}{0.14 E_v + E_{LPM}} \right) \quad (21)$$

The convolution theorem states that multiplication of two functions in the Fourier domain is identical to convolving those functions in the time domain. Eq. (20) multiplies the scalar effective height formula for a single frequency (h_{eff}) with the electric field. Thus, Eq. (20) is like the proper convolution of the electric field and antenna response ($h_{rx}(t)$) with the complex phase factor neglected. For pure ice, $E_{LPM} \approx 0.3$ PeV [35], depending on the ice density, and the cascade begins to elongate near 2 PeV. The nominal ice density of 0.92 g/cc is assumed here. The frequency f_0 is the same as above. Antenna beam widths of 60° and 120° are used as the Gaussian widths in G in Eq. (20), for the E- and H-planes respectively, and θ_E and θ_H are the incoming angles in the respective antenna planes. This description of the antenna main lobe is an approximation best suited for directions within one beam-width of the forward direction.

The full calculation of the antenna voltage yields a number meant to be compared to rms voltage fluctuations from thermal noise. The fractional deviation of ShelfMC from the maximum voltage in this work's model is shown in Fig. 19, with θ_E and θ_H varied through all the angles measured in the anechoic chamber, subject to $\theta_E < 60^\circ$. The convolution method from this work is denoted TD for time-domain. The Askaryan pulse comes from [14], using $E_v = 3 \times 10^{18}$ eV, $\theta_{obs} - \theta_c = 0.3^\circ$, $f_{em} = 1$. No distance, reflection, or attenuation effects were applied to either the TD or ShelfMC numbers, since these effects equally shift both distributions. Thus, a comparison can be made between the ShelfMC expression for the maximum voltage, and the maximum voltage of the signal templates.

Fig. 19 demonstrates that the fractional difference between ShelfMC and TD is typically 10%. The χ^2/dof indicates a good fit. The excess near -0.4 comes from an overestimation by ShelfMC, where the Gaussian functions G describing the radiation pattern over-predict the LPDA relative gain (Eq. (20)). In reality, the Gaussian approximation is valid only for angles well within one or two beam widths in the E-plane (about 60° , centered on forward direction), because the real radiation pattern (Fig. 4) decreases more quickly. Fig. 19 indicates that the errors in the signal to noise $V_{ant}/V_{thermal}$ from ShelfMC are modest (for constant $V_{thermal}$) when the more realistic TD model is employed. The TD model incorporates

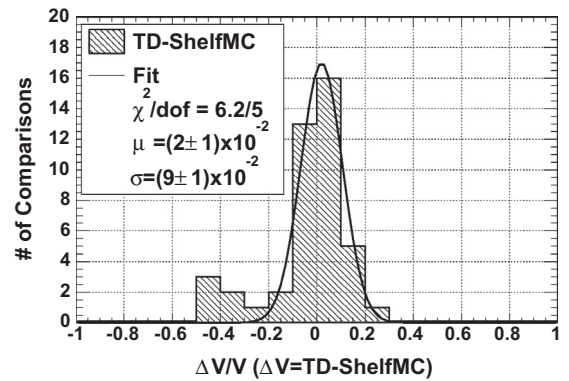


Fig. 19. The fractional voltage difference between ShelfMC (which relies on the formalism of Eqs. (18)–(20)) and the TD model of this work. The Askaryan signal is convolved with the each LPDA $h_{rx}(t)$ measured in the anechoic chamber, for each θ_E, θ_H from the chamber turn-table positioning system. A restriction of $\theta_E < 60^\circ$ has been applied (approximately two beam widths), for a total of 43 comparisons.

antenna phase effects, and even predicts the waveform shape (the templates). The thermal fluctuations are characterized by the system temperature, which remains constant because the antenna aperture and bandwidth are constant in either case.

7. Summary and conclusions

The RF response of the ARIANNA DAQ has been measured, with the purpose of predicting and quantifying the signatures from high energy neutrino interactions in Antarctic ice. This includes an iterative procedure to compute the effective height of the log-periodic dipole arrays (LPDA) serving as receiving antennas for the system, and the amplifier transfer function of the amplifier feeding the antenna signal to the digitizer. The LPDA response was determined in air, but prior work [19] and evidence presented in this paper demonstrates that the response remains valid for LPDA embedded in low density firn less than a few meters from the surface. This work has defined a procedure to compute the time-dependent signal Askaryan signal from the RF response, and this calculation is used to produce signal templates in several examples. The measured response is confirmed by data from multiple field contexts. The level of agreement between predicted and observed time domain waveforms produced correlation coefficients larger than 0.79. The predicted time-dependent wave packet is approximately 40 ns wide, changing shape according to the observation angle with respect to the Cerenkov cone, and the arrival direction with respect to the antenna. The change in shape due to the arrival direction is smooth and continuous in the forward lobe of the LPDA.

The example neutrino templates were computed from theoretical calculations of the time dependent signals generated from electromagnetic cascades [13,14,37] and convolved with the RF response function of the detector. The correlation coefficient between templates obeys $\rho \geq 0.8$, for variation of the E- and H-plane angles, and the observation angle. This result indicates that imprecise knowledge of the viewing angle has little impact on the overall form of the waveform, because the duration of electromagnetic pulse is short compared to the time scales of the system response. For similar reasons, there is little variation in the time-dependent waveform from hadronic or electromagnetic cascades, except in the case where the LPM effect is strong. Thus, it is acceptable to use the time-dependent pulse generated from an electromagnetic cascade at energies below the influence of the LPM, and scale it to higher energies to predict the waveforms from the dominant hadronic cascades. Though LPM-dominated events are sub-dominant in ARIANNA, [12], future development

of this work will extend the template production to include a broader range of LPM associated physics. Finally, it was also shown that the additional frequency dependence introduced by ice attenuation has negligible impact on the time dependent shape of the waveform for interaction distances relevant to ARIANNA.

The ARIANNA digitizers operate via a positive and negative voltage threshold trigger that separates random thermal noise from signal-like templates like those presented in this work. Rates are kept low, while maintaining low voltage thresholds, by requiring that a signal rise above a positive threshold and drop below a negative threshold. Such a system is triggered by a generic bi-polar waveform. While there are risks to searching for a specific signal shape in data, the potential benefits include highly efficient thermal-noise trigger rejection. It has been shown in this work that the signal templates are bi-polar, and contain high-frequency (1 GHz) content in spite of ice absorption and antenna effects. Further, an understanding of the energy-scaling of the signal is required for energy measurement. The template analysis provides this benefit, confirmed at the 10%-level by Monte Carlo simulation (for events near the Cerenkov angle).

Finally, correlations between all computed templates (for varying Cerenkov observation angles, and incoming angles in the LDPA main lobe) remain above 0.85, implying that the templates are consistent enough to use in ARIANNA data analysis routines [27], without *a priori* knowledge of the observation or incoming angles. By comparing the average ρ -value between data channels and templates, random thermal triggers are rejected for entire seasons of data with relatively few complex calculations. Future directions along the lines published here include studying cross-polarized measurements to constrain Askaryan field polarization, and the production of templates corresponding to high-energy cosmic rays. The latter effort involves use of the CoREAS code [38,39].

Acknowledgements

We wish to thank the staff of Antarctic Support Contractors, Raytheon Polar Services and Lockheed Martin, and the entire crew at McMurdo Station for excellent logistical support. We would like to acknowledge and thank the CReSIS project and the Anechoic Chamber facility management for the use of the world class anechoic chamber at the University of Kansas. This work was supported by generous funding from the Office of Polar Programs and Physics Division of the US National Science Foundation, grant awards ANT-08339133, NSF-0970175, and NSF-1126672.

Appendix A. Further equations

This section reviews the definition of the antenna effective height used in Section 2, and the assumption that $Z_{in} \approx Z_L$. Eq. (9), which produces the result for the signal recorded in the anechoic chamber (used to solve for the antenna effective height), has been simplified assuming $Z_{in} \approx Z_L$. The signal $V_L(t)$ recorded in a line impedance-matched configuration on an oscilloscope, in response to an incident electric field $E(t)$, is given by Eq. (3):

$$V_L(t) = 2 \left(\frac{Z_L}{Z_L + Z_{in}} \right) h_{rx}(t) \circ E(t) \quad (\text{A.1})$$

The operator (\circ) refers to convolution. The left-hand side of this equation is strictly real. Taking the imaginary part of both sides:

$$\text{Im}V_L(t) = 2\text{Im} \left(\frac{Z_L}{Z_L + Z_{in}} \right) h_{rx} \circ E(t) \quad (\text{A.2})$$

$$0 = \text{Im} \left(\frac{Z_L}{Z_L + Z_{in}} \right) \quad (\text{A.3})$$

$$0 = \text{Im}\{Z_L Z_{in}^*\} \quad (\text{A.4})$$

$$\text{Im}Z_L \text{Re}Z_{in} = \text{Im}Z_{in} \text{Re}Z_L \quad (\text{A.5})$$

From the last statement, it follows that the phases of Z_L and Z_{in} must be equal. If the real parts are equal, then the imaginary parts are equal as well, and $Z_{in} = Z_L$. For most RF equipment, the real part is just 50Ω , and this is true for the cables in this work. As discussed in Section 5.2, however, the real part of the LDPA impedance is 80Ω on average. When placed in snow with an index of refraction $n = 1.3$, however, $|Z_{in}|$ drops to $\approx 50\Omega$, and the assumptions hold.

For an impulsive electric field, described by $E(t) = E_0 \delta(t - t_0)$, the voltage read out by the antenna is

$$V_L(t) = 2 \left(\frac{Z_L}{Z_L + Z_{in}} \right) h_{rx}(t) \circ E(t) = h_{rx} \circ E_0 \delta(t - t_0) \quad (\text{A.6})$$

$$V_L(t) = E_0 h_{rx}(t) \circ \delta(t - t_0) = E_0 h(t - t_0) \quad (\text{A.7})$$

The antenna cannot reproduce the impulsive signal, and instead reads out a copy of the response function h_{rx} at a time $t - t_0$, with the units of volts versus time, proportional to the electric field amplitude.

References

- [1] K. Greisen, Phys. Rev. D 16 (1966) 748–750, <http://dx.doi.org/10.1103/PhysRevLett.16.748>.
- [2] G.T. Zatsepin, V.A. Kuz'min, JETP Lett. 4 (1966) 78–80.
- [3] V.S. Berezinsky, G.T. Zatsepin, Phys. Lett. B 28 (1969) 423.
- [4] S.W. Barwick, J. Phys. Conf. Ser. 60 (2007) 276–283, <http://dx.doi.org/10.1088/1742-6596/60/1/060>.
- [5] J.C. Hanson, The performance and initial results of the ARIANNA prototype (Ph.D. thesis), University of California at Irvine, 2013.
- [6] J.C. Hanson et al. (The ARIANNA Collaboration), Proceedings of the 32nd International Cosmic Ray Conference, Beijing, China. doi:<http://dx.doi.org/10.7529/ICRC2011/V04/0340>.
- [7] C.S. Neal, J. Glaciol. 24 (1979) 295–307.
- [8] G. Askaryan, Sov. Phys. JETP 14 (1962) 441–443.
- [9] I. Kravchenko et al. (The RICE Collaboration), Phys. Rev. D 85. doi:<http://dx.doi.org/10.1103/PhysRevD.85.062004>.
- [10] P.W. Gorham et al., The ANITA Collaboration, J. Astropart. Phys. 32 (2009) 10–41, <http://dx.doi.org/10.1016/j.astropartphys.2009.05.003>.
- [11] S. Klein, Nucl. Phys. Proc. Supl. 229–232 (2012) 284–288, <http://dx.doi.org/10.1016/j.nuclphysbps.2012.09.045>.
- [12] K. Dookayka, Characterizing the search for ultra-high energy neutrinos with the ARIANNA detector (Ph.D. thesis), University of California at Irvine, 2011.
- [13] J. Alvarez-Muniz, A. Romero-Wolf, E. Zas, Phys. Rev. D 81 (2010) 123009.
- [14] J. Alvarez-Muniz, A. Romero-Wolf, E. Zas, Phys. Rev. D 84 (2011) 103003, <http://dx.doi.org/10.1103/PhysRevD.84.103003>.
- [15] W. Sorgel, W. Wiesbeck, EURASIP J. Appl. Signal Process. 2005 (2005) 296–305, <http://dx.doi.org/10.1155/ASP.2005.296>.
- [16] A. Shilivski, E. Heyman, R. Kastner, IEEE Trans. Antennas Propag. 45 (1997) 1140–1149, <http://dx.doi.org/10.1109/8.596907>.
- [17] C. Baum, IEEE Trans. Electromagn. Compat. 44 (2002) 18–24, <http://dx.doi.org/10.1109/15.990707>.
- [18] P. Miocinovic et al., Phys. Rev. D 74 (2006) 043002, <http://dx.doi.org/10.1103/PhysRevD.74.043002>.
- [19] J.C. Hanson, L. Gerhardt, S. Klein, T. Stezelberger, S.W. Barwick, K. Dookayka, R. Nichol, Nucl. Instrum. Methods A 624 (2010) 85–91, <http://dx.doi.org/10.1016/j.nima.2010.09.032>.
- [20] T. Barrella, D. Saltzberg, S.W. Barwick, J. Glaciol. 57 (2011) 61–66, <http://dx.doi.org/10.3189/002214311795306691>.
- [21] Gerald Burke, Andrew Poggio, <http://en.wikipedia.org/wiki/Numerical_Electromagnetics_Code>.
- [22] C. Balanis, *Antenna Theory: Analysis and Design*, 3rd ed., John Wiley and Sons, 2005.
- [23] J. McClean, R. Sutton, Antennas and Propagation Society Intl. Symposium 3, 2003, pp. 571–574. doi:<http://dx.doi.org/10.1109/ICUWB.2009.5288811>.
- [24] J. McClean, H. Foltz, R. Sutton, Conference on Ultra-Wide Band Systems and Technologies, 2004, pp. 317–321. doi:<http://dx.doi.org/10.1109/UWBST.2004.1320987>.
- [25] S.A. Kleinfelder et al., The ARIANNA Collaboration, IEEE Trans. Nucl. Sci. 60 (2013) 612–618, <http://dx.doi.org/10.1109/TNS.2013.2252365>.
- [26] C.S. Neal, Ann. Glaciol. 3 (1982) 216–221.
- [27] J. Tatar, Performance of sub-array of arianna detector stations during first year of operation (Ph.D. thesis), University of California at Irvine, 2013.
- [28] S.O. Rice, Bell Syst. Tech. J. 23 (1944) 282–332, <http://dx.doi.org/10.1002/j.1538-7305.1944.tb00874.x>.

- [29] V.V. Bogorodsky, C.R. Bentley, P.E. Gudmandsen, *Radioglaciology*, D. Reidel Publishing, 1985.
- [30] J. Kraus, R. Marhefka, *Antennas*, 3rd ed., McGraw-Hill, 2003.
- [31] D. Seckel, Int. J. Mod. Phys. A 21-1 (2006) 70–74, <http://dx.doi.org/10.1142/S0217751X06033398>.
- [32] P.W. Gorham et al., The ANITA Collaboration, Phys. Rev. Lett. 99 (2007) 171101, <http://dx.doi.org/10.1103/PhysRevLett.99.171101>.
- [33] D. Saltzberg et al., Phys. Rev. Lett. 86 (2001) 2802, <http://dx.doi.org/10.1103/PhysRevLett.86.2802>.
- [34] E. Zas, F. Halzen, T. Stanev, Phys. Rev. D 45 (1992) 362–376.
- [35] L. Gerhardt, S. Klein, Phys. Rev. D 82 (2010) 074017, <http://dx.doi.org/10.1103/PhysRevD.82.074017>.
- [36] K. Kotera, D. Allard, A.V. Olinto, JCAP 10 (2010), <http://dx.doi.org/10.1088/1475-7516/2010/10/013>.
- [37] J. Alvarez-Muniz et al., Phys. Rev. D 62 (2000) 063001, <http://dx.doi.org/10.1103/PhysRevD.62.063001>.
- [38] D. Heck, J. Knapp, J.N. Capdevielle, G. Schatz, T. Thouw, Report FZKA 6019, 1998, Forschungszentrum Karlsruhe.
- [39] T. Huege, M. Ludwig, C.W. James. arXiv:1301.2132.

Radar absorption, basal reflection, thickness and polarization measurements from the Ross Ice Shelf, Antarctica

Jordan C. HANSON,^{1,2} Steven W. BARWICK,¹ Eric C. BERG,¹ Dave Z. BESSON,^{2,3} Thorin J. DUFFIN,¹ Spencer R. KLEIN,⁴ Stuart A. KLEINFELDER,⁵ Corey REED,¹ Mahshid ROUMI,¹ Thorsten STEZELBERGER,⁴ Joulien TATAR,¹ James A. WALKER,¹ Liang ZOU¹

¹Department of Physics and Astronomy, University of California, Irvine, Irvine, CA, USA

²Department of Physics and Astronomy, University of Kansas, Lawrence, KS, USA

³Moscow Physics and Engineering Institute, Moscow, Russia

⁴Lawrence Berkeley National Laboratory, Berkeley, CA, USA

⁵Department of Electrical Engineering and Computer Science, University of California, Irvine, CA, USA

Correspondence: Jordan C. Hanson <918particle@gmail.com>

ABSTRACT. Radio-glaciological parameters from the Moore's Bay region of the Ross Ice Shelf, Antarctica, have been measured. The thickness of the ice shelf in Moore's Bay was measured from reflection times of radio-frequency pulses propagating vertically through the shelf and reflecting from the ocean, and is found to be 576 ± 8 m. Introducing a baseline of 543 ± 7 m between radio transmitter and receiver allowed the computation of the basal reflection coefficient, R , separately from englacial loss. The depth-averaged attenuation length of the ice column, $\langle L \rangle$ is shown to depend linearly on frequency. The best fit (95% confidence level) is $\langle L(\nu) \rangle = (460 \pm 20) - (180 \pm 40)\nu$ m (20 dB km $^{-1}$), for the frequencies $\nu = [0.100\text{--}0.850]$ GHz, assuming no reflection loss. The mean electric-field reflection coefficient is $\sqrt{R} = 0.82 \pm 0.07$ (1.7 dB reflection loss) across [0.100–0.850] GHz, and is used to correct the attenuation length. Finally, the reflected power rotated into the orthogonal antenna polarization is <5% below 0.400 GHz, compatible with air propagation. The results imply that Moore's Bay serves as an appropriate medium for the ARIANNA high-energy neutrino detector.

KEYWORDS: ice/ocean interactions

INTRODUCTION

The vast Antarctic ice sheet has become important to high-energy neutrino physics in recent years (Barwick, 2007; ANITA Collaboration, 2010; Klein, 2012; Kravchenko and others, 2012; IceCube Collaboration, 2013), motivated by the convenient properties of glacial ice, including optical and radio-frequency (RF) dielectric properties. High-energy cascades induced by neutrinos emit Cherenkov photons; photons with 350–500 nm wavelengths can propagate 10–100 m in Antarctic ice before being detected by photomultiplier tubes (AMANDA Collaboration, 2006). Similarly, at energies 0.1 EeV, neutrinos begin to produce measurable Askaryan pulses (Askaryan, 1962), a form of coherent Cherenkov radiation in the RF regime. Moore's Bay, part of the Ross Ice Shelf, presents an attractive target volume for studying these particle interactions, because the radiation experiences minimal attenuation in the cold ice, and can be reflected back towards the surface by the ocean. Knowledge of the dielectric properties of the ice shelf is required to build such an experiment.

By transmitting a ~1 ns pulse through a transmitting antenna downwards through the ice shelf, and recording the reflections from the oceanic interface, bulk ice attenuation and the reflection coefficient of the interface can be inferred. Using reflected radio pulses to study ice sheets and shelves is known as radio-echo sounding, and has been used to study glaciers and ice shelves in various locations on the Ross Ice Shelf (RIS) and the high plateau (Neal, 1979, 1982;

Besson and others, 2008; Allison and others, 2012; Fretwell and others, 2013).

Basal reflection in Moore's Bay has been studied previously. Neal (1979, 1982) reported on the RIS, using a 60 ns wide, 60 MHz pulse, recording the returned power vs location. Flights 1 km above the RIS were performed, including several points over Moore's Bay. Basal reflection coefficients were derived in 10 dB increments, assuming no losses from dust or other impurities, for contours across the shelf. Moore's Bay produces reflection coefficients near the Fresnel limit (~0.82 dB, or ~0.91 for the electric field), and two explanations were offered. First, Moore's Bay is far from brine percolation zones that are traced from the grounding line to the shelf front, which are correlated with ice velocity. Second, the melt rate near the grounding line for basal ice prevents the formation of an abrupt basal layer of saline ice, and instead replaces glacial ice with saline ice over time. The freeze-on of saline ice at the shelf bottom does occur; however, these regions are far from the location of the Antarctic Ross Ice-Shelf ANtenna Neutrino Array (ARIANNA), and the average accumulation rate of bottom saline ice is only 0.3 ± 0.1 m a $^{-1}$ in the east RIS (Rignot and others, 2013).

Neal (1982) showed that two parameters besides peak power can be extracted from the data. First, the width of the peak power distribution for a specific location pertains to vertical roughness at the oceanic interface. Second, the spatial correlation of power measurements reveals horizontal correlation lengths for roughness. These measurements must

be compared to theoretical distributions of the same parameters, from the theory of rough-surface scattering (Dookayka, 2011). The most general statistical surface, with the fewest parameters, was chosen: a Gaussian surface roughness described by normal fluctuations about a mean depth, and a specified horizontal correlation length. Neal reports vertical root-mean-square (rms) of 3 cm at the ocean/ice boundary, spread over correlation lengths of 27.5 m, 30 km east of Ross Island. The results make no use of absolute power measurements, and thus are independent of assumptions of RF absorption.

To measure the reflection coefficient separately from englacial loss, the transmitting and receiving antennas may be separated by a baseline comparable to the shelf depth. The signal path is longer with the baseline, providing different absorption but the same reflection loss (Hanson, 2011, 2013). By comparing total loss in the set-up with and without a baseline, absorption and reflection loss can be measured separately. A map of the site studied in this work is shown in Figure 1.

RF attenuation length

The amplitude of an electric field decreases by $1/e$ after propagating one attenuation length. For an electromagnetic plane wave travelling through a dielectric medium with a complex index of refraction $n = n' - in''$, the electric field is

$$\mathbf{E} = \mathbf{E}_0 \exp(-i(nkx - \omega t)) = \mathbf{E}'_0 \exp\{-n''kx\} \quad (1)$$

The electric field attenuation length is then $(n''k)^{-1} = L$ (ω is the angular frequency). When measured over a volume of material with varying dielectric absorption, the attenuation length is averaged over the effect of depth on the dielectric constant $\epsilon = \epsilon' - i\epsilon''$, and in turn the loss tangent, $\tan \delta = \epsilon''/\epsilon'$. If $\tan \delta \ll 1$, it can be shown that

$$\langle L \rangle^{-1} = (\pi\nu/c)\sqrt{\epsilon'} \tan \delta (\text{m}^{-1}) \quad (2)$$

$$N_L (\text{dB km}^{-1}) = 8686.0 \langle L[m] \rangle^{-1} \quad (3)$$

Equation (3) is the conversion from attenuation length to absorption loss, N_L . The Debye model shows that $\nu \tan \delta$ is approximately constant, provided the frequency is far from any molecular resonances (this is true for 0.1–1 GHz). Additionally, ϵ' (in ice) is constant for the bandwidth 0.1–2 GHz. Thus, frequency dependence in $\langle L \rangle$ is attributed to other effects, such as acids and sea-salt impurities (Bogorodsky and others, 1985; Matsuoka and others, 2012).

Reflection coefficient

Under the Debye model, with a single relaxation time, the ice conductivity is $\sigma = 2\pi\epsilon_0\epsilon'\nu\tan \delta \approx 10 \mu\text{S m}^{-1}$ at 100 MHz (Dowdeswell and Evans, 2004). By comparison, sea water has a conductivity of a few S m^{-1} , with a skin depth of 30 mm, at 60 MHz (Dowdeswell and Evans, 2004; Somaraju and others, 2006). The reflection coefficient for the electric fields (\sqrt{R} , where R refers to power) is given by $(n_1 - n_2)/(n_1 + n_2)$, given the complex $n_1 = \sqrt{\epsilon_1}$ and $n_2 = \sqrt{\epsilon_2}$ for the dielectric and conductive media, respectively.

$$\begin{aligned} \lim_{\tan \delta_2 \gg 1, \tan \delta_1 \rightarrow 0} |\sqrt{R}| &= \frac{1 - n_2/n_1}{1 + n_2/n_1} \\ &= \frac{1 - \sqrt{\alpha}e^{-i\delta_2/2}}{1 + \sqrt{\alpha}e^{-i\delta_2/2}} = \left(\frac{1 + \alpha - \sqrt{2\alpha}}{1 + \alpha + \sqrt{2\alpha}} \right)^{1/2} \end{aligned} \quad (4)$$

Equation (4) demonstrates that $|\sqrt{R}| \rightarrow 1$, where n_1 refers to

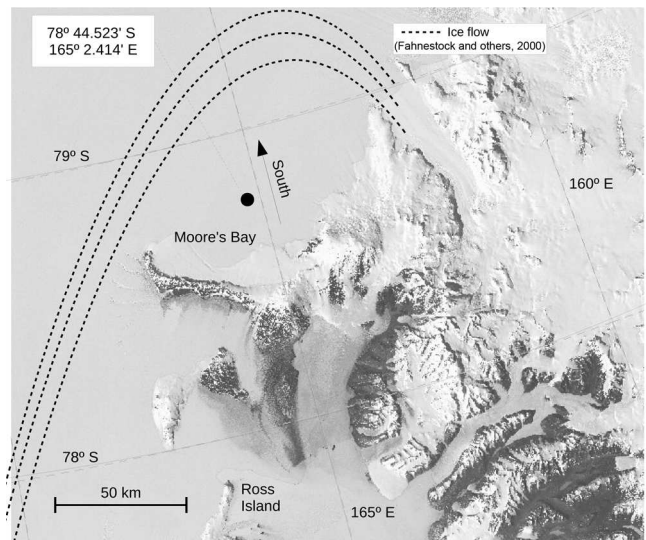


Fig. 1. The site studied in this work is marked with the black circle. Moore's Bay is the area south of Ross Island, enclosed by Minna Bluff. The satellite data are available by the US Geological Survey (USGS, 2012). The main ice flowlines are illustrated with dashed lines. Fahnestock (2000) provides further analysis and discussion.

the ice and n_2 refers to the ocean, given the limits $\tan \delta_2 \gg 1$, and $\tan \delta_1 \approx 0$, and $\alpha = \epsilon_2''/\epsilon_1'$. In Eqn (4), the fact that $\delta_2 \rightarrow \pi/2$ has been used. Equation (4) is completely general as long as the limit is satisfied. The right-hand side has a global minimum at $\alpha = 1$, or $\epsilon_2'' = \epsilon_1'$, corresponding to a minimum electric field reflection coefficient of $\sqrt{R}_{\min} \approx 0.41$. Realistic values for both ice and sea water indicate α ranges from 20 to 30, depending on the salinity and temperature of the sea water (Dowdeswell and Evans, 2004; Somaraju and others, 2006). Neal (1979) suggested that the reflection coefficient in Moore's Bay is approximately -0.82 dB , or $\sqrt{R} = 0.91$, based on the properties of the sea water beneath the RIS. These upper and lower bounds form an allowed range of $\sqrt{R} = 0.41\text{--}0.91$.

In addition to vertical radio echoes, measurements were taken with a baseline distance between transmitter and receiver, introducing a new overall path length. In this work, these measurements are named angled bounce studies. For the angled bounce studies reported here, Eqn (5) shows that the reflected power limits to the expression for normal incidence (for s-polarized waves). Also, the initial transmission angle from normal is reduced, because the upper firn layer bends the transmitted pulse downward (to $\theta \gtrsim 30^\circ$), given the initial antenna orientation of 45° . Ignoring the cosine dependence in Eqn (5) amounts to a 1–5% correction, depending on n_2 :

$$\sqrt{R} \approx \frac{n_1(1 - \theta^2/2) - n_2(1 - \frac{1}{2}(\epsilon\theta)^2)}{n_1(1 - \theta^2/2) + n_2(1 - \frac{1}{2}(\epsilon\theta)^2)} \approx \frac{n_1 - n_2}{n_1 + n_2} \quad (5)$$

Ice thickness calculation

The upper 60–70 m of the ice shelf is firn with density $\approx 0.4 \text{ g cm}^{-3}$ near the surface (Gerhardt and others, 2010). This result is in agreement with the value 0.36 g cm^{-3} from Dowdeswell and Evans (2004). Looyenga's equation, n_{ice} and the firn surface density predict the firn index to be $n_{\text{firn}} \approx 1.3$. This value was confirmed with pulse propagation timing at the surface, over a distance of $543 \pm 7 \text{ m}$ (see

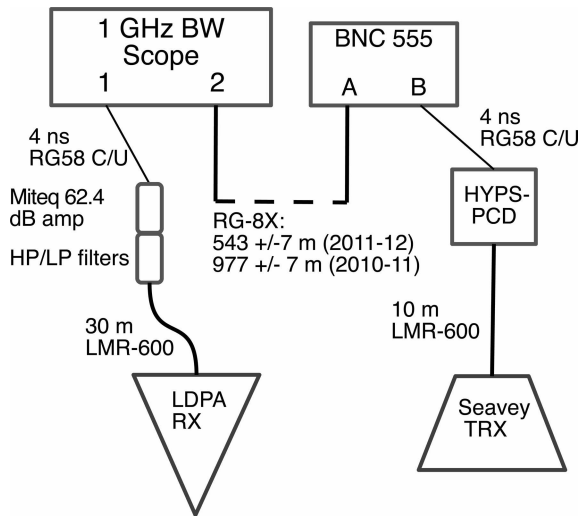


Fig. 2. The general set-up of the radio-sounding experiments. Measured and physical time delays are shown in Table 2.

below for detail). From the pulse arrival time, the implied wave speed indicated an index of $n_{\text{surf}} = 1.29 \pm 0.02$ (Hanson, 2013).

The density and thus the index of refraction has an exponential depth dependence, according to the Schytt model:

$$n(z) = 1.78 = n(z \geq 67\text{m}) \quad (6)$$

$$n(z) = n_0 + p \exp(-z/q) \quad (z < 67\text{m}) \quad (7)$$

In Eqn (7), $n_0 = 1.86$, $p = -0.55$ and $q = 35.4\text{ m}$, with the upper layer density $\rho \approx 0.4\text{ g cm}^{-3}$, and $z > 0$ for increasing depth. A different model with a constant firn correction (to sounding propagation times) and no exponential density profile yields shelf depths consistent within errors (Gerhardt and others, 2010). Equations (6) and (7) are based on measurements taken at Williams Field near McMurdo station (Schytt, 1958; Barrella and others, 2011). Given the measured physical delay between pulse and reflection, Δt , the shelf depth can be obtained from integrating over the total path length d (Eqns (8) and (9)). Error propagation yields Eqn (10), where $D_f = 67 \pm 10\text{ m}$ is the firn depth (Dowdeswell

Table 1. The various experimental configurations used, by year, for the data in this work. S stands for Seavey horn, and L stands for LDPA (log-periodic dipole array)

Year	Vertical/Angled	Ant. (TX/RX)	$G_1 G_2$
2010	Vertical	L/L	1.0
2011	Vertical	S/L	1.0
2011	Angled	S/L	0.5
2011	Vertical	L/L	1.0

and Evans, 2004). A density profile for the RIS in figure 2 of the latter reference is consistent with this model.

$$\frac{c\Delta t}{2} = \int_0^{d_{\text{ice}}} n(z) dz \quad (8)$$

$$d_{\text{ice}} = \frac{c\Delta t}{2n} - \frac{D_f(n_0 - n)}{n} + \frac{qp}{n} (e^{-D_f/q} - 1) \quad (9)$$

$$\sigma_{d, \text{ice}} = \sqrt{\left(\frac{\sigma_t c}{2n}\right)^2 + \left(\frac{\sigma_n c \Delta t}{2n^2}\right)^2 + k \sigma_{D_f}^2} \quad (10)$$

$$\approx \frac{c}{2n} \sqrt{\left(\frac{\sigma_n}{n}\right)^2 \Delta t^2 + \sigma_t^2}$$

The fractional difference between n_0 and n is small, and $\exp(-D_f/q)$ is small, so k turns out to be of order 10^{-2} . The term in Eqn (10) involving k is a factor of 10 below the others so it may be dropped. For similar reasons, cross-terms involving firn properties and σ_n have been neglected.

EXPERIMENTAL TECHNIQUE

The experimental set-up is shown in Figure 2, with additional detail in Table 1. Figure 3 shows the vertical and angled bounces. To create broadband RF pulses, a 1 ns wide, 1–2.5 kV pulse was delivered from the HYPS Pockels Cell Driver (PCD) to a transmitting antenna, and the reflection is received by a second antenna. The PCD and the 1 GHz bandwidth oscilloscope (Tektronix TDS540A in 2010, Agilent HP54832D thereafter) were triggered with a tunable delay generator (Berkeley Nucleonics 555 2-port). From the programmed delay, reflection time and relevant cable delays, the shelf depths were derived for each season. The RG-8X cable between port A of the BNC 555 and the oscilloscope enabled the introduction of a long baseline between the antennas.

Voltage standing wave ratio (VSWR) measurements were performed to study antenna transmission in snow. In all cases, the VSWR of the transmitting and receiving antennas demonstrates good transmission and reception when buried in the surface snow (Gerhardt and others, 2010; Barrella and others, 2011). Noise above and below the receiver bandwidth was filtered with MiniCircuits NHP and NLP filters, and amplified by a 62.4 dB Miteq AM-1660 low-noise amplifier (typical noise figure of 1.5 dB). Signals were attenuated by 3–20 dB where appropriate, to remain in the linear regime of the amplifier.

For the 2006 season (Barrella and others, 2011), the transmitter and receiver were Seavey radio horns used in the ANITA (ANTarctic Impulsive Transient Antenna) experiment (ANITA Collaboration, 2009), with a bandwidth of [200–1300] MHz. In the data from the 2010 season, the receiver and transmitter were log-periodic dipole arrays (LPDAs;

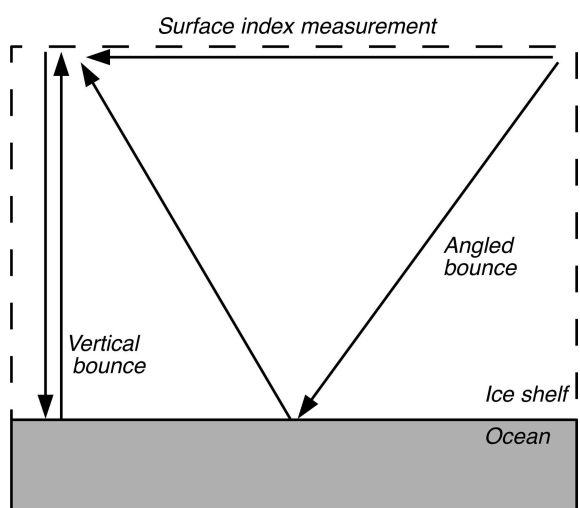


Fig. 3. The vertical and angled bounce tests. The surface propagation set-up was used to derive the surface index of refraction, n_{surf} .

Create Corp. CLP5130-2N) with a bandwidth of [100–1300] MHz. The Seavey is a dual polarization quad-ridge horn antenna that has higher gain above 200 MHz than the LPDA. The LPDA antennas have a wider bandwidth, but stretch the signal in time with respect to the horn (Barwick and others, 2015). In the 2011 season, the data were recorded with a Seavey transmitter and an LPDA receiver. The 2010 data have been published (Hanson, 2011, 2013). In this work, the thickness results from 2010 are compared to three new measurements, and a new reflection coefficient and attenuation length analysis are presented.

In the surface test, we measured the pulse propagation time over the 543 ± 7 m baseline, and extracted the surface index of refraction from the speed. The result was $n_{\text{surf}} = 1.29 \pm 0.02$, and is needed for the boundary conditions in the shelf-thickness model. In the *vertical bounce* measurements, where the transmitter and receiver are co-located, the separation in 2006 was typically 9 m. In 2010 and 2011 the separation was 19 and 23 m, respectively. This ensures that the receiver is in the far field of the transmitter during calibration. Comparing vertical bounce soundings to calibration measurements allows derivation of $\langle L \rangle$ assuming a value for \sqrt{R} .

The *angled-bounce* measurements are also compared to calibration measurements and vertical bounce cases to measure both $\langle L \rangle$ and \sqrt{R} . Angled signals were captured without having to account for complex ray tracing near the surface. During angled bounce tests, the transmitter and receiver were angled 45° downward from horizontal. For the angled bounce measurements, the 2010 baseline was 977 ± 7 m, and the 2011 baseline was 543 ± 7 m. The angled bounce measurements in 2010 and 2011 had signal path lengths of 1517 ± 8 m and 1272 ± 7 m, respectively. The incident angle with respect to normal refracts closer to 30° when the pulse reaches the ocean, because the firn index $n_{\text{firn}} = 1.3$ is smaller than the bulk ice index $n_{\text{ice}} = 1.78$.

The Friis equation relates the power received, P_r , to the transmitted power P_t in a lossless medium at a given wavelength. For two identical antennas in air, it may be written

$$P_r = \frac{P_t(G_a c)^2}{(4\pi\nu d)^2} = \frac{P_0}{d^2} \quad (11)$$

Here G_a is the intrinsic gain of the antennas and ν is the frequency. P_r and P_t are the received and transmitted power, respectively. To account for absorption losses and possible losses upon reflection, the Friis equation is modified to

$$P_r = \frac{P_0 R G_1 G_2}{d^2} \exp\left(-\frac{2d}{\langle L \rangle}\right) \quad (12)$$

By convention, the factor of 2 in the exponential means $\langle L \rangle$ refers to electric field, and the reflection coefficient for the power is R . The factor $G_1 G_2$ accounts for the relative power radiation pattern of the transmitter and receiver (Table 1). G_1 and G_2 are 1 for the vertical bounce measurements, in which the signal is transmitted and received in the forward direction of the antennas. As the angle at which the signal interacts with the antenna increases, $G_1 G_2$ decreases from 1 according to the antenna radiation patterns. The radiation patterns have been both simulated and measured (ANITA Collaboration, 2009; Barwick and others, 2015). Manipulating Eqn (12) gives Eqn (13), the left-hand side of which may be plotted vs path length d to obtain a line with a slope $-1/\langle L \rangle$, and a constant y-intercept. The reflection coefficient is treated as a free parameter in the fit. The error in the

Table 2. A summary of total and physical time delays for the various seasons, and calculated shelf thicknesses. The physical time delay Δt_{phys} is the measured delay Δt_{meas} , with equipment delays subtracted. The total precision is quoted in the earlier measurements (Gerhardt and others, 2010; Barrella and others, 2011). The width of the reflected pulse, σ_{pulse} , is caused by the response of the antennas

Year	Δt_{meas}	Δt_{phys}	σ_{stat}	σ_{sys}	σ_{pulse}	σ_{tot}	d_{ice}
	ns	ns					m
2006	–	6783	–	–	–	10	577.5 ± 10
2009	–	6745	–	–	–	15	572 ± 6
2010	7060	6772	5.0	8.0	10	14	576 ± 6
2011	6964	6816	4.0	5.0	10	12	580 ± 6

left-hand side of Eqn (13) is given by Eqn (14).

$$f(d) = \ln \sqrt{\frac{d^2 P_r}{R G_1 G_2}} = -d/\langle L \rangle + \text{const} \quad (13)$$

$$\sigma_f = \sqrt{\left(\frac{\sigma_d}{d}\right)^2 + \left(\frac{\sigma_{P_r}}{2P_r}\right)^2} \quad (14)$$

ICE-THICKNESS RESULTS

The measured propagation times, both total and corrected for cable delays, are shown in Table 2, along with statistical and systematic uncertainties. Using Eqns (8–10), the times are converted to thickness. Systematic errors arise from cables, the response time of the pulser, and delay generator precision (see Fig. 2). For the long cables, a conservative 5% error in the propagation time is assumed, because the endpoints of the baselines were measured with GPS, with waypoint precision of 5 m. The distance between the 2006 site and the site for the remaining three thickness measurements was ~ 1 km, and the GPS location of the latter site is accurate to within a horizontal uncertainty of 5 m.

The reflected pulse from the 2009 set-up was only several mV above noise backgrounds, so the entire pulse width was included as systematic error (Gerhardt and others, 2010). For the 2011 data, the location and uncertainty in peak voltage oscillations in the reflections were used instead, because the signal was well above backgrounds. The low-frequency ringing in the reflected data originates from group delay in the LPDA, which is 10 ns at 0.2 GHz (the lowest frequency emitted by the transmitter). When folded into the timing uncertainties, smaller but comparable errors to 2006 are obtained for the thickness. Timing uncertainties are lowest in 2006 because both transmitter and receiver were Seavey horns, which have lower group delay than the LPDA.

In general, statistical errors come from Eqn (10), with $n = 1.78 \pm 0.02$, and total timing error from Table 2. The magnitude of σ_n comes from measurements made at the surface ($n_{\text{surf}} = 1.29 \pm 0.02$) (Hanson, 2013). Fluctuations in n are largest at the surface, making this a conservative estimate for the bulk ice, and it is similar to previous work (Gerhardt and others, 2010; Barrella and others, 2011). The total error from 2006 is higher because a larger error on the dielectric constant was used. The mean thickness over all seasons is $d_{\text{ice}} = 576 \pm 8$ m (statistical and systematic added in quadrature). Errors in Table 2 other than from the index of refraction are treated as systematic. A linear fit to the four

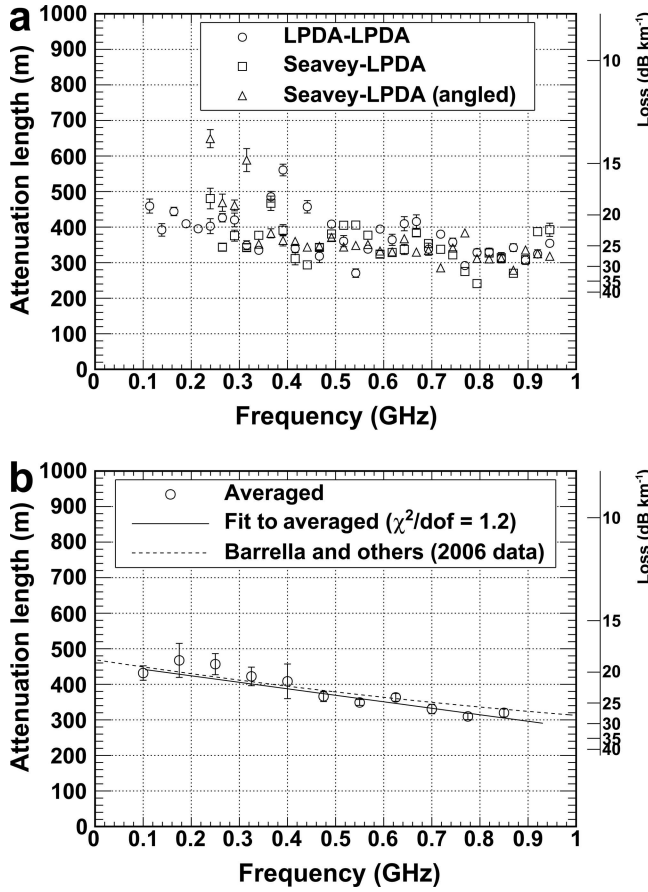


Fig. 4. (a) The depth-averaged attenuation length vs frequency, with standard deviations from error propagation in Eqn (18). The attenuation length is converted to englacial loss (dB km^{-1}), at right. (b) The data from (a) averaged into 75 MHz bins, with standard deviations. The linear fit has $\chi^2/\text{dof} = 1.2$, a slope of $-180 \pm 40 \text{ m GHz}^{-1}$ and an offset of $460 \pm 20 \text{ m}$. The dashed line is a fit to prior data taken 1 km from our site (Barrella and others, 2011).

data points together yields a slope consistent with zero (within errors). The measurement from 2006 took place 1 km from the location of subsequent seasons, and does not deviate strongly from the mean.

AVERAGE ATTENUATION LENGTH, $\langle L \rangle$, VS FREQUENCY

The technique of measuring \sqrt{R} and $\langle L \rangle$ simultaneously is more challenging than assuming a constant \sqrt{R} and comparing the raw power spectra of only vertical bounce data and calibration data. Assuming a uniform reflection coefficient with respect to frequency assumes that the reflecting surface is dominated by specular, rather than diffuse, reflection. As long as the first few Fresnel zones D_m of the transmitted pulse are not significantly larger than the horizontal correlation length L_C of roughness features along the shelf base, then the effect of the vertical roughness scales on the reflection coefficient is avoided (Peters and others, 2005). Prior data collected at two locations on the Ross Ice Shelf, near Moore's Bay, indicate horizontal correlation lengths $L_C = 12.5 \text{ m}$ and $L_C = 27.5 \text{ m}$ at the two sites (Neal, 1982). The glaciological Fresnel zone equation, for an observation point a distance h above the snow surface, with a shelf thickness of z , shelf index of refraction n , Fresnel

zone number m , and an in-air wavelength λ is

$$D_m \approx \sqrt{2m\lambda\left(h + \frac{z}{n}\right)} \quad (15)$$

The approximation arises from the small angle approximation, and is sound because the Fresnel zones are small compared to z . The measurements take place at the surface, so $h = 0$. Using $n = 1.78$, $\lambda = 3 \text{ m}$ and the measured shelf thickness, Eqn (15), gives $D_1 = 10\text{--}40 \text{ m}$, for the bandwidth. Vertical rms fluctuations at the ocean/ice surface were reported to be 3 cm and 10 cm for two sites, spread out over a typical length scale of L_C . Vertical height fluctuations of 10 cm and 3 cm spread out over 12.5 m and 27.5 m, respectively, mean that specular reflection is a good approximation for this bandwidth (Neal, 1982). The attenuation lengths derived assuming constant \sqrt{R} are revised in the next section, to account for reflection loss ($\sqrt{R} < 1.0$).

Consider the calibration pulse, V_C , the vertical bounce pulse, V_{ice} , and the depth-averaged attenuation length vs frequency, $\langle L(\nu) \rangle$, all at a frequency ν :

$$V_C(\nu) = V_0/d_C \quad (16)$$

$$V_{\text{ice}}(\nu) = \frac{V_0}{d_{\text{ice}}} \exp\left(-\frac{d_{\text{ice}}}{\langle L(\nu) \rangle}\right) \quad (17)$$

$$\langle L(\nu) \rangle = \frac{d_{\text{ice}}}{\ln((V_C(\nu)d_C)/(V_{\text{ice}}(\nu)d_{\text{ice}}))} \quad (18)$$

Because the surface of the firn is snow, with a density of 0.4 g cm^{-3} and an index of refraction $n = 1.3$, the reflection coefficient (for power) between air and snow is ~ 0.02 , so potential interference from surface reflections is not expected to modify Eqn (16). The antennas were placed at the maximum height allowed by the cables and other equipment (1.5 m), and this calibration was compared to the case with the antennas buried in snow slots. Because of the low snow density, dielectric absorption is negligible over the calibration distances (23 m). The antenna calibrations produced similar waveforms with the antennas lowered in snow. The waveform amplitude increases when LPDAs are in the snow, due to the shift in the lower cut-off frequency by the index of refraction. This effect is confirmed in Numerical Electromagnetic Code (NEC) antenna simulations, and VSWR data (Barwick and others, 2015).

The 2011 data are shown in Figure 4a. In Eqns (16–18), the voltages are defined $V \propto \sqrt{P(\nu)}$, where P is the measured power at the frequency ν . The antenna impedance is the same for the calibration and bounce studies, making it irrelevant in the ratio in Eqn (18) (Barwick and others, 2015). The 2011 power spectra begin at the low-frequency cut-offs of the transmitter type (200 MHz for the Seavey, and 100 MHz for the LPDA). The englacial loss (dB km^{-1}) is also shown (Eqn (3)).

The 2011 data extend to 0.850 GHz, where the signal-to-noise ratio is close to 1.0, and the error bars are the standard deviation from error propagation in Eqn (18). About 10 m of the error is due to uncertainty in the shelf thickness, and 10 m is due to uncertainty in the power spectrum. Data above 0.850 GHz appear to be rising due to noise floor contributions. Also, systematic fluctuations in the vertical bounce power spectra lead to systematic fluctuations in $\langle L(\nu) \rangle$. Systematic errors arise from differences in system frequency response after changing the transmitter location and type, and reflections within the system. The angled bounce data at 0.240 and 0.315 GHz, in particular, are

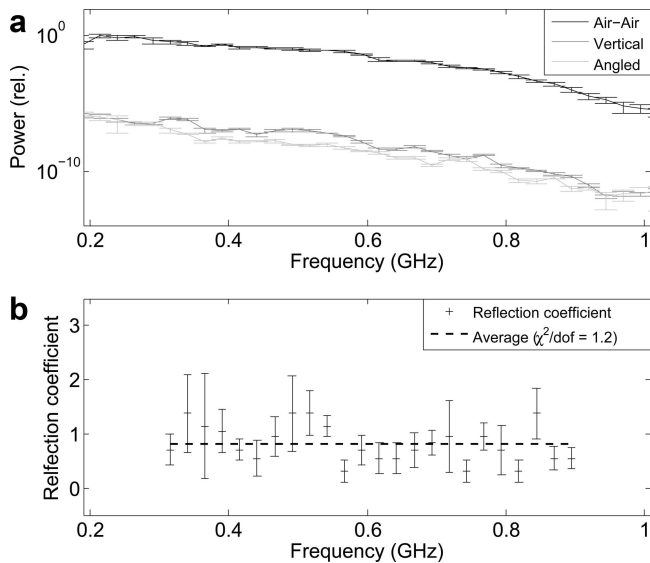


Fig. 5. The electric-field reflection coefficient, \sqrt{R} , vs frequency. The three power spectra correspond to three measurements: a surface power calibration (black), vertical bounce (dark grey) and angled bounce (light grey) cases. The three measurements at each frequency determine a reflection coefficient through a linear fit to Eqn (13), with errors from Eqn (14) attributed to \sqrt{R} .

systematically high. The Seavey transmitter was placed in a snow cavity rather than fully buried for the angled test, which can lead to cavity resonance effects.

The frequency resolution is maximized in Figure 4a, with no window function. A higher resolution extends the upper frequency limit by avoiding folding noise into the highest-frequency bins. The correction for potential angular dependence of the reflection coefficient only applies to the angled bounce data (~ 4 m). In Figure 4a, the data are averaged into 0.075 GHz bins, with a linear fit. The best-fit slope is $-180 \pm 40 \text{ m GHz}^{-1}$, and the best-fit offset is $460 \pm 20 \text{ m}$ (95% confidence level, $\chi^2/\text{dof} = 1.2$). Data above 0.850 GHz are neglected in the average and fit shown in Figure 4; however, the χ^2/dof only increases to 1.8 if it is included. As in Figure 4a, the averaged attenuation length is converted to dB km^{-1} on the right-hand y-axis using Eqn (3).

Despite the systematic fluctuations, the fit to the data in Figure 4 is in close agreement with the quadratic fit to the data from 2006 (Barrella and others, 2011). In the publication of the 2006 data, the reflection loss was assumed to be 0 dB. If a lower value is assumed (see below), the attenuation length increases, because the returned voltage per unit frequency in Eqn (18) must remain constant. The level of systematic variation in \sqrt{R} shown below will also generate $\sim 5\%$ systematic uncertainty in $\langle L \rangle$, but only to increase it. The 2006 and 2011 data agree, even though the measurements were made 1 km apart. The area of Moore's Bay near Minna Bluff is far from any zones of high glacial velocity that could cause depth or basal reflection variations, and crevasses have not been observed in the area, so the ice is expected to be relatively uniform.

BASAL REFLECTION COEFFICIENT

The 2006 season $\langle L \rangle$ results were derived from vertical bounce measurements assuming $\sqrt{R} = 1.0$. Using the path lengths derived from shelf thickness, and the measured

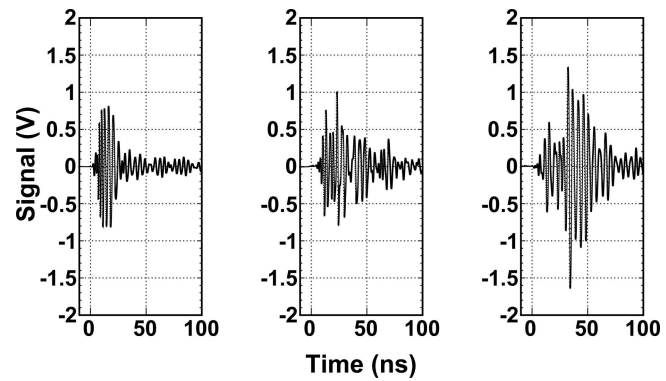


Fig. 6. Typical waveforms from 2011, averaged over 100 triggers. (a) The calibration pulse. (b) The vertical bounce reflection. (c) The angled bounce reflection. The vertical and angled bounce data have been amplified by the 60 dB Miteq amplifier. The data have been scaled to account for in-line attenuators (the data were kept within the amplifier linear range).

power spectra of the calibration, vertical bounce and angled bounce reflections, \sqrt{R} can be derived separately from the attenuation length. The errors in \sqrt{R} arise from propagating errors in path length (from thickness, and geometry) and returned power through Eqn (13).

The three tests (calibration, vertical and angled bounce) serve as three measurements of $f(d)$ for different values of the path length d , given the free parameter \sqrt{R} . The measurements are compared to the linear model $f_{\text{model}} = -d/\langle L \rangle + f_0$, which is scanned through $(\sqrt{R}, \langle L \rangle)$ parameter space. The y-intercept is irrelevant to the physics, coming from the linear fit upon each iteration. (The overall power at a given frequency is relative to the calibration pulse power.) Each iteration produces a χ^2 value, and $(\sqrt{R}, \langle L \rangle)$ were scanned until a global minimum was reached at each frequency.

The averaged power spectra of the time-dependent waveforms are shown in Figure 5a. The spectra are constructed from averaging the modulus-squared of the fast Fourier transform of the time-dependent signals, and plotted relative to the maximum calibration power. The error bars are the error in the mean for each bin. Examples of waveforms from which these power spectra are derived are shown separately in Figure 6. For all recorded waveforms, a sampling rate of 5 GHz was used on the 1 GHz bandwidth oscilloscope. The spectra in Figure 5 have a frequency resolution of 0.025 GHz.

The 2010 data for \sqrt{R} vs $\langle L \rangle$ have been analysed by Hanson (2011, 2013). The basic results were $480 \text{ m} \leq \langle L \rangle \leq 510 \text{ m}$ ($17\text{--}18 \text{ dB km}^{-1}$), and $0.72 \leq \sqrt{R} \leq 0.88$ ($1.1\text{--}2.8 \text{ dB loss}$), for the average attenuation length and reflection coefficient (68% confidence level). The set-up (Fig. 2) demonstrated good transmission through surface snow for frequencies below 0.180 GHz that season, and the LDPA lower limit in the snow is 0.080 MHz. The index of refraction of snow extends the LPDA response to 0.080 GHz from a lower limit of 0.105 GHz (Barwick and others, 2015). A shorter angled bounce baseline ($543 \pm 7 \text{ m}$) was chosen for the 2011 season, relative to the prior year, to boost signal at higher frequencies; however, the snow absorption effect was not observed in 2011.

Figure 5b shows the \sqrt{R} results from the 2011 season. The baseline sets the path length difference between the

Table 3. Summary of dielectric parameters. The first column is the frequency, ν , followed by the attenuation lengths, which are uncorrected ($\langle L_0 \rangle$) and corrected ($\langle L \rangle$) for $\sqrt{R} = 0.82 \pm 0.07$. The fourth column is $\langle L \rangle$ expressed in dB km $^{-1}$. The imaginary part of the dielectric constant, ϵ'' , is shown in the fifth column. The final column shows $\nu \tan \delta$ (GHz). The typical error on the quantity $\nu \tan \delta$ is 0.2×10^{-4}

ν GHz	$\langle L_0 \rangle$ m	$\langle L \rangle$ m	$\langle L \rangle$ dB km $^{-1}$	$\epsilon'' \times 10^3$	$\nu \tan \delta \times 10^4$ GHz
0.100	432	449	19.3	3.8	1.2
0.175	467	487	17.8	2.0	1.1
0.250	457	476	18.2	1.4	1.1
0.325	422	438	19.8	1.2	1.2
0.400	408	423	20.5	1.0	1.3
0.475	366	378	23.0	0.95	1.4
0.550	349	360	24.1	0.86	1.5
0.625	363	375	23.2	0.72	1.4
0.700	331	341	25.5	0.71	1.6
0.775	310	319	27.2	0.69	1.7
0.850	320	329	26.4	0.61	1.6
Ave.	380 ± 16	400 ± 18	22 ± 1	1.3 ± 0.3	1.37 ± 0.06

angled and vertical cases, introducing a trade-off. A shorter baseline causes the attenuation length to become large compared to the difference in path length between the angled and vertical bounce tests (~ 130 m in 2011). At low frequencies, the difference in power loss between vertical and angled cases becomes smaller than the errors in the power spectra (~ 3 dB at 0.300 GHz). Alternatively, the baseline for the angled bounce can be increased, which increases the path length difference between angled and vertical bounces. While this increases the low-frequency precision, the high-frequency precision suffers due to increased absorption in the angled bounce data. The vertical and angled signal power are equal within statistical errors up to 0.300 GHz in Figure 5a, but differences in the vertical and angled power are measurable up to 0.850 GHz.

Figure 5b shows \sqrt{R} , with statistical errors from the fit, at each frequency. The errors are conservative, in that all the deviation from a perfect linear model (Eqn (14)) is attributed to error in \sqrt{R} . The mean is $\sqrt{R} = 0.82 \pm 0.07$ (-1.7 dB), and a flat model at this mean has a chi-squared result of $\chi^2/\text{dof} = 1.2$. Despite fluctuations in the data, no data point deviates above the physical region by much more than one standard deviation. At each point in the bandwidth where the gap between the reflected and calibration spectra randomly decreases, the parameter \sqrt{R} must fluctuate upwards to produce a linear fit to $f(d)$. These data have larger error bars, because the deviation in $f(d)$ from a linear model is larger for those bins. An unweighted flat-line fit to the data is shown; this fit produces the same results, within statistical uncertainties, as a weighted fit (that de-emphasizes the points with large errors). If the bins with $\sqrt{R} > 1$ are ignored in the fit, then the mean decreases by 20% ($\sqrt{R} = 0.6$).

Ignoring the data above 1.0, however, would raise the attenuation length results, because the total power loss must be conserved (Table 3). As the attenuation length has the stronger impact on the design of the future ARIANNA detector, relative to the reflection coefficient, it is important to be conservative with regard to the attenuation length in

Table 3 (Dookayka, 2011). The origin of the roughness in the reflected spectra is likely noise interference, since the signal-to-noise ratio is lower than in the calibration study.

Finally, knowledge of the basal reflection coefficient allows the correction of the attenuation length numbers in Figure 4 to more realistic values. If $\langle L_0 \rangle$ is the measured attenuation length, assuming $\sqrt{R} = 1.0$, then the actual attenuation length $\langle L \rangle$ can be expressed as

$$\frac{\langle L \rangle}{\langle L_0 \rangle} = \left(1 + \frac{\langle L_0 \rangle}{2d_{\text{ice}}} \ln R \right)^{-1} \quad (19)$$

Using the $\langle L_0 \rangle$ values from Figure 4, Table 3 shows the $\langle L \rangle$ results for the mean value of $\sqrt{R} = 0.82 \pm 0.07$, vs frequency. Table 3 also shows the imaginary part of the dielectric constant, derived from n'' , via $\langle L \rangle^{-1} = n''k$, where k is the free-space wavenumber. Assuming $\tan \delta \ll 1$, the expression $\epsilon'' = 2n''\sqrt{\epsilon'}$, with $\sqrt{\epsilon'} = 1.78$, relates the two quantities.

The ϵ'' results are in agreement with an earlier low-frequency projection for typical ice-shelf temperatures (Matsuoka and others, 1996). The Debye model predicts $\epsilon'' \propto \nu^{-1}$ for frequencies below 2 GHz, and the ϵ'' data follow this trend. The quantity $\nu \tan \delta$ is expected to be small and constant for a simple dielectric material, and Table 3 also displays this quantity in the final column, which agrees with an estimate from analysis of the 2006 data (Barrella and others, 2011). Although $\nu \tan \delta$ varies with frequency, this variation is such that no measurement is more than one standard deviation (0.2×10^{-4}) from the mean (1.37 ± 0.06).

POLARIZATION MEASUREMENTS

The \sqrt{R} result shows that little power is lost from the basal reflection. In this section, we assess potential losses by scattering or rotation of the linearly polarized signal. For any non-ideal linearly polarized antenna system, a small amount of power can leak into the cross-polarized channel. Significant transfer of power into the cross-polarized direction would indicate polarization rotation in the ice, and bias the attenuation length results. Birefringence and surface roughness effects at the water–ice interface at the bottom of the ice shelf are expected to generate power in the cross-polarized direction.

To quantify the polarization rotation, the cross-polarization fraction, F_{ice} , was measured in the vertical bounce configuration, and compared to F_{air} . F is defined in Eqn (20), where P_{\perp} and P_{\parallel} refer to the measured power in the cross-polarized and co-polarized direction with respect to the linear polarization of the transmitter at a given frequency:

$$F = \frac{P_{\perp}}{P_{\perp} + P_{\parallel}} \quad (20)$$

The leakage between co-polarized and cross-polarized channels is expected to be low across the bandwidth, but difficult to observe at high frequencies. Cross-polarized signals are weaker than co-polarized, and the vertical bounce data in the cross-polarized state are subject to noise interference above 0.4 GHz. The intrinsic transfer into the cross-polarized direction of a specified antenna pair was estimated by facing the transmitter toward the receiver in air. F_{air} is computed from the power observed between co-polarized and cross-polarized orientation of the receiver. The results of this study are shown in the third column of

Table 4. It was verified that the snow surface 1.5 m below the antennas scatters back a negligible amount of power.

F_{ice} was obtained from the vertical bounce set-up, with a Seavey transmitter and LPDA receiver. The Seavey antenna transmits very little power below 0.175 GHz, and the cross-polarized signal is weaker than the co-polarized signal, limiting F_{ice} results to frequencies below 0.4 GHz. These measurements are shown in column 4 of Table 4. These data can be compared to measurements taken in 2010, in which F_{ice} and F_{air} were shown to agree at 0.1 GHz with a LPDA transmitter and LPDA receiver at the same location as the 2011 measurements (Hanson, 2011). A comparison of F_{air} with F_{ice} reveals no excess power in the cross-polarization direction, with the possible exception of data at 0.400 GHz, which show a 2σ deviation from intrinsic antenna effects. These data do not confirm the F_{ice} analysis of the 2006 data, which showed $F_{\text{ice}} = 0.7$ at 0.4 GHz.

DISCUSSION

The data are in agreement with independent analyses and models. A study from Greenland found the total transfer function of the Greenland ice sheet, and models the different contributions from basal reflection and attenuation (Paden and others, 2005). A reflection coefficient (for power) of -37 dB is reported for the North Greenland Ice Core 2 (NGRIP2) location, and ice absorption of ~ 56 dB. Given the depth of 3.1 km, a loss rate of ~ 9.0 dB km $^{-1}$ is obtained. (The Greenland study was limited to 0.11–0.5 GHz.) The upper half of the Greenland ice sheet is colder than Moore's Bay, lowering the attenuation rate through temperature dependence of ϵ'' . The reflection coefficient from that study (-37 dB) is much smaller than that of Moore's Bay. However, other authors have estimated it to be higher (Bamber and others, 2001; Avva and others, 2014), with an absorption rate of 9.2 dB km $^{-1}$, conservatively assuming no reflection loss (attributing all loss to absorption). The Greenland site also exhibits a frequency dependence that produces a change of 8.5 dB km $^{-1}$ over the bandwidth (0.11–0.5 GHz). The slope of the loss rate vs frequency is therefore $8.5/(0.55 - 0.11) \approx 22$ dB km $^{-1}$ GHz $^{-1}$. The corresponding value for the ARIANNA site is 9.3 dB km $^{-1}$ GHz $^{-1}$, from Table 3.

Another study presents models for ice absorption across the entire Antarctic continent, given an array of inputs, such as temperature and chemistry data (Matsuoka and others, 2012). That expansive study presents results for shelf and sheet depth across the continent, and the portion depicting the Ross Ice Shelf, near the ARIANNA site, is in agreement with our thickness measurements. The RIS depth is peaked at 500 m in that model, and we find 576 ± 8 m. The inputs to this model indicate that the Ronne Ice Shelf has smaller absorption rates (dB km $^{-1}$) than the Ross Ice Shelf, which leads to a double-peaked distribution of loss rates, with one peak near 12.5 dB km $^{-1}$, and the other near 22.5 dB km $^{-1}$. The ARIANNA site average absorption rate is within one standard deviation of the mean for the entire distribution (15.1 ± 6.2 dB km $^{-1}$), and is in agreement with the second peak in the distribution of loss rates, corresponding to the Ross Ice Shelf.

Finally, a study of the Ross Ice Shelf at 2 MHz reveals large-scale thickness uniformity in the shelf, up to 40 km from the grounding line of the glaciers flowing into the shelf

Table 4. A comparison of cross-polarization fraction measurements vs frequency

Frequency GHz	F_{air}	F_{ice}
0.175	0.06 ± 0.02	0.08 ± 0.05
0.200	0.04 ± 0.01	0.01 ± 0.01
0.225	0.04 ± 0.02	0.02 ± 0.01
0.250	0.02 ± 0.01	0.01 ± 0.01
0.275	0.02 ± 0.01	0.02 ± 0.01
0.300	0.02 ± 0.01	0.07 ± 0.04
0.325	0.01 ± 0.005	0.03 ± 0.01
0.350	0.04 ± 0.01	0.08 ± 0.03
0.375	0.02 ± 0.01	0.11 ± 0.07
0.400	0.03 ± 0.01	0.22 ± 0.09

(MacGregor, 2011). The measurements are obtained from basal echoes with travelling transmitters and receivers at the surface. In some cases, multiple echoes are observed, corresponding to multiple round trips made by the signal, from surface to base. This technique provides excellent constraints on the thickness and absorption rate. Specifically, this study shows that our depth measurement is typical for large expanses of ice, a key requirement for large-scale ground arrays in neutrino detectors.

CONCLUSION

During the 2011/12 Antarctic season, radio-echo sounding measurements were performed in Moore's Bay with high-voltage broadband RF pulses in the 0.1–0.850 GHz bandwidth, to understand the dielectric properties of the ice shelf. The shelf thickness determined from the total propagation time was 576 ± 8 m. The echo soundings revealed depth-averaged attenuation lengths well fit by the linear function $\langle L(\nu) \rangle = (460 \pm 20) - (180 \pm 40) \times \nu \text{ m}$ (19.3–26.4 dB km $^{-1}$), where ν is the frequency (GHz). The χ^2/dof of this linear fit to the combination of multiple datasets was 1.2, with 9 degrees of freedom. The fit is consistent with prior measurements (Barrella and others, 2011), and the functional dependence is compatible with theoretical expectations (Matsuoka and others, 1996; Somaraju and others, 2006).

Vertical echo soundings were compared to echo soundings with a 543 ± 7 m baseline between transmitter and receiver, which allowed independent measurement of the basal reflection coefficient, found to be $\sqrt{R} = 0.82 \pm 0.07$ (-1.7 dB). The slope of \sqrt{R} vs frequency is consistent with a flat-mirror approximation. The average value of \sqrt{R} is consistent with earlier studies performed at lower frequencies (Neal, 1979). The short duration of the observed pulses (90% of the power contained within 100 ns) precludes significant multi-path effects. The Fresnel zones of the pulses at the shelf base are not significantly larger than measured horizontal correlation lengths. After correcting attenuation lengths for the effect of \sqrt{R} on returned power, dielectric quantities like ϵ'' and $\nu \tan \delta$ were derived. The results for ϵ'' and $\nu \tan \delta$ agree with theoretical expectations (Matsuoka and others, 1996). Finally, the fraction of scattered power by the ice into the cross-polarized direction, F_{ice} , is $< 10\%$ (0.100–0.400 GHz), compatible with the fraction of power

due to intrinsic limitations of the transmitting and receiving antennas. Both the large value of \sqrt{R} and the small value of F_{ice} suggest that the bottom surface of the Ross Ice Shelf at Moore's Bay is smooth. The measurements of F_{ice} do not demonstrate any significant features below 0.400 GHz, where cross-polarized power is noise-limited. This result, combined with the measured field attenuation length at frequencies between 0.100 and 0.850 GHz, suggests that the Moore's Bay region of the Ross Ice Shelf will be an excellent medium for the ARIANNA high-energy neutrino project.

ACKNOWLEDGEMENTS

We thank the staff of Antarctic Support Contractors, Lockheed, Raytheon Polar Services, and the entire crew at McMurdo station for excellent logistical support. This work was supported by generous funding from the Office of Polar Programs and Physics Division of the US National Science Foundation, grant awards ANT-08339133, NSF-0970175 and NSF-1126672. In 2010, additional funding was provided through the US Department of Energy under contract DE-AC-76SF-00098. Finally, we thank David Saltzberg for comments and suggestions throughout the expeditions and analysis.

REFERENCES

- Allison P and 47 others (2012) Design and initial performance of the Askaryan Radio Array prototype EeV neutrino detector at the South Pole. *Astropart. Phys.*, **35**, 457–477
- AMANDA Collaboration (2006) Optical properties of deep glacial ice at the South Pole. *J. Geophys. Res.*, **111**(D13), D13203 (doi: 10.1029/2005JD006687)
- ANITA Collaboration (2009) The Antarctic Impulsive Transient Antenna ultra-high energy neutrino detector: design, performance, and sensitivity for 2006–2007 balloon flight. *Astropart. Phys.*, **32**(1), 10–41
- ANITA Collaboration (2010) Observational constraints on the ultrahigh energy cosmic neutrino flux from the second flight of the ANITA experiment. *Phys. Rev. D*, **82**(2), 022004 (doi: 10.1103/PhysRevD.82.022004)
- Askaryan GA (1962) Excess charge of an electron-photon shower and its coherent radio emission. *Sov. Phys. JETP*, **14**(2), 441–442
- Avva J, Kovac JM, Miki C, Saltzberg D and Vieregg AG (2014) An in situ measurement of the radio-frequency attenuation in ice at Summit Station, Greenland. arXiv:1409.5413
- Bamber JL, Layberry RL and Gogineni SP (2001) A new thickness and bed data set for the Greenland ice sheet: 1. Measurement, data reduction, and errors. *J. Geophys. Res.*, **106**(D24), 33 773–33 780
- Barrella T, Barwick S and Saltzberg D (2011) Ross Ice Shelf (Antarctica) in situ radio-frequency attenuation. *J. Glaciol.*, **57**(201), 61–66
- Barwick SW (2007) ARIANNA: a new concept for UHE neutrino detection. *J. Phys. Conf. Ser.*, **60**, 276–283 (doi: 10.1088/1742-6596/60/1/060)
- Barwick SW and 14 others (2015) The time-domain response of the ARIANNA detector. *Astropart. Phys.*, **62**, 139–151 (doi: 10.1016/j.astropartphys.2014.09.002)
- Besson D and 42 others (2008) In-situ radioglaciological measurements near Taylor Dome, Antarctica and implications for UHE neutrino astronomy. *Astropart. Phys.*, **29**(2), 130–157
- Bogorodsky VV, Bentley CR and Gudmandsen PE (1985) *Radio-glaciology*. Reidel Publishing Co., Dordrecht
- Dookayka K (2011) Characterizing the search for ultra-high energy neutrinos with the ARIANNA Detector. (PhD thesis, University of California, Irvine)
- Dowdeswell JA and Evans S (2004) Investigations of the form and flow of ice sheets and glaciers using radio-echo sounding. *Rep. Progr. Phys.*, **67**(10), 1821–1861
- Fahnestock MA, Scambos TA, Bindschadler RA and Kvaran G (2000) A millennium of variable ice flow recorded by the Ross Ice Shelf, Antarctica. *J. Glaciol.*, **46**(155), 652–664
- Fretwell P and 55 others (2013) Bedmap2: improved ice bed, surface and thickness datasets for Antarctica. *Cryosphere*, **7**(1), 375–393 (doi: 10.5194/tc-7-375-2013)
- Gerhardt L and 6 others (2010) A prototype station for ARIANNA: a detector for cosmic neutrinos. *Nucl. Instrum. Meth. Phys. Res. A*, **624**(1), 85–91
- Hanson JC (2011) Ross Ice Shelf thickness, radio-frequency attenuation and reflectivity: implications for the ARIANNA UHE neutrino detector. *Proceedings of the 32nd International Cosmic Ray Conference, 11–18 August, Beijing, China*. Institute of High Energy Physics, Beijing
- Hanson JC (2013) The performance and initial results of the ARIANNA prototype. (PhD thesis, University of California, Irvine)
- IceCube Collaboration (2013) Evidence for high-energy extra-terrestrial neutrinos at the IceCube detector. *Science*, **342**(6161), 1242856 (doi: 10.1126/science.1242856)
- Klein, SR (2012) Radiodetection of neutrinos. *Nucl. Phys. Proc. Suppl.*, **229–232**, 284–288
- Kravchenko I and 8 others (2012) Updated results from the RICE experiment and future prospects for ultra-high energy neutrino detection at the south pole. *Phys. Rev. Lett. D*, **85**, 062004
- MacGregor J, Anandakrishnan S, Catania GA and Winebrenner DP (2011) The grounding zone of the Ross Ice Shelf, West Antarctica, from ice-penetrating radar. *J. Glaciol.*, **57**(205), 917–928
- Matsuoka K, Fujita S and Mae S (1996) Effect of temperature on dielectric properties of ice in the range 5–39 GHz. *J. Appl. Phys.*, **80**(10), 5884–5890
- Matsuoka K, MacGregor JA and Pattyn F (2012) Predicting radar attenuation within the Antarctic ice sheet. *Earth Planet. Sci. Lett.*, **359–360**, 173–183 (doi: 10.1016/j.epsl.2012.10.018)
- Neal CS (1979) The dynamics of the Ross Ice Shelf revealed by radio echo-sounding. *J. Glaciol.*, **24**(90), 295–307
- Neal CS (1982) Radio echo determination of basal roughness characteristics on the Ross Ice Shelf. *Ann. Glaciol.*, **3**, 216–221
- Paden J, Allen CT, Gogineni S, Jezek KC, Dahl-Jensen D and Larsen LB (2005) Wideband measurements of ice sheet attenuation and basal scattering. *Geosci. Remote Sens. Soc. Newslett.*, **2**(2) (doi: 10.1109/LGRS.2004.842474)
- Peters M, Blankenship DD and Morse DL (2005) Analysis techniques for coherent airborne radar sounding: application to West Antarctic ice streams. *J. Geophys. Res.*, **110**(B6), B06303 (doi: 10.1029/2004JB003222)
- Rignot E, Jacobs S, Mouginot J and Scheuchl B (2013) Ice-shelf melting around Antarctica. *Science*, **341**(6143), 266–270 (doi: 10.1126/science.1235798)
- Schytt V (1958) The inner structure of the ice shelf at Maudheim as shown by core drilling. In *Norwegian–British–Swedish Antarctic Expedition, 1949–52, scientific results*. Norsk Polarinstitutt, Oslo, 113–151
- Somaraju R and others (2006) Frequency, temperature and salinity variation of the permittivity of seawater. *IEEE Trans. Antennas Propag.*, **54**(11), 3441–3448
- United States Geological Survey (USGS) (2012) *Landsat Image Mosaic of Antarctica (LIMA)*. lima.usgs.gov/



Ross Ice Shelf Thickness, Radio-frequency Attenuation and Reflectivity: Implications for the ARIANNA UHE Neutrino Detector

JORDAN C. HANSON¹, FOR THE ARIANNA COLLABORATION

¹*Department of Physics and Astronomy, University of California at Irvine, Irvine, CA 92697*

jchanson@uci.edu

DOI: 10.7529/ICRC2011/V04/0340

Abstract: The ARIANNA high energy neutrino detector is planned to be deployed on the surface of the Ross Ice Shelf to search for astrophysical neutrinos. Collisions with nuclei in the ice generate showers of particles that emit short pulses of radiation, created by the Askaryan mechanism, in the frequency range of 100 MHz to 1 GHz. The ARIANNA site is located about 65 miles from McMurdo Station, the main hub of US Antarctic operations, and is protected from ambient RF interference by a geologic formation known as Minna Bluff. In this work, we report preliminary results for the frequency interval 90-180 MHz from site studies of the field attenuation length (averaged over depth), and reflection and polarization properties of the saltwater-ice boundary.

Keywords: ARIANNA, Antarctica, GZK, neutrino astronomy, Ross Ice Shelf, attenuation length

1 Introduction

The Antarctic Ross Ice Shelf Antenna Neutrino Array (ARIANNA) is designed to detect ultra-high energy (UHE) cosmogenic neutrinos, via the Askaryan effect [1, 2, 3, 4, 5]. When a neutrino interacts in bulk matter with an index of refraction, the resulting hadronic and electromagnetic cascades can produce coherent GHz radiofrequency (RF) pulses. High energy scattering processes and positron annihilation cause a negative charge excess to build up in the cascades, creating an effective radiating dipole moment. This radiation is coherent, since the coherent radiated power from Cherenkov radiation scales quadratically with the charge of the emitter [6], and the wavelengths are set by the lateral size of the shower initiated by the original neutrino interaction. Simulation studies show that the signal pulses from high energy neutrinos usually arrive at ARIANNA surface receivers by first reflecting from the ice-water interface at the bottom of the Ross Ice Shelf (RIS), and then propagating through the bulk ice [7]. Relatively few neutrino signals propagate directly from the interaction vertex to the surface receivers. Therefore, the sensitivity and capabilities of ARIANNA depends on the ice properties such as the attenuation length and reflection efficiency. In this work, we report on several key properties of the ARIANNA site.

The ARIANNA detector consists of an array of autonomous stations deployed on the surface of the RIS, viewing 513 km³ of glacial ice centered at (77° 44' 523" S, 165° 02' 414" E) in western Antarctica. Prior studies of the electromagnetic properties of the ARIANNA site have

measured the electric field attenuation length by using vertically reflected pulses and assumed a value for the reflection coefficient from the ice-water boundary at the bottom [11]. In this work, we examine reflected pulses over several baselines to determine both the field attenuation length and reflection coefficient. We also show that the reflected pulse preserves its polarization orientation. Measurements of the reflection coefficient have been made independently [8, 9], revealing strongly reflected RF pulses in regions free of sub-glacial flow lines and sea-ice freezing zones. ARIANNA is in Moore's Bay, which is far from glacial irregularities [8] and in good RF isolation. For a similar study of attenuation lengths performed in ice located in a different region of Antarctica, see Besson (2008) [10].

We quantify absorptive losses experienced by an electromagnetic wave by adding an imaginary component to the dielectric constant, parameterized by

$$\alpha = -8.686(\pi\nu/c)(\sqrt{\epsilon'}\tan\delta) \quad (\text{dB/m}) \quad (1)$$

Here, the vacuum speed of light is c , ν is the frequency in Hz, ϵ' is the real part of the dielectric and the loss tangent $\tan\delta$ is the imaginary part of the dielectric over the real part ϵ''/ϵ' . The electric field attenuation length is then defined as [11]

$$L_\alpha = 1/\ln\sqrt{10^{\alpha/10}} \quad (2)$$

which is the distance the electromagnetic wave travels before decreasing in amplitude by a factor e^{-1} .

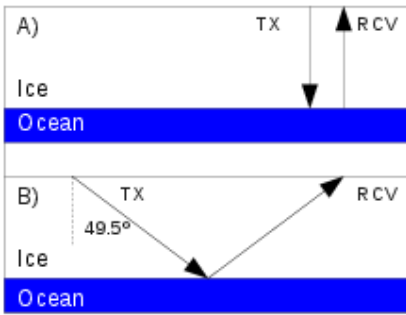


Figure 1: A) A schematic of the direct bounce experimental geometry. B) The angled bounce experimental geometry.

2 Experimental Methods

To create broad band RF pulses for propagation through the ice shelf, a short duration (1 ns wide), kilovolt pulse is delivered from the HYPS Pockel Cell Driver to a log-periodic dipole array (LPDA) transmitter (105 MHz-1300 MHz), supplied by Creative Design Corp (CLP5130-2). These antennas are directional, with a gain of 6-7 dBi. An identical LPDA serves as a receiver. Along with a precise measurement of the ice-shelf depth at the ARIANNA site, we have the S11 and voltage standing wave ratio (VSWR) parameters for the antennas as they couple to the dielectric properties of the snow around them [5]. The lowest frequency measurable by the LPDA in snow decreases to approximately 80 MHz because the wave speed slows down in the snow, while the antenna response remains constant. The VSWR is close to one for all relevant frequencies in this work. The signal from the receiver is filtered with both a NHP-50+ highpass filter and a NLP-1200+ lowpass filter, and amplified by a 1 GHz Miteq AM-1660 low-noise amp before being recorded on a Tektronix oscilloscope with 1 GHz bandwidth. We also attenuate by 20 dB where appropriate to obtain manageable signal amplitudes.

Figure 1 shows two distinct reflection geometries employed in these studies for the antennas, both of which are buried in the low density firn snow and pointed down. The direct bounce configuration (1a) is indicated by the vertical path between the transmitter and receiver antennas, which are separated by 18.7 m. The radio pulse travels 576 m to the water-ice interface and reflected back to the surface for a total path length of 1152 m. The angled bounce configuration (1b) is similar to the direct bounce, where the two antennas oriented vertically downward, but the separation between the two antennas is increased to 977 m, which increases the total path length to 1510 m (see Table 1). The unattenuated signal amplitude is determined by rotating the LPDA antennas to point toward each other through the surface snow while separated by 18.7 m. The path length for this test is the shortest of the three configurations. In practice, R, G, and the exponential factor are set to 1 in eqn. (4).

Since the signal in this test is relatively strong, the amplifier is removed for this measurement.

The analysis presented here focuses on the frequency range between 90 MHz and 180 MHz, where the measured power was well above thermal noise for the three configurations. It assumes that losses due to RF scattering in the ice medium are negligible for the frequencies of interest, and that the field reflection coefficient does not depend significantly on incidence angle of the two reflection configurations. We verified with a noise source that cable losses are negligible at these frequencies.

The Friis equation relates the power received (P_r) to the transmitted power (P_t) in a lossless medium at a given wavelength. For two identical antennas, separated by a distance d , it becomes

$$P_r = \frac{G_a^2 \lambda^2}{(4\pi)^2 d^2} = \frac{P_0}{d^2} \quad (3)$$

where G_a is the intrinsic gain of the antenna and λ is the electromagnetic wavelength. The factor P_0 can be treated as a constant at each frequency for all configurations since the variation in LPDA intrinsic gain is small for the frequency interval of this study. P_0 was determined from the short distance configuration with the antennas rotated to point toward each other. To account for absorption losses and possible losses upon reflection, the Friis equation is modified to

$$P_r = \frac{P_0 R G^2}{d^2} \exp\left(-2 \frac{d}{\langle L_\alpha \rangle}\right) \quad (4)$$

The factor R is the reflection coefficient, defined for power. The factor of 2 is required in the exponential if $\langle L_\alpha \rangle$ is the electric field attenuation length, rather than a quantity associated with the power. The brackets around $\langle L_\alpha \rangle$ indicate that the attenuation length is averaged over the full depth of the ice, and thereby integrated over the temperature dependence of the path¹. Following convention, the reflection coefficient for the electric field is then $R^{1/2}$. The factor G^2 accounts for the difference in relative antenna gain for each antenna. G is 1 for the direct bounce, where the returned signal is aligned along the receiver boresight. The orientation of the antennas remained vertical for the angled bounce configuration, so the signal pulses were emitted and received at an angle of 49.5°. At this angle in the H-plane of the antennas, $G = 0.80$.

1. This temperature dependence arises from the modest temperature dependence of the imaginary part of the dielectric constant of bulk ice, which is roughly one part in a thousand.

Year/site	Delay (ns)	Depth (m)
2006 [11]	6783 ± 10	577.5 ± 10
2009 [12]	6745 ± 15	572 ± 6
2010 [this work]	6772 ± 15	576 ± 10

Table 1: The result from this work was produced using the same $n(z)$ model as the result in the first row. The larger final uncertainties come from using slightly larger uncertainties on the index of refraction of bulk ice.

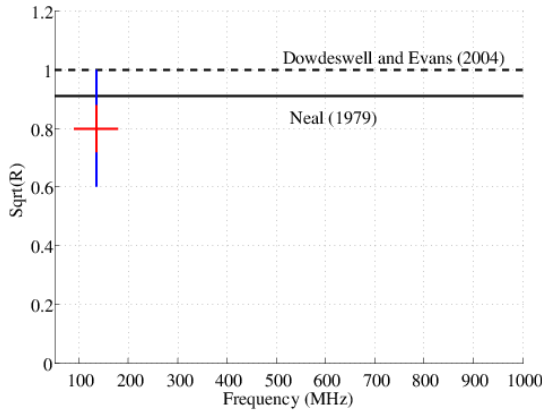


Figure 2: Expected field reflection coefficient $R^{1/2}$ vs. frequency, for an ideal flat surface. The longest vertical error bar indicates 95% confidence. The horizontal error bar indicates the range of frequencies used in this analysis.

3 Data and Analysis

3.1 Depth of the Ice Shelf

The thickness of the ice at the ARIANNA site can be determined by the round-trip travel time and knowledge of the index of refraction, $n(z)$, as a function of depth. For depths greater than 65–75 m, the ice is uniform with $n = 1.78$. At shallower depths, the mass density of the firn is characterized with an exponential dependence [11]. Along with the linear dependence between index of refraction and mass density, we have a complete description of $n(z)$ in the firn ice. Table 1 summarizes the calculations of ice thickness at the ARIANNA site. The 2009 and 2010 measurements were performed at the same geographical location on the ice shelf, whereas the 2006 measurement was performed at a location about 1 km from the 2009 and 2010 tests. The round trip travel times agree to within two standard deviations. The uncertainties in the depth measurements include statistical errors in the round trip travel time and index of refraction in the uniform ice, and systematic errors due to the functional variation of $n(z)$. The larger errors associated with the 2006 and 2010 depths are due to slightly larger uncertainties for the index of refraction in the bulk ice.

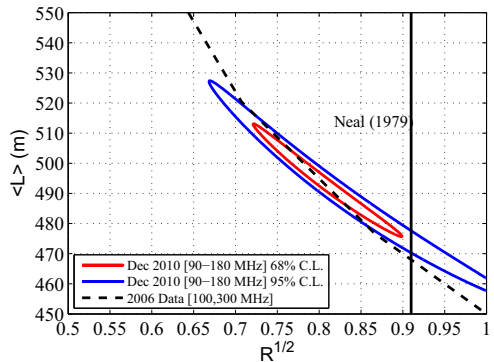


Figure 3: Contour plot of the depth averaged attenuation length $\langle L_\alpha \rangle$ (m) vs. $R^{1/2}$ showing 1 and 2- σ errors. Dashed curve was obtained from [11], as explained in the text. Vertical line indicates theoretical expectation of $R^{1/2} = 0.91$ from [9].

3.2 Attenuation Length, Reflectivity and Signal Polarization

After correcting for the geometrical effects of path length for the three different configurations and relative antenna gain, the field reflection coefficient $R^{1/2}$ and $\langle L_\alpha \rangle$ are treated as free parameters in eqn. (4). The statistical errors in P_r were obtained from the rms fluctuation over the entire frequency band. The 1 and 2- σ contours in figure 3 were obtained from a reduced chi-squared fit. The contours match the dashed curve, which was derived by varying the reflection coefficient $R^{1/2}$ assumed in [11] for the quoted attenuation lengths at 100 and 300 MHz. The attenuation length is determined to be 495 ± 15 m at 68 % C.L., in agreement with previous values from 2006 [11], and the field reflection coefficient $R^{1/2} = 0.80 \pm 0.08$ at 68% C.L., in agreement with a theoretical expectation ($R^{1/2} = 0.91$) for an ideal ice-saltwater interface [9].

Our measurements indicate that the field reflection coefficient at the ARIANNA site is compatible with an ideal flat surface, although values as small as 0.7 are also permitted. The reflection coefficient is not expected to vary significantly with frequency for specular reflection, as shown in figure 2. If the permittivity of sea-water is assumed to be very large for 100–1000 MHz, then the field reflection coefficient is 1 with no frequency dependence (the upper horizontal line in figure 2) [12]. In addition, multi-path effects are safely ignored in this analysis because the maximum duration of our signal pulses (100 ns) is small compared to the total propagation time.

The radio pulse from the neutrino interaction is perfectly linearly polarized, with the orientation perpendicular to the direction of the propagation of the pulse. It lies in the plane defined by the neutrino direction vector and propagation vector. Therefore, the polarization information helps to determine the direction of the neutrino, and reflected signals must retain a known correlation with the initial polarization.

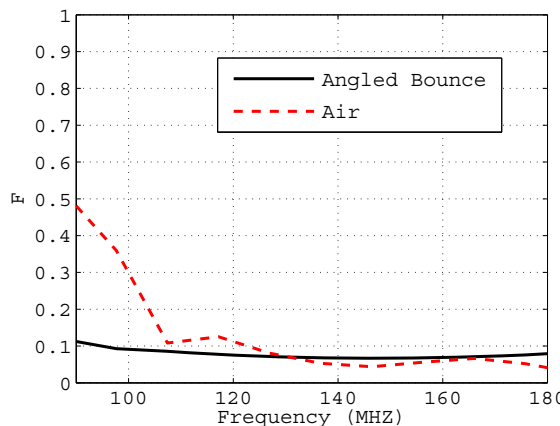


Figure 4: Polarization fraction, F , is shown as a function of frequency for transmission through air (dashed line) and for the angled bounce configuration at the ARIANNA site (solid line).

We investigate this by comparing the co-polarized power, P_{\parallel} , to the cross-polarized power, P_{\perp} for the angled bounce configuration. The fraction of cross-polarized power to total power is

$$F = \frac{P_{\perp}}{P_{\parallel} + P_{\perp}} \quad (5)$$

Figure 4 compares F for the angled bounce configuration (solid curve) to a study performed in air (dashed curve). Due to imperfections in the LPDA antennas, some power will leak into the cross-polarized configuration, representing a lower limit to F . This is estimated by air measurements with the LPDA antennas oriented to point toward each other, and separated by 10 m to avoid near-field effects. The sudden rise to a value of 0.5 (the value of F for unpolarized noise) at frequencies below 105 MHz is due to the antenna response. In air, the VSWR of the LPDA increases dramatically below 105 MHz, whereas the VSWR for LPDAs buried in snow remains low down to 80 MHz [5]. The good agreement between the angled bounce configuration and the air studies suggests that little power is transferred from the co-polarized direction to the cross polarized direction after reflection from the water-ice boundary.

4 Conclusion

Preliminary studies of the site properties in the frequency band 90-180 MHz confirm large field attenuation lengths (495 ± 15 m), and show that the reflection coefficient is compatible with theoretical expectations for a smooth saltwater-ice interface ($R^{1/2} = 0.80 \pm 0.08$), and signal polarization is preserved. Further work is required over multiple baselines to distinguish the smooth water-ice hypothesis from potential small losses due to surface roughness

at the ARIANNA site. We note that Neal [9] reported very small levels of surface roughness at sites in the RIS characterized by large reflection coefficients at 60 MHz. Such small effects will have little, if any, impact on signal attenuation and time profiles if similar values for vertical rms fluctuations from flatness and horizontal correlation lengths are found at higher frequencies.

5 Acknowledgements

This work was supported by the U.S. NSF Office of Polar Programs and the U.S. NSF Physics Division, award numbers 0839133 and 0970175, and by the Dept. of Energy under contract DE-AC-76SF-00098. We also thank the dedicated staff of Raytheon Polar Services for their logistical support of the ARIANNA program.

References

- [1] Askaryan,G., Soviet Physics JETP, 1962, **14**: 441-442
- [2] Barwick,S. (ARIANNA Collab.), J. Phys.: Conf. Ser., 2007, **60**: 276-283
- [3] Hoffman, K. *et al.* (ARA Collab.) J. Phys.: Conf. Ser., 2007, **81**(1): 012022
- [4] Gorham, P. *et al.* (ANITA Collab.), Phys. Rev. D, 2010 **82**: 022004
- [5] Gerhardt, L. *et al.* Nucl. Inst. and Meth., 2010 **624**(1): 85-91
- [6] Gorham, P. *et al.* (ANITA Collab.), Phys. Rev. 2007, **99**: 171101
- [7] ARIANNA Collaboration, paper 0144, these proceedings.
- [8] Neal, C.S., J. Glaciology, 1979, **24**(90): 295-307
- [9] Neal, C.S., Annals of Glac., 1982, **3**: 216-221
- [10] Besson, D. *et al.* Astropar. Phys., 2008, **2**: 130-157
- [11] Barrella, T. *et al.* J. Glaciology, 2011 **57**(201): 61-66
- [12] Dowdeswell, J.A. and Evans, S. Rep. Prog. Phys. **67**: 1821

Research Application: Exploration of Antarctic Ice Sheets with Drones

A gap exists in Askaryan-based UHE-v science. We have made detailed measurements of the RF attenuation length in ice, a critical parameter in our detector designs. However, we cannot currently repeat this measurement throughout detector ice volumes, which would cover kilometers of ice in every direction away from the center of IceCube-Gen2 at the South Pole. Though measurements from aircraft have been collected elsewhere, there is very little aircraft data near the South Pole.

The Open Polar Server Data Gaps, and Drones

The Open Polar Server (OPS) is a service provided by CReSIS at the University of Kansas (KU). Researchers may download data from Greenland and Antarctica. The data are recorded from aircraft over the ice, and the RF attenuation length can be extracted from radar echoes. There are three disadvantages to flight data. First, there may not be a flight near the detector. Second, flights only give a snapshot of the ice at the time. Third, the bandwidth of CReSIS radar does not always overlap with the proposed IceCube-Gen2 bandwidth. There is a trade-off between spatial and temporal data in radio sounding. A plane flight covers hundreds of kilometers, once. Conversely, an embedded station records data over time, but only at one location.

A dedicated drone could constrain the attenuation length in both regimes. In my machine shop and RF design lab, a student and I constructed a 3D printed drone, with 1 kg payload, powered by LiPo batteries. Before the pandemic hit, we had plans to equip it with solar charging and cold-temperature components. A similar effort is underway at CReSIS at KU: Prof. Emily Arnold of the KU Dept. of Aerospace Engineering has begun an NSF CAREER grant to utilize RC military drones to study the Jakobshavn glacier in Greenland. Thus, there is a potential for collaboration between CReSIS and IceCube-Gen2 and PUEO to solve a common problem: the rechargeable ice attenuation length measurement system. Our drone design can be 3D printed and assembled from commercial parts for < \$1k.

Connection to Whittier Scholars Program, Office of Naval Research, and Climate Science

This research ties together several aspects of our other research programs at Whittier College, connecting climate science, neutrino physics research, and RF engineering. We seek to mount RF transmitting antennas to the drone, along with a transceiver payload. We need a lightweight, broadband RF antenna suited to the task. Thus, our ONR research into 3D printing RF antennas designed with the MIT Electromagnetic Equation Propagation (MEEP) package connects to the drone research. We are currently working on 3D printed RF antennas designed with MEEP that will serve IceCube Gen2 and the Navy in a variety of ways. By constructing a drone capable of landing and recharging in a polar environment, we would unlock a new regime of climate-related measurements by improving the time and spatial resolution of glaciological measurements.

Two undergraduate researchers have helped with this research. The first was a physics and business double major, who helped design and 3D-print the drone, which has autonomous flight capability. The second is a Whittier Scholars Program major who graduated after completing several expeditions to Iceland, Alaska, and Montana to study glaciers. The hope was that he could have performed test flights in Antarctica with the drone, however that expedition was impeded by the pandemic. This student helped further design and test the drone. Finally, we wrote a Whittier Scholars Program thesis exploring the evolution of glaciers within a climate science context, and the connection between glaciers and culture. The work was informed by data collected from our student's expeditions, my past glaciological research, and work connected to the drone (Fig. 1). *A copy of the Whittier Scholars Program Thesis has been included in this dossier.*



Figure 1. Our custom designed, 3D printed quad-rotor drone with autonomous flight capability. The communications antenna is visible atop the hull. The four engines are mounted on carbon fiber arms, within 3D printed housing components. The guidance, power, and communications electronics are all contained within the hull.

Research Application: Workforce Development for Naval Surface Warfare Systems (NSWC), Corona Division

In the Summers of 2020, 2021, and 2022, I have received Summer Faculty Research Fellowship grants from the Office of Naval Research (ONR). One of my tasks given by ONR was to develop online interactive engineering courses for new personnel. New personnel often join Navy operations, either as civilians or soldiers, with a need for customized training in fields like radar or digital signal processing (DSP).

As a STEM educator at a liberal arts institution, I have a unique set of skills that is highly valued by the Navy. I continue to create interactive engineering courses designed for a diverse audience that has a varying level of expertise in the RF engineering field. Course audiences have been new sailors or field engineers tasked with radar or RF equipment maintenance on aircraft carriers and other warships, and acquisition personnel tasked with purchasing and overseeing new surveillance, GPS, and weapons systems. These diverse personnel need to understand relevant engineering topics quickly, at the right level of detail, and at their own pace.

Luckily, my research often involves synthesizing concepts from RF, radar, DSP, and mathematical physics. I have been able to leverage my knowledge and research experiences in these areas to deliver two summer online courses for the Navy. The first was a general introduction to RF Field Engineering. The second, currently in progress, is an Introduction to GPS M-Code signals for On-boarding of Navy Personnel. Examples of content from each course are included in this dossier.

RF Field Engineer Course: A Practical Introduction

Jordan Hanson

June 8, 2021

Whittier College Department of Physics and Astronomy

Course Introduction

1. Professor Jordan Hanson
2. Email: jhanson2@whittier.edu, 918particle@gmail.com
3. Mobile: 562-351-0047
4. Zoom Credentials: (ID) 796 092 0745 (Passcode) 667725
5. **Reading: Stimson's Introduction to Airborne Radar, 3rd Edition.** (Hughes Radar Handbook)
6. Box Folder: <https://app.box.com/s/qalsptcztyeq8hjvu3pmf4mlodmopop7>

Summary

Reading: Stimson3 ch. 1-6

- **Week 1:** Units and estimation. **Key skills:** mental math, wave concepts
 - Electromagnetic units, estimation, and decibels
 - Waves and the wave equation
 - Reflections, refraction, and diffraction
 - Phase, amplitude, frequency, polarization
- **Week 2:** Basic Training in Mathematics. **Key skills:** estimate pulse bandwidth, pulse trains and uncertainty principle
 - **Complex numbers:** applications to phasors and radio waves, complex impedance of filters and antennas
 - **Fourier series and transforms,** filters and attenuation, properties of waveforms, power spectra, and spectrograms, cross-correlation and convolution
 - **Statistics and probability:** applications to noise, signal-to-noise ratio

Reading: Stimson3 ch. 7-11

- Week 3: RF Antenna Properties. **Key skills:** characterize an antenna, diagnose a problem with an antenna system
 - Radiation pattern, directivity, and gain
 - Complex impedance and reflection coefficient, S11, S21
 - Bandwidth, narrow and wide
 - Antenna temperature
 - Angular resolution
 - Attenuation: applications to remote sensing
- Week 4: **Electronically Scanned Antenna Systems**
 - **Basics:** spacing, wavelength, and scan angle
 - **Design classes:** AESA and PESA
 - **Wideband considerations:** Scan losses, time-delays
 - **Bonus:** FDTD demonstrations of ESAs
- Week 5: Review of Weeks 1-4, pulsed radar concepts

Reading: Stimson3 ch. 12-13, part IV (18-22), 23

- Week 6: Range Equations. Key skills: diagnose issues with distance target detection, estimate radar cross section (RCS)
 - Radar cross-section
 - Noise and noise figure, signal-to-noise ratio (SNR)
 - Thermal noise floor and detection probability
 - Ranging techniques: pulse compression, frequency modulation
- Week 7: Overview of Pulse Doppler Radar (Cumulative Example)
 - Connections with Telemetry
 - See Stimson3 part IV
 - Connections to digital signal processing: sampling and digitization
- Week 8: Clutter and Attenuation
 - Clutter: sources and spectra
 - Attenuation: absorption and scattering, components

Course Summary

- Week 9: Link Budgets (Cumulative Example)
 - Assembling the pieces
 - Example calculations
- Week 10: Course Review
 - Review Weeks 1-9
 - Skill Review
 1. Estimation and approximations
 2. Conceptual challenge questions
 3. Worked examples



Introduction to GPS M-Code Signals for Onboarding of Navy Personnel

Jordan Hanson

Assistant Professor of Physics and Computer Science

Department of Physics and Astronomy, Whittier College

Summer Research Fellow with the Office of Naval Research

June 24, 2022

Outline

Outline

Introduction to GPS M-Code Signals - Six Easy Pieces

1. Radio transmission equation and signal strengths
2. Signals: amplitude versus time
3. More on binary signals
4. Power spectral densities
5. Mixing signals, carrier frequencies
6. Auto-correlation functions

Synthesis: Putting the pieces together

Artemis Program: The Internet of Things (IoT) and Wearable Technology

Dr. Jordan Hanson - Whittier College Dept. of Physics and Astronomy

January 22, 2020

Abstract

Electronics engineering has become an activity available to the benchtop tinkerer thanks to low-cost microprocessors, vibrant maker communities and simple, widely-distributed computer-code packages. In this version of the Artemis program, we will attempt to design an electronic safety bracelet system that sends location data of a lost loved one. The project involves Arduino circuit boards and code development, as well as integration of WiFi and GPS hardware and data.

Regular meeting times: Mondays, 4:30 - 5:45 pm in Science and Learning Center, Room 228. Optional meetings on Wednesdays, same time and place, as needed.

Instructor contact information: jhanson2@whittier.edu, tel. 562.351.0047

Attendance/Absence: Participants are encouraged to attend as many meetings as possible. If a participant misses more than one meeting that will preclude participation in SCCUR and URSCA conferences.

Program expectations:

- Attend as many meetings as possible
- Bring laboratory notebook and take notes during meetings
- Perform a weekly study activity outside meeting times
- Construct a piece of wearable circuitry (for example, a bracelet) that signals the location of the wearer if the wearer is lost
- Gain experience with the Arduino development platform
- Prepare a scientific poster to present at URSCA and SCCUR. URSCA stands for Undergraduate Research, Scholarship, and Creative Activity, which is conference and poster session held annually at Whittier College. SCCUR stands for Southern California Conferences for Undergraduate Research, and is held annually at a college or university in Southern California.

Schedule:

1. Meeting 1: February 5th, 2020. **Introduction to Arduino development, 1**
 - (a) Powering up devices, using the software development environment, LEDs and printing to screen
 - (b) *Weekly assignment: download Arduino SDE and practice toggling an LED, code practice*
2. Meeting 2: February 10th, 2020. **Introduction to Arduino development, 2**
 - (a) Code control flow and the event loop
 - (b) Adding conditional features to code, involving switch and if/else statements
 - (c) *Weekly assignment: Activate LED with a button or switch*
3. Meeting 3: February 17th, 2020. **Pinouts, schematics, and other nerdy things**
 - (a) Learn how to read a pinout schematic
 - (b) Learn how to search for parts and diagram prototype
 - (c) *Weekly assignment: search for schematic of GPS module for our Arduino boards*
4. Meeting 4: February 24th, 2020. **Breadboards, power supplies, and connectors**
 - (a) Practice hooking things together, prototyping and troubleshooting
 - (b) Common laboratory equipment: voltmeters, probes and power supplies
 - (c) *Weekly assignment: measure car battery voltage*

5. Meeting 5: March 2nd, 2020. **Arduino and GPS**

- (a) Major milestone no. 1: print GPS coordinates to screen, from Arduino over USB.
- (b) What is GPS, and what are latitude and longitude? What distances do they represent?
- (c) *No pre-defined assignment: troubleshoot issues that arise.*

6. Meeting 6: March 9th, 2020. **Arduino and WiFi**

- (a) Connect WiFi shield to Arduino and demonstrate signal RX/TX (receiving and transmitting)
- (b) *No pre-defined assignment: troubleshoot issues that arise.*
- (c) **March 13th: URSCA abstracts are due.**

7. **March 16th - 20th: Whittier College Spring Break**

8. Meeting 7: March 23rd, 2020. **Arduino + WiFi + GPS, 1**

- (a) Systems integration of main board, GPS receiver, and WiFi shield
- (b) First attempt to share GPS data over WiFi via SMS text message
- (c) Begin with breadboard setup, investigate form factor solution
- (d) *Weekly assignment: search for code/example to send SMS message or email over WiFi from Arduino*

9. Meeting 8: March 30th, 2020. **Arduino + WiFi + GPS, 2**

- (a) Continuation of activities from previous week
- (b) *Code/example to send SMS message or email over WiFi from Arduino*

10. Meeting 9: April 6th, 2020. **Arduino + WiFi + GPS, 3**

- (a) Integration into wearable technology
- (b) Battery power and power consumption calculations
- (c) *Weekly assignment: determine the power consumption of a household appliance or piece of technology in your home*

11. Meeting 10: April 13th, 2020. **Final production, 1**

- (a) Arduino + WiFi + GPS + battery power.
- (b) Troubleshooting and testing.
- (c) Guidelines for creating a polished figure for presentations
- (d) *Weekly assignment: test WiFi on network other than that of Whittier College*
- (e) **Poster presentation due: April 15th, 2020 (send to Samantha Ruiz)**

12. Meeting 11: April 20th, 2020. **Final production, 2**

- (a) Arduino + WiFi + GPS + battery power + wearable fitting.
- (b) Troubleshooting and testing.
- (c) *Weekly assignment: test different modes of carrying and wearing, battery life*
- (d) April 23rd, 2020: optional URSCA practice with Samantha Ruiz

13. **April 25th (Saturday), 2020: URSCA.**

14. Meeting 12: April 27th, 2020. **Final wrap-up, program summary**

- (a) Review of accomplishments
- (b) Logistics for SCCUR

15. Meeting 13: May 4th, 2020

- (a) Additional optional meeting, in case we need more time (we will).
- (b) May the 4th be with you!

Application for Diversity, Equity & Inclusion Innovative Initiatives Grants

Jordan C. Hanson, PhD

Department of Physics and Astronomy

Whittier College

Abstract: Whittier College serves a diverse set of undergraduates with a variety of preparation levels for introductory STEM courses. These courses serve large cohorts of students and are required for many majors and professional schools. Our goal is to develop a mobile application infused with machine-learning and educational data-mining (EDM) that will boost equity and inclusiveness in foundational physics courses. Based on published examples developed at other institutions, we will create a customized tool that will strengthen our students' skills and abilities. Diverse undergraduate experts in digital storytelling and design will drive and shape the digital presentation of content. Our application will include the voices, narrative themes, and imagery of the diverse students actually attending foundational physics courses. The result will be an open educational resource (OER) designed to foster equity and inclusion for Whittier College Physics students.

Physics education at Whittier College represents a precious opportunity: to engage and inspire students of color and women to a wide variety of scientific, mathematical, and engineering principles. A pervasive myth at Whittier College is that “STEM tends to be white and male-dominated.”¹ *This is not true.* According to our institutional research, 25% of all white male Whittier College students select major in STEM disciplines, but represent just 10% of STEM majors at Whittier College (data selected for the period of 2019-2022). White men accounted for just 18% of all majors in disciplines tied to engineering, 10% of all KNS majors, and just 6.3% of all biology majors. Introductory physics students are mostly biology and biochemistry majors who plan to attend medical school, KNS majors who plan to attend physical therapy school, and engineering students.² Bolstering student success in these courses is intrinsically anti-racist, because this large group of students is on the pathway to join and diversify fields in medicine, biotechnology, and engineering.

Another myth is that “systems designed by white men” cannot “address the needs of students of color and women who are marginalized in STEM.”³ *Again, not true.* Consider a proof by contradiction: introductory STEM courses at Whittier College are “systems” often created by white men, so by this logic no students of color or female students should succeed in such courses. But many do, as evidenced by course evaluation data and in our learning outcomes. If they did not, a large fraction of introductory physics students would fail. Introductory physics instructors regularly attend American Associated of Physics Teachers (AAPT) conferences on teaching techniques for undergraduates. Currently, we are attending Cottrell Scholars Network webinars on *Inclusivity in Introductory STEM Courses*. In the first of this 3-part series, the speaker presented social science research that reveals how affirming the dignity of students builds a sense of belonging as a scientist. One major motivation for this proposal is to

1 Though this quote is taken from the initial response to this grant proposal, the sentiment being shared has been shared informally in a variety of faculty forums.

2 Note that in the data period (2019-2021), there were $N = 530$ students who took introductory physics courses. Student demographic data at the course-level was not available. Disciplines tied to engineering include physics, math, computer science, and the 3-2 program.

3 As your friend and colleague, I was astonished to read such a strong remark in the initial response to this proposal. We must always trust the goodness of colleagues’ motivations.

affirm the dignity of students of color and young women by providing them with a tool designed for them by myself *and by their peers*. There are two underlying problems, according to research, for those that struggle in introductory physics courses. (1) They perceive themselves to be less effective at science despite having the same grades as others, and (2) when they do struggle with physics concepts, they must be helped in a way that affirms their dignity. We propose to develop a tool that helps them automatically by showing them that (a) they are not alone in their anxiety about physics courses, and (b) peers have built tools designed to strengthen their skills. According to the social science research, differences in self-efficacy vanish when one addresses (a), and addressing (b) through dignity-affirming peer-built tools should strengthen the students.

Currently, in introductory physics courses, students engage with self-designed laboratory experiments, group projects, and active-learning strategies that include peer-learning. These elements are used because Physics Education Research (PER) has shown them to be more effective than traditional physics teaching techniques [1]. One major reason we propose this new application in DEI innovation is the engagement of students of color and young women *before* they begin foundational STEM courses. Physics instructors already collect data on student performance during the introductory courses, which informs us on how well students' conceptual understanding shifts between the beginning to the end of the semester [2]. Similar to our post-doctoral experience with bridge programs for first-year students [3], we seek to *prime* the students via digital content.

This strategy serves multiple purposes. The first is to affirm the students' dignity and foster belonging. Students of color and young women often wonder why the instructor "is not like them." By infusing the digital content with the voices and identities of their peers, and avatars created by their peers, the incoming students' dignity and identities will be affirmed in advance to foster a sense of shared belonging in the course. Our current strategy for fostering belonging in *Calculus-Based Physics I* (PHYS150) places the instructor's cohort of first-year advisees in the same sections of PHYS150 and INTD100 (College Writing Seminar). The digital strategy proposed here is extensible to all introductory physics courses. The second purpose for such a digital instructional tool is to sharpen and refresh the students' skills before the course begins. This strategy allows the instructor to tailor precious course time for the needs of the diverse population of students. Online physics homework systems already give some insight, but the data is collected *during* the course and contains no demographic data [4]. Gains in equity could be larger if we could tailor the course to people of color and young women *before it began*.

We propose to enhance student belonging and learning by creating an application that combines digital storytelling with machine learning. Physics instructors already work with staff from Wardman Library to help infuse our courses with training in digital storytelling (www.diglibarts.whittier.edu), so our students learn to present the results of self-designed scientific experiments to their peers using tools like WeVideo (<https://www.wevideo.com>). Within the Math and Physics departments, we have experience using machine-learning techniques [5, 6]. Further, the literature on educational data mining (EDM) contains a plethora of examples used to understand undergraduate STEM learning patterns [7]. An example of such an application using this two-pronged strategy for language learning is DuoLingo (<https://www.duolingo.com>), in

which digital storytelling is used to welcome and strengthen the learner in stages. Learners of all backgrounds are affirmed through the visual storytelling aspect of the application, and their skills are strengthened incrementally such that the user feels empowered, rather than deficient. These ideas are at the core of this proposal. Finally, the EDM literature also recognizes that the earlier struggling students are identified and aided by the instructor, the better their outcomes [9]. Several examples of such digital tools have been created specifically for STEM courses [10,11]. Our hypothesis is that the digital storytelling aspect will raise student engagement by relating the content to their own experiences. One final point about the tool we propose: this tool is not based around any “deficit model” of student achievement. Rather, as we argue above and below, this strategy focuses on building strengths and building belonging within introductory STEM courses. To this end, more data from the *Inclusivity in Introductory STEM Courses* is relevant.

In the second of the 3-part series, *Inclusivity in Introductory STEM Courses* through the Cottrell Scholars Network, the speaker discusses self-efficacy and long-term success in STEM fields for women and people of color. If our proposed tool could show the students (anonymously) that they are not the only one who gets wrong answers initially, self-efficacy gaps tend to vanish [8]. Thus, it is important to note that any such data collection the tool might perform will be anonymous. Thus, the tool we propose actually has nothing to do with so-called “deficit models,” but is more aptly described as an **antidote** to deficit models. Students will be shown that they are *not alone*, rather than be shown that they are the only one who struggles. Digital tools have already helped our students connect and grow, despite the quarantines induced by COVID-19.

The COVID-19 pandemic forced our department to shift to digital educational platforms. Normally, our introductory STEM curricula is centered on both laboratory and lecture courses. In 100-level physics courses, we have merged lecture and lab at the introductory level, using concepts from workshop physics models and peer-instruction (PI) [1]. Peer-instruction models have the students play an active role in teaching each other, and the content is transmitted through the instructor *and peers*, leading to better learning outcomes. Components of our courses remain online and asynchronous going forward. One example is the Pivot Interactives lab platform, in which students can complete lab activities remotely in a way that fits into their schedule [13]. Thus, there is precedent for the further use of digital tools to boost student success in STEM.

One final idea for the proposed digital tool is derived from a novel entitled *The Diamond Age*, by Neal Stephenson. In the book, a digital tool called *The Primer* falls into the hands of a young orphan named Nell. Nell engages with the tool, which teaches her mathematics, design principles, physics, and leadership skill. The key to her development is that *The Primer adapts* to her educational needs in real time, and provides a narrative for her growth in terms of creating a land for her fellow orphans. The MathBot project [10] already has achieved a conversational model similar to that of *The Primer*. To these already-successful models, we would add the narrative through digital storytelling of *The Primer* by incorporating digital-storytelling and graphic design from Whittier College. As the story progresses, students would be prompted to solve progressively more challenging problems in order to build strength. Duolingo combines digital storytelling and machine-learning in this way. Thus, the project would have a liberal arts component, and a software design component. In the coming sections, we describe the software design and digital storytelling of the proposed tool. We also

provide an assessment plan with more detail regarding important objectives and milestones.

Two essential actions would be performed by the software as the student progresses.

First, exercise and demographic data such as response rate and time, correct percentage, and student race and gender, would be recorded anonymously for further analysis. Machine-learning algorithms (see below) would be run on trial data to help instructors understand student learning patterns. Insights derived could be taken into account in our courses. If we find, for example, that students of color regularly struggle with vector addition and momentum conservation (most likely due to non-exposure to these topics in high-school or at Whittier) then providing more in-class practice in those topics should *boost* equity, rather than exacerbate it. The second action performed by the code would be to establish the pace and intensity of the course. If we find that historically marginalized students demonstrate strength in certain topics, relatively less in-class practice should be spent on those topics. The net gain for marginalized students is that they are exposed to *more content* than they would experienced without the data-driven model. Thus, the software facilitates an adaptable course that maximizes the learning of people who have traditionally been marginalized.

Whenever one encounters digital storytelling or narrative anywhere in this proposal, do not forget that it will not be and should not be a physics instructor creating these stories and themes.

Rather, we plan to recruit Whittier Scholars Program students, digital design students, and staff members from Wardman Library to drive creation in this area. There are three reasons it makes sense to do the project this way. First, the Digital Liberal Arts area already has the experience to help students tell their own stories. As stated above, we regularly invite staff members such as Sonia Chaidez from Digital Liberal Arts to train students in introductory physics courses how to create a digital story about their science projects (usually with WeVideo). Having gained experience with tools like WeVideo, we now have access to a plethora of institutional wisdom in digital storytelling. Second, undergraduates from diverse backgrounds will be recruited to create the digital storytelling piece, so the narrative themes should be recognizable and dignity-affirming to the user, unlike a sterile traditional textbook. Third, the format will move the data collection and analysis anonymously to the back end, so that the students are anonymously helping their instructors learn about them.

Current physics students at Whittier College already generate data that goes unused, and our students of color and female students are not yet benefiting from its analysis.

There are many examples in EDM literature that demonstrate how clustering and classification algorithms are used in STEM education. One example of clustering algorithms was [14], in which researchers identified patterns in self-regulated learning (SRL) in a large asynchronous online statistics course. Another example was [15], in which student problem-solving clusters emerged from data generated in a physics MOOC (massive open online course). On occasion, EDM researchers develop educational protocols and tools based on the results. Probably the most applicable example to our introductory physics courses is the MathBot [10].

In introductory physics courses, we have been using the Force and Motion Concept Evaluation (FMCE) in introductory physics courses [2]. We use the FMCE data primarily to evaluate our progress as instructors. However, we do not *continue* to record data that *re-informs* our picture of our students, nor do we systematically tailor content to the

students as they evolve. In addition, we would like to make our proposed tool cognizant of student demographic data. To strive to be as equitable as possible in our 100-level physics courses, we should at least be using the data that students of color and young women generate. No matter the background of the student, the adaptability the machine-learning tools in EDM literature should be deployed to form an equitable foundation of skills for Whittier Poets.

Equity and inclusion are core values of Whittier College. The idea that each student could be given free access to a digital tool that helps train them in advance of and during introductory physics courses fosters equity and inclusion at our institution. It is our hope that we will affirm the dignity of our physics students and customize their course content by creating this tool. Seventy percent of our student body identify as people of color, which is not true of Whittier faculty. By allowing students to drive the creation of the digital-storytelling, we will infuse it with narrative themes and imagery that align with the identities of the very people we instruct.

The ideas behind this project are in alignment with our Racial Justice and Equity Action Plan. For example, part of the plan calls for increased data collection and analysis with a focus on equity, inclusion, and retention of Black students. We should strive to collect educational data so that their educational experience may be improved. Another portion of the plan calls for an associate dean to “lead efforts in evaluating, modifying, and implementing policy and practices and augmenting faculty development.” Bringing this tool to the instructional landscape will demonstrate exactly how faculty can evolve their teaching practices to better serve our students.

Project Timeline and Project Assessment

- *Team recruitment and planning stages*
 - Because we propose designing an app for Android OS, it would be helpful to recruit a computer science student involved in the Whittier Scholars Program. Prof. Hanson of the Dept. of Physics and Astronomy advises at least one such student per year, so this should not be difficult. Other programming expertise can come from projects created via PHYS396: Physics Research for Credit.
 - We need to recruit motivated Whittier Scholars Program (WSP) and digital design students interested in creating digital artwork and storytelling themes for the application. We had anticipated being able to reward these students financially. Those in charge of the POET internship program have indicated this is a strong proposal for such a POET intern, however, funding would have to arrive in the next academic year because the application window is closed. This should not hinder progress, however, because the nature of this project is such that we must create a skeleton of software first before infusing it with digital narratives.
 - We estimate a timeline of 1 month for software design recruitment
- *Character creation, story development, and STEM content generation*
 - We assume that the digital storytelling side of this project will undergo refinement such that there is a workable story and set of digital designs that can be implemented as the visual content of the application. The portfolio should be broad, to account for students moving through it via multiple pathways. We estimate two semesters to complete this, starting in Fall 2022.
 - On the coding and analysis side, we must have the minimum ability to collect data from a device running the application in a central location, and separately run machine-learning algorithms on it. We estimate two semesters in parallel with the digital storytelling side for this work.

- Optimally, we should determine how to execute machine-learning algorithms tools within the application. Ideally, we'd like to have this integrated at the end of the second semester.
- *Initial machine-learning studies*
 - In the second and third semesters of this work, we will run machine-learning studies on the data generated by volunteer users.
 - We will investigate the usage of cited EDM algorithms, but we will make time for more detailed and broad studies of how this data is processed. The analysis of this data could form the backbone of a Whittier Scholars Program major design.
 - In the final stages, we must demonstrate that the application can change based on the user, in the same sense as DuoLingo.
 - We estimate this work taking place during the third semester of the project.
- *Expanded testing on larger sets of student volunteers*
 - This would mark a useful stopping point for this work.
 - If we succeed up to this phase, the moment would be ripe to apply for an external grant focused on scaling up the processes to incorporate more introductory STEM courses.

Financial Compensation

Given that external sources such as POET internships will be sought for student compensation, there is no financial component to that part of the project. However, Prof. Hanson will be writing software for this project, so we do request the maximum of \$500.00 from the proposal call.

Bibliography

- [1] E. Mazur, Peer Instruction: A User's Manual. Pearson Education, 2013.
- [2] Ramlo, Susan. "Validity and reliability of the force and motion conceptual evaluation," American Journal of Physics vol 76. (2008) p. 882
- [3] The Ohio State University Young Scholars Program (YSP). For more information, visit <https://odi.osu.edu/young-scholars-program>
- [4] One example for STEM: "The OpenStax Tutor System," <https://tutor.openstax.org/>?
- [5] J.C. Hanson et al. "Time-Domain Response of the ARIANNA Detector." Astroparticle Physics Journal vol. 62 (2015) pp. 139-151
- [6] K. Bui, F. Park, S. Zhang, Y. Qi, J. Xin, "l₀ Regularized Structured Sparsity Convolutional Neural Networks," Pre-print manuscript on arXiv.org: arXiv:1912.07868 (2019)
- [7] Dongjo Shin and Jaekwoun Shim. "A Systematic Review on Data Mining for Mathematics and Science Education," International Journal of Science and Mathematics Education (2020) pp. 1-21
- [8] Binning, K. R. et al. "Changing Social Contexts to Foster Equity in College Science Courses: An Ecological-Belonging Intervention." Psychological Science, vol. 31, n. 9, pp.
- [9] Cameron Cooper and Paul Pearson. "A Genetically Optimized Predictive System for Success in General Chemistry Using a Diagnostic Algebra Test," Journal of Science Education and Technology vol. 21 no. 1 (2011)
- [10] J. Grossman, Z. Lin, H. Sheng, J. Wei, J. Williams, and S. Goel. "MathBot: Transforming Online Resources for Learning Math into Conversational Interactions," Copyright, 2019 Association for the Advancement of Artificial Intelligence (www.aaai.org)
- [11] H.S. Lee et al. "Automated text scoring and real - time adjustable feedback: Supporting revision of scientific arguments involving uncertainty," Science Education Journal vol. 103 no. 3 (2019)
- [12] "PhysPort: Supporting Physics Teaching with Research Based Resources." <https://www.physport.org/> methods/method.cfm?G=Peer_Instruction. A teaching material repository for PI module questions.
- [13] "Pivot Interactives." www.pivotinteractives.com. Copyright Pivot Interactives 2020 SBC. Example of online physics laboratory instruction modules.
- [14] D. Kim, M. Yoon, I. H. Jo, and R. M. Branch. "Learning analytics to support self-regulated learning in asynchronous online courses: A case study at a women's university in South Korea," Computers & Education vol. 127 (2018)
- [15] Y. Lee. "Using Self-Organizing Map and Clustering to Investigate Problem-Solving Patterns in the Massive Open Online Course: An Exploratory Study," Journal of Educational Computing Research vol. 57 no. 2 (2018)

CHANGING GLACIERS: SO MUCH MORE THAN SEA LEVEL RISE

How changing glaciers will influence every aspect of life on earth, case study: Iceland, and
photo essay.

Nicolas Bakken-French

March 8, 2021

Project Sponsor: Jordan Hanson

Undergraduate in Environmental Science and Policy

Minor in Glaciology

Abstract: Glaciology is an evolving science during a time in which our increased understanding of glaciers will become critical to understanding and adapting to our future of life on earth. Current glaciological research can predict the impacts of glacial change on a warming planet with steadily increasing precision in a variety of contexts. This study catalogues a diverse range of glacial impacts on human activity through a variety of geographic case studies. First, glacial influence on ocean currents and sea level rise is analyzed through our understanding of the Greenland and Antarctic ice sheets. Second, glacial influence on fresh water availability, agriculture, fisheries, tourism, and biodiversity is analyzed through our understanding of the Himalaya region, Wyoming state, Washington state, New Zealand, and California state. Third, glacial ice cores from Antarctica reveal information on past climate, and geological analysis of Yosemite National Park offers further insight. Fourth, the influence of glacial change on cultures and spiritual practice is analyzed. Because Iceland presents a unique combination of glacial influences, the geological and cultural impacts of glaciers there are analyzed. Finally, this study is further contextualized by a photo essay of Iceland's Glaciers by the author.

Table of Contents

Introduction.....	3
Defining Glaciers	4
Glaciers Influence on Global Climate.....	6
IPCC & Sea Level Rise	7
Albedo	7
Ocean Currents.....	8
Polar Glacial Dynamics.....	9
Operation Icebridge.....	11
Glacial Influences Downstream.....	13
Fresh Water Source: Himalaya, the Water Tower of Asia.....	15
Impacts on agriculture: Wyoming.....	17
Impacts on fisheries: Washington Salmon.....	18
Glacier Tourism: New Zealand.....	21
Biodiversity & Endemic Species: Trinity Alps, CA.....	23
What Glaciers Can Tell Us About the Past.....	24
Ice Cores.....	24
Previously Glaciated Landscapes: Yosemite, CA.....	25
Glacial Impacts on Culture and Identity.....	26
Indigenous Perspectives.....	27
Iceland.....	29
Geological Impacts.....	29
Natural and Anthropogenic, Post Little Ice-Age Recessions.....	30
Proglacial Lake Formation & Glacial Behavior.....	33
Future of the Southeast Iceland Landscape.....	34
Cultural Impacts.....	36
Iceland's Booming Tourism.....	37
Photo Essay: Vatna > Jökull.....	38
Conclusion.....	48
Acknowledgments.....	48
References.....	49

PHOTO ESSAY: VATNA > JÖKULL

Perhaps thinking about a glacier's aliveness is to think about living, about what living means, about how we respond to the livingness of the world around us. In many ways, thinking about glaciers is also thinking about us.

- Dr. M Jackson

In Fall 2020, I travelled to Iceland on an undergraduate study program centered on climate changes impacts on the Arctic and stayed in Hali, Hornafjörður, just a few kilometers from Breiðamerkurjökull. I was quickly exposed to islands changing glaciers and to the lives of those who centered around glaciers. Through experiencing and learning about Icelanders interaction with glaciers and perceptions of glacial change, I developed a sense of how powerful these bodies of ice were. Coupled with moments walking along the ice, the crunch of my crampons interrupted by the deep and full echos of moving ice, pulsating glacial streams, and the loud thud of ice calving off the glacier terminus and into the water, I began to understand why some Icelanders perceive glaciers as alive. The intense beauty of the ice that would stop me in my tracks, as I paused to breathe with the glacier, to feel and listen to its heartbeat, and try and comprehend what was before me. This glacier demands my respect, our fates tied together, and through that connection, it was hard not to feel its aliveness myself. With the photographs I captured, with my 35mm Canon AE-1, I hope to capture that feeling....



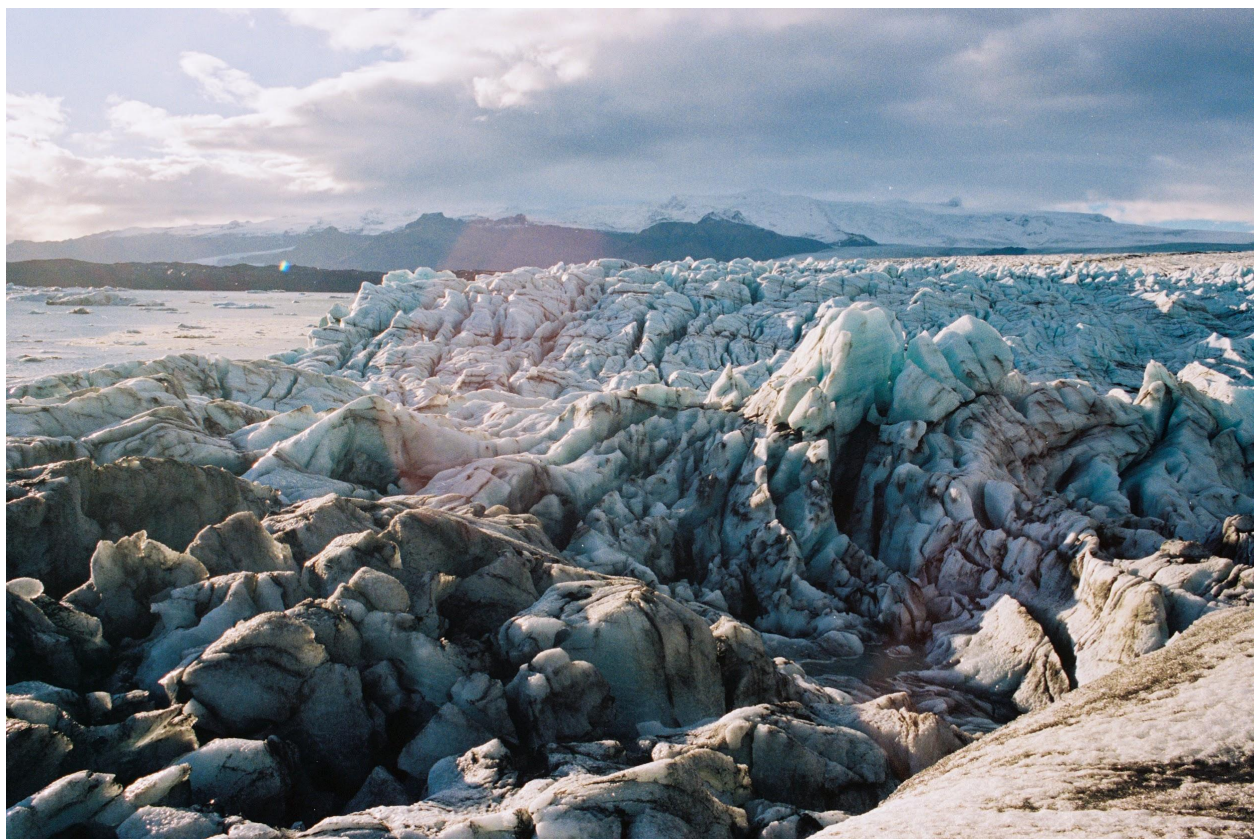


















Conclusion

The case studies that have been presented are only a few of the many examples of the impacts of glacial change, every place on earth will be impacted by glacial change either directly through downstream changes or indirectly through global changes. There are countless stories to tell about how people interact and connect with ice. Our understanding of glaciers must dramatically improve if we are to best prepare ourselves for the inevitable changes that will occur. Our understanding must be rooted in stories that help connect people with ice and our dependence on it as much as it must be rooted in our physical understanding of ice. It is through our increased connection with, as well as understanding of, glaciers that we may come to better adapt to the changes that will occur and try to prevent the total loss of our planet's diverse and magical ice.

Acknowledgments

There are so many people I wish to thank in my process of developing my understanding of glaciers and glacial change, and the incredible places it has taken me and the soul filling experiences it has exposed me too. My mothers for their never-ending support of my passions. Jordan Hanson, my mentor, who has guided me through this work and whose own work in Antarctica has inspired mine. Cheryl Swift, for expanding my capabilities in field work and showing me the joy of working in the field. Haukur Igni Einersson, owner and operator of Glacier Adventure, for inviting me to Hali, Iceland to experience the glaciers of his homeland and generously providing a helping hand whenever it was needed. My thanks, as well, to Mike Reid, lead guide at Glacier Adventure, for showing me how to properly travel and climb across glaciers and have a whole lot of fun doing it. My thanks to Þorvarður Árnason, for showing me the beauty of working at “the border of art and science,” whose photographs of the glaciers of Iceland are and will continue to be an inspiration. To Whittier College, NOLS, and SIT: Study Abroad for providing me with the opportunities to discover my passion for glaciers. My family and friends, whose adventurous spirits and full hearts make life exciting and meaningful.